INFORMATION TO USERS

This manuscript has been reproduced from the microfilm master. UMI films the text directly from the original or copy submitted. Thus, some thesis and dissertation copies are in typewriter face, while others may be from any type of computer printer.

The quality of this reproduction is dependent upon the quality of the copy submitted. Broken or indistinct print, colored or poor quality illustrations and photographs, print bleedthrough, substandard margins, and improper alignment can adversely affect reproduction.

In the unlikely event that the author did not send UMI a complete manuscript and there are missing pages, these will be noted. Also, if unauthorized copyright material had to be removed, a note will indicate the deletion.

Oversize materials (e.g., maps, drawings, charts) are reproduced by sectioning the original, beginning at the upper left-hand corner and continuing from left to right in equal sections with small overlaps.

Photographs included in the original manuscript have been reproduced xerographically in this copy. Higher quality 6" x 9" black and white photographic prints are available for any photographs or illustrations appearing in this copy for an additional charge. Contact UMI directly to order.

ProQuest Information and Learning
300 North Zeeb Road, Ann Arbor, MI 48106-1346 USA
800-521-0600

UMI®

Downloaded from SHAREOK. Persistent Handle URL: https://hdl.handle.net/11244/409

UNIVERSITY OF OKLAHOMA

GRADUATE COLLEGE

APPLICATION OF PEBI GRID SIMULATION TO ANALYZE PRESSURE-TRANSIENT BEHAVIOR OF HYDRAULICALLY FRACTURED VERTICAL WELLS

A Dissertation

SUBMITTED TO THE GRADUATE FACULTY

In partial fulfillment of the requirements for the

Degree of

Doctor of Philosophy

By

FREDDY HUMBERTO ESCOBAR
Norman, Oklahoma
2002

UMI Number: 3034892

UMI®

UMI Microform 3034892

Copyright 2002 by ProQuest Information and Learning Company.
All rights reserved. This microform edition is protected against
unauthorized copying under Title 17, United States Code.

ProQuest Information and Learning Company
300 North Zeeb Road
P.O. Box 1346
Ann Arbor, MI 48106-1346

© Copyright by Freddy Humberto Escobar 2002
All Rights Reserved

APPLICATION OF PEBI GRID SIMULATION TO ANALYZE TRANSIENT-PRESSURE BEHAVIOR OF HYDRAULICALLY FRACTURED VERTICAL WELLS

A Dissertation APPROVED FOR THE MEWBOURNE SCHOOL
OF PETROLEUM AND GEOLOGICAL ENGINEERING

BY

ACKNOWLEDGEMENTS

First and foremost, I express my eternal gratitude to my major advisor, Dr. Djebbar Tiab, for his teaching, advise, guidance, understanding and funding given throughout the completion of my doctoral studies. I have always felt I have the support of my advisor. I appreciate his respectful attitude for my opinions. An extensive thank you is given to Dr. Faruk Civan, my former supervisor, for his kindly acceptance to be part of my committee and for all the teaching and background I obtained from.... "just" five courses I took from him. My appreciation is also extended to the other members of my committee: Dr. Michael L. Wiggins, Dr. Luther W. White and Dr. Subhash N. Shah.

The financial support obtained from Universidad Surcolombiana and Colciencias is very much appreciated.

I am greatly greatful with Dr. Sergio Berumen-Campos, PEMEX E&P, for all the ideas and help provided along my doctoral studies. I also express my gratitude to Mr. Eduard May, GeoQuest, for the great support received during my dissertation work.

At Universidad Surcolombiana, I am thankful with Professor Jairo A. Sepulveda and Professor Jaime Rojas Puentes for cosigning for my financial support. Profound thanks are equally extended to Professor Yamil Armando Cerquera, Professor Jorge Antonio Polania and Ms. Maria Nelfy Leon Medina for all the help provided.

I also thank Dr. Susan Smith Nash for assisting me with the English corrections of this work.

Special thanks to my brother Leonardo Fabio Escobar for all his help and to my wife Matilde Montealegre for her companionship, help and understanding.

The discussions with Sarfraz A. Jokhio, Arturo Diaz-Perez and Gherson Penuela and all their cooperation are truly appreciated.

Although, I have not had the pleasure to meet them personally, I express my gratitude to Mrs. Irina Merazka and Mr. Abdelhakim Deghmoum, in Algeria, who worried about my dissertation work and tried to help as much as they could. Also, Mrs. Merazka has been a great help in my job as *Distance Learning Program Assistant* and it has been a delight to work with her.

I very much appreciate all the help and cooperation provided by Mrs. Chryl Yerdon, Graduate Secretary at the Mewbourne School of Petroleum and Geological Engineering.

I am also thankful to my Colombian friends Walter Nuñez, Julio R. Ronderos, Katherine Moncada, Abel Chacón, Irina Desiré Katime M., Alejandro Carrascal, Luis Fernando Bonilla, Luis José Abaunza, Alvaro Prada, Alfonso Varela and Gustavo A. Gómez who contributed to my having a rewarding experience at the University of Oklahoma.

Finally, but not lastly, I am thankful to God for ..... everything!.

DEDICATIONS

This work and all my graduate studies are dedicated to:

..... My parents Sotero Escobar (RIP) and Delfina Macualo, my wife Matilde Montealegre, my children Jennifer Andrea and Freddy Alonso Escobar, my siblings Sotero Alonso (RIP), Leonardo Fabio and Dayra Stella Escobar.

..... My nephews Daniel Alfredo Escobar, Juan David and Gabriel Fernando Betancourt.

..... My godchildren Raul Alejandro Vageón and José Gabriel Rangel.

..... My cousin Demetrio Alfonso Escobar (RIP) who has not died in my heart.

..... My uncle José Demetrio Escobar who is very proud of my acievements.

..... Gloria Celis de Escobar who taught me how to read and write.

..... My mother-in-law, my sisters-in-law and brothers-in-law. Special dedication to the memory of my brother-in-law Heiler Giovanni Forero (R.I.P.).

..... My godparents: Angelica Mackualo, Romulo A. Mackualo, Milton "Tacho" Duarte and Hernán Villegas Alvarez (R.I.P.)

..... The Liceo Tame High School at my hometown Tame (Arauca-Colombia) and Universidad Surcolombiana at Neiva (Huila-Colombia).

..... All my friends and relatives.

..... The following friends and their families: Luis Elias Quiroga, Daniel Augusto Gutierrez, Omar Enrique Arciniegas, José Luis Cantini, Yamil Armando Cerquera, Pedro Antonio Vanegas, Emiliano Bohórquez, Alfonso Guerrero Pinillos, Benito Espinel, Carlos Jose Elpidio "Pillo" Rangel Camacho and Juan Manuel Cepeda.

TABLE OF CONTENTS

ACKNOWLEDGEMENTS iv

DEDICATIONS vi

LIST OF FIGURES xi

LIST OF TABLES xix

ABSTRACT xxv

CHAPTER I 1

PROBLEM BACKGROUND 1

CHAPTER II 14

PEBI GRID APPLICATION TO TRANSIENT 14

2.1. INTRODUCTION 14

2.2. THEORETICAL CONCEPTS ON PEBI GRIDS 15

2.2.1. DEFINITION 15

2.2.2. GRID AND BLOCK CONSTRUCTION 18

2.2.3. PEBI GRID STYLES 22

2.2.4. GRID CONTROLS 23

2.3. PEBI GRIDS APPLICATION TO SIMULATE PRESSURE TRANSIENT BEHAVIOR 23

2.3.1. VERTICAL WELLS 24

2.3.2. VERTICAL WELLS INTERSECTED BY A HYDRAULICAL FINITE-DONDUCTIVITY FRACTURE 31

2.3.2.1. EFFECT OF FRACTURE CONDUCTIVITY 32

2.3.2.2. EFFECT OF NON-ORTHOGONALITY 42

2.3.3. HORIZONTAL WELLS 43

CHAPTER III 48

MATHEMATICAL FORMULATION AND SOLUTION 48

3.1. HYDRAULIC FRACTURED VERTICAL WELL WITH A BRANCH FRACTURE 48

3.2. A SEALING FAULT INTERSECTED BY A VERTICAL HYDRAULIC FRACTURE 60

CHAPTER IV 65

ANALYSIS OF RESULTS 65

4.1. HYDRAULIC FRACTURED VERTICAL WELL WITH A BRANCH FRACTURE 65

4.1.1. EFFECT OF BRANCH FRACTURE ANGLE 74

4.1.2. EFFECT OF BRANCH FRACTURE 75

CHAPTER V 99

THE TIAB'S DIRECT SYNTHESIS TECHNIQUE 99

5.1.2. WELLBORE STORAGE AND BILINEAR FLOW 104

5.1.3. LINEAR AND BILINEAR FLOW 106

5.1.4. RADIAL AND BILINEAR FLOW 109

5.1.4. RADIAL AND LINEAR FLOW RELATIONSHIPS 110

5.1.5. BRANCH FRACTURE REGIME RELATIONS 111

5.1.8. APPLICATIONS 123

5.2. HYDRAULIC FRACTURED INTERSECTING A SEALING FAULT 135

5.2.2. STEP-BY-STEP PROCEDURES 138

5.2.3. APPLICATIONS 141

CHAPTER VI 155

SUMMARY, CONCLUSIONS AND RECOMENDATIONS 155

6.1. SUMMARY 155

6.2. CONCLUSIONS 157

6.3. RECOMMENDATIONS 158

NOMENCLATURE 159

REFERENCES 162

APPENDIX A 172

ANALYTICAL SOLUTIONS 172

A.1. LINE SOURCE WELL IN AN INFINITE SYSTEM – PRODUCTION AT CONSTANT RATE 173

A.2. WELL IN AN INFINITE SYSTEM – PRODUCTION AT CONSTANT RATE – WELLBORE STORAGE AND SKIN FACTOR 173

A.3. FINITE-CONDUCTIVITY FRACTURED WELL – NEITHER SKIN NOR WELLBORE STORAGE CONSIDERED 174

A.3.1. FRACTURE FLOW MODEL 175

A.3.2. RESERVOIR FLOW MODEL 176

A.3. HORIZONTAL WELLS 180

APPENDIX B 183

FIGURES 183

APPENDIX C 258

GRIDS 258

APPENDIX D 293

TABLES 293

APPENDIX E 387

RESERVOIR MODEL 387

APPENDIX F 398

FRACTURE MODEL 398

LIST OF FIGURES

Fig. 1.1. Hydraulic branching in Sandstone (After Ref. 1) 2
Fig. 1.2. Granitic dike propagation through the interface between two gabbros at Wichita Mountains area 2
Fig. 1.3. Near-wellbore and far-field multiple fractures 3
Fig. 1.4. Injection Microseismic Map 3
Fig. 1.5. Injection Microseismic Map 4
Fig. 1.6. Fracture Geometries conceibed for the Couper basin. Left: Fracture turning (movement in one plane). Right: Multiple fracturing 4
Fig. 2.1. Voronoi or PEBI grid block example 16
Fig. 2.2. Generalized PEBI grid block example (GPEBI) 17
Fig. 2.3. Demonstration of the flexibility of Voronoi Grids (generated with the Eclipse Suit). Upper left: horizontal well, Lower left: vertical well, Center: vertical fractured well, Right: A linear fault intersecting a non-linear fault 18
Fig. 2.1. Grid network and block system 19
Fig. 2.5. Voronoi grid systems 21
Fig. 2.6. Pressure and pressure derivative curves generated using different PEBI grid styles 26
Fig. 2.7. Pressure plot for a vertical well simulated numerically using elliptical, hexagonal and rectangular PEBI grid styles 27
Fig. 2.8. Pressure plot for a vertical well having damage and wellbore storage generated using a circular PEBI grid style 28
Fig. 2.9. Pressure plot for a vertical fractured (C_{fD}=1) simulated using Circular, Hexagonal, Rectangular, variable and Elliptical PEBI grid styles 35
Fig. 2.10. Pressure plot for a vertical fractured (C_{fD}=0.1) simulated an Elliptical PEBI grid (Case 1 – 899 gridpoints) 36
Fig. 2.11. Pressure plot for a vertical fractured (C_{fD}=0.5) simulated using an Elliptical PEBI grid (Case 2 –3462 gridpoints) 37
Fig. 2.12. Pressure plot for a vertical fractured simulated using an Elliptical PEBI grid for several dimensionless 38
Fig. 2.13. Pressure plot for a vertical fractured simulated using an Elliptical PEBI grid for dimensionless fracture conductivity values of 1 and 50 and fracture inclination angle values of 45 and 75 degrees 39
Fig. 2.14. Pressure plot for a vertical fractured simulated using an Elliptical PEBI grid for a dimensionless fracture conductivity value of 50 and a fracture inclination angle of 60 degrees 40
Fig. 2.15. Pressure plot for a vertical fractured simulated using an Elliptical PEBI grid for dimensionless fracture conductivity values of 1, 100 and 300 and fracture inclination angles of 15, 30 and 90 degrees 41
Fig. 2.16. Pressure Log-Log plot for a horizontal well simulated using all the studied PEBI grid styles 46

Fig. 2.17. Pressure Semilog plot for a horizontal well simulated using all the studied PEBI grid styles 47
Fig. 3.1. Schematic view of the reservoir-fracture system 51
Fig. 3.2. Plane view of the reservoir-fracture system 51
Fig 3.3. Reservoir coodinates and boundary conditions 53
Fig 3.4. Translation and rotation of cartesian axis[98] 54
Fig. 3.5. Schematic representation of the solution to the main fracture-branch fracture system used with the Eclipse suit 59
Fig. 3.6. Schematic view of the reservoir-fracture-fault system 61
Fig. 3.7. Plane view of the reservoir-fracture-fault system 62
Fig. 3.8. Fracture-fault system cases studied (a) Fracture intersects fault at 75 % of fault length (b) fracture and fault meet at their tips 63
Fig. 4.1. Position of the branch fractured along the main fracture 66
Fig. 4.2. Well pressure behavior for a fractured well with a branch fracture for cases a and b, X_{fbD}=0 and 0.6 and θ=30° 68
Fig. 4.3. Plan view of the fracture system of this study and the asymmetric fracture of Ref. 36 69
Fig. 4.4. Dimensionless pressure for a fractured well with no branch fracture 72
Fig. 4.5. Dimensionless pressure for a symmetry fractured well as reported in Ref. 36 73
Fig. 4.6.a. Dimensionless Pressure and pressure derivative plot for a fractured well with a branch fracture for X_{fbD}=0 and 0.6. 77
Fig. 4.6.b. Dimensionless Pressure and pressure derivative plot for a fractured well with a branch fracture for X_{fbD}=0 and 0.6, θ=30° and C_{fD}=10 78
Fig. 4.6.c. Dimensionless Pressure and pressure derivative plot for a fractured well with a branch fracture for X_{fbD}=0 and 0.6, θ=30° and C_{fD}=50 79
Fig. 4.6.d. Dimensionless Pressure and pressure derivative plot for a fractured well with a branch fracture for X_{fbD}=0 and 0.6, θ=30° and C_{fD}=100 80
Fig. 4.6.e. Dimensionless Pressure and pressure derivative plot for a fractured well with a branch fracture for X_{fbD}=0 and 0.6, θ=30° and C_{fD}=300 81
Fig. 4.7. Radial and pseudoradial flows 82
Fig. 4.8.a. Dimensionless pressure and pressure derivative curve for a hydraulic fracture intersecting a fault at its middle part forming an angle of 90°. C_{fD}=1 ..87
Fig. 4.8.b. Dimensionless pressure and pressure derivative curve for a hydraulic fracture intersecting a fault at its middle part forming an angle of 90°. C_{fD}=10.88
Fig. 4.8.c. Dimensionless pressure and pressure derivative curve for a hydraulic fracture intersecting a fault at its middle part forming an angle of 90°. C_{fD}=50.89
Fig. 4.8.d. Dimensionless pressure and pressure derivative curve for a hydraulic fracture intersecting a fault at its middle part forming an angle of 90°. C_{fD}=100 90
Fig. 4.8.e. Dimensionless pressure and pressure derivative curve for a hydraulic fracture intersecting a fault at its middle part forming an angle of 90°. C_{fD}=300 91
Fig. 4.8.f. Dimensionless pressure and pressure derivative curve for a hydraulic fracture intersecting a fault at its middle part. C_{fD}=1 and L_D=80 92

Fig. 4.8.g. Dimensionless pressure and pressure derivative curve for a hydraulic fracture intersecting a fault at its middle part. C_{fD}=1 and L_D=162 93
Fig. 4.9. Sketch of flow regimes for a hydraulic fracture intersecting the middle part of a fault and forming an angle of 90° 94
Fig. 4.10. Sketch of flow regimes for a hydraulic fracture intersecting the fourth part of a fault and forming an angle less than 90° 95
Fig. 5.1. Flow Regimes governing pressure behavior at a well interrupting a finite capacity vertical fracture[22] 101
Fig. 5.2. Actual and simulated data to detect a branch fracture in a low conductivity fracture system 116
Fig. 5.3. Log-log plot of pressure and pressure derivative for example 1 125
Fig. 5.4. Log-log plot of pressure and pressure derivative for example 2 131
Fig. 5.5. Log-log plot of pressure and pressure derivative for example 2 compared to a simulation using C_{fD}=118.3 132
Fig. 5.6. Average correlation between maximum time and maximum pressure derivative for a fault-fracture system 137
Fig. 5.7. Average correlation between maximum time and maximum pressure derivative for a fault-fracture system 137
Fig. 5.8. Log-log plot of pressure and pressure derivative for example 3 143
Fig. 5.9. Log-log plot of pressure and pressure derivative for example 4 144
Fig. 5.10. Log-log plot of pressure and pressure derivative for example 5 145
Fig. A.1. Fracture flow model 177
Fig. A.2. Reservoir flow model 178
Fig. A.3. Fracture divided into 2N equal segments 178
Fig. A.4. Horizontal well configuration 181
Fig. B.1.a. Pressure and pressure derivative curves for a fractured well with a branch fracture 184
Fig. B.1.b. Pressure and pressure derivative curves for a fractured well with a branch fracture 185
Fig. B.1.c. Pressure and pressure derivative curves for a fractured well with a branch fracture 186
Fig. B.1.d. Pressure and pressure derivative curves for a fractured well with a branch fracture 187
Fig. B.1.e. Pressure and pressure derivative curves for a fractured well with a branch fracture 188
Fig. B.2.a. Dimensionless Pressure obtained for a hydraulic fractured well with an asymmetric factor of 0.2 189
Fig. B.2.b. Dimensionless Pressure obtained for a hydraulic fractured well with an asymmetric factor of 0.4 190
Fig. B.2.c. Dimensionless Pressure obtained for a hydraulic fractured well with an asymmetric factor of 0.6 191
Fig. B.3.a. Dimensionless Pressure obtained for a hydraulic fractured well with dimensionless 192
Fig. B.3.b. Dimensionless Pressure obtained for a hydraulic fractured well with dimensionless 193

Fig. B.3.c. Dimensionless Pressure obtained for a hydraulic fractured well with dimensionless *194*
Fig. B.4.a. Dimensionless Pressure and pressure derivative curves for hydraulically fractured well with a branch fracture. Dimensionless fracture conductivity of 1 and angle of zero degrees *195*
Fig. B.4.b. Dimensionless Pressure and pressure derivative curves for hydraulically fractured well with a branch fracture. Dimensionless fracture conductivity of 10 and angle of zero degrees *196*
Fig. B.4.c. Dimensionless Pressure and pressure derivative curves for hydraulically fractured well with a branch fracture. Dimensionless fracture conductivity of 50 and angle of zero degrees *197*
Fig. B.4.d. Dimensionless Pressure and pressure derivative curves for hydraulically fractured well with a branch fracture. Dimensionless fracture conductivity of 100 and angle of zero degrees *198*
Fig. B.4.e. Dimensionless Pressure and pressure derivative curves for hydraulically fractured well with a branch fracture. Dimensionless fracture conductivity of 300 and angle of zero degrees *199*
Fig. B.5.a. Dimensionless pressure and pressure derivative curve for a hydraulic fracture intersecting a fault at its fourth part forming an angle of 90°. C_{fD}=1..200
Fig. B.5.b. Dimensionless pressure and pressure derivative curve for a hydraulic fracture intersecting a fault at its fourth part forming an angle of 90°. C_{fD}=10201
Fig. B.5.c. Dimensionless pressure and pressure derivative curve for a hydraulic fracture intersecting a fault at its fourth part forming an angle of 90°. C_{fD}=50202
Fig. B.5.d. Dimensionless pressure and pressure derivative curve for a hydraulic fracture intersecting a fault at its fourth part forming an angle of 90°. C_{fD}=100 ..... *203*
Fig. B.5.e. Dimensionless pressure and pressure derivative curve for a hydraulic fracture intersecting a fault at its fourth part forming an angle of 90°. C_{fD}=300 ..... *204*
Fig. B.6.a. Dimensionless pressure and pressure derivative curve for a hydraulic fracture intersecting a fault at its tip forming an angle of 90°. C_{fD}=1 ..... *205*
Fig. B.6.b. Dimensionless pressure and pressure derivative curve for a hydraulic fracture intersecting a fault at its tip forming an angle of 90°. C_{fD}=10 ..... *206*
Fig. B.6.c. Dimensionless pressure and pressure derivative curve for a hydraulic fracture intersecting a fault at its tip forming an angle of 90°. C_{fD}=50 ..... *207*
Fig. B.6.d. Dimensionless pressure and pressure derivative curve for a hydraulic fracture intersecting a fault at its tip forming an angle of 90°. C_{fD}=100 ..... *208*
Fig. B.6.e. Dimensionless pressure and pressure derivative curve for a hydraulic fracture intersecting a fault at its tip forming an angle of 90°. C_{fD}=300 ..... *209*
Fig. B.7.a. Dimensionless pressure and pressure derivative curve for a hydraulic fracture intersecting a fault at its tip forming an angle of 75°. C_{fD}=1 ..... *210*
Fig. B.7.b. Dimensionless pressure and pressure derivative curve for a hydraulic fracture intersecting a fault at its middle part forming an angle of 75°. C_{fD}=10 ..... *211*

Fig. B.7.c. Dimensionless pressure and pressure derivative curve for a hydraulic fracture intersecting a fault at its middle part forming an angle of 75°. C_{fD}=50 ..... *212*
Fig. B.7.d. Dimensionless pressure and pressure derivative curve for a hydraulic fracture intersecting a fault at its middle part forming an angle of 75°. C_{fD}=100 ..... *213*
Fig. B.7.e. Dimensionless pressure and pressure derivative curve for a hydraulic fracture intersecting a fault at its middle part forming an angle of 75°. C_{fD}=300 ..... *214*
Fig. B.8.a. Dimensionless pressure and pressure derivative curve for a hydraulic fracture intersecting a fault at its fourth part forming an angle of 75°. C_{fD}=1..215
Fig. B.8.b. Dimensionless pressure and pressure derivative curve for a hydraulic fracture intersecting a fault at its fourth part forming an angle of 75°. C_{fD}=10216
Fig. B.8.c. Dimensionless pressure and pressure derivative curve for a hydraulic fracture intersecting a fault at its fourth part forming an angle of 75°. C_{fD}=50217
Fig. B.8.d. Dimensionless pressure and pressure derivative curve for a hydraulic fracture intersecting a fault at its fourth part forming an angle of 75°. C_{fD}=100 ..... *218*
Fig. B.8.e. Dimensionless pressure and pressure derivative curve for a hydraulic fracture intersecting a fault at its fourth part forming an angle of 75°. C_{fD}=300 ..... *219*
Fig. B.9.a. Dimensionless pressure and pressure derivative curve for a hydraulic fracture intersecting a fault at its tip forming an angle of 75°. C_{fD}=1 ..... *220*
Fig. B.9.b. Dimensionless pressure and pressure derivative curve for a hydraulic fracture intersecting a fault at its tip forming an angle of 75°. C_{fD}=50 ..... *221*
Fig. B.9.c. Dimensionless pressure and pressure derivative curve for a hydraulic fracture intersecting a fault at its tip forming an angle of 75°. C_{fD}=300 ..... *222*
Fig. B.10.a. Dimensionless pressure and pressure derivative curve for a hydraulic fracture intersecting a fault at its middle part forming an angle of 60°. C_{fD}=1 223
Fig. B.10.b. Dimensionless pressure and pressure derivative curve for a hydraulic fracture intersecting a fault at its middle part forming an angle of 60°. C_{fD}=10 ..... *224*
Fig. B.10.c. Dimensionless pressure and pressure derivative curve for a hydraulic fracture intersecting a fault at its middle part forming an angle of 60°. C_{fD}=50 ..... *225*
Fig. B.10.d. Dimensionless pressure and pressure derivative curve for a hydraulic fracture intersecting a fault at its middle part forming an angle of 60°. C_{fD}=100 ..... *226*
Fig. B.10.e. Dimensionless pressure and pressure derivative curve for a hydraulic fracture intersecting a fault at its middle part forming an angle of 60°. C_{fD}=300 ..... *227*
Fig. B.11.a. Dimensionless pressure and pressure derivative curve for a hydraulic fracture intersecting a fault at its fourth part forming an angle of 60°. C_{fD}=1..228
Fig. B.11.b. Dimensionless pressure and pressure derivative curve for a hydraulic fracture intersecting a fault at its fourth part forming an angle of 60°. C_{fD}=10229

Fig. B.11.c. Dimensionless pressure and pressure derivative curve for a hydraulic fracture intersecting a fault at its fourth part forming an angle of 60°. C_{fD}=50230
Fig. B.11.d. Dimensionless pressure and pressure derivative curve for a hydraulic fracture intersecting a fault at its fourth part forming an angle of 60°. C_{fD}=100 231
Fig. B.11.e. Dimensionless pressure and pressure derivative curve for a hydraulic fracture intersecting a fault at its fourth part forming an angle of 60°. C_{fD}=300 232
Fig. B.12.a. Dimensionless pressure and pressure derivative curve for a hydraulic fracture intersecting a fault at its tip forming an angle of 60°. C_{fD}=1 233
Fig. B.12.b. Dimensionless pressure and pressure derivative curve for a hydraulic fracture intersecting a fault at its tip forming an angle of 60°. C_{fD}=10 234
Fig. B.12.c. Dimensionless pressure and pressure derivative curve for a hydraulic fracture intersecting a fault at its tip forming an angle of 60°. C_{fD}=50 235
Fig. B.12.d. Dimensionless pressure and pressure derivative curve for a hydraulic fracture intersecting a fault at its tip forming an angle of 60°. C_{fD}=100 236
Fig. B.12.e. Dimensionless pressure and pressure derivative curve for a hydraulic fracture intersecting a fault at its tip forming an angle of 60°. C_{fD}=300 237
Fig. B.13.a. Dimensionless pressure and pressure derivative curve for a hydraulic fracture intersecting a fault at its middle part forming an angle of 30°. C_{fD}=1 238
Fig. B.13.b. Dimensionless pressure and pressure derivative curve for a hydraulic fracture intersecting a fault at its middle part forming an angle of 30°. C_{fD}=10 239
Fig. B.13.c. Dimensionless pressure and pressure derivative curve for a hydraulic fracture intersecting a fault at its middle part forming an angle of 30°. C_{fD}=50 240
Fig. B.13.d. Dimensionless pressure and pressure derivative curve for a hydraulic fracture intersecting a fault at its middle part forming an angle of 30°. C_{fD}=100 241
Fig. B.13.e. Dimensionless pressure and pressure derivative curve for a hydraulic fracture intersecting a fault at its middle part forming an angle of 30°. C_{fD}=300 242
Fig. B.14.a. Dimensionless pressure and pressure derivative curve for a hydraulic fracture intersecting a fault at its fourth part forming an angle of 30°. C_{fD}=1..243
Fig. B.14.b. Dimensionless pressure and pressure derivative curve for a hydraulic fracture intersecting a fault at its fourth part forming an angle of 30°. C_{fD}=10244
Fig. B.14.c. Dimensionless pressure and pressure derivative curve for a hydraulic fracture intersecting a fault at its fourth part forming an angle of 30°. C_{fD}=50245
Fig. B.14.d. Dimensionless pressure and pressure derivative curve for a hydraulic fracture intersecting a fault at its fourth part forming an angle of 30°. C_{fD}=100 246
Fig. B.14.e. Dimensionless pressure and pressure derivative curve for a hydraulic fracture intersecting a fault at its fourth part forming an angle of 30°. C_{fD}=300 247

Fig. B.15.a. Dimensionless pressure and pressure derivative curve for a hydraulic fracture intersecting a fault at its tip forming an angle of 30°. $C_{fD}=1$ 248
Fig. B.15.b. Dimensionless pressure and pressure derivative curve for a hydraulic fracture intersecting a fault at its tip forming an angle of 30°. $C_{fD}=10$ 249
Fig. B.15.c. Dimensionless pressure and pressure derivative curve for a hydraulic fracture intersecting a fault at its tip forming an angle of 30°. $C_{fD}=50$ 250
Fig. B.15.d. Dimensionless pressure and pressure derivative curve for a hydraulic fracture intersecting a fault at its tip forming an angle of 30°. $C_{fD}=100$ 251
Fig. B.15.e. Dimensionless pressure and pressure derivative curve for a hydraulic fracture intersecting a fault at its tip forming an angle of 30°. $C_{fD}=300$ 252
Fig. B.16.a. Dimensionless pressure and pressure derivative curve for a hydraulic fracture intersecting a fault at its tip forming an angle of 0°. $C_{fD}=1$ 253
Fig. B.17.b. Dimensionless pressure and pressure derivative curve for a hydraulic fracture intersecting a fault at its tip forming an angle of 0°. $C_{fD}=50$ 254
Fig. B.17.c. Dimensionless pressure and pressure derivative curve for a hydraulic fracture intersecting a fault at its tip forming an angle of 0°. $C_{fD}=300$ 255
Fig. B.18.a. Dimensionless pressure and pressure derivative curve for a hydraulic fracture intersecting a fault at its middle part. $C_{fD}=300$ and $L_D=80$ 256
Fig. B.18.b. Dimensionless pressure and pressure derivative curve for a hydraulic fracture intersecting a fault at its middle part. $C_{fD}=300$ and $L_D=162$ 257
Fig. C.1.a. Variable PEBI grid for a vertical well without wellbore storage 259
Fig. C.1.b. Variable PEBI grid for a vertical well without wellbore storage (closer view) 260
Fig. C.2.a. Elliptical PEBI grid for a vertical well without wellbore storage 261
Fig. C.2.b. Elliptical PEBI grid for a vertical well without wellbore storage (closer view) 262
Fig. C.3.a. Circular PEBI grid for a vertical well without wellbore storage 263
Fig. C.4.a. Hecagonal PEBI grid for a vertical well without wellbore storage 264
Fig. C.4.b. Hexagonal PEBI grid for a vertical well without wellbore storage (closer view) 265
Fig. C.5.a. Rectangular PEBI grid for a vertical well without wellbore storage 266
Fig. C.5.b. Rectangular PEBI grid for a vertical well without wellbore storage (closer view) 267
Fig. C.6. Rectangular PEBI grid for a vertical well without wellbore storage. 3708 gridpoints 268
Fig. C.7.a. Circular PEBI grid used to simulate fractured well pressure behavior. $C_{fD}=1$ 269
Fig. C.7.b. Circular PEBI grid used to simulate fractured well pressure behavior. $C_{fD}=1$ (closer view) 270
Fig. C.8. Hexagonal PEBI grid used to simulate fractured well pressure behavior. $C_{fD}=1$ (closer view) 271
Fig. C.9.a. Rectangular PEBI grid used to simulate fractured well pressure behavior. $C_{fD}=1$ 272
Fig. C.9.b. Rectangular PEBI grid used to simulate fractured well pressure behavior. $C_{fD}=1$ (closer view) 273

Fig. C.10.a. Variable PEBI grid used to simulate fractured well pressure behavior. $C_{fD}=1$ 274
Fig. C.10.b. Variable PEBI grid used to simulate fractured well pressure behavior. $C_{fD}=1$ (closer view) 275
Fig. C.11. Elliptical PEBI grid used to simulate fractured well pressure behavior. $C_{fD}=1$ (closer view) 276
Fig. C.12. Elliptical PEBI grid used to simulate fractured well pressure behavior. $C_{fD}=300$ and $\theta=15°$ (closer view) 277
Fig. C.13. Elliptical PEBI grid used to simulate fractured well pressure behavior. $C_{fD}=50$ and $\theta=45°$ (closer view) 278
Fig. C.14. Elliptical PEBI grid used to simulate fractured well pressure behavior. $C_{fD}=50$ and $\theta=60°$ (closer view) 279
Fig. C.15. Elliptical PEBI grid used to simulate fractured well pressure behavior. $C_{fD}=1$ and $\theta=75°$ (closer view) 280
Fig. C.16. Elliptical PEBI grid used to simulate horizontal well pressure behavior. $\theta=45°$ (closer view) 281
Fig. C.17. Circular PEBI grid used to simulate horizontal well pressure behavior. $\theta=45°$ 282
Fig. C.18. Hexagonal PEBI grid used to simulate horizontal well pressure behavior. $\theta=45°$ 283
Fig. C.19. Rectangular PEBI grid used to simulate horizontal well pressure behavior. $\theta=45°$ 284
Fig. C.20. Variable PEBI grid used to simulate horizontal well pressure behavior. $\theta=45°$ 285
Fig. C.21.a. Close view of an elliptical PEBI grid for a hydraulically fractured well with a Branch fracture starting from the wellbore (Horizontal well) 286
Fig. C.21.b. Close view of an elliptical PEBI grid for a hydraulically fractured well with a Branch fracture starting at the middle distance between wellbore and main fracture tip (Horizontal well) for $\theta=30°$ and $X_{fbD}=0.6$ 287
Fig. C.21.c. Close view of an elliptical PEBI grid for a hydraulically fractured well with a Branch fracture starting at the main fracture tip (Horizontal well) for $\theta=30°$ and $X_{fbD}=0.6$ 288
Fig. C.22.a. Close view of an elliptical PEBI grid (showing centers and pressure profile) for a hydraulically fractured well with $C_{fD}=1$ intersecting a fault with L_D of 1 and an angle of 90° 289
Fig. C.22.b. Close view of an elliptical PEBI grid for a hydraulically fractured well with $C_{fD}=1$ intersecting a fault at its tip. L_D of 3 and an angle of 90° 290
Fig. C.2.c. Close view of an elliptical PEBI grid for a hydraulically fractured well with $C_{fD}=1$ intersecting a fault at its fourth part. L_D of 7.5 and an angle of 60° 291
Fig. C.22.d. Close view of an elliptical PEBI grid for a hydraulically fractured well with $C_{fD}=1$ intersecting a fault at its tip. L_D of 1 and an angle of 0° 292

LIST OF TABLES

Table 2.1. Reservoir coordinates 23
Table 2.2. Reservoir, well and rock data used for simulation 24
Table 2.3. Main simulation parameters used in the Eclipse Suit 25
Table 2.5. Grid controls 25
Table 2.6. Absolute errors for several PEBI grids 25
Table 2.7. Grid controls for hexagonal, elliptical and rectangular PEBI grids 30
Table 2.8. Grid controls for hexagonal, elliptical and rectangular PEBI grids 30
Table 2.9. Fracture parameters 31
Table 2.10. Grid control parameters applied to all studied PEBI grids applied to fractured wells 31
Table 2.11. Absolute errors for several PEBI grids (hydraulically fracture vertical wells) 32
Table 2.12. Grid control parameters for Elliptical PEBI grids applied to fractured wells 33
Table 2.13. Absolute errors for Elliptical PEBI grids and C_{fD}=0.1 and 0.5 34
Table 2.14. Recommended grid control parameters to simulate transient pressure behavior of vertical wells using an Elliptical PEBI grids 34
Table 2.15. Grid control parameters for Elliptical PEBI grids applied to fractured wells with different fracture conductivities 42
Table 2.16. Grid control parameters for Elliptical PEBI grids applied to fractured wells with different fracture conductivities and different fracture-orientation angles 43
Table 2.17. Reservoir coordinates 44
Table 2.18. Reservoir, well and rock data used for simulation 45
Table 2.19. Grid control parameters 45
Table 2.20. Number of grid points 45
Table 2.21. Absolute errors for a horizontal well using all the studied PEBI grids 45
Table 3.1. Equivalent horizontal wellbore length and wellbore radius to fracture conductivity 59
Table 4.1. Absolute average errors for the pressure solutions between a 66
Table 4.2. Average absolute errors obtained from the solution of this study and the 70
Table 4.3. Equivalent horizontal wellbore length and wellbore radius to branch fracture conductivity 76
Table 4.4. Equivalent horizontal wellbore length and wellbore radius to branch fracture conductivity 76
Table 4.5. Slopes observed in a hydraulic fractured well with a branch fracture 82
Table 5.1. Simulated test data for example 1 124
Table 5.2. Simulated test data for example 2 129
Table 5.3. Coefficients and correlation coefficients for Eq. 5.63 136
Table 5.4. Pressure data for example 3 142
Table 5.5. Pressure data for example 4 149
Table 5.6. Pressure data for example 5 152
Table D.1.a. Dimensionless pressure for a vertical well. Numerical solutions were obtained using Hexagonal, Circular and rectangular PEBI grids 294

Table D.1.b. Dimensionless pressure for a vertical well generated by analytical solution and Variable and Elliptical PEBI grids 297
Table D.2.a. Dimensionless pressure for a vertical well. Numerical solution generated using Circular PEBI grids (S=0) 300
Table D.2.b. Dimensionless pressure for a vertical well. Numerical solutions generated using Circular PEBI grids (C_D=10000, S=0 and S=5) 304
Table D.3.a. Dimensionless pressure for a vertical well intersected by a hydraulic fracture. Numerical solutions generated using Hexagonal, Circular, and 308
Table D.3.b. Dimensionless pressure for a vertical well intersected by a hydraulic fracture. Numerical solutions generated using Variable and Elliptical PEBI grids. C_{fD}=1 310
Table D.4. Dimensionless pressure for a vertical well intersected by a hydraulic fracture (C_{fD}=0.1). Numerical solutions generated using an Elliptical PEBI grid 312
Table D.5. Dimensionless pressure for a vertical well intersected by a hydraulic fracture (C_{fD}=0.5). Numerical solutions generated using an Elliptical PEBI grid 314
Table D.6.a. Dimensionless pressure for a vertical well intersected by a hydraulic fracture (C_{fD}=1 and C_{fD}=50). Numerical solutions generated using an 316
Table D.6.b. Dimensionless pressure for a vertical well intersected by a hydraulic fracture (C_{fD}=100 and C_{fD}=300). Numerical solutions generated using an 319
Table D.7.a. Dimensionless pressure for a vertical well intersected by a rotated hydraulic fracture. Numerical solutions generated using an Elliptical PEBI grid 322
Table D.7.b. Dimensionless pressure for a vertical well intersected by a rotated hydraulic fracture. Numerical solutions generated using an Elliptical PEBI grid 324
Table D.8. Dimensionless pressure for a horizontal well (θ=0, 45 and 90°). Numerical solutions generated using all available PEBI grid 326
Table D.9. Number of gridblocks used for simulating hydraulic fracture well with a branch fracture (horizontal well) 328
Table D.10. Dimensionless pressure for a hydraulic fractured well with a branch fracture starting from the wellbore, θ = 30° and X_{fbD}=0.6 329
Table D.11. Dimensionless pressure for a hydraulic fractured well with a branch fracture starting from the middle distance from the wellbore and the 331
Table D.12.a. Absolute errors obtained between the pressure solutions for a branch fracture starting from the wellbore and a fractured well with X_{fbD}=0 (no branch) and X_{fbD} =0.6 and angle of 30° 333
Table D.12.b. Absolute errors obtained between the pressure solutions for a branch fracture starting from the middle distance between wellbore and main fracture tip and a fractured well with X_{fbD}=0 (no branch) and X_{fbD} =0.6 and angle of 30° ... 334
Table D.13.a. Pressure solution obtained in this study for a hydraulically fractured well with no branch 335
Table D.13.b. Pressure solution obtained in Ref. 36 for a symmetric hydraulic fractured well 336

Table D.13.c. Absolute error between the pressure solution of this study and the one from Ref. 36 (tables D.13.a and D.13.b) 337
Table D.14.a. Pressure solution obtained in this study for a hydraulically fractured well with dimensionless branch fracture length, X_{fbD}, of 0.2 (angle = 0°) 338
Table D.14.b. Pressure solution obtained in Ref. 36 for a hydraulically fractured well with fracture asymmetric factor of 0.2 339
Table D.14.c. Absolute error between the pressure solution of this study (X_{fbD}=0.2) and the one from Ref. 36 for fracture asymmetric factor of 0.2 (tables D.14.a and D.14.b) 340
Table D.15.a. Pressure solution obtained in this study for a hydraulically fractured well with dimensionless branch fracture length, X_{fbD}, of 0.4 (angle = 0°) 341
Table D.15.b. Pressure solution obtained in Ref. 36 for a hydraulically fractured well with fracture asymmetric factor of 0.4 342
Table D.15.c. Absolute error between the pressure solution of this study (X_{fbD}=0.4) and the one from Ref. 36 for fracture asymmetric factor of 0.4 (tables D.15.a and D.15.b) 343
Table D.16.a. Pressure solution obtained in this study for a hydraulically fractured well with dimensionless branch fracture length, X_{fbD}, of 0.6 (angle = 0°) 344
Table D.16.b. Pressure solution obtained in Ref. 36 for a hydraulically fractured well with fracture asymmetric factor of 0.6 345
Table D.16.c. Absolute error between the pressure solution of this study (X_{fbD}=0.6) and the one from Ref. 36 for fracture asymmetric factor of 0.4 (tables D.16.a and D.16.b) 346
Table D.17.a. Pressure solution for a branch fracture inclined 10° with respect the main fracture and its deviation with respect to the pressure solution obtained for the angle of 0°. C_{fD}=1 347
Table D.17.b. Pressure solution for a branch fracture inclined 10° with respect the main fracture and its deviation with respect to the pressure solution obtained for the angle of 0°. C_{fD}=10 348
Table D.17.c. Pressure solution for a branch fracture inclined 10° with respect the main fracture and its deviation with respect to the pressure solution obtained for the angle of 0°. C_{fD}=50 349
Table D.17.d. Pressure solution for a branch fracture inclined 10° with respect the main fracture and its deviation with respect to the pressure solution obtained for the angle of 0°. C_{fD}=100 350
Table D.17.e. Pressure solution for a branch fracture inclined 10° with respect the main fracture and its deviation with respect to the pressure solution obtained for the angle of 0°. C_{fD}=300 351
Table D.18.a. Pressure solution for a branch fracture inclined 20° with respect the main fracture and its deviation with respect to the pressure solution obtained for the angle of 0°. C_{fD}=1 352
Table D.18.b. Pressure solution for a branch fracture inclined 20° with respect the main fracture and its deviation with respect to the pressure solution obtained for the angle of 0°. C_{fD}=10 353

Table D.18.c. Pressure solution for a branch fracture inclined 20° with respect the main fracture and its deviation with respect to the pressure solution obtained for the angle of 0°. C_{fD}=50 354
Table D.18.d. Pressure solution for a branch fracture inclined 20° with respect the main fracture and its deviation with respect to the pressure solution obtained for the angle of 0°. C_{fD}=100 355
Table D.18.e. Pressure solution for a branch fracture inclined 20° with respect the main fracture and its deviation with respect to the pressure solution obtained for the angle of 0°. C_{fD}=300 356
Table D.19.a. Pressure solution for a branch fracture inclined 30° with respect the main fracture and its deviation with respect to the pressure solution obtained for the angle of 0°. C_{fD}=1 357
Table D.19.b. Pressure solution for a branch fracture inclined 30° with respect the main fracture and its deviation with respect to the pressure solution obtained for the angle of 0°. C_{fD}=10 358
Table D.19.c. Pressure solution for a branch fracture inclined 30° with respect the main fracture and its deviation with respect to the pressure solution obtained for the angle of 0°. C_{fD}=50 359
Table D.19.d. Pressure solution for a branch fracture inclined 30° with respect the main fracture and its deviation with respect to the pressure solution obtained for the angle of 0°. C_{fD}=100 360
Table D.19.e. Pressure solution for a branch fracture inclined 30° with respect the main fracture and its deviation with respect to the pressure solution obtained for the angle of 0°. C_{fD}=300 361
Table D.20.a. Pressure solution for a branch fracture (C_{fbD}=0.75) inclined 30° with respect the main fracture (C_{fD}=1) and its deviation with respect to the pressure solution obtained for the angle of 30° with constant dimensionless fracture conductivity (C_{fbD}=1 and C_{fD}=1) 362
Table D.20.b. Pressure solution for a branch fracture (C_{fbD}=7.5) inclined 30° with respect the main fracture (C_{fD}=10) and its deviation with respect to the pressure solution obtained for the angle of 30° with constant dimensionless fracture conductivity (C_{fbD}=10 and C_{fD}=10) 363
Table D.20.c. Pressure solution for a branch fracture (C_{fbD}=37.5) inclined 30° with respect the main fracture (C_{fD}=50) and its deviation with respect to the pressure solution obtained for the angle of 30° with constant dimensionless fracture conductivity (C_{fbD}=50 and C_{fD}=50) 364
Table D.20.d. Pressure solution for a branch fracture (C_{fbD}=75) inclined 30° with respect the main fracture (C_{fD}=100) and its deviation with respect to the pressure solution obtained for the angle of 30° with constant dimensionless fracture conductivity (C_{fbD}=100 and C_{fD}=100) 365
Table D.20.e. Pressure solution for a branch fracture (C_{fbD}=225) inclined 30° with respect the main fracture (C_{fD}=300) and its deviation with respect to the pressure solution obtained for the angle of 30° with constant dimensionless fracture conductivity (C_{fbD}=300 and C_{fD}=300) 366

Table D.21.a. Pressure solution for a branch fracture (C_{fbD}=0.5) inclined 30° with respect the main fracture (C_{fD}=1) and its deviation with respect to the pressure solution obtained for the angle of 30° with constant dimensionless fracture conductivity (C_{fbD}=1 and C_{fD}=1) 367
Table D.21.b. Pressure solution for a branch fracture (C_{fbD}=5) inclined 30° with respect the main fracture (C_{fD}=10) and its deviation with respect to the pressure solution obtained for the angle of 30° with constant dimensionless fracture conductivity (C_{fbD}=10 and C_{fD}=10) 368
Table D.21.c. Pressure solution for a branch fracture (C_{fbD}=25) inclined 30° with respect the main fracture (C_{fD}=50) and its deviation with respect to the pressure solution obtained for the angle of 30° with constant dimensionless fracture conductivity (C_{fbD}=50 and C_{fD}=50) 369
Table D.21.d. Pressure solution for a branch fracture (C_{fbD}=50) inclined 30° with respect the main fracture (C_{fD}=100) and its deviation with respect to the pressure solution obtained for the angle of 30° with constant dimensionless fracture conductivity (C_{fbD}=100 and C_{fD}=100) 370
Table D.21.e. Pressure solution for a branch fracture (C_{fbD}=150) inclined 30° with respect the main fracture (C_{fD}=300) and its deviation with respect to the pressure solution obtained for the angle of 30° with constant dimensionless fracture conductivity (C_{fbD}=300 and C_{fD}=300) 371
Table D.22. Number of PEBI cells used to simulate a branch fracture 372
Table D.23.a. Number of PEBI cells used to simulate a fracture well intersecting a fault at its middle part and forming an angle of 90° 372
Table D.23.b. Number of PEBI cells used to simulate a fracture well intersecting a fault at its fourth part and forming an angle of 90° 373
Table D.23.c. Number of PEBI cells used to simulate a fracture well intersecting a fault at its tip and forming an angle of 90° 373
Table D.23.e. Number of PEBI cells used to simulate a fracture well intersecting a fault at its fourth part and forming an angle of 75° 374
Table D.23.f. Number of PEBI cells used to simulate a fracture well intersecting a fault at its tip and forming an angle of 75° 374
Table D.23.g. Number of PEBI cells used to simulate a fracture well intersecting a fault at its middle part and forming an angle of 60° 374
Table D.23.h. Number of PEBI cells used to simulate a fracture well intersecting a fault at its fourth part and forming an angle of 60° 374
Table D.23.i. Number of PEBI cells used to simulate a fracture well intersecting a fault at its tip and forming an angle of 60° 375
Table D.23.j. Number of PEBI cells used to simulate a fracture well intersecting a fault at its middle part and forming an angle of 30° 375
Table D.23.k. Number of PEBI cells used to simulate a fracture well intersecting a fault at its fourth part and forming an angle of 30° 375
Table D.23.l. Number of PEBI cells used to simulate a fracture well intersecting a fault at its tip and forming an angle of 30° 375
Table D.23.m. Number of PEBI cells used to simulate a fracture well intersecting a fault at its tip and forming an angle of 0° 376

Table D.23.n. Number of PEBI cells used to simulate a fracture well intersecting a fault at its middle distance and forming different angles. L_D=80 (almost half reservoir is crossed by the fault) 376
Table D.23.o. Number of PEBI cells used to simulate a fracture well intersecting a fault at its middle distance and forming different angles. L_D=162 (The whole reservoir is crossed by the fault) 376
Table D.24.a. Pressure solution for a hydraulic fracture intersecting the a fault in its middle part forming and angle of 90°, C_{fD}=1 377
Table D.24.b. Pressure solution for a hydraulic fracture intersecting the a fault in its middle part forming and angle of 90°, C_{fD}=10 379
Table D.24.c. Pressure solution for a hydraulic fracture intersecting the a fault in its middle part forming and angle of 90°, C_{fD}=50 381
Table D.24.d. Pressure solution for a hydraulic fracture intersecting the a fault in its middle part forming and angle of 90°, C_{fD}=100 383
Table D.24.e. Pressure solution for a hydraulic fracture intersecting the a fault in its middle part forming and angle of 90°, C_{fD}=300 385

ABSTRACT

This study provides new findings in the transient pressure analysis of finite conductivity hydraulically fractured vertical wells, and in particular, the cases of the presence of a hydraulic fracture which possesses a branch and a hydraulic fracture intersecting a sealing fault.

The introduction of a branch or a fault makes the mathematical/numerical treatment of the fractured wells more difficult. Numerical techniques require the implementation of a gridding method that is different than the traditionally rectangular system to better capture the effects of the non-orthogonality problem introduced by either the branch fracture or the fault. In this study, PEBI grids, implemented in a commercial simulator (Eclipse Suit) were employed to solve the mathematical models. However, it was first necessary to study the use of five PEBI grids to establish their application and limitations. It was found that a circular PEBI grid describes with great accuracy the transient pressure behavior of unfractured vertical wells. Elliptical PEBI grids do the same for fracture vertical wells (including fracture rotation) while any of the PEBI grids works well on horizontal wells.

Due to simulator limitations, only a single branch fracture was simulated at three different positions along the main fracture and three different angles. New pressure response was found when the branch is attached at the tip of the main branch and no significant effect of the angle was found. The pressure behavior is very similar to cases of fracture asymmetry already reported in the literature.

As far as the fracture-fault system forming an angle of 90 degrees is concerned, the pressure response is characterized by a maximum point in the pressure derivative which takes place once the transient response of the fracture has vanished. This occurs because the fault inhibits the development of the pseudoradial flow regime. If the fault divides the reservoir into two parts of practically same size, the pseudoradial flow regime will never be developed, and instead, a new flow regime here called as *semiradial* or *semi-pseudoradial* is formed. If not handled carefully, this new flow regime can be easily confused with the behavior of a complete reservoir and its analysis will lead to serious errors.

As the angle of the fault is reduced from 90 to zero degrees and when fault and fracture conjoin at their tips, the characteristic signature, the "hump," is less notorious or can be completely absent. The rotation of the fault provides more space for the formation of radial flow then the maximum is diminished.

Mathematical expressions for estimating the length of the branch fracture were developed using the philosophy of the *Tiab's Direct Synthesis Technique*. Correlations were also developed for estimation of fault length when the intersecting angle fracture-fault is 90 degrees. The procedure has a major effect in improving the analysis of fractured-well pressure response since it allows us to understand previously unconsidered new scenarios for simulation and modeling. Interpretation of pressure transient tests for finite-conductivity fractured wells by *the Tiab's Direct Synthesis Technique* is now extended to cover these two new aspects.

CHAPTER I

PROBLEM BACKGROUND

Initially, hydraulic fracturing was considered a good stimulation technique for increasing the productivity of low permeability formations. Lately, the technique has been extended so that may be applied to higher permeability reservoirs to improve their productivity.

The idea of studying the pressure behavior of a hydraulic fractured well whose reservoir contains long bifurcating fractures, called "branches" was originated in a study conducted by Germanovich et al[1,2]. The authors indicated that hydraulic fractures are not single, symmetric and planar features in rocks, but instead, the fractures have irregular patterns which vary in size, and which bifurcate from each other in branches. Their research was based upon direct observation on fractured cores, geological evidence and laboratory experiments. A clear example is illustrated in Fig. 1.1, which shows a photograph of an 18-in cube sample of Red Sandstone after being hydraulically fractured with water. Even though the sample was homogeneous and without pre-existing fractures/joints and anisotropy, crack front segmentation took place.

Germanovich et al[2] also collected observations concerning dike segmentation in reservoir type rocks. Their observations concluded that dikes exhibit similar

fracture patterns as the hydraulic fractures created in hydrocarbon wells. (See Fig. 1.2.) An unstable growth process of the crack causes the fracture segmentation.

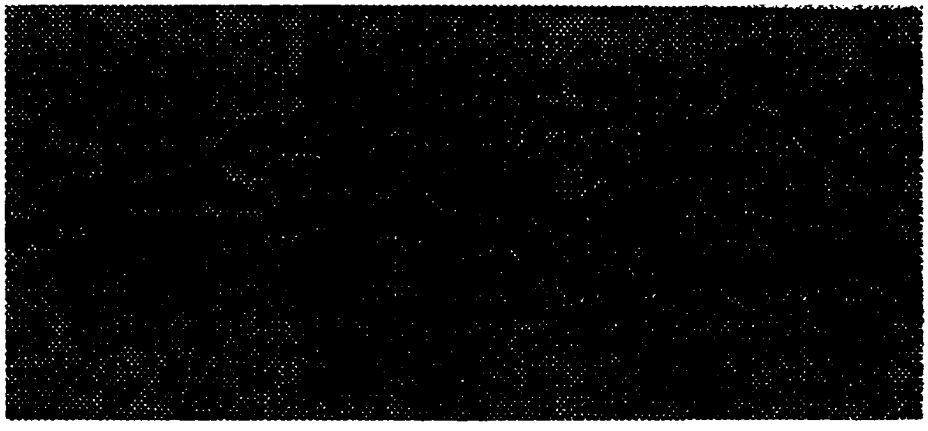

Fig. 1.1. Hydraulic branching in sandstone (After Ref. 1)

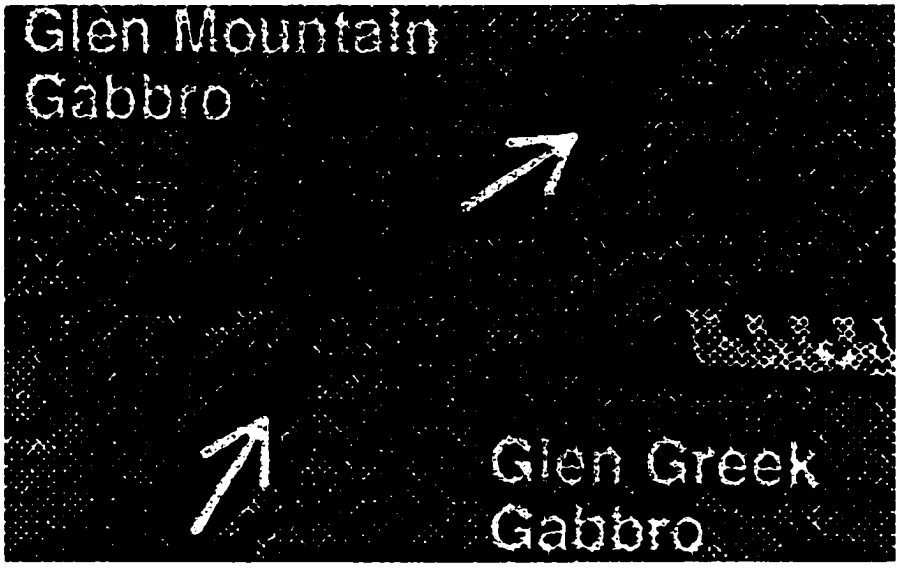

Fig. 1.2. Granitic dike propagation through the interface between two gabbros at Wichita Mountains area (After Ref. 1)

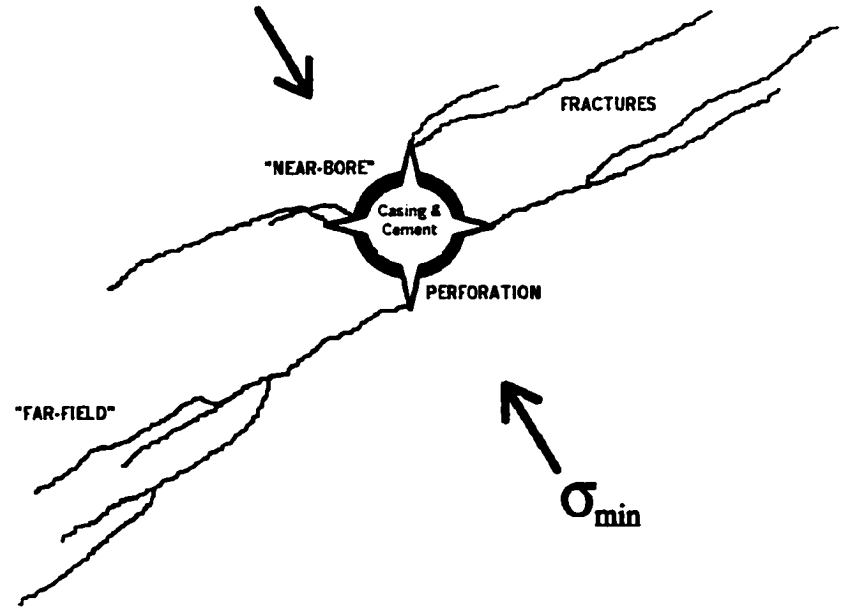

Fig. 1.3. Near-wellbore and far-field multiple fractures (After Ref. 1)

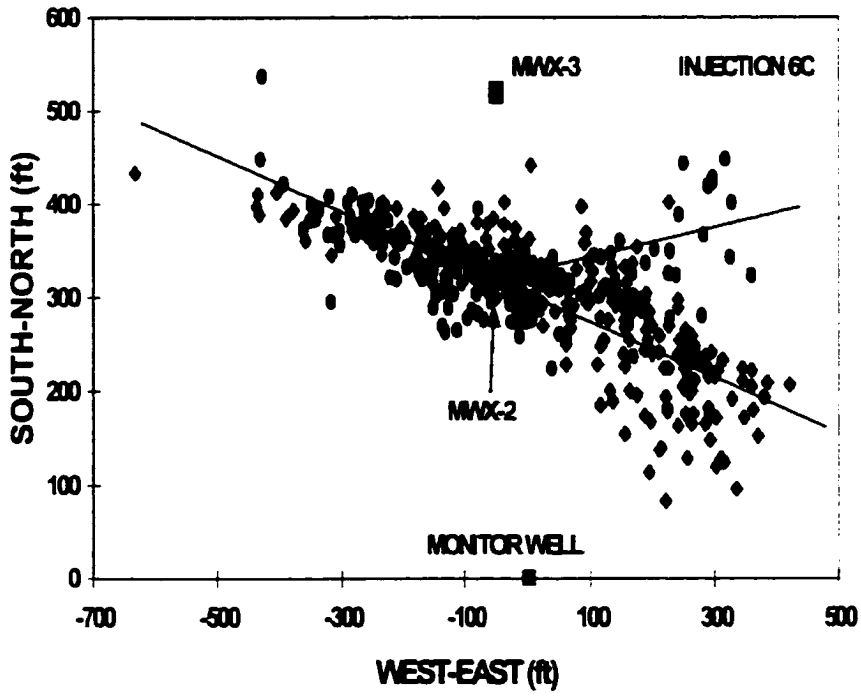

Fig. 1.4. Injection Microseismic Map (After Ref. 3 and 4)

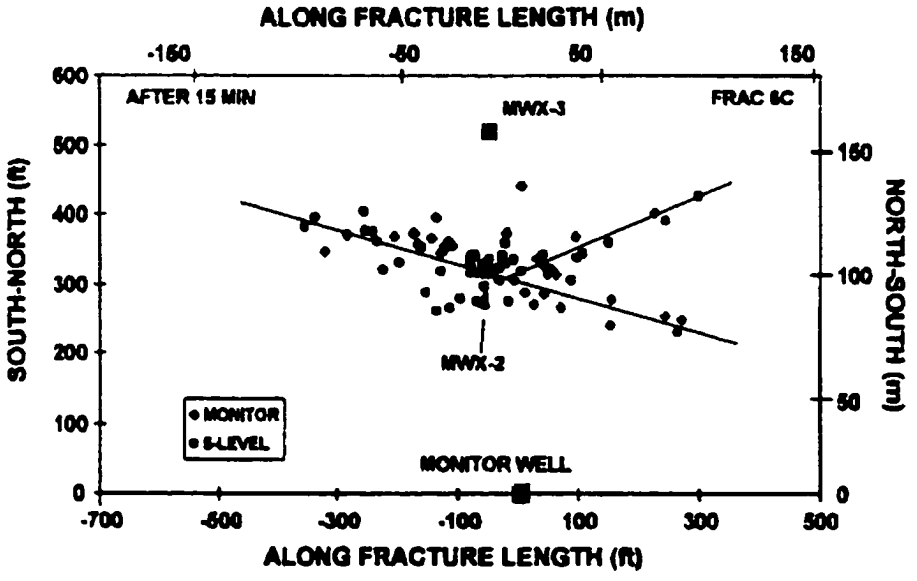

Fig. 1.5. Injection Microseismic Map (After Ref. 3 and 4)

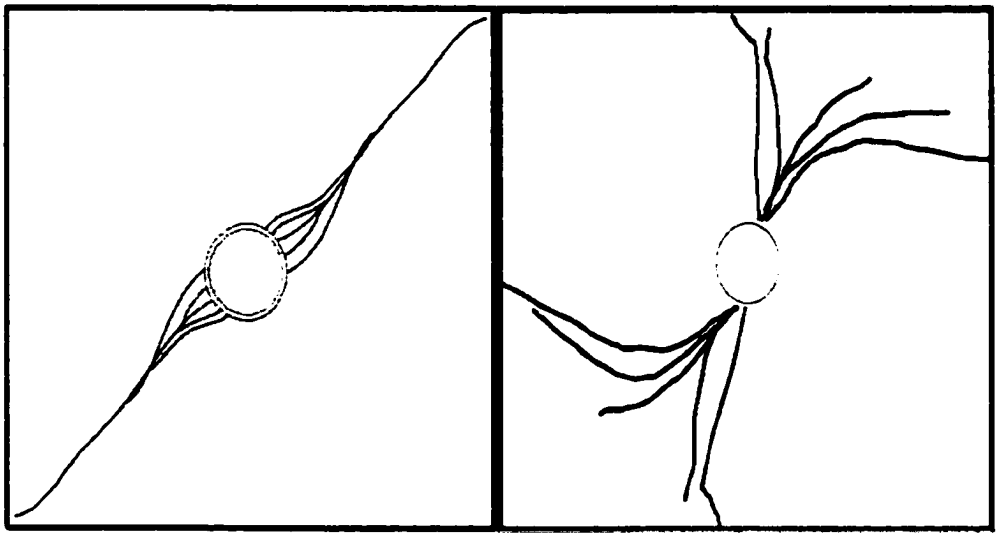

Fig. 1.6. Fracture Geometries conceived for the Couper basin. Left: Fracture turning (movement in one plane). Right: Multiple fracturing (After Ref. 6)

Multiple fractures can occur a) near the wellbore or 2) far field. Fig. 1.3 demonstrates via a sketch the way fracture propagation may develop according to the theory expounded by Germanovich et al[1-2].

It appears that more evidence of branch fractures is obtained by microseismic and deformation imaging of hydraulic fracturing growth. These techniques can be implemented either post-fracture or during the fracturing process by means of real-time data acquisition[3-5]. Mapping images are presented in Figs. 3.4 and 3.5 on which the main fracture and the branch fracture were drawn. Additionally, near-wellbore pressure loss (NWBPL) detected in a hydraulic fracturing program conducted in the Cooper basin of Central Australia[6] was associated with multiple fracturing. NWBPL is a friction pressure drop in the near-wellbore region, which can be caused by either insufficient perforation area or complex near-wellbore fracture geometry (tortuosity). NWBPL is the most serious obstacle to successful proppant placement. Fig. 1.6 illustrates possible fracture geometries conceived for this basin.

Well test analysis in hydraulically fractured wells has been a topic of interest to the oil industry since the early 1950's[7-10]. Since then, different approaches have been presented to study their pressure transient behavior. Numerical, physical semi-analytic and analytic models have been analyzed[7-16].

In 1955, Crawford and Landrum[7] studied the impact of fracture asymmetry and the angle of fracture separation on the production capacity using an electrical model. They determined a maximum reduction of 10 % in well productivity when the angle of fracture varied from 180 to 90 degrees. They also found an increment in production

capacity from 155 to almost 200 percent when the fracture length is 20 percent of the drainage radius.

Russell and Truit[10] conducted the first numerical study performed in this field. They proposed a numerical solution for a well with an infinite-conductivity fracture using an explicit finite-difference solution. In spite of their simplistic approach and the fact that the solution was carried out using an explicit finite-difference formulation, later on, Gringarten et al[11-12] found out that Russell and Truit's solution approached very well their proposed analytic solution for the case of $x_e/x_f = 10$. Gringarten et al[11-12] presented analytical solution for both infinite-conductivity and uniform flux fractured wells. An infinite conductivity fracture considers a negligible pressure drop along the fracture. In a uniform flux fracture the fluid enters the fracture at a uniform flow rate per unit area of fracture so pressure drop is taken into account. The most important practical contribution of Gringarten et al[11-12] were their type curves.

In 1972 Raghavan et al[13] demonstrated the general characteristics of all common buildup graphs for fractured wells and concluded that the Hornet plot is superior for permeability calculations.

Sawyer at al[14] used the Alternating-Direction Implicit Procedure (ADIP) to study the behavior of fracture gas wells under Darcy flow. They used a non-uniform grid to account for higher pressure drop around the fracture. Another numerical simulation, this time using the finite element method, was presented by Barker[15] in 1978.

Wattenberger and Ramey[16] considered the effects of turbulent flow in the reservoir on the behavior of fractured wells. They concluded that turbulence within the

fracture itself is sometimes more important than turbulence in the formation. A later numerical study by Holditch and Morse[17] on non-Darcy flow behavior in fractured gas wells determined that the larger pressure drops are located near the wellbore. For fractures with low conductivity, the produced gas enters the fracture close to the wellbore which is seen by an increase of non-Darcy flow near the wellbore and for low conductivity fractures, most of the produced gas enters the fracture close to the tip. They[17] also found out that calculation of fracture length when neglecting non-Darcy flow will result in values that are far too small. Non-Darcy flow can reduce the fracture conductivity 20 times or more.

A very important contribution in this field was presented by Cinco-Ley et al[18]. They developed a semi-analytical solution to analyze the pressure behavior of a vertical well intersected by a symmetric finite-conductivity vertical fracture in an infinite slab reservoir. Their model assumes constant properties in both fracture and reservoir, negligible gravity forces, laminar flow. Neither wellbore storage nor damage were included. This investigation led to characterize the bilinear flow and establish new concepts on the finite nature of fracture conductivity. They recognized that in some cases their solution may not follow some field data. Such cases are pressure sensitive reservoirs, variable fracture conductivity and different fracture patterns.

Dowdle and Hyde[19] conducted a numerical investigation to account for the effects of turbulence, pressure-dependent permeability and porosity, damage, wellbore storage crossflow and partial penetration in hydraulically fractured gas wells with uniform flux. The pressure transient analysis was achieved via type- curve matching.

Ekie et al[20] generalized correlations to analyze and design pulse tests in fractured wells. They[20] presented a method for estimation of the compass orientation of a vertical fracture as well as the degree of reservoir anisotropy provided that formation permeability and fracture length are known.

In 1977, Cinco-ley and Samaniego[21] extended the work of Cinco-Ley et al[18] to include the effects of wellbore storage and damage. They found that the pressure behavior is greatly affected by the fracture damage. They also found that relevant information about fracture characteristics might not be determined when wellbore storage effects are present because it masks the bilinear or linear response. Later on, Cinco-Ley and Samaniego[22] showed that a plot of flowing pressure versus fourth root of time yields a straight line which slope depends upon fracture conductivity.

Narasimhan and Berkeley[23] elaborated on fracture asymmetry by means of a numerical Integral Finite Difference Model using a curvilinear mesh with locally grid refinement in both near-wellbore and tip fracture regions. They reported that the number of grid points has to be increased as the fracture conductivity value decreases.

By means of a numerical approach, Guppy et al[24] determined that the dimensionless fracture conductivity is smaller than estimated if Non-Darcy flow is not considered in gas wells. They presented a correlation to correct fracture conductivity including non-Darcy effects.

Fracture orientation can be estimated by either interference[25] or pulse testing[26]. For this purpose, Mousli et al[25] presented a type-curve method applied to interference tests while Tiab and Aboubise[26] presented an analytical technique for pulse testing

which utilizes graphical correlations instead of type curves. In any case, at least three wells have to be tested to find fracture orientation.

Bennett et al[27] conducted a numerical study of fracture behavior which included variable fracture conductivity and fracture asymmetry. This is the unique source in the literature which provides valuable suggestions, tips, and details on grid size and time step distribution[27-28]. They found that if the fracture conductivity decreases as a function on the distance from the wellbore, then at a later time the response of the variable fracture conductivity behaves as the arithmetic average of the conductivity.

The application of the pressure derivative concept to fracture wells was applied in 1986 and 1988 by Wong et al[29] and Tiab and Puthigai[30], respectively. Both techniques used type-curve matching procedures. In addition, type-curves were generated to analyze fractured well responses in naturally fractured reservoirs[31]. The technique was extended for multilayer double porosity reservoirs with analytical, numerical and semi-analytical numerical solutions[32].

The application of the *Tiab's Direct Synthesis Technique* to analyze the pressure behavior was introduced by Tiab[33] in 1994 for infinite conductivity and uniform flux fractures in closed systems. This technique was extended for finite conductivity wells by Tiab et al[34] in 1999. Berumen[35] also applied the *Tiab's Direct Synthesis Technique* to fractured wells in pressure-sensitive formations. He considered fracture asymmetry and variable fracture conductivity. Berumen et al[36] elaborated a more detailed study on fracture asymmetry in a later investigation.

The first attempt of simulating the pressure behavior of fractured wells with multiple branches was presented by Escobar et al[37]. The investigators presented a numerical solution for infinite conductivity vertical fractures and found that the response was identical as if no branches existed. They used a rectangular grid to force the non-orthogonal system to be orthogonal. This assumption could lead to losing the physical and mathematical meaning of the problem since Cartesian grids are very inflexible in describing real geometries that do not follow the Cartesian coordinate system. By using this approach, the grid orientation effects[38-40] can be more pronounced.

Most reservoir simulators are defined using a rectangular Cartesian coordinate system, which has the advantage of familiarity; the equations describing physical phenomena are traditionally written in Cartesian coordinate form; then, it is a straightforward process to construct rectangular grid systems. These types of grids appear to be both natural and intuitive. However, the use of Cartesian coordinates imposes a rectangular grid on model that may possess no physical relation to the studied problem.

The first attempt found in the petroleum literature for modeling reservoir geometry with non-rectangular grid was presented in 1980 by Wadsley[41]. Their construction consisted of approximating an orthogonal curvilinear system by straight line segments and incorporating a new method to estimate inter-block transmissibilities and block-pore volume.

In the early 1980's, the need for reducing grid orientation effects was receiving more attention. Pruess and Bodvarsson[42] presented a seven-point finite difference

scheme to reduce grid orientation effects in steamflood patterns. As a result a hexagonal grid system was employed. Their method alleviates more the grid orientation effects as compared with the existing five-point and nine-point finite difference schemes.

With the purpose of improving the treatment of wells in reservoir simulators, Pedrosa and Aziz presented a technique that used an orthogonal curvilinear grid system (cylindrical or elliptical) near the wellbore and rectangular grid elsewhere with special treatment in the neighboring between the two regions. The technique was referred to as a hybrid grid system. They use simultaneous solutions while IMPES solution in the reservoir region.

It was also found that the accuracy of the finite difference formulation applied to fluid equations is affected tremendously by the grid size. Finer grid system will lead to less truncation errors and consequently a more accurate solution is obtained. Also, the refinement of grid systems is also an effective tool for decreasing the numerical dispersion in the displacement front. However, a conventional grid system requires larger storage and computation time. Then, great interest was paid to local grid refinement[44-47].

PEBI grids, also known as Voronoi grids, have been recently introduced to reservoir engineering. The first application in petroleum engineering was made by Heinemann et al[48]. They describe techniques for equation discretization and grid construction. They also found that the grid orientation effects when a PEBI grid is used is lower than that occurring when a five-point Cartesian grid is used and slightly higher compared to the nine-point formulation. The second application found was

presented by Palagi and Aziz[49]. They found that hybrid Cartesian and hybrid hexagonal are less sensitive to grid orientation effects that pure hexagonal grids or even the nine-point scheme.

Due to its flexibility, PEBI or Voronoi grids have been used in several other areas of the sciences, namely: fluid mechanics[50], mathematics[51], physics[52], rock characterization[53] and crystallography[54], electrical engineering[55], biology[56], geostatistics[57] and groundwater flow[58].

Few applications of PEBI grids to reservoir engineering are reported in the literature. Deimbacher and Heinemann[59] applied PEBI grids to large-scale reservoir simulation. Naccache[60] developed a reservoir simulator to model the injection of steam into heavy oil. Verma and Aziz[61] presented techniques to generate two- and three-dimensional flexible grids for reservoir simulation and for calculation of flow over these grids. Recently, Mlacnik and Heinemann[62] applied windowing and local timestepping techniques to a full scale simulation model. Pattay and Ganzer[63] implemented a dual porosity/permeability system into a PEBI grid reservoir simulator. Ahmed and Singh[64] employed PEBI grids to simulate the Eastern Shallow oil zone of the Elk Hills Field. Two comparative studies[65-66] have been conducted to study the effectiveness of PEBI grids.

Heinemann[67] developed a study of the application of PEBI grids with faults, windows, dual time-stepping, transient well testing, horizontal-well modeling and aquifer modeling. He found an overall enhanced reservoir description. For the case of well testing he found an excellent match between the numerical results and analytical solution. However, there was no specification of the type of PEBI grid used.

Gunasekera and Lindsey[68] elaborated upon the classification of PEBI grids and applied them to study transient pressure behavior in vertical and horizontal wells. In spite of the difference among the results obtained for four different grid types, they considered that there is not sufficient experience with PEBI grids to recommend one method over other. They determined that hexagonal PEBI grids result in a low grid orientation effect for isotropic and anisotropic cases.

CHAPTER II

PEBI GRID APPLICATION TO TRANSIENT PRESSURE ANALYSIS

2.1. INTRODUCTION

Accuracy and efficiency of reservoir simulators in complex systems are highly dependent upon a proper grid selection. Grids based on a Cartesian coordinate system have been widely used, but possess some disadvantages: (a) inflexibility in description of faults, pinchouts, hydraulic fractures, horizontal wells and general discontinuities presented in reservoirs, (b) inflexibility in representing well location; (c) unavoidable inaccuracies due to grid orientation effects.

Local grid refinement[44-47], nine-point[38-39] and thirteen-point[40] finite difference schemes were introduced to enhance the performance of Cartesian grids. Research has covered other techniques to reduce grid orientation effects, starting from the development of a uniform hexagonal grid block pattern[42] until the application of Voronoi or PEBI grids. However, as pointed out by Gunasekera and Lindsey[68], the experience with PEBI grids is very limited since their application is still in its infancy. Application of PEBI grids in the oil industry has been no more than a decade. Besides, last applications are being introduced during the past three years. On the other hand, generation and construction of PEBI grids are not as easy as Cartesian grids. The construction of a PEBI grid for a reservoir is feasible only if it is done by a numerical

grid generation procedure[69]. The Eclipse suit[70-71], which was used in this study (finite-difference simulator), recognizes five types of grids but there is no evidence of the limitations and applicability of them to simulate well transient behavior. Therefore, the point of this chapter is to provide some basic definitions on PEBI grids and establish and recommend their applications for simulating the transient pressure behavior of horizontal wells, vertical wells and vertical fractures artificially created in vertical wells. We will see that PEBI grids are not a panacea for solving the above-mentioned cases.

2.2. THEORETICAL CONCEPTS ON PEBI GRIDS[48-49,59,67-75]

2.2.1. DEFINITION

A Voronoi grid is defined as the region of space that is closer to its gridpoint than to any other gridpoints[40,73-75]. The PEBI grid is locally orthogonal. It means the block boundaries are normal to lines joining the nodes on the two sides of each boundary. (See Fig. 2.1.) This allows a reasonably accurate computation of interblock transmissibility for heterogeneous but isotropic permeability distribution[48, 67]. This is the type of grid supported by the Eclipse Suit[70]. Heinemann and Brand[48] also presented a method of implementing the PEBI grid method to full and anisotropic symmetric permeability tensors. The grid block boundaries in this case are not locally orthogonal but oriented in a manner such the vector $\bar{k}\bar{n}$ (being $\bar{k}$ the permeability tensor in the triangle and $\bar{n}$ is the outward normal to the block surface) is parallel to vector $\bar{s}$, the vector pointing to node j from node i. A result of this simplification is

that flow across any surface becomes only a function of potentials at the nodes on either side of the surface[48]. Such grids have been called *k*-orthogonal or generalized perpendicular bisector (GPEBI) grids[66]. See Fig. 2.2. This approach presents problems for regions having high permeability anisotropy[80].

Actually, a Voronoi grid block has been used not only for numerical simulation but also to discretize a domain in many other fields[50-59]. Although, the gridblocks have been referred as such names as Wigner cells[76], Dirichlet tesellation[77], PEBI grid[72] (PErpendicular BIsection), or polygons of influence[58], it is more common found in the literature as Voronoi polyhedra in honor of the mathematician Voronoi[78] who first defined these polygonal regions.

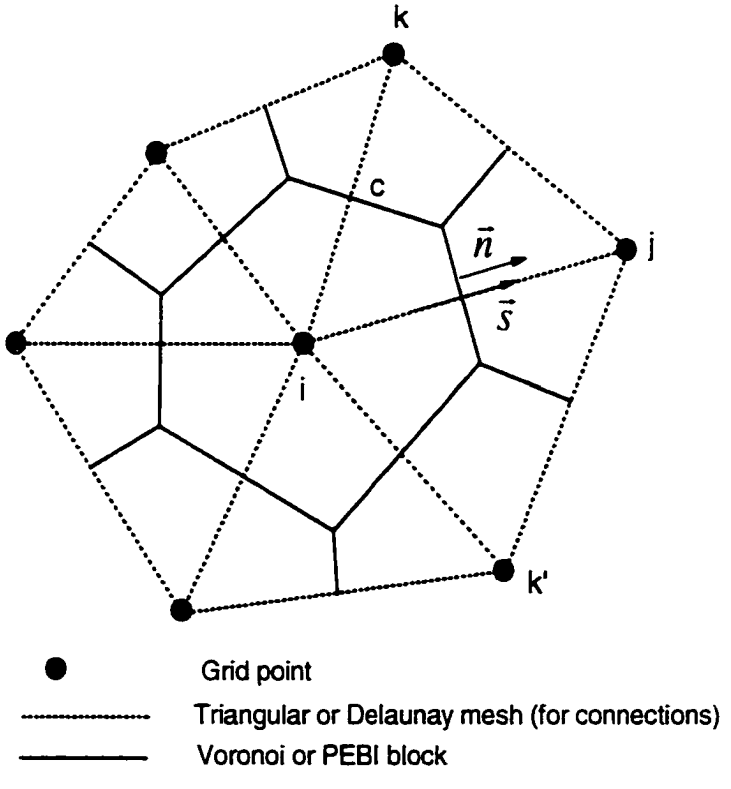

Fig. 2.1. Voronoi or PEBI grid block example

Voronoi grids provide ways to connect the locally refined grid with the base coarse grid. Conventional local grid refinement techniques have some restrictions regarding the grid refinement. Voronoi grids do not have this limitation. Any combination of Cartesian, cylindrical, hexagonal, curvilinear, hydrid-Cartesian, locally refined Cartesian, hydrid hexagonal, etc. can be used in a single domain which increase their flexibility for representing major reservoir features and flow around wells and capturing local details. Besides, the grid system can be generated in the domain by a combination of modules of simple geometry (Cartesian, cylindrical or hexagonal). Each module can be located, rotated and scaled in the physical domain such that the grid geometry conforms to major direction of flow around wells and geologic features[79]. Several modules can be combined in the same domain. Fig. 2.3 presents an example of a PEBI grid generated with the Eclipse Suit.

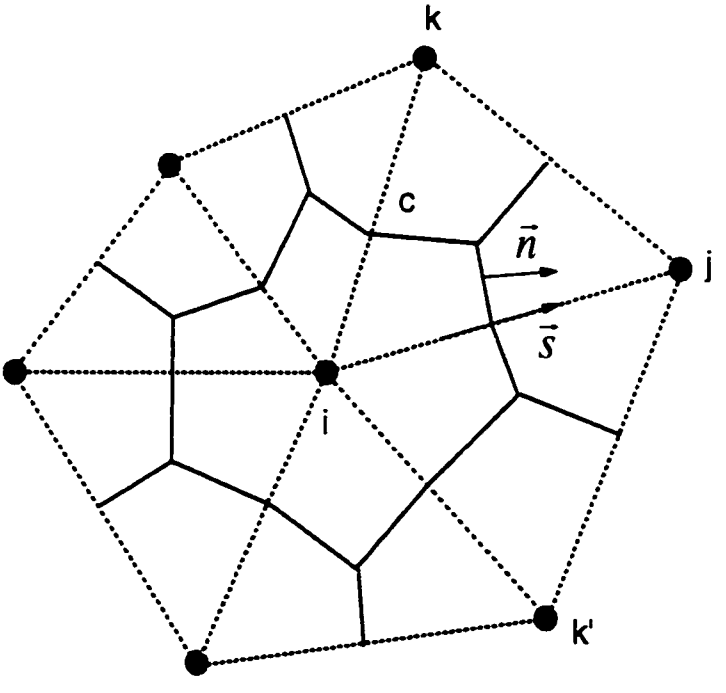

Fig. 2.2. Generalized PEBI grid block example (GPEBI)

2.2.2. GRID AND BLOCK CONSTRUCTION

Several methods have been developed for the generation of PEBI grids. Some of them use to start a triangular mesh (Delaunay mesh), others use a hexagonal mesh, convex quadrangles, radial or other curvilinear meshes. Even though, there are methods on which grid points are arbitrarily distributed inside the domain.

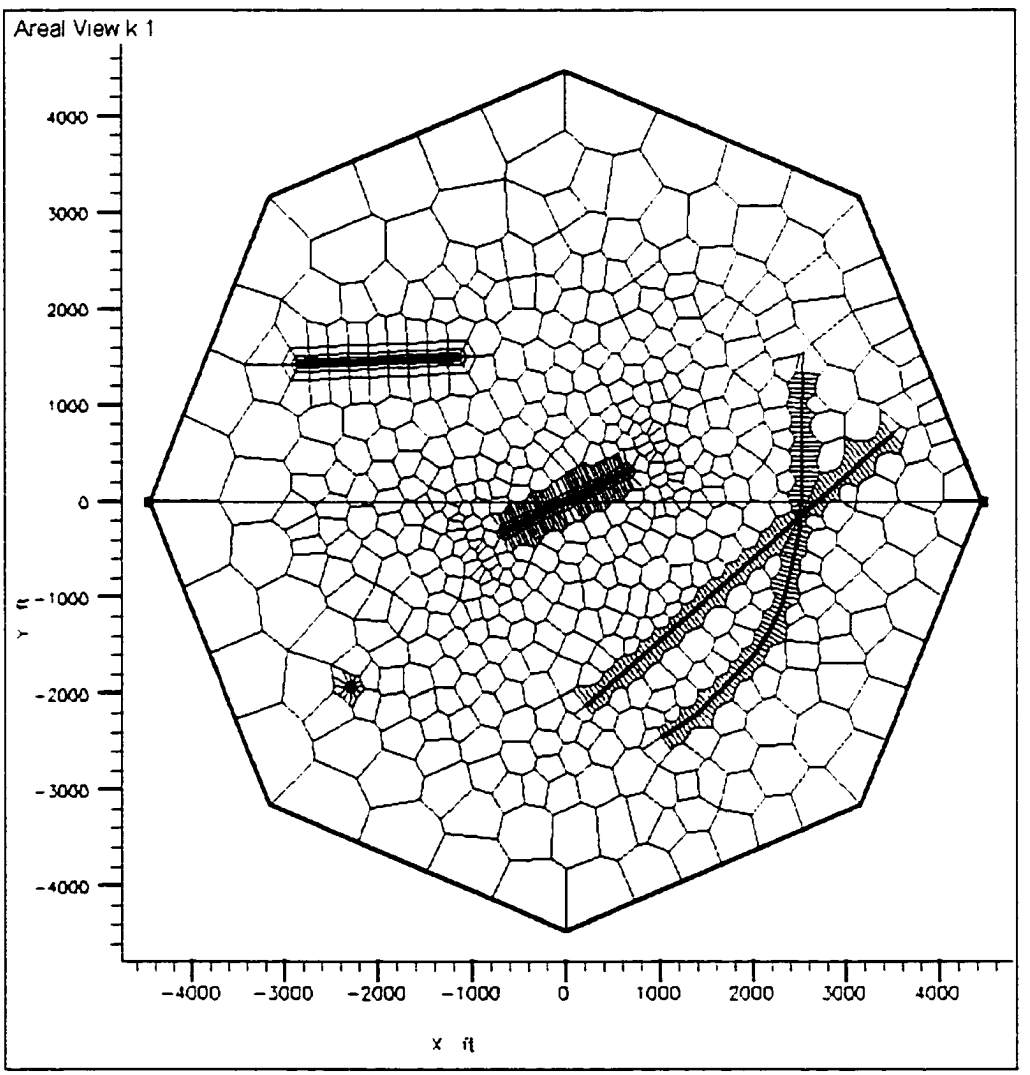

Fig. 2.3. Demonstration of the flexibility of Voronoi Grids (generated with the Eclipse Suit). Upper left: horizontal well, Lower left: vertical well, Center: vertical fractured well, Right: A linear fault intersecting a non-linear fault

Not all discretizations on irregular grids are based on perpendicular bisectors. For a rectangular grid, there are two different ways of constructing grid blocks: block-centered and point-distributed, the latter being equivalent to the perpendicular bisection method.

A complete review of grid generation algorithms was presented by Ho-Le[81]. The one described here, only for 2D PEBI grids, uses the procedure outlined by Frederick et al[82] to generate internal points, but it differs from it by the way the boundaries are treated to satisfy reservoir simulation needs.

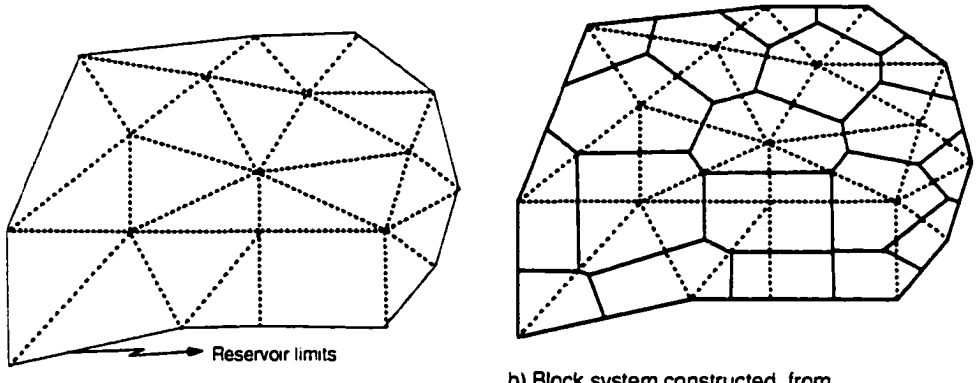

Fig. 2.1. Grid network and block system

Construction of a 2D PEBI grid starts with defining the position of gridpoints and connecting them by straight lines so that a triangular (or rectangular for other methods) mesh is formed. See Fig. 2.4.a. This grid network has to fulfill the following regularity conditions: (1) for any two adjacent triangles, the sum of the two angles at the vertices opposite the common edge of the two triangles must not exceed π and (2) for a triangle at the boundary, the angle at the vertex opposite the boundary must not

exceed $\pi/2$. A triangulation satisfying both conditions is known as Delauney triangulation (See Figs. 2.1 and 2.2). For triangular meshes, considering accuracy, equilateral triangles are optimal. However, for reasons of flexibility, some triangles must be irregular. Once the triangulation is complete, the block system is constructed from the grid network as shown in Fig. 2.4.b.

The main steps for block construction generation is given below[49,75]:

1) Select a grid point i.
2) Select a set of potential neighbors, j, such that the distance between the points i and j is less than two times r_{max} ($L_{ij} < 2\ r_{max}$). All other points are not considered in the following steps.
3) Find the closest neighbor j (minimum L_{ij}).
4) Based on segment ij, look for the next neighbor k in a counter-clockwise sequence, such that the angle $i\hat{k}j$ is the maximum one.
5) Evaluate the radius, r_c, of a circle that passes through points i, j and k. The center of this circle is a corner of the Voronoi polygon (gridblock) of these three points. The corner may be outside of the domain (Fig. 2.5).
6) If $r_c < r_{max}$, then point k is a valid neighbor. Set point $j = k$ and repeat steps 4 and 5. If the first neighbor (the one from step 3) is reached again, then the block i is an internal one, and step 1 should be repeated for a new grid point. r_{max} is an user-input property which defines the maximum size for grid construction.
7) If $r_c > r_{max}$, or no point is found in the search, then segment ij is part of the external boundary. Proceed to step 8.

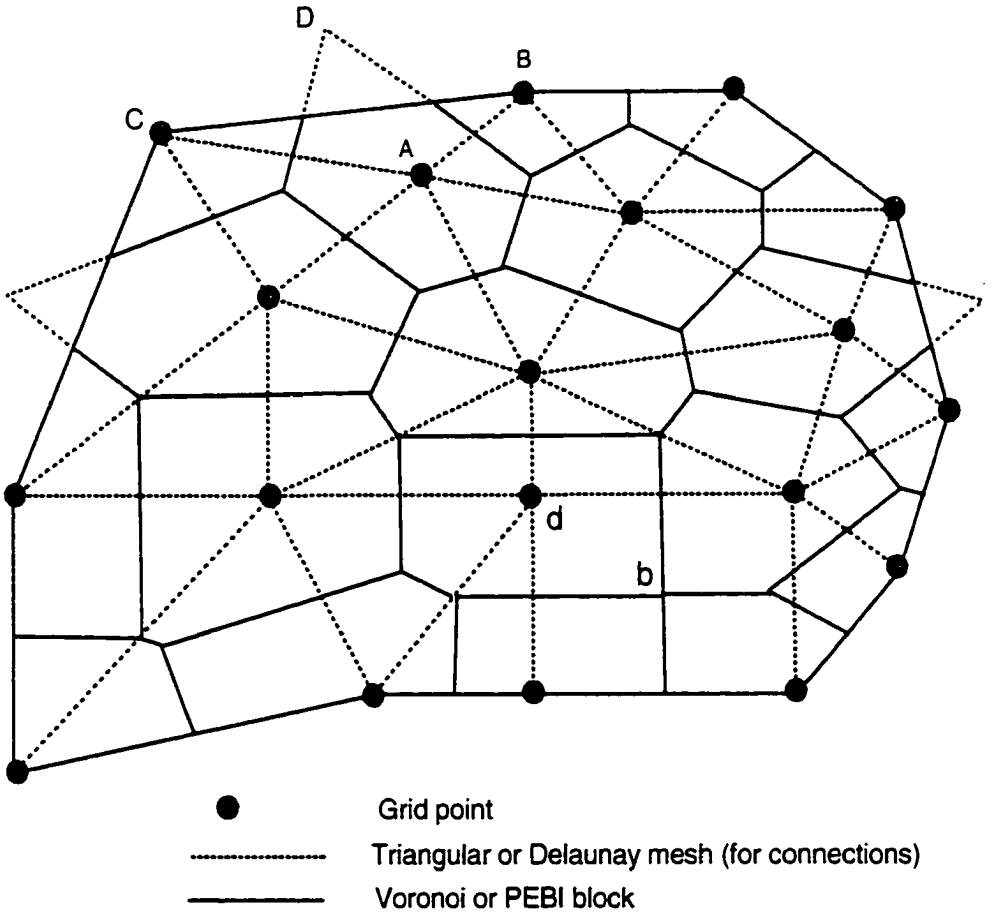

Fig. 2.5. Voronoi grid systems

8) After all the grid connections and boundaries have been generated (steps 1 through 8) then go back to the boundary blocks and evaluate the angles between boundary points and adjacent interior points, such as $C\hat{A}B$ in Fig. 2.5.

9) If $C\hat{A}B < \pi/2$ then the middle point of the segment BC is a corner of the Voronoi polygon (gridblock) of points B and C.

10) If $C\hat{A}B > \pi/2$ then cut the part of block A that would lie outside the boundary and adjust the geometry of blocks B and C (Fig. 2.5).

11) Finally, remove all connections with width b less than a very small number (recommended 0.001 times the block perimeter[49]).

The above described method suffer from several deficiencies[75]:

a) If is not possible to control the final position of the grid points.

b) The grid increasing in density in some parts of the domain causes grid coarsening in other parts as the number of grid points inside the domain remains the same.

c) A totally irregular gridblock system also causes problems in the output and in the graphics.

2.2.3. PEBI GRID STYLES[70]

The Eclipse Suit recognizes five types of PEBI grids[70]. Uniform grids specified with fixed x and y dimensions:

- Hexagonal
- Rectangular

Expanding grids with a growth factor from some location out to a uniform grid boundary beyond which no further growth takes place:

- Variable
- Circular
- Elliptical

Circular and elliptical grid styles should only be used with models with one well[70].

2.2.4. GRID CONTROLS[70]

In the Eclipse Suit, this controls the type of local grid used around the well. It is very important to have small grid blocks near the well in order to model the transient response. The following parameters control the grid:

- Grid style. If a radial style is chosen then the number of theta and radial divisions can be set. If another style is chosen the local grid will be a single cell with a radius of the same size of the radius field. For bulk style gridding the cell radius is the same as that for the main volume.
- Radius. Outer radius of the local grid region
- Radial cells, sector/sides. The number of radial and azimuthal divisions within the local grid or the number of sides of the single cell.

Table 2.1. Reservoir coordinates

X	Y	Boundary	X	Y	Boundary
4565.4	0	Closed	-4565.4	0	Closed
3228.2	3228.2	Closed	-3228.2	-3228.2	Closed
0	4565.4	Closed	0	-4565.4	Closed
-3228.2	3228.2	Closed	3228.2	-3228.2	Closed

2.3. PEBI GRIDS APPLICATION TO SIMULATE PRESSURE TRANSIENT BEHAVIOR

This section will focus on the application of PEBI grids to simulate the pressure transient behavior (drawdown) of single vertical wells, single horizontal wells and single artificially fractured vertical wells. Numerical solutions are compared to analytical solutions to determine the accuracy and applicability of a given grid style.

Table 2.2. Reservoir, well and rock data used for simulation

Property	Value
k, md	30
h, ft	50
ϕ, %	23
c_f, psia	$1x10^{-6}$
T, °F	200
Tops depth, ft	10000
Rock type	Limestone
p_i, psia	5200
r_w, ft	0.4
q, bpd	3000
μ, cp	0.3
c_o, $psia^{-1}$	$1.28x10^{-5}$
B, rb/STB	1.48
ρ_o, lbm/ft^3	55
ρ_w, lbm/ft^3	62.428
ρ_g, lbm/ft^3	0.05
T_{sc}, °F	60
P_{sc}, psia	14.7

2.3.1. VERTICAL WELLS

The analytical solution including wellbore storage and damage for vertical wells is given in Appendix A. Several numerical simulation runs were performed using the five grid styles above mentioned. Reservoir, fluid, PVT data and rock properties are defined in tables 2.1 through 2.4. The reservoir was assumed to possess an octagonal shape with a well centered in it at 0, 0 ft and radius 4565.4 ft. This particular shape reduces the possibilities of failure of the gridding algorithms.

Table 2.3. Main simulation parameters used in the Eclipse Suit

Time step mode	Transient
Timestep pressure change	2.3932 psia
Initial time step	0.0001 hrs
Maximum time step	15 hrs
Maximum time step growth	1.2 hrs
Simulation length	150 hrs
Report steps per period	1
Restart option	On
Fluid model	Black oil
Grid type	Corner point
Model type	2D
Solution type	Fully implicit

Table 2.5. Grid controls

Grid style	**Radius of radial grid, ft**	**number of radial cells**	**Sectors/ Sides**	**Dimensions**	**Total number of cells**
Variable	68.9655	19	12	102*20*1	546
Elliptical	30.0000	32	32	48*33*1	1088
Circular	68.9655	19	12	40*20*1	427
Hexagonal	68.9655	19	12	52*21*1	546
Rectangular	68.9655	19	12	48*20*1	520

Table 2.6. Absolute errors for several PEBI grids

Grid style	**Absolute error, %**
Variable	0.375
Elliptical	18.775
Circular	0.455
Hexagonal	3.153
Rectangular	3.364

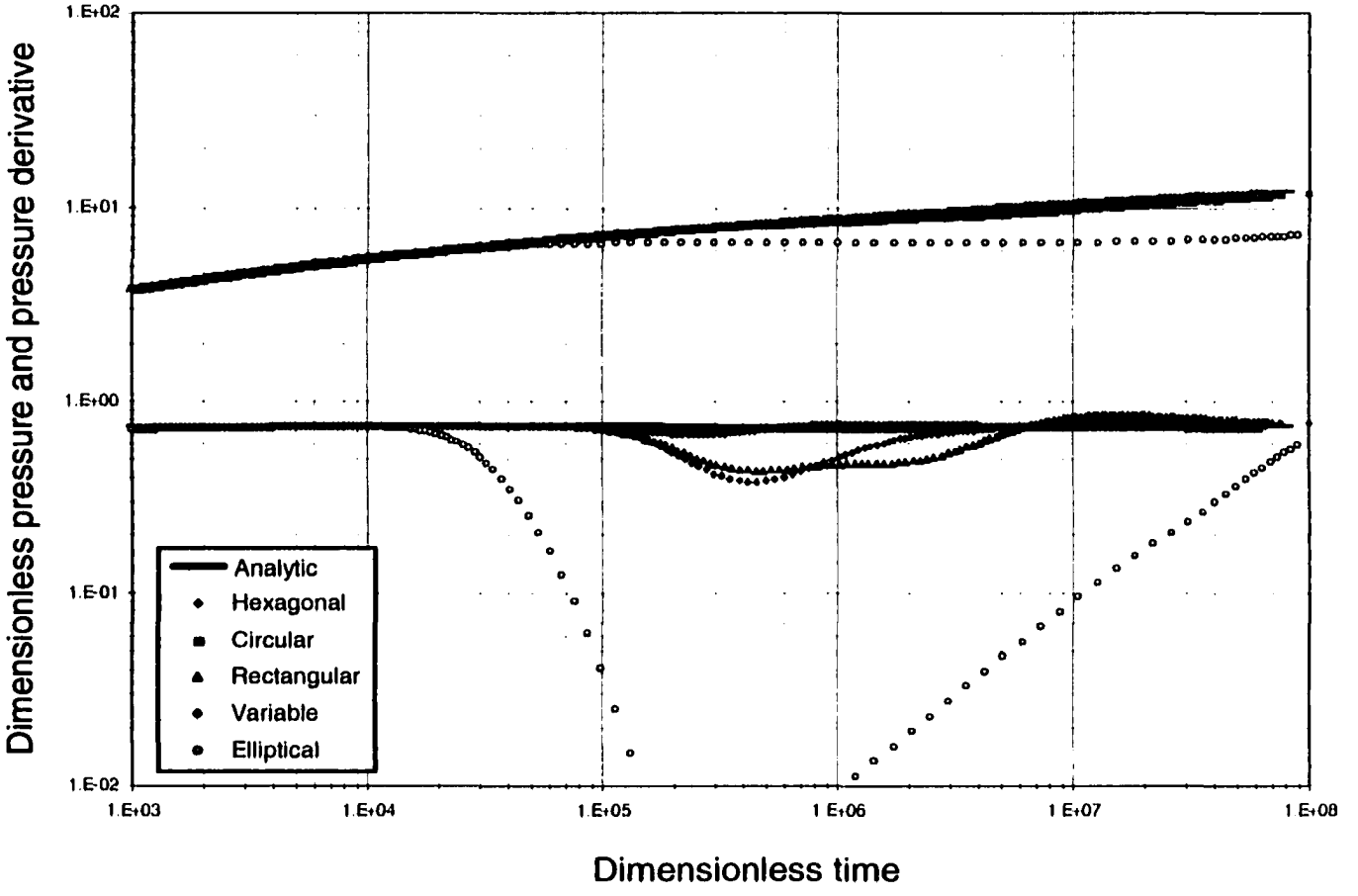

Fig. 2.6. Pressure and pressure derivative curves generated using different PEBI grid styles

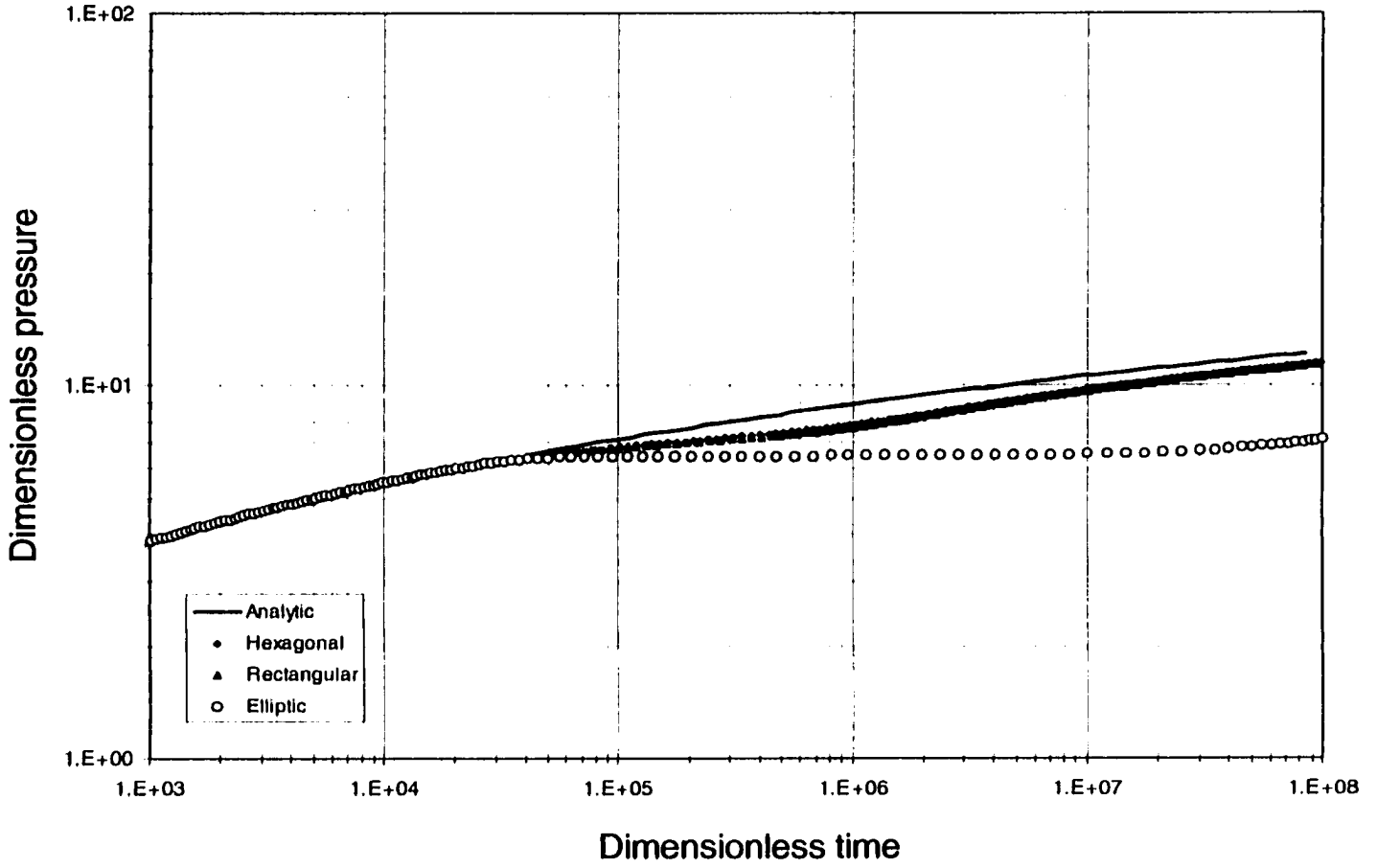

Fig. 2.7. Pressure plot for a vertical well simulated numerically using elliptical, hexagonal and rectangular PEBI grid styles

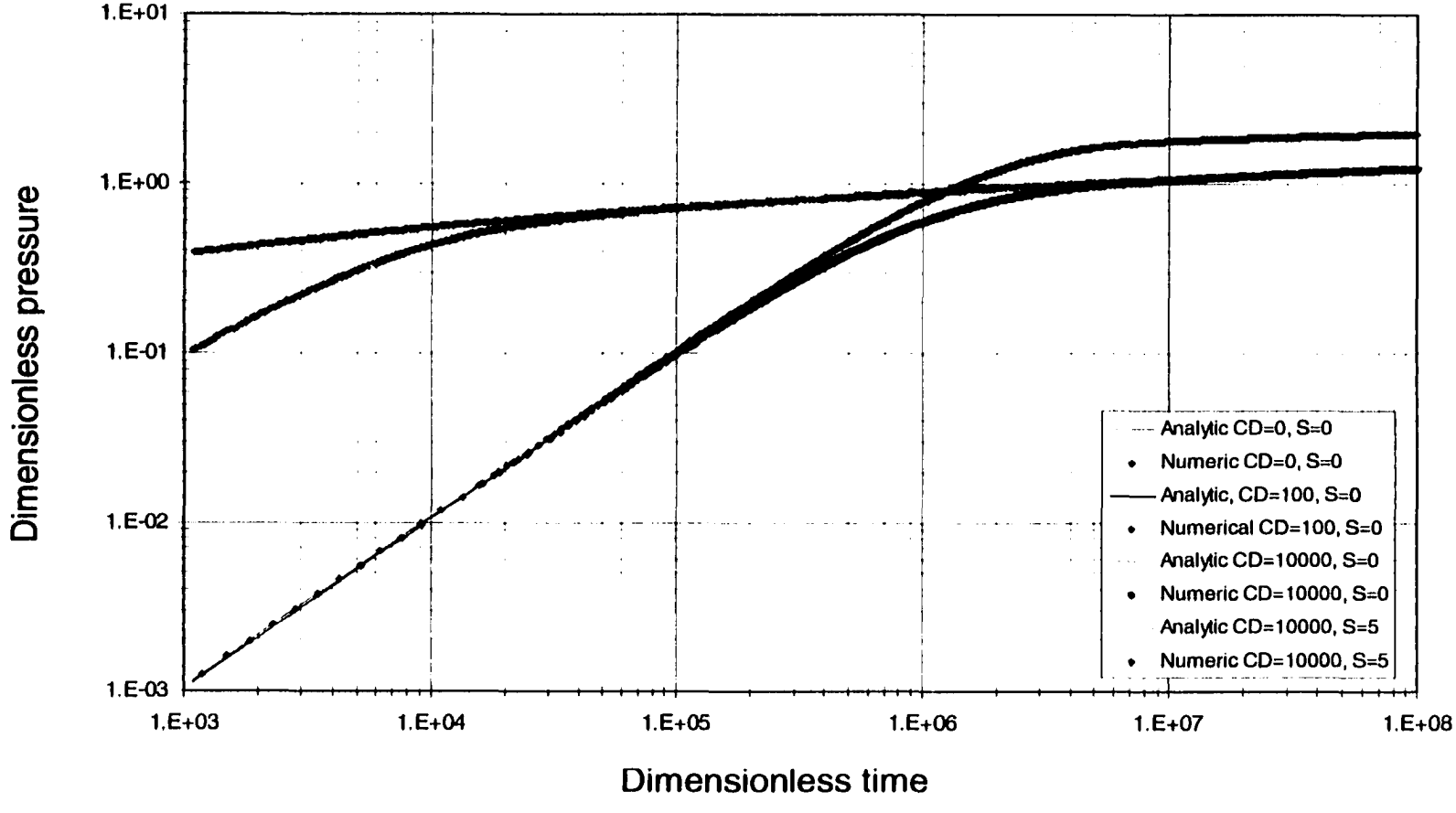

Fig. 2.8. Pressure plot for a vertical well having damage and wellbore storage generated using a circular PEBI grid style

The number of grid points was gradually increased until the numerical solutions close matches the analytical solutions. In several cases increasing the number of gridpoints did not improve significantly the numerical solution. The grids used for simulation are shown in Figs. C.1 through C.5. Simulation results are reported in Fig. 2.6 and tables D.1.a and D.1.b. Table 2.6 shows the absolute error deviation of the numerical solution from the analytical one. Notice in Fig. 2.6 that the elliptical grid provides very erroneous solutions for this case. Besides, the absolute error keeps increasing. The absolute error estimated from the numerical results for an Elliptical grid to the analytical solution has a mathematical average of 18.77 %, see table 2.6. Moreover, the behavior of the pressure derivative curve differs significantly from the actual analytical case. A similar behavior, although less severe, is observed for the rectangular grid case. The best solutions were attained with the variable and circular grid styles. Arithmetical errors for these cases were below 0.5 %. It is evident, from Table 2.6 that the number of grid points is about the same for all the grid styles but the elliptical. Even though, the number of grid points used for this grid style (elliptical) is about as much as twice the remaining grid styles, the numerical solution is highly mistaken. The fact that the numerical solution at early time is very good, does not make the general behavior to be unreliable.

For the three worse solutions, namely: elliptical, rectangular and hexagonal, new runs were performed increasing the number of grid points by a factor of 2.4, 7.02 and 7.13, respectively, to see the improvement of the numerical solutions. Table 2.7 contains the gridding parameters and Fig. C.6 presents the grid system used for these simulations. Results are reported in Fig. 2.7. In spite of the increment of computational

time, the solutions improved insignificantly and do not compensate the involved computation effort.

Table 2.7. Grid controls for hexagonal, elliptical and rectangular PEBI grids

Grid style	**Radius of radial grid, ft**	**number of radial cells**	**Sectors/ Sides**	**Dimensions**	**Total number of cells**
Elliptical	30	64	32	56*65*1	2632
Hexagonal	30	64	40	103*65*1	3863
Rectangular	30	64	40	96*65**1	3708

Table 2.8. Grid controls for hexagonal, elliptical and rectangular PEBI grids

Wellbore storage, C_D	**Skin Factor, S**	**Radius of radial grid, ft**	**number of radial cells**	**Sectors /Sides**	**Dimensions**	**Total number of cells**
0	0	68.9655	19	12	102*20*1	546
100	0	68.9655	19	12	102*20*1	546
10000	0	68.9655	19	12	102*20*1	546
10000	5	68.9655	19	12	102*20*1	546

It has been shown that for vertical wells, the circular and variable PEBI grids provide very good results with the smaller number of gridpoints. Even though, the variable grid gives the smallest average error, its pressure derivative suffers a slight deviation from the actual path, as can be seen in Fig. 2.6. It is thereafter concluded that circular PEBI grids are the best tool for this case.

The application of circular PEBI grids was extended to vertical wells having damage and wellbore storage. Table 2.8 shows the grid controls for these runs. As can be seen in tables D.2.a and D.2.b the average absolute error is lower than 0.5 %. Refer also to Fig. 2.8 to observe how well the numerical curves match the analytical solutions.

2.3.2. VERTICAL WELLS INTERSECTED BY A HYDRAULICAL FINITE-DONDUCTIVITY FRACTURE

In order to establish which grid style should be appropriate to better describe fractured-well performance, the five grid styles namely: variable, rectangular, hexagonal, circular and elliptical were used to simulate pressure drawdown tests. Dimensionless fracture conductivities ranging from 0.1 to 300 were employed in the simulations. The semi-analytical solution presented by Cinco-Ley et al[18], and provided in appendix A, is used as the matching criterion. The mathematical models are provided in chapter 3.

The fracture orientation, traditionally lying over the x-axis, was rotated from 0 to 90 degrees to observe the capability of PEBI grids handling non-orthogonal systems. Fracture parameters are given in Table 2.9.

Table 2.9. Fracture parameters

Parameter	Value
x_f, ft	100
ϕ_f, %	10
w, ft	0.05
k_f, D	6 to 18000
c_t, 1/psia	$1x10^{-6}$

Table 2.10. Grid control parameters applied to all studied PEBI grids applied to fractured wells

Grid Style	Radius of radial grid, ft	No. of radial cells	Sectors /Sides	Fracture cell length, ft	Dimensions	Total number of cells
Elliptical	15	4	32	20	92*19*1	702
Circular	5	20	64	5	78*55*1	2602
Hexagonal	5	4	32	5	70*31*1	1044
Rectangular	5	4	32	5	66*31*1	1018
Variable	5	4	32	5	287*31*1	1610

Table 2.11. Absolute errors for several PEBI grids (hydraulically fracture vertical wells)

Grid style	Absolute error, %
Variable	12.59
Elliptical	1.43
Circular	64.29
Hexagonal	12.35
Rectangular	11.72

Fig. 2.9 presents the pressure behavior obtained numerically for a vertical fractured well using the whole set of PEBI grid styles under study. The gridding control parameters are reported in Table 2.10. The dimensionless fracture conductivity used was 1. Refer to Figs. C.7 through C.10 to see the grid systems used for these simulations. Data for generating such a plot are presented in tables D.3.a and D.3.b. From Fig. 2.9 is virtually seen the high efficiency performed by the simulation run with an elliptical PEBI grid. Its average absolute error was less than 1.5 %. See Table 2.11. Although, the circular grid performs very well at very early times, the overall performance is very poor since the numerical solution deviates continuously from the numerical one. The other three grid styles display a more constant behavior. However, the resulting deviation error above 10 % leads us to not apply them to study transient fractured well behavior.

2.3.2.1. EFFECT OF FRACTURE CONDUCTIVITY

It was also found that the Elliptical PEBI grids, which provide the best numerical solution for vertical fractured wells, have a limited application for

dimensionless fracture conductivities greater or equal to 1. Another experiment was run for dimensionless fracture conductivities of 0.1 and 0.5. The gridding parameters for these two cases are given in Table 2.12. Results of simulation runs are reported in Table D.4 and D.5 and Figs. 2.10 and 2.11.

Table 2.12. Grid control parameters for Elliptical PEBI grids applied to fractured wells

C_{fD} - Case	Radius of radial grid, ft	No. of radial cells	Sectors /Sides	Fracture Cell length, ft	Dimensions	Total Number of cells
0.1 - Case 1	15	8	32	25	84*26*1	899
0.1 - Case 2	5	8	32	5	148*40*1	3462
0.5 - Case 1	15	8	32	25	84*26*1	899
0.5 - Case 2	5	8	32	5	148*40*1	3462

For a dimensionless fracture conductivity of 1, it was seen that simulations using an Elliptical grid provides reliable results since absolute error was 1.43 %. Refer to Table 2.13 to note that the error reduces as the gridpoint number increases and as the fracture conductivity goes from 0.1 to 0.5. For the first case, C_{fD}=0.1 the deviation errors are around 30 % even though the gridpoint numbers was increased almost 4 times. For the second case, increasing 3.85 times the number of gridpoints took down the deviation error from 11.33 to 4.15 %. It still does not satisfy a good matching criteria. Then, we conclude that the Elliptical PEBI grids do not provide accurate results for dimensionless fracture conductivities below 1.0. An explanation to this phenomenon is that the pressure gradients in the fracture become extremely high as the fluid approaches the wellbore, then the computation of transmissibilities is not accurate.

Table 2.13. Absolute errors for Elliptical PEBI grids and C_{fD}=0.1 and 0.5.

Case 1 - Error, %	Case 2 - Error, %
35.25	27.16
11.33	4.15

Table 2.14. Recommended grid control parameters to simulate transient pressure behavior of vertical wells using an Elliptical PEBI grids

Dimensionless fracture conductivity	Maximum Radius of radial grid, ft	Minimum Number of radial cells	Sectors /Sides	Minimum Fracture cell length, ft
1	15	4-8	32	5-20
10	15	4	32	5-20
20	10	4	32	5-20
30	5-10	2	32	5-20
50	5-15	2	32	5-20
70	5-15	2	32	5-10
80	5-15	2	32	5-10
100	5-20	2-4	32	10-30
150	5-20	2	32	5-30
200	5-20	2	32	5-30
300	5-20	2	32	5-30

From several numerical simulation runs performed during this study, the range of grid control parameters provided in Table 2.14 are recommended to obtain reliable simulated results for the use of PEBI Elliptical grids in hydraulically fractured wells. Simulations results for dimensionless fracture conductivities other than one were also performed. See results in tables D.6.a and D.6.b. It is shown there a deviation error lower than 1.5 %. Comparison of the simulation results against analytical solutions can be better observed in Fig. 2.12. Grid control parameters are presented in Table 2.15. An example of the used grids is shown in Fig. C.11.

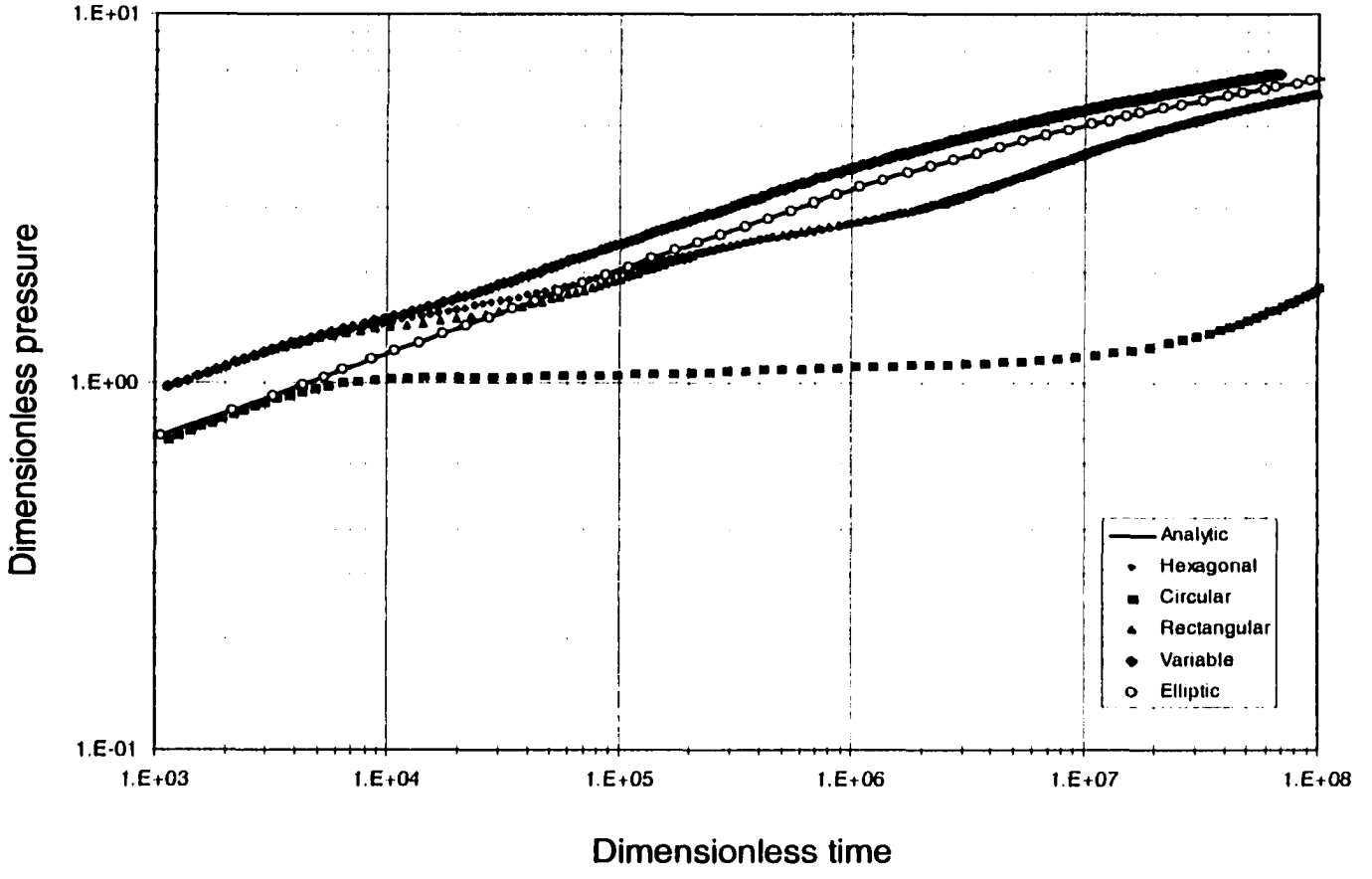

Fig. 2.9. Pressure plot for a vertical fractured (C_{fD}=1) simulated using Circular, Hexagonal, Rectangular, variable and Elliptical PEBI grid styles

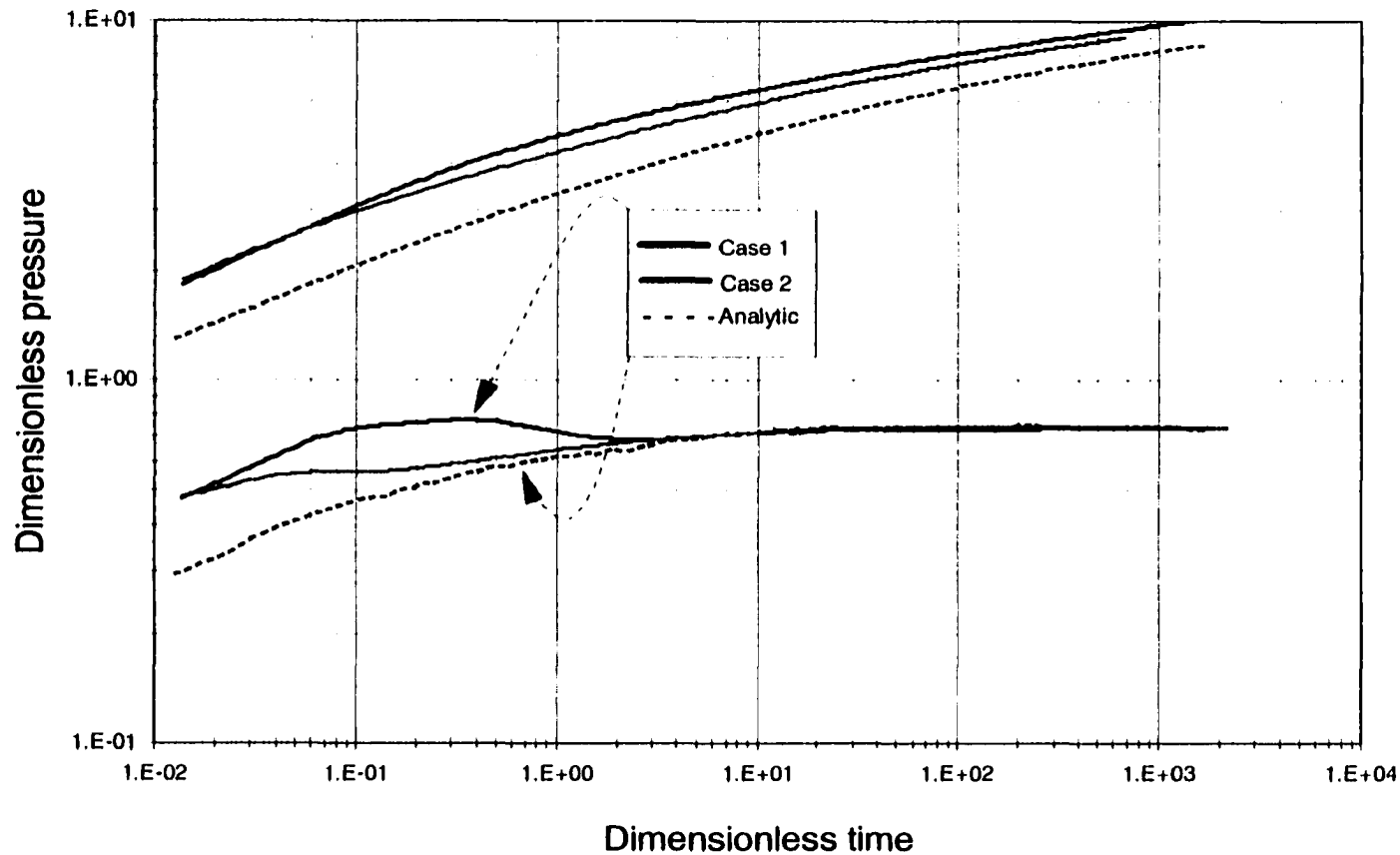

Fig. 2.10. Pressure plot for a vertical fractured (C_{fD}=0.1) simulated an Elliptical PEBI grid (Case 1 – 899 gridpoints)

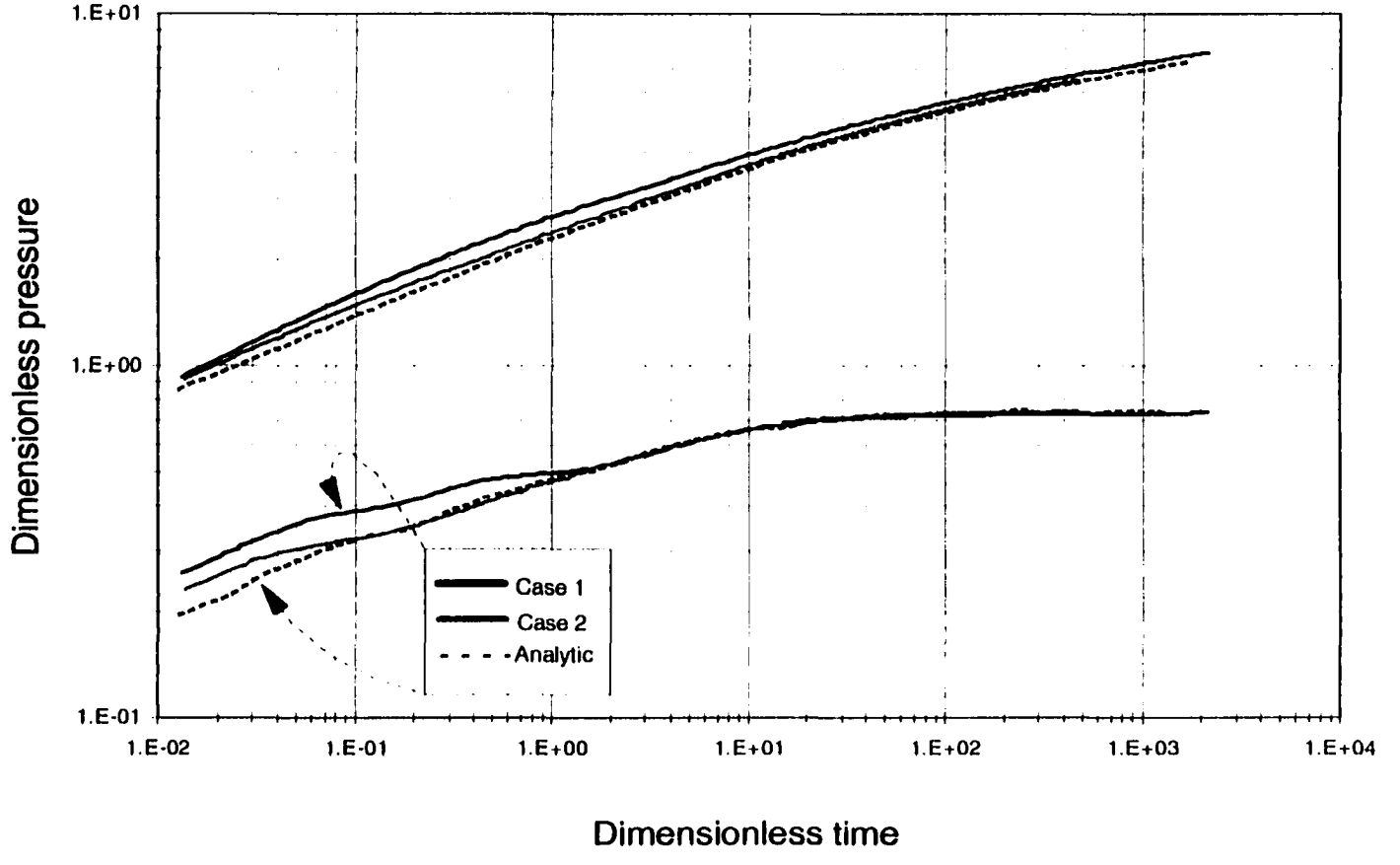

Fig. 2.11. Pressure plot for a vertical fractured (C_{fD}=0.5) simulated using an Elliptical PEBI grid (Case 2 –3462 gridpoints)

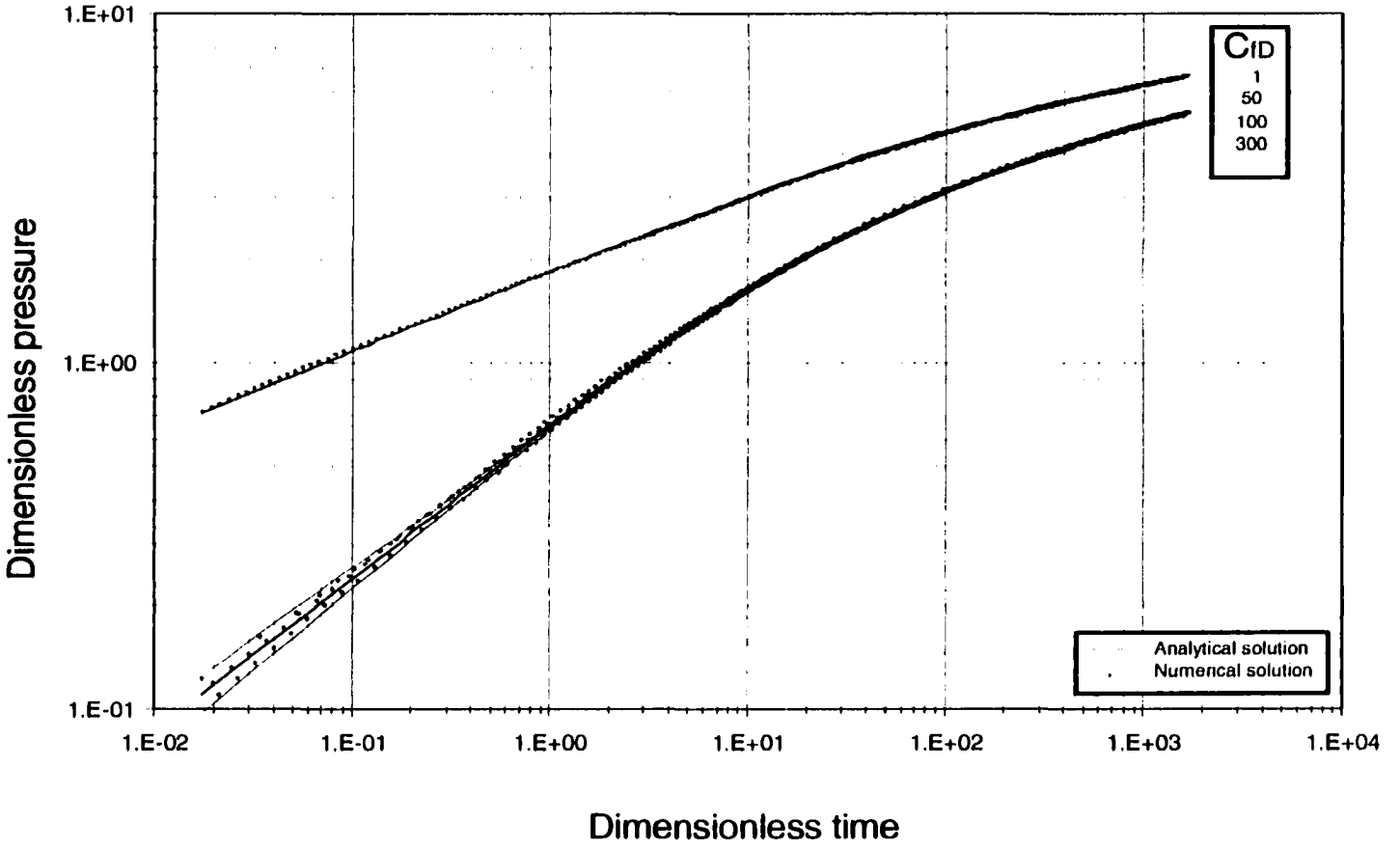

Fig. 2.12. Pressure plot for a vertical fractured simulated using an Elliptical PEBI grid for several dimensionless fracture conductivity values

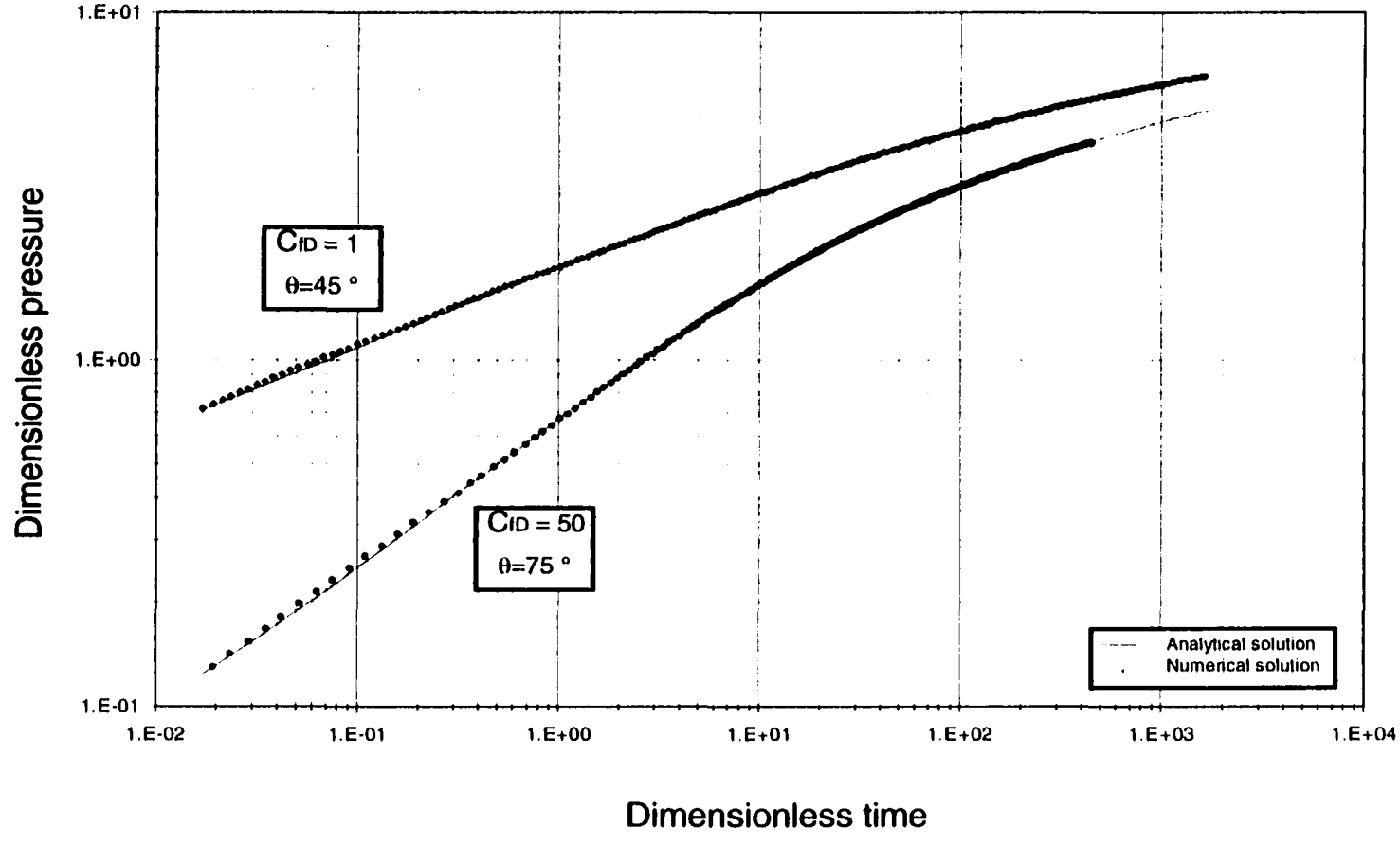

Fig. 2.13. Pressure plot for a vertical fractured simulated using an Elliptical PEBI grid for dimensionless fracture conductivity values of 1 and 50 and fracture inclination angle values of 45 and 75 degrees

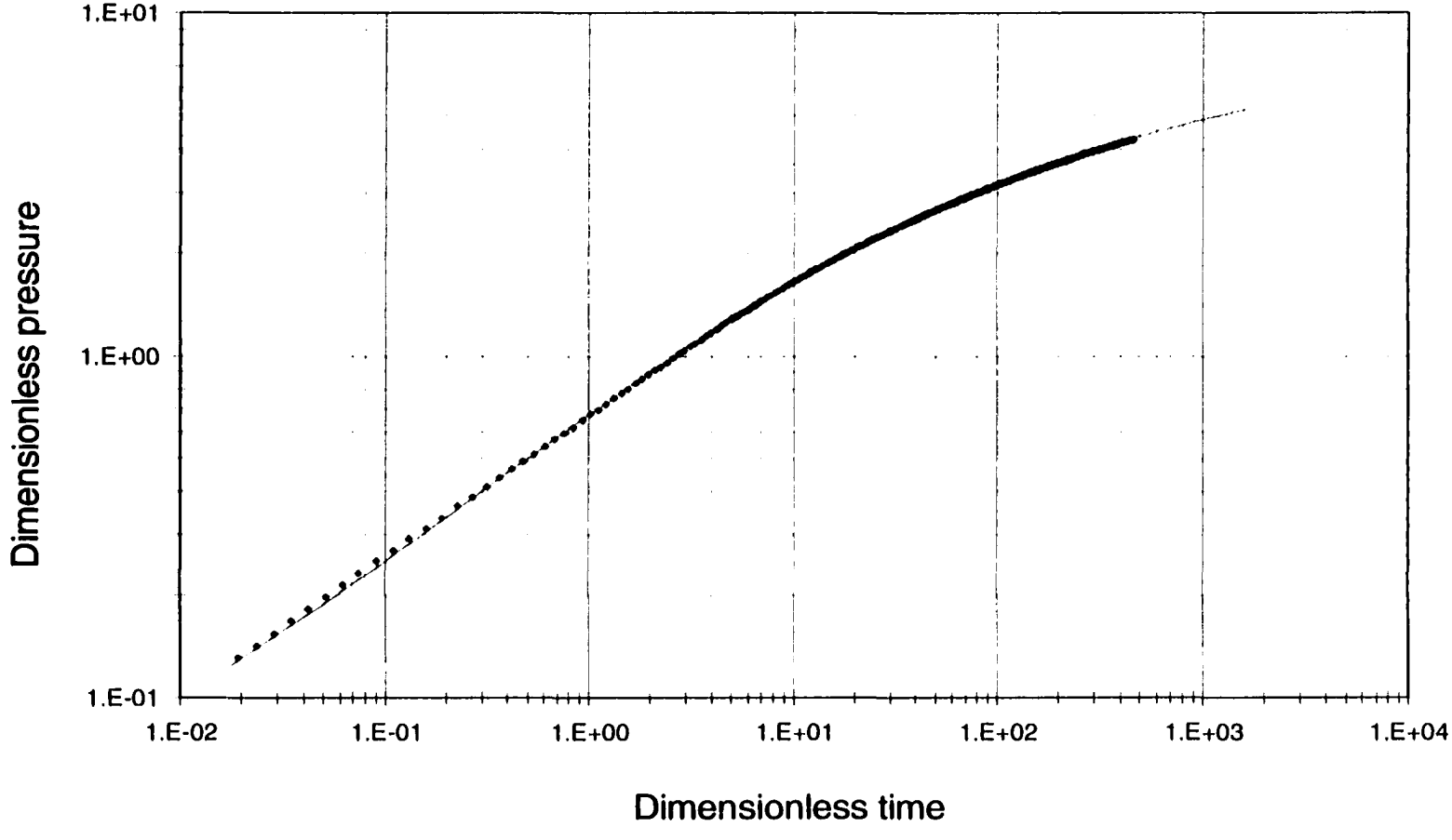

Fig. 2.14. Pressure plot for a vertical fractured simulated using an Elliptical PEBI grid for a dimensionless fracture conductivity value of 50 and a fracture inclination angle of 60 degrees

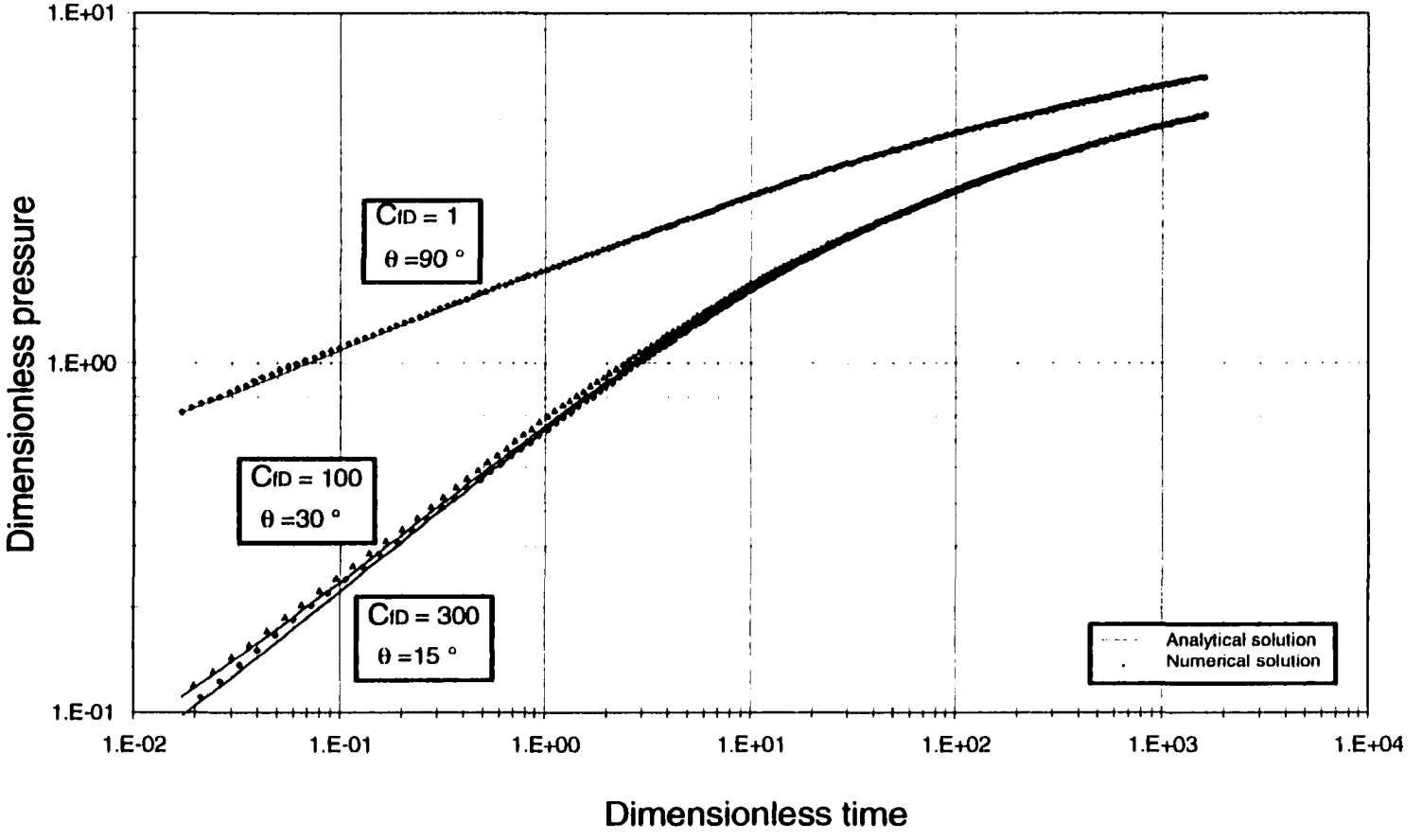

Fig. 2.15. Pressure plot for a vertical fractured simulated using an Elliptical PEBI grid for dimensionless fracture conductivity values of 1, 100 and 300 and fracture inclination angles of 15, 30 and 90 degrees

Table 2.15. Grid control parameters for Elliptical PEBI grids applied to fractured wells with different fracture conductivities

C_{fD}	Radius of radial grid, ft	No. of radial cells	Sectors/ Sides	Dimen-sions	Total No. of cells	Fracture cell length, ft
1	4	4	32	92*19*1	702	15
50	2	2	32	112*20*1	985	10
100	2	2	32	88*16*1	498	20
300	2	2	32	112*20*1	985	10

2.3.2.2. EFFECT OF NON-ORTHOGONALITY

It is of crucial importance to determine if the Elliptical PEBI grid has the flexibility of accurately provide numerical results when the fracture is not oriented along the x-axis and it has been rotated any angle, instead. Therefore, Elliptical PEBI grids were designed to run numerical simulations with certain rotation of the hydraulic fracture within a wide range of fracture conductivities. The gridding control parameters used during this experiment are shown in Table 2.16 and results are reported in tables D.7.a and D.7.b and Figs. 2.13 through 2.15. See the type of designed grid systems in Figs. C.12 through C.15.

From the results just obtained, it is therefore demonstrated that PEBI grids, specifically Elliptical style, are capable of reliably handle non-orthogonal systems that lie on the Cartesian coordinate plane.

Table 2.16. Grid control parameters for Elliptical PEBI grids applied to fractured wells with different fracture conductivities and different fracture-orientation angles.

C_{fD}	θ, Degrees	Radius of radial grid, ft	No. of radial cells	Sectors/ Sides	Dimensions	Total No. of cells	Fracture cell length, ft
300	15	5	2	32	148*29*1	1571	5
100	30	20	2	32	104*18*1	714	20
50	45	5	2	32	148*29*1	1570	5
50	60	5	2	32	148*29*1	1578	5
1	75	15	4	32	92*19*1	702	15
1	90	15	4	32	92*19*1	702	15

2.3.3. HORIZONTAL WELLS

In a similar fashion, the five PEBI grid styles under consideration were employed to perform numerical simulation of transient well pressure in horizontal wells. Numerical drawdown solutions were compared to the analytical solution proposed by Goode and Thambynayagam[86]. Input data for these simulations are given in Table 2.17 through 2.20. Reasonable accurate numerical solutions were obtained and no effort was concentrated to improve the accuracy of the solution by increasing the number of gridpoints. Moreover, to capability of PEBI grids to handle non-orthogonal system, the horizontal well was rotated with respect to the x and y coordinate systems. The Numerical solution for an angle of zero degrees was very slightly different to those from angles of 45 and 90 degrees. Then, reports for 45 and 90 degrees, which were essentially the same, are provided. Examples of the designed grid systems for these cases are shown in Figs. C.16 though C.20.

Notice from Figs. 2.16 and 2.17 that all the mentioned PEBI grids provide good results for horizontal wells in any angle. It is easy to improve more the accuracy

of the solutions by incrementing the number of gridpoints. However, it was considered no need of doing so since the numerical results are with an acceptable margin of about 2.5 %. The pressure derivative curve is provided in both log-log and semilog scale. The reason of the semilog scale is to be able to distinguish the solution trends. Absolute error deviations are shown in Table 2.21. Notice that although the absolute errors are about the same, the elliptical grid provides an overall trend which better matches the analytical solution. However, any of the studied PEBI grids can be used to simulate horizontal well pressure behavior.

As a final remark, the mathematical and numerical conceptions of treating horizontal wells is the same as for vertical wells. In other words, mathematically speaking, a fracture is identical to a horizontal well. Horizontal wells just have a radial profile instead of a rectangular profile in vertical wells. To the simulator this means very little, as connections are connections. If this is the case, the following question arises: why are horizontal wells described by all the studied PEBI grid styles and vertical wells with hydraulic fractures not ? A possible explanation to that question is due to the flow geometry. In a vertical well, there exists a bilinear flow inside the fracture from the tips to the well while in horizontal wells a linear behavior is observed. Therefore, the estimation of the average transmissibilities is more uniform for horizontal wells, then the simulation results could be more reliable.

Table 2.17. Reservoir coordinates

X	Y	Boundary	X	Y	Boundary
16405	0.0	Closed	-16405	0.0	Closed
11600	11600	Closed	-11600	-11600	Closed
0.0	16405	Closed	0.0	-16405	Closed
-11600	11600	Closed	11600	-11600	

Table 2.18. Reservoir, well and rock data used for simulation

Parameter	Value	Parameter	Value
k, md	200	T, °F	200
K_z/k_r	1	Tops depth, ft	6000
H, ft	60	Rock type	Limestone
L_w, ft	3000	P_i, psia	3000
Well position	0, 0	r_w, ft	0.4
r_e, ft	16405	q, bpd	4000
Perforation length, ft	3000	μ, cp	0.65
C_D	500	c_o, $psia^{-1}$	$2x10^{-5}$
S	5	β_o, rb/STB	1.25
Simulation time, hr	160	ρ_o, lbm/ft^3	54
ϕ, %	20	T_{sc}, °F	60
C_f, psia	$1x10^{-6}$	P_{sc}, psia	14.7

Table 2.19. Grid control parameters

Parameter	Value
Extent of Cartesian grid, ft	413.7931
Distance to first point, ft 0.8	0.8
Number of transverse cells	14
Number of Longitude cells	14

Table 2.20. Number of grid points

Type of Cell	Number of cells
Circular	4795
Elliptical	4851
Rectangular	5495
Hexagonal	5684
variable	4403

Table 2.21. Absolute errors for a horizontal well using all the studied PEBI grids

Grid style	Absolute Error, %
Elliptical	2.38
Hexagonal	2.38
Variable	2.44
Rectangular	2.57
Circular	2.36

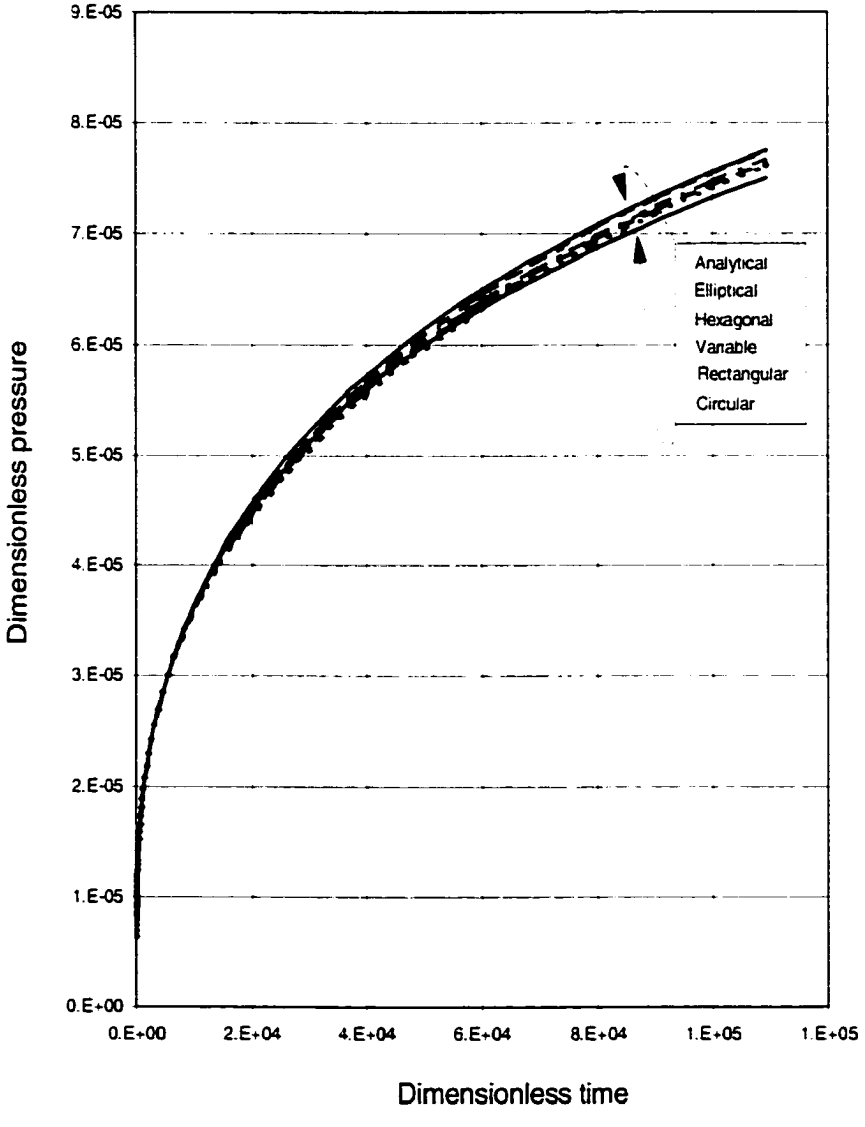

Fig. 2.16. Pressure Log-Log plot for a horizontal well simulated using all the studied PEBI grid styles

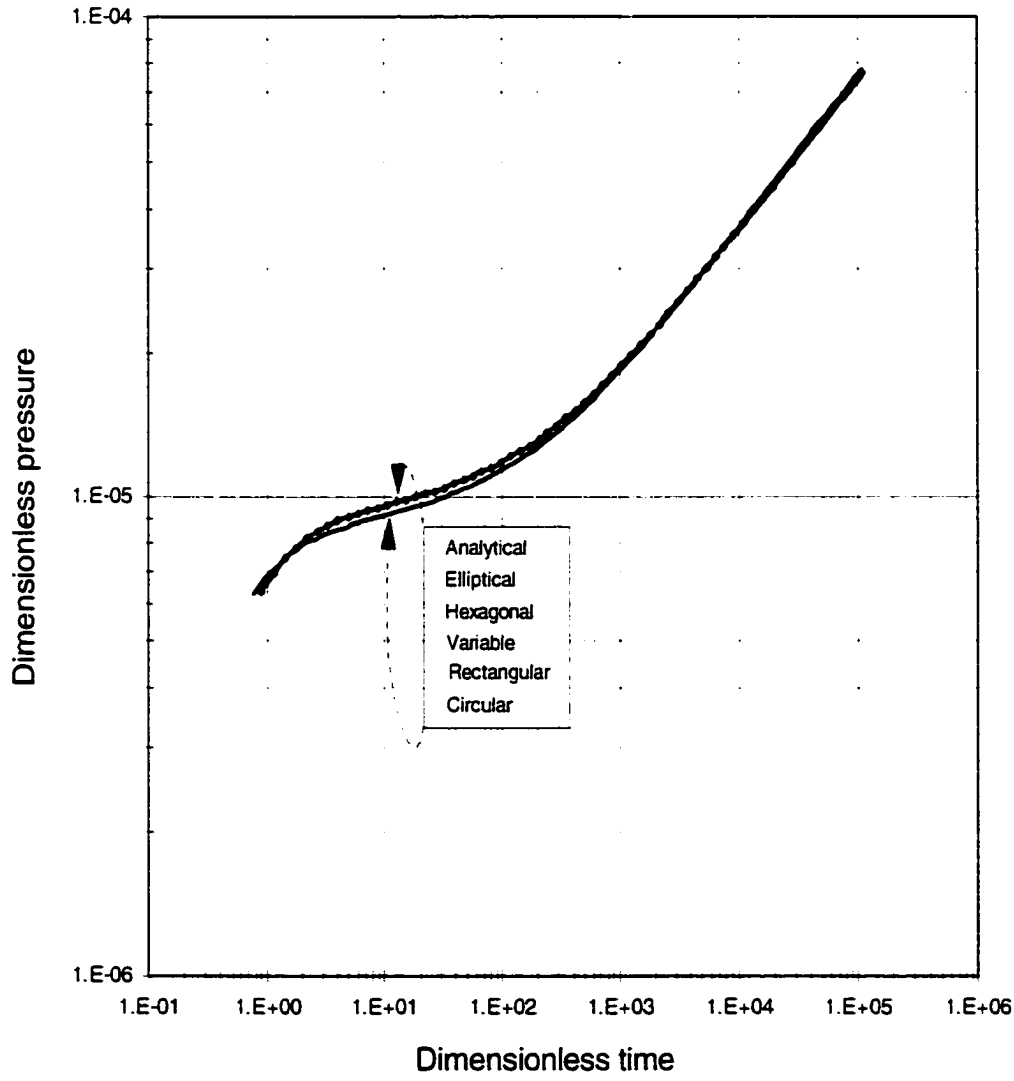

Fig. 2.17. Pressure Semilog plot for a horizontal well simulated using all the studied PEBI grid styles

CHAPTER III

MATHEMATICAL FORMULATION AND SOLUTION

The purpose of this chapter is to describe the physical systems used in this study by introducing a set of mathematical equations. Before the equations are presented, all the required assumptions are stated. Then, models for reservoir and fracture systems are described along with the respective initial and boundary conditions to which the systems are subject. We also define a set of dimensionless quantities to better understand and generalize the transient pressure behavior so that the *Tiab's Direct Synthesis Technique* can be derived.

3.1. HYDRAULIC FRACTURED VERTICAL WELL WITH A BRANCH FRACTURE

Fig. 3.1 illustrates a schematic view of the reservoir situation in which we are interested. The following assumptions are stated:

- The physical system is a single layer circular reservoir that is being drained by a hydraulically fractured well. However, for practical purposes the circular system has been approached to an octagon as shown in Fig. 3.1.
- The porous medium is isotropic, homogeneous and bounded by upper and lower impermeable strata.
- A horizontal reservoir with uniform thickness, h, is considered. Therefore, gravity effects are neglected.

- Skin and wellbore storage effects are not considered to take place neither in the fracture nor in the well.
- The reservoir and fractures are completely saturated with a slightly compressible single-phase liquid fluid of constant compressibility, c_f, and constant viscosity, μ. Flow in both fracture and reservoir is laminar and described by Darcy's law. Rapid flow effects (non-Darcy flow) are significant for gas flow in fractured wells[17,24]. Therefore, the derivation of the flow equations included non-Darcy effects with the sole purpose of future extension of this work to gas flow.
- No chemical reactions take place in the porous media. Also, the dispersion term is neglected.
- The inner boundary condition is set to constant production rate. Fluid enters the well only from the fracture. Fluid enters the fracture from the fracture face.
- The vertical fracture extends over the entire stratum. In other words, the model assumes that the fracture height, h_f, is equal to the formation thickness, h.
- The fracture is length $2X_f$, width, w, and fully penetrates the wellbore. The fracture permeability, k_f, is assumed to be constant.
- Neither dilation nor compaction of the reservoir-fracture system are considered.
- The main fracture yields parallel to the drainage area in the x-direction while the branch fracture has an inclined position. For the experiments run in chapter II, where only main fracture exists, the fracture can have any arbitrary rotation.
- No mechanical interaction takes place between the main and branch fractures.
- The main fracture system is symmetric with respect to the well and the well is located in coordinates 0,0 (center of octagon).

- The fractures –main and branch- are considered to be another porous medium which properties differ from those of the reservoir. The width, w, and length, x_f, of the fracture do not depend on the vertical coordinate. The fracture si assumed to possess finite conductivity.

Since the fracture covers the whole vertical interval and no gravity effects are involved, the problem can be represented in two-dimensional coordinates as depicted in Fig. 3.2.

Using the assumptions above stated, the partial differential equation governing the fluid flow for the reservoir depicted by Fig. 3.1 is:

In the reservoir:

$$\delta_x \frac{\partial^2 p_D}{\partial X_D^2} + \xi_x \left(\frac{\partial p_D}{\partial X_D}\right)^2 + \delta_y \frac{\partial^2 p_D}{\partial Y_D^2} + \zeta_y \left(\frac{\partial p_D}{\partial Y_D}\right)^2 \pm \frac{\pi q_{fD}(x_{Di}, y_{Di}, t_D)}{\Delta x_D \Delta y_D} = \frac{\partial p_D}{\partial t_D} \quad (3.1)$$

The above equation, constituting the first initial value boundary problem, has been derived with detail in Appendix E. As stated in the assumptions, consideration of non-Darcy flow is relevant for gas flow but is not very significant for liquid flow, then Eq. 3.1 becomes:

$$\frac{\partial^2 P_D}{\partial X_D^2} + \frac{\partial^2 P_D}{\partial Y_D^2} \pm \frac{\pi q_{fD}(x_{Di}, y_{Di}, t_D)}{\Delta x_D \Delta y_D} = \frac{\partial P_D}{\partial t_D} \quad (3.2)$$

Since the physical system has been assumed to be isotropic, then Eq. 3.2 can be written, in dimensional form, as:

$$\frac{\partial^2 p}{\partial x^2} + \frac{\partial^2 p}{\partial y^2} + \frac{Q(x_i, y_i, t)\mu}{hk} = \frac{\phi c_t \mu}{k} \frac{\partial p}{\partial t} \quad (3.3)$$

which is applied to the reservoir domain given in Fig. 3.1, excluding the fracture.

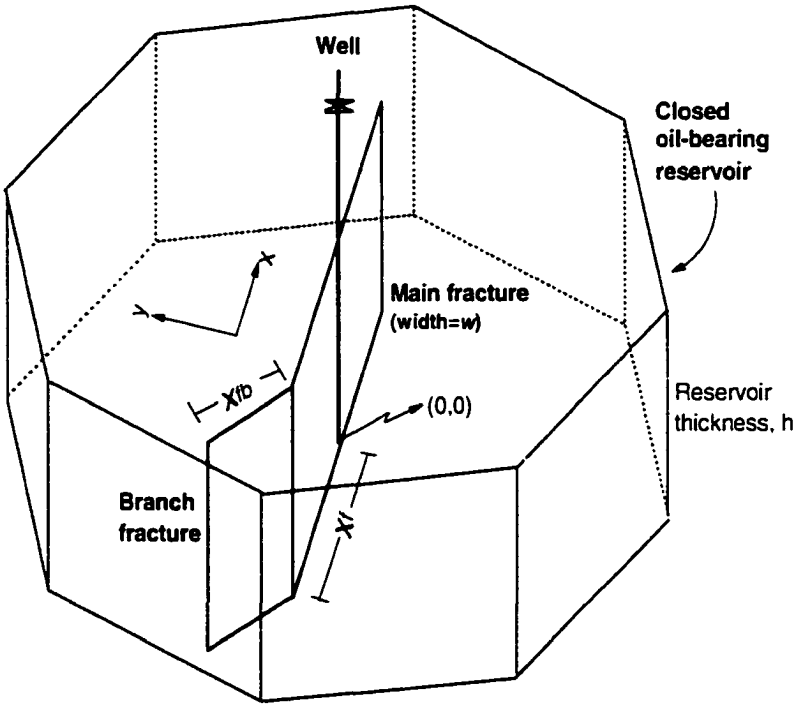

Fig. 3.1. Schematic view of the reservoir-fracture system

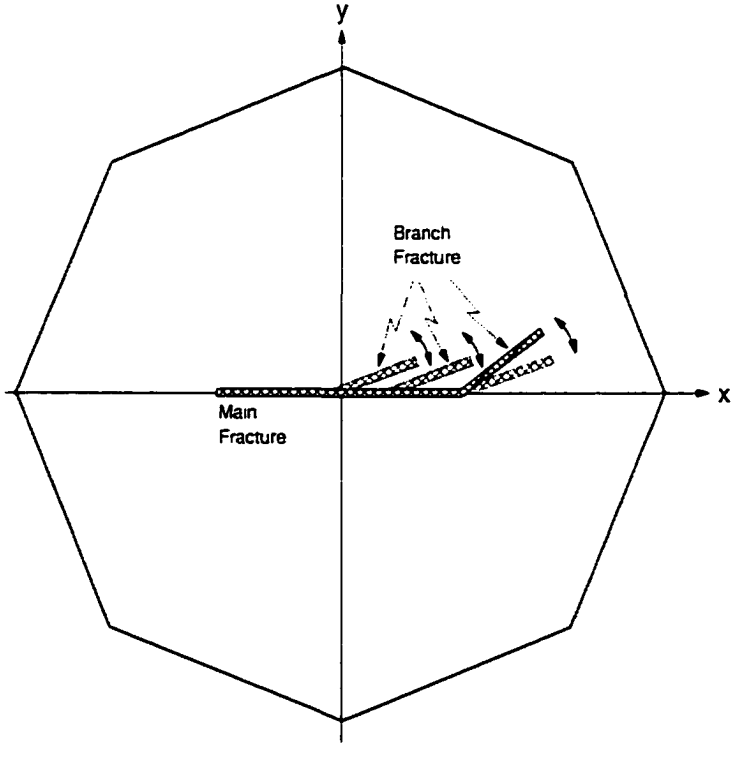

Fig. 3.2. Plane view of the reservoir-fracture system

Eq. 3.3 is subject to the following initial and boundary conditions:

$$p(x, y, 0) = p_i \tag{3.4}$$

which is expressed in dimensionless form as:

$$p_D(X_D, Y_D, 0) = 0 \tag{3.5}$$

As shown in Fig. 3.3, the outer no-flow boundary conditions at the east and west sides of the reservoir are given by:

$$\frac{\partial p}{\partial x'}(x', y', t) = 0 \tag{3.6}$$

and the outer no-flow boundary conditions at the north and south sides of the reservoir are given by:

$$\frac{\partial p}{\partial y'}(x', y', t) = 0 \tag{3.7}$$

where x' and y' are defined by[98]:

$$x' = (x - a)\cos\omega + (y - b)\sin\omega \tag{3.8}$$

$$y' = -(x - a)\sin\omega + (y - b)\cos\omega \tag{3.9}$$

being a and b the translation values along the x and y directions, respectively, and ω is the rotation angle with respect to the x-axis. Refer to Fig. 3.4.

The dimensionless form of Eqs. 3.6 through 3.9 is given by:

$$\frac{\partial p_D}{\partial X_D'}(X_D', Y_D', t_D) = 0 \tag{3.10}$$

$$\frac{\partial p_D}{\partial Y_D'}(X_D', Y_D', t_D) = 0 \tag{3.11}$$

$$X_D' = (X_D - a/r_e)\cos\omega + (Y_D - b/r_e)\sin\omega \tag{3.12}$$

$$Y_D' = -(X_D - a/r_e)\sin\omega + (Y_D - b/r_e)\cos\omega \tag{3.13}$$

In the fracture:

The second initial boundary problem for the system under discussion consists of a fracture which governing equation is given by:

$$\frac{\partial^2 p_{fD}}{\partial X_D^2} + \frac{\partial^2 p_{fD}}{\partial Y_D^2} - \frac{\pi w_D}{C_{fD}\Delta X_{Dt}\Delta Y_{Dt}} q_{fD}(X_{Dt}, Y_{Dt}, t_D) + \frac{4\pi w_D}{C_{fD}\Delta X_{Dw}\Delta Y_{Dw}} q_{wD}(t_D) = \left(\frac{\pi C_{fD}^*}{C_{fD}}\right)\frac{\partial p_{fD}}{\partial t_D} \tag{3.14}$$

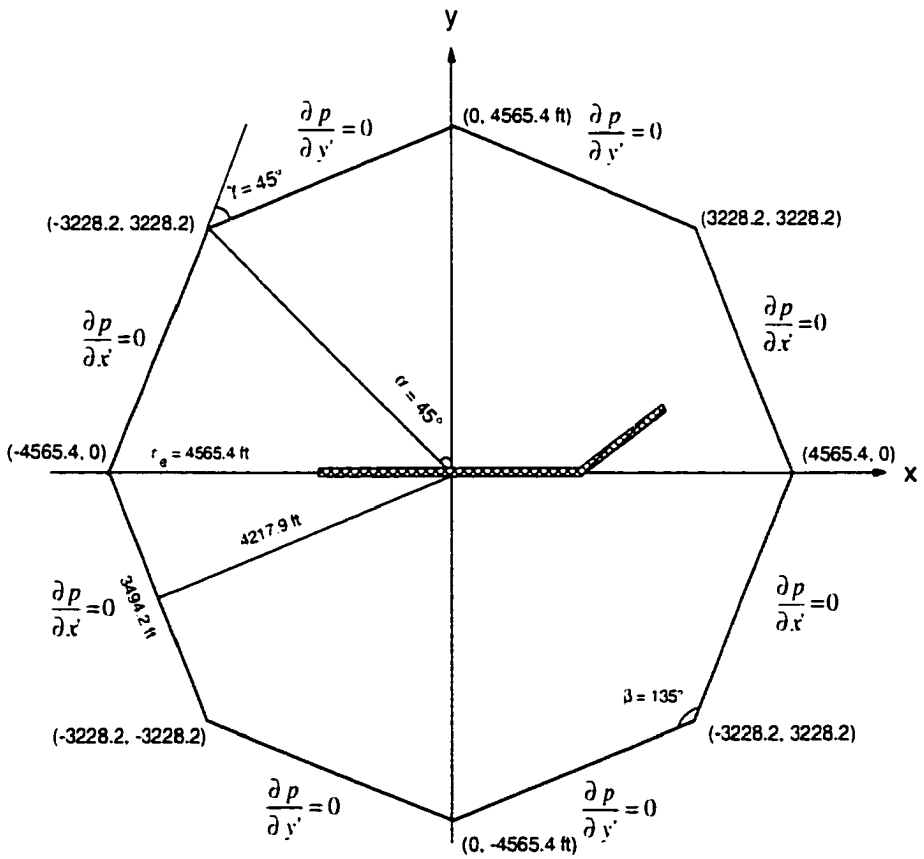

Fig 3.3. Reservoir coodinates and boundary conditions

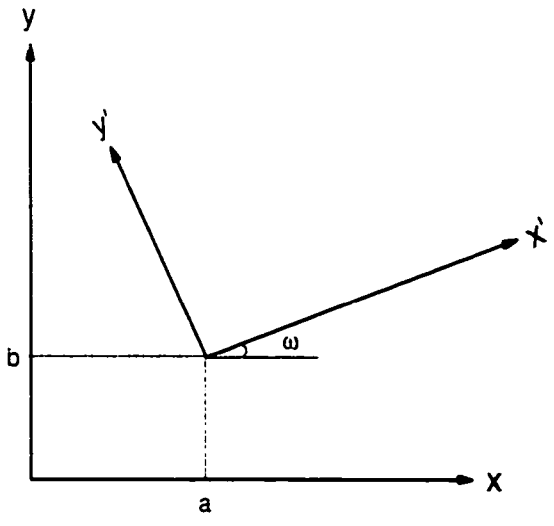

Fig 3.4. Translation and rotation of Cartesian axis[98]

Eq. 3.6 was derived with detail in Appendix F. After neglecting rapid flow effects, the dimensional form for Eq. 3.6 is:

$$\frac{\partial^2 p_f}{\partial x^2}+\frac{\partial^2 p_f}{\partial y^2}-\frac{\mu q_f(x,y,t)}{k_f whx_f}+\frac{\mu q_w(t)}{k_f whx_f}=\frac{\mu\phi_f c_{tf}}{k_f}\frac{\partial p_f}{\partial t} \tag{3.15}$$

The initial condition is:

$$p_f(x,y,0)=p_i \tag{3.16}$$

where x includes both the main and branch fractures.

The domain of the above equation is the whole fracture system. In dimensionless form, the above conditions are expressed as:

$$p_{fD}(X_D,Y_D,0)=0 \tag{3.17}$$

The dimensional and dimensionless no-flow conditions at the fracture tip are:

$$\frac{\partial p_f}{\partial x}(x_f,0,t)=0 \tag{3.18}$$

$$\frac{\partial p_{fD}}{\partial X_D}(1.0, t_D) = 0 \tag{3.19}$$

Compatibility and continuity conditions[1]:

$$q_f(x, y, t) = q(x, y, t) \tag{3.20}$$

$$p_f(x, y, t) = p(x, \frac{w}{2}, t) \tag{3.21}$$

$$p_f(x, y, t) = p(x, -\frac{w}{2}, t) \tag{3.22}$$

$$k_f \frac{\partial p_f}{\partial y}\Big|_{Fracture} = k \frac{\partial p}{\partial y}\Big|_{Reservoir} \text{ along the fracture} \tag{3.23}$$

The above conditions expressed in dimensionless form are:

$$q_{fD}(X_D, Y_D, t_D) = q_D(X_D, Y_D, t_D) \tag{3.24}$$

$$p_{fD}(X_D, Y_D, t_D) = p(X_D, \frac{w_D}{2}, t_D) \tag{3.25}$$

$$p_{fD}(X_D, Y_D, t_D) = p_{fD}(X_D, -\frac{w_D}{2}, t_D) \tag{3.26}$$

$$k_f \frac{\partial p_{fD}}{\partial Y_D}\Big|_{Fracture} = k \frac{\partial p_D}{\partial Y_D}\Big|_{Reservoir} \quad \text{along the fracture} \tag{3.27}$$

Wellbore Conditions

Two types of inner boundary conditions are possible: constant rate and constant pressure. As said before, this study considers only constant flow rate case as inner condition.

---

[1] Mathematical development applied to a symmetric fracture along the x-direction

For the main fracture, the constant rate boundary condition can be obtained by integration of Eq. 3.15 over the length of the fracture, thus:

$$\frac{\mu}{k_f whx_f}\int_{-x_f}^{x_f} q_w dx = -\int_{-x_f}^{x_f}\left[\frac{\partial^2 p_f}{\partial x^2}+\frac{\partial^2 p_f}{\partial y^2}-\frac{\mu q_f(x,t)}{k_f whx_f}-\frac{\mu\phi_f c_{tf}}{k_f}\frac{\partial p_f}{\partial t}\right]dx \qquad (3.28)$$

The boundary conditions expressed by Eq. 3.18 indicates that $\partial p_f/\partial x$ at the fracture tip is equal to zero, then, the above equation simplifies to:

$$\frac{2\mu q_w}{k_f wh} = \frac{\mu}{k_f whx_f}\int_{-x_f}^{x_f}\left[q_f(x,t)+\frac{\phi_f c_{tf}}{k_f}\frac{\partial p_f}{\partial t}\right]dx \qquad (3.29)$$

from where the flow rate q_w can be solved, as follows:

$$q_w = \frac{1}{2x_f}\int_{-x_f}^{x_f} q_f(x,t)dx + \frac{wh\phi_f c_{tf}}{2}\int_{-x_f}^{x_f}\frac{\partial p_f}{\partial t}dx \qquad (3.30)$$

Define the fracture pore volume, V_{pf}, as:

$$V_{pf} = wh\phi_f x_f \qquad (3.31)$$

Then:

$$q_w = \frac{1}{2x_f}\left[\int_{-x_f}^{x_f} q_f(x,t)dx + V_{pf}c_{tf}\int_{-x_f}^{x_f}\frac{\partial p_f}{\partial t}dx\right] \qquad (3.32)$$

Dimensionless Parameters

Dimensionless distances

$$X_D = \frac{x}{x_f} \qquad (3.33)$$

$$Y_D = \frac{y}{x_f} \qquad (3.34)$$

Dimensionless time

$$t_D = \frac{kt}{\phi \mu c x_f^2} \tag{3.35}$$

Refer to Appendix E for derivation of the dimensionless time equation.

Dimensionless fracture storage capacity

$$C_{fD}^{\cdot} = \frac{w\phi_f c_{tf}}{\pi \phi_f c_t x_f} \tag{3.36}$$

Dimensionless fracture conductivity

$$C_{fD} = \frac{k_f w}{k x_f} \tag{3.37}$$

Dimensionless pressure in the reservoir

$$p_D(X_D, Y_D, t_D) = \frac{2\pi kh}{q_w \mu B}(p_i - p(x, y, t)) \tag{3.38}$$

Dimensionless pressure drop in the fracture

$$p_{Df}(X_D, Y_D, t_D) = \frac{2\pi kh}{q_w \mu B}(p_i - p_f(x, y, t)) \tag{3.39}$$

Dimensionless flow rate at the wellbore

$$q_{wD} = 1 = \frac{q_w \mu B}{2\pi kh(p_i - p_f(x, y, t))} \tag{3.40}$$

Dimensionless flow rate at the fracture is:

$$q_{fD} = \frac{2q_f(x, y, t)\mu B x_f}{2\pi kh(p_i - p_f(x, y, t))} \tag{3.41}$$

$$q_{fD} = \frac{2q_f(x, y, t)\mu B x_f}{q_w} \tag{3.42}$$

$$w_D = \frac{w}{r_e} \tag{3.43}$$

This model was solved numerically using the Eclipse Suit which uses a finite-difference formulation. However, the solution had to be handle in a very special manner. Actually, as seen in the second chapter, PEBI grids are the best tool for fractured well simulation. However, there are limitations in the gridders since they are very new. We can say that PEBI grids are in a childhood stage. The used numerical tool, eclipse suit, does not currently support the simulation of one hydraulic fracture with branches or a hydraulic fracture connected to another one. Asymmetric fractures are not support either. When trying to connect two hydraulic fractures, the gridding fails and no grid system is generated. Then, a recursive procedure was employed. Mathematically, a fracture is identical to a horizontal well: it just has a radial wellbore instead of a rectangular profile. To a reservoir simulator, this means very little, as connections are connections[96]. Therefore, the branch fracture was simulated as it were a horizontal well connected to the main fracture at the center point of the fracture's vertical extension. The whole horizontal well extension was simulated as perforated and crossflow was allowed. In this way, it does not produce but allows fluids to move along it to the main fracture. Fig. 3.5. illustrates this situation. Three different horizontal wells lengths were simulated (20, 40 and 60 % the length of the main fracture) and three different values of the angle formed between main fracture and branch fracture were analyzed. The horizontal well meets the fracture in three different locations along the main fracture. One at the fracture tip, another at the middle

distance between the wellbore and the fracture tip, and the last one at the wellbore. Fig. 3.2 illustrates this situation.

The simulation parameters used were the same as given in section 2.3.2. But, the initial time used was $1x10^{7-}$ hours, permeability was 150 md, reservoir thickness was 200 ft and the timestep pressure change was set to 1 psia (see tables 2.2 and 2.3). Of course, the elliptical PEBI grid was chosen to run the simulations.

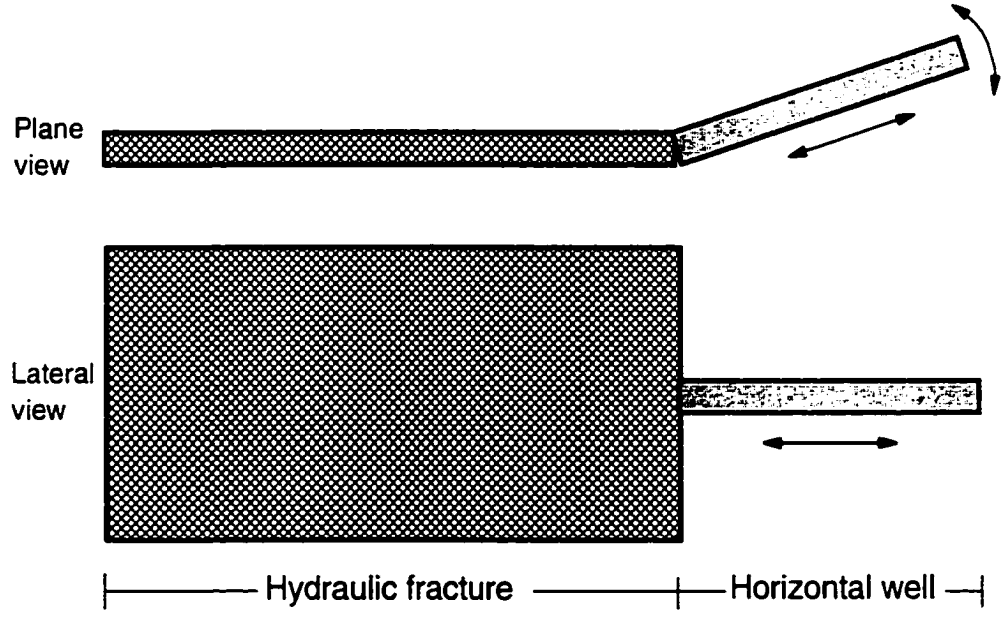

Fig. 3.5. Schematic representation of the solution to the main fracture-branch fracture system used with the Eclipse suit

Table 3.1. Equivalent horizontal wellbore length and wellbore radius to fracture conductivity

Equivalent, C_{fD}	L_w=20 ft	L_w=40 ft	L_w=60 ft	L_w=20 ft	L_w=40 ft	L_w=60 ft
	r_w, ft	r_w, ft	r_w, ft	D_w, in	D_w, in	D_w, in
1	0.0095	0.0113	0.0125	0.228	0.271	0.300
10	0.0169	0.0201	0.0222	0.405	0.482	0.533
50	0.0252	0.0300	0.0332	0.606	0.720	0.797
100	0.0300	0.0357	0.0395	0.720	0.857	0.948
300	0.0395	0.0470	0.0520	0.948	1.127	1.248

According to Ozkan et al[97], as in the case of fractured wells, it is possible to define the dimensionless conductivity, C_{hD}, for horizontal wells using the following relationship:

$$C_{hD} = 7.395x10^{13}\frac{r_w^4}{khL_w} \tag{3.44}$$

Table 3.1 presents the dimensionless conductivities estimated using Eq. 3.44 for the cases studied here.

A dimensionless branch-fracture length, X_{fbD}, is defined as:

$$X_{fbD} = \frac{L_w}{x_f} \tag{3.45}$$

3.2. A SEALING FAULT INTERSECTED BY A VERTICAL HYDRAULIC FRACTURE

Fig. 3.6 illustrates the reservoir-fracture-fault system under consideration. Additionally to the assumptions given in section 3.1, it is also assumed:

- The fault stops the growing path of the fracture.
- The fracture is completely vertical (no dip angle), it means not tilt is presented, therefore fault and fracture meet along a vertical line.
- Fracture flow direction takes place along the x direction.
- Fault covers the whole reservoir thickness.
- No proppant enters the fault path.
- Fracture lies over the x direction.

- The stress field is assumed to be homogeneous, then, the pressure drop in the wellbore does not cause failure/slip of any of the fault blocks.

The mathematical model for the reservoir system is the same as given by Eq. 3.2 or 3.3:

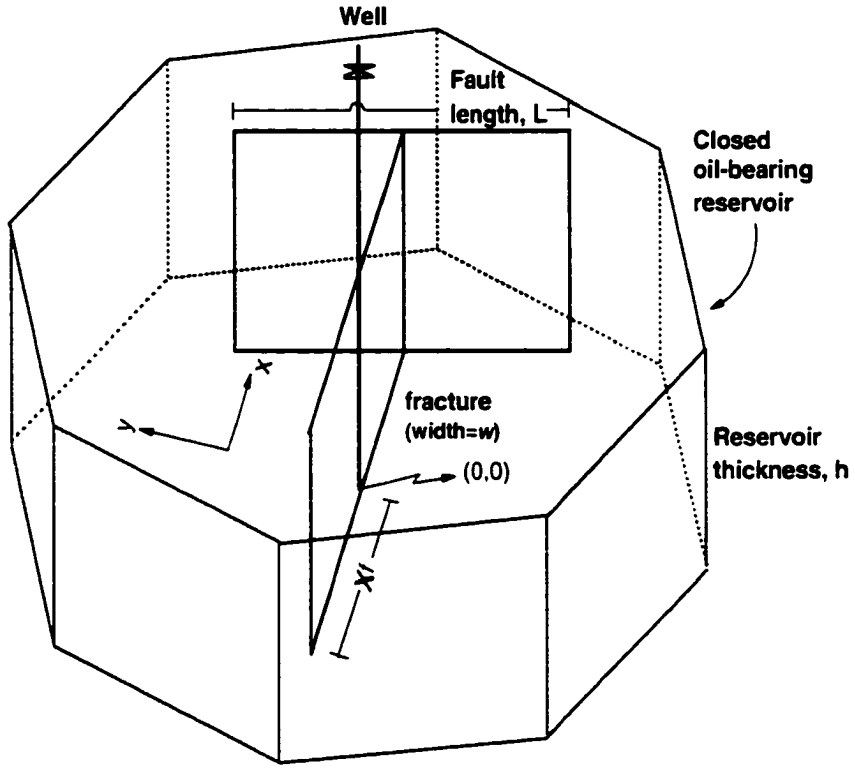

Fig. 3.6. Schematic view of the reservoir-fracture-fault system

$$\frac{\partial^2 P_D}{\partial X_D^2}+\frac{\partial^2 P_D}{\partial Y_D^2}\pm\frac{\pi q_{fD}(x_{Di},y_{Di},t_D)}{\Delta x_D \Delta y_D}=\frac{\partial P_D}{\partial t_D} \tag{3.2}$$

$$\frac{\partial^2 p}{\partial x^2}+\frac{\partial^2 p}{\partial y^2}+\frac{Q(x_i,y_i,t)\mu}{hk}=\frac{\phi c_t \mu}{k}\frac{\partial p}{\partial t} \tag{3.3}$$

The above equations are subject to the same initially, boundary and internal conditions as in section 3.1. Along the fault, a no-flow boundary condition is set as:

A sealing fault indicates that no flow takes place neither along the fault nor through the fracture, then the no-flow internal conditions are:

$$\frac{\partial p}{\partial x'}(x', y', t) = 0 \tag{3.46}$$

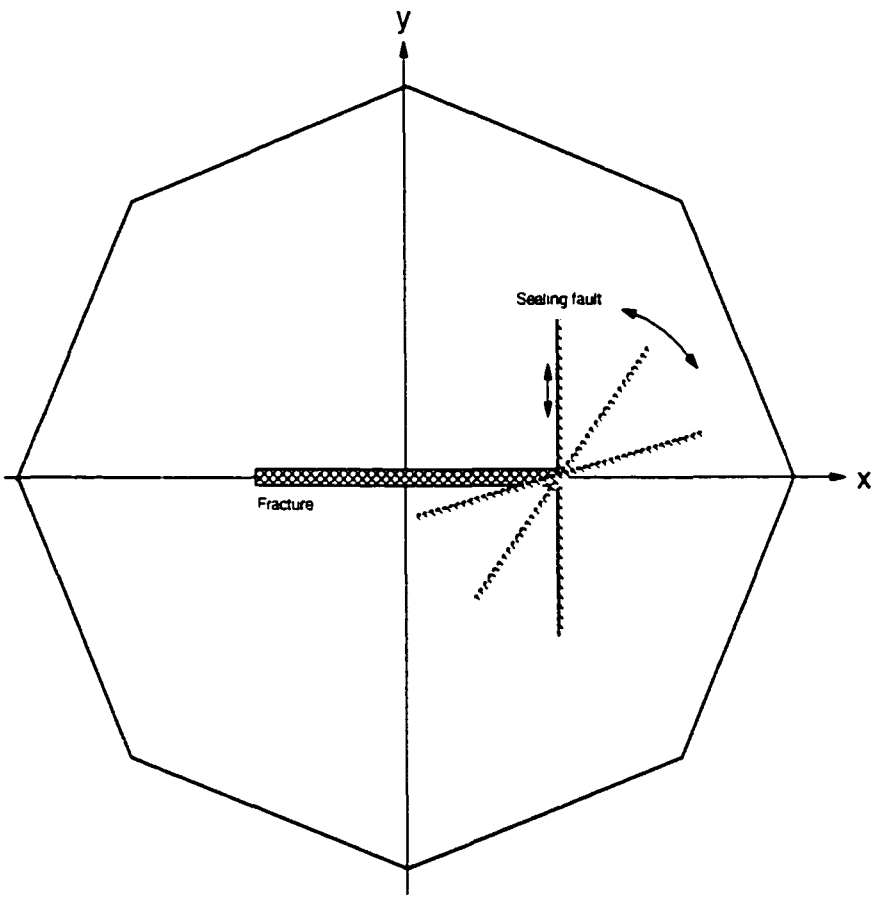

Fig. 3.7. Plane view of the reservoir-fracture-fault system

$$\frac{\partial p}{\partial y'}(x', y', t) = 0 \tag{3.47}$$

where x' and y' are defined by[98]:

$$x' = (x - a)\cos\omega + y\sin\omega \tag{3.48}$$

$$y' = -(x - a)\sin\omega + y\cos\omega \tag{3.49}$$

being a the translation values along the x direction and ω is the rotation angle with respect to the x-axis. Refer to Fig. 3.4.

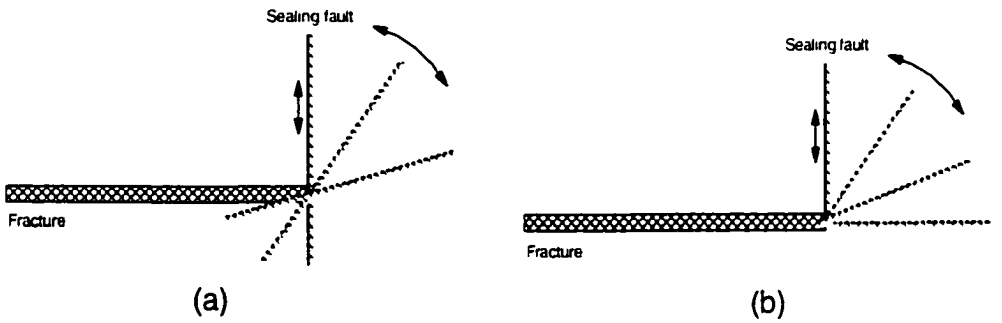

Fig. 3.8. Fracture-fault system cases studied (a) Fracture intersects fault at 75 % of fault length (b) fracture and fault meet at their tips

In dimensionless form, Eqs. 3.46 through 3.49 are expressed as:

$$\frac{\partial p_D}{\partial X'_D}(X_D, Y_D, t_D) = 0 \tag{3.50}$$

$$\frac{\partial p_D}{\partial Y'_D}(X_D, Y_D, t_D) = 0 \tag{3.51}$$

$$X_D' = (X_D - a/r_e)\cos\omega + Y_D \sin\omega \tag{3.52}$$

$$Y_D' = -(X_D - a/r_e)\sin\omega + Y_D \cos\omega \tag{3.53}$$

The mathematical model for the fracture system is the same as given by Eq. 3.6 or 3.7 but with the fracture lying over the x axis, such that:

$$\frac{\partial^2 p_{fD}}{\partial X_D^2} - \frac{\pi w_D}{C_{fD}\Delta X_{Di}\Delta Y_{Di}} q_{fD}(X_{Di}, Y_{Di}, t_D) + \frac{4\pi w_D}{C_{fD}\Delta X_{Dw}\Delta Y_{Dw}} q_{wD}(t_D) = \left(\frac{\pi C^*_{fD}}{C_{fD}}\right)\frac{\partial p_{fD}}{\partial t_D} \tag{3.54}$$

$$\frac{\partial^2 p_f}{\partial x^2} - \frac{\mu q_f(x, y, t)}{k_f whx_f} + \frac{\mu q_w(t)}{k_f whx_f} = \frac{\mu \phi_f c_{tf}}{k_f}\frac{\partial p_f}{\partial t} \tag{3.55}$$

A dimensionless fault length, L_D, is defined as:

$$L_D = \frac{L}{x_f} \tag{3.56}$$

Dimensionless fault lengths starting between 0.5 and 30 were used to analyze the transient pressure behavior. The simulation parameters used were the same as given in section 2.3.2 with no changes as in section 3.1. Additionally, some simulation runs were performed using dimensionless fracture lengths of 80 and 162. The former covers half the reservoir volume and the later divides the reservoir into two sections of about the same size. Initially, the hydraulic fracture intersects the fault in its middle part forming a pure symmetric system since the intersecting angle was set to 90 degrees. Then, the intersecting point takes in one-fourth part of the fault size. In other words, the fracture intersects the fault at a distance from the fault tip of 25 percent of the total fault extension. Then, it is analyzed the case when both fault and fracture meet at their tips. Fig. 3.7 illustrates these descriptions.

To further extend the analysis, the fault angle was varied from 90 to zero degrees as can be also noted in Fig. 3.8. This experiment concludes the simulation runs for sealing faults intersected by a hydraulic vertical fracture.

CHAPTER IV

ANALYSIS OF RESULTS

This may be the most important chapter of this study. Its purpose is to present the results in graphical format and analyze them to establish patterns and differentiate pressure behaviors for both a branch fracture and a fracture intersected by a fault. The analysis takes into account the explanation of the causes of the given transient pressure behaviors which contributes to the extension of *the Tiab's Direct Synthesis Technique* to provide a step-by-step methodology to estimate branch fracture length, and fault lengths in each individual case (Chapter 5). The introduction of the semi-radial or semi-pseudoradial flow is introduced here.

4.1. HYDRAULIC FRACTURED VERTICAL WELL WITH A BRANCH FRACTURE

As explained in Chapter 2, the branch fracture was connected to the main fracture at three particular positions along the main fracture: (a) from the wellbore, (b) from the middle distance between well and fracture tip, and (c) from the fracture tip, as sketched in Fig. 4.1.

Three different angles of 10, 20 and 30° and three different dimensionless branch fracture lengths of 0.2, 0.4 and 0.6 were investigated. Limitations on simulator gridding did not allow simulation of other scenarios. Using angle values higher than

30° has no physical meaning. Refer to Figs. C.21.a through C.21.c to observe the grid system utilized. A number of grid points are provided in Table D.22.

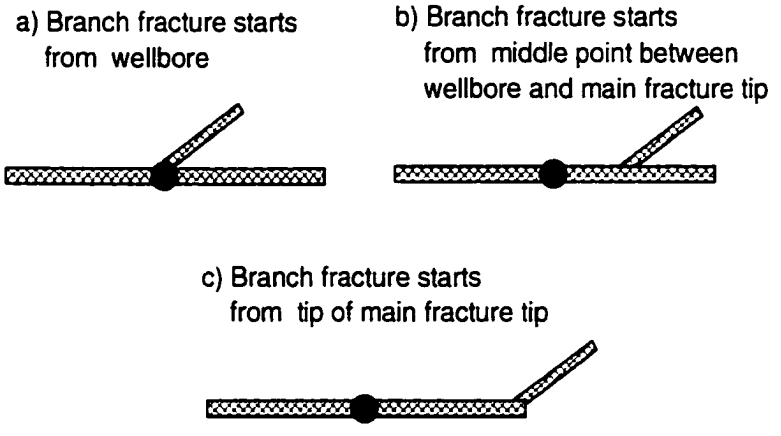

Fig. 4.1. Position of the branch fractured along the main fracture

Table 4.1. Absolute average errors for the pressure solutions between a fractured well with no branch and a fractured well with a branch (X_{fbD}=0.6)

CASE	C_{fD} =1	C_{fD} =10	C_{fD} =50	C_{fD} =100	C_{fD} =300
	Absolute Average Errors, %				
(a)	0.1283	0.1242	0.1216	0.1241	0.1263
(b)	0.0575	0.0585	0.1542	0.1424	0.0609

For cases *a* and *b*, it means, when the branch fracture starts from other position than the main fracture tip, the pressure response for all the branch fracture lengths and angles were essentially the same. Therefore, results for an angle of 30° and dimensionless branch fracture of 0.6 are reported for these two cases. See tables D.10 and D.11. Also Figs. C.21.a thorough C.21.c show the typical grid systems handle for simulating a fractured well with a branch fracture.

Fig. 4.2 shows the behavior of a fractured well obtained for cases *a* and *b*. It includes the case without a branch fracture. These curves are shown separately for dimensionless fracture conductivity in Figs B.1.a through B.1.e. Notice that for each dimensionless fracture conductivity a single curve is observed. This is because the solutions for a branch fracture starting from either the wellbore or the middle distance between wellbore a main fracture tip (cases *a* and *b*) is essentially the same for the case where no branch fracture exists. Tables D.12.a and D.12.b show the absolute error between the pressure solution for a hydraulic fracture with a branch (X_{fbD}=0.6) and without a branch and table 4.1 summarizes these errors. Notice that an average difference less than 0.13 % is observed. This leads us to establish that for cases *a* and *b*, the response of a branch fracture and without a branch fracture is the same. As possible explanation, we could say that a very early time, even before the starting of the bilinear flow regime, the largest pressure drop between wellbore and fracture is detected. Since the main fracture tip is located at the farthest point from the wellbore, then that pressure drop is detected and pressure drop from the branches is then masked for this. One can think that as the dimensionless time becomes smaller, a pressure response from the fracture branch may be detected. However, going to smaller dimensionless time may not have real sense since current pressure gauges are not designed to work under such small time values. The impact of branch fracture conductivity will be studied in case *c*.

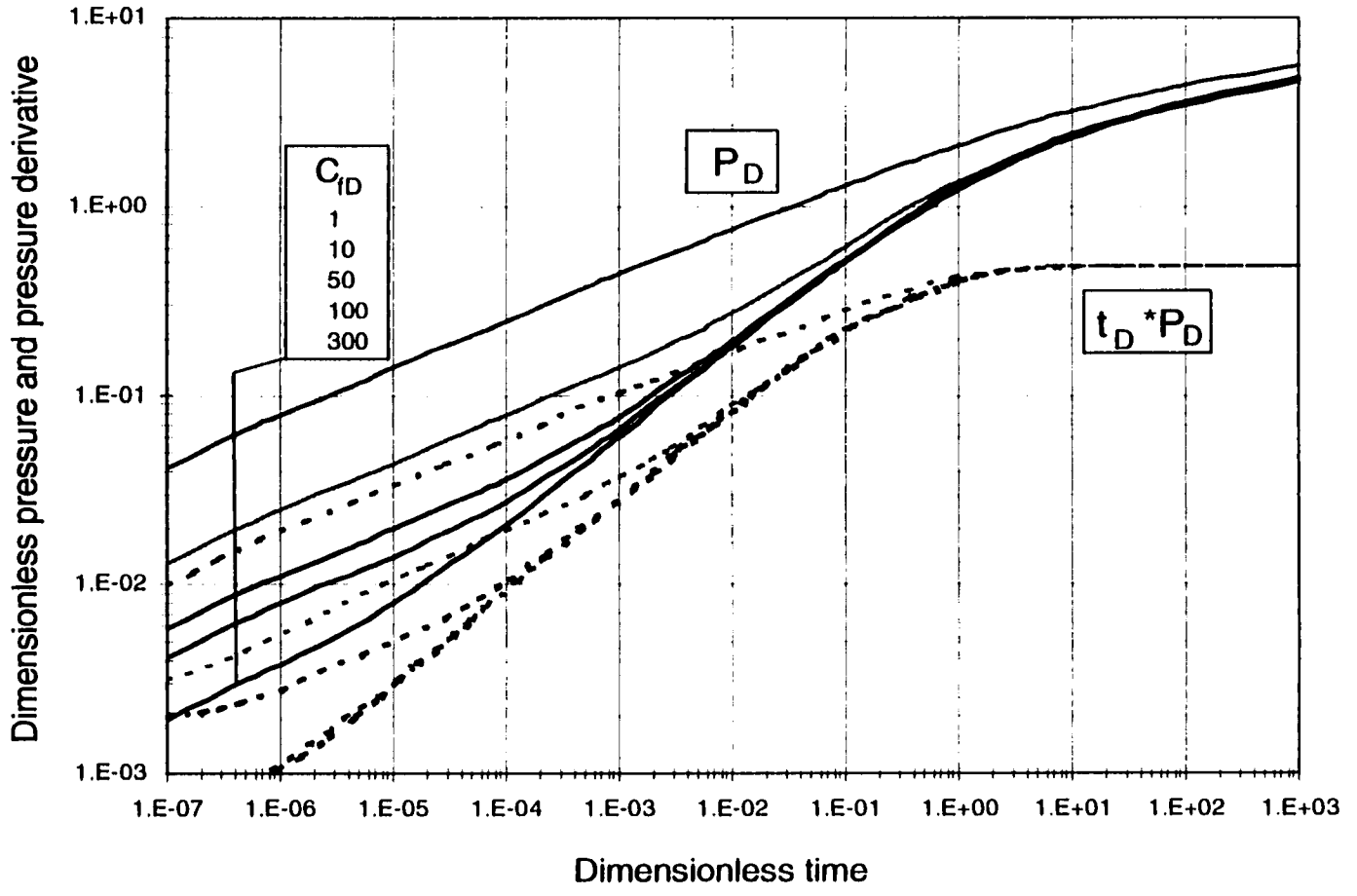

Fig. 4.2. Well pressure behavior for a fractured well with a branch fracture for cases a and b, X_{fbD}=0 and 0.6 and θ=30°

Observations of the pressure behavior for cases *a* and *b*, which essentially is the same as for a single main fracture, have been already studied in the literature. As noted in previous investigations, as the fracture conductivity increases, the bilinear flow duration is shorter until it practically disappears. See Figs. B.1.a through B.1.e and Fig. 4.2.

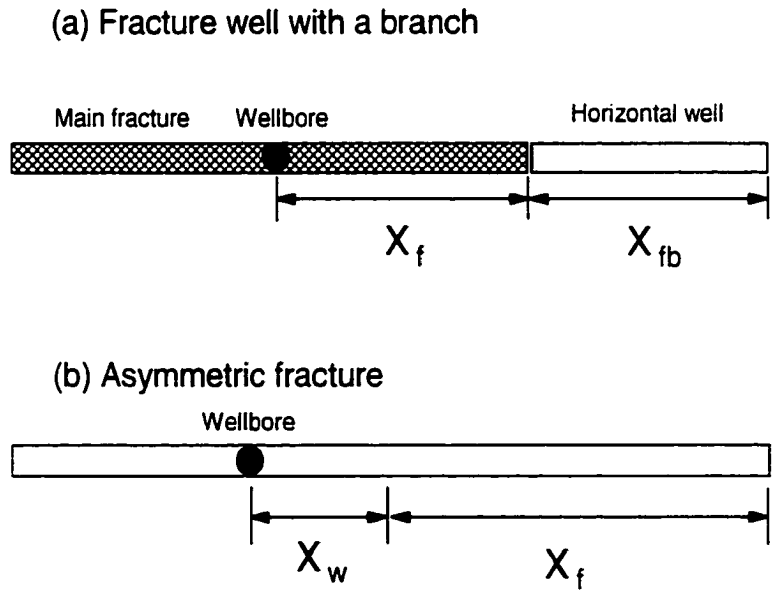

Fig. 4.3. Plan view of the fracture system of this study and the asymmetric fracture of Ref. 36

Case *c*, when the branch fracture starts from the tip of the main fracture, presents a different behavior than that from the other two cases. However, before attempting to analyze the pressure behavior, some experimental runs were performed to verify if the assumed approach-horizontal well acting as the branch fracture works well. This was done by using a zero angle formed between the horizontal well and the main fracture and comparing to the results of fracture asymmetry obtained by

Berumen et al[36]. Three cases of fracture asymmetry, $\xi = 0.2$, 0.4 and 0.6 (See Fig. 4.3) where considered. Fracture asymmetry is defined as[36]:

$$\xi = \frac{X_w}{X_f} \tag{4.1}$$

Recalling the dimensionless branch-fracture length, X_{fbD}, definition:

$$X_{fbD} = \frac{L_w}{X_f} \tag{3.45}$$

Table 4.2. Average absolute errors obtained from the solution of this study and the Cases of fracture asymmetry from Ref. 36

C_{fD}	X_{fbD}=0	X_{fbD}=0.2	X_{fbD}=0.4	X_{fbD}=0.6
	Average Absolute Error, %			
1	0.105029	0.96516	1.43062	1.52769
10	0.105640	0.99246	1.42970	1.53364
50	0.105158	1.21740	1.43095	1.52677
100	0.105411	1.23845	1.42307	1.53045

The solution for a system with no branch fracture was compared to the symmetric fracture case of Ref. 36. Results are reported in tables D.13.a, D.13.b, Fig. 4.4 and Fig. 4.5; absolute errors are given in table D.13.c and summarized in the second column of Table 4.2. Notice that a very low absolute difference, of about 0.1 %, was obtained between the two simulation studies. This indicates that both simulation results are reliable.

The next step was to compare the results using dimensionless branch fractures of 0.2, 0.4 and 0.6 to the solutions presented by Berumen et al[36] for values of fracture asymmetry of 0.2, 0.4 and 0.6. In this particular case, fracture branch and fracture asymmetry are basically same definitions. Tabulated results for the above-mentioned

cases are shown in tables D.14.a, D.15.a and D.16.a, covering branch fractures, and D.14.b, D.15.b and D.16.b, covering asymmetric fracture, respectively. Absolute errors obtained between the two studies are summarized in Table 4.2 and reported in detail in tables D.14.c, D.15.c and D.16.c.

The results reported by Berumen et al[36] are also plotted in Figs. B.2.a through B.2.c for asymmetric fracture factors of 0.2, 0.4 and 0.6, respectively. Results from this study are presented in Figs. B.3.a, B.3.b and B.3.c for dimensionless branch fractures of 0.2, 0.4 and 0.6, respectively. Moreover, the pressure derivative curves are provided for each of the studied dimensionless fracture conductivities in Figs. B.4.a through B.4.e.

Notice in Table 4.2 that there are very insignificant differences between the results of this study and those reported by Berumen et al[36]. However, as the dimensionless branch fracture increases from 0.2 to 0.6, the absolute deviation also increases. This small discrepancies may be due to the fact that the branch fracture provides a radial profile which is due to the presence of the horizontal well while Berumen et al's[36] asymmetric fractures have a rectangular profile. In spite of this fact, the difference is considered negligible and we can conclude that the solution of the branch fractured simulated as a horizontal well is reliable.

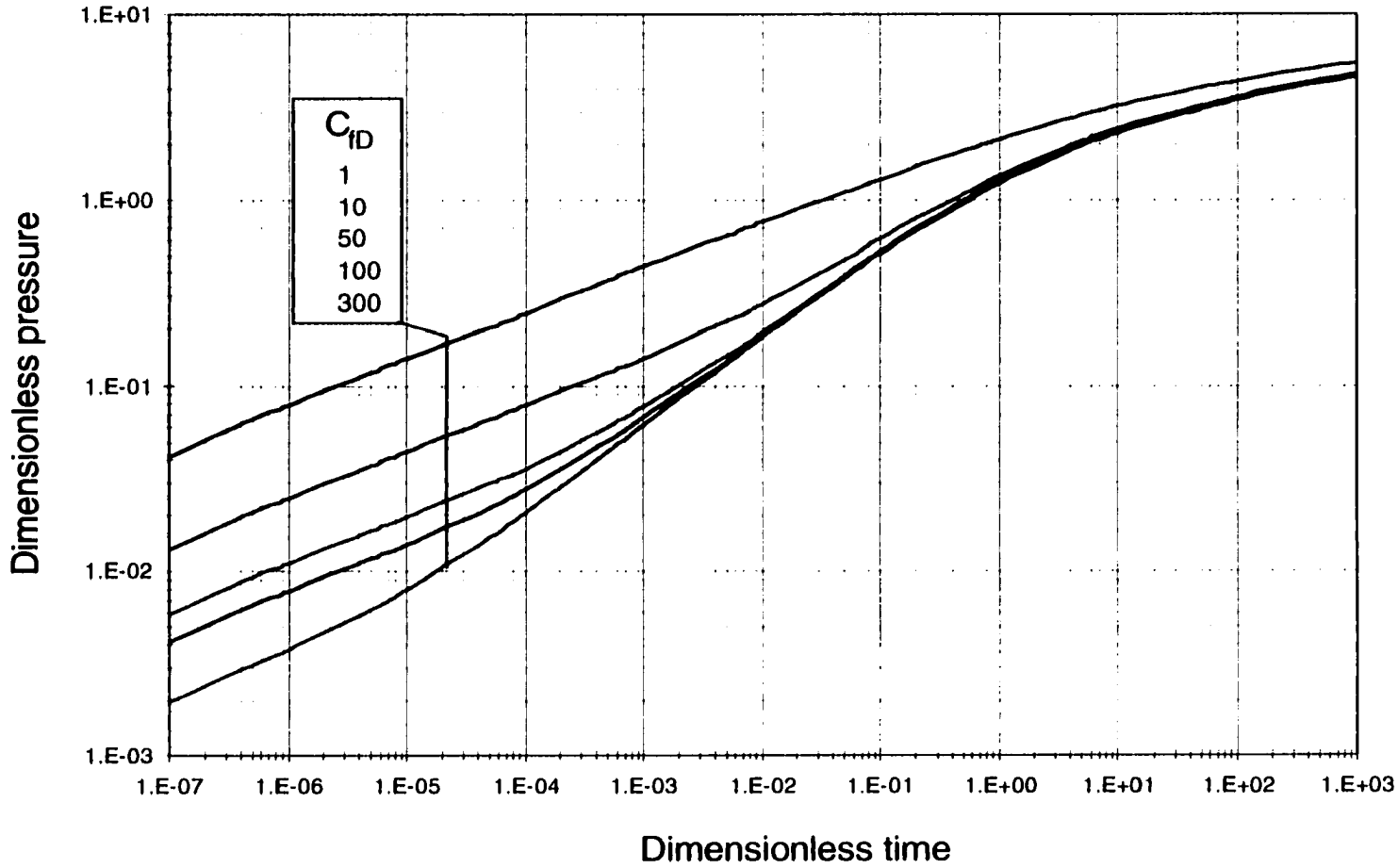

Fig. 4.4. Dimensionless pressure for a fractured well with no branch fracture

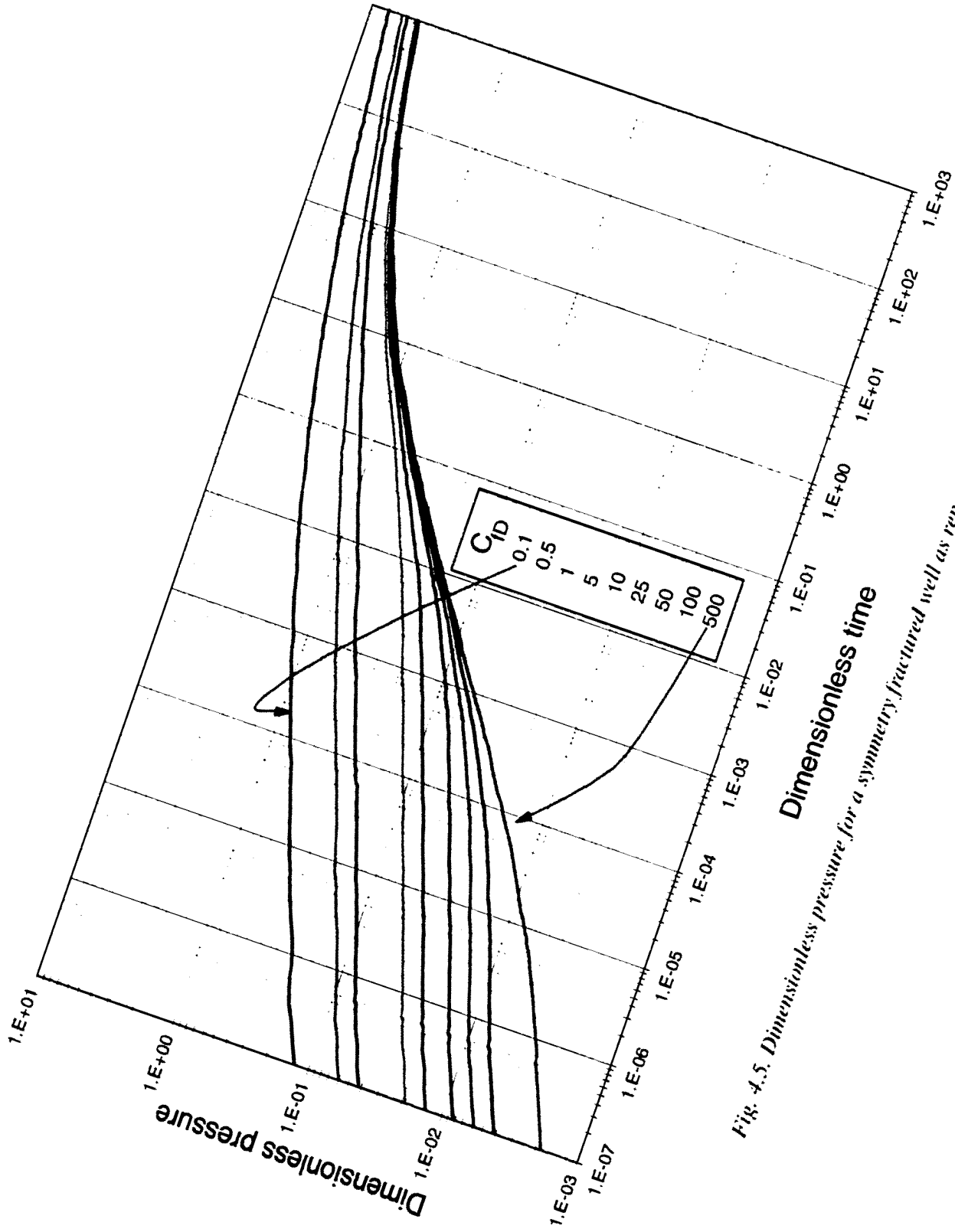

Fig. 4.5. Dimensionless pressure for a symmetry fractured well as reported in Ref. 36

4.1.1. EFFECT OF BRANCH FRACTURE ANGLE

As commented earlier in this chapter, the branch fracture was inclined 10, 20 and 30° with respect to the direction of the main fracture. It is observed that varying the angle from zero, in the case of asymmetric fracturing, to 10 has more effect than when the angle is changed from 10 to 20 or from 20 to 30°. This observation is explained by an increase in the pressure drop due to the friction caused by the angle. As the angle increases, the friction remains and only a very small increase in pressure drop is observed. As shown in tables D.17a-D.17.e, the increment in pressure drop with respect the case of no angle is about 6.6 percent. However, the pressure profile is still the same as if no angle exists, therefore no graphic results are reported to avoid repetition. When, the angle increases from 10 to 20°, there is an overall pressure increase of about 6.9 percent and also the pressure profile is kept as in the former case. See results in tables D.18.a-D.18.e. A similar behavior is seen when the angle value is set to 30°, a slight increase in pressure drop of about 7.1 % compared to the zero angle is observed. Of course, the pressure trend keeps behaving as in the case of zero angle. Results are presented in tables D.19.a-D.19.e.

From the above observations, we conclude that a slight inclination of the angle causes a friction for the pressure transient to travel. Then, a small increase in pressure drop is observed. Duplicating the value of the angle causes a pressure drop, which is very slightly higher than the former case, and so on. Then, the pressure behavior for angles of 10, 20 or 30° may be considered the same.

4.1.2. EFFECT OF BRANCH FRACTURE DIMENSIONLESS CONDUCTIVITY

Because of failure in the gridding algorithms, it was only possible to reduce the branch fracture dimensionless conductivity to 75 percent and 50 percent of the value of the main fracture dimensionless conductivity. Variations of branch fracture conductivity were attained by modifying the horizontal well radius. Refer to tables 4.3 and 4.4.

The first experimental exercise consisted of reducing the branch fracture dimensionless conductivity 75 percent of the value of the main fracture dimensionless conductivity. As shown in tables D.20.a through D.20.e, this reduction causes approximately a 0.15-percent increase in the pressure trend compared to the constant fracture dimensionless conductivity case. Furthermore, reducing the dimensionless fracture conductivity to 50 percent of the value of the main fracture dimensionless conductivity causes a slight pressure drop which deviates about 0.21 % from the constant dimensionless fracture conductivity case, as can be seen from tables D.21.a through D.21.e. Then, for these two specific cases, we conclude that the impact of branch fracture conductivity is insignificant.

4.1.3. OBSERVATIONS ON PRESSURE BEHAVIOR

As mentioned before, the pressure behavior for a branch fracture is practically independent of the angle (for angle > 0) and the contrast in conductivity between the main fracture and the branch fracture. Therefore, refer to Figs. B.4.a through B.4.e for

the proceeding analysis since the curves for different angles demonstrate practically identical behavior. The case of a branch fracture forming an angle of 30° is studied here.

Table 4.3. Equivalent horizontal wellbore length and wellbore radius to branch fracture conductivity

Equivalent, C_{fD}	L_w=20 ft r_w, ft	L_w=40 ft r_w, ft	L_w=60 ft r_w, ft	L_w=20 ft D_w, in	L_w=40 ft D_w, in	L_w=60 ft D_w, in
0.75	0.0088	0.0105	0.0116	0.212	0.252	0.279
7.50	0.0157	0.0187	0.0207	0.377	0.448	0.496
37.50	0.0235	0.0279	0.0309	0.564	0.670	0.742
75.00	0.0279	0.0332	0.0368	0.670	0.797	0.882
225.00	0.0368	0.0437	0.0484	0.882	1.049	1.161

Table 4.4. Equivalent horizontal wellbore length and wellbore radius to branch fracture conductivity

Equivalent, C_{fD}	L_w=20 ft r_w, ft	L_w=40 ft r_w, ft	L_w=60 ft r_w, ft	L_w=20 ft D_w, in	L_w=40 ft D_w, in	L_w=60 ft D_w, in
0.50	0.0080	0.0095	0.0105	0.192	0.228	0.252
5.00	0.0142	0.0169	0.0187	0.341	0.405	0.448
25.00	0.0212	0.0252	0.0279	0.509	0.606	0.670
50.00	0.0252	0.0300	0.0332	0.606	0.720	0.797
150.00	0.0332	0.0395	0.0437	0.797	0.948	1.049

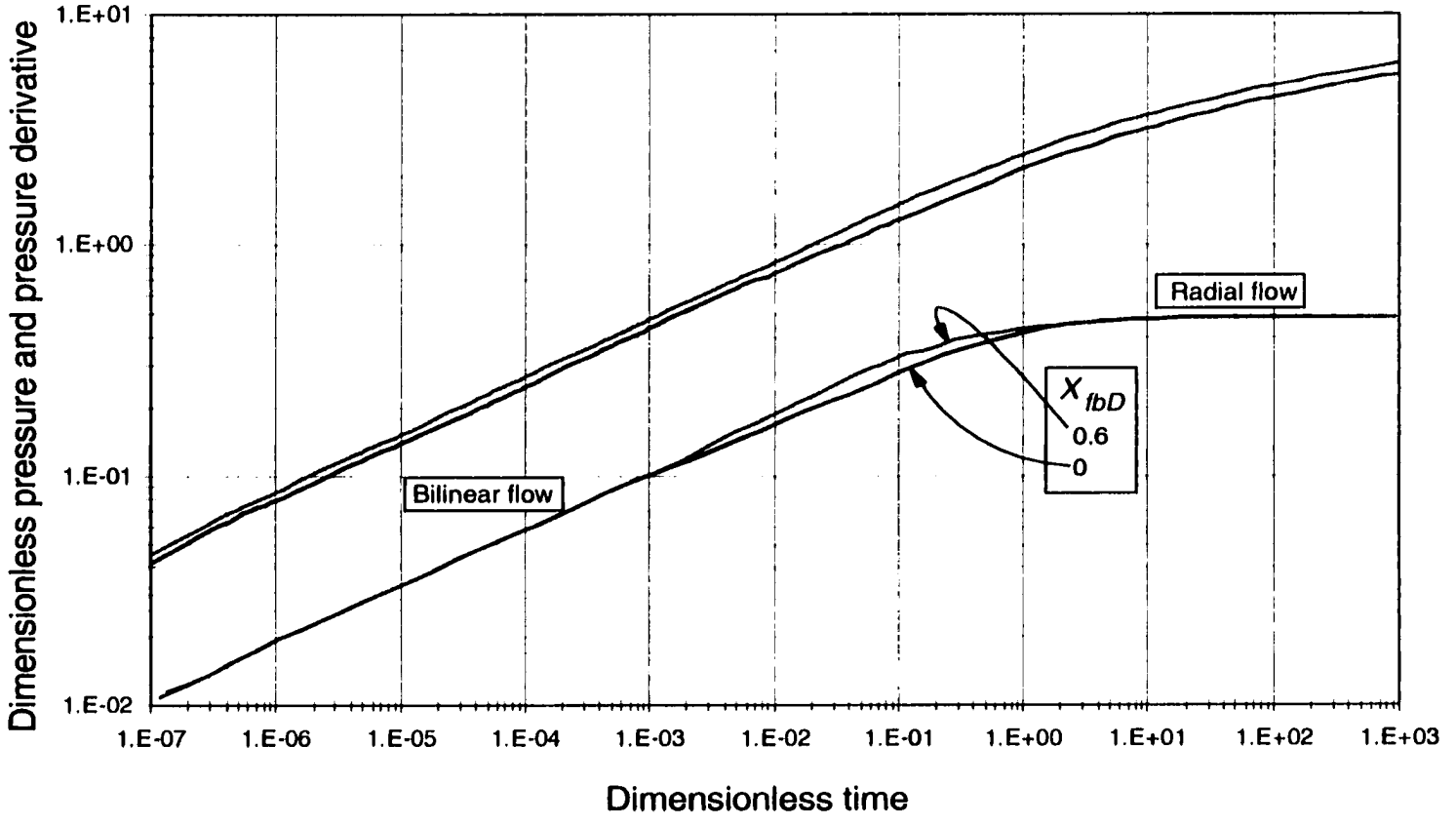

Fig. 4.6.a. Dimensionless Pressure and pressure derivative plot for a fractured well with a branch fracture for X_{fbD}=0 and 0.6, θ=30° and C_D=1

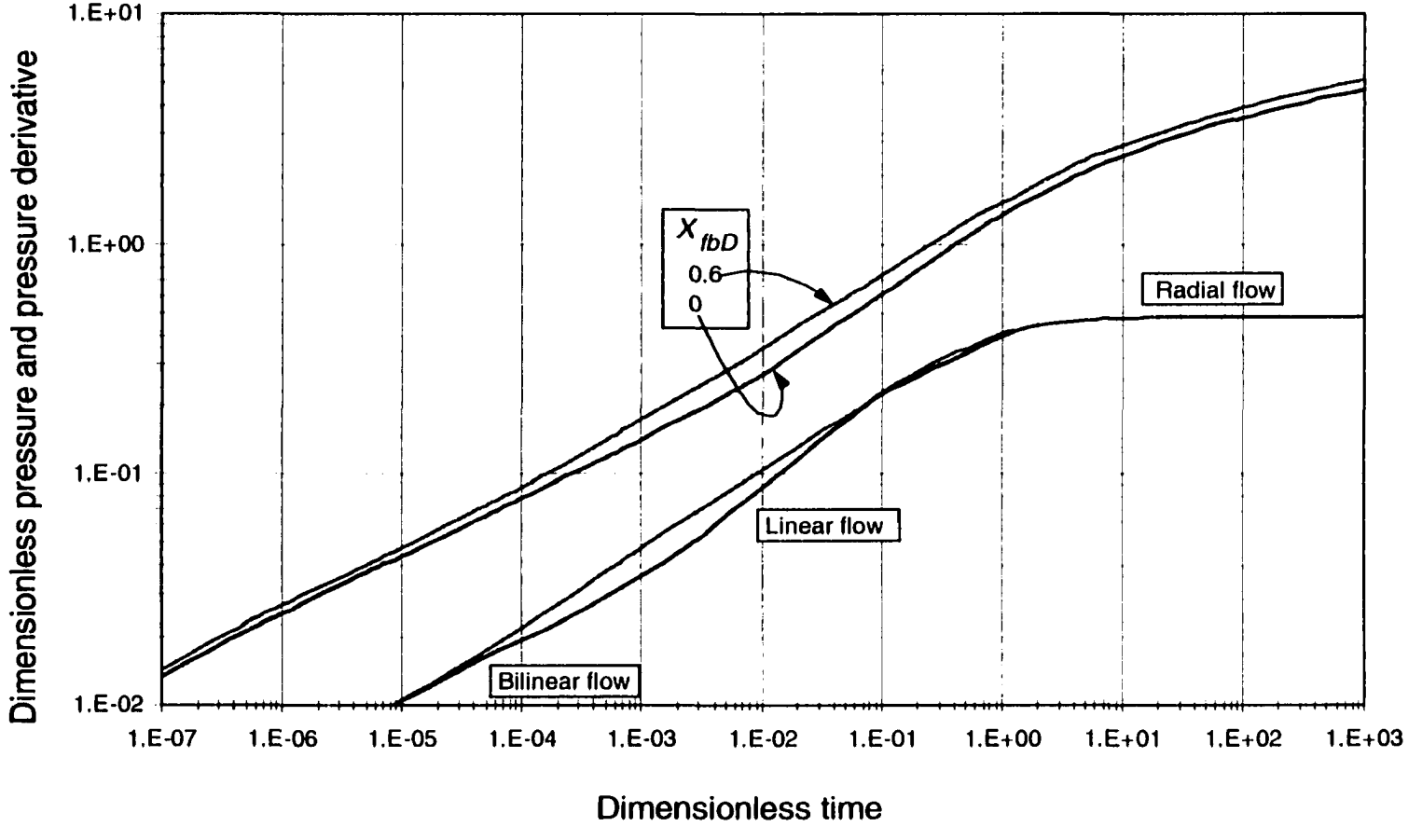

Fig. 4.6.b. Dimensionless Pressure and pressure derivative plot for a fractured well with a branch fracture for X_{fbD}=0 and 0.6, θ=30° and C_D=10

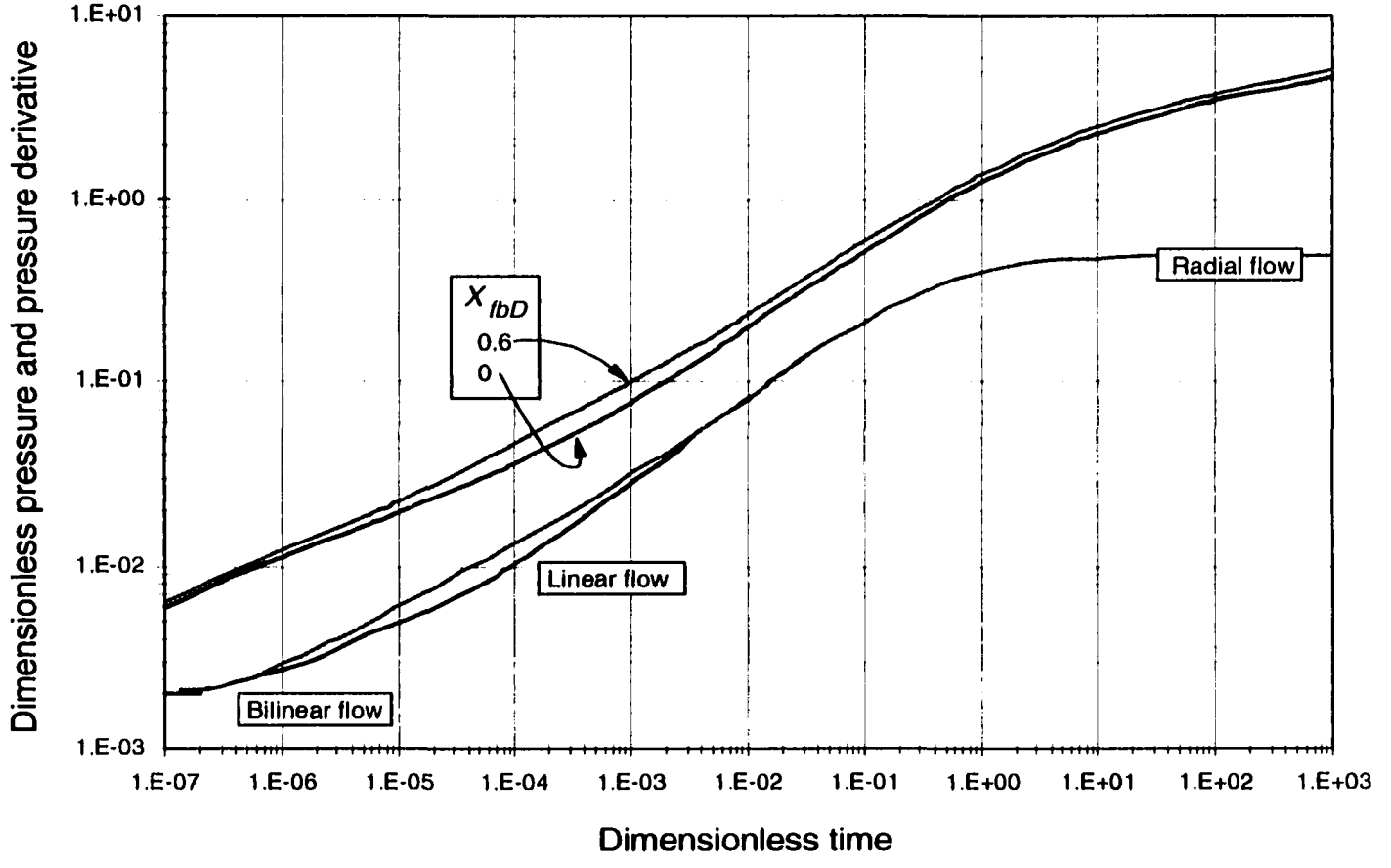

Fig. 4.6.c. Dimensionless Pressure and pressure derivative plot for a fractured well with a branch fracture for X_{fbD}=0 and 0.6, θ=30° and C_{fD}=50

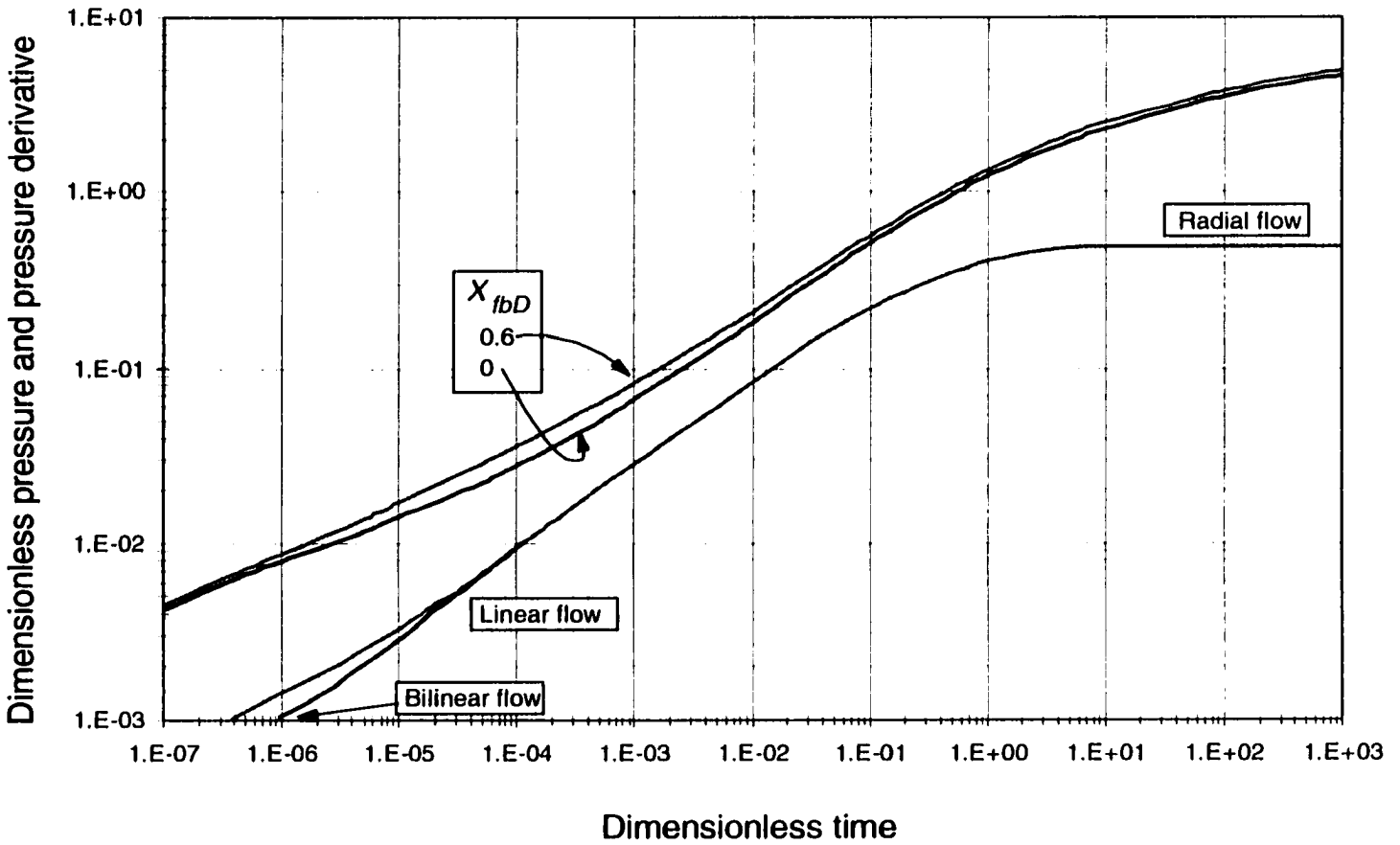

Fig. 4.6.d. Dimensionless Pressure and pressure derivative plot for a fractured well with a branch fracture for X_{fbD}=0 and 0.6, θ=30° and C_D=100

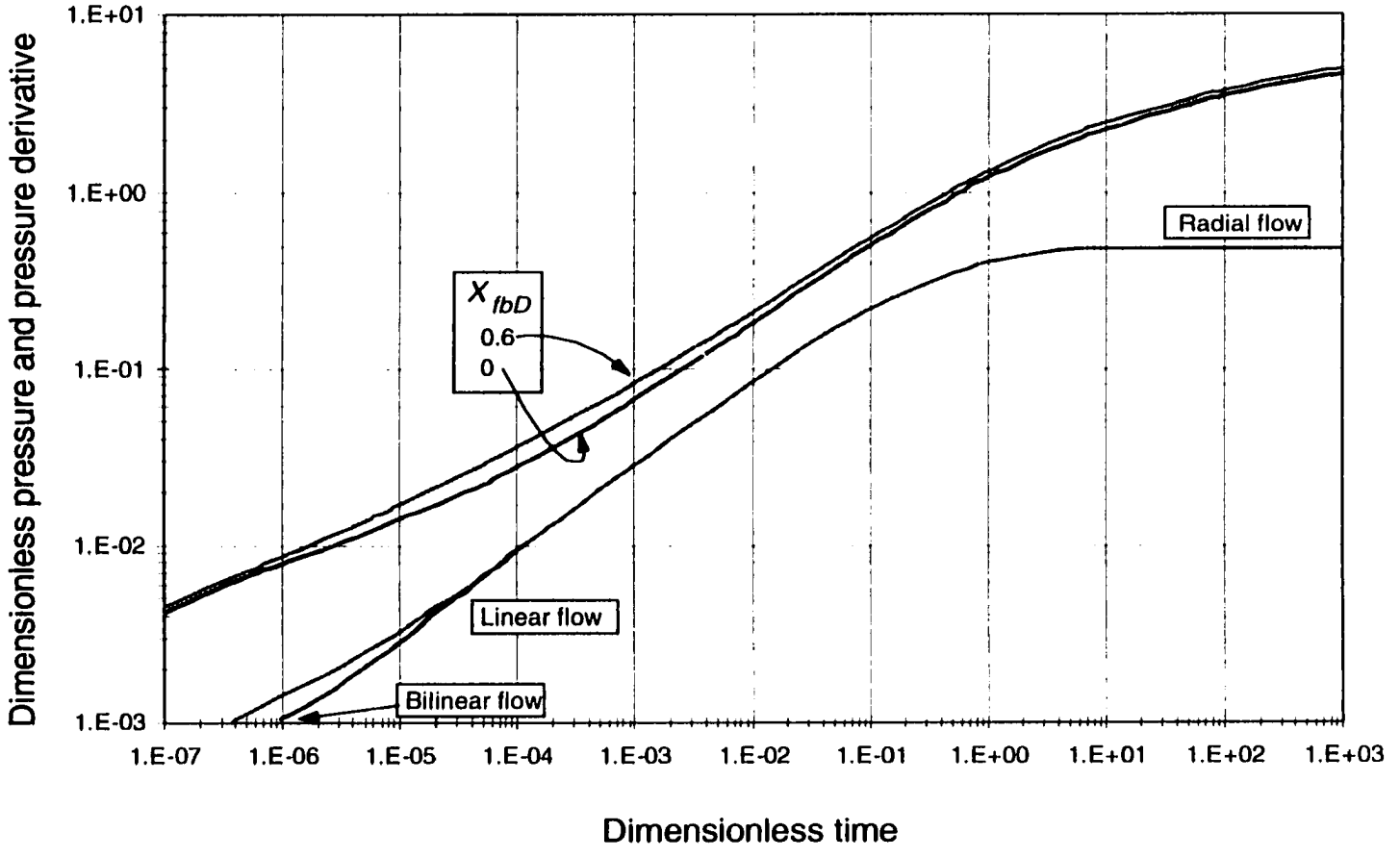

Fig. 4.6.e. Dimensionless Pressure and pressure derivative plot for a fractured well with a branch fracture for X_{fbD}=0 and 0.6, θ=30° and C_D=300

Table 4.5. Slopes observed in a hydraulic fractured well with a branch fracture

C_{fD}	X_{fbD}	Slope	Duration (log Cycles)	Intercept	$10^{Intercept}$
1	0.2	0.25			
1	0.4	0.25			
1	0.6	0.25			
10	0.2	0.34	3	-0.2913	0.511
10	0.4	0.34	2	-0.343	0.454
10	0.6	0.34		-0.379	0.418
50	0.2	0.35	3	-0.46	0.347
50	0.4	0.35	<2	-0.5	0.316
50	0.6	0.35		-0.56	0.275
100	0.2	0.35	> 1	-0.74	0.182
100	0.4	0.38	~ 1	-0.594	0.255
100	0.6	0.42	~ 1	-0.4	0.398
300	0.2	0.25	>1	-1.27	0.054
300	0.4	0.34	>1	-0.75	0.178
300	0.6	0.4	1	-0.48	0.331

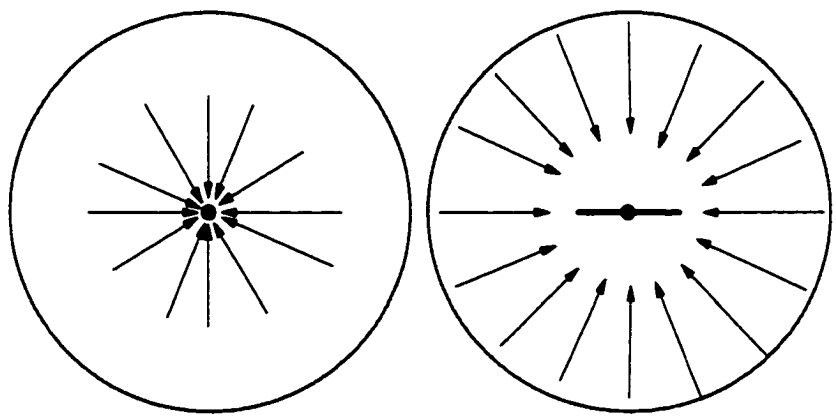

Fig. 4.7. Radial and pseudoradial flows

Most of the observations will be based on Figs. 4.6.a-4.6.e, and only cases with no branch and for X_{fbD}=0.6 are shown here for visual purposes. For the case of low fracture conductivity, C_{fD}=1, it may be difficult to identify a branch fracture since the behavior of it is very close to the case when no branch exists. This is due to the fact

that the low conductivity does not permit a rapid answer from the fracture tip, as it occurs for higher conductivity systems. Notice that the unbranched case has a longer transition period from bilinear to pseudoradial flow. It has been customary to call the radial flow period to the transient response of a well immediately after wellbore storage effects end. See Fig. 4.7. In fracture wells, the radial flow regime is formed (if the test is long enough and the reservoir boundaries do not interfere) after the bilinear or linear flow periods end. That flow period has been customarily[18] referred to as pseudoradial flow. Since both flow regimes are used to estimate reservoir permeability, in this study these flow regimes are treated indistinguishably.

If we extend our analysis for the moderate fracture conductivity, C_{fD}=10, the presence of a branch fracture can now be better seen, than for the low conductivity case. The reader is referred to Fig. 4.6.b. The unbranched fracture case presents a long bilinear flow period followed by a short linear period of about two log cycles. For the case of a branch fracture, the 0.25 slope is practically absent when X_{fdD}=0.6 but tends to appear as the branch fracture size is reduced. Refer to table 4.5. The branch case shown in Fig. 4.6.b deserves especial attention. It has a almost constant 0.34 slope followed by a transition period before the radial flow appears. A close behavior is observed for an infinite conductivity fracture when the ratio between fracture length and drainage radius is bigger than 16[33] in which a slope of 0.36, known a biradial flow by Tiab[33] or elliptical flow by others, is presented. However, this behavior is expected for fracture conductivities above or around 300. Therefore, our case may not be confused with the just mentioned particular case. For the branch case discussed here, the main fracture conductivity and fracture conductivity should be estimated from the

intersection between linear and radial flow regimes as indicated in reference 34. If moderate fracture conductivity is obtained from that calculation, then we may conclude that we are dealing with a branch fracture. In addition, it is advisable to simulate the pressure behavior using the obtained fracture conductivity value[18] and compare to the actual pressure test.

A similar analysis is applied for the case of medium fracture conductivity, C_{fD}=50, which for the unbranched case has a shorter bilinear flow period. As seen in Table 4.5, the branch fracture has a 0.35 slope which duration reduces as the branch fracture length reduces. See Fig. 4.6.c. Again, this case should not be confused with the infinite fracture conductivity case as commented in the former paragraph. For unbranched cases, it is not expected that a finite conductivity fracture possesses a 0.35 slope during either the bilinear or linear acting periods.

The same analysis is applied for the high conductivity case, C_{fD}=100, when X_{fbD}=0.6, however, notice that the duration of the 0.35 slope is shorter. Slopes of 0.38 and 0.42 are present for dimensionless branch fracture lengths of 0.4 and 0.2, respectively. This is because as the branch fracture becomes smaller the behavior approaches the unbranched case which has a 0.5 slope since practically the earliest stages and time.

The infinite conductivity case exhibits a very special behavior. As shown in Fig. 4.6.e, a slope of 0.25 is observed at early time, then the linear flow regime appears. The slope increases, although of shorter duration, as the branch fracture length is reduced. In the unbranched case, it is never expected that it would have an infinite conductivity fracture showing a bilinear flow regime (slope of 0.25). It does

not mean that for these cases the bilinear flow regime does not exist. It does exist, but the duration is so short that the current devices do not detect it since impractically small time steps are involved. The pressure drop along the fracture is practically negligible. Thereby, this type of fracture is regarded as an infinite conductivity fracture. For this case, it is also recommended to estimate fracture length and fracture conductivity as indicated in Ref. 34 and then simulate a pressure test with the recently calculated fracture conductivity and fracture length. If comparison with the simulated curve and the actual trend gives some differences at early time, we may be in the presence of a high conductivity branch.

4.2. HYDRAULIC FRACTURED VERTICAL WELL INTERSECTING A SEALING FAULT

There was no evidence of a similar study reported in the literature. As illustrated in Figs. 3.7 and 3.8, the experiments of a hydraulic fracture intersecting a fault analyzes different intersecting angles and three intersecting points fracture-fault. The numbers of grid cells used in all the simulation are reported in tables D.23.a through D.23.o. Some few grid systems are presented in Figs. C.22.a through C.22.d.

At early points in time, in a pressure test conducted in a well with a hydraulic fracture presents bilinear flow when the fracture has a finite conductivity. This period is characterized by simultaneous flow inside the fracture and another flow from the formation to the fracture, as identified by Cinco-Ley et al[18]. This flow period is identified by a straight line having a one-fourth slope in the pressure derivative curve on a logarithmic plot. As the fracture conductivity increases, the duration of the ¼

slope tends to be reduced and it completely disappears for the case of infinite fracture conductivity since the pressure drop along the fracture becomes smaller. It has been conventionally established[18] that for dimensionless fracture conductivity higher than 300, the bilinear flow is no present and only a linear flow from the formation to the fracture takes place giving origin to the onset of infinite hydraulic conductivities. The linear flow is characterized by a one-half slope at early time of the pressure test seen on the derivative curve of a log-log plot.

Once the linear or bilinear effect has ended, the answer from the reservoir itself is then expected. That answer is conventionally referred as pseudoradial flow and for Newtonian flow behavior is characterized by a straight line with a zero slope found in the derivative curve on a log-log plot.

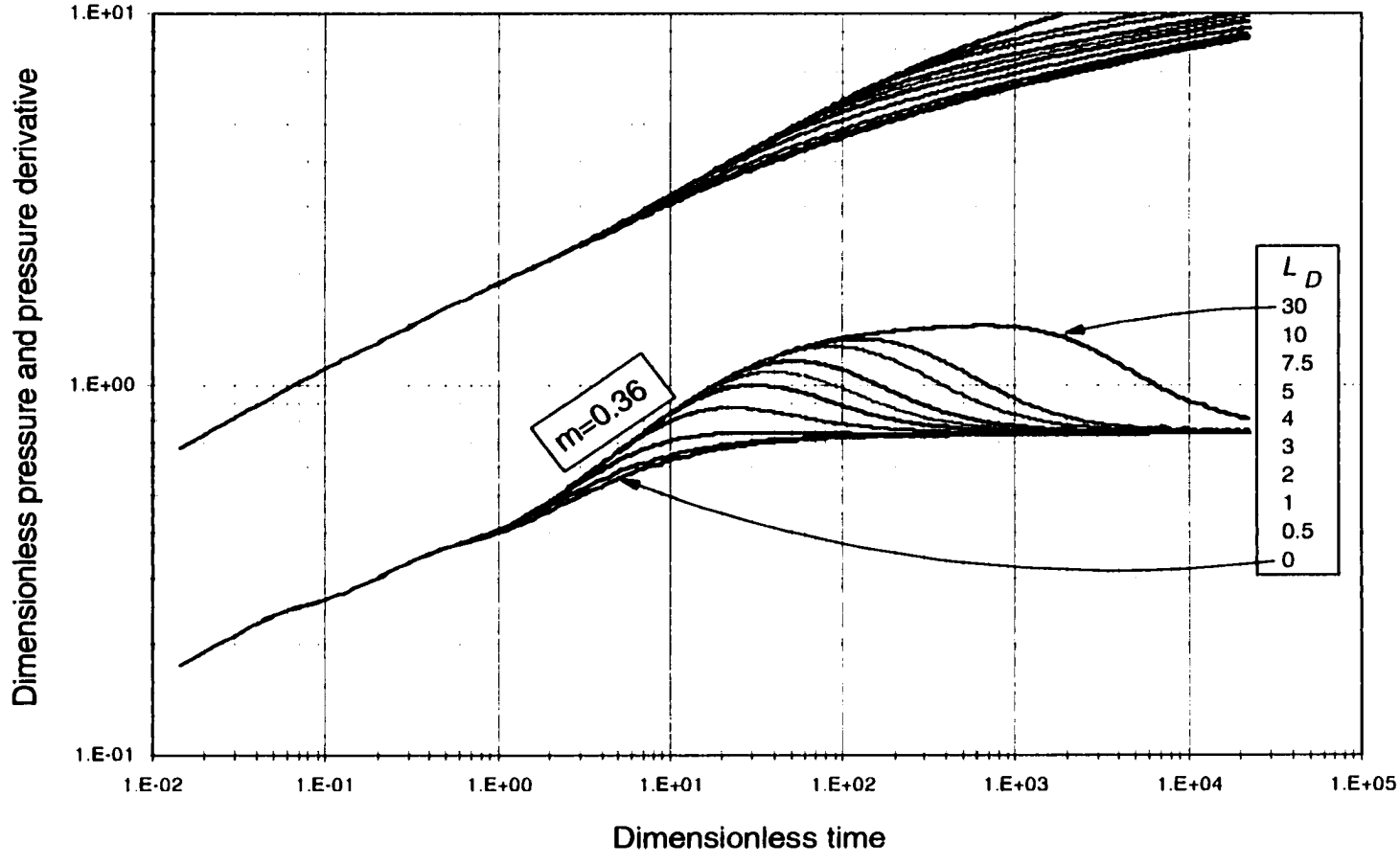

Fig. 4.8.a. Dimensionless pressure and pressure derivative curve for a hydraulic fracture intersecting a fault at its middle part forming an angle of 90°. C_D=1

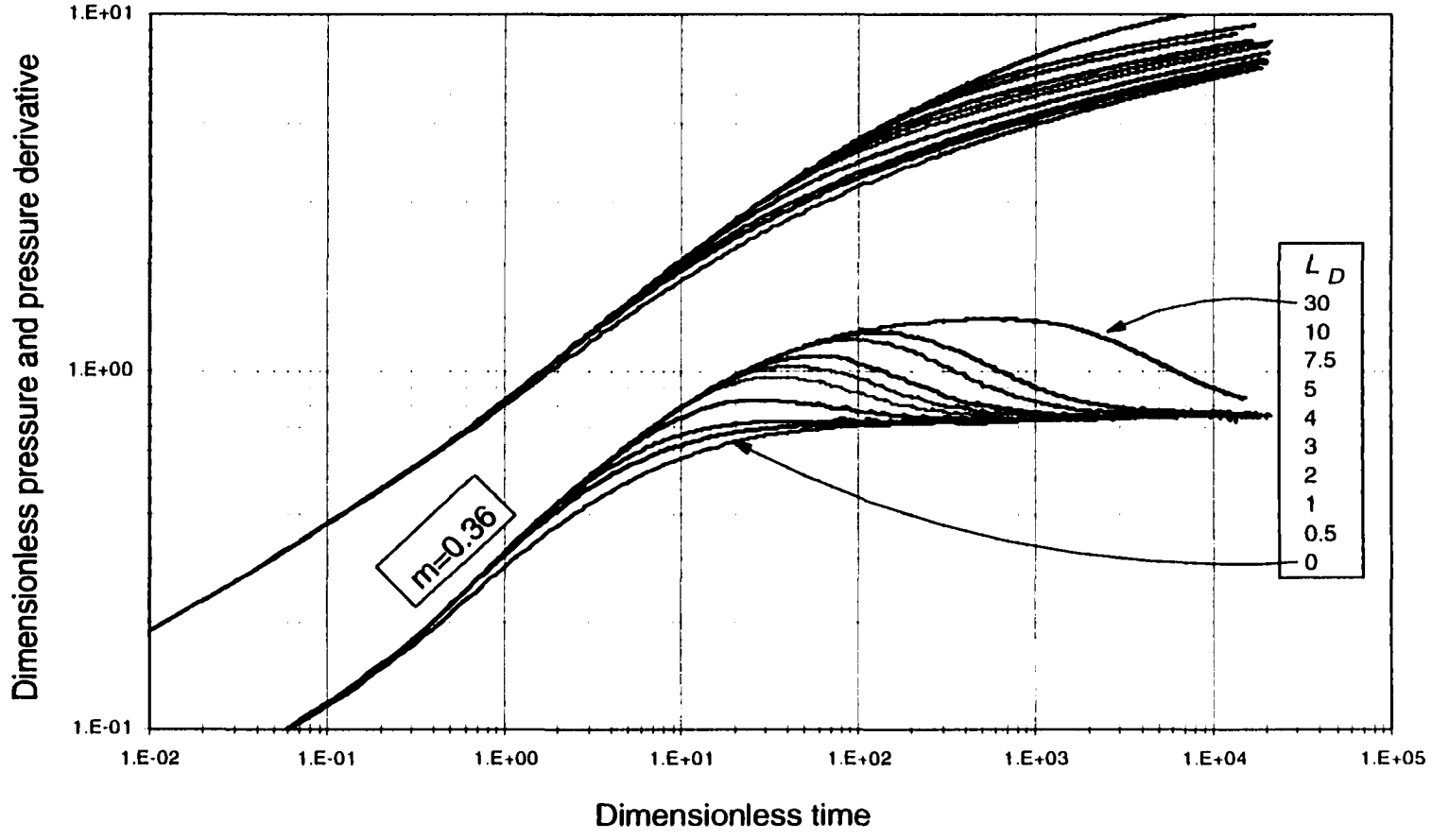

Fig. 4.8.b. Dimensionless pressure and pressure derivative curve for a hydraulic fracture intersecting a fault at its middle part forming an angle of 90°. C_D=10

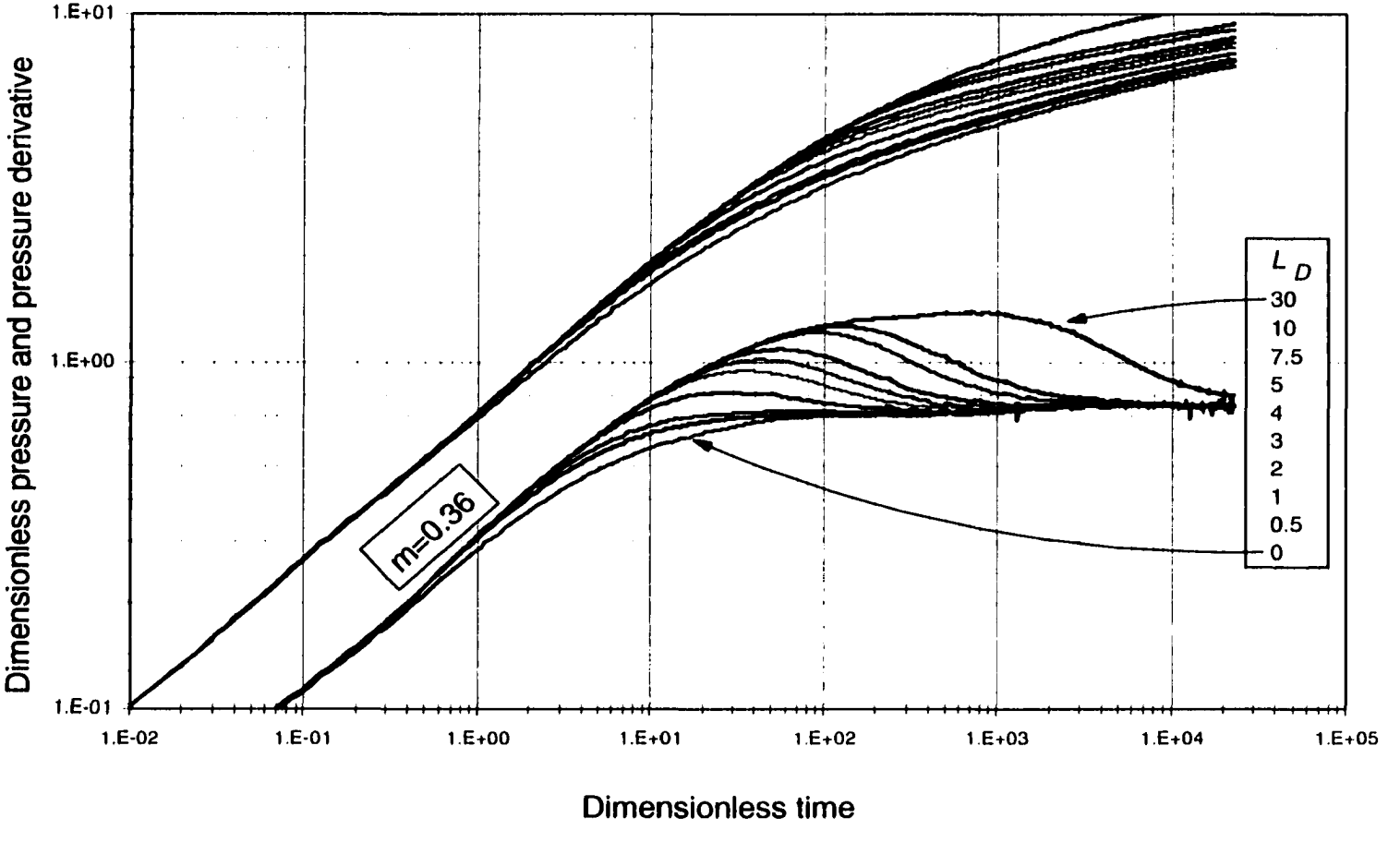

Fig. 4.8.c. Dimensionless pressure and pressure derivative curve for a hydraulic fracture intersecting a fault at its middle part forming an angle of 90°. C_D=50

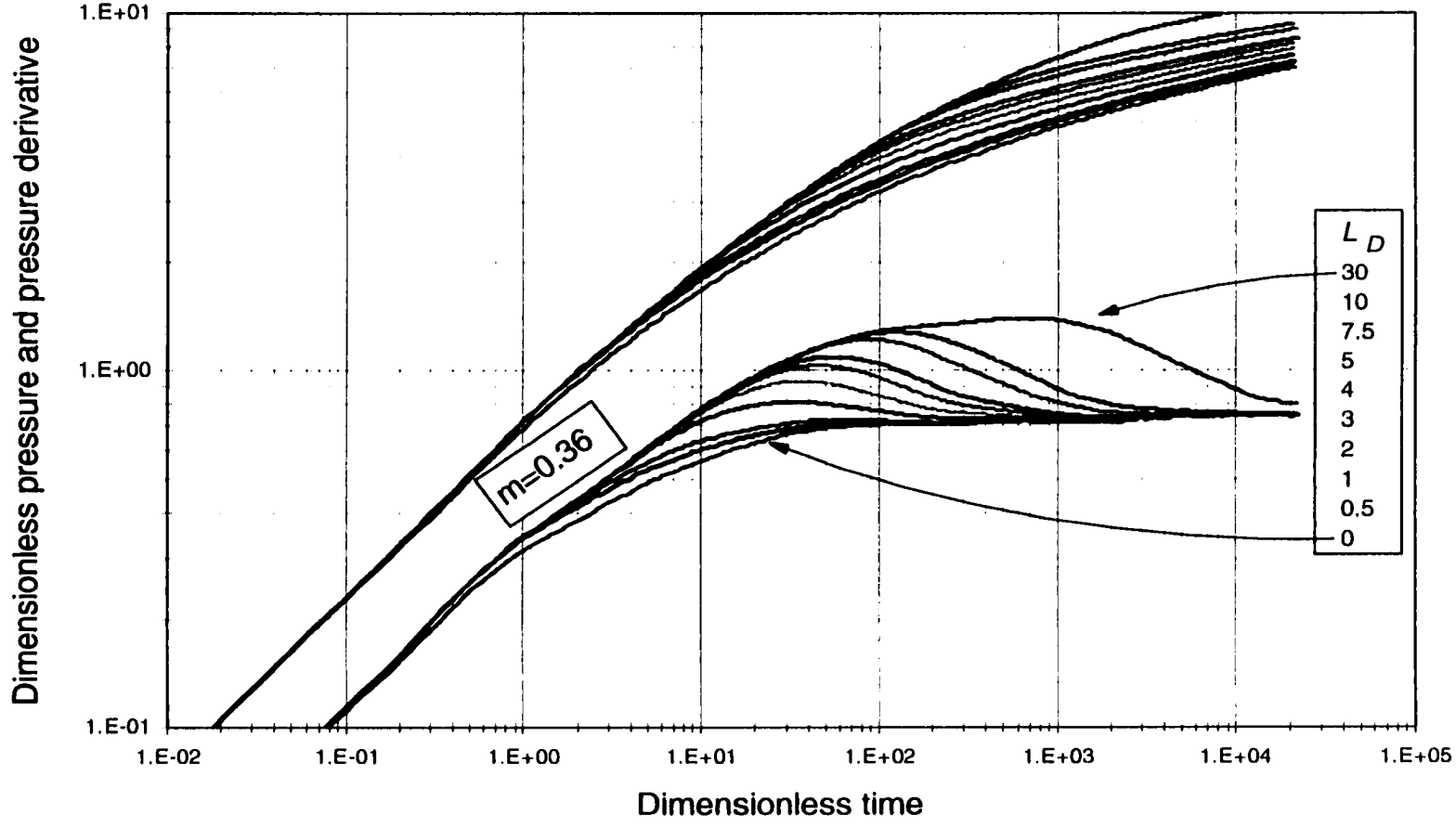

Fig. 4.8.d. Dimensionless pressure and pressure derivative curve for a hydraulic fracture intersecting a fault at its middle part forming an angle of 90°. C_D=100

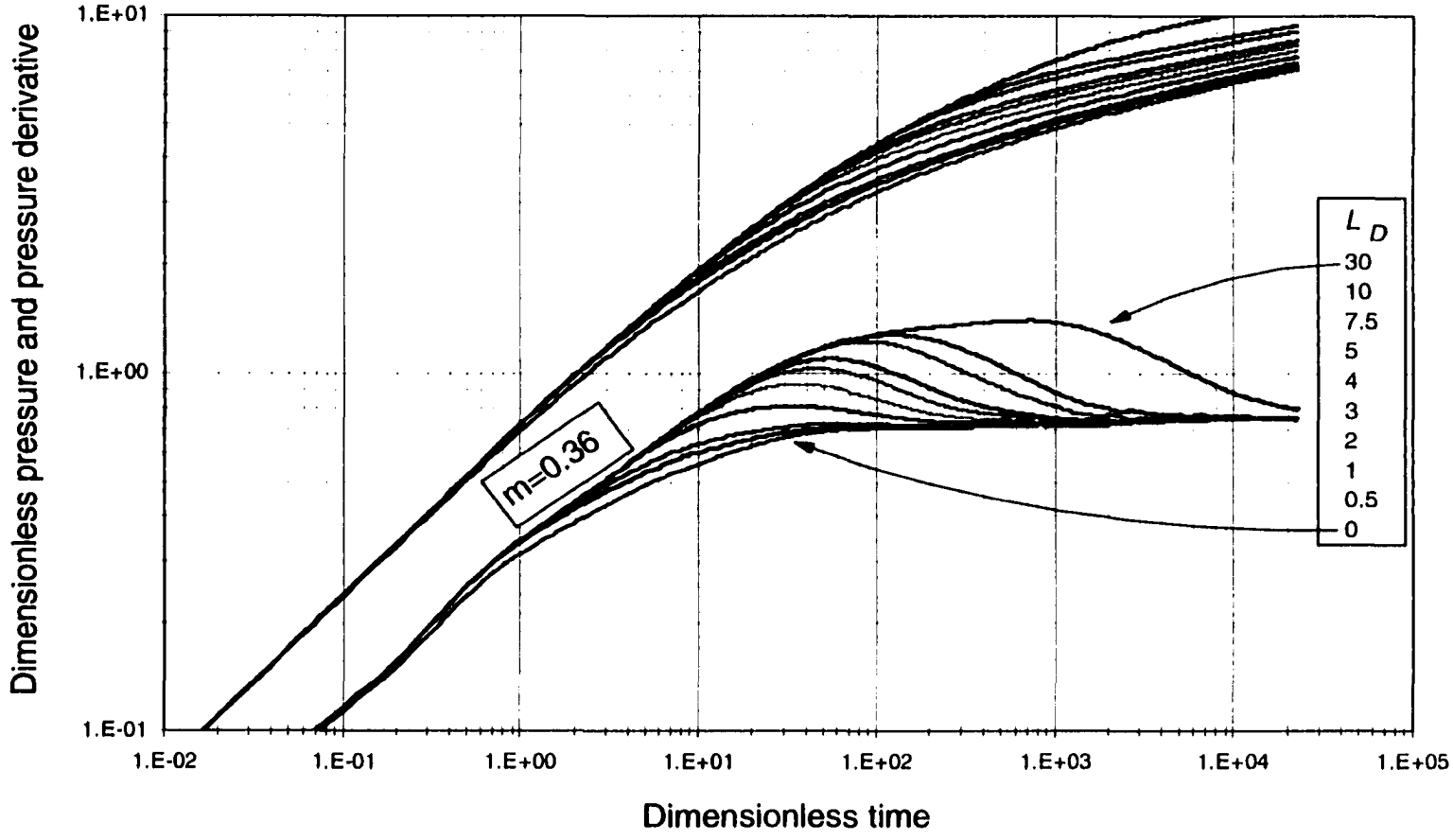

Fig. 4.8.e. Dimensionless pressure and pressure derivative curve for a hydraulic fracture intersecting a fault at its middle part forming an angle of 90°. C_{fD}=300

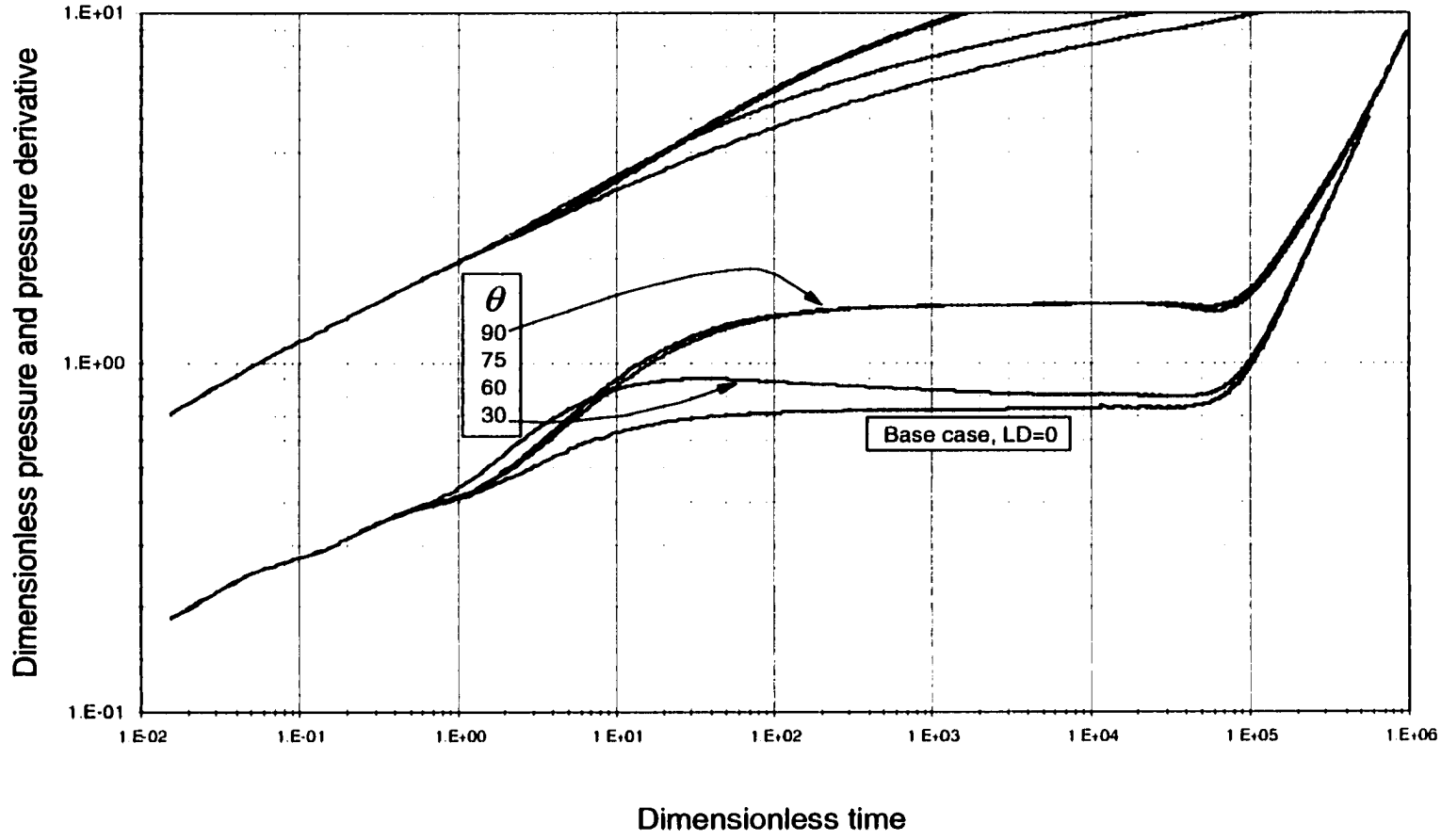

Fig. 4.8.f. Dimensionless pressure and pressure derivative curve for a hydraulic fracture intersecting a fault at its middle part. C_D=1 and L_D=80

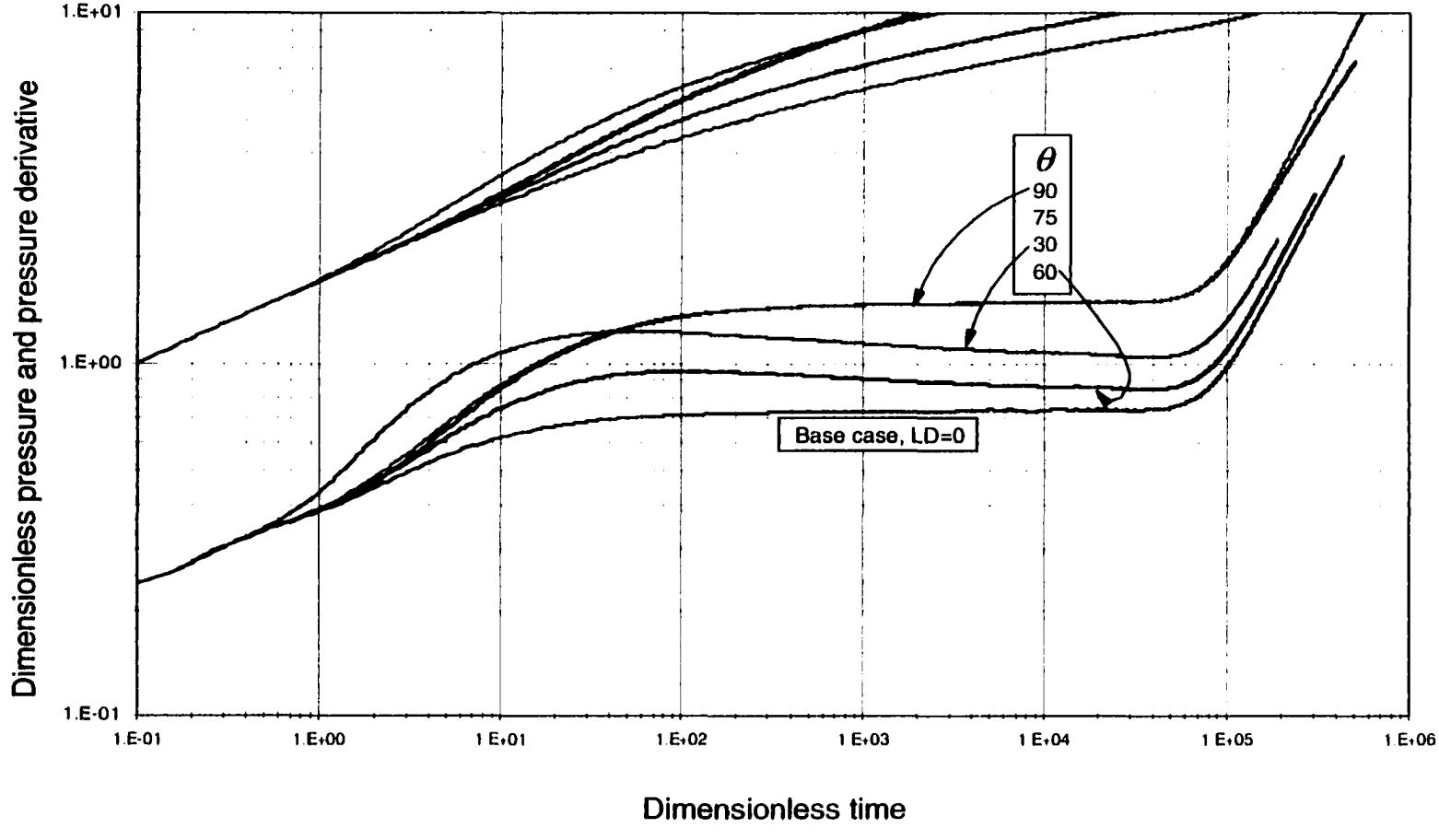

Fig. 4.8.g. Dimensionless pressure and pressure derivative curve for a hydraulic fracture intersecting a fault at its middle part. $C_{fD}=1$ and $L_D=162$

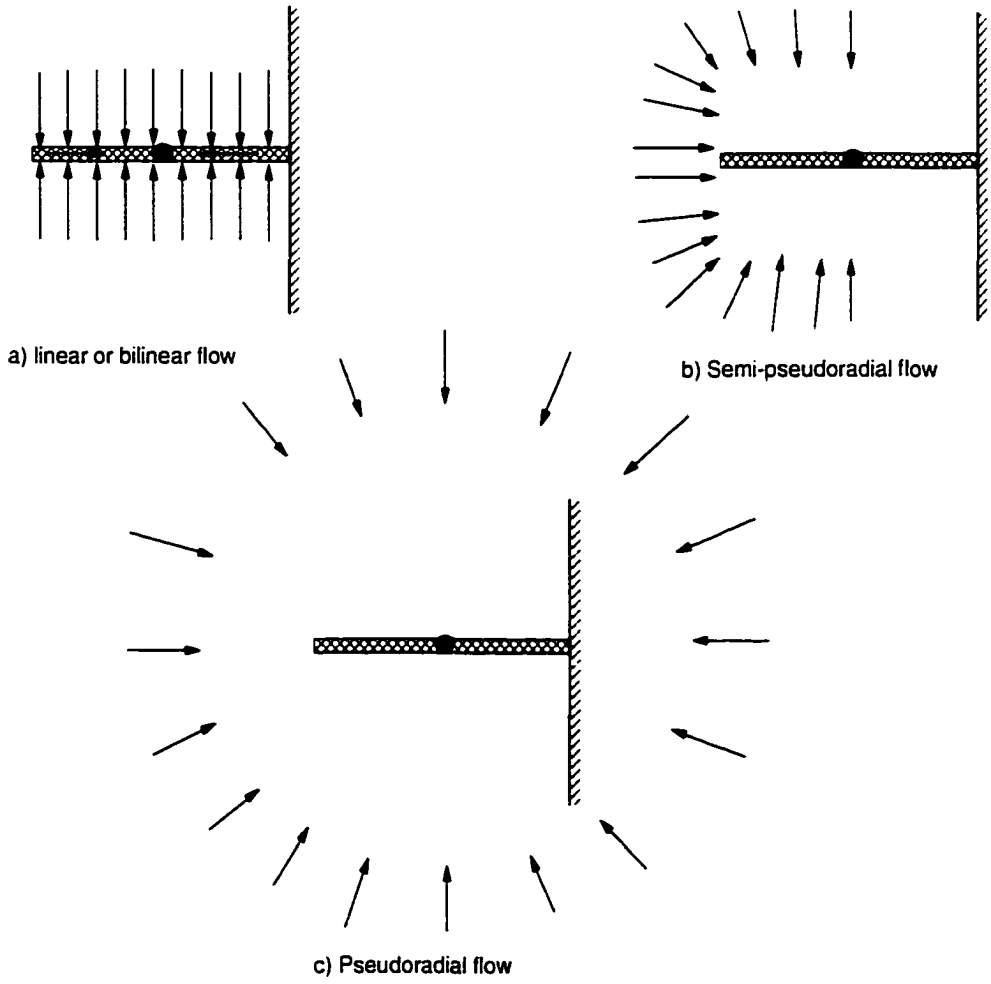

Fig. 4.9. Sketch of flow regimes for a hydraulic fracture intersecting the middle part of a fault and forming an angle of 90°

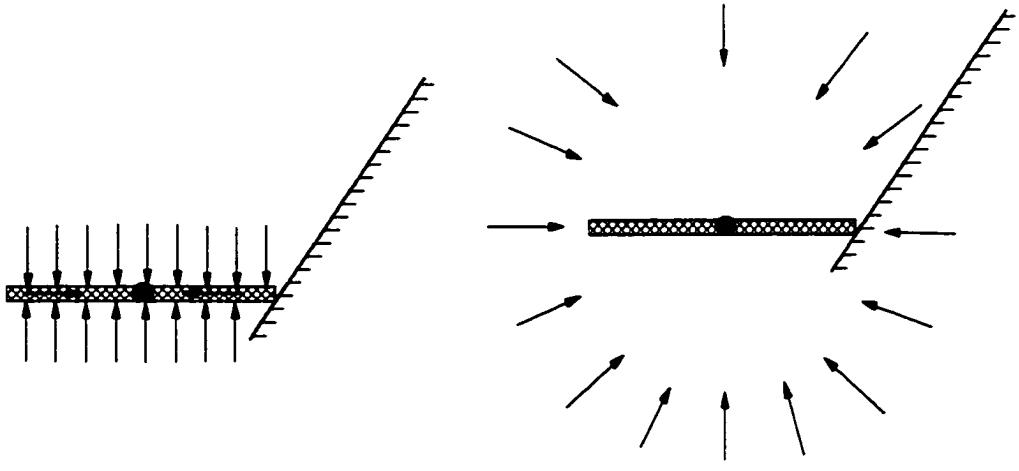

Fig. 4.10. Illustration of flow regimes for a hydraulic fracture intersecting the fourth part of a fault and forming an angle less than 90° (angle measured clockwise)

As seen in Figs. 4.8.a through 4.8.f if a fracture intersects a fault at its middle part and forming an angle of 90 degrees, this fault tends to delay the formation of the pseudoradial flow period. Actually, the fault may act as a boundary which effect depends upon its length. In the mentioned figures, if comparing a faulted system with an unfaulted one, after the bilinear/linear flow ends, the pressure derivative curve for the faulted system starts deviation upwards from the unfaulted one. This deviation is more pronounced as the fault length increases upwards.

Notice that for $r_e/L_f \leq 16405/3000 \leq 5.5$ radial flow will not develop.

For a better understanding of the above phenomenon, refer first to the upper curve on the pressure derivative plot of Fig. 4.8.g which presents the behavior of a hydraulic fracture-symmetric fault system when the intersecting angle is either 90 or 75°. The fault crosses completely the reservoir and practically divides it into two

semicircles. Notice that after the bilinear flow has ended, a zero-slope straight line is observed. At first instance, we may tend to suggest that the pseudoradial (or as stated before radial) flow period has been reached. This is a wrong conclusion and will lead to underestimation of reservoir permeability. If the proportion is linear, we may end up estimating half permeability value. This type of system will never develop a pseudoradial flow period because that requires the response from the whole reservoir. If taking a glance to Fig. 4.8.b, the response is obtained from, practically, half reservoir portion then this period is here named as *semi-pseudoradial* radial or *semiradial flow*.

If considering another fault length, let us say L_D=5, for a finite fracture conductivity system, it is first observed the bilinear flow regime as pointed out before. See Fig. 4.9.a. Once, the effects of bilinear flow has been vanished, the curves fall into a straight line which slope is 0.36. This may indicate the presence of elliptical flow. The length of this slope depends on fault length. After a transition period, the response of half part of the reservoir is felt as indicated in Fig. 4.9.b and the semiradial flow tries to develop. As the time goes by and the pressure transient has passed the fault tip, then the pseudoradial flow regime takes place as sketched in Fig. 4.9.c.

Besides the fault length, there are two key factors which affect the presence of the semiradial flow regime. They are fracture-fault intersecting point and fracture-fault intersecting angle. If the fracture meets the fault at a point different of the fault's middle point, the possibilities of radial flow development is higher since the shorter distance from the meeting point to the fault tip provides more room for the faster formation of the radial flow regime. When fracture and fault meet at their tips, the

presence of the semiradial flow is practically undetectable as seen in Figs. B.6.a thorough B.6.e.

A slight rotation of the fault angle causes the semiradial flow to be much shorter as it can be appreciated from Figs. B.7.a. through B.7.e which shows the pressure behavior for a fracture-fault system forming an angle of 75°. As the angle increases, the pressure "hump" observed on the pressure derivative plots no longer shows up, therefore the duration of the semiradial flow regime is reduced. See Figs. 4.10.a and 4.10.b.

As observed in Figs. B.17.a through B.17.c, when the angle of intersection is zero (or 180°) the fault is not felt by the pressure transient response. Once the bilinear or linear effect has ended, the formation of the radial flow regime takes place without any influence of the fault.

Fig. 4.8.g deserves a especial observation. Notice that during the radial acting part of the plot, the derivative curve of 30 degrees falls between the 90°/75° and 60° curves. This is due to the fact that in the 30 degrees system, immediately after the bilinear/linear flow period, the presence of a boundary is felt by the pressure transient, then a pseudosteady state flow regime tries to develop. As the transient travels, neither de semiradial nor the radial flow regimes are observed because the reservoir boundaries avoid it.

Tables D.24.a though D.24.e present some value of the pressure response for a fracture-fault system intersecting with an angle of 90° at the middle part of the fault. Only the case of dimensionless fracture conductivity of one is reported.

Refer to Figs. B.5.a through B.18.b to observe all the cases studied here for fracture-fault systems. Notice that the effects of the fracture conductivity on the transient characterization of the fault is negligible.

CHAPTER V

THE *TIAB'S DIRECT SYNTHESIS TECHNIQUE*

The *Tiab's Direct Synthesis Technique* is a modern and revolutionary method for interpretation of pressure transient tests in hydrocarbon reservoirs. This technique, introduced by Tiab[99] in 1993, utilizes characteristic points and lines commonly found in the pressure and pressure derivative curves to determine reservoir, well and fracture parameters. Its greatest advantage is that it utilizes exact analytical solutions determined for each particular flow regime then the use of type-curve matching is fully eliminated. The *Tiab's Direct Synthesis Technique* has been extended to several reservoir and well conditions among which we can name fractured vertical wells, horizontal wells in heterogeneous media, horizontal wells in naturally fractured reservoirs, gas well testing, etc.

Since this work deals with a finite-conductivity vertical fractured well, the extension of the *Tiab's Direct Synthesis Technique* very closely follows the procedure outlined in Ref. 34. Therefore, new equations and procedures to determine branch fracture length and fault length are added.

5.1. HYDRAULIC FRACTURED VERTICAL WELL WITH A BRANCH FRACTURE

As mentioned in chapter 4, during a pressure transient test conducted in a vertically fractured well, it is theoretically expected to find first a linear flow regime in the fracture, which is characterized by a slope of 0.5 on the log-log plot. However, the occurrence of this flow period is too short and normally is never seen. Once this flow period ends, a simultaneous linear flow in the fracture and a linear flow from the formation to the fracture take place. This flow period has been called[18] bilinear flow and is identified by a slope of one quarter on the log-log plot. Once the linear flow in the formation -or the bilinear flow- vanishes, the pseudo-radial flow takes place. Fig. 5.1 illustrates the mentioned flow regimes for a hydraulically fractured vertical well.

Assuming the fractured well is produced long enough to observe the infinite acting behavior then the log-log plot of pressure and pressure derivative data versus time would yield unique characteristics, which can be used to analyze pressure transient tests by the *Tiab's Direct Synthesis Technique*.

These unique characteristics are: (a) an early slope of 0.34-0.35 (although values of 0.25, 0.38, 0.4 and 0.42 may be observed, see Table 4.5) characterizing the branch fracture. (b) The bilinear flow line of slope 0.25, (c) The formation linear flow line of slope 0.5, and (d) The late-time horizontal line which corresponds to the radial flow regime.

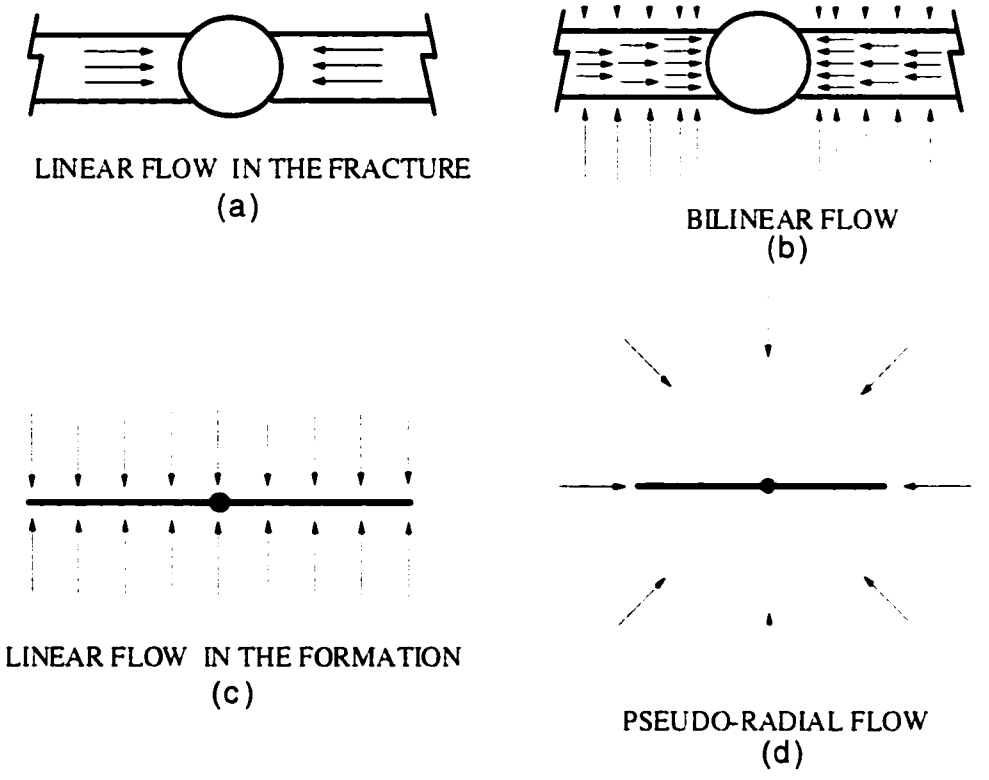

Fig. 5.1. Flow Regimes governing pressure behavior at a well interrupting a finite capacity vertical fracture[22]

5.1.1. BILINEAR FLOW REGIME[34]

During the bilinear flow regime, the dimensionless well pressure behavior is given by:

$$P_D = \left(\frac{2.451}{\sqrt{C_{fD}}} \right) t_D^{0.25} \tag{5.1}$$

where the dimensionless fracture conductivity, C_{fD}, is defined by:

$$C_{fD} = k_{fD} w_D = \left(\frac{k_f}{k}\right)\left(\frac{w_f}{x_f}\right) \tag{3.37}$$

The dimensionless time, t_D, and dimensionless well pressure, P_D, are given by:

$$t_D = \frac{0.0002637kt}{\phi\mu c_t x_f^2} \tag{3.35}$$

$$P_D = \frac{kh}{141.2q\mu B}\Delta p \tag{3.38}$$

Combining Eqs. 5.1, 3.35, 3.37 and 3.38 and solving for the well pressure drop, Δp, yields :

$$\Delta p = m_{BL} t^{0.25} \tag{5.2}$$

where the subscript BL stands for bilinear and m_{BL} is defined by:

$$m_{BL} = \frac{44.13}{(\phi\mu c_t k)^{0.25}}\left(\frac{q\mu B}{h\sqrt{k_f w}}\right) \tag{5.3}$$

Taking the logarithm of both sides of Eq. 5.2 yields,

$$\log \Delta p = 0.25 \log t + \log m_{BL} \tag{5.4}$$

The above expression indicates that a plot of ΔP versus time on a log-log graph will yield a straight line portion of slope 0.25, if the fracture has a finite conductivity.

Let $(\Delta P)_{BL1}$ be the value of ΔP_W at time t = 1 hour on the bilinear flow straight line (extrapolated if necessary), then the Eq. 5.4 becomes:

$$(\Delta P)_{BL1} = m_{BL} \tag{5.5}$$

Combining Eqs. 5.3 and 5.5 and solving for the fracture conductivity, $k_f w$, we have:

$$k_f w = 1947.46 \frac{1}{\sqrt{\phi \mu c_t k}} \left(\frac{q \mu B}{h(\Delta P)_{BLI}} \right)^2 \tag{5.6}$$

Fracture conductivity also can be determined from the pressure derivative straight line corresponding to the bilinear flow regime. The derivative of the dimensionless well pressure during this regime is:

$$t_D \cdot P'_D = \left(\frac{0.6127}{\sqrt{k_{fD} w_D}} \right) \cdot t_D^{0.25} \tag{5.7}$$

Substituting for the dimensionless parameters and solving for the derivative of well pressure, it yields:

$$t \cdot \Delta p'_w = 0.25 m_{BL} \cdot t^{0.25} \tag{5.8}$$

Taking the logarithm of both sides of Eq. 5.8, gives

$$\log (t \cdot \Delta p') = 0.25 \cdot \log t + \log (0.25 m_{BL}) \tag{5.9}$$

This expression also shows that a log-log plot of $(t\Delta p')$ versus time will yield a straight line of slope 0.25 if the bilinear flow is dominant. Let $(t^*\Delta p')_{BLI} = (t^*\Delta p')$ be the value of $(t^*\Delta p')$ at time t=1 hr on the bilinear flow straight line, extrapolated if necessary, then Eq. 5.9 becomes

$$(t \cdot \Delta p')_{BLI} = 0.25 m_{BL} \tag{5.10}$$

Comparing Eqs. 5.5 and 5.10, gives at time t=1 hr:

$$(t \cdot \Delta p')_{BLI} = 0.25 (\Delta p)_{BLI} \tag{5.11}$$

The conductivity of the finite conductivity fracture from the pressure derivative line is obtained by replacing $(t^*\Delta p')_{BLI}$ in Eq. 5.6 with $4(t^*\Delta p')_{BLI}$, thus

$$k_f w = \frac{121.74}{\sqrt{\phi\mu c_t k}}\left(\frac{q\mu B}{h(t\cdot\Delta p')_{BLI}}\right)^2 \qquad (5.12)$$

Eq. 5.11 is very important because it relates the pressure and the pressure derivative functions at a unique point, and can be used for verification purposes.

Generally, near-wellbore conditions affect the pressure derivative curve much more than the pressure curve during bilinear flow, making it difficult to locate the quarter-slope line. In such case, calculate the fracture conductivity from the bilinear flow line of the pressure curve, using Eq. 5.6. Then, estimate $(t^*\Delta p')_{BLI}$ from Eq. 5.11 and draw a straight line of slope 0.25 across this point.

5.1.2. WELLBORE STORAGE AND BILINEAR FLOW

This works does not consider wellbore storage effects because it masks the early answer from a fracture. However, for completeness purposes, if the unit slope straight line, corresponding to the wellbore storage flow regime, is present, then the wellbore storage coefficient can be determined from the usual equations, i.e., from the pressure curve:

$$C = \left(\frac{qB}{24}\right)\frac{t}{\Delta p} \qquad (5.13)$$

or from the pressure derivative curve:

$$C = \left(\frac{qB}{24}\right)\frac{t}{t\cdot\Delta p'} \qquad (5.14)$$

The coordinates of the point of intersection of the unit slope and bilinear flow lines on the pressure curve can be obtained by combining Eq. 5.2 and 5.13:

$$m_{BL} \cdot t^{0.25} = \left(\frac{qB}{24C} \right) t \tag{5.15}$$

Replacing t with t_{USBL} yields:

$$t_{USBL} = 24^{4/3} \left(\frac{Cm_{BL}}{qB} \right)^{4/3} \tag{5.16}$$

At the intersection point, on the pressure curve:

$$(\Delta p)_{USBL} = m_{BL} (t_{USBL})^{0.25} \tag{5.17}$$

The coordinates of the point of intersection of the unit slope and bilinear flow lines on the derivative curve can be obtained by combining Eqs. 5.8 and 5.14; thus,

$$0.25 m_{BL} t^{0.25} = \left(\frac{qB}{24C} \right) \cdot t \tag{5.18}$$

Replacing t with t'_{USBL} yields:

$$t'_{USBL} = 6^{4/3} \left(\frac{cm_{BL}}{qB} \right)^{4/3} \tag{5.19}$$

and:

$$(t \cdot \Delta p')_{USBL} = 0.25 m_{BL} (t'_{USBL})^{0.25} \tag{5.20}$$

The coordinates of the intersection points on the Δp and $t^*\Delta p'$ curves are related as follows:

$$t_{USBL} = 4^{4/3} t'_{USBL} \tag{5.21}$$

$$(\Delta p)_{USBL} = 4 \cdot (t \cdot \Delta p')_{USBL} \tag{5.22}$$

These two expressions are very useful for verification purposes.

5.1.3. LINEAR AND BILINEAR FLOW INTERRELATIONSHIPS[34]

If the formation linear flow regime is observed after the bilinear flow line, then the equations developed by Tiab[33] for the infinite conductivity fracture and uniform flux fracture cases can be used to determine the fracture length:

$$\Delta p = m_L \sqrt{t} \tag{5.23}$$

$$(t \cdot \Delta p') = 0.5 m_L \sqrt{t} \tag{5.24}$$

Replacing the dimensionless groups, we obtain:

$$m_L = 4.064 \left(\frac{qB}{h} \right) \sqrt{\frac{\mu}{\phi c_t k x_f^2}} \tag{5.25}$$

Taking the logarithm of both sides of Eq. 5.23 and solving for the half-fracture length, x_f at time t=1 hr yields:

$$x_f = 4.064 \left(\frac{qB}{h(\Delta p)_{LI}} \right) \sqrt{\frac{\mu}{\phi c_t k}} \tag{5.26}$$

where $(\Delta p)_{LI}$ is the value of Δp at time t=1 hour on the straight line portion of slope 0.5 (extrapolated if necessary). The half-fracture length can be determined from the derivative curve by replacing $(\Delta p)_{LI}$, in Eq. 5.26 with $2(t\Delta p')_{LI}$, since at time t = 1 hour:

$$(t \cdot \Delta p')_{LI} = 0.5 \cdot (\Delta p)_{LI} \tag{5.27}$$

OBSERVATION:

(a) The coordinates of the intersection point of the lines on the Δp curve can be obtained by combining Eqs. 5.2 and 5.23:

$$m_{BL}t^{0.25} = m_L t^{0.5} \tag{5.28}$$

Replacing t with t_{BLLi}, where the subscript "*BLLi*" stands for intersection of the bilinear and linear flow lines, yields:

$$t_{BLLi} = \left(\frac{m_{BLLi}}{m_L}\right)^4 \tag{5.29}$$

$$(\Delta p)_{BLLi} = m_L\sqrt{t_{BLLi}} \tag{5.30}$$

or:

$$(\Delta p)_{BLLi} = m_{BL}(t_{BLLi})^{0.25} \tag{5.31}$$

Substituting for m_{BL} (Eq. 5.3) and m_L (Eq. 5.25) into Eq. 5.29 we obtain:

$$t_{BLLi} = 13910\phi\mu c_t\left(\frac{x_f^2\sqrt{k}}{k_f w}\right)^2 \tag{5.32a}$$

Solving permeability, k, yields:

$$k = \left(\frac{k_f w}{x_f^2}\right)^2 \frac{t_{BLLi}}{13910\phi\mu c_t} \tag{5.32b}$$

Eqs. 5.32a and 5.32b can be used for verification purposes, if all three flow regimes are observed. If the test is too short to observe the radial flow line, or a pre-frac test is not possible such as in low-permeability formation, then Eq. 5.32b may be used to calculate the formation permeability.

A useful relationship for design and verification purposes may be derived by combining the dimensionless fracture conductivity, Eq. 3.37, and Eq. 5.29.

$$t_{BLL} = 13910 \frac{\phi \mu c_t}{k} \left(\frac{x_f^2}{c_{fD}} \right)^2 \tag{5.33}$$

(b) Using a similar approach, the coordinates of the point of intersection of the bilinear and linear straight lines on the derivative curve, we have:

$$t'_{BLL} = \left(\frac{m_{BL}}{2 \cdot m_L} \right)^4 = \frac{1}{16} \left(\frac{m_{BL}}{m_L} \right)^4 \tag{5.34}$$

$$(t \cdot \Delta p')_{BLL} = 0.5 m_L \cdot (t'_{BLL})^{0.5} \tag{5.35}$$

or:

$$(t \cdot \Delta p')_{BLL} = 0.25 m_{BL} \cdot (t'_{BLL})^{0.25} \tag{5.36}$$

A relationship between t_{BLL} and t'_{BLL} can be derived by combining Eqs. 5.26 and 5.24:

$$t_{BBL} = 16 t'_{BBL} \tag{5.37}$$

Combining Eqs. 5.31 and 5.36 yields:

$$(\Delta p)_{BLL} = 4 \cdot (t \cdot \Delta p')_{BLL} \tag{5.38}$$

Thus, it is possible to "locate" the straight lines corresponding to the two flow regimes on the pressure derivative curve from the pressure curve, even when the pressure derivative data are extremely noisy.

5.1.4. RADIAL AND BILINEAR FLOW INTERRELATIONSHIPS[34]

The pressure derivative portion corresponding to the infinite acting radial flow line is a horizontal straight line. This flow regime is given by;

$$(t \cdot \Delta p')_R = \frac{70.6q\mu B}{kh} \tag{5.39a}$$

The subscript "*R*" stands for radial flow. The formation permeability is therefore[99]:

$$k = \frac{70.6q\mu B}{h(t \cdot \Delta p')_R} \tag{5.39b}$$

where $(t\Delta p')_R$ is obtained by extrapolating the horizontal line to the vertical axis. The radial flow line can also be used to calculate the skin factor from the equation[99]:

$$s = 0.5\left[\frac{(\Delta p)_R}{(t \cdot \Delta p')_R} - \ln\left(\frac{kt_R}{\phi\mu c_t r_w^2}\right) + 7.43\right] \tag{5.40}$$

The time-coordinate of the intersection point of the bilinear and radial flow straight lines can be determined from a combination of Eqs. 5.8 and 5.3:

$$0.25 m_{BL} t^{0.25} = \frac{70.6q\mu B}{kh} \tag{5.41}$$

$$t_{RBLi}^{0.25} = \frac{70.6q\mu B}{kh}\frac{4}{m_{BL}} \tag{5.42}$$

Substituting for m_{BL} from Eq. 5.3 yields:

$$t_{RBLi} = 1677\frac{\phi\mu c_t}{k^3}\left(k_f w_f\right)^2 \tag{5.43}$$

This expression should preferably be used for verification purposes. Radial and linear flow interrelationships are presented in Ref. 2.

If there is a certainty that *semiradial* or *pseudo-semiradial* flow is present, the equation to estimate permeability should be:

$$k = \frac{141.2q\mu B}{h(t \cdot \Delta p')_{SR}} \tag{5.39c}$$

where the suffix SR stands for *semiradial.*

5.1.4. RADIAL AND LINEAR FLOW RELATIONSHIPS[34]

As presented in Ref. 33, combining Eqs. 5.24 and 2.25 and solving for the half-fracture length, x_f, we obtain:

$$x_f = \frac{2.032Bq}{h(t*\Delta p')_{L1}}\sqrt{\frac{\mu}{\phi c_t k}} \tag{5.44}$$

Besides, if we let $(\Delta p)_{L1}$ be the value of Δp on the straight line (extrapolated if necessary) at time t=1 hr and using Eq. 3.26[33] we are able to estimate x_f.

$$x_f = \frac{4.064Bq}{h(\Delta p)_{L1}}\sqrt{\frac{\mu}{\phi c_t k}} \tag{5.26}$$

The point of intersection of the linear flow line and the infinite-acting radial flow line is unique. For further verification, Ref. 33 presents an equation to estimate the ratio x_f^2/k from this intersection point:

$$\frac{x_f^2}{k} = \frac{t_{LRi}}{1207\phi\mu c_t} \tag{5.45}$$

For completeness of the set of equations, Ref. 33 provides relationships to estimate x_f and drainage area from the intersection point between the linear line with the pseudosteady-state line and with the radial line, respectively, thus:

$$kx_f^2 = \frac{7544\phi\mu c_t A}{t_{LP_1}} \tag{5.46}$$

$$A = \frac{7544\phi\mu c_t}{kx_f^2 t_{LP_1}} \tag{5.47}$$

$$A = \frac{kt_{RP_1}}{301.77\phi\mu c_t} \tag{5.48}$$

5.1.5. BRANCH FRACTURE REGIME RELATIONS

We have seen that the response of a hydraulic fracture having a branch is very similar to the response of an asymmetric fracture. Therefore, the application of the technique may be applied to both systems.

In the above systems, we observe (See. Figs. B.4.a. – B.4.e) for hydraulic fractures having low and moderate fracture conductivity, i.e. C_{fD}=10 or 50, that it may be difficult to identify the bilinear flow regime because it is masked by the branch fracture regime. However, it should exist at very early time during the test.

Let us define m_{bf} and b_{bf} as the slope of intercept of the branch fracture. Then, the derivative curve for that flow regime closely follows this relationship:

$$t_D \cdot P_D' = b_{bf} t_D^{m_{bf}} \tag{5.49}$$

The main fracture and branch fracture dimensional conductivities are assumed to be the same. Then:

$$C_{fbD} = k_{fbD} w_{bD} = \left(\frac{k_f}{k}\right)\left(\frac{w}{x_{fb}}\right) \tag{5.50}$$

Redefining the dimensionless time as:

$$t_D = \frac{0.0002637kt}{\phi\mu c_t x_{fb}^2} \tag{5.51}$$

Combination of Eqs. 5.49 through 5.51 and Eq. 3.38 gives:

$$t \cdot \Delta p' = \frac{535456.96 b_{hf} Bc_t \mu^2 (0.0002637k/\phi\mu c_t)^{m_{hf}} \phi x_{fb}^{2(1-m_{hf})}}{k^2 h} t^{m_{hf}} \tag{5.52}$$

Recalling Eq. 5.8,

$$t \cdot \Delta p' = 0.25 m_{BL} \cdot t^{0.25} \tag{5.8}$$

The intersection point between the line of slope m_{bf} with the bilinear line leads to the estimation of the branch fracture length. After combining Eqs. 5.52 with 5.8 and solving for x_{fb}, yields:

$$x_{fb} = \left[\frac{k^2 h m_{BL}}{2141827.8 b_{hf} Bc_t \mu^2 (0.0002637k/\phi\mu c_t)^{m_{hf}} \phi t_{BFBLi}^{m_{hf}-0.25}}\right]^{1/2(1-m_{hf})} \tag{5.53}$$

where the suffix *BFBLi* stands for the intersection between bilinear and branch fracture lines and m_{BL} is given by Eq. 5.3. Notice that x_f was substracted in Eq. 5.53 because the computed fracture length includes the total fracture length.

Recalling Eq. 5.24:

$$(t \cdot \Delta p') = 0.5 m_L \sqrt{t} \tag{5.24}$$

The intersection point between the line of slope m_{bf} with the linear line can be used to estimate the branch fracture length. Combination of Eqs. 5.52 with 5.24 and solving for x_{fb}, yields:

$$x_{fh} = \left[\frac{k^2 h m_L t_{BFLi}^{0.5-m_{hf}}}{1070913.9 b_{hf} B c_t \mu^2 (0.0002637 k / \phi \mu c_t)^{m_{hf}} \phi} \right]^{1/2(1-m_{hf})} \tag{5.54}$$

where the suffix *BFLi* stands for the intersection between linear and branch fracture lines and m_L is given by Eq. 5.25:

If both linear and bilinear flow periods are observed Eqs. 5.53 and 5.54 should be used simultaneously for verification purposes.

If neither linear flow nor bilinear flow are identified, combination of Eqs. 5.39.a with 5.52 should be used to estimate the branch fracture length when this two lines intersect at the point t_{BFRi}. Then:

$$x_{fh} = \left[\frac{0.00013185 kq}{b_{hf} c_t \mu (0.0002637 k / \phi \mu c_t)^{m_{hf}} \phi t_{BFRi}^{m_{hf}}} \right]^{1/2(1-m_{hf})} \tag{5.55}$$

To confirm the value of the branch fracture length, read the value of the pressure derivative curve, $(t^*\Delta p')_{BFI}$, for the time t=1 hr. Then, from Eq. 5.52 we obtain:

$$x_{fh} = \left[\frac{(t \cdot \Delta p')_{BFI} k^2 h}{535456.96 b_{hf} B c_t \mu^2 (0.0002637 k / \phi \mu c_t)^{m_{hf}} \phi} \right]^{1/2(1-m_{hf})} \tag{5.56}$$

Once the branch fracture length is computed, the dimensionless branch fracture conductivity is calculated using Eq. 5.50.

Care has to be taken with the use of Eqs. 5.53 through 5.54. For moderate and low fracture conductivities, the resulting branch fracture length may result in a larger number than the main fracture permeability which may not be the case. Then, the estimated main fracture conductivity should be substracted from the branch fracture

conductivity value. For high or infinite fracture conductivities, the linear flow dominates over the bilinear period –most of the times bilinear flow does not exist- and the answer corresponds to the main fracture only which is the responsible for the linear flow, for these cases, the value reported by Eqs. 5.54 through 5.56 should be the correct one.

5.1.6. SPECIAL CASES

The above analysis assumes that all flow regimes (branch fracture, bilinear, formation linear, and radial) are observed during the pressure test and that they are well defined in the pressure derivative curve. In many instances, at least one of the flow regimes is not observed or not well defined. Because of the short duration of the flow period answer from a branch fracture, the presence of wellbore storage effects may mask this behavior.

(a) **Formation Linear flow is not observed.** For a low conductivity fracture, $C_{fD} \leq 1$, the straight line corresponding to the linear flow regime will probably not be observed. After the bilinear flow line, the pressure derivative curve generally enters a transition flow and it is very difficult to estimate the branch fracture length. Later, if the test is run long enough, a horizontal line on the pressure derivative curve is observed corresponding to the infinite-acting radial flow regime. In this case, the formation permeability is calculated from Eq. 39b and the fracture conductivity is determined from the bilinear flow line (Eqs. 5.6 or 5.12).

If this case is presented, the recommended procedure is to estimate fracture conductivity and main fracture length using the bilinear and radial relationships

presented in sections 5.1.1 and 5.1.3 which were developed in reference 33. Once this is done, use the estimated values to simulate a pressure test for that particular case. Plot the simulated pressure and pressure derivative on the same log-log graph and verify the presence of the branch fracture by looking the part of the curve which does not match with the simulated data. Refer to Fig. 5.2. Then, find the slope and intercept of the line which does not match with the simulated results and determine the intersection point between the bilinear and the branch fracture lines. Calculation of branch fracture length is possible by using Eq. 5.53 is the slope of the branch fracture is not 0.25.

Ref. 33 presents the following equations which relate the half-fracture length, x_f, formation permeability, k, fracture conductivity, wk_f, and post-frac skin factor, s:

$$x_f = \frac{1.92173}{\frac{e^s}{r_w} - \frac{3.31739k}{wk_f}} \tag{5.57}$$

Knowing the fracture conductivity, wk_f, from the bilinear flow, and formation permeability, k, and skin, s from radial flow, Eq. 5.57 can be used to calculate the half-fracture length, x_f.

(b) Bilinear flow is not observed. If the bilinear flow line of slope 0.25 is not well defined or not observed due to wellbore phenomena, then the fracture conductivity, wk_f, can be calculated from[33]:

$$w k_f = \frac{3.31739k}{\frac{e^s}{r_w} - \frac{1.92173}{x_f}} \tag{5.58}$$

where the formation permeability is determined from Eq. 5.39b (if a pre-frac is not possible) and post-frac skin from Eq. 5.40. The half-fracture length is obtained from Eq. 5.26 and branch fracture length is determined from Eq. 5.54.

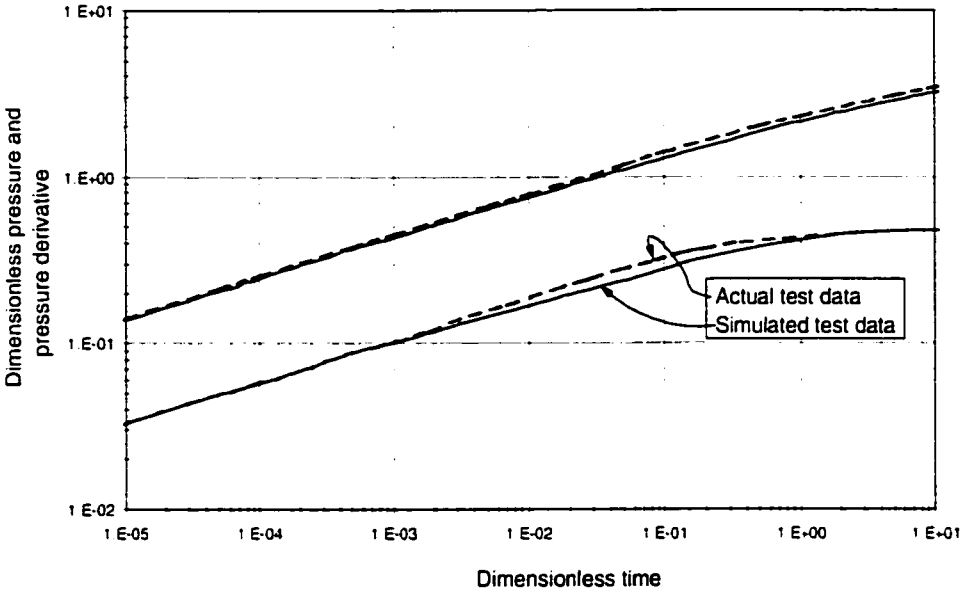

Fig. 5.2. Actual and simulated data to detect a branch fracture in a low conductivity fracture system

(c) **Radial flow line is not observed.** For short tests such as in low permeability formations, the horizontal straight line on the pressure derivative, which corresponds to the infinite acting behavior might not be observed during the limited period of time of a conventional drawdown or buildup test. In this case, Eq. 5.40 cannot be used to calculate the post-frac skin factor. If both bilinear and formation linear flow regimes are well defined in the pressure and pressure derivative curves, then the formation permeability is calculated from Eq. 5.32b (assuming there is no pre-frac test), while the post-frac skin factor is obtained either from:[33]

$$s = \ln\left[r_w \left(\frac{1.92173}{x_f} - \frac{3.31739k}{wk_f} \right) \right] \tag{5.59}$$

or from the following equation[100]:

$$s = \ln\frac{r_w}{x_f} + \frac{1.65 - 0.32u + 0.11u^2}{1 + 0.18u + 0.064u^2 + 0.005u^3} \tag{5.60}$$

where:

$$u = \ln\left(\frac{w_f k_f}{x_f k} \right) \tag{5.61}$$

It is important to emphasize that accurate values of k, x_f, and wk_f can only be obtained when, respectively, the radial, formation linear and bilinear flow regimes are well defined in the pressure and pressure derivative curves. In the absence of anyone of the three flow regimes Eqs. 5.57 – 5.61 are accurate enough (with less than one percent error) for determining these parameters[33].

5.1.7. STEP-BY-STEP PROCEDURES

Case 1. Ideal Case (All flow regimes are observed)

The following **step-by-step procedure** is for the case where all the straight lines corresponding to various flow regimes of a finite conductivity fracture are well defined.

Step 1 - Plot the pressure change Δp and pressure derivative ($t^*\Delta p'$) values versus test time.

Step 2 - Identify and draw the straight lines corresponding to branch fracture, bilinear flow (slope = 0.25), formation linear flow (slope = 0.5), and infinite acting radial flow (horizontal line). If wellbore storage is absent, as assumed here, go to **step 4**.

Step 3 - Calculate the wellbore storage coefficient from Eq. 5.13.

Step 4 - Calculate the formation permeability, k, from the infinite acting radial flow line on the pressure derivative curve, using Eq. 5.39b.

Step 5 - Read the value of Δp and $(t^*\Delta p')$ at time t=1 hr from the bilinear flow line (extrapolated if necessary), and calculate the fracture conductivity, $k_f w$, from Eqs. 5.6 and 5.12. For noise derivative, use Eq. 5.11 to identify the quarter slope line on the $(t^*\Delta p')$ curve. Equations 5.6 and 5.12 of course must yield the same value of $k_f w$.

Step 6 - Calculate the time of intersection of the bilinear and radial flow lines using Eq. 5.42, and compare with the observed intersection time t_{RBLi} in the graph. If the calculated and the observed values of t_{RBLi} are approximately equal, we can conclude that the calculated values of the formation permeability, k and the fracture conductivity $(k_f w_f)$ are correct. If they are different, adjust one of the two straight lines or both and recalculate k and $k_f w$ until the two values of t_{RBLi} are equal.

Step 7 - Calculate the skin factor from Eq. 5.40

Step 8 - Calculate the half-fracture length from Eq. 5.26. Verify this value of x_f by calculating t_{BLLi} from Eq. 5.32a and then comparing it with the observed value of t_{BLLi}. If these two values of t_{BLLi} are approximately equal we can conclude that x_f is correct. If the two values of t_{BLLi} are different shift the half-slope line until the observed and calculated t_{BLLi} are equal.

Step 9 - Calculate the dimensionless fracture conductivity, C_{fD}, from Eq. 3.37.

Step 10 - If wellbore storage effects observed stop the procedure here.

Step 11 - Read the coordinates of the intersection point of the branch fracture straight and the bilinear lines, t_{BFBLi} and $(t^*\Delta p')_{BFBLi}$. Read any lower coordinates over the branch fracture curve t_{BF2} and $(t^*\Delta p')_{BF2}$. Estimate the slope, m_{bf}, and intercept, b_{mf}, of the branch fracture straight line. The following equations may be used:

$$m_{bf} = \frac{\log(t^*\Delta p')_{BFBLi} - \log(t^*\Delta p')_{BF2}}{\log(t_{BFBLi}) - \log(t_{BF2})} \tag{5.62}$$

$$b_{bf} = \log(t^*\Delta p')_{BF2} - m_{bf} * \log(t_{BF2}) \tag{5.63}$$

Step 12 - Extrapolate the straight line over the branch fracture and read the value of the pressure derivative, $(t^*\Delta p')_{BF1}$, at time t=1 hr, and estimate branch fracture length using Eq. 5.56.

Step 13 - Recalculate branch fracture length, x_{fb}, using Eq. 5.53. If the linear flow period is very well observed then read the time of intersection between linear and branch fracture, t_{BFLi} and estimate x_{fb} from Eq. 5.54. The values of x_{fb} obtained in step 12 and 13 ought to be the same. If the linear line is not very well developed, read the time of intersection between the radial line and the branch fracture line, t_{BFRi} and estimate x_{fb} value using Eq. 5.55.

Step 14 - If the pseudosteady-state flow behavior is observed estimate the intersection times between the linear line with the pseudosteady-state line, t_{PL}, and with the radial line, t_{PRi}, then estimate x_f (or drainage area) and drainage area from Eqs. 5.47 and 5.48, respectively.

Step 15 – If branch fracture length is higher than the main fracture value, the branch fracture length should be the difference between the two value.

Step 16 - If at early time, the branch fracture presents a slope of 0.25 or close. Read the supposed value of the pressure derivative, $(t^*\Delta p')_{BLI}$, at time t= 1hr. Estimate the fracture conductivity using Eq. 5.12 and then estimate fracture conductivity using Eq. 3.37. Then simulate a well pressure test using the procedure outline in section A.3. If the simulated results agree very well with the actual pressure and pressure derivative trend, there is an indication of the absence of a branch fracture, otherwise, the branch fracture is present and the value estimated in the former steps should be correct.

Case 2. Low conductivity fracture (Linear flow line is not observed)

For a low conductivity fracture, the formation linear flow regime will probably be too short-lived to be well defined, making it difficult to draw the half- slope line, or will not be observed at all. Also, the behavior of the branch fracture may not be detected and can be confused with the bilinear line.

Steps 1 - 7: Same as above (ideal case)

Step 8 - Calculate the half-fractured length from Eq. 5.57.

Step 9 - same as above.

Step 10 – If the bilinear flow regime is very long, using the values of fracture conductivity and fracture length estimated in the above steps, simulate a pressure test using the semi-analytical approach presented by Cinco-Ley et al[18]. and reported in section A.3. Identify the branch fracture line, if any, and determine its slope and

intercept. If the slope is greater than 0.25 continue with step 11, otherwise the branch fracture length cannot be determined.

Step 11 - 12 - Same as case 1.

Step 13 - Recalculate branch fracture length, x_{fb}, using Eq. 5.53. The values of x_{fb} obtained in step 12 and 13 ought to be the same. Read the time of intersection between the radial line and the branch fracture line, t_{BFRi} and estimate x_{fb} value using Eq. 5.55.

Step 14 - 15 - Same as case 1.

Case 3. Intermediate conductivity fracture

A pressure test in a well with an intermediate-conductivity fracture should yield all four flow regimes, i.e. branch fracture, bilinear, formation-linear and radial. However, if the effect of wellbore storage and/or noise on the early-time pressure data are severe, then it would be difficult to draw the quarter-slope line and identify the branch fracture line.

Steps 1-4: Same as in the ideal case.

Step 5 - Calculate the half-fracture length from Eq. 5.26.

Step 6 - Select any convenient time t_R during the infinite acting radial portion of the pressure and pressure derivative curves, and read the corresponding values of $(\Delta p)_R$ and $(t\Delta p')_R$ then calculate the skin factor, s, from the Eq. 5.40.

Step 7 - Estimate the fracture conductivity, k_fw, from Eq. 5.58.

Step 8 - Same as **step 9** of the ideal case.

Step 10 - 11 - 16 - Same as **Step 14, 15** and **16** of the ideal case.

Case 4. High to infinite fracture conductivity (only branch fracture line and linear flow are observed)

Step 1 - 4 - Same as case 1.

Step 5 - Read the value of Δp and $(t^*\Delta p')$ at time t=1 hr from the linear flow line (extrapolated if necessary), and calculate the half-fracture length, x_f, from Eqs. 5.44 and 5.26. Eqs. 5.44 and 5.26 must provide the same value of x_f.

Step 6 - Calculate the skin factor from Eq. 5.40.

Step 7 - Estimate the time of intersection between the linear line and the radial line, t_{LRi}, and recalculate half fracture length, x_f, from Eqs. 5.45.

Step 8 – Find the slope and intercept of the branch fracture line. Determine the intersection time between the branch fracture and the linear flow line, t_{BFLi}, the value of the pressure derivative of the branch fracture line when the time t=1 hr, $(t^*\Delta p')_{BFI}$ and estimate branch fracture length using Eqs. 5.54 and 5.56. If easy to find, determine the intersection point of the radial line and the branch fracture line and re-estimate branch fracture length using Eq. 5.55.

Step - 8: Dimensionless fracture conductivity may be obtained by using a numerical fitting of a graphical correlation presented Ref. 22:

$$x = s + \ln\left(\frac{x_f}{r_w}\right); \quad 0.67 \le x \le 2.8 \tag{5.62a}$$

$$C_{fD} = 10^{\left(\frac{0.59222806 - 1.77955x + 0.86571983x^2}{1 - 1.5944514x + 0.010112x^2}\right)} \tag{5.62b}$$

Step 9 - Same as step 15, case 1.

Case 5. Short post-frac tests

For low permeability reservoirs, the portion of the curve corresponding to the radial infinite acting behavior may not be observed. Then, the permeability should be estimated from a pre-frac test.

Steps 1-3 - Same steps as in the ideal case

Step 4 - The permeability value is determined from a pre-frac test.

Step 5 - Calculate the fracture conductivity $k_f w$ as discussed in **Step 5** of the ideal case.

Step 6 - Calculate the half-fracture length, x_f, as discussed in **step 8** of the ideal case.

Step 7 - Calculate skin from Eq. 5.59.

Step 8 - same as **step 9** of the ideal case

Step 10 - 11 - Same as steps 15 and 16, case 1.

Step 11 – Optionally, use Eq. 5.39a to estimate $(t^*\Delta p)_R$ which corresponds to the infinite acting radial flow line. Draw a horizontal line over this point. This horizontal line corresponds to the radial line and, according to the case, apply cases 1, 2 or three.

5.1.8. APPLICATIONS

Example 1. A simulated drawdown test data is given in Table 5.1. The data used to simulate the test were:

k = 10 md	h = 54 ft	x_f = 250 ft
x_{fb} = 75 ft (angle of 30°)	ϕ = 12 %	$c_t = 5\text{x}10^{-5}$ 1/psi
μ = 1.45 cp	q = 700 BPD	B = 1.23 rb/STB
r_w = 0.3 ft	C_{fD} = 10	

Determine reservoir permeability, fracture conductivity, fracture length, skin factor, and branch fracture length.

Solution:

Step 1 – A plot the pressure change Δp and pressure derivative ($t^*\Delta p'$) values versus test time is presented in Fig. 5.3.

Step 2 – In the plot, we observe the bilinear flow regime and another line having a slope of 0.336 which corresponds to the branch fracture. Linear behavior is not seen, so we fall in case two. The radial flow line presents few points.

Step 3 – No unit-slope line is found then no wellbore storage is estimated.

Table 5.1. Simulated test data for example 1

t, hrs	Δp', psi	t*Δp', psi	t, hrs	Δp', psi	t*Δp', psi
0.0003	7.6282	1.9253	3.3784	106.7556	33.7210
0.0010	10.7652	2.5249	16.8919	179.2711	57.9701
0.0017	12.5916	2.9303	33.7838	225.8651	73.1268
0.0034	15.0328	3.4206	84.4596	305.5466	97.1023
0.0084	18.4287	4.4522	168.9192	380.4991	115.9581
0.0169	21.7047	5.6272	253.3788	430.1309	126.0522
0.0338	26.1511	7.2383	337.8385	467.7891	132.4400
0.0422	27.8982	7.9118	1013.5154	627.5401	149.4166
0.1689	42.7768	12.3856	1689.1923	708.3349	153.5865
0.3378	53.0460	15.7226	2702.7076	784.8546	155.9250
0.4561	58.1475	17.3940	3378.3845	821.6295	156.6644
2.5338	97.6910	30.6587			

Step 5 – The following values are read: $(\Delta p)_{BL1} = 65$ psi and $(t^*\Delta p')_{BL1} = 16.25$ psi, the fracture conductivity, $k_f w$, is estimated from Eqs. 5.6 and 5.12.

$$k_f w = 1947.46 \frac{1}{\sqrt{\phi \mu c_t k}} \left(\frac{q \mu B}{h(\Delta P)_{BL1}} \right)^2$$

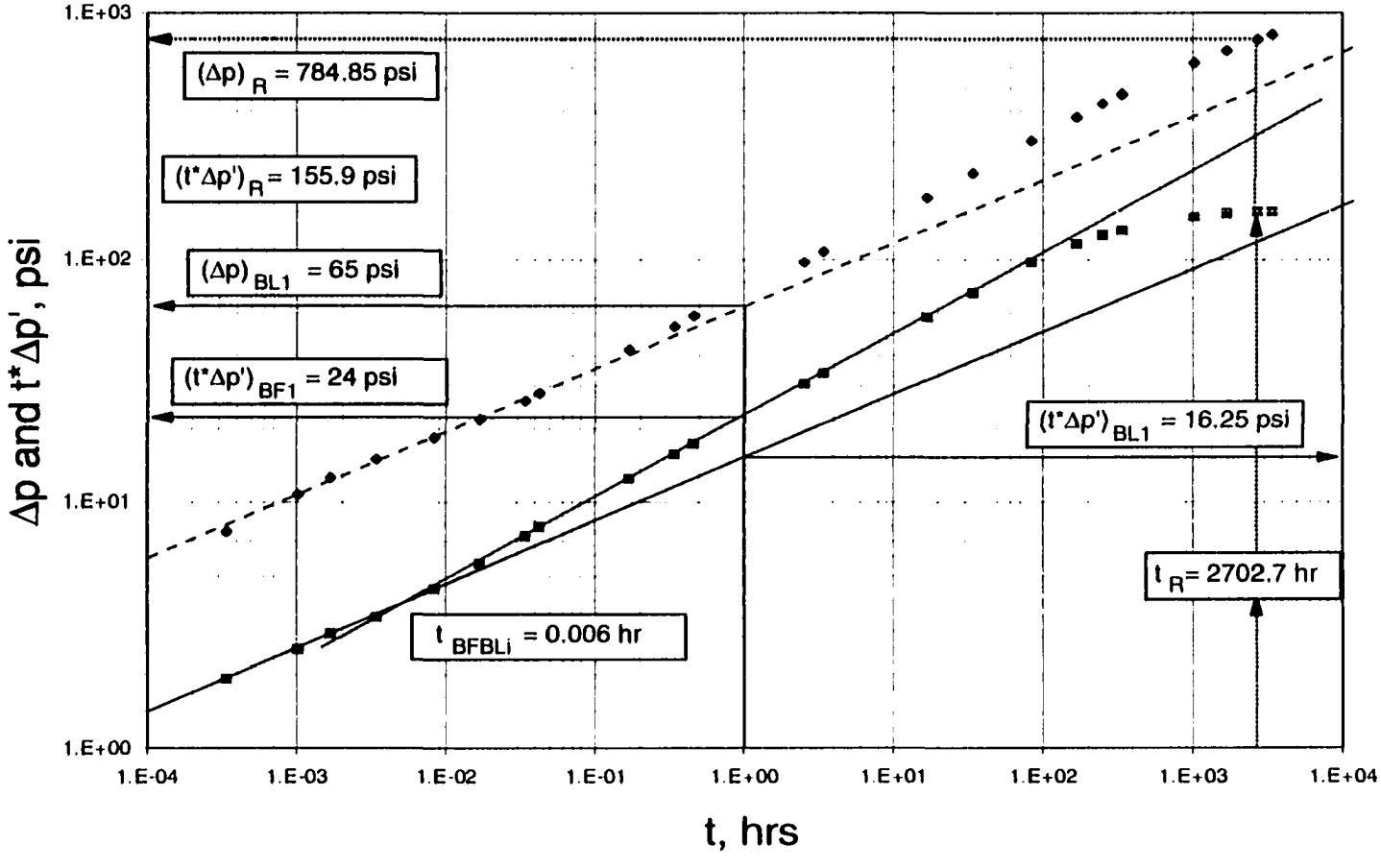

Fig. 5.3. Log-log plot of pressure and pressure derivative for example 1

$$k_f w = 1947.46 \frac{1}{\sqrt{0.12(1.45)(5x10^{-5})(10.46)}}\left(\frac{700(1.45)(1.23)}{54(65)}\right)^2 = 25826.8\ md-ft$$

$$k_f w = \frac{121.74}{\sqrt{\phi\mu c_t k}}\left(\frac{q\mu B}{h(t\cdot\Delta p')_{BL1}}\right)^2 = \frac{121.74}{\sqrt{0.12(1.45)(5x10^{-5})(10.46)}}\left(\frac{700(1.45)(1.23)}{54(16.25)}\right)^2$$

$k_f w = 25830\ md\text{-}ft$

The values of fracture conductivity calculated by Eqs. 5.6 and 5.12 are in very close agreement.

Step 6 - Calculate the time of intersection of the bilinear and radial flow lines using Eq. 5.42, but first, m_{BL} is calculated using Eq. 5.3, as:

$$m_{BL} = \frac{44.13}{(\phi\mu c_t k)^{0.25}}\left(\frac{q\mu B}{h\sqrt{k_f w}}\right) = \frac{44.13}{\sqrt[4]{(0.12)(1.45)(5x10^{-5})(10.46)}}\left(\frac{700(1.45)(1.23)}{54\sqrt{25830}}\right)$$

$m_{BL} = 64.996$

$$t_{RBL}^{0.25} = \frac{70.6q\mu B}{kh}\frac{4}{m_{BL}} = \frac{70.6(700)(1.45)(1.23)}{(10.46)(54)}\frac{4}{64.996}$$

$t_{RBL} = 8504.4\ hr$

A close value of t_{RBL} is observed on Fig. 5.3.

Step 7 – The following characteristic values are read from the log-log plot in Fig. 5.3:

t_R = 2702.7 hrs

Δp_R = 784.85 psi

Then, skin factor is calculated from Eq. 5.40, thus:

$$s = 0.5\left[\frac{(\Delta p)_R}{(t\cdot\Delta p')_R} - \ln\left(\frac{kt_R}{\phi\mu c_t r_w^2}\right) + 7.43\right]$$

$$s = 0.5\left[\frac{784.85}{155.9} - \ln\left(\frac{10.46(2702.7)}{0.12(1.45)(1.23)(5x10^{-5})0.3^2}\right) + 7.43\right] = -5.923$$

Step 8 - half fracture length is estimated using Eq. 5.57

$$x_f = \frac{1.92173}{\frac{e^s}{r_w} - \frac{3.31739k}{wk_f}} = \frac{1.92173}{\frac{e^{-5.923}}{0.3} - \frac{3.31739(10.46)}{25830}} = 253.51\ ft$$

This value matches very well with the value of 250 ft input for the simulation.

Step 9 - Calculate the dimensionless fracture conductivity, C_{fD}, from Eq. 3.37.

$$C_{fD} = \left(\frac{k_f}{k}\right)\left(\frac{w_f}{x_f}\right) = \frac{25830}{10.46 * 253.5} \approx 10$$

which corresponds to a moderate fracture conductivity.

Step 10 – The branch fracture line has been identified. Its slope, m_{bf}, and intercept, b_{bf}, are 0.336 psi/hr and 1.15987 hr, respectively.

Step 11 - The time of the intersection point of the branch fracture straight and the bilinear lines is, $t_{BFBLi} = 6x10^{-3}$ hr.

Step 12 – The value of $(t*\Delta p')_{BFI}$ = 24 psi at time t=1 hr. The branch fracture length is obtained using Eq. 5.56.

$$x_{fb} = \left[\frac{(t\cdot\Delta p')_{BFI} k^2 h}{535456.96 b_{bf} B c_t \mu^2 (0.0002637k/\phi\mu c_t)^{m_{bf}} \phi}\right]^{1/2(1-m_{bf})}$$

$$x_{fb} = \left[\frac{24(10.46)^2(54)}{535456.96(1.16)(1.23)(5x10^{-5})1.45^2\left(\frac{0.0002637(10.46)}{0.12(1.45)(5x10^{-5})}\right)^{0.336}(0.12)}\right]^{0.753}$$

$$x_{fb} = 320.23$$

Since branch fracture length is higher that main fracture length, then.

$$x_{fb} = 320.23 - 251.51 = 66.7\ ft$$

Step 13 - Recalculate branch fracture length, x_{fb}, using Eq. 5.53.

$$x_{fb} = \left[\frac{k^2 h m_{BL}}{2141827.8 b_{hf} B c_t \mu^2 (0.0002637 k / \phi \mu c_t)^{m_{hf}} \phi t_{BFBLi}^{m_{hf}-0.25}} \right]^{1/2(1-m_{hf})}$$

$$x_{fb} = \left[\frac{10.46^2 (54)(64.996)}{2141827.8(1.15)(1.23)(5x10^{-5})1.45^2 \left(\frac{0.0002637(10.46)}{0.12(1.45)(5x10^{-5})} \right)^{0.336} (0.12)0.006^{0.086}} \right]^{0.753}$$

$$x_{fb} = 332.51 \; ft$$

Again, since branch fracture length is higher that main fracture length, then.

$$x_{fb} = 332.51 - 253.51 = 79 \; ft$$

Although, there is a slight difference between the two values of branch conductivity, they are reasonably acceptable. A better attempt of reading the value of $(t^*\Delta p')_{BFI}$ could be make. However, for practical purposes this exercises can be stop here.

Example 2. A simulated drawdown test data is presented in Table 5.1. The data used to simulate the test were:

k = 5 md	h = 70 ft	x_f = 200 ft
x_{fb} = 10 ft (angle of 30°)	ϕ = 8 %	$c_t = 5x10^{-5}$ 1/psi
μ = 3 cp	q = 100 BPD	B = 1.3 rb/STB
r_w = 0.3 ft	C_{fD} = 300	

Determine reservoir permeability, fracture length, skin factor, and branch fracture length.

Table 5.2. Simulated test data for example 2

t, hrs	Δp', psi	t*Δp', psi
5.55E-05	0.4074	0.1754
9.35E-05	0.4508	0.1941
1.63E-04	0.5327	0.2117
2.36E-04	0.6006	0.2375
3.76E-04	0.6947	0.2666
6.52E-04	0.8245	0.3139
1.01E-03	0.9444	0.3527
1.60E-03	1.0921	0.4091
2.54E-03	1.2587	0.4904
4.54E-03	1.5473	0.6076
8.85E-03	2.0754	0.7779
1.58E-02	2.5535	0.9960
2.99E-02	3.2748	1.3399
8.24E-02	4.9958	2.1606
2.27E-01	7.8074	3.6008
4.97E-01	11.1483	5.1740
1.09	16.0251	7.5580
2.83	25.0716	11.7925
7.36	39.1472	17.8032
18.60	59.7341	26.8775
55.93	96.2793	39.2617
141.39	139.3862	51.9535
401.32	201.6729	64.3633
903.44	258.4574	71.0513
2420.00	333.4596	76.3673
7713.43	425.0070	76.3673

Solution:

Step 1 – A plot the pressure change Δp and pressure derivative ($t^*\Delta p'$) values versus test time is presented in Fig. 5.3. This example falls in case 4.

Step 2 – In the plot, we observe a linear flow regime and another line having a slope of 0.25 which corresponds to the branch fracture. Notice that the pressure derivative and the pressure change curves have a separation smaller than that in example 1, which indicates that the fracture should have infinite conductivity. Then, the first slope

should not be confused with a bilinear flow regime. The radial flow line is present as indicated in the plot.

Step 3 – No unit-slope line is found then no wellbore storage is estimated.

Step 4 - Calculate the formation permeability, k, from the infinite acting radial flow line on the pressure derivative curve, using Eq. 5.39b.

From Fig. 5.4, $(t^*\Delta p')_R = 76.37$ psi.

$$k = \frac{70.6q\mu B}{h(t\cdot\Delta p')_R} = \frac{70.6(100)(3)(1.3)}{(70)(76.37)} = 5.15\ md$$

Notice that the above permeability value is in close agreement with the value used for the simulation (5 md).

Step 5 - The following values are read:

$(\Delta p)_{LI} = 14.6$ psi and $(t^*\Delta p')_{LI} = 7.3$ psi, the half fracture length, x_f, is estimated from Eqs. 5.44 and 5.26, respectively:

$$x_f = \frac{2.032Bq}{h(t^*\Delta p')_{LI}}\sqrt{\frac{\mu}{\phi c_t k}} = \frac{2.032(1.3)(100)}{70(7.3)}\sqrt{\frac{3}{0.08(5x10^{-5})(5.15)}} = 197.3\ ft$$

$$x_f = \frac{4.064Bq}{h(\Delta p)_{LI}}\sqrt{\frac{\mu}{\phi c_t k}} = \frac{4.064(1.3)(100)}{70(14.6)}\sqrt{\frac{3}{0.08(5x10^{-5})(5.15)}} = 197.3\ ft$$

Observe the excellent match between the above values of half-fracture length.

Step 6 - The following characteristic values are read from the log-log plot in Fig. 5.4:

$t_R = 2420$ hrs

$\Delta p_R = 333.46$ psi

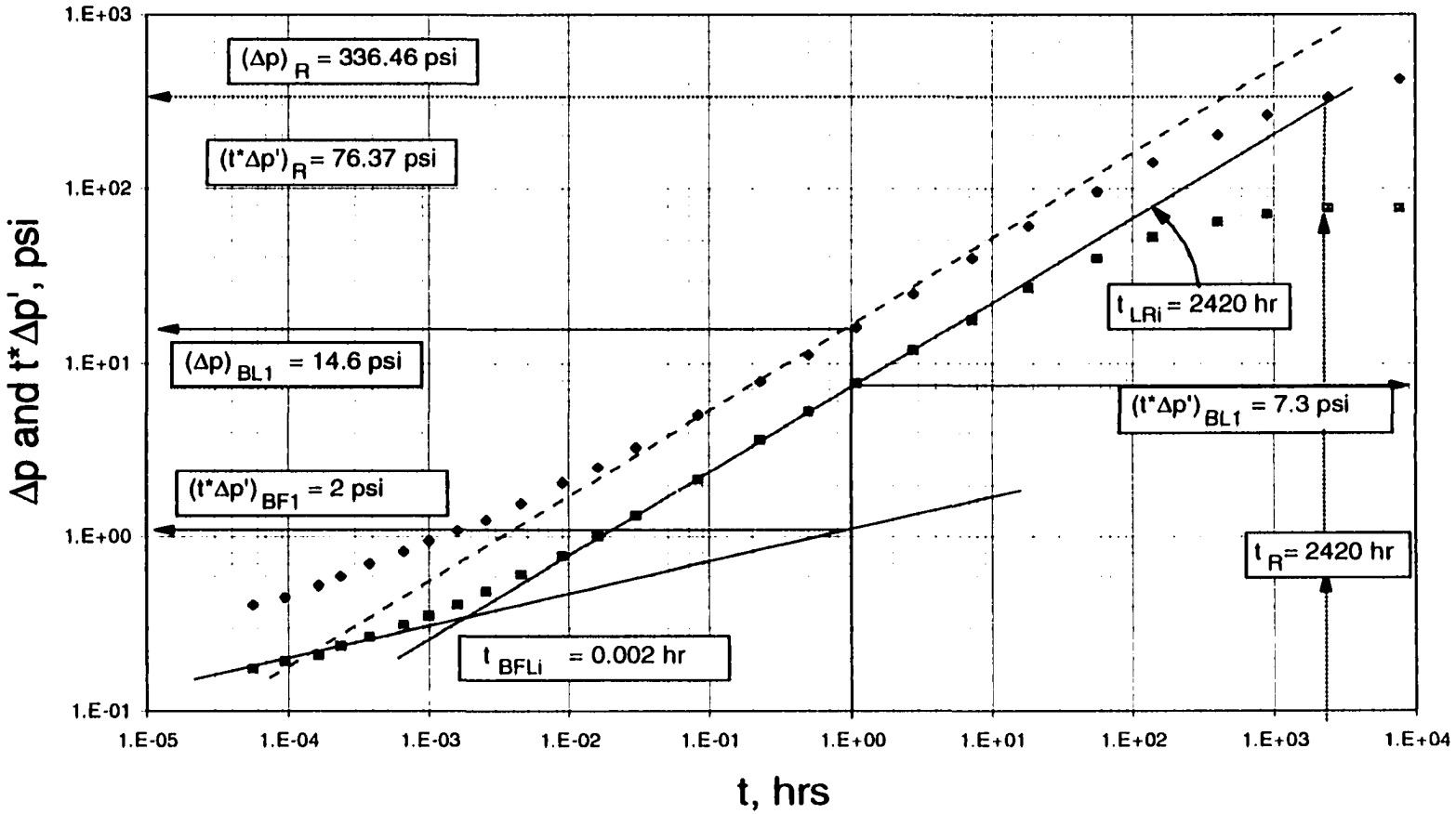

Fig. 5.4. Log-log plot of pressure and pressure derivative for example 2

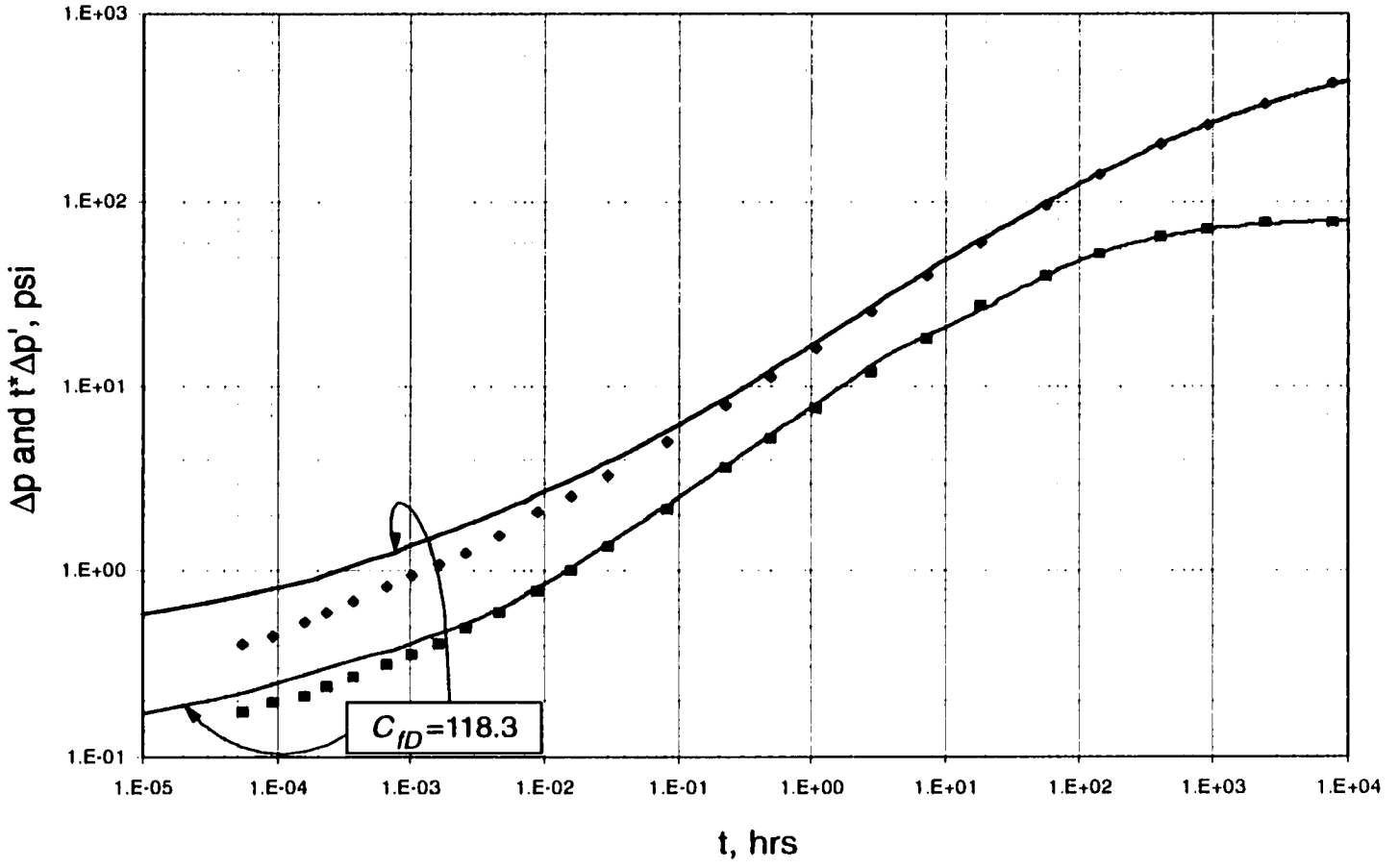

Fig. 5.5. Log-log plot of pressure and pressure derivative for example 2 compared to a simulation using C_{fD}=118.3

Then, skin factor is calculated from Eq. 5.40, thus:

$$s = 0.5\left[\frac{(\Delta p)_R}{(t\cdot\Delta p')_R} - \ln\left(\frac{kt_R}{\phi\mu c_t r_w^2}\right) + 7.43\right]$$

$$s = 0.5\left[\frac{333.46}{76.37} - \ln\left(\frac{5.15(2420)}{0.08(3)(1.3)(5x10^{-5})0.3^2}\right) + 7.43\right] \approx -5.8$$

Step 7 - The time of intersection between the linear line and the radial line, t_{LRi}, is 115 hr. Half fracture length, x_f, is calculated using Eq. 5.45.

$$\frac{x_f^2}{k} = \frac{t_{LRi}}{1207\phi\mu c_t} = \frac{115}{1207(0.08)(3)(5x10^{-5})}$$

$$x_f = \sqrt{\frac{115*5.15}{1207(0.08)(3)(5x10^{-5})}} = 202.2\ ft$$

Step 8 – An estimate of dimensionless fracture conductivity can be obtained from Eqs. 5.62a and 5.62b, as follows:

$$x = s + \ln\left(\frac{x_f}{r_w}\right) = -5.8 + \ln\left(\frac{197.3}{0.3}\right) = 0.6871; \quad 0.67 \le x \le 2.8$$

$$C_{fD} = 10^{\left(\frac{0.59222806 - 1.77955(0.7887) + 0.86571983(0.7887)^2}{1 - 1.5944514(0.7887) + 0.010112(0.7887)^2}\right)}$$

$$C_{fD} = 275.8$$

Step 9 – The slope and intercept of the branch fracture line are 0.25 and 0.67, respectively. The intersection time between the branch fracture and the linear flow line, t_{BFLi}, is read from Fig. 5.4 to be 0.002 hrs. The value of the pressure derivative of the branch fracture line when the time t=1 hr, $(t*\Delta p')_{BFI}$ is 2 psi. Estimation of branch fracture length from Eqs. 5.54 and 5.56 is performed as follows:

$$x_{fb} = \left[\frac{k^2 h m_L t_{BFLi}^{0.5-m_{hf}}}{1070913.9 b_{hf} B c_t \mu^2 (0.0002637 k / \phi \mu c_t)^{m_{hf}} \phi} \right]^{1/2(1-m_{hf})}$$

$$x_{fb} = \left[\frac{5.15^2 (70)(41.388) 0.002^{0.25}}{1070913.9(0.67)(1.3)(3^2) \left(\frac{0.0002637(5.15)}{0.08(3)(5 \times 10^{-5})} \right)^{0.25} (0.08)} \right]^{0.6667} = 9.7 \; ft$$

$$x_{fb} = \left[\frac{(t \cdot \Delta p')_{BFI} k^2 h}{535456.96 b_{hf} B c_t \mu^2 (0.0002637 k / \phi \mu c_t)^{m_{hf}} \phi} \right]^{1/2(1-m_{hf})}$$

$$x_{fb} = \left[\frac{(2)(5.15)^2 (70)}{535456.96(0.67)(1.3)(3^2) \left(\frac{0.0002637(5.15)}{0.08(3)(5 \times 10^{-5})} \right)^{0.25} (0.08)} \right]^{0.667} = 16.63 \; ft$$

This example can easily be confused with an unbranched system. Notice that the early line has a slope of ¼. At first sight, the interpreter may think that this is finite conductivity fracture in which the bilinear flow regime is observable. Now, if we assume that we have a bilinear flow regime instead a branch fracture, then, $(t^*\Delta p')_{BLI}$ is 2 psi. Using Eq. 5.12, the fracture conductivity is:

$$k_f w = \frac{121.74}{\sqrt{\phi \mu c_t k}} \left(\frac{q \mu B}{h (t \cdot \Delta p')_{BLI}} \right)^2 = \frac{121.74}{\sqrt{0.08(3)(5 \times 10^{-5})(5.15)}} \left(\frac{100(3)(1.3)}{70(2)} \right)^2$$

$$k_f w = 120174.46 \; md - ft$$

From Eq. 3.37, the dimensionless fracture conductivity is:

$$C_{fD} = \left(\frac{k_f}{k} \right) \left(\frac{w_f}{x_f} \right) = \frac{120174.46}{(197.3)(5.15)} = 118.3$$

Numerical and semi-analytical simulations were performed using the input data for this example and the calculated data (x_f = 197.3 ft, C_{fD} = 118.3 and k = 5.15 md) to compare with the pressure and pressure derivative of this example. Results are reported in Fig. 5.5. Notice at early time, there exists a disagreement between the data for example 2 and the data simulated with the calculated fracture conductivity. This procedure may help us to differentiate between a branch fracture and a finite-conductivity fracture.

5.2. HYDRAULIC FRACTURED INTERSECTING A SEALING FAULT

Most of the mathematical fracture treatment procedures are similar to those presented in section 5.1. This apart focused on the estimation of the fault length for which a correlation is developed. The model assumes that reservoir permeability is known from other sources, i.e. pre-frac tests, well logging, core analysis, etc. to be able to apply the analysis.

As seen in Figs. B.5.a through B.17.c, when the fracture intersects a fault forming an angle of 90°, the pressure derivative shows a maximum and then it reaches the pseudoradial flow line. When fault and fracture meet at their tips, the effect is less pronounced since the system provides more room for the development of the pseudoradial flow regime. Also, for angles less than 90°, without matter of the fault-fracture meeting point, the maximum point is difficult to observe and vanishes as the angle reduces. Then, the correlations to estimate fracture length only take into account

cases when the fracture and fault form an angle of 90 degrees and the pseudoradial period has to be developed.

Fig. 5.6 presents a plot of the maximum dimensionless coordinates found on a pressure derivative plot. Fig. 5.7 presents a plot of the dimensionless fracture length against the dimensionless maximum pressure derivative and the dimensionless time at which this maximum takes place. Observe that the variables follow a defined pattern, then they can be correlated.

Eq. 5.63 presents a correlation to determine the fault length that is intersected by a fault forming an angle of 90°. The range of application of this correlation applies to eight values of dimensionless fracture conductivities ranging from 1 to 300. See Table 5.3. Other values maybe either interpolated or extrapolated. If for any reason, fracture conductivity cannot be estimated, then an average correlation may be used. The non-linear regression coefficients are above 0.99 and are reported individually in Table 5.3. No correlation was found to determine the fault-fracture angle since no defined pattern was observed. The angle of the intersection of the fracture-fault system may be identified by multiple well testing which is beyond the scope of this study.

Table 5.3. Coefficients and correlation coefficients for Eq. 5.63

C_{fD}	a	$b \cdot 10^{-5}$	$c \cdot x10^{-6}$	$d \cdot x10^{-6}$	r^2
Average	-4.582930	2.071981	1.919560	9.372899	0.9996
1	-2.850635	2.262125	2.083126	6.071802	0.9998
10	-4.563090	1.772448	1.455560	10.483443	0.9984
25	-3.652506	1.797033	1.095081	7.964444	0.9992
50	-3.270727	2.318344	2.166801	6.252563	0.9985
100	-5.440014	2.009004	1.873956	11.339665	0.9984
150	-3.443053	2.094285	1.767972	6.642798	0.9999
225	-5.446653	2.721045	2.974173	8.764386	0.9994
300	-7.195004	1.758969	1.652864	15.748184	0.9989

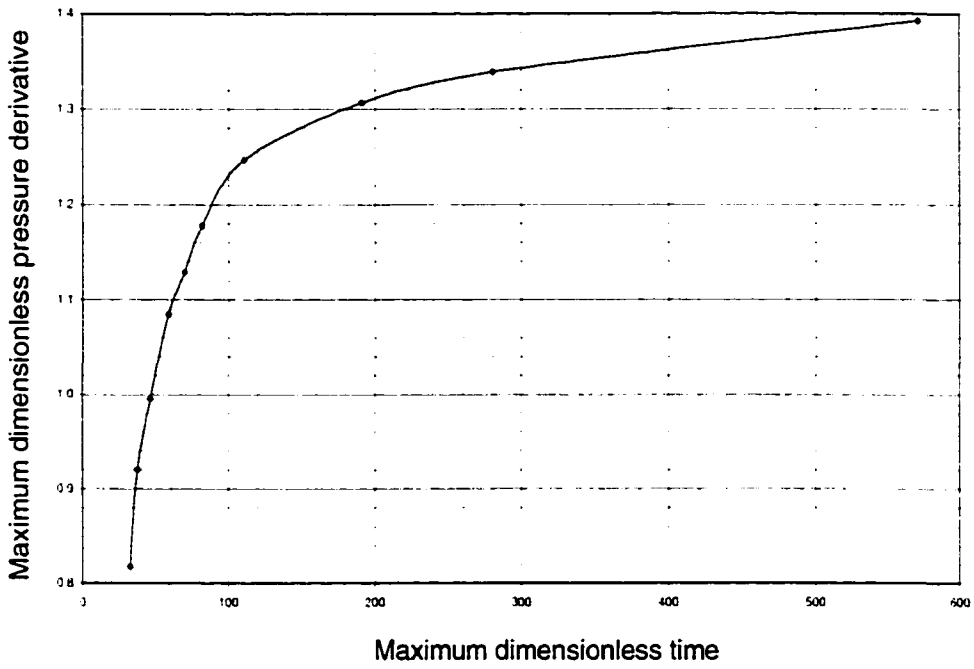

Fig. 5.6. Average correlation between maximum time and maximum pressure derivative for a fault-fracture system

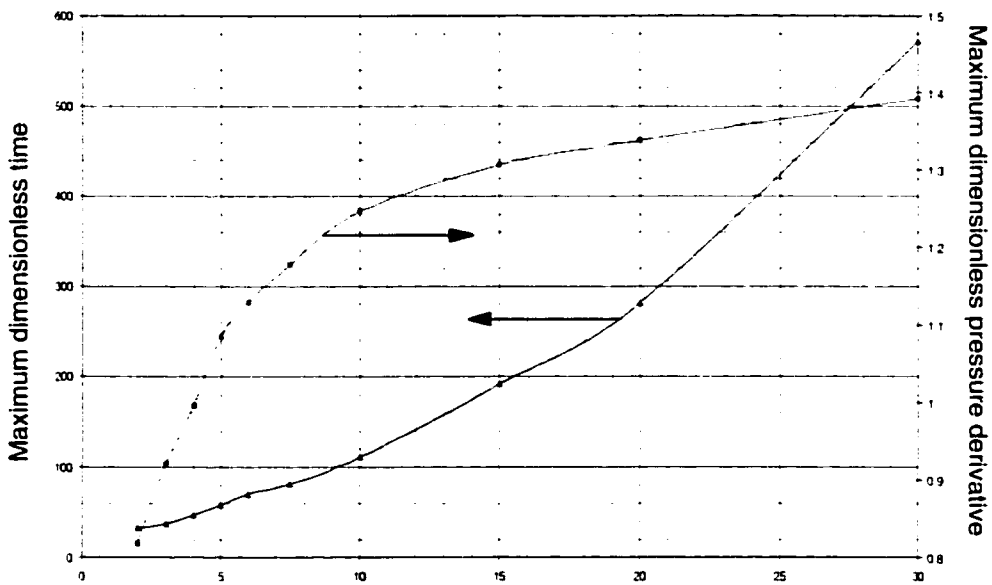

Fig. 5.7. Average correlation between maximum time and maximum pressure derivative for a fault-fracture system

$$L = \left| ax_f + \frac{bkt_x}{\phi \mu c_t x_f} - \left(\frac{ckt_x}{\phi \mu c_t x_f^{3/2}} \right)^2 + \left(\frac{dk^2 h (t * \Delta p')_x}{\phi \mu^2 c_t x_f q B} \right) \right| \qquad (5.63)$$

Eq. 5.63 may be applied for angles different than 90 degrees. If a maximum is observed on the pressure derivative curve and the angle is known, the equivalent fault length may be estimated by dividing the result from Eq. 5.63 by the cosine of the angle.

Eq. 5.63 can be used only if the pseudoradial flow regime develops regardless the presence of a maximum in the pressure derivative curve.

5.2.2. STEP-BY-STEP PROCEDURES

Case 1. Ideal Case (All flow regimes are observed)

The following step-by-step procedure is for the case where all the straight lines corresponding to various flow regimes of a finite conductivity fracture and the maximum pressure derivative point are well defined.

Step 1 - Plot the pressure change Δp and pressure derivative ($t^*\Delta p'$) values versus test time.

Step 2 - With the permeability obtained from another sources, determine the value of the pressure derivative at which the infinite acting radial flow line takes place, $(t^*\Delta p')_R$, using Eq. 5.39a. In the log-log plot of pressure and pressure derivative, draw a horizontal line along this value.

Step 3 - Identify and draw the straight lines corresponding to bilinear flow (slope=0.25), formation linear flow (slope=0.5), and infinite acting radial flow (horizontal line).

Step 4 - Calculate the wellbore storage coefficient, if exists, from Eq. 5.13.

Step 5 - 9 - Same as ideal case of section 5.1.7.

Step 10 - Verify that the acting radial flow line coincides with the horizontal line drawn in step 2. If so, read the maximum pressure derivative value, $(t^*\Delta p')_r$ and the time at which this occurs, t_r, and using the dimensionless fracture conductivity value find the appropriate values of the constants a, b, c and d and determine the fault length using Eq. 5.63. If the dimensionless fracture conductivity is not listed in table 5.3, interpolation or extrapolation of the fault length between two close known values may be applied.

Case 2. Low conductivity fracture (Linear flow line is not observed)

For a low conductivity fracture, the formation linear flow regime will probably not be well defined, making it difficult to draw the half slope line, or will completely absent.

Steps 1 - 4: Same as above (ideal case)

Step 5 - 7: Same as ideal case, section 5.1.7

Step - 8: Calculate the half-fractured length from Eq. 5.57.

Step 9 - Calculate the dimensionless fracture conductivity, C_{fD}, from Eq. 3.37.

Step 10 – Same as **step 11** ideal case.

Case 3. Intermediate conductivity fracture

A pressure test in a well with an intermediate-conductivity fracture should yield all three flow regimes, i.e. bilinear, formation-linear and radial. However, if the effect of wellbore storage and/or noise on the early-time pressure data is severe, then it would be difficult to identify the bilinear flow regime.

Steps 1-4: Same as in the ideal case

Step 5 - Calculate the half-fracture length from Eq. 5.26.

Step 6 - Select any convenient time t_R during the infinite acting radial portion of the pressure and pressure derivative curves, and read the corresponding values of $(\Delta p)_R$ and $(t\Delta p')_R$ then calculate the skin factor, s, from the Eq. 5.40. Be sure that the values are read on the truly pseudoradial flow period.

Step 7 - Estimate the fracture conductivity, $k_f w$, from Eq. 5.58.

Step 8 - Same as **step 9** of the ideal case.

Step 10 - Same as Step 11 of ideal case.

Case 4. High to infinite fracture conductivity (only linear flow is observed)

Step 1 - 4 - Same as case 1.

Step 5 - Read the value of Δp and $(t^*\Delta p')$ at time t=1 hr from the linear flow line (extrapolated if necessary), and calculate the half fracture length, x_f, from Eqs. 5.44 and 5.26. Equations 5.44 and 5.26 of course must yield the same value of x_f.

Step 6 - Calculate the skin factor from Eq. 5.40.

Step 7 - Estimate the time of intersection between the linear line and the radial line, t_{LRi}, and recalculate half fracture length, x_f, from Eqs. 5.45.

Step 8 – Same as Step 8, case 4 of section 5.1.7.

Step 9 –Verify that the acting radial flow line coincides with the horizontal line drawn in step 2. If so, read the maximum pressure derivative value, $(t^*\Delta p')_r$ and the time at which this occurs, t_r. Since fracture conductivity cannot be estimated, find the appropriate values of the constants a, b, c and d for the average case and determine the fault length using Eq. 5.63.

5.2.3. APPLICATIONS

Example 3. A simulated pressure transient test on a hydraulically fracture well was conducted and reported in Table 5.4. The fracture intersects a fault forming an angle of 90 degrees. The fracture-fault meeting point is at 70 % of the distance from one of the faults tip. The following information was used for the simulation:

k = 30 md	h = 50 ft	x_f = 100 ft
L = 450 ft	ϕ = 23 %	c_t = 1.35x10^{-6} 1/psi
μ = 0.3 cp	q = 3000 BPD	B = 1.48 rb/STB
r_w = 0.4 ft	C_{fD} = 10	

Determine fracture length and fault length.

Solution: In this example, all the flow regimes are present. The procedure given in case 1 will be followed.

Step 1 - A log-log plot of pressure change Δp and pressure derivative $(t^*\Delta p')$ values versus test time is provided in Fig. 5.8.

Table 5.4. Pressure data for example 3

t, hr	Δp, psi	t*Δp', psi	t, hr	Δp, psi	t*Δp', psi	t, hr	Δp, psi	t*Δp', psi
0.00034	13.07	3.27	0.16	92.21	34.52	15.26	422.36	83.12
0.00041	13.71	3.42	0.20	100.72	38.11	20.28	445.37	78.60
0.00049	14.39	3.58	0.27	112.08	42.91	28.52	471.31	73.74
0.00060	15.07	3.75	0.34	123.45	47.59	40.98	497.31	70.23
0.00072	15.79	3.99	0.43	134.82	52.08	50.49	511.81	68.65
0.00087	16.54	4.24	0.56	149.04	57.41	59.87	523.42	67.04
0.00104	17.36	4.53	0.70	163.26	62.42	71.31	534.97	65.43
0.00126	18.18	4.85	0.84	174.62	66.23	85.18	546.47	64.61
0.00151	19.11	5.22	1.03	188.83	70.66	106.78	561.03	63.91
0.00219	21.17	6.03	1.26	203.02	74.79	128.14	572.63	63.35
0.00316	23.54	6.94	1.51	217.22	78.58	153.88	584.17	63.10
0.00455	26.25	7.94	1.80	231.42	81.99	185.12	595.85	62.95
0.00656	29.32	9.16	2.21	248.47	85.50	244.22	613.22	62.96
0.00946	32.86	10.75	2.69	265.52	88.37	255.81	616.18	62.90
0.01363	37.05	12.73	3.36	285.41	90.88	353.34	636.51	62.94
0.01636	39.45	13.84	4.17	305.32	92.47	444.99	650.99	62.93
0.02330	44.81	16.19	5.17	325.22	93.10	535.12	662.61	63.11
0.02731	47.53	17.41	5.49	330.91	93.08	790.47	687.48	63.31
0.03643	53.01	19.81	6.40	345.15	92.72	1111.81	709.06	63.91
0.04724	58.53	22.00	7.70	362.25	91.68	1431.92	725.12	63.66
0.06719	66.86	24.97	7.95	365.10	91.44	1958.13	744.94	63.35
0.09224	75.26	27.92	9.91	385.10	89.24	2000.00	746.29	63.33
0.12283	83.71	31.09	12.05	402.28	86.69			

Step 2 - With the given permeability of 30 md, the value of pressure derivative at which the infinite acting radial flow line takes place, $(t^*\Delta p')_R$, is obtained using Eq. 5.39a. In the log-log plot of pressure and pressure derivative, the horizontal line along this value is drawn.

$$(t \cdot \Delta p')_R = \frac{70.6 q \mu B}{kh} = \frac{70.6(3000)(0.3)(1.48)}{(30)(50)} = 63 \; psi$$

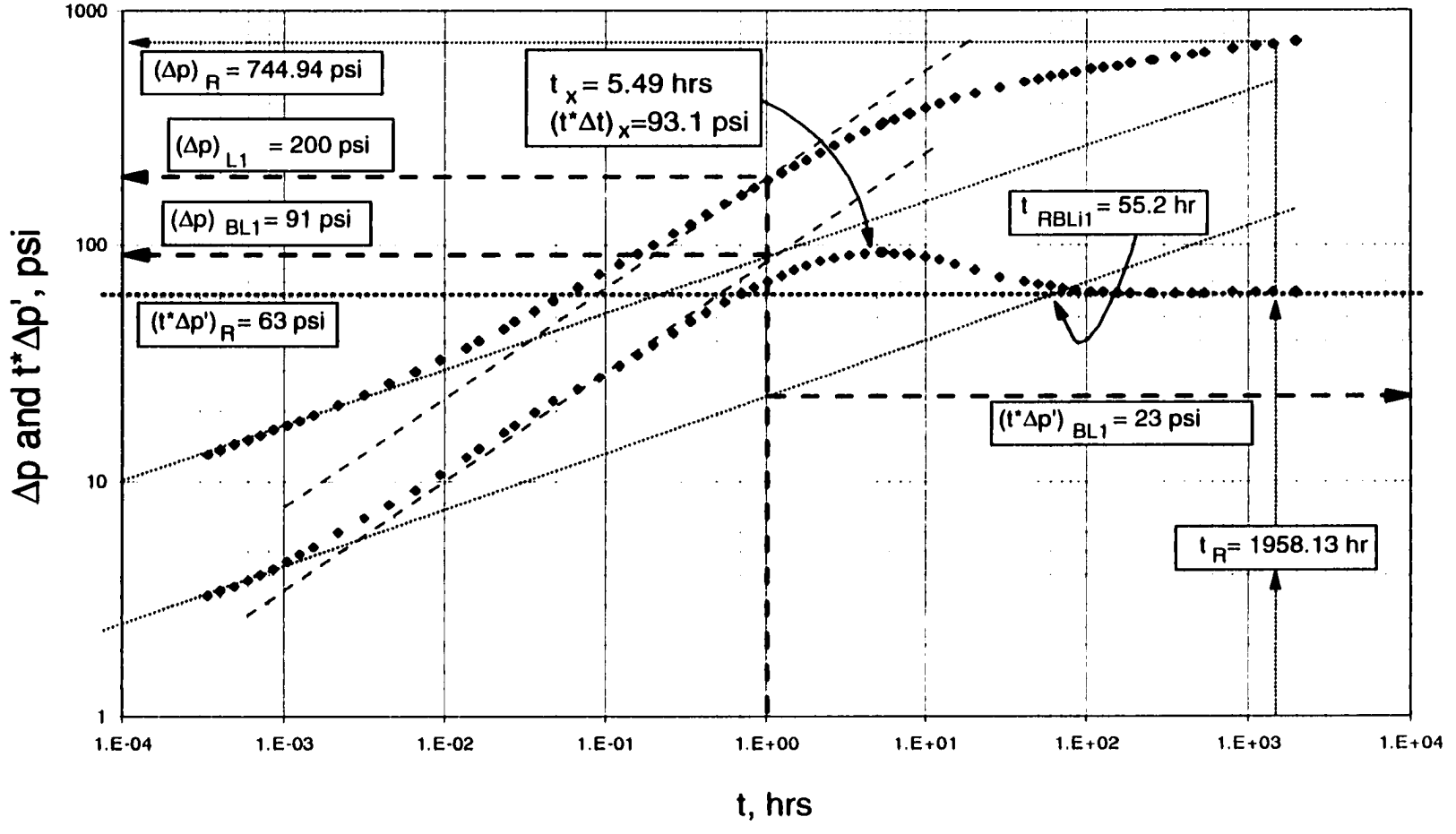

Fig. 5.8. Log-log plot of pressure and pressure derivative for example 3

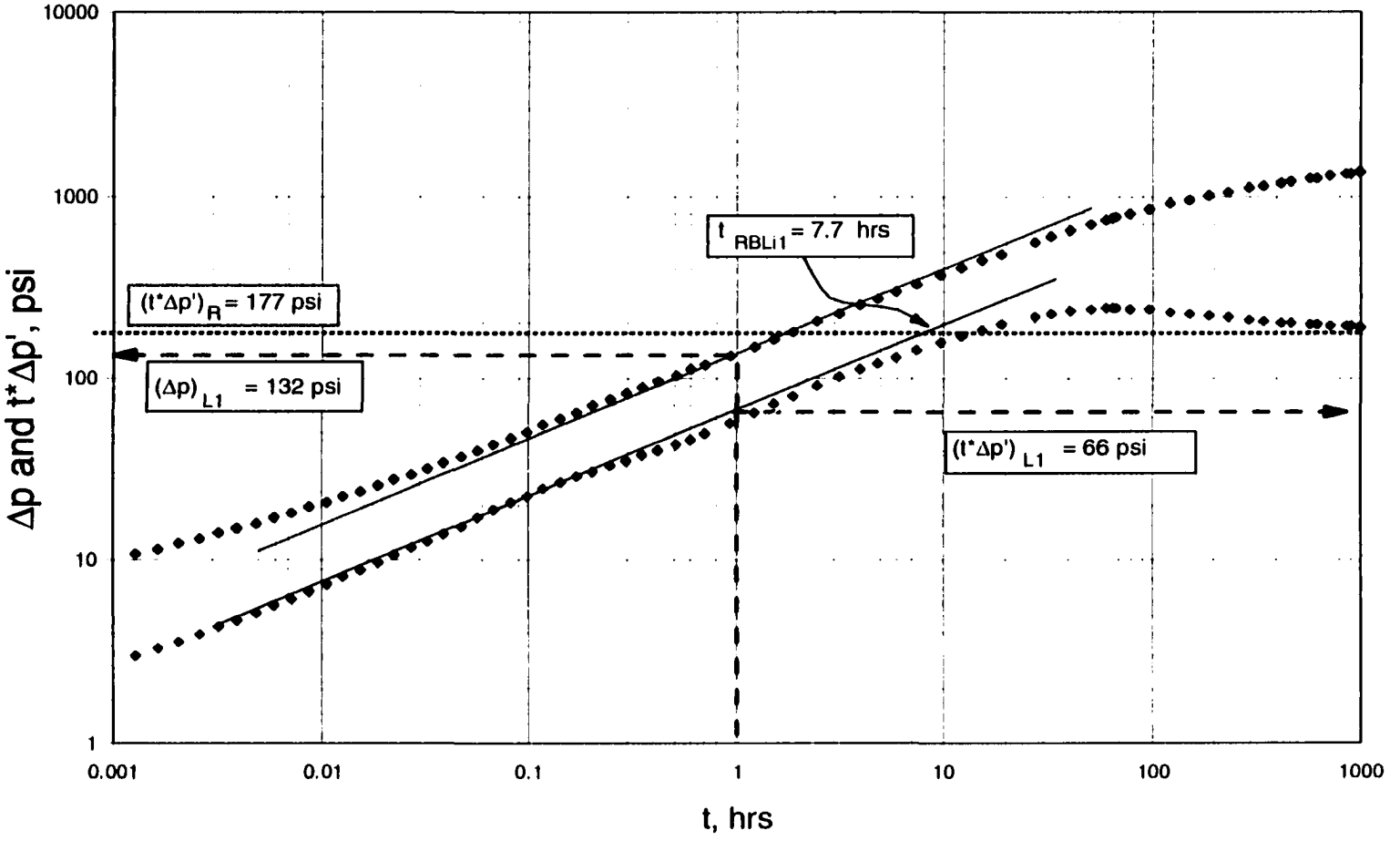

Fig. 5.9. Log-log plot of pressure and pressure derivative for example 4

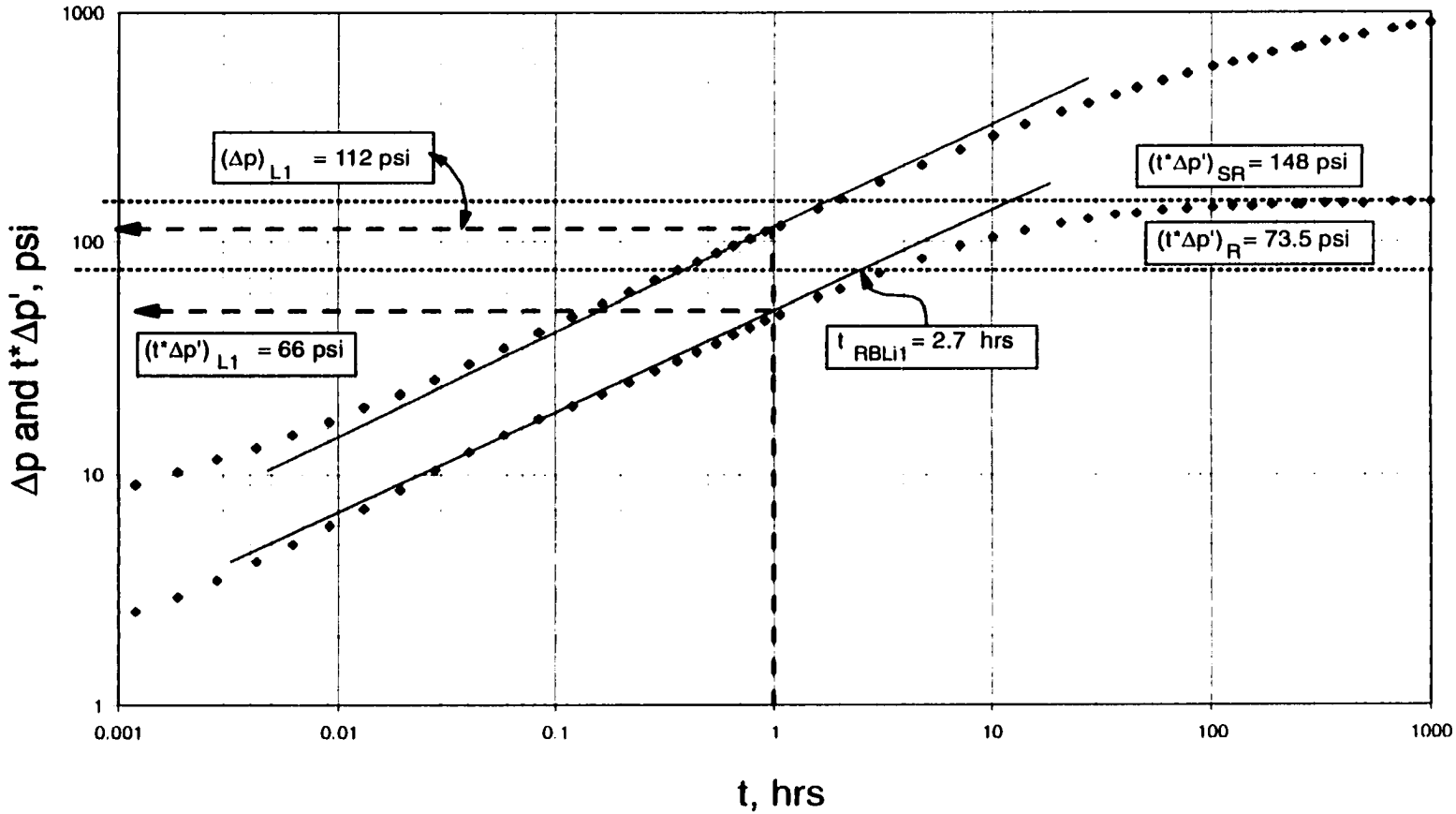

Fig. 5.10. Log-log plot of pressure and pressure derivative for example 5

In Fig. 5.8, it is observed that the pseudoradial flow regime is developed and corresponds to the obtained value.

Step 3 – The different flow regimes have been identified and drawn in Fig. 5.8.

Step 4 – No wellbore storage coefficient is calculated since the unit slope line does not exist.

Step 5 – The following values are read: $(\Delta p)_{BL1} = 60$ psi and $(t^*\Delta p')_{BL1} = 15$ psi. Fracture conductivity, $k_f w$, is estimated from Eqs. 5.6 and 5.12.

$$k_f w = 1947.46 \frac{1}{\sqrt{\phi \mu c_t k}} \left(\frac{q\mu B}{h(\Delta P)_{BL1}} \right)^2$$

$$k_f w = \frac{1947.46}{\sqrt{0.23(0.3)(1.35x10^{-5})(30)}} \left(\frac{3000(0.3)(1.48)}{50(92)} \right)^2 = 30889.4 \; md - ft$$

$$k_f w = \frac{121.74}{\sqrt{\phi \mu c_t k}} \left(\frac{q\mu B}{h(t \cdot \Delta p')_{BL1}} \right)^2 = \frac{121.74}{\sqrt{0.23(0.3)(1.35x10^{-5})(30)}} \left(\frac{3000(0.3)(1.48)}{50(23)} \right)^2$$

$k_f w = 30895.4$ *md-ft*

The values of fracture conductivity calculated by Eqs. 5.6 and 5.12 are close agreement. The average value of 30892.4 *md-ft* is taken.

Step 6 - Calculate the time of intersection of the bilinear and radial flow lines using Eq. 5.42, but first, m_{BL} is calculated using Eq. 5.3, as:

$$m_{BL} = \frac{44.13}{(\phi \mu c_t k)^{0.25}} \left(\frac{q\mu B}{h\sqrt{k_f w}} \right) = \frac{44.13}{\sqrt[4]{0.23(0.3)(1.35x10^{-5})(30)}} \left(\frac{3000(0.3)(1.48)}{50\sqrt{30892.4}} \right)$$

$$m_{BL} = 92$$

$$t_{RBL}^{0.25} = \frac{70.6 q\mu B}{kh} \frac{4}{m_{BL}} = \frac{70.6(3000)(0.3)(1.48)}{(30)(50)} \frac{4}{92}$$

$$t_{RBL} = 55.2 \; hr$$

A close value of t_{RBLi} is observed on Fig. 5.8.

Step 7 – The following characteristic values are read from the log-log plot in Fig. 5.8:

t_R = 1958.13 hrs

Δp_R = 744.944 psi

Then, skin factor is calculated from Eq. 5.40, thus:

$$s = 0.5\left[\frac{(\Delta p)_R}{(t\cdot\Delta p')_R} - \ln\left(\frac{kt_R}{\phi\mu c_t r_w^2}\right) + 7.43\right]$$

$$s = 0.5\left[\frac{744.944}{63} - \ln\left(\frac{30(1958.13)}{0.23(0.3)(1.48)(1.35x10^{-5})0.4^2}\right) + 7.43\right] \approx -3.53$$

Step 8 – half-fracture length is estimated using Eq. 5.26, extrapolating the linear line to read $(\Delta P)_{LI}$=200 psi, thus:

$$x_f = 4.064\left(\frac{qB}{h(\Delta p)_{LI}}\right)\sqrt{\frac{\mu}{\phi c_t k}} = 4.064\left(\frac{3000(1.48)}{50(200)}\right)\sqrt{\frac{0.3}{(0.23)(1.35x10^{-5})(30)}} = 102.4\ ft$$

Verifying the above value using Eq. 5.32a:

$$t_{BLLi} = 13910\phi\mu c_t\left(\frac{x_f^2\sqrt{k}}{k_f w}\right)^2 = 13910(0.23)(0.3)(1.35x10^{-5})\left(\frac{102.4^2\sqrt{30}}{30892.4}\right)^2$$

t_{BLLi} = 0.0015 hrs

This value matches very well with the value of 100 ft input for the simulation and also with the observed value of t_{BLLi} on Fig. 5.8.

Step 9 - Calculate the dimensionless fracture conductivity, C_{fD}, from Eq. 3.37.

$$C_{fD} = \left(\frac{k_f}{k}\right)\left(\frac{w_f}{x_f}\right) = \frac{30892.4}{30(102.4)} = 10.05$$

Step 10 – Since the acting radial flow line coincides with the horizontal line drawn in step 2, then the maximum value pressure derivative value, $(t^*\Delta p')_r$ and the time at which this occurs, t_r, are read to be 5.49 hrs and 93.1 psi, respectively, then with the values of the constants a, b, c and d corresponding to C_{fD}=10 the fault length is estimated using Eq. 5.63, as follows:

$$|L| = -4.56309(102.4) + \frac{(1.7725x10^{-5})(5.49)}{(0.23)(0.3)(1.35x10^{-5})(102.4)} - \left(\frac{1.095x10^{-6}(5.49)}{(0.23)(0.3)(1.35x10^{-5})(102.4)^{3/2}}\right)^2$$

$$+\frac{10.48344x10^{-6}(30^2)(50)(93.1)}{(0.23)(0.3^2)(1.35x10^{-5})(102.4)(3000)(1.48)} = 429.8\ ft$$

Notice that the correlation given by Eq. 5.63 works well if compared with the input fracture length value of 450 ft.

Example 4. Estimate fracture length and fault length for the simulated pressure test data are reported in Table 5.5. Other parameters are given below:

k = 50 md	h = 100 ft	x_f = 200 ft
L = 850 ft	ϕ = 10 %	c_t = 3.7x10^{-5} 1/psi
μ = 2 cp	q = 5000 BPD	B = 1.25 rb/STB
r_w = 0.3 ft	C_{fD} = 25	

Solution:

Step 1 - A log-log plot of pressure change Δp and pressure derivative $(t^*\Delta p')$ values versus test time is provided in Fig. 5.8.

Table 5.5. Pressure data for example 4

t, hr	Δp, psi	t*Δp', psi	t, hr	Δp, psi	t*Δp', psi	t, hr	Δp, psi	t*Δp', psi
0.00129	10.80	3.02	0.14	59.29	26.53	27.55	565.81	218.15
0.00165	11.58	3.31	0.17	64.34	28.57	32.93	605.59	226.49
0.00208	12.37	3.61	0.20	69.75	30.63	40.53	653.44	234.12
0.00260	13.22	3.95	0.25	75.52	32.75	51.30	709.38	239.67
0.00322	14.10	4.30	0.29	81.66	34.96	60.56	749.39	241.36
0.00396	15.03	4.70	0.35	88.18	37.29	64.71	765.39	241.49
0.00485	16.01	5.14	0.42	95.13	39.82	66.89	773.40	241.44
0.00592	17.07	5.62	0.51	102.53	42.56	78.98	813.45	240.34
0.00720	18.21	6.15	0.60	110.01	45.57	96.57	861.50	237.07
0.00874	19.44	6.75	0.71	117.58	48.85	122.66	917.54	231.07
0.01059	20.78	7.39	0.94	132.90	56.12	151.40	965.54	224.89
0.01281	22.23	8.10	1.22	148.36	63.81	187.95	1013.49	218.62
0.01547	23.81	8.86	1.53	163.88	71.54	234.73	1061.40	214.48
0.01867	25.54	9.69	1.87	179.46	79.11	294.09	1109.10	209.78
0.02250	27.41	10.60	2.47	202.92	90.02	343.03	1140.92	204.06
0.02710	29.44	11.61	3.16	226.45	100.38	417.44	1180.78	201.70
0.03262	31.65	12.73	3.95	250.05	110.33	463.06	1201.65	199.50
0.03925	34.06	13.99	4.84	273.65	119.95	580.29	1246.18	198.01
0.04720	36.71	15.40	5.85	297.27	129.23	616.89	1258.23	196.46
0.05674	39.62	16.98	7.38	328.77	141.26	717.96	1287.89	194.63
0.06819	42.83	18.70	9.61	368.13	155.99	857.25	1322.29	192.81
0.08192	46.39	20.55	12.23	407.52	170.26	901.92	1332.10	192.71
0.09841	50.31	22.50	15.28	446.98	183.87	978.73	1347.77	190.86
0.11819	54.61	24.50	18.81	486.50	196.52	1000.00	1351.87	190.67

Step 2 - With the given permeability of 50 md, the value of pressure derivative at which the infinite acting radial flow line takes place, $(t^*\Delta p')_R$, is obtained using Eq. 5.39a. On the log-log plot of pressure and pressure derivative, the horizontal line along this value is drawn.

$$(t\cdot\Delta p')_R = \frac{70.6q\mu B}{kh} = \frac{70.6(5000)(2)(1.25)}{(50)(100)} = 177\ psi$$

In Fig. 5.9, it is observed that the pseudoradial flow regime is not very well developed.

Step 3 – The different flow regimes have been identified and drawn in Fig. 5.9. Notice that the bilinear flow regime is not very well identified. Instead, there is a transition period between bilinear and bilinear.

Step 4 – No wellbore storage coefficient is calculated since the unit slope line does not exist.

Step 5 - The values of Δp and $(t^*\Delta p')$ at time t=1 hr read from the plot as 210 and 90 psi, respectively. The half fracture length, x_f, is calculated from Eqs. 5.44 and 5.26, giving an excellent match, as follows:

$$x_f = \frac{2.032Bq}{h(t^*\Delta p')_{L1}}\sqrt{\frac{\mu}{\phi c_t k}} = \frac{2.032(1.25)(5000)}{100(66)}\sqrt{\frac{2}{0.1(3.7x10^{-5})(50)}} = 200.08\ ft$$

$$x_f = \frac{4.064Bq}{h(\Delta p)_{L1}}\sqrt{\frac{\mu}{\phi c_t k}} = \frac{4.064(1.25)(5000)}{100(132)}\sqrt{\frac{2}{0.1(3.7x10^{-5})(50)}} = 200.08\ ft$$

Step 6 - Skin factor should be calculated using Eq. 5.40 which requires knowledge of Δp_R and $(t^*\Delta p')_R$ which cannot be obtained accurately since the radial flow regime has not been developed very well. Also, the intersection between linear and bilinear flow regimes is not clearly defined, so for this example is not possible to accurately estimate the skin factor.

Step 7 – From Fig. 5.9, the time of intersection between the linear line and the radial line, t_{LRi}, is 7.7 hrs, then the half fracture length, x_f, is recalculated from Eq. 5.45.

$$\frac{x_f^2}{k} = \frac{t_{LRi}}{1207\phi\mu c_t}$$

$$\frac{x_f^2}{50} = \frac{7.7}{1207(0.1)(2)(3.7x10^{-5})} \Rightarrow x_f = 207.6\ ft$$

which agrees with the values obtained from Eqs. 5.44 and 5.26.

Step 8 – Although, the infinite acting radial flow line does not coincides very well with the horizontal line drawn in step 2, use of correlation 5.63 can be still effective. The maximum pressure derivative value, $(t^*\Delta p')_x$ and the time at which this occurs, t_x are, respectively, 241.4 psi and 66.9 hrs. Since fracture conductivity cannot be estimated, find the appropriate values of the constants a, b, c and d for the average case and determine the fault length using Eq. 5.63, thus:

$$|L| = 200(-4.58293) + \frac{2.072x10^{-5}(50)(66.9)}{(0.1)(2)(3.7x10^{-5})(200)} - \left(\frac{1.9196x10^{-6}(50)(66.9)}{(0.1)(2)(3.7x10^{-5})(200)^{3/2}}\right)^2 +$$

$$\frac{9.379x10^{-6}(50^2)(100)(241.4)}{(0.1)(2^2)(3.7x10^{-5})(200)^{3/2}(5000)(1.25)} = 870\ ft$$

This demonstrate the validity of Eq. 5.63 since the obtained value agrees well with the value of 850 ft used for the simulation.

Example 5. Simulated pressure test data are reported in Table 5.6. It is known that a sealing fault is intercepted by the well's hydraulic fracture forming an angle of 90 degrees. Other parameter used to perform the simulation are given below:

k = 120 md	h = 100 ft	x_f = 150 ft
L = 10000 ft	ϕ = 10 %	$c_t = 3.7x10^{-5}$ 1/psi
μ = 2 cp	q = 5000 BPD	B = 1.25 rb/STB
r_w = 0.3 ft	C_{fD} = 25	

What is the value of permeability that can be estimated from this test? Estimate the fracture half length. Can the fault length be calculated for this example?

Table 5.6. Pressure data for example 5

t, hr	Δp, psi	t*Δp', psi	t, hr	Δp, psi	t*Δp', psi	t, hr	Δp, psi	t*Δp', psi
0.0012	9.10	2.54	0.36	74.88	30.57	36.85	440.26	130.38
0.0019	10.32	2.96	0.45	81.90	33.54	45.97	469.46	133.44
0.0028	11.65	3.51	0.55	88.94	36.58	60.27	506.05	136.62
0.0042	13.15	4.18	0.66	96.02	39.62	78.63	542.71	139.13
0.0062	14.91	5.00	0.78	103.11	42.65	102.18	579.44	141.05
0.0091	16.97	5.97	0.92	110.20	45.65	125.76	608.86	142.27
0.0133	19.38	7.14	1.07	117.31	48.61	154.56	638.30	143.27
0.0193	22.24	8.60	1.60	138.68	57.22	189.74	667.77	144.13
0.0279	25.67	10.42	2.02	152.91	62.71	244.84	704.64	145.06
0.0403	29.85	12.57	3.07	181.33	73.09	257.61	712.02	145.25
0.0582	34.87	14.94	4.82	216.90	84.90	331.84	748.91	146.08
0.0839	40.80	17.35	7.16	252.58	95.36	406.00	778.43	146.70
0.1198	47.45	19.77	10.23	288.36	104.49	496.33	807.96	147.25
0.1645	54.19	22.29	14.25	324.28	112.37	669.98	852.25	148.00
0.2192	61.01	24.94	20.67	367.60	120.36	817.71	881.78	148.41
0.2845	67.92	27.69	27.74	403.87	125.86	1000.00	911.71	148.00

Solution:

Step 1 - A log-log plot of pressure change Δp and pressure derivative ($t^*\Delta p'$) values versus test time is provided in Fig. 5.10.

Step 2 – From the log-log plot, at first sight, it looks that the pseudoradial flow regime is very well developed. A line over the value of 148 is drawn on Fig. 5.10. However, using the given permeability of 120 md which is assumed to be obtained from another sources, the value of pressure derivative at which the infinite acting radial flow line takes place, $(t^*\Delta p')_R$, is obtained by means of Eq. 5.39a:

$$(t \cdot \Delta p')_R = \frac{70.6 q\mu B}{kh} = \frac{70.6(5000)(2)(1.25)}{(120)(100)} \approx 73.5 \; psi$$

On the log-log plot of pressure and pressure derivative, the horizontal line along this value is drawn. This is a typical case of development of *semiradial* flow regime. Notice the difference between the true radial line (73.5 psi) and the *semiradial* line (on 148 psi). If permeability is calculated with the value of ($t^*\Delta p'$) for the semiradial flow regime, using Eq. 5.39b, we obtain:

$$k = \frac{70.6 q\mu B}{h(t \cdot \Delta p')_R} = \frac{70.6(5000)(2)(1.25)}{(100)(148)} \approx 59.63 \; md$$

Under the mentioned circumstances, notice that Eq. 5.39b predicts a value of permeability which corresponds to half the true value. Then, the applicability of Eq. 5.39c is here demonstrated:

$$k = \frac{141.2 q\mu B}{h(t \cdot \Delta p')_{SR}} = \frac{141.2(5000)(2)(1.25)}{(100)(148)} \approx 119.3 \; md$$

which is much closer to the permeability value of 120 md.

Step 3 – The different flow regimes have been identified and drawn in Fig. 5.10. Notice that the bilinear flow regime is not very well identified. Instead, there is a transition period between bilinear and bilinear.

Step 4 – No wellbore storage coefficient is calculated since the unit slope line does not exist.

Step 5 - The values of Δp and ($t^*\Delta p'$) at time t=1 hr read from the plot as 210 and 56 psi, respectively. The half-fracture length, x_f, is calculated from Eqs. 5.44 and 5.26, as follows:

$$x_f = \frac{2.032Bq}{h(t*\Delta p')_{LI}}\sqrt{\frac{\mu}{\phi c_t k}} = \frac{2.032(1.25)(5000)}{100(56)}\sqrt{\frac{2}{0.1(3.7x10^{-5})(120)}} = 152.2\ ft$$

$$x_f = \frac{4.064Bq}{h(\Delta p)_{LI}}\sqrt{\frac{\mu}{\phi c_t k}} = \frac{4.064(1.25)(5000)}{100(112)}\sqrt{\frac{2}{0.1(3.7x10^{-5})(50)}} = 152.21\ ft$$

Notice the excellent agreement between the input value of half-fracture length used for the simulation and the values obtained from Eqs. 5.44 and 5.26.

Step 6 - Skin factor should not be calculated using Eq. 5.40 since the truly pseudoradial flow is unknown. Eqs. 5.59 or 5.60 cannot be also used because fracture conductivity was not estimated since the bilinear flow regime is not very well defined in this exercise.

Step 7 – From Fig. 5.10, the time of intersection between the linear line and the radial line, t_{LRi}, is 2.7 hr, then the half fracture length, x_f, is recalculated from Eq. 5.45.

$$\frac{x_f^2}{k} = \frac{t_{LRi}}{1207\phi\mu c_t}$$

$$\frac{x_f^2}{120} = \frac{2.7}{1207(0.1)(2)(3.7x10^{-5})} \Rightarrow x_f = 190.5\ ft$$

which is close to the values obtained from Eqs. 5.44 and 5.26.

Step 8 – Dimensionless fracture conductivity cannot be estimate because skin factor is unknown.

Step 9 – Because pseudoradial flow regime was never developed and no maximum point is observed, Eq. 5.63 cannot be applied.

CHAPTER VI

SUMMARY, CONCLUSIONS AND RECOMENDATIONS

6.1. SUMMARY

It has been found that the five studied PEBI grid styles work well for simulating horizontal well pressure behavior. The average deviation error was about 2.5 %. No improvement effort in the accuracy of the solution was performed which means that deviation error could be further reduced. Vertical wells, whether or not damage and wellbore storage effects are included, can be accurately simulated using either circular or variable PEBI grid styles. Deviation errors lower than 0.5 % were obtained with a relative small number of gridpoints. PEBI grids are not the panacea to simulate vertical fractured well pressure behavior. Only the Elliptical grid style was able to provide reliable and accurate solutions with absolute deviation less than 1.5 %. It is being demonstrated through several examples that PEBI grids handle very well non-orthogonal systems. Accurate simulation results where obtaining by changing the horizontal well angle with respect to the x-y plane. For vertical wells, similar results were found by rotating the fracture angle from 0 to 90 degrees. Traditionally and numerically speaking, a fracture has been oriented along the x-direction.

For a branch fracture, a slight inclination of the angle causes a friction for the pressure transient to travel. Then, a small increase in pressure drop is observed. Duplicating the value of the angle causes a pressure drop which is very slightly higher

than the former case, an so on. Then, the pressure behavior for angles of 10, 20 or 30° may be considered the same. Same situation occurs when the branch fracture conductivity was reduced 75 or even 50 %.

Some branch fracture transient behaviors present an early slope of 0.34 or 0.35 which may be confused with the pressure behavior obtained from an infinite conductivity fracture when the ratio of fracture to drainage ratio is bigger than 16 since the biradial or elliptical flow (slope=0.36) is observed at very early times.

For case of intermediate to high fracture conductivity, a branch fracture may be confused with a bilinear flow regime if a slope of 0.25 is present at early time. The fracture conductivity can be estimated from the supposed bilinear flow regime to be used to simulate a pressure test. If the results of the simulation do not match the well the pressure and pressure derivative actual trend, we may conclude that a branch fracture takes place, otherwise, the bilinear flow regime was correctly assumed.

A fracture intersecting a fault causes a delaying of the formation of the pseudoradial flow period since the fault acts as a boundary which effect depends upon its length. This is manifested by a hump on the pressure derivative curve. This deviation is more pronounced as the fault length grows up but is less noticeable as the intersecting angle goes from 90 to zero degrees and as the fracture-fault meeting point goes from the fault middle point to the fault tip. When the fault fully crosses the reservoir gives origin to the introduction of a new flow regime period, called here as *semiradial* (or *semi-pseudoradial*). This flow regime results from the partial answer of the reservoir system because the fault acts as a boundary.

6.2. CONCLUSIONS

1) Any of the five studied PEBI grids can be used to simulate horizontal well pressure behavior. Circular PEBI grids and elliptical PEBI grids are appropriate to simulate pressure transient behavior in unfractured vertical wells and fractured vertical wells, respectively.
2) In vertical fractured wells, the elliptical PEBI grid is not recommended for dimensionless fracture conductivities lower than 1.
3) The pressure response for a branch fracture starting from either the wellbore or the middle distance between wellbore and main fracture tip is practically the same as the case without branch.
4) Verification the acceptance of the branch fracture simulated as horizontal well was performed by comparison its solution to the solution presented by Berumen et al[36] with resulting maximum absolute deviation of about 1.5 %.
5) Reduction of branch fracture conductivity and branch fracture angle do not affect the pressure response of the branch fracture.
6) A sealing fault intercepted by a fracture tends to delay the formation of the psudoradial flow regime. If the fault is too long, the radial flow regime may never develop. This effect is reduced as the intercepting angle is different than 90°.
7) The effects of the fracture conductivity on the transient characterization of the fault is negligible.
8) The *Tiab's Direct Synthesis Technique* was applied for estimation of branch fracture length and correlations were developed to estimate fault length when the

fracture-fault angle is 90 degrees and a new relation to estimate permeability for *semiradial* flow regime is introduced.

6.3. RECOMMENDATIONS

1) The use of a fracture, instead of horizontal well, to simulate one or more branch fractures should be motive of a later study with the use of PEBI elliptical grids.
2) For the case of a hydraulic fracture intersecting a fault, simulation of multiple well tests may be studied to attempt to determine fault-fracture angle.
3) Study the case of hydraulic fractures intersecting leaky faults.
4) Include in the simulations the criteria concerning to fault failure.
5) Select the PEBI grid and the gridding control parameters provided in chapter two according to the system dealt with.

NOMENCLATURE

For the modeling part nomenclature is given in CGS units. However, oilfield units are used for the application of the *Tiab's Direct Synthesis Technique*.

A Drainage area, Ac
B Oil formation factor, rb/STB
b Straight line intersect
C Wellbore storage coefficient, bbl/psi
C_D Dimensionless wellbore storage coefficient
C_{fD} Dimensionless fracture storage capacity
C_{fD} Dimensionless fracture conductivity
c_f Formation, fracture or fluid compressibility, 1/psi
C_{HD} Horizontal well dimensionless conductivity
c_o Oil compressibility, 1/psi
c_t Total system compressibility, c_f+c_o, 1/psi
c_{tf} Total compressibility in the fracture, 1/psi
D_w Wellbore diameter, ft
G Source/sink term
h Reservoir thickness, ft
h_f Fracture/fault thickness, ft
i Node
j Node
k Formation permeability, md
k_f Fracture permeability, md
k_fw Fracture conductivity, md-ft
k_x x-direction permeability, md
k_z z-direction permeability, md
L Fault length, ft
L_D Dimensionless fault length
L_w Horizontal well length, md
m Straight line slope
p Pressure, psi
p_i Initial reservoir pressure, psi
P_D Dimensionless pressure
P_D' Dimensionless pressure derivative
q Oil flow rate, BPD
Q Mass flow rate per unit area of grid block

R_e Reynolds number in porous media
r_e Reservoir drainage radius, ft
r_w Wellbore radius, ft
q Oil flow rate, BPD
q_f Flow rate at fracture
q_w Flow rate at wellbore
s Skin factor
t Time, hr
T Reservoir temperature, °F
t_D Dimensionless time
$t*\Delta p'$ Pressure derivative, psi
u Flow velocity, ft
V_{pf} Fracture pore volume
x_f Half-fracture length
x_{fb} Branch fracture length
x_{fbD} Dimensionless branch fracture length
w Fracture width, ft
w_D Dimensionless fracture width, ft
x x-direction
y y-direction

Greek

β Rapid flow coefficient
Δx Block size in x-direction
Δy Block size in y-direction
Δt Time step, hrs
Δp Pressure drop, psi
δ $(1+R_e)^{-1}$
ϕ Porosity, cp
ρ Density, lbm/ft^3
θ Fracture inclination angle with respect to the x-axis, or angle formed between main fracture and branch fracture, degrees
ξ_x $\delta_x c_f/(2-\delta_x)$
ξ_y $\delta_y c_f/(2-\delta_y)$

Subscripts

1	1 hr
Bf	Branch fracture
BF1	Branch fracture at 1 hr
BFBLi	Branch fracture-bilinear intersection
BFLi	Branch fracture-linear intersection
BL	Bilinear
BLLi	Bilinear-linear intersection
BL1	Bilinear at 1 hr
L1	Linear at 1 hr
D	Dimensionless
F	Formation, fracture
G	Gas
LPi	Linear-Pseudosteady state intersection
LRi	Linear-Radial intersection
o	Oil
SC	Standard conditions
SR	Semiradial
R	radial
RBLi	Radial-bilinear intersection
RLi	Radial-linear intersection
USBLi	Unit slope-bilinear intersection
w	Water

REFERENCES

1. Germanovich, L. N., Astakhov, D. K., Mayerhofer, J. S. and Ring, L. M.: "*Hydraulic Fracture with Multiple Segments I. Observations an Model Formulation.*" Int. J. Rock. Mech. & Sci. 34 : 3-4, Paper No. 00097, 1997.

2. Germanovich, L. N., Astakhov, D. K., Mayerhofer, J. S. and Ring, L. M.: "*Hydraulic Fracture with Multiple Segments II. Effect of Interaction.*" Int. J. Rock. Mech. & Sci. 34 : 3-4, Paper No. 00098, 1997.

3. Warpinski, N. R., Braganan, T. P., Peterson, R. E., Fiz, J. E., Engler, B. P., and Wilmer, R.: "*Microseismic and Deformation Imaging of Hydraulic Fracture Growth and Geometry in the C Sand Interval, GRI/DOE M-Site Project*". Paper SPE 38573 presented at the 1997 Annual Technical Conference and Exhibition held in Dallas, TX, 5-8 Oct. 1997.

4. Warpinski, N. R., Braganan, T. P., Peterson, R. E., Walhort, S. L. and Uhl, J. E.: "*Mapping Hydraulic Growth and Geometry Using Microseismic Events Detected by Wireline Retrievable Accelorometer Array*". Paper SPE 40014 presented at the 1998 Gas Technology Symposium held in Calgary, Canada, March 15-18, 1998.

5. Cipolla, C. L., and Wright, C. A.: "*State-of-the-Art in Hydraulic Fracture Diagnosis*". Paper SPE 64434 presented at SPE Asia Pacific Oil and Gas Conference and Exhibition held in Brisbane, Australia, Oct. 16-18, 2000.

6. Roberts, G. A., Chipperfield, S. T. and Miller II, W. K.,: "*The Evolution of a High Near-Wellbore Pressure-Loss-Treatment Strategy for the Australian Cooper Basin*". Paper SPE 63029 presented at the 2000 SPE Annual Technical Conference and Exhibition held in Dallas, TX, Oct. 1-4, 2000.

7. Crawford, P. B., and Landrum, B. L.: "*Effect of Unsymmetrical Vertical Fractures on Production Capacity*". Technical Note 275. Soc. Pet. Eng. Of AIME, Vol. 204, p. 251-254. 1955,

8. McGuire, W. J. and Sikora, V. J.: "*The Effect of Vertical Fractures on Well Productivity*". Trans. AIME (1960) 219, p. 401.

9. Scott, J. O.: "*The Effect of Vertical Fractures in Transient Pressure Behavior of Wells.*" JPT (Dec. 1963). P. 1365.

10. Russell, D. G. and Truitt, N. E.: "*Transient Pressure Behavior in Vertically Fractured Reservoirs.*" JPT (Oct. 1964). P. 1159-1170.

11. Gringarten, A. C. and Ramey, H. Jr.: "*Pressure Analysis for Fractured Wells.*" Paper SPE 4051 presented at the 47th Annual Fall Meeting of the Society of Petroleum Engineers of AIME held in San Antonio, TX, Oct. 8-11, 1972.

12. Gringarten, A. C., Ramey, H. Jr. and Raghavan, A.: "*Unsteady-State Pressure Distributions Created by a Well with a Single Infinite-Conductivity Vertical Fracture.*" SPEJ (Aug. 1974). P. 347-560.

13. Raghavan, R., Cady, G. V. and Ramey, H. J., Jr.: "*Well-Test Analysis for Vertically Fractured Wells.* JPT (aug. 1972). P. 1014-1020.

14. Sawyer, W. K., Locke, C. D., and Overbey, W. K. Jr.: "*Simulation of a finite-Capacity Vertical Fracture in a Gas Reservoir*". Paper SPE 4593 presented at the 48th Annual Fall Meeting of the SPE of AIME held in Las Vegas, NV, Sept. 30-Oct. 3, 1973.

15. Barker, B. J.: "*Transient Flow to Finite Conductivity Vertical Fractures*". PhD Dissertation. Stanford University. 1977.

16. Wattenberger, R .A. and Ramey, H. J., Jr.: "*Well Test Interpretation in Vertically Fractured Gas Wells*" JPT (May 1969), p. 625-632. Trans. AIME 246.

17. Holditch, S. A. and Morse, R. A.: "*The Effects of Non-Darcy Flow on the Behavior of Hydraulically Fractured Gas Wells*". Paper SPE 5586. JPT (Oct. 1976), p. 1169-1179.

18. Cinco-Ley, H., Samaniego, V. F. and Rodriguez, F.: "*Transient Pressure Behavior for a Well with a Finite-Conductivity Fracture*". Paper SPE 6014 presented at the SPE-AIME 51st Annual Fall Technical Conference and Exhibition, held in New Orleans, LA, Oct. 3-6, 1976.

19. Dowdle, W. L. and Hyde, P.: "*Well Test Analysis of Hydraulically Fractured Gas Wells*". Paper SPE 6437 presented at the 1977 Deep Drilling and Production Symposium of the SPE of AIME held in Amarillo, TX, Apr. 17-19, 1977.

20. Ekie, S., Hadinoto, N., and Raghavan, R.: "*Pulse-Testing of Vertically Fractured Wells*". Paper SPE 6751 presented at the 52nd Annual Fall Technical Conference and Exhibition of the SPE of AIME held in Denver, CO, Oct. 9-12, 1977.

21. Cinco_Ley, H. and Samaniego, F.: "*Effect of Wellbore Storage and Damage on the Transient Pressure Behavior of Vertical Wells*". Paper SPE 6752 presented at the 52nd Annual Fall Technical Conference and Exhibition of the SPE of AIME held in Denver, CO, Oct. 9-12, 1977.

22. Cinco_Ley, H. and Samaniego, F.: "*Transient Pressure Analysis for Fractured Wells*". Paper SPE 7490 presented at the 53rd Annual Fall Technical Conference and Exhibition of the SPE of AIME held in Houston, TX, Oct. 1-3, 1978.

23. Narasimhan, T. N. and Berkeley, L.: "*A Purely Numerical Approach for Analysing Fluid Flow to a Well Intercepting a Vertical Fracture*". Paper SPE 7983 presented at the 1979 California Regional Meeting of the SPE of AIME held in Ventura, CA, Par. 18-20, 1979.

24. Guppy, K. H., Cinco-Ley, H., Ramey, H. Jr., Samaniego, F.: "*Non-Darcy Flow in Well with Finite-Conductivity Vertical Fractures*" SPEJ, p. 681-698, Oct. 1982. Paper SPE 8281.

25. Naelan A. M. and Raghavan, R.: "*The Influence of Vertical Fractures Intercepting Active and Observation Wells on Interference Tests*". Paper SPE 9346 presented at the 55th Annual Fall Technical Conference and Exhibition of the SPE of AIME held in Dallas, TX, Sept. 21-24, 1980.

26. Tiab, D. and Abobise, E. O.: "*Determining Fracture Orientation from Pulse Testing*". SPE Formation Evaluation, p. 459-474. Sept. 1989. Paper SPE 11027.

27. Bennett, C. O., Rosato, N. D., Reynolds, A. C. Jr., and Raghavan, R.: "*Influence of Fracture Heterogeneity and Wing Length on the Response of Vertically Fractured Wells*". Paper SPE 9886 presented at the 1981 SPE/DOE Low Permeability Symposium held in Denver, CO, May. 27-29, 1981.

28. Bennett, C. O., Reynolds, A. C. Jr., and Raghavan, R. and Elbel, J. L.: "*Performance of Finite-Conductivity, Vertically Fractured Wells in Single-Layer Reservoirs*". SPE Formation Evaluation, p. 399-420. Aug. 1986.

29. Wong, D. W., Harrington, A. G. and Cinco-Ley, H.: "*Application of the Pressure-Derivative Function in the Pressure-Transient Testing of Fractured Wells*". SPE Formation Evaluation, p. 470-480, Oct. 1986. Paper SPE 13056.

30. Tiab, D. and Puthigai, S. K.: "*Pressure Derivative Type Curves for Vertically Fractured Wells*". SPE Formation Evaluation, p. 156-158, March 1988.

31. Cinco-Ley, H. and Meng, H. -Z.: "*Pressure Transient Analysis of Wells with Finite Conductivity Vertical Fractures in Double Porosity Reservoirs*". Paper SPE 18172 presented at the 63rd Annual technical Conference and Exhibition of the SPE held in Houston, TX, Oct. 2-6, 1988.

32. Okoye, C. U., Oshinuga, A. D. and Ghalambor, A.: "*Pressure Transient Behavior in Multilayer Vertically Fractured gas Reservoir with Finite Conductivity*". Paper SPE 18960 presented at the SPE Joint Rocky Mountain Regional/Low

Permeability reservoirs Synposium and Exhibition held in Denver, CO, March 6-8, 1989.

33. Tiab, D.: "*Analysis of Pressure and Pressure Derivative without Type-Curve Matching: Vertically Fractured Wells in Closed Systems*". Journal of Petr. Sci. and Engr. 11 (1994) p. 323-333.

34. Tiab, D., Azzougen, A., Escobar, F. H., and Berumen, S.: "*Analysis of Pressure Derivative Data of a Finite-Conductivity Fractures by the 'Direct Synthesis Technique'*". Paper SPE 52201 presented at the 1999 SPE Mid-Continent Operations Symposium held in Oklahoma City, OK, March 28-31, 1999 and presented at the 1999 SPE Latin American and Caribbean Petroleum Engineering Conference held in Caracas, Venezuela, 21–23 April 1999.

35. Berumen-Campos, Sergio.: "*Evaluation of Fractured Wells in Pressure-Sensitive Formations.*" PhD Dissertation. The University of Oklahoma. 1995.

36. Berumen, S., Rodriguez, F. and Tiab, D.: "*An Investigation of Fracture Asymmetry on the Pressure Response of Fractured Wells*". Paper SPE 38972 presented at the 5th Latin American and Caribbean Petroleum Engineering Conference and Exhibition held in Rio de Janeiro, Brazil, Aug. 30-Sept-3, 1997.

37. Escobar, F. H., Tiab, D. and Jokhio, S.: "*Pressure Analysis for a Well Intersected by a Hydraulic Fracture with Multiple Segments*". Paper SPE 71035 presented at the SPE Rocky Mountain Petroleum Technology Conference held in Keystone, CO. May. 21-23, 2001.

38. Yanosik, J. L., and McCracken, T.A.: "A Nine-Point Finite-Difference Reservoir Simulator for Realistic Prediction of Adverse Mobility Ratio Displacements". Paper SPE 5734. 1979, pp. 253-262.

39. Coats, K. H. and Modine, A. D.: "A Consistent Method for Calculating Transmissibilities in Nine-point Difference Equations". Paper SPE 12248 presented at the reservoir simulation symposium held in San Francisco, CA, Nov. 15-18, 1983.

40. Escobar, F. H.: "*Thirteen-Point Finite Difference Solution for Prediction of Waterflood Sweep Efficiency*". M.S. Thesis. The University of Oklahoma. 1995.

41. Wadsley, W. A.: "*Modeling Reservoir Geometry with Non-Rectangular Coordinate Grids*". Paper SPE 9369 presented at the 55th Annual Technical Conference and Exhibition of the Society of Petroleum Engineers of AIME, held in Dallas, TX, Sept. 21-24, 1980.

42. Pruess, K. and Bodvarsson, G. S.: "*A Seven-Point Finite Difference Method for Improved Grid Orientation Performance in Pattern Steamfloods*". Paper SPE 12252 presented at the Reservoir Simulation Symposium held in San Francisco, CA., Nov. 15-18, 1983.

43. Pedrosa, O. A., Jr., Aziz, K.: "*Use of Hybrid Grid in reservoir Simulation*". SPE Reservoir Engineering, November 1986, p. 611-621. Paper SPE 13507.

44. Han, D. K., Han D. L., Yan, C. Z. and Peng, L. T.: "*A more Flexible Approach of Dynamic Local Grid Refinement for reservoir Modeling*". Paper SPE 16014 presented at the ninth SPE Symposium on Reservoir Simulation held in San Antonio, TX, Feb. 1-4. 1987.

45. Ewing, R. E., and Lazarov, R. D.: "*Adaptive Local grid Refinement*". Paper SPE 17806 presented at the SPE Rocky Mountain Regional Meeting, held in Casper, WY, May 11-13, 1988.

46. Nacul, E. C., Leprete, C., Pedrosa, O. A., jr., Girad, P. and Aziz, K.: "*Efficient Use of Domain Decomposition and Local grid Refinement in Reservoir Simulation*". Paper SPE 20740 Presented at the 65th Annual technical Conference and Exhibition of the Society of Petroleum Engineers held in New Orleans, LA, Sept. 23-26, 1990.

47. Wallis, J. R., and Nolen, J. S.: "*Efficient Iterative Linear Solution of Locally refined Grids Using Algebraic Multilevel Approximate Factorizations*". Paper SPE 25239 presented at the 12th SPE symposium in reservoir Simulation held in New Orleans, LA, Feb. 28-March 3, 1993.

48. Heinemann, Z. E. and Brand, C. W., Munka, M. and Chen, Y. M.: "*Modeling Reservoir Geometry with Irregular Grids*". SPE Reservoir Engineering, May 1991, p. 225-232. Paper SPE 18412.

49. Palagi, C. L. and Aziz, K.: "*Use of Voronoi Grid in reservoir Simulation*" Paper SPE 22889 presented at the 66th Annual technical Conference and Exhibition of the Society of Petroleum Engineers held in Dallas, TX, Oct. 6-9, 1991.

50. Trease, H.: "*Three-Dimensional Free Lagrangian Hydrodynamics*". The Free-Lagrange Method, eds. M.J. Fritts, W.P. Crowley and H.E. Trease, Lecture Notes in Physics, Springer-Verlag, New York (1985) 238, p. 145-157.

51. Voronoi, G.: "*Nouvelles Applications des Parametres Continus a la Therie des formes quadratiques*" J. Reine Agew. Math (1908) 134, p. 198-287.

52. Winterfield, P. H. Scriven, L. E. and Davis, H. T.: "*Percolation and Conductivity of Random Two-Dimensional Composites*" Jour. Phys. C.: Solid State Phys. (1981) 95, p. 217-227.

53. Pathak, P., Winterfeld, P. H., Davis, H. T., and Scriven, L. E.: "*Rock Structure and Transport thre in: Unifying with Voronoi Models and Percolation Concepts*" Paper SPE 8846 presented at the First joint SPE/DOE symposium of Enhanced Oil Recovery held in Tulsa, OK, April 1980.

54. Mackay, A. L.: "*Stereological Characteristics of Atomic Arrangements in Crystals*", Journal of Microscopy (1972) 95, p. 217-227.

55. McNeal, R. H.: "*An Asymmetrical Finite Difference Network*". Quart. Appl. Math. (1953) 11, p. 295-310.

56. Richards, F. D.: "*The Interpolation of Protein Structures: Total Volume Group Distribution and Packing Density*", Journal of Molecular Biology (1974) 82, p. 1-14.

57. Deimbacher, F. X., and Heinemann, Z. E.: "*Time-Dependent Incorporation of Locally Irregular Grids in Large Reservoir Simulation Models*". Paper SPE 25260 presented at the 12th SPE symposium on Reservoir Simulation held in New Orleans, LA, Feb. 28-March 3, 1993.

58. Isaaks, E. H. and Srivastava, R. M.: "*An Introduction to Applied Geostatistics*". Ozford University Press. New York, 1989.

59. Narasimhan, T. N. and Witherspoon, P. A.: "*An Integrated Finite Difference Method for Analyzing Fluid Flow in Porous Media*". Water Resources Res. (Feb. 1976) 12, No. 1., p. 57-64.

60. Naccache, P. F.: "*A Fully-Implicit Thermal Reservoir Simulator*". Paper SPE 37985 presented at the 14th Symposium in Reservoir Simulation held in Dallas, TX, June 8-11, 1997.

61. Verma, S. and Aziz, K.: "*A Control Volume Scheme for Flexible Grids in reservoir Simulation*" Paper SPE 37999 presented at the 14th Symposium in Reservoir Simulation held in Dallas, TX, June 8-11, 1997.

62. Mlacnik, M. J. and Heinemann, Z. E.: "*Using Well Windows in Full Field Reservoir Simulation*". Paper SPE 66371 presented at the SPE Symposium in Reservoir Simulation held in Houston, TX, Feb. 11-14, 2001.

63. Von Pattay, P. W., and Ganzer, L. J.: "*Reservoir Simulation Model for Fractured and Partially Fractured Reservoirs Based on PEBI Grids*". Paper SPE 66384

presented at the SPE Symposium in Reservoir Simulation held in Houston, TX, Feb. 11-14, 2001.

64. Ahmed, M. and Singh, S. P.: "*Application of Flexible Gridding Technique to Simulate Gravity Drainage in ESOZ*". Paper SPE 68842 presented at the SPE Western regional Meeting held in Bakersfield, CA, March 26-30, 2001.

65. Quandalle, P.: "*Eighth SPE Comparative Solution Project: Gridding Tecniques in reservoir Simulation*" Paper SPE 25263 presented at the 12th SPE Symposium in Reservoir Simulation held in New Orleans, LA, Feb. 28-March 3, 1993.

66. Trujillo, D., Blanc, G. Estebenet, T., Qettier, L. and Thomas, J. M.: "*Comparison of Finite Volume Schemes for Reservoir Simulation on Unstructured Grids: Application to productivity Index Calculations*". Paper SPE 38011 presented at the 1997 SPE Reservoir Simulation Simposium held in Dallas, TX, June 8-11, 1997.

67. Helnemann, Z. E.: "*Interactive Generation of Irregular Simulation Grids and Its Practical Applications*". Paper SPE 27998 presented at the University of Tulsa Centennial Petroleum Engineering Symposium held in Tulsa, OK, Aug. 29-31, 1994.

68. Gunasereka, D. and Lindsey, P.: "*The Generation and Application of K-Orthogonal Grid Systems*". Paper SPE 37998 presented at the 14th Symposium in Reservoir Simulation held in Dallas, TX, June 8-11, 1997.

69. Thompson, J. F., Warsi, Z. and Wayne Mastin, C.: "*Numerical Grid generation*", Elsevier Science Publishing Co. Inc., New York City. 1985.

70. Schlumberger.: "*Welltest 200: User Guide*". Version 2000A.

71. Schlumberger.: "*Welltest 200: Technical Description*". Version 2000A.

72. Heinemann, Z. E. and Brand, C. W. "*Gridding Techniques in Reservoir Simulation*". First and Second International Forum on Reservoir Simulation. Alpbach, Austria, Sept. 12-16, 1988 and Sept. 4-8, 1989, p. 339-424.

73. Aziz, K.: "Lectures: *Handling of Wells in reservoir Simulators*". Fourth International Forum on Reservoir Simulation. Salzburg, Austria, Aug. 31-Sept. 4, 1992.

74. Heinemann, Z. E.: "Lectures: *Gridding in Reservoir Simulation*". Fourth International Forum on Reservoir Simulation. Salzburg, Austria, Aug. 31-Sept. 4, 1992.

75. Heinemann, Z. E. and Deimbach, F. X. "Lectures: Advances in *Reservoir Simulation Gridding*". Fourth International Forum on Reservoir Simulation. Salzburg, Austria, Aug. 31-Sept. 4, 1992.

76. Ziman, J. M.: "*Principles of the Theory of Solids*". Cambridge University press, London, 1965.

77. Green, P. J. and Sibson, R.: "*Computing Dirichlet Tessellation in the Plane*". The Computer J. (1977), 21, No. 2, p. 168-173.

78. Voronoi, G.: "*Novel Applications des Parametres Continus a la Theorie des Formes Quadratiques*". J. Reine Agew. Math. (1908) 134, p. 198-287.

79. Palagi, C. L.: "*Flexible Grids: its Generation and Application to Heterogeneous reservoirs*". Paper presented at the seventh Stanford Reservoir Simulation Workshop, Stanford, May 14, 1990.

80. Verma, S.: "*A Flexible Gridding Scheme for Reservoir Simulation*". Proceedings, Production Operations and Engineering/General, SPE ACTE, Oct. 22-25, 1995, Dallas, TX, 657-672.

81. Ho-Le, K.: "*Finite Element Mesh Generation Methods: A Review and Classification*". Compute-aided Design, Jan./Feb. 1988, 20, p. 27-38.

82. Frederick, C. O., Wong, Y. C., and Edge, F. W.: "*Two-Dimensional Automatic Mesh generation for Structural Analysis*". Intern. Jour. Numer. Meth. Eng. (1970) 2, p. 133-144.

83. Van Everdingen, A. F. and Hurst, W.: "*The Application of the Laplace Transform to Flow Problems in Reservoirs*". Trans. AIME (1949) 186, p. 305-324.

84. Raghavan, R.: "*Well Test Analysis*". Prentice Hall Petroleum Engineering Series. Englewoods Cliffs, NY, 558p. 1993.

85. Horne, R. N.: "*Modern Well Test Analysis: A Computer-Aided Approach*". Second Edition. Petroway, Inc. Palo Alto, Ca. 1998.

86. Goode, P. A. and Thambynayagam, R. K. M.: "*Pressure Drawdown and Buildup Analysis of Horizontal Wells in Anisotropic Media*". SPEFE (Dec. 1987) p. 683-697.

87. Collins, R. E.: "*Flow of Fluids Through Porous Material*". Research & Engineering Consultants Inc., Englewood, Colorado, 2nd reprint, 1990.

88. Forchheimer, P.: "*Wasserbewegung Durch Boden*" Z. Ver. Deutsch (1901) 45 p. 1782-1788.

89. Civan, F., and Evans, R. D.: "*Determining the Parameters of the Forchheimer Equation from Pressure-Squared vs. Pseudopressure Formulations.*" SPE Res. Evaluation and Eng., Feb. 1998.

90. Civan, F., and Evans, R. D.: "*Determination of the Non-Darcy Flow Parameters Using a Differential Formulation of the Forchhheimer Equation.*" Paper SPE 35621 presented at the SPE Gas Technology Symposium held in Calgary, Canada, Apr. 28-May 1, 1996.

91. Civan, F., and Evans, R. D.: "*New Insights in the Formulation of Porous Media Mass Momentum Equations.*" Paper SPE 26149 presented at the SPE Gas Technology Symposium held in Calgary, Canada, Jun. 28-30, 1993.

92. Liu, X, Civan, F. and Evans, R. D.: "*Correlation for Non-Darcy Flow Coefficient.*" JCPT (Dec. 1995) 50.

93. Geertsma, J.: "*Estimating the Coefficient of Inertial Resistance in Fluid Flow Through Porous Media.*" SPEJ (Oct. 1974). p. 445-450.

94. Firoozabadi, E., and Katz, D. L.: "*An Analysis of High Velocity Flow through Porous Media.*" JPT)Feb. 1979. p. 211-216.

95. Yale, D. P., Nabor, G. W. Russell, J. E., Pham, H. D. and Yousef, M.: "*Application of Variable Formation Compressibility for Improved Reservoir Analysis.*" paper SPE 26647 presented at the 68th Annual Fall Technical Meeting of SPE, Houston, TX, Oct. 3-6, 1993.

96. May, Edward. Geoquest Schlumberger. Electronic communication. Aug. 2001

97. Ozkan, E., Sarica, U. C., Haciislamoglu, M., and Raghavan, R.: "*A Complete and Comprehensive Mathematical Model is Developed to Study Wellbore Hydraulics in Horizontal Wells.*" SPE Adavanced Technology Series, Vol. 3, No. 1, p. 85-94, 1995.

98. Tuma, J. J. and Walsh, R. A.: "*Engineering Mathematics Handbook.*" McGraw-Hill, 4th Ed., 1998.

99. Tiab, D.: "*Analysis of Pressure and Pressure Derivative without Type-Curve Matching: 1- Skin and Wellbore Storage.*" Paper SPE 25423 presented at the Production Operations Symposium held in Oklahoma City, OK, Mar. 21-23, 1993. P. 203-216. Also, Journal of Petroleum Science and Engineering 12 (1995), p. 171-181.

100. Economides, M. J., Watters, Dunn-Norman, S: "*Petroleum Well Construction*," John Wiley & Sons, New York (1988). 622 pages.

APPENDIX A

ANALYTICAL SOLUTIONS

A.1. LINE SOURCE WELL IN AN INFINITE SYSTEM – PRODUCTION AT CONSTANT RATE

The solution to the diffusivity equation for this case is given by[83]:

$$P_D(r_D,t_D) = -\frac{1}{2}Ei\left(-\frac{r_D^2}{4t_D}\right) \tag{A.1}$$

where:

$$Ei(u) = -0.5772 - \ln|u| + \sum_{n=1}^{\infty}\frac{(-1)^{n-1}}{nn!}u^n \tag{A.2}$$

The pressure derivative is evaluated by:

$$\frac{\partial P_D}{\partial t_D} = P_D' = \frac{1}{2t_D}e^{-\frac{r_D^2}{4t_D}} \tag{A.3}$$

The dimensionless variables are defined as:

$$t_D = \frac{0.0002637kt}{\phi\mu c_t r_w^2} \tag{A.4}$$

$$P_D(r_D,t_D) = \frac{kh}{141.2q\mu B}\left[P_i - P(r_w,t)\right] \tag{A.5}$$

A.2. WELL IN AN INFINITE SYSTEM – PRODUCTION AT CONSTANT RATE – WELLBORE STORAGE AND SKIN FACTOR[84]

$$P_D = \frac{4}{\pi^2}\int_0^{\infty}\frac{1-e^{-v^2t_D}}{v^3\left\{\left[vC_DJ_0(v)-f(v)J_1(v)\right]^2+\left[vC_DY_0(v)-f(v)Y_1(v)\right]^2\right\}}dv \tag{A.6}$$

The pressure derivative is estimated by differentiating Eq. A.1 as:

$$\frac{dP_D}{dt_D} = \frac{4}{\pi^2}\int_0^\infty \frac{1-e^{-v^2 t_D}}{v\left\{\left[vC_D J_0(v) - f(v)J_1(v)\right]^2 + \left[vC_D Y_0(v) - f(v)Y_1(v)\right]^2\right\}} dv \qquad (A.7)$$

being $J_0(v)$ and $J_1(v)$ are the Bessel functions of the first kind of order zero and one, respectively, and $Y_0(v)$ and $Y_1(v)$ are the Bessel functions of the second kind of order zero and one, respectively, and $f(v)=1 - C_D s v^2$.

The dimensionless wellbore storage coefficient is defined by:

$$C_D = \frac{0.89359}{\phi c_t h r_w^2} C \qquad (A.8)$$

A.3. FINITE-CONDUCTIVITY FRACTURED WELL – NEITHER SKIN NOR WELLBORE STORAGE CONSIDERED

An analytical expression for the pressure distribution in the reservoir created by a finite conductivity fracture was presented by Cinco-Ley et al[18]. The dimensionless pressure drop at any point in the reservoir may be obtained from the following equation:

$$P_D(x_D, y_D, t_D) = \frac{1}{4}\int_0^{t_D}\int_{-1}^{1} q_D(x,\tau)\frac{\exp\left(-\frac{(x_D - x)^2 + y_D^2}{4\tau}\right)}{\tau} dx\, d\tau \qquad (A.9)$$

where:

$$P_D(x_D, y_D, t_D) = \frac{kh(P_i - P(x, y, t))}{141.2qB\mu} \qquad (A.10)$$

$$q_D(x,\tau) = \frac{2q(x,\tau).x_f}{q} \qquad (A.11)$$

$q(x,\tau)$ is the flow rate per unit of a fracture length. The dimensionless pressure derivative is as follows:

$$t_D \times P_D' = \frac{1}{4}\int_{-1}^{1} q_D(x,t_D)\exp(-\frac{(x_D - x)^2 + y_D^2}{4t_D})\ dx \qquad (A.12)$$

The finite conductivity solution is obtained by considering two flow regions: (1) the fracture, and (2) the reservoir.

A.3.1. FRACTURE FLOW MODEL

Fluid enters the fracture at a rate $q(x,\tau)$ per unit of a fracture length, and flow across the edges of this porous medium is negligible as depicted in Fig. A.1.

The dimensionless pressure drop in the fracture is proposed by Cinco-Ley et al[18] as follows:

$$P_{FD}(x_D,t_D) = \frac{1}{C_{fDf}}\sqrt{\frac{1}{\pi\eta_{fD}}}\sum_{n=1}^{\infty}\int_{0}^{t_D}\left\{\frac{e^{\frac{(x_D-2n)^2}{4\eta_{fD}\tau}}}{\sqrt{\tau}} - \int_{2n-1}^{2n+1} q_{fD}(x,\tau)\times\frac{e^{\frac{(x_D-x)^2}{4\eta_{fD}\tau}}}{2\sqrt{\tau}}\ dx\right\}d\tau \qquad (A.13)$$

where:

$$P_{fD}(x_D,t_D) = \frac{kh(P_i - P_f(x,t))}{141.2qB\mu} \qquad (A.14)$$

$$q_{fD}(x,\tau) = \frac{2q_f(x,\tau)x_f}{q} \qquad (A.15)$$

$$C_{fDf} = \frac{w\phi_f c_{ft}}{\pi x_f \phi . c_t} \qquad (A.16)$$

$$\eta_{fD} = \frac{k_f \phi . c_t}{k\phi_f c_{ft}} \qquad (A.17)$$

A.3.2. RESERVOIR FLOW MODEL

The transient pressure behavior in the reservoir may be studied by considering the fracture as a plane source of flux density $q_f(x,t)$ (See Fig. A.2). The dimensionless pressure drop at any point in the reservoir can be obtained from equation A.9.

To solve equations A.9, A.11 through A.13 simultaneously, continuity between the two flow regions must be established. Thus:

$$P_{fD}(x_D,t_D) = P_D(x_D, y_D = 0, t_D) \tag{A.18}$$

and $$q_{fD}(x_D,t_D) = q_D(x_D,t_D) \tag{A.19}$$

for $-1 \le x_D \le 1$ and $t_D > 0$.

After combining equations A.9, A.13, A.18 and A.19, using the Poisson's summation formula, and discretizing in space and time so that the fracture is divided into 2N equal segments (Fig. A.3) and time is divided into K different intervals, one could end up with the following system:

$$\begin{cases} q_D(1,k)z(1,1,k) + q_D(2,k)z(2,1,k) + \cdots + q_D(N,k)z(N,1,k) = g(1) - \sum_{i=1}^{N}\sum_{l=1}^{k-1} q_D(i,l)z(i,1,l) \\ q_D(1,k)z(1,2,k) + q_D(2,k)z(2,2,k) + \cdots + q_D(N,k)z(N,2,k) = g(2) - \sum_{i=1}^{N}\sum_{l=1}^{k-1} q_D(i,l)z(i,2,l) \\ \cdots\cdots\cdots\cdots \\ q_D(1,k)z(1,j,k) + q_D(2,k)z(2,j,k) + \cdots + q_D(N,k)z(N,j,k) = g(j) - \sum_{i=1}^{N}\sum_{l=1}^{k-1} q_D(i,l)z(i,j,l) \\ \cdots\cdots\cdots\cdots \\ q_D(1,k)z(1,N,k) + q_D(2,k)z(2,N,k) + \cdots + q_D(N,k)z(N,N,k) = g(N) - \sum_{i=1}^{N}\sum_{l=1}^{k-1} q_D(i,l)z(i,N,l) \end{cases}$$

(A.20)

The system is solved at each step time level where the $q_D(i,l=1)$ equal zero at the first step time level. The $g(j)$ and $z(i,j,l)$ parameters are defined as follows:

$$g(j)=\frac{1}{C_{fDf}}\left\{t_D(k)+\frac{2}{\pi^2\eta_{fD}}\sum_{n=1}^{\infty}\frac{1}{n^2}\left[1-\exp(-(\pi n)^2\eta_{fD}t_D(k)\right]\cos(n\pi x_{D_j})\right\} \quad \text{(A.21)}$$

being:

$$x_{D_j}=\frac{j-0.5}{N} \quad \text{(A.22)}$$

$$z(i,j,l)=\frac{\sqrt{\pi}}{4}m(i,j,l)+\frac{\Delta x}{C_{fDf}}\Delta t_{l,l-1}+\frac{4}{\pi^3\eta_{fD}C_{fDf}}v(i,j,l) \quad \text{(A.23)}$$

where:

$$\Delta t_{l,l-1}=t_D(l)-t_D(l-1) \quad \text{(A.24)}$$

$$v(i,j,l)=\sum_{n=1}^{\infty}\frac{1}{n^3}\left[\exp(-(\pi n)^2\eta_{fD}\Delta t_{k,l})-\exp(-(\pi n)^2\eta_{fD}\Delta t_{k,l-1})\right] \times\cos(n\pi x_{D_j})\cos(n\pi x_{D_i})\sin\left(\frac{n\pi}{2N}\right) \quad \text{(A.25)}$$

$$m(i,j,l)=X_{i,j}^{k,l-1}-X_{i,j}^{k,l}+Y_{i,j}^{k,l-1}-Y_{i,j}^{k,l} \quad \text{(A.26)}$$

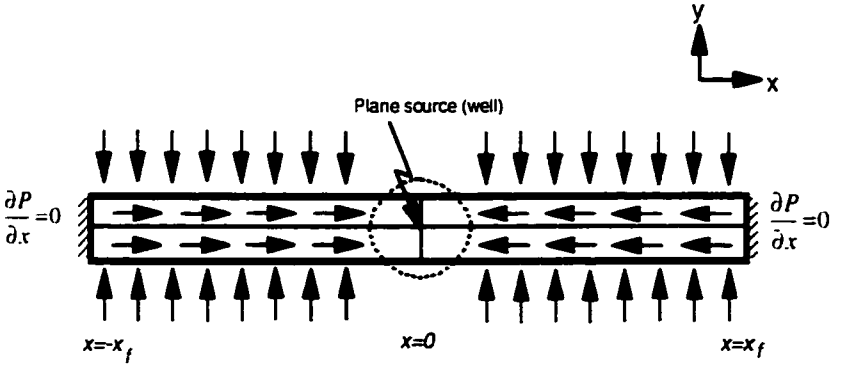

Fig. A.1. Fracture flow model[18]

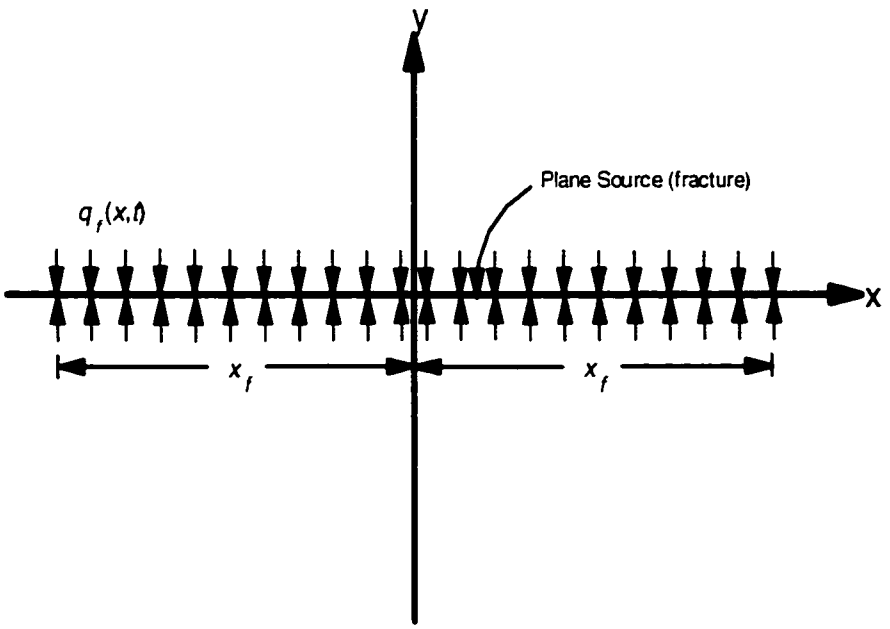

Fig. A.2. Reservoir flow model[18]

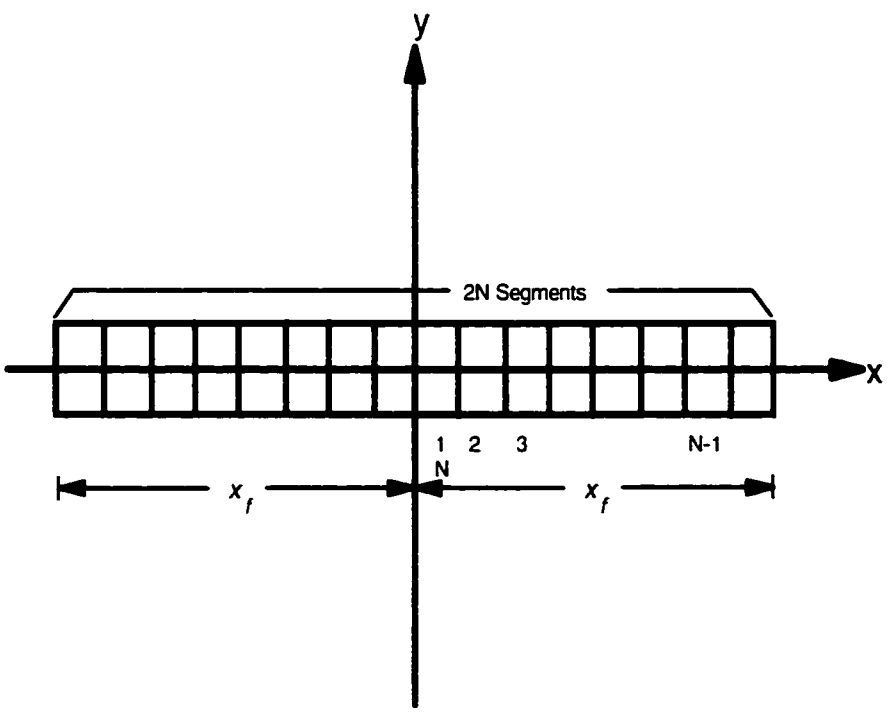

Fig. A.3. Fracture divided into 2N equal segments[18]

being:

$$X_{i,j}^{k,l} = 2\sqrt{\Delta t_{k,l}}\left\{ erf\left[\frac{\alpha_{i,j}}{\sqrt{\Delta t_{k,l}}}\right] - erf\left[\frac{\beta_{i,j}}{\sqrt{\Delta t_{k,l}}}\right] + erf\left[\frac{\gamma_{i,j}}{\sqrt{\Delta t_{k,l}}}\right] - erf\left[\frac{\delta_{i,j}}{\sqrt{\Delta t_{k,l}}}\right]\right\} \tag{A.27}$$

$$Y_{i,j}^{k,l} = -\frac{2}{\sqrt{\pi}}\left\{ \alpha_{i,j} Ei\left[-\frac{\alpha_{i,j}^2}{\Delta t_{k,l}}\right] - \beta_{i,j} Ei\left[-\frac{\beta_{i,j}^2}{\Delta t_{k,l}}\right] + \gamma_{i,j} Ei\left[-\frac{\gamma_{i,j}^2}{\Delta t_{k,l}}\right] - \delta_{i,j} Ei\left[-\frac{\delta_{i,j}^2}{\Delta t_{k,l}}\right]\right\} \tag{A.28}$$

The arguments of the error function, *erf*, and Exponential Integral, *Ei*, functions are defined as:

$$\alpha_{i,j} = \frac{j-i+0.5}{2N} \tag{A.29}$$

$$\beta_{i,j} = \frac{j-i-0.5}{2N} \tag{A.30}$$

$$\gamma_{i,j} = \frac{j+i-0.5}{2N} \tag{A.31}$$

$$\delta_{i,j} = \frac{j+i-1.5}{2N} \tag{A.32}$$

The pressure derivative was computed numerically by the following relationship[85]:

$$t\left(\frac{\partial P}{\partial t}\right)_i = t\left(\frac{\partial P}{\partial \ln t}\right)_i = \left\{ \frac{\ln(t_i/t_{i-k})\Delta P_{i+j}}{\ln(t_{i+j}/t_i)\ln(t_{i+j}/t_{i-k})} + \frac{\ln(t_{i+j}t_{i-k}/t_i^2)\Delta P_i}{\ln(t_{i+1}/t_i)\ln(t_i/t_{i-1})} - \frac{\ln(t_{i+j}/t_i)\Delta P_{i-1}}{\ln(t_i/t_{i-k})\ln(t_{i+j}/t_{i-k})} \right\} \tag{A.33}$$

where:

$$\ln t_{i+j} - \ln t_i \geq 0.2 \tag{A.34}$$

$$\ln t_i - \ln t_{i-k} \geq 0.2 \tag{A.35}$$

A.3. HORIZONTAL WELLS

The reservoir fluid is single phase and slightly compressible, flowing through an anisotropic, homogeneous reservoir. The solution of Goode And Thambynayagam[86] is also adopted in this section because of its convenient and simple form. The dimensionless solution for an infinite or semi-infinite reservoir penetrated by a horizontal well in an anisotropic, homogeneous porous media is given by:

$$P_D = \frac{2 L_w r_{wa}}{h_x h_z}\left[\sqrt{\pi t_D} + \frac{h_x^2}{\pi^2 v_x}\sum_{n=1}^{\infty} erf(v_x \pi n\sqrt{t_D})\frac{\xi_n^2}{n} + \frac{h_x h_z}{L_w v_z \pi}\sum_{m=1}^{\infty} erf(v_z \pi m\sqrt{t_D})\frac{\xi_m}{m}\cos(m\pi z_e)\right] + \sqrt{\frac{k_x}{k_z}}\, s_m \tag{A.36}$$

The derivative with respect to time of Eq. A.36 is:

$$\frac{\partial P_D}{\partial t_D} = \frac{2 L_w r_{wa}}{h_x h_z}\sqrt{\frac{\pi}{t_D}}\left[\frac{1}{2} + \frac{h_x^2}{\pi^2}\sum_{n=1}^{\infty}\exp[-(v_x \pi n)^2 t_D]\xi_n^2 + \frac{h_x h_z}{L_w \pi}\sum_{m=1}^{\infty}\exp[-(v_z \pi m)^2 t_D]\xi_m\cos(m\pi z_e)\right] \tag{A.37}$$

where, the dimensionless variables are:

$$P_D = \frac{k_y L_w \Delta P}{141.2 q \mu B} \tag{A.38}$$

$$t_D = \frac{0.0002637 k_y t}{\phi \mu c_t (L_{zb} - L_{za})^2} \tag{A.39}$$

$$v_x = \frac{L_{zb} - L_{za}}{h_x}\sqrt{\frac{k_x}{k_y}} \tag{A.40}$$

$$v_z = \frac{L_{zb} - L_{za}}{h_z}\sqrt{\frac{k_z}{k_y}} \tag{A.41}$$

$$\xi_n = \frac{\sin\frac{m\pi L_{x1}}{h_z} - \sin\frac{m\pi L_{xd}}{h_z}}{m(L_{x1} - L_{xd})} \tag{A.42}$$

$$\xi_m = \frac{\sin\frac{m\pi L_{za}}{h_z} - \sin\frac{m\pi L_{zb}}{h_z}}{m(L_{zb} - L_{za})} \tag{A.43}$$

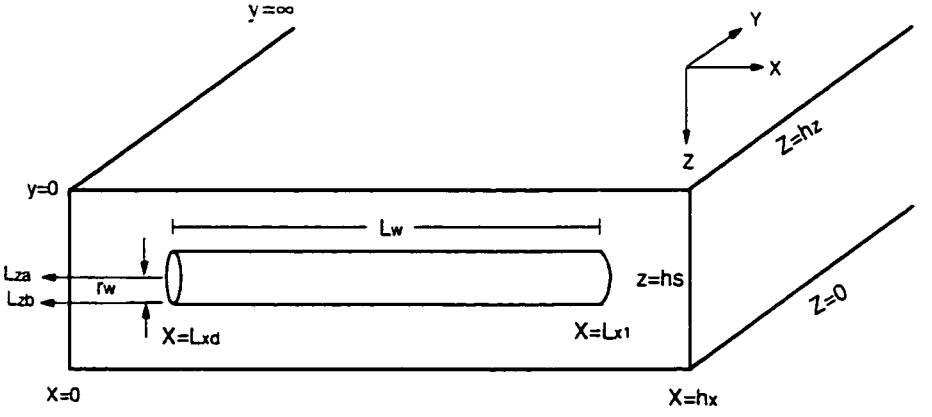

Fig. A.4. Horizontal well configuration[86]

The apparent wellbore radius converts the strip source to a well of radius r_w. Accounting for anisotropy the relationship can be expressed as:

$$4\,r_{wa} = 4\,r_w\left(\frac{k_z}{k_y}\right)^{1/4} = (L_{zb} - L_{za}) \tag{A.44}$$

The dimensionless wellbore length is defined as:

$$L_D = \frac{h_z}{2\,L_w}\sqrt{\frac{k_z}{k_h}} \tag{A.45}$$

The point at which the effective pressure is measured in the horizontal well is expressed by:

$$z_e = \frac{1}{h_z}(h_s + 1.47\,r_{wa}) \tag{A.46}$$

Conversion from the adopted dimensionless variables of Goode and Thambynayagam[86] to the other widely used definitions is given for comparative purposes.

Dimensionless time:

$$\frac{t_{D_j}}{t_{D_{G+T}}} = \left(\frac{r_{wa}}{L_w}\right)^2 \sqrt{\frac{k_x}{k_y}} \qquad \text{(A.47)}$$

where the subscript j refers to Joshi type dimensionless variables and $g+t$ to the Goode and Thambynayagam[86] dimensionless variables.

Dimensionless pressure:

$$\frac{p_{D_j}}{p_{D_{g+t}}} = \frac{h_z}{L_w}\sqrt{\frac{k_x}{k_y}} \qquad \text{(A.48)}$$

APPENDIX B

FIGURES

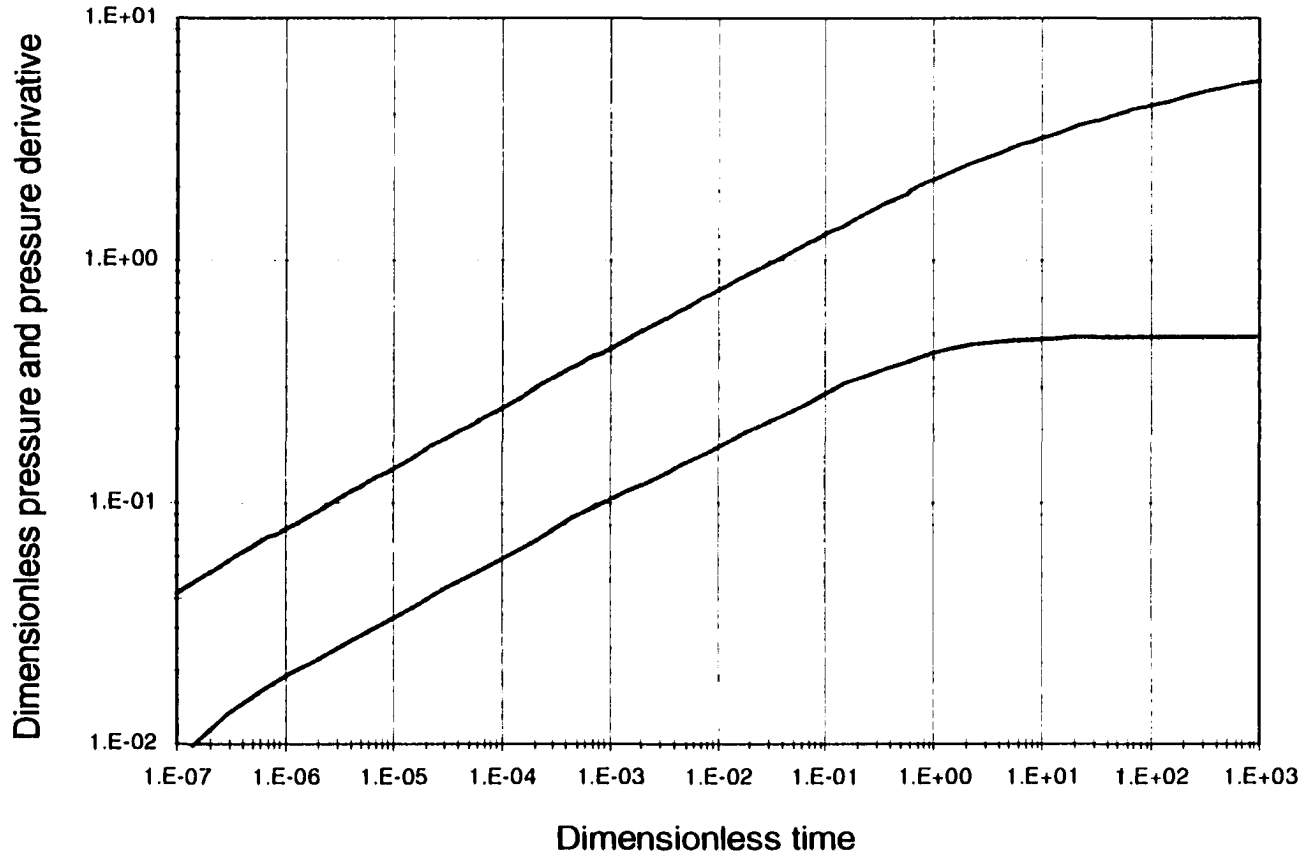

Fig. B.1.a. Pressure and pressure derivative curves for a fractured well with a branch fracture Starting from the well and a branch fracture starting from the middle distance between wellbore a Main fracture tip. $C_{fD}=1$, $X_{fbD}=0$ *and* $X_{fbD}=0.6$

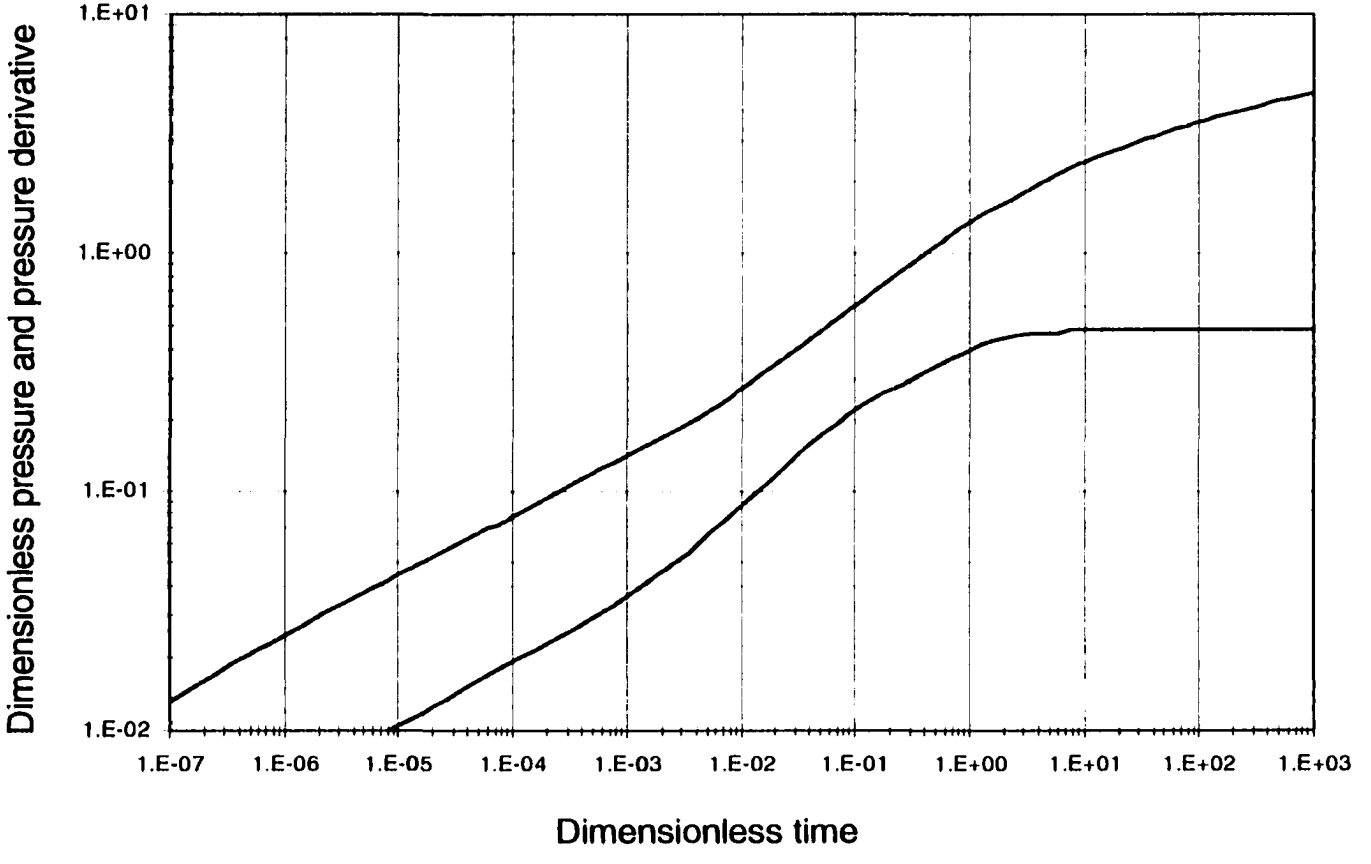

Fig. B.1.b. Pressure and pressure derivative curves for a fractured well with a branch fracture Starting from the well and a branch fracture starting from the middle distance between wellbore a Main fracture tip. C_{fD}=10, X_{fbD}=0 and X_{fbD}=0.6

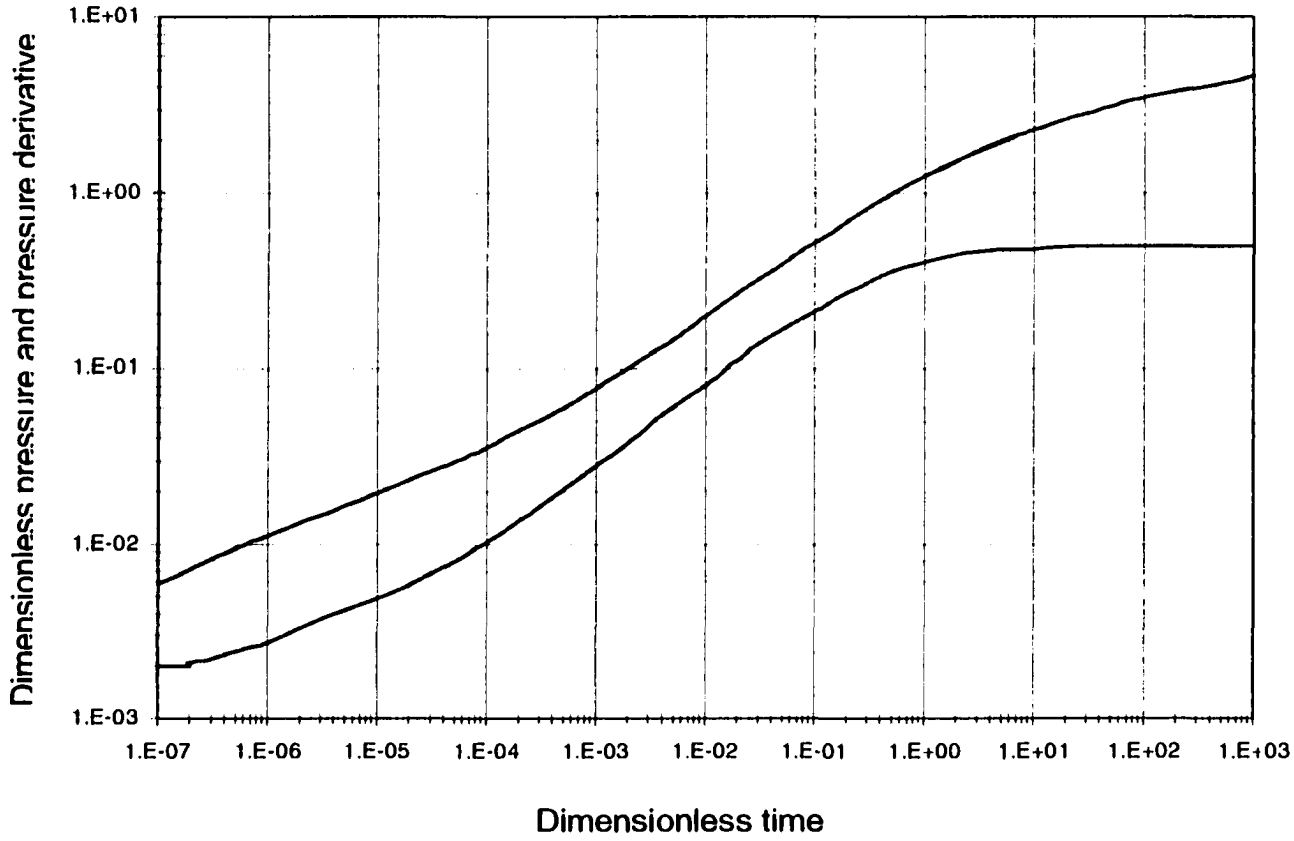

Fig. B.1.c. Pressure and pressure derivative curves for a fractured well with a branch fracture Starting from the well and a branch fracture starting from the middle distance between wellbore a Main fracture tip. C_{fD}=50, X_{fbD}=0 and X_{fbD}=0.6

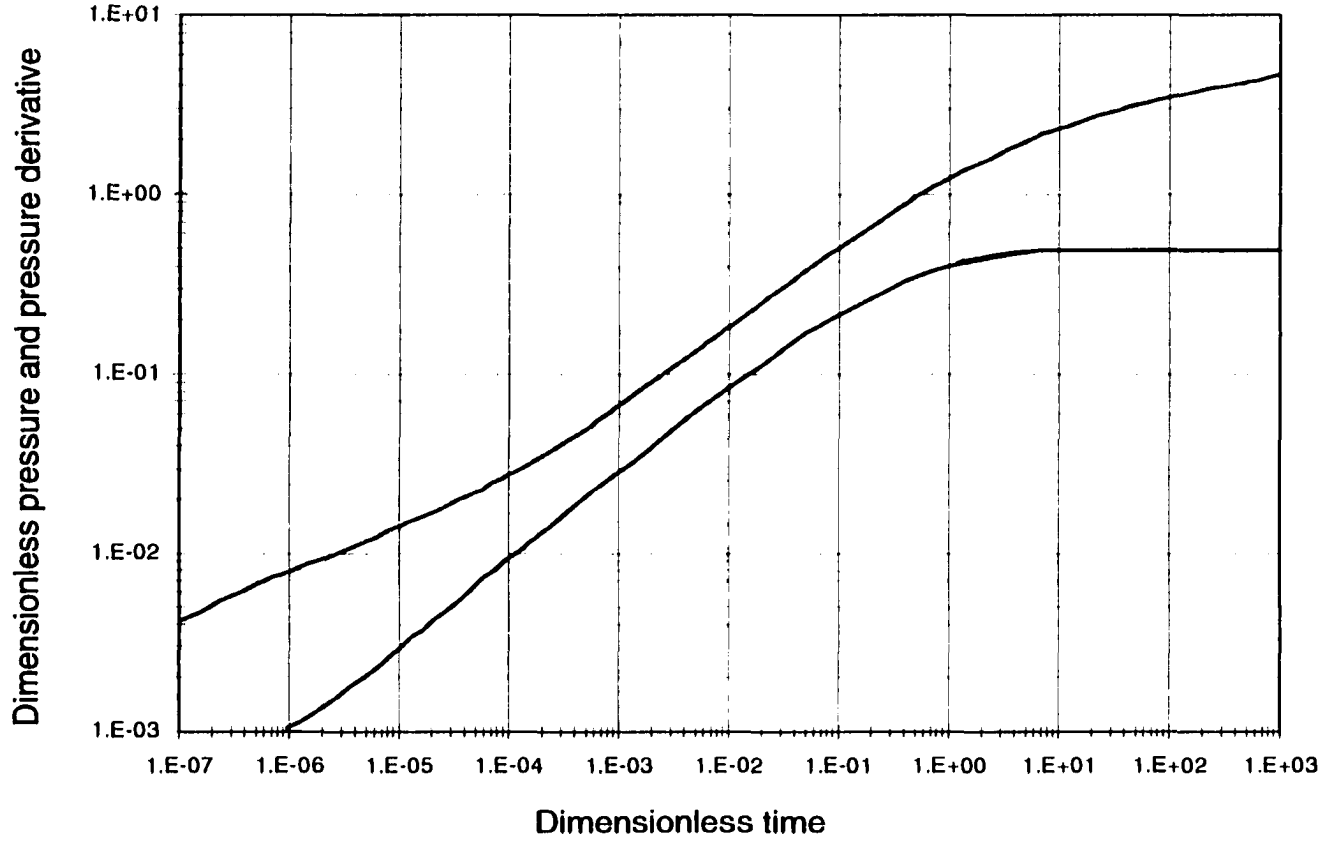

Fig. B.1.d. Pressure and pressure derivative curves for a fractured well with a branch fracture Starting from the well and a branch fracture starting from the middle distance between wellbore a Main fracture tip. $C_{fD}=100$, $X_{fbD}=0$ *and* $X_{fbD}=0.6$

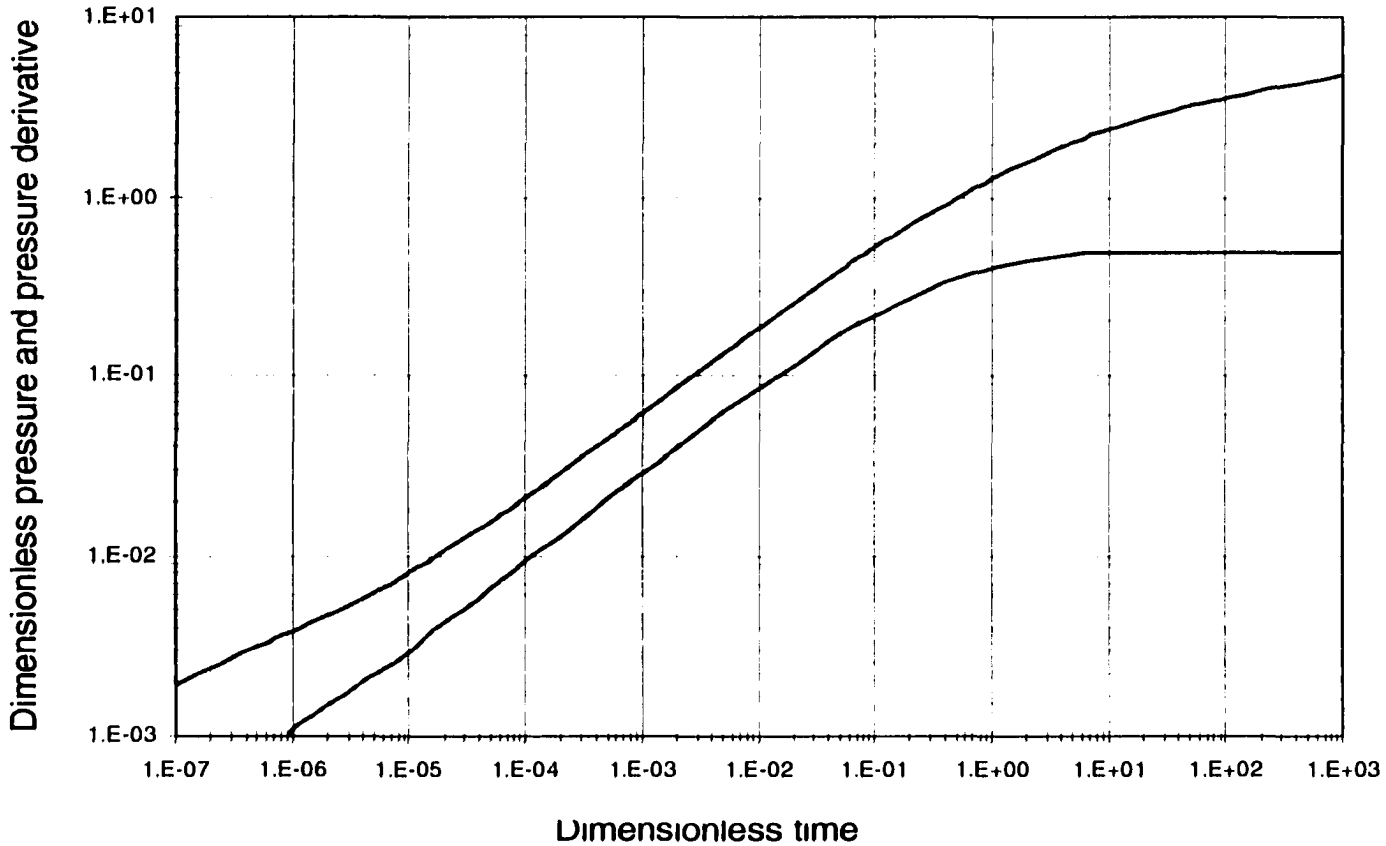

Fig. B.1.e. Pressure and pressure derivative curves for a fractured well with a branch fracture Starting from the well and a branch fracture starting from the middle distance between wellbore a Main fracture tip. CfD=300, XfbD=0 and XfbD=0.6

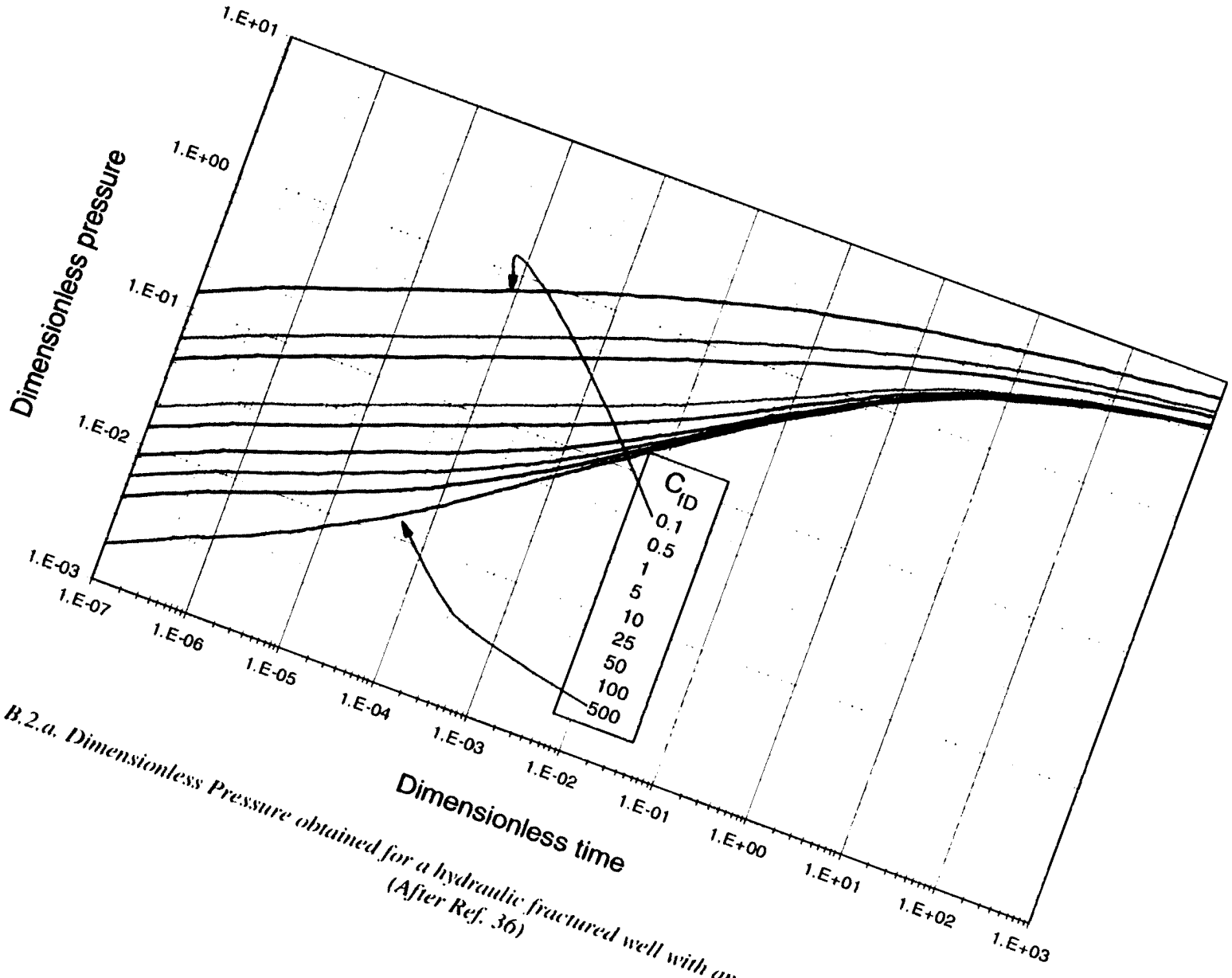

Fig. B.2.a. Dimensionless Pressure obtained for a hydraulic fractured well with an asymmetric factor of 0.2 (After Ref. 36)

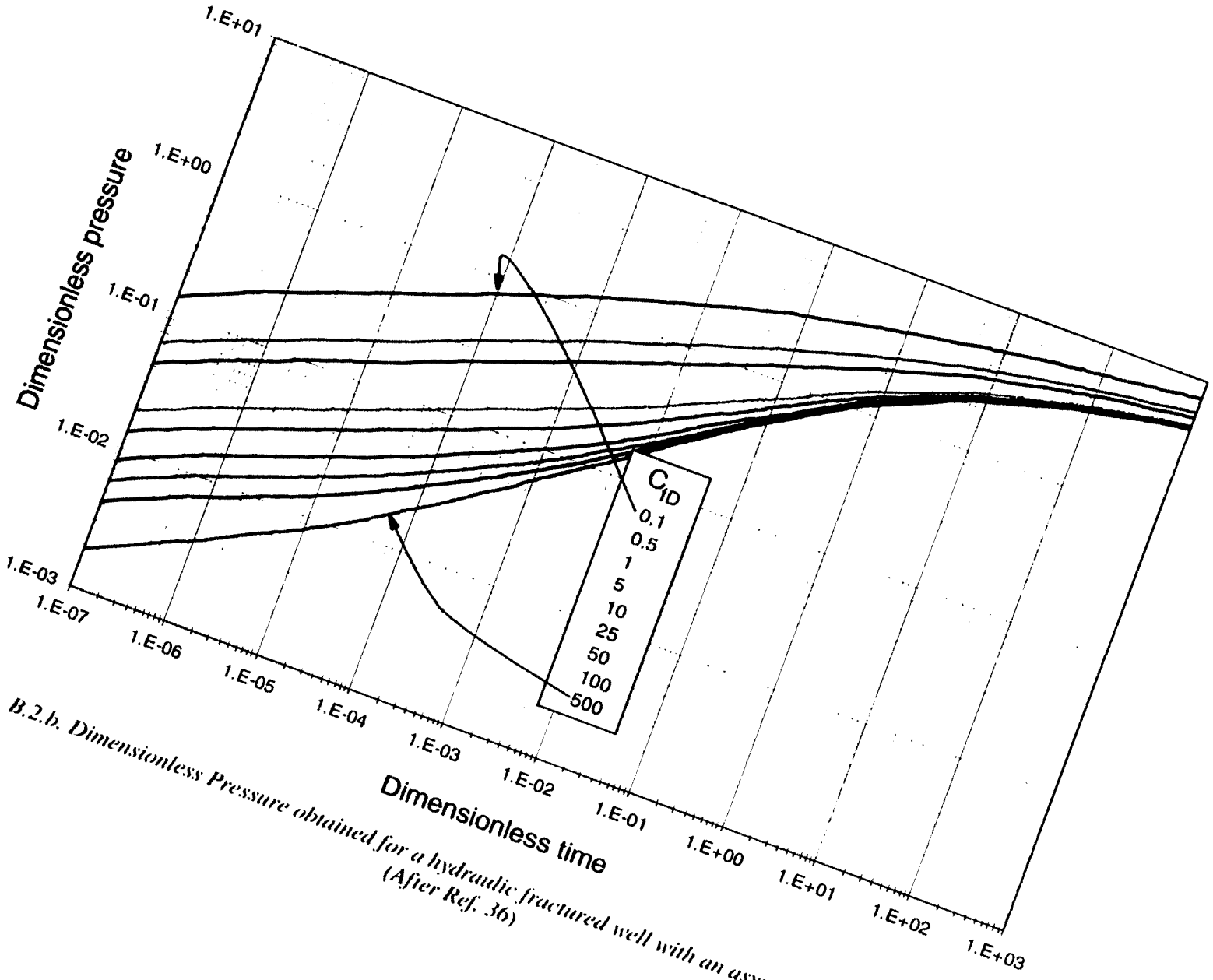

Fig. B.2.b. Dimensionless Pressure obtained for a hydraulic fractured well with an asymmetric factor of 0.4 (After Ref. 36)

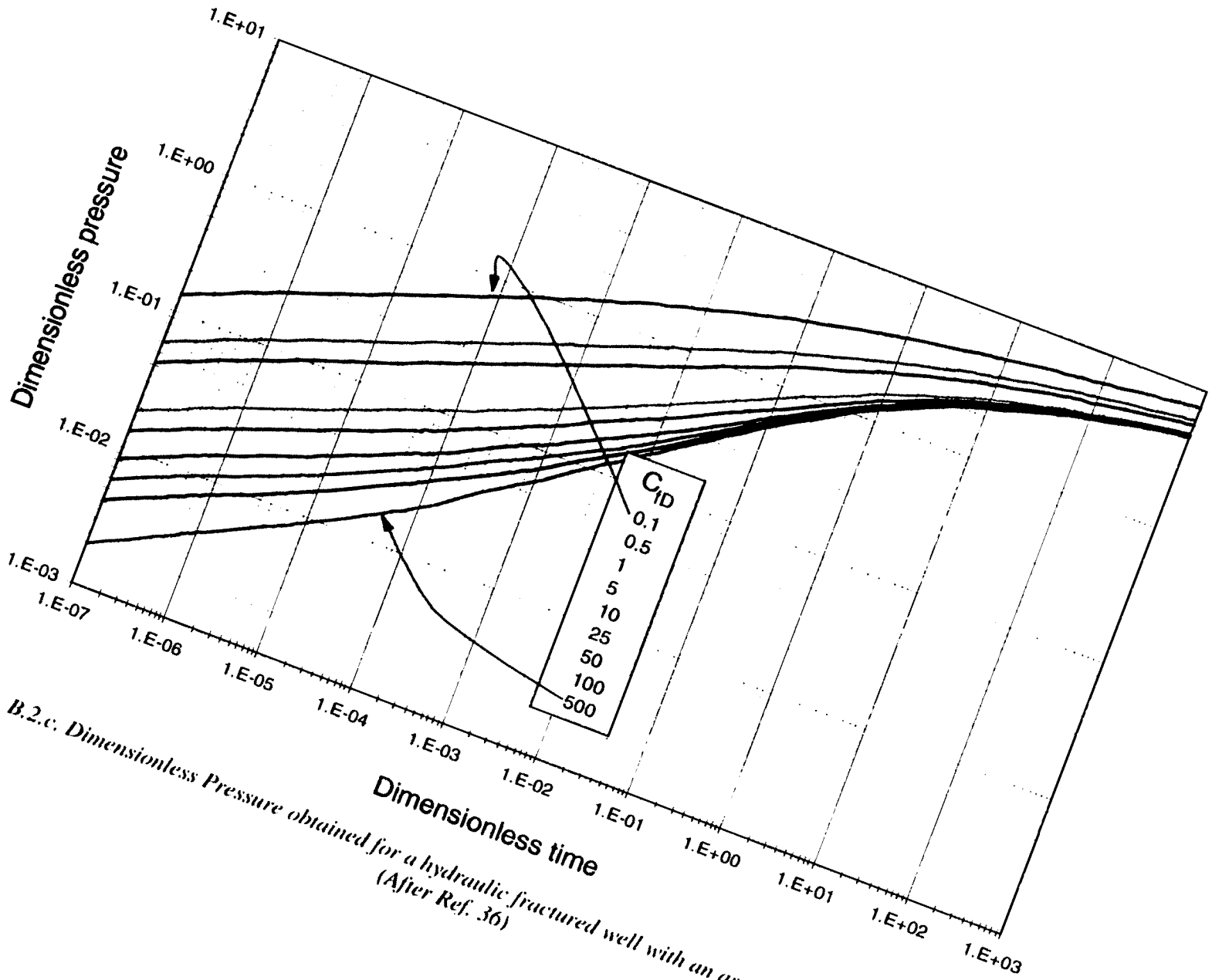

Fig. B.2.c: Dimensionless Pressure obtained for a hydraulic fractured well with an asymmetric factor of 0.6 (After Ref. 36)

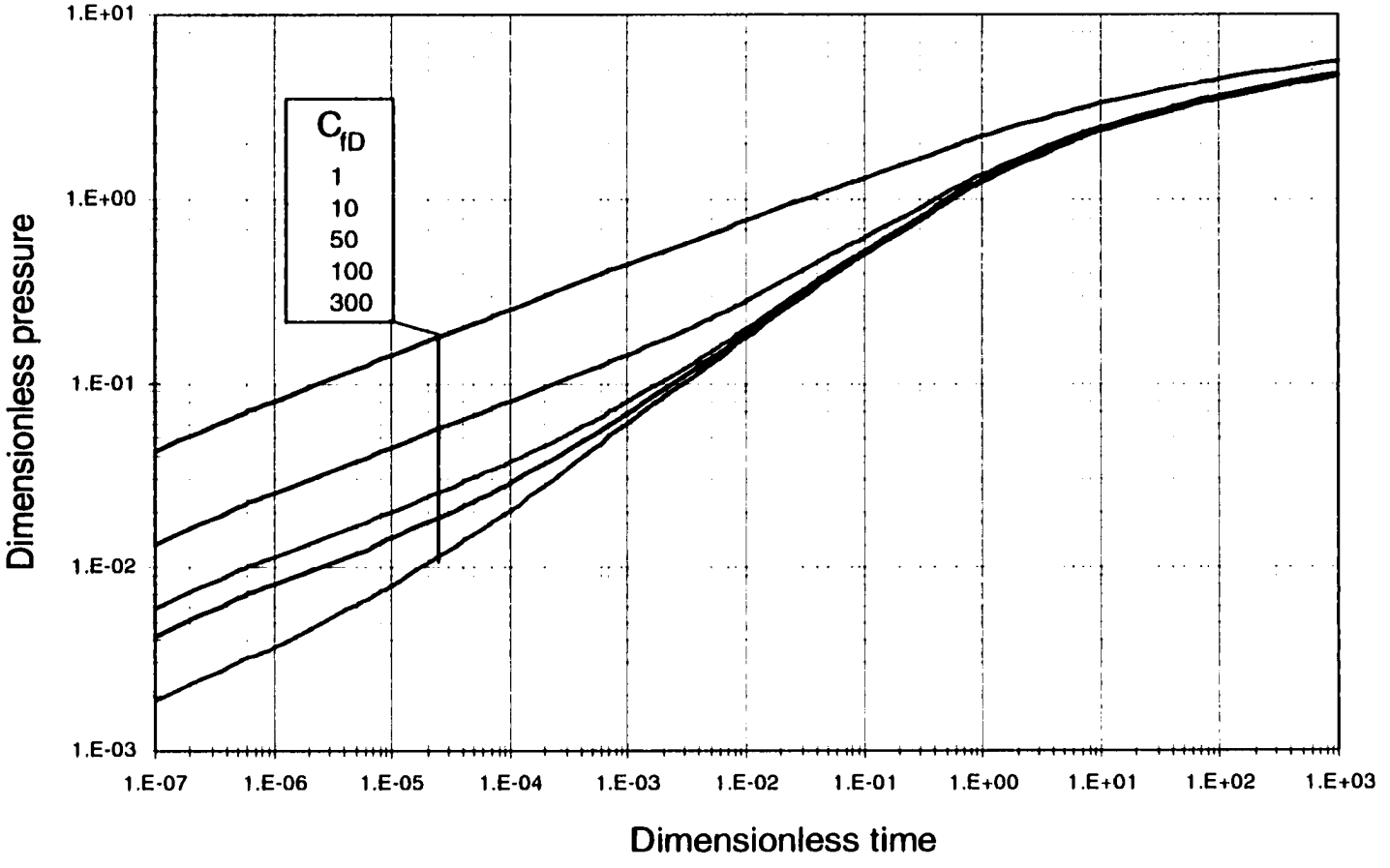

Fig. B.3.a. Dimensionless Pressure obtained for a hydraulic fractured well with dimensionless Branch fracture of 0.2 (this study)

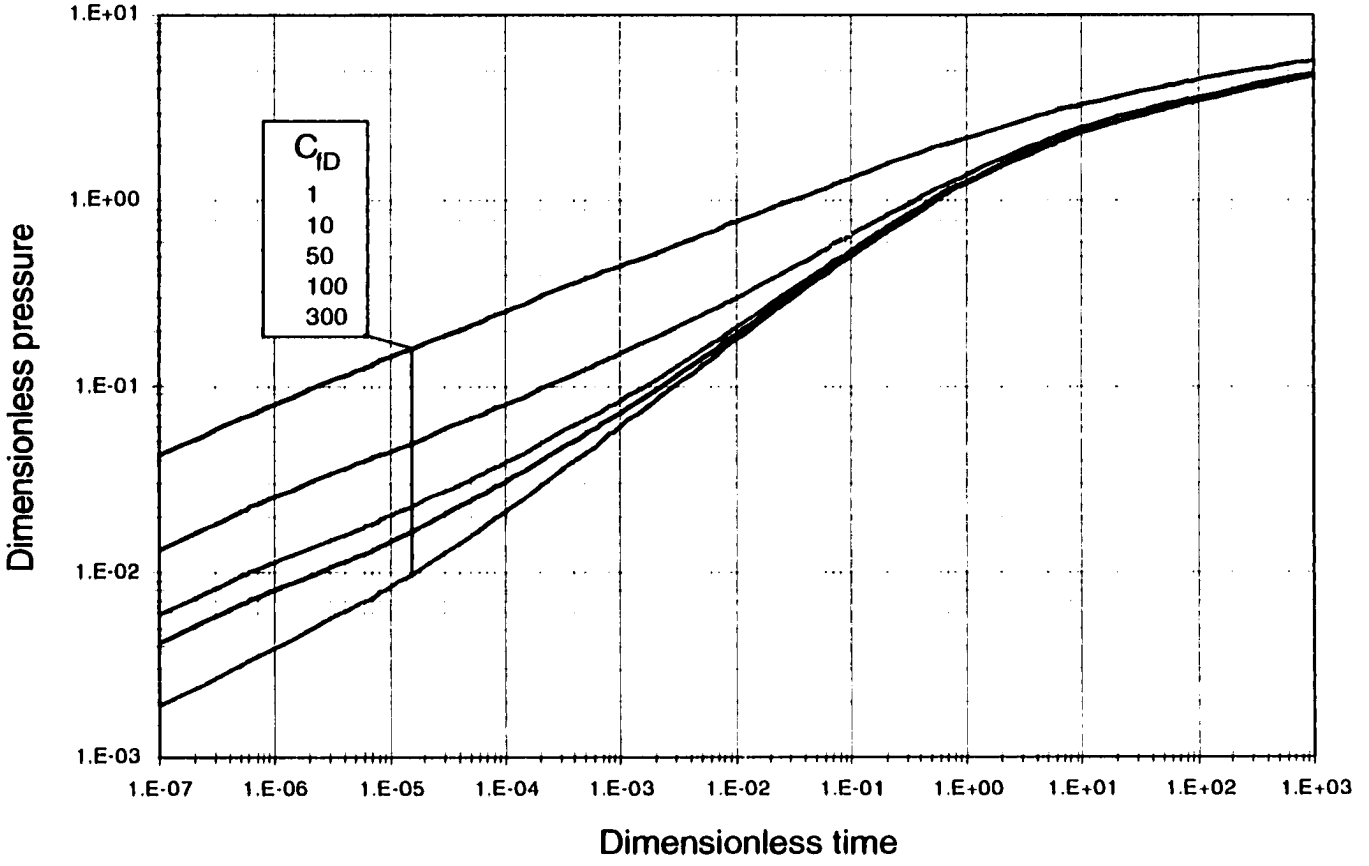

Fig. B.3.b. Dimensionless Pressure obtained for a hydraulic fractured well with dimensionless Branch fracture of 0.4 (this study)

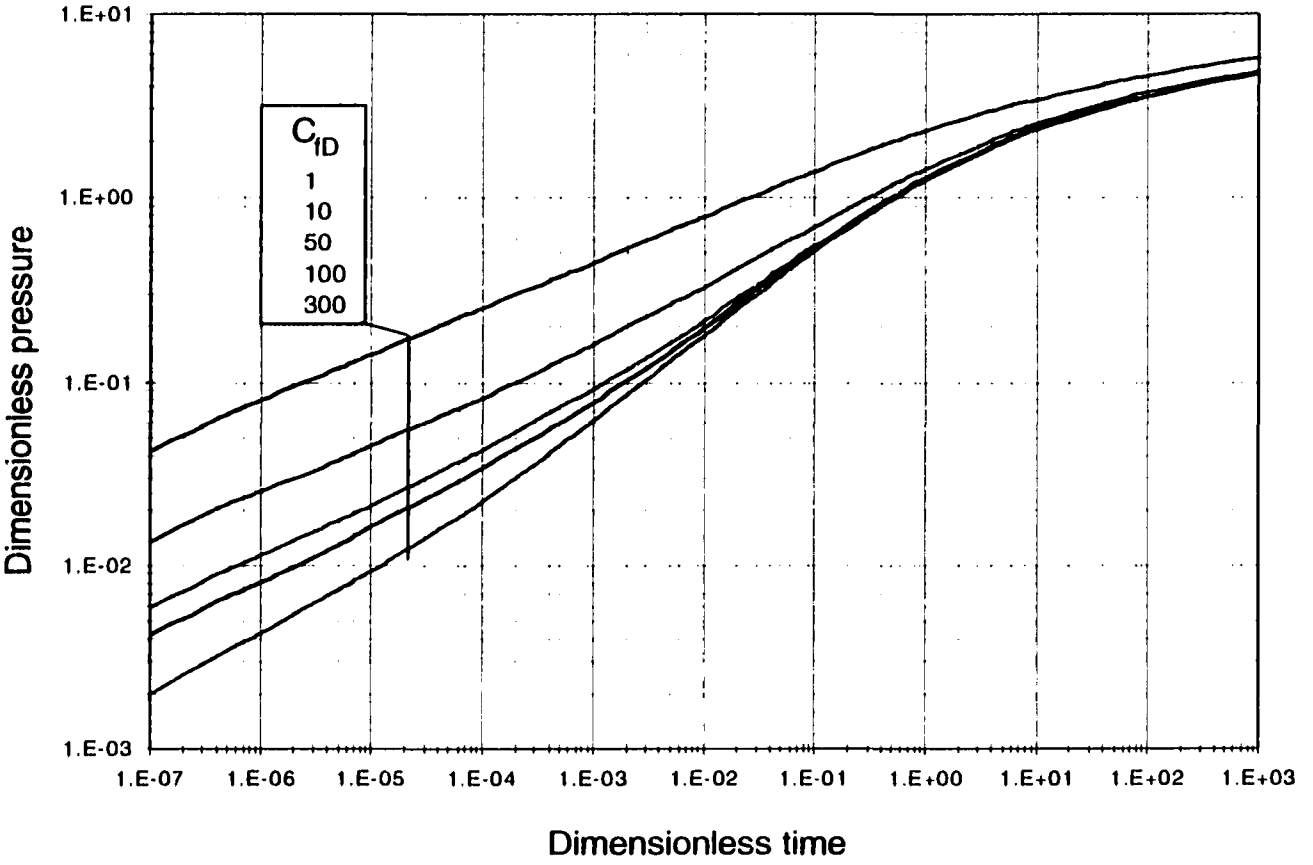

Fig. B.3.c. Dimensionless Pressure obtained for a hydraulic fractured well with dimensionless Branch fracture of 0.6 (this study)

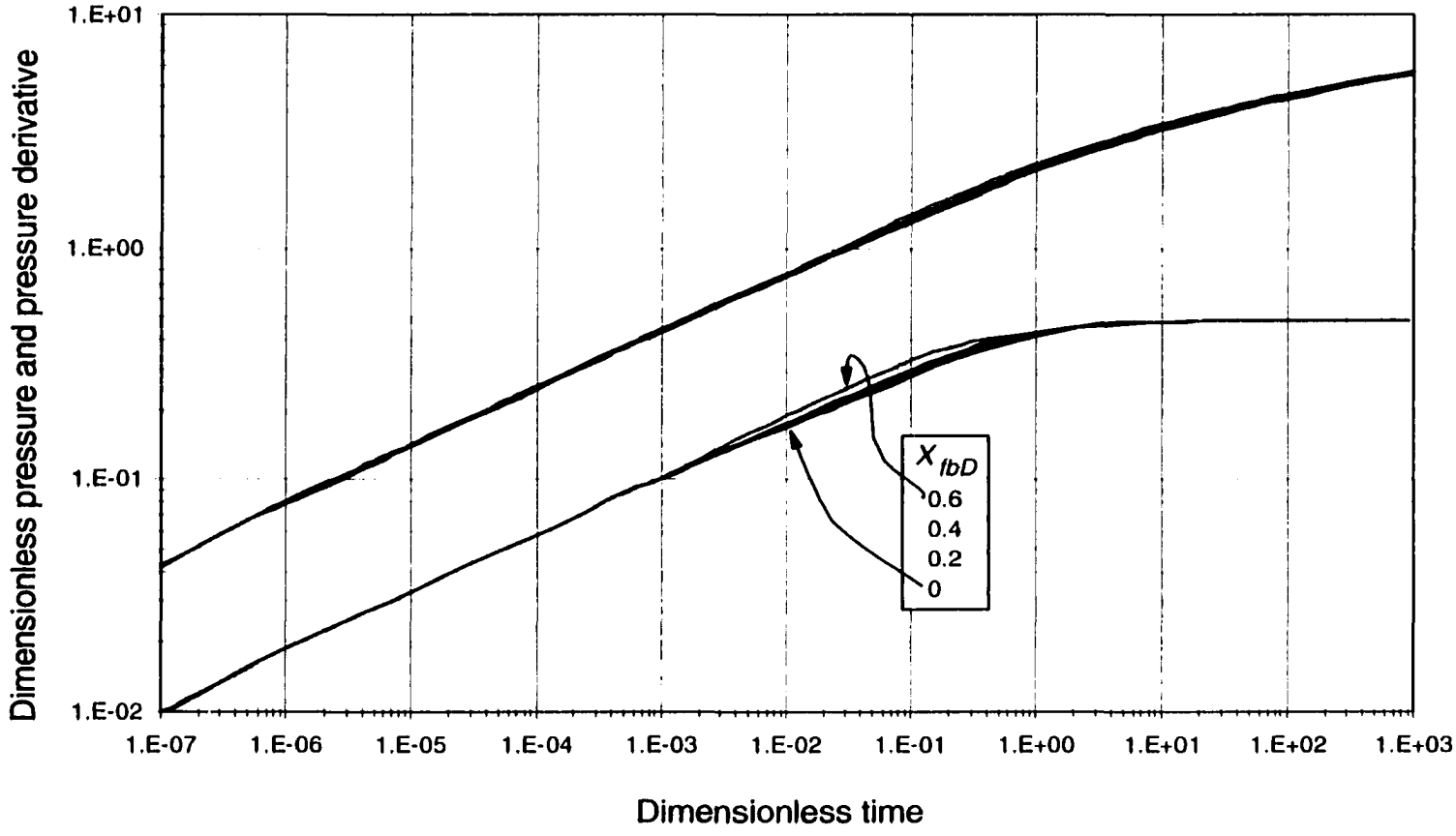

Fig. B.4.a. Dimensionless Pressure and pressure derivative curves for hydraulically fractured well with a branch fracture. Dimensionless fracture conductivity of 1 and angle of zero degrees

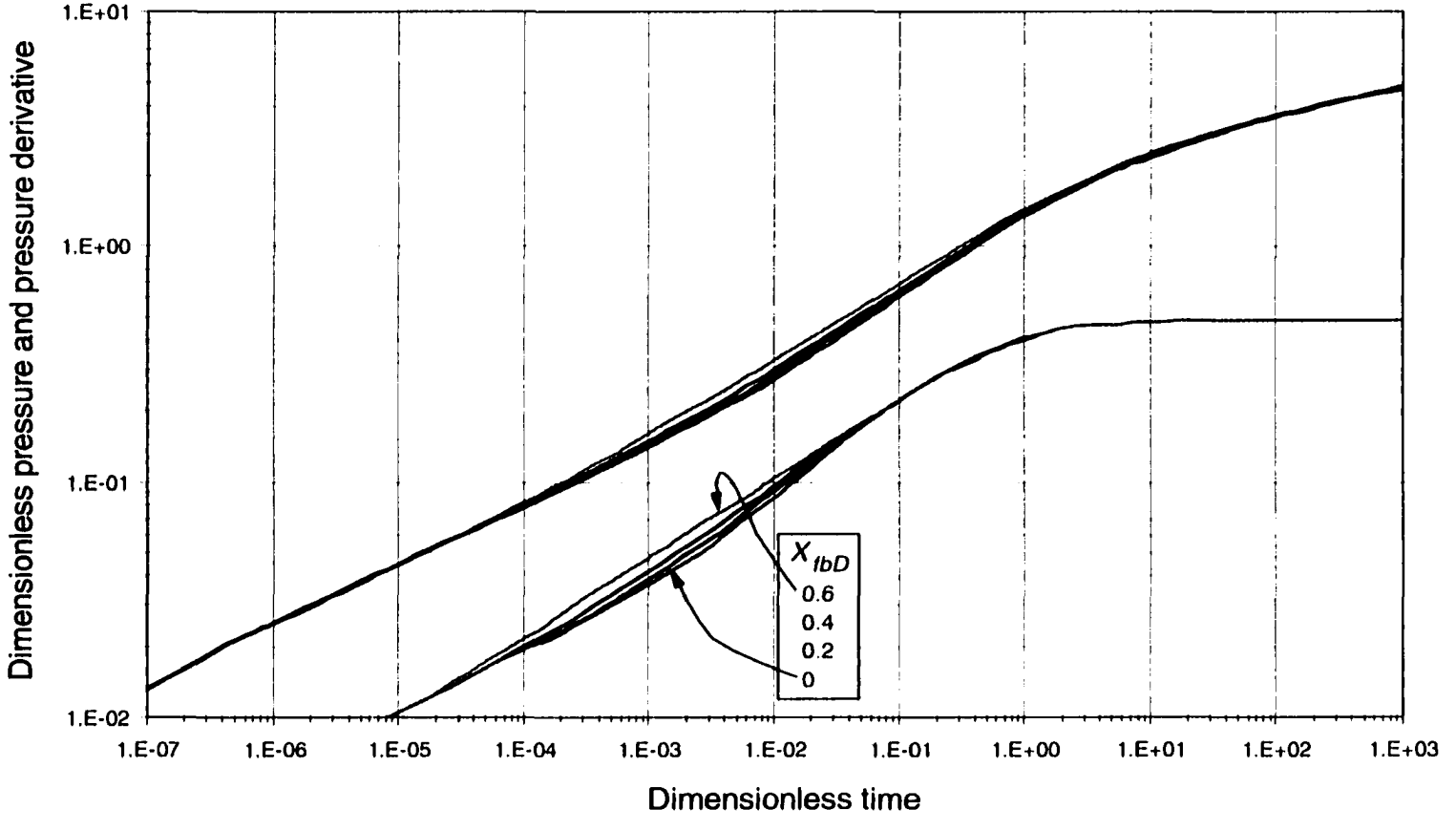

Fig. B.4.b. Dimensionless Pressure and pressure derivative curves for hydraulically fractured well with a branch fracture. Dimensionless fracture conductivity of 10 and angle of zero degrees

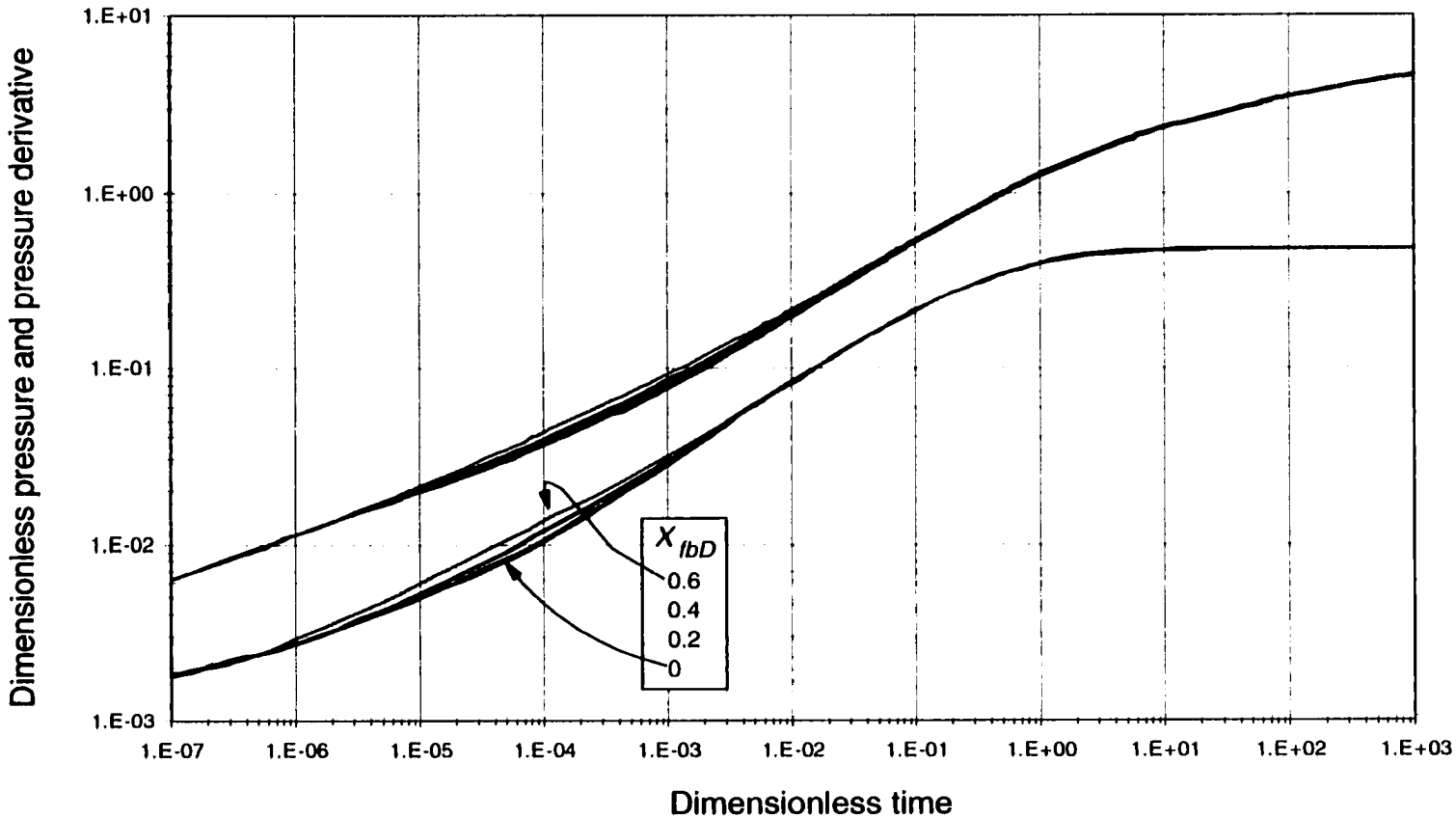

Fig. B.4.c. Dimensionless Pressure and pressure derivative curves for hydraulically fractured well with a branch fracture. Dimensionless fracture conductivity of 50 and angle of zero degrees

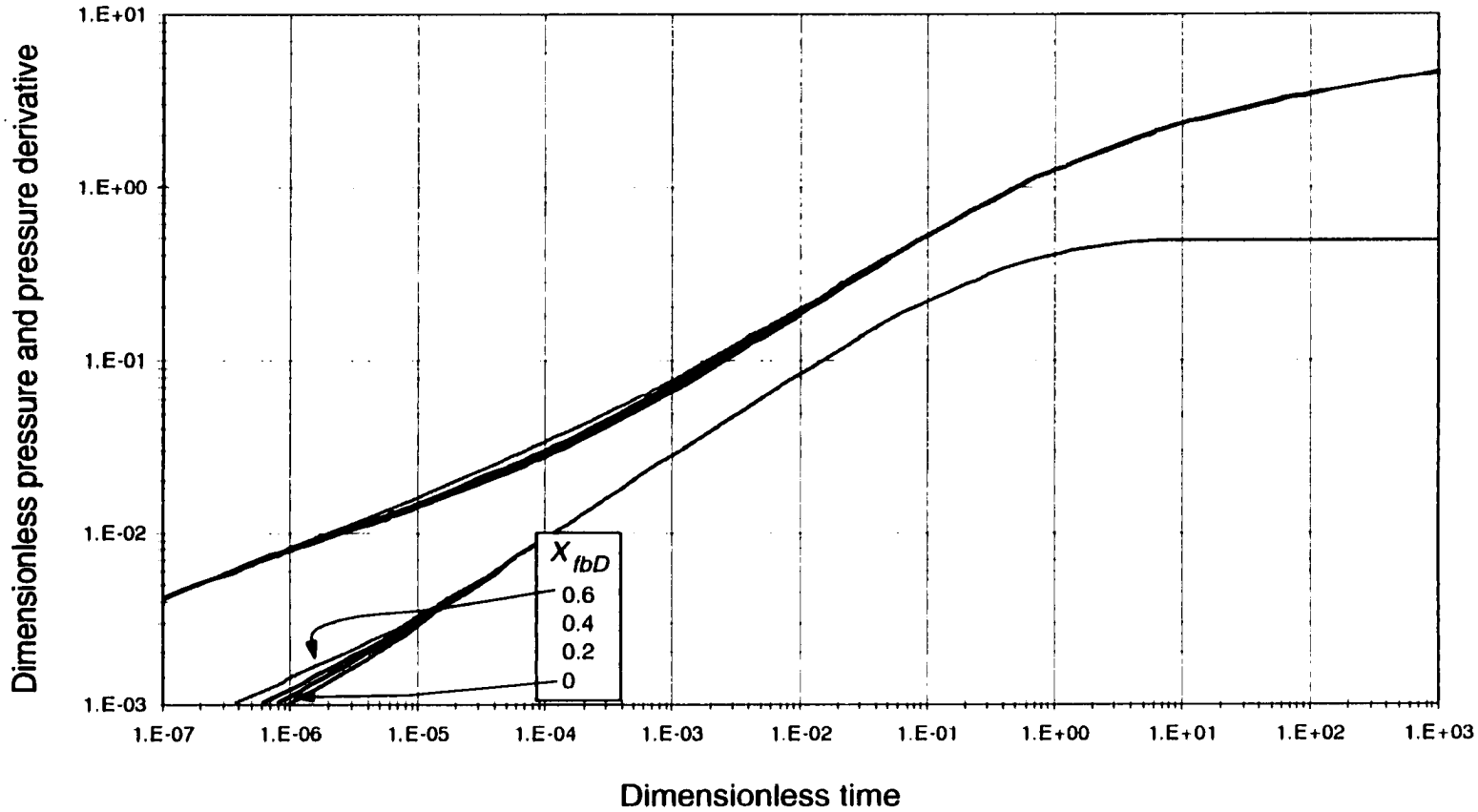

Fig. B.4.d. Dimensionless Pressure and pressure derivative curves for hydraulically fractured well with a branch fracture. Dimensionless fracture conductivity of 100 and angle of zero degrees

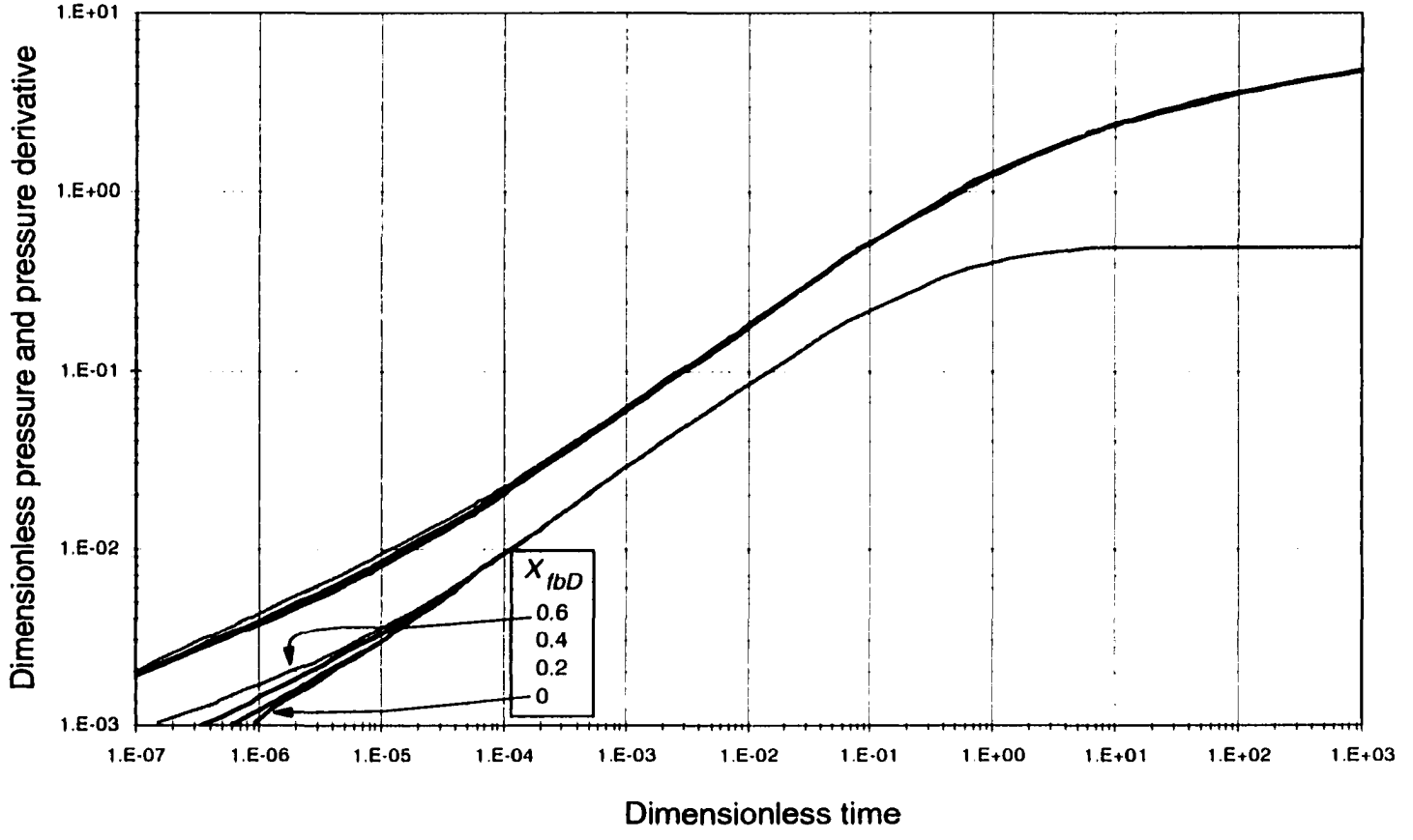

Fig. B.4.e. Dimensionless Pressure and pressure derivative curves for hydraulically fractured well with a branch fracture. Dimensionless fracture conductivity of 300 and angle of zero degrees

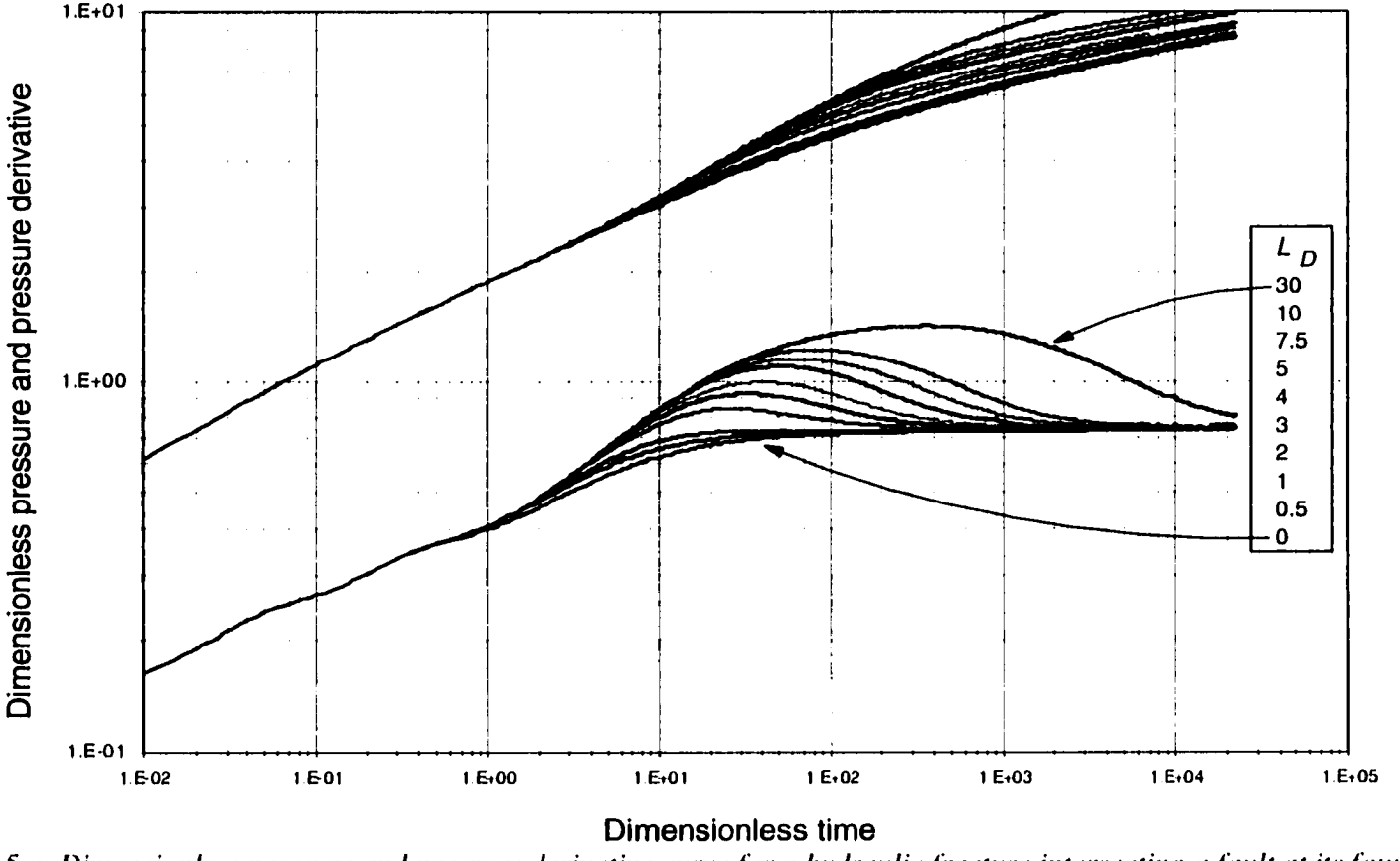

Fig. B.5.a. Dimensionless pressure and pressure derivative curve for a hydraulic fracture intersecting a fault at its fourth part forming an angle of 90°. C_{fD}=1

Fig. B.5.b. Dimensionless pressure and pressure derivative curve for a hydraulic fracture intersecting a fault at its fourth part forming an angle of 90°. C_D=10

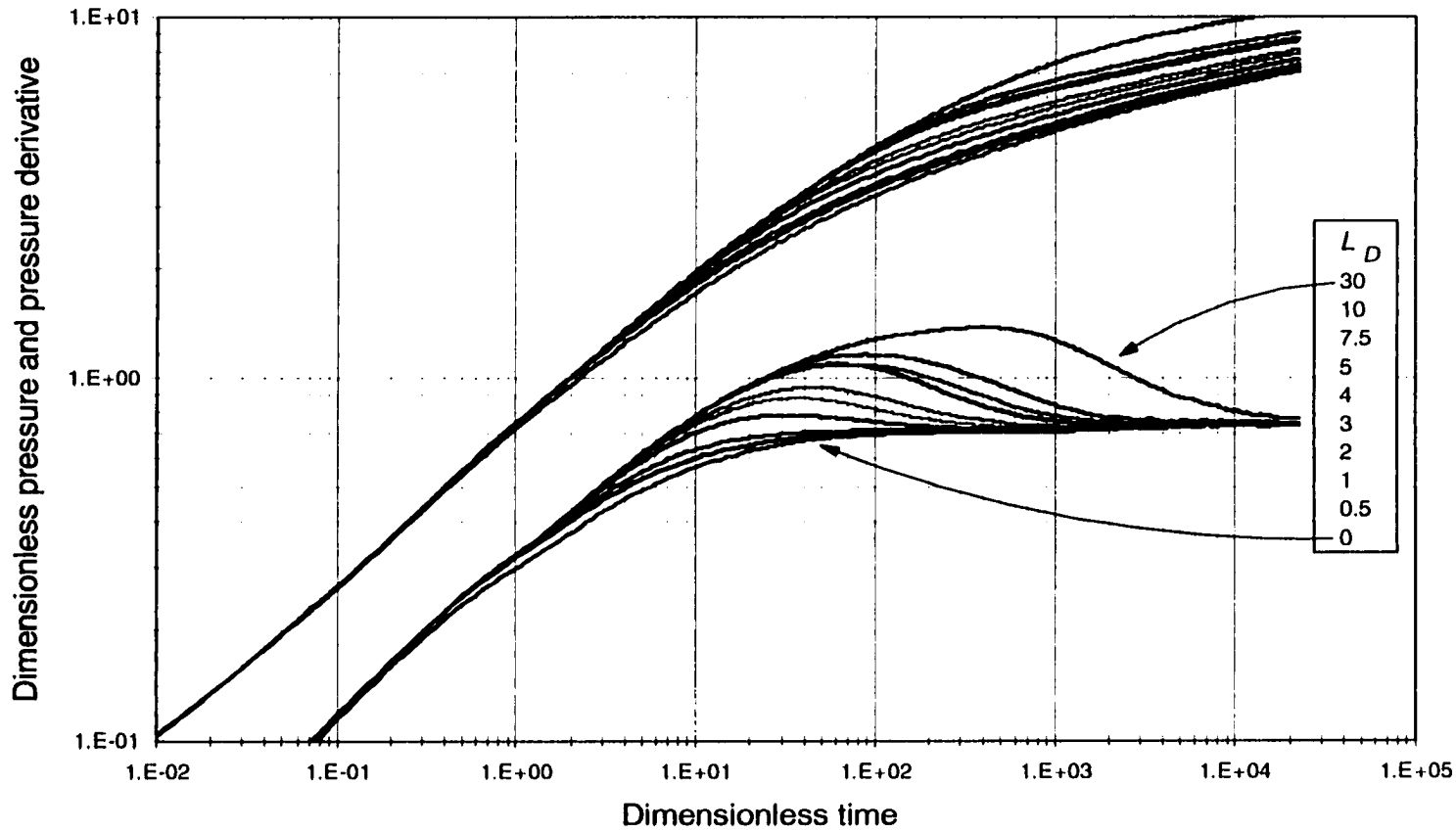

Fig. B.5.c. Dimensionless pressure and pressure derivative curve for a hydraulic fracture intersecting a fault at its fourth part forming an angle of 90°. C_D=50

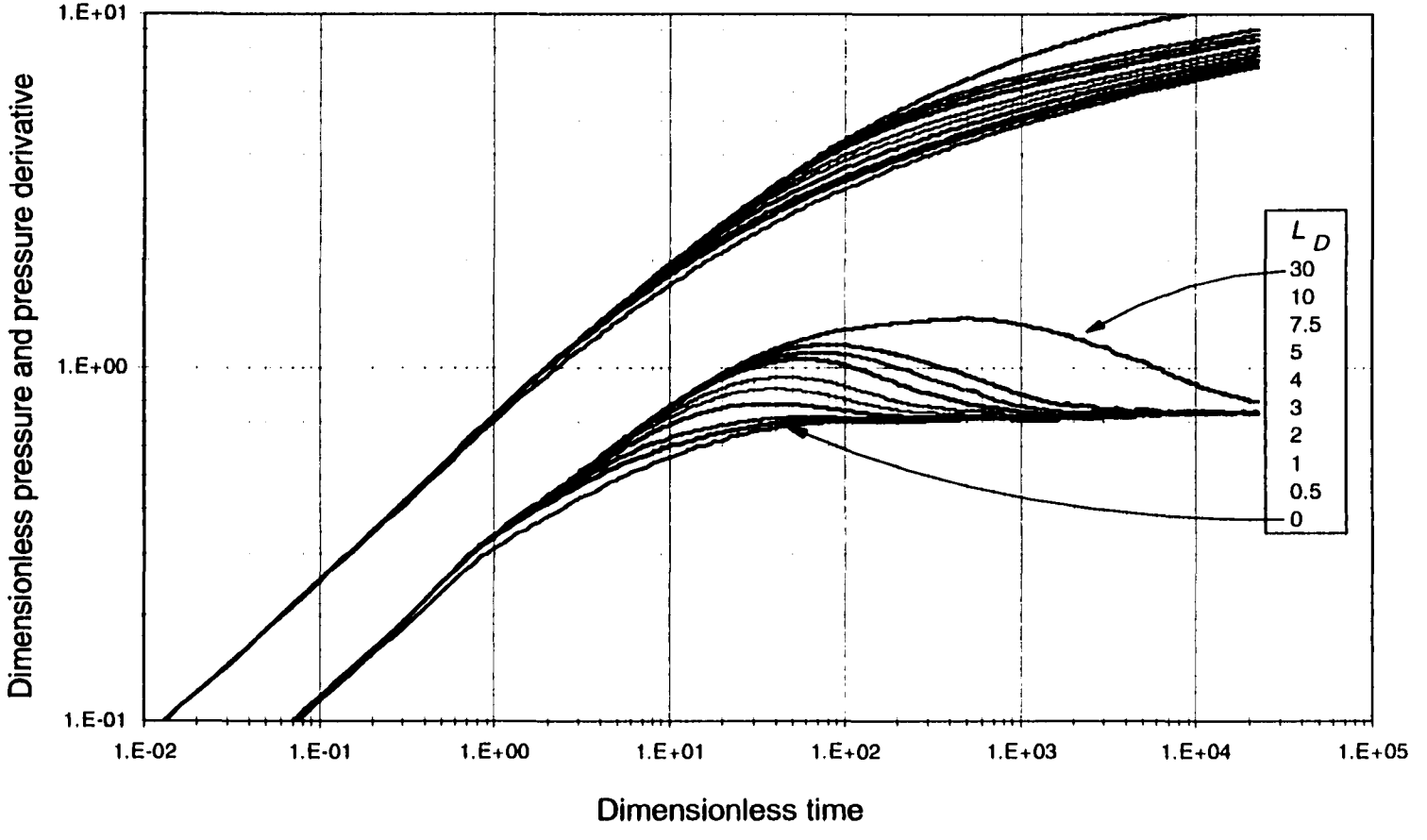

Fig. B.5.d. Dimensionless pressure and pressure derivative curve for a hydraulic fracture intersecting a fault at its fourth part forming an angle of 90°. C_D=100

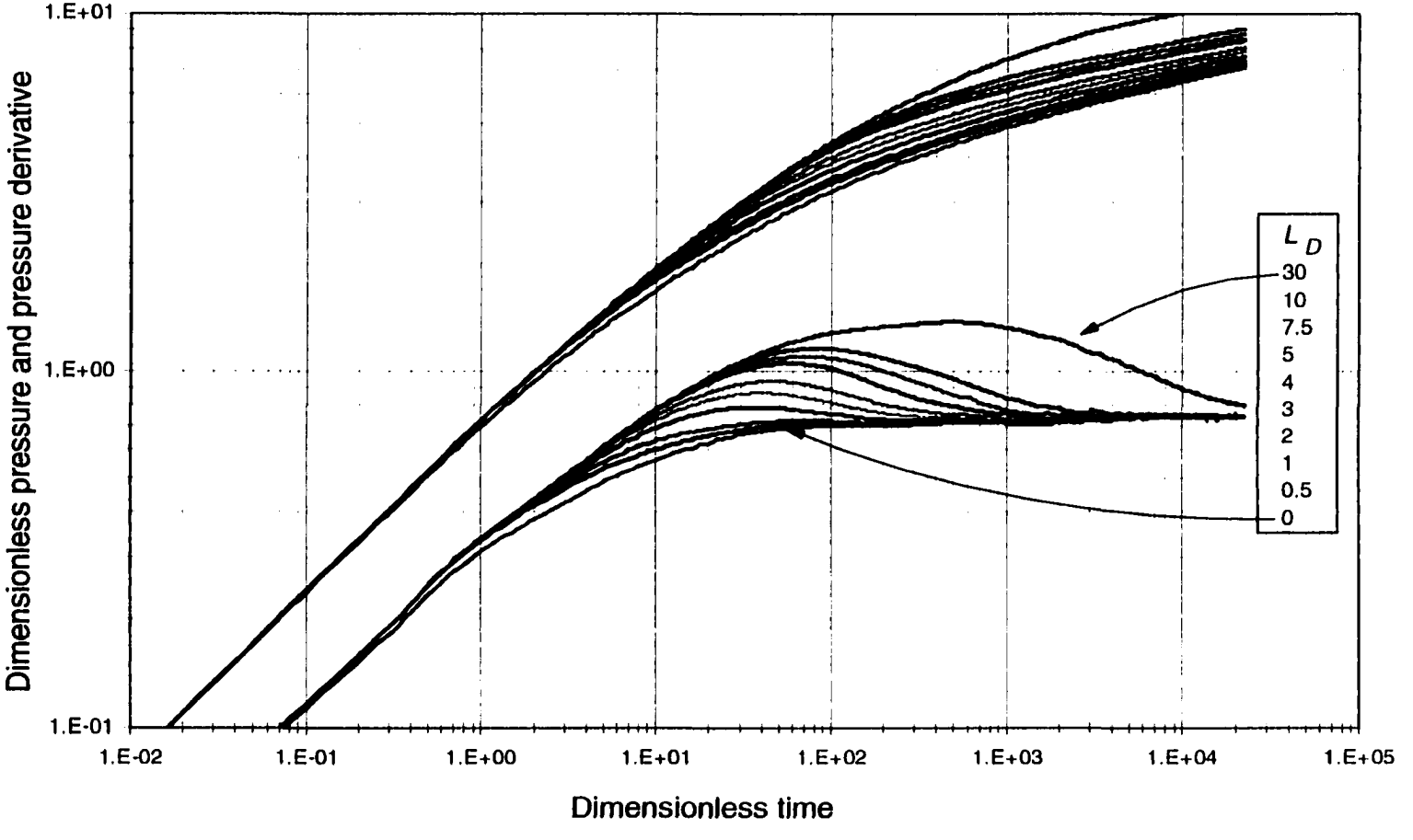

Fig. B.5.e. Dimensionless pressure and pressure derivative curve for a hydraulic fracture intersecting a fault at its fourth part forming an angle of 90°. C_{fD}=300

Fig. B.6.a. Dimensionless pressure and pressure derivative curve for a hydraulic fracture intersecting a fault at its tip forming an angle of 90°. C_{fD}=1

Fig. B.6.b. Dimensionless pressure and pressure derivative curve for a hydraulic fracture intersecting a fault at its tip forming an angle of 90°. C_D=10

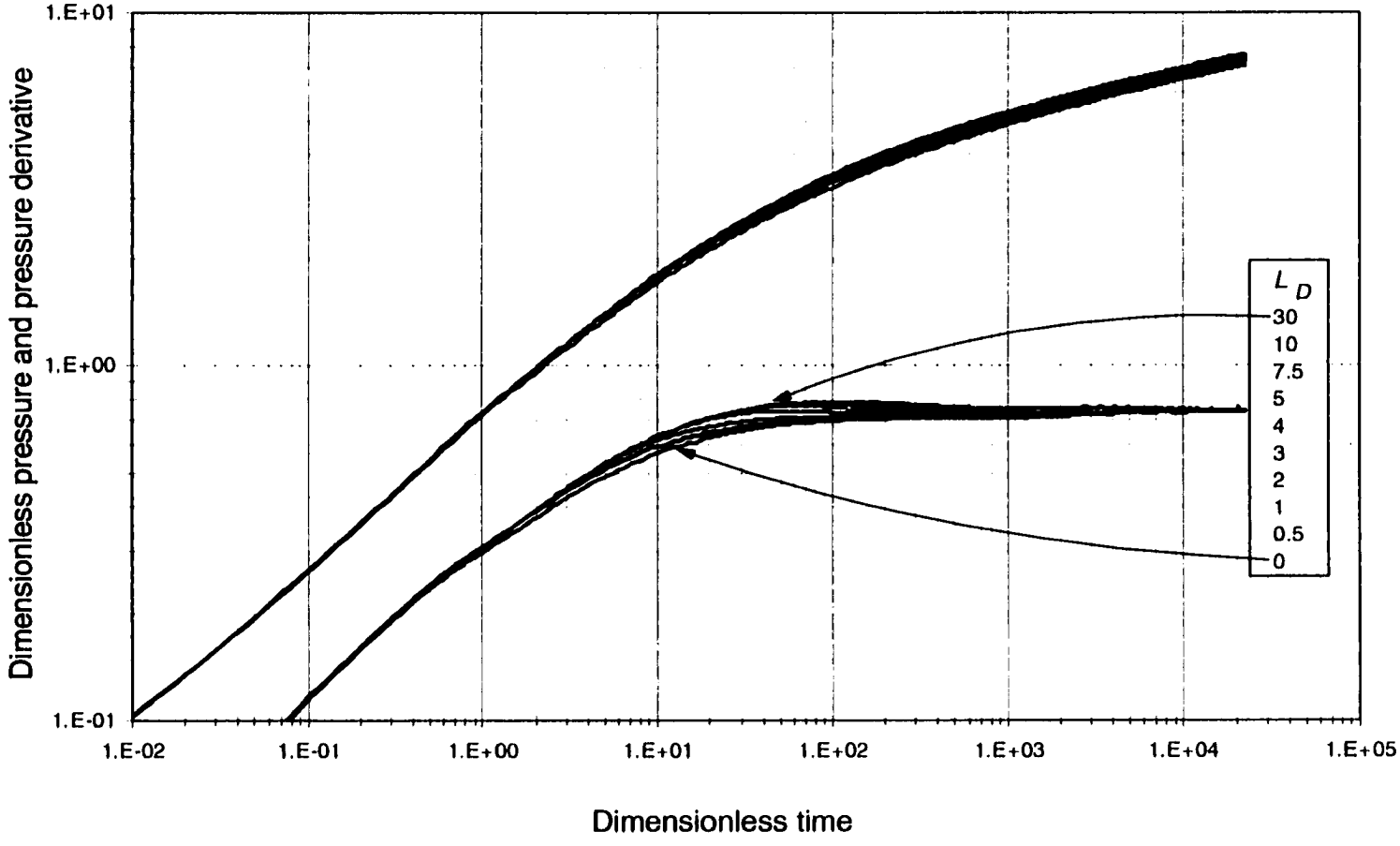

Fig. B.6.c. Dimensionless pressure and pressure derivative curve for a hydraulic fracture intersecting a fault at its tip forming an angle of 90°. C_{fD}=50

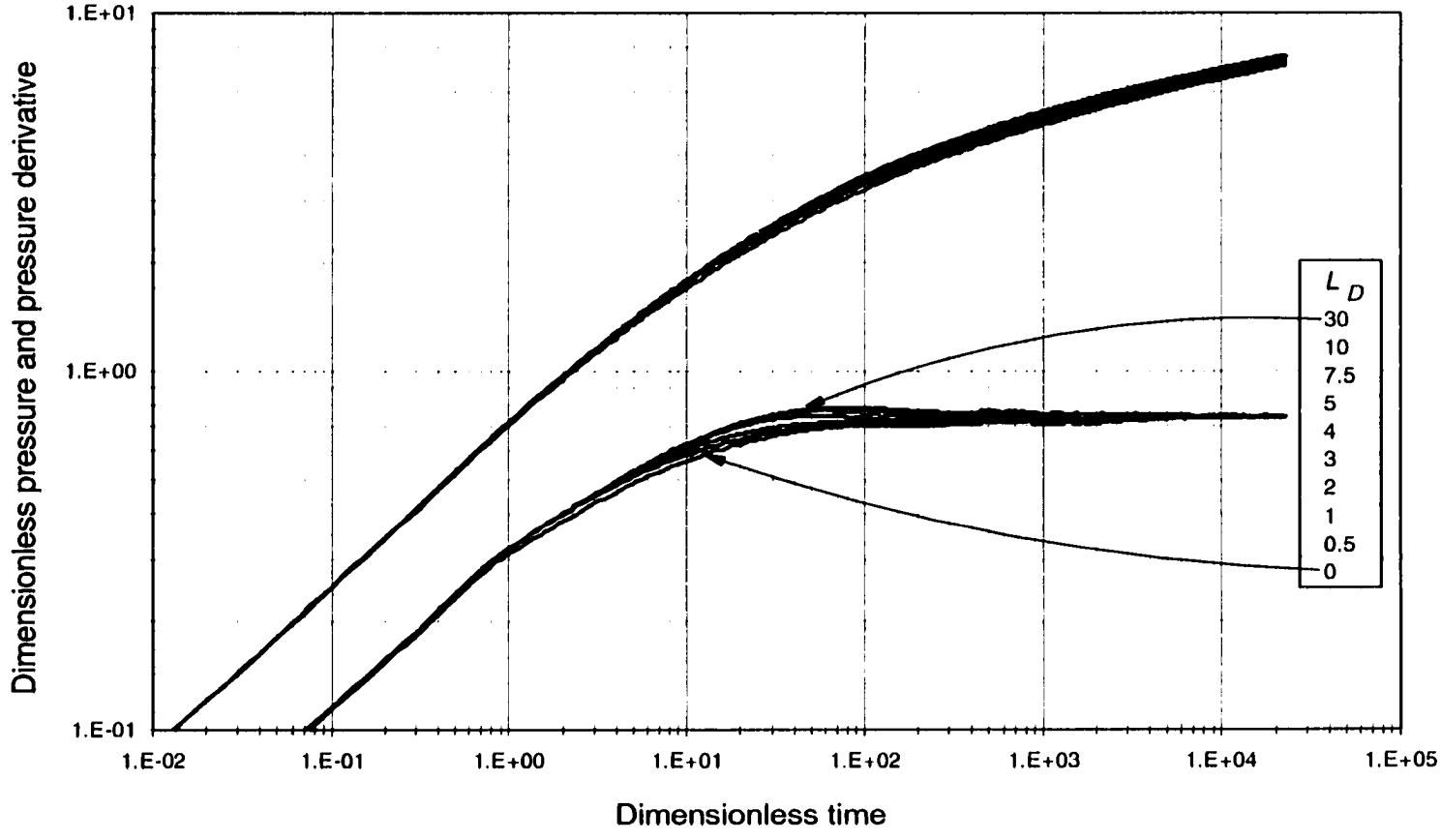

Fig. B.6.d. Dimensionless pressure and pressure derivative curve for a hydraulic fracture intersecting a fault at its tip forming an angle of 90°. C_{fD}=100

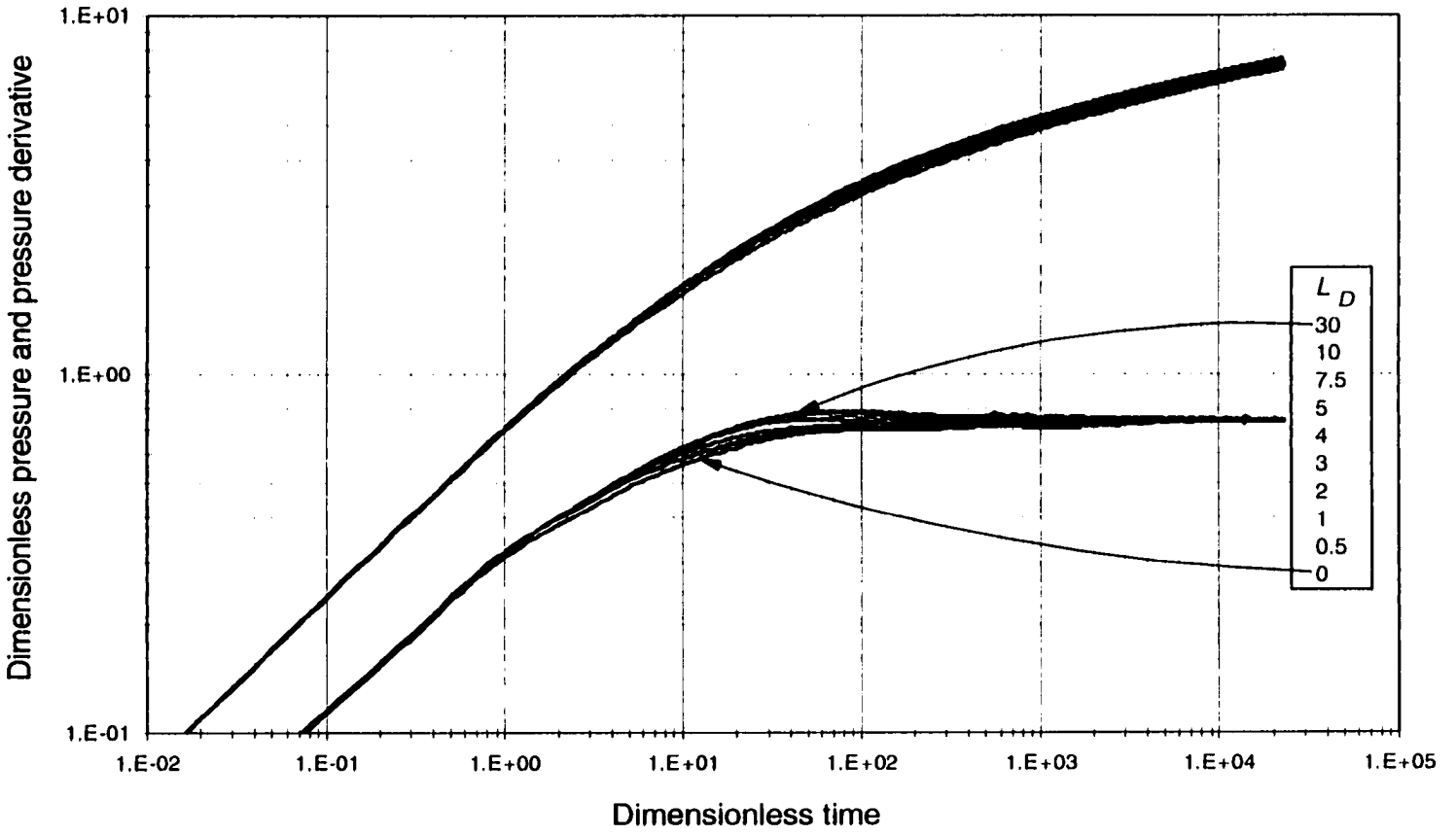

Fig. B.6.e. Dimensionless pressure and pressure derivative curve for a hydraulic fracture intersecting a fault at its tip forming an angle of 90°. C_{fD}=300

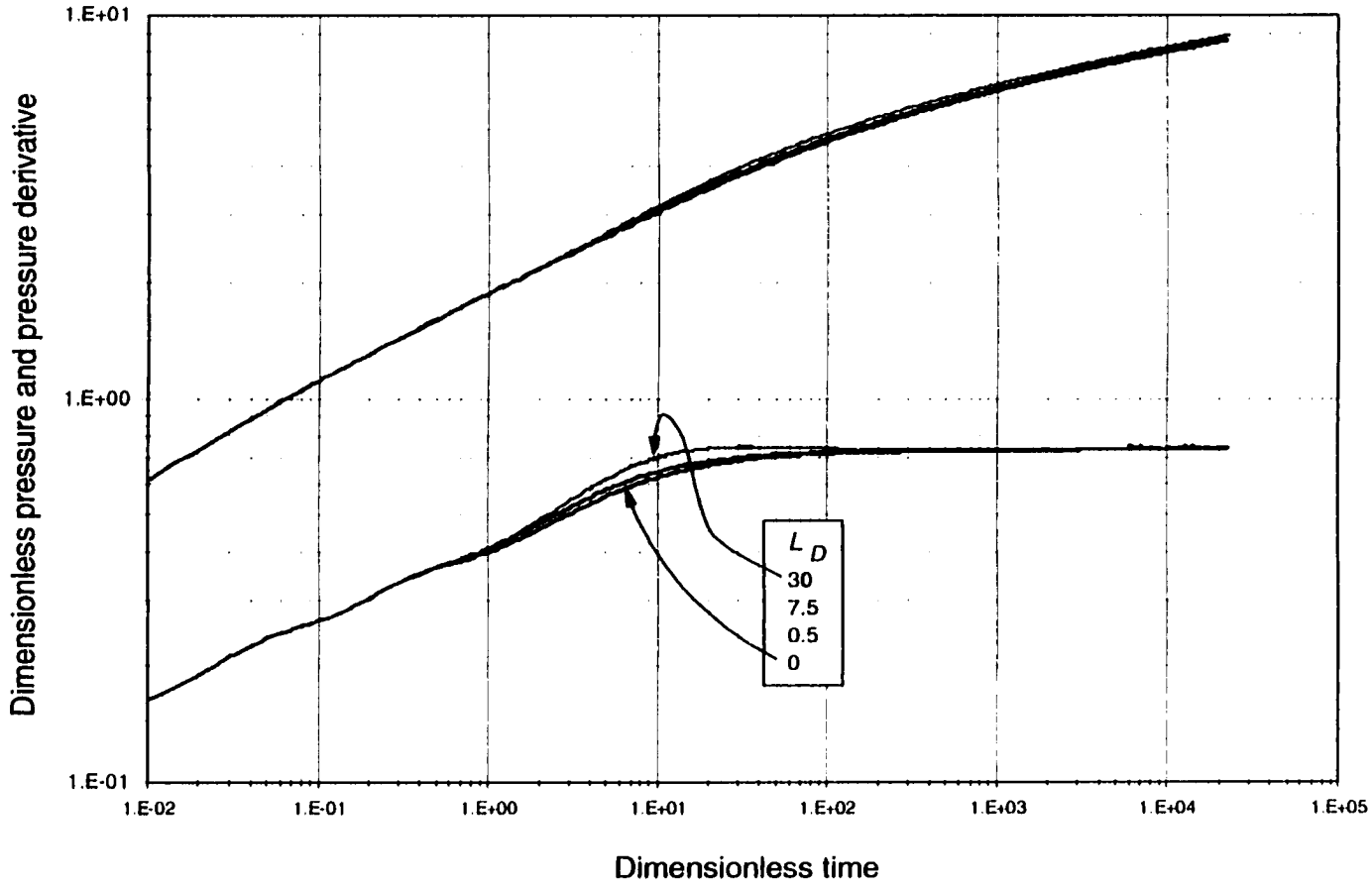

Fig. B.7.a. Dimensionless pressure and pressure derivative curve for a hydraulic fracture intersecting a fault at its tip forming an angle of 75°. $C_{fD}=1$

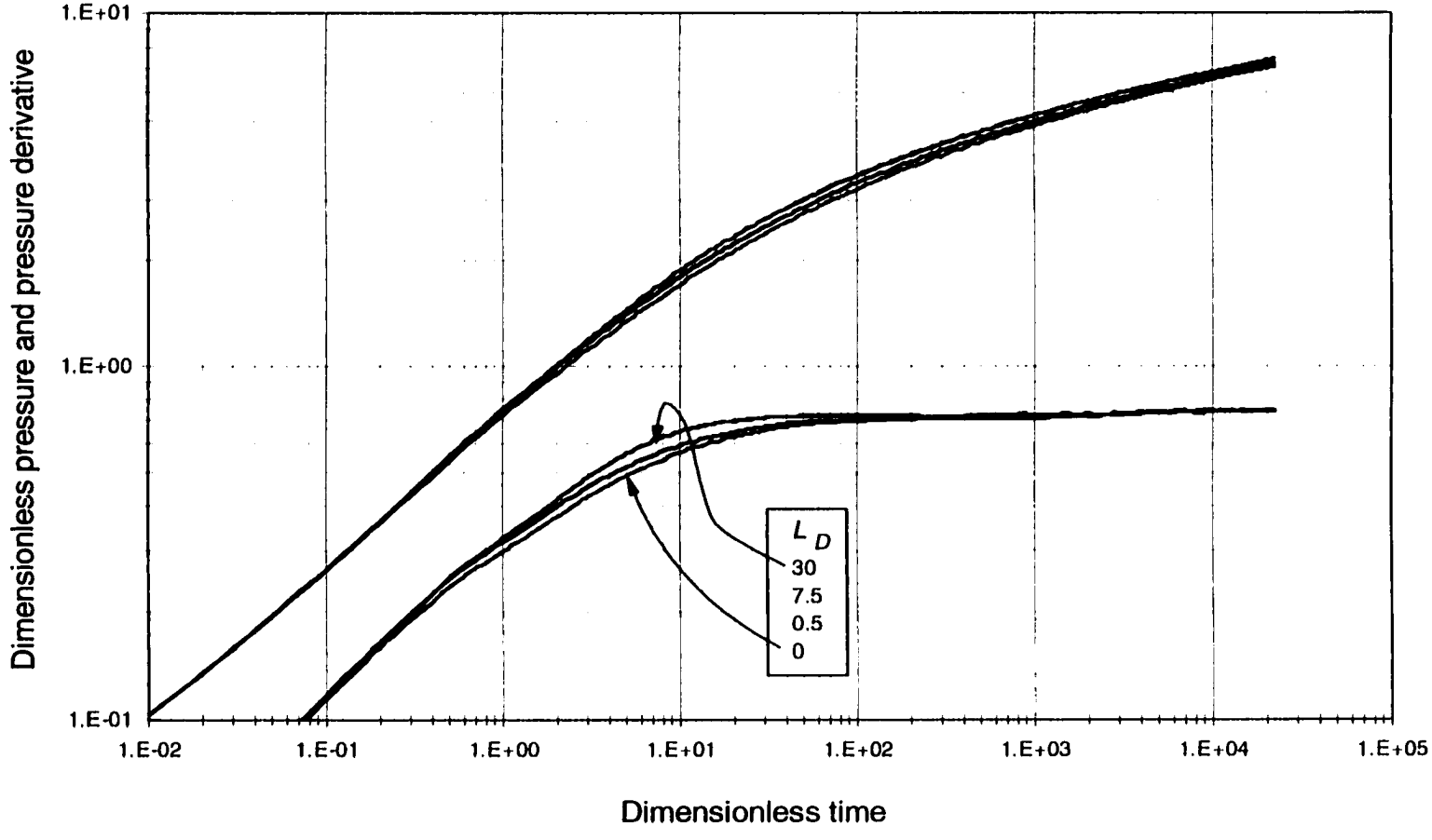

Fig. B.7.b. Dimensionless pressure and pressure derivative curve for a hydraulic fracture intersecting a fault at its middle part forming an angle of 75°. C_{fD}=10

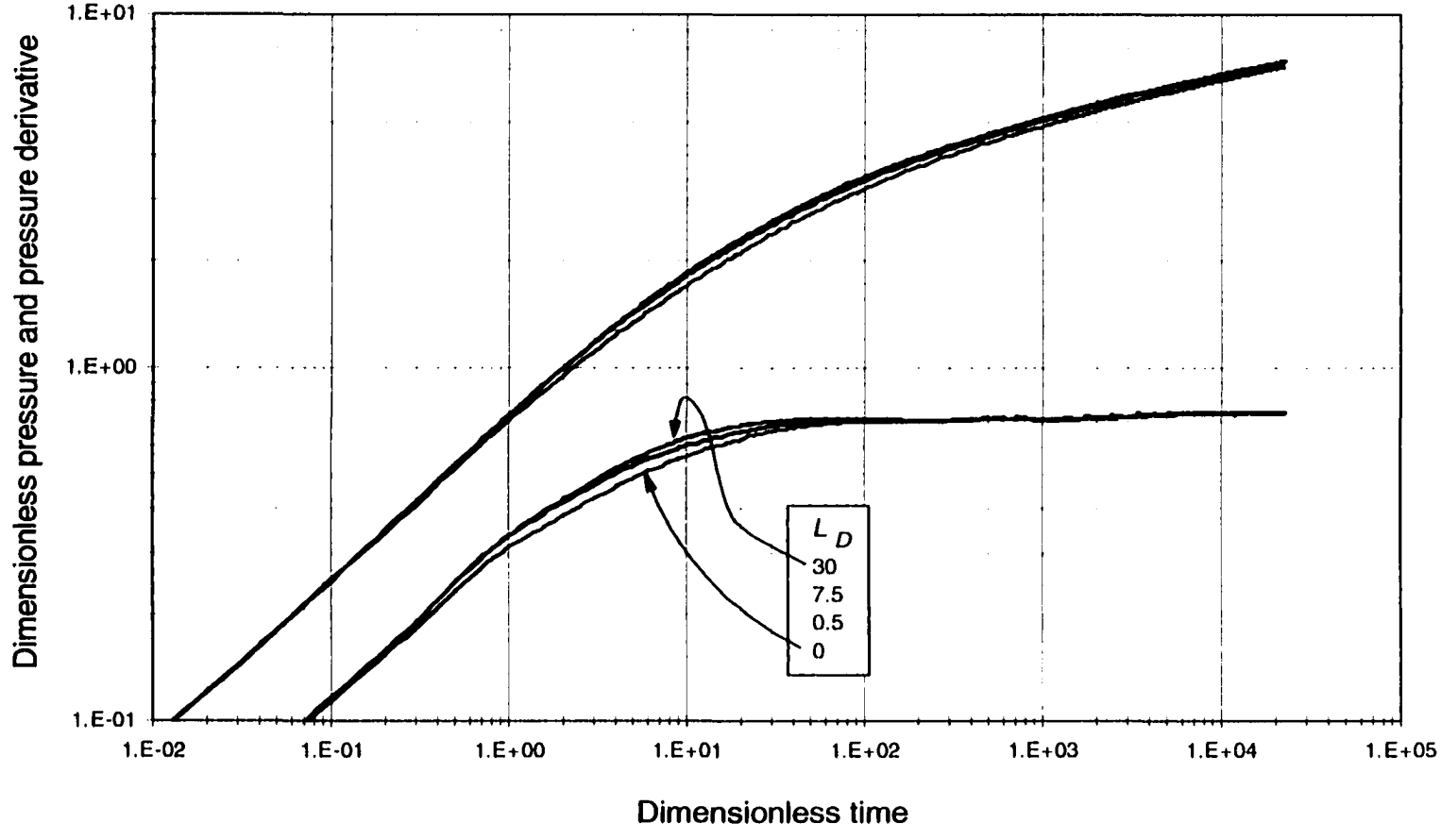

Fig. B.7.c. Dimensionless pressure and pressure derivative curve for a hydraulic fracture intersecting a fault at its middle part forming an angle of 75°. C_D=50

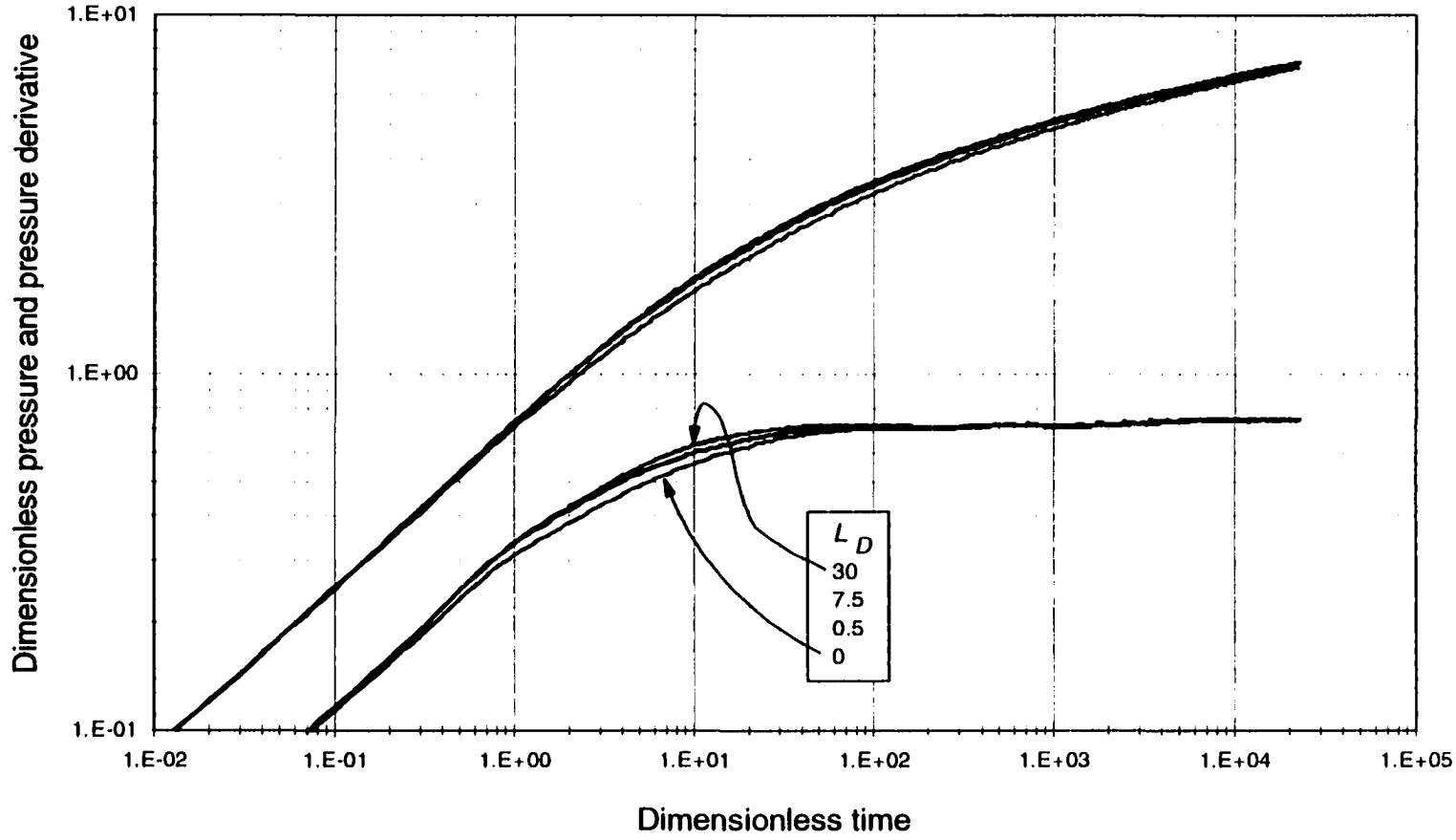

Fig. B.7.d. Dimensionless pressure and pressure derivative curve for a hydraulic fracture intersecting a fault at its middle part forming an angle of 75°. C_D=100

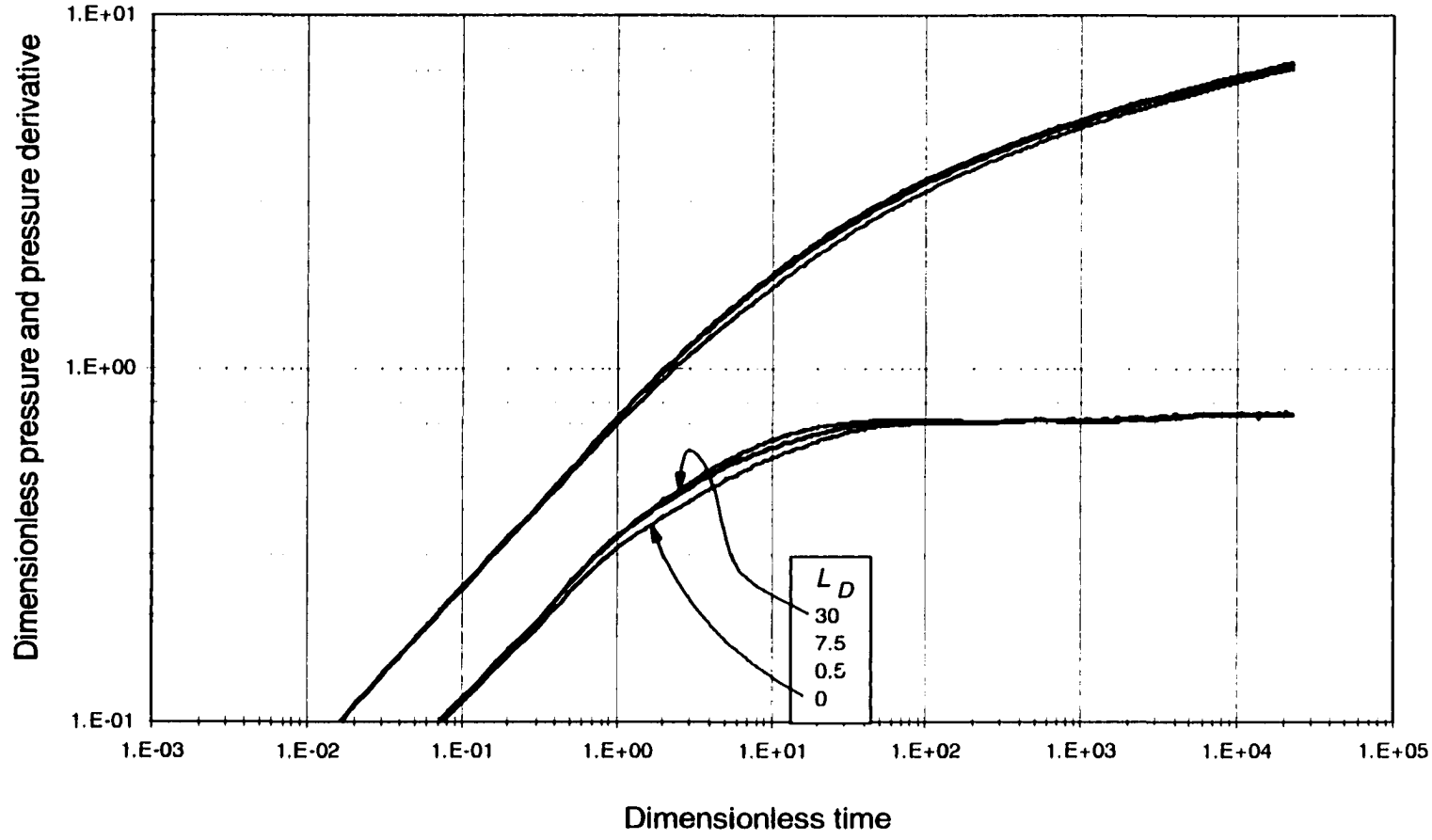

Fig. B.7.e. Dimensionless pressure and pressure derivative curve for a hydraulic fracture intersecting a fault at its middle part forming an angle of 75°. C_D=300

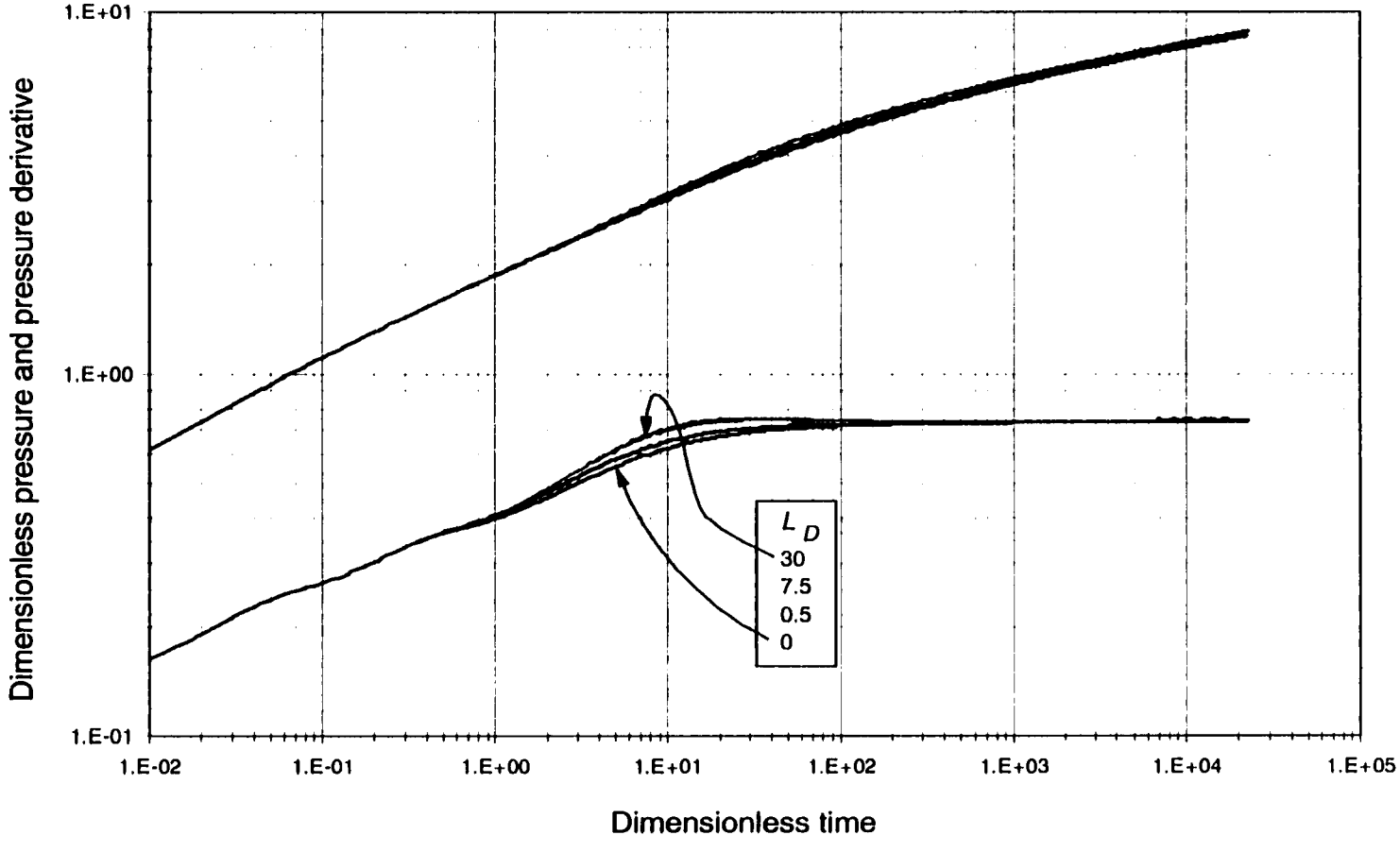

Fig. B.8.a. Dimensionless pressure and pressure derivative curve for a hydraulic fracture intersecting a fault at its fourth part forming an angle of 75°. $C_{fD}=1$

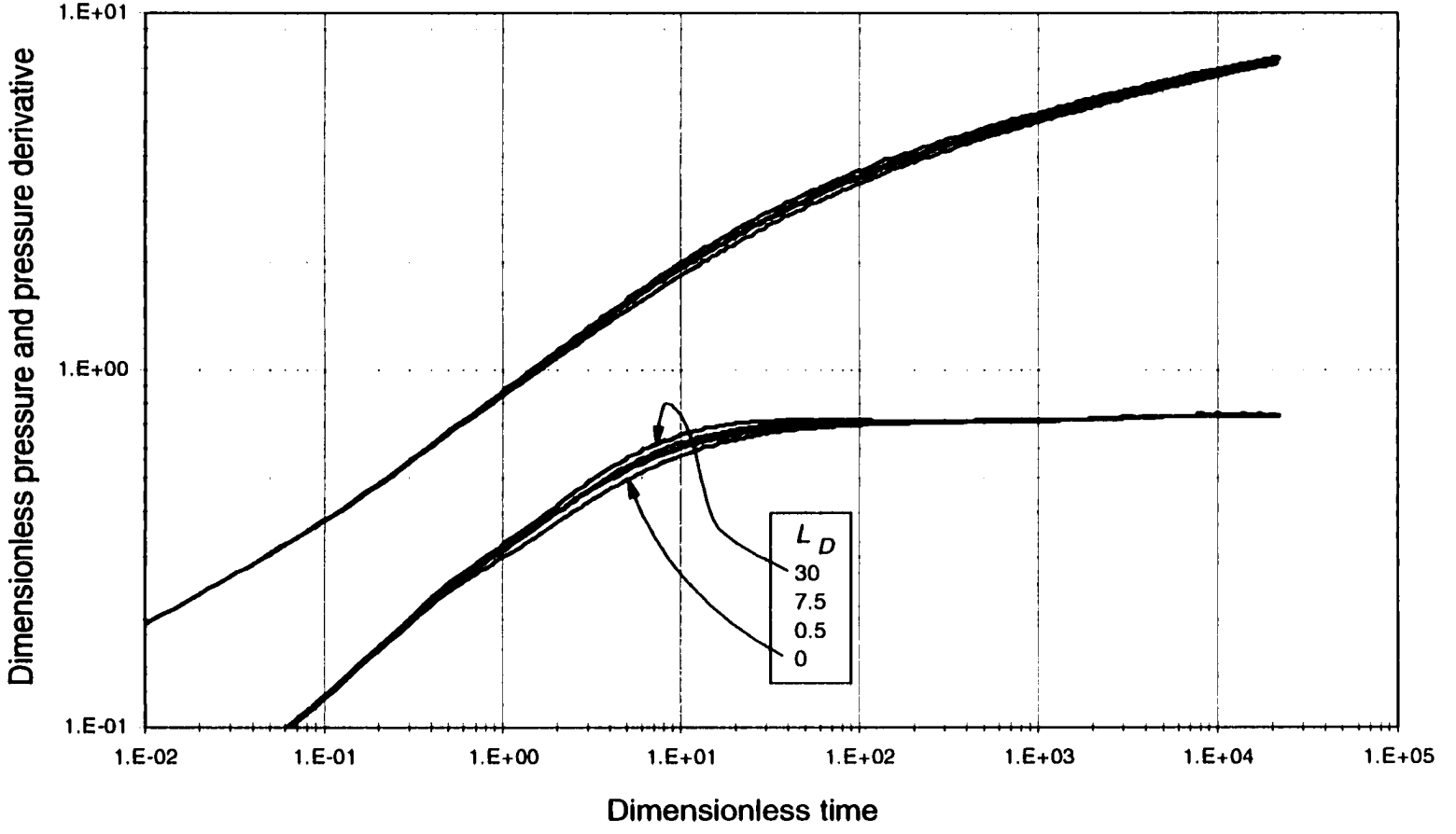

Fig. B.8.b. Dimensionless pressure and pressure derivative curve for a hydraulic fracture intersecting a fault at its fourth part forming an angle of 75°. C_{fD}=10

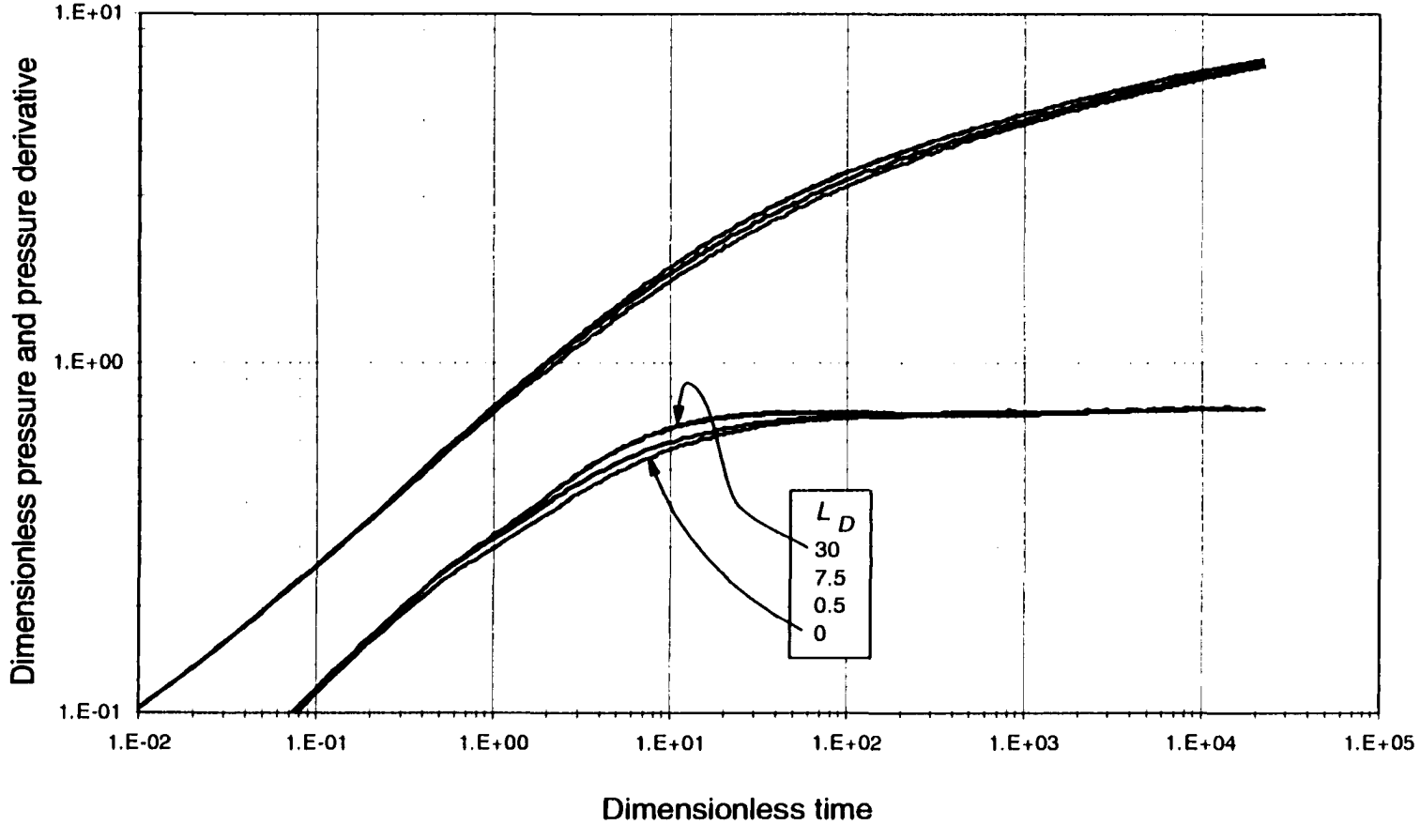

Fig. B.8.c. Dimensionless pressure and pressure derivative curve for a hydraulic fracture intersecting a fault at its fourth part forming an angle of 75°. C_D=50

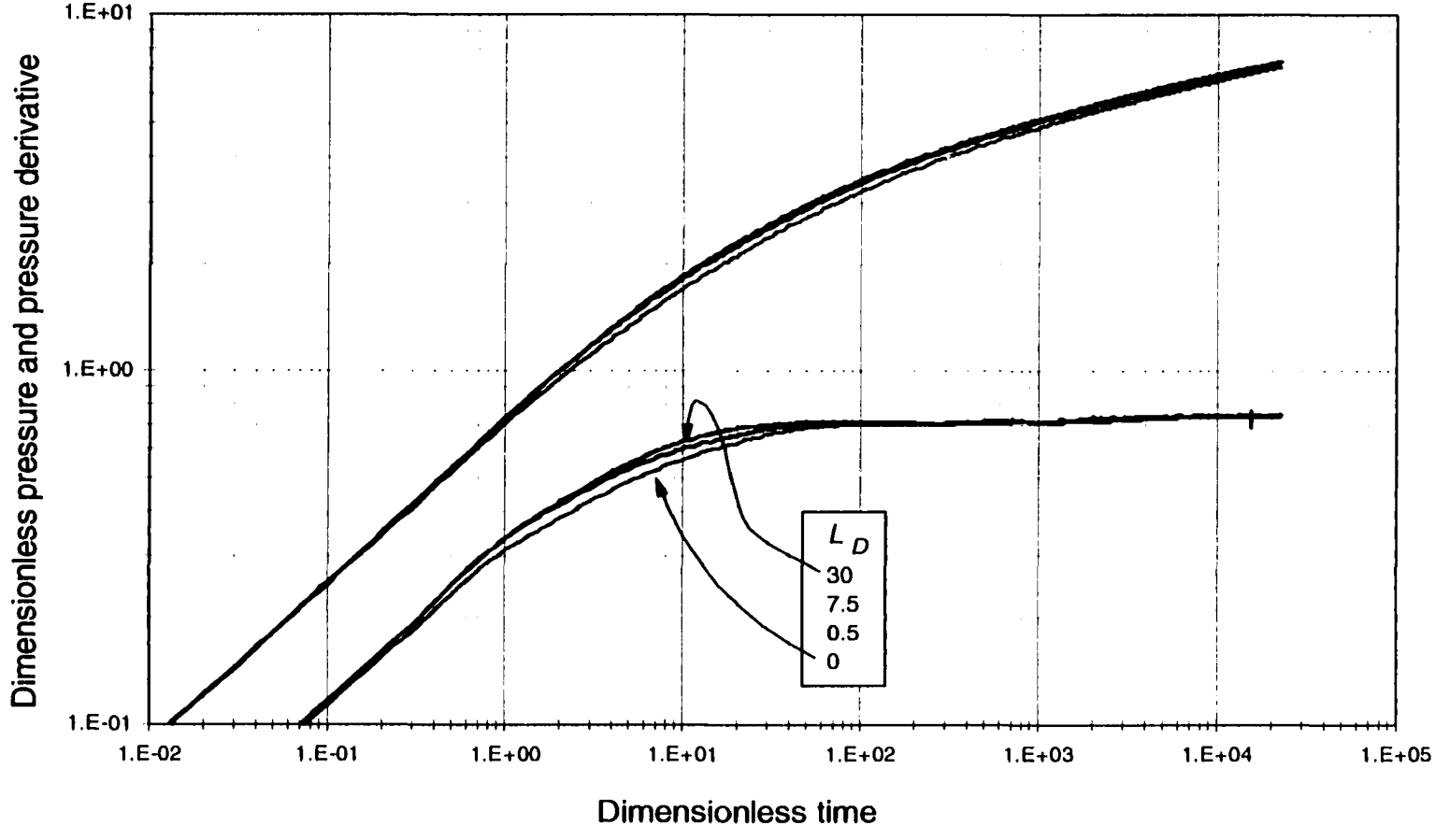

Fig. B.8.d. Dimensionless pressure and pressure derivative curve for a hydraulic fracture intersecting a fault at its fourth part forming an angle of 75°. C_D=100

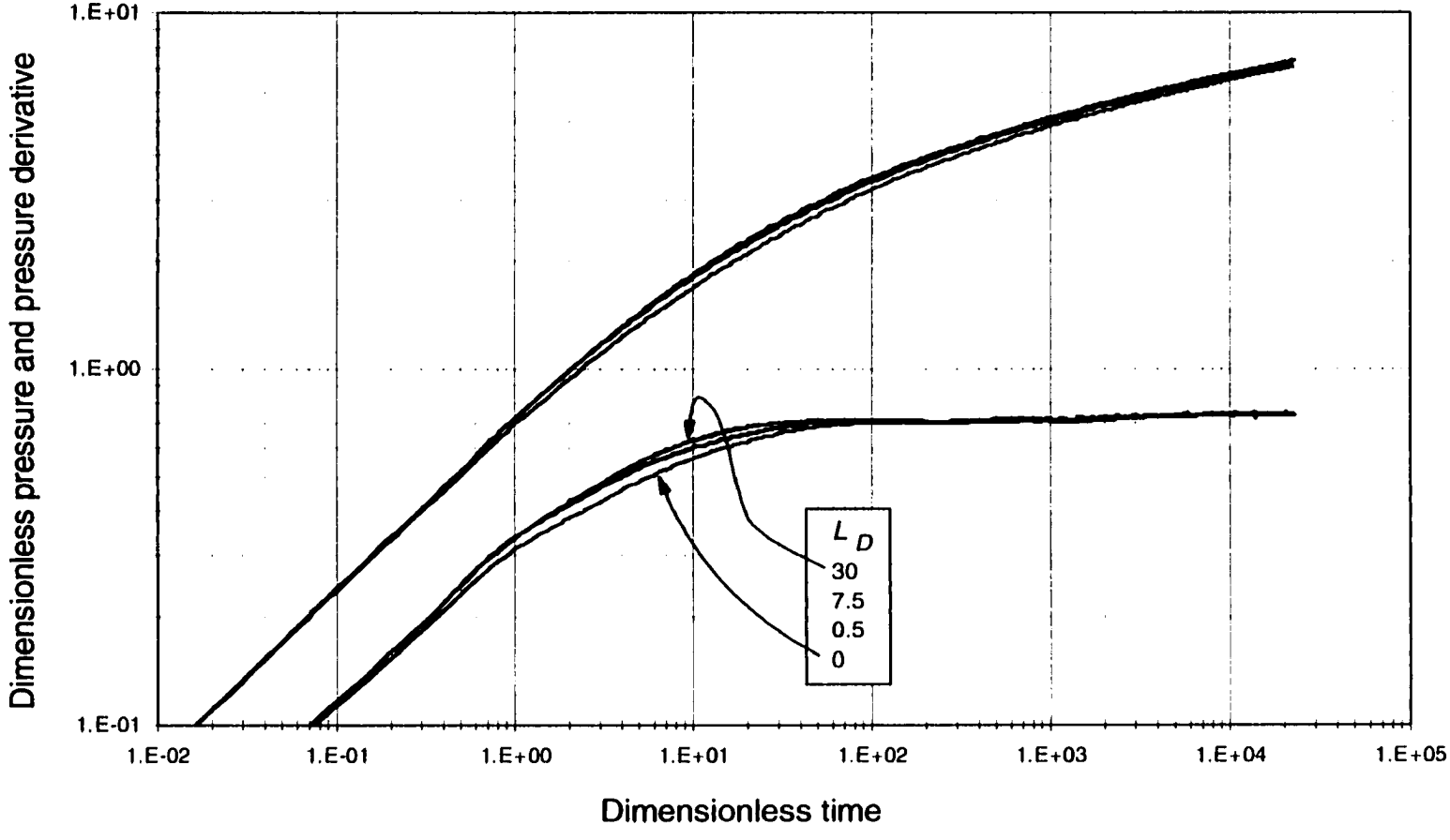

Fig. B.8.e. Dimensionless pressure and pressure derivative curve for a hydraulic fracture intersecting a fault at its fourth part forming an angle of 75°. C_D=300

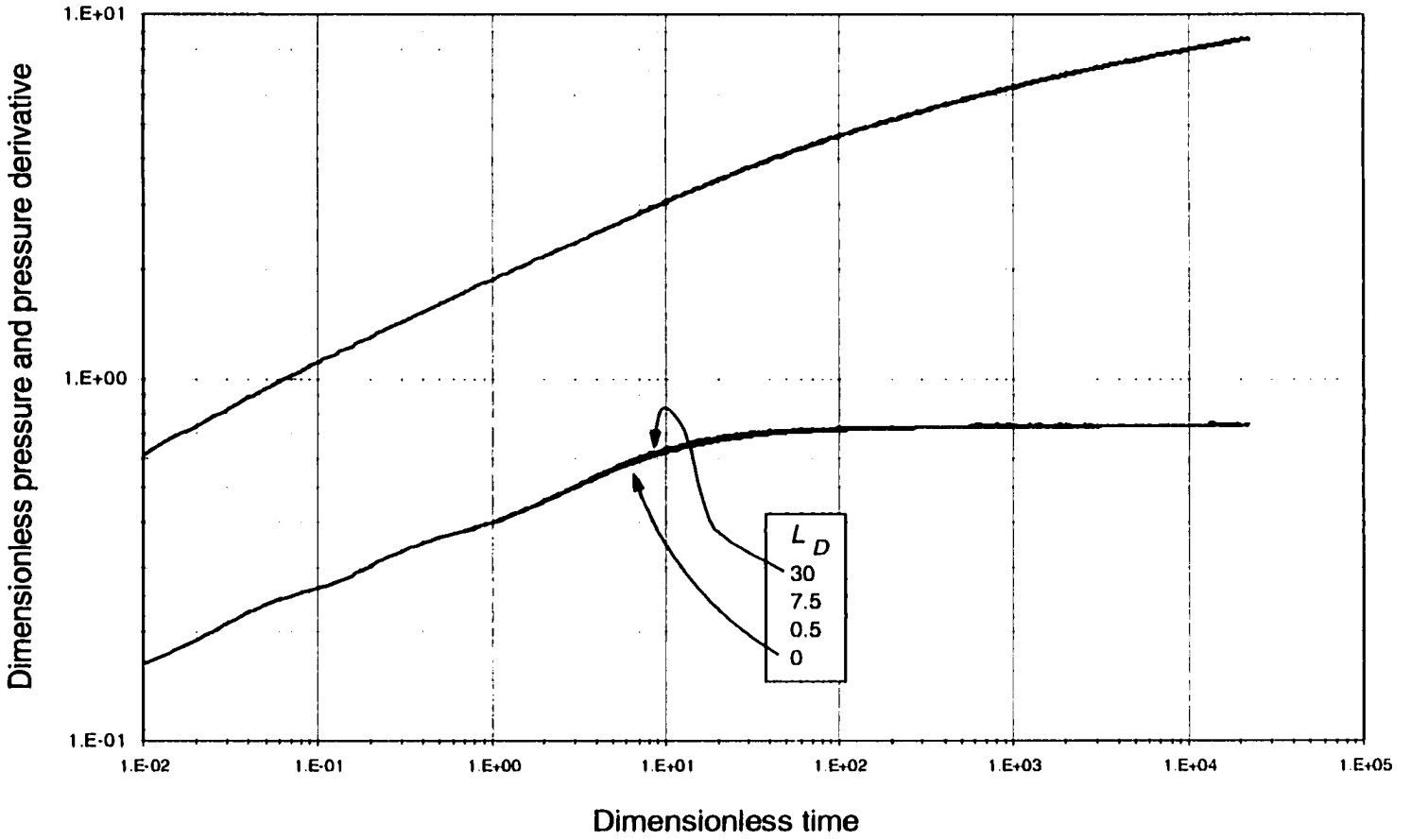

Fig. B.9.a. Dimensionless pressure and pressure derivative curve for a hydraulic fracture intersecting a fault at its tip forming an angle of 75°. C_D=1

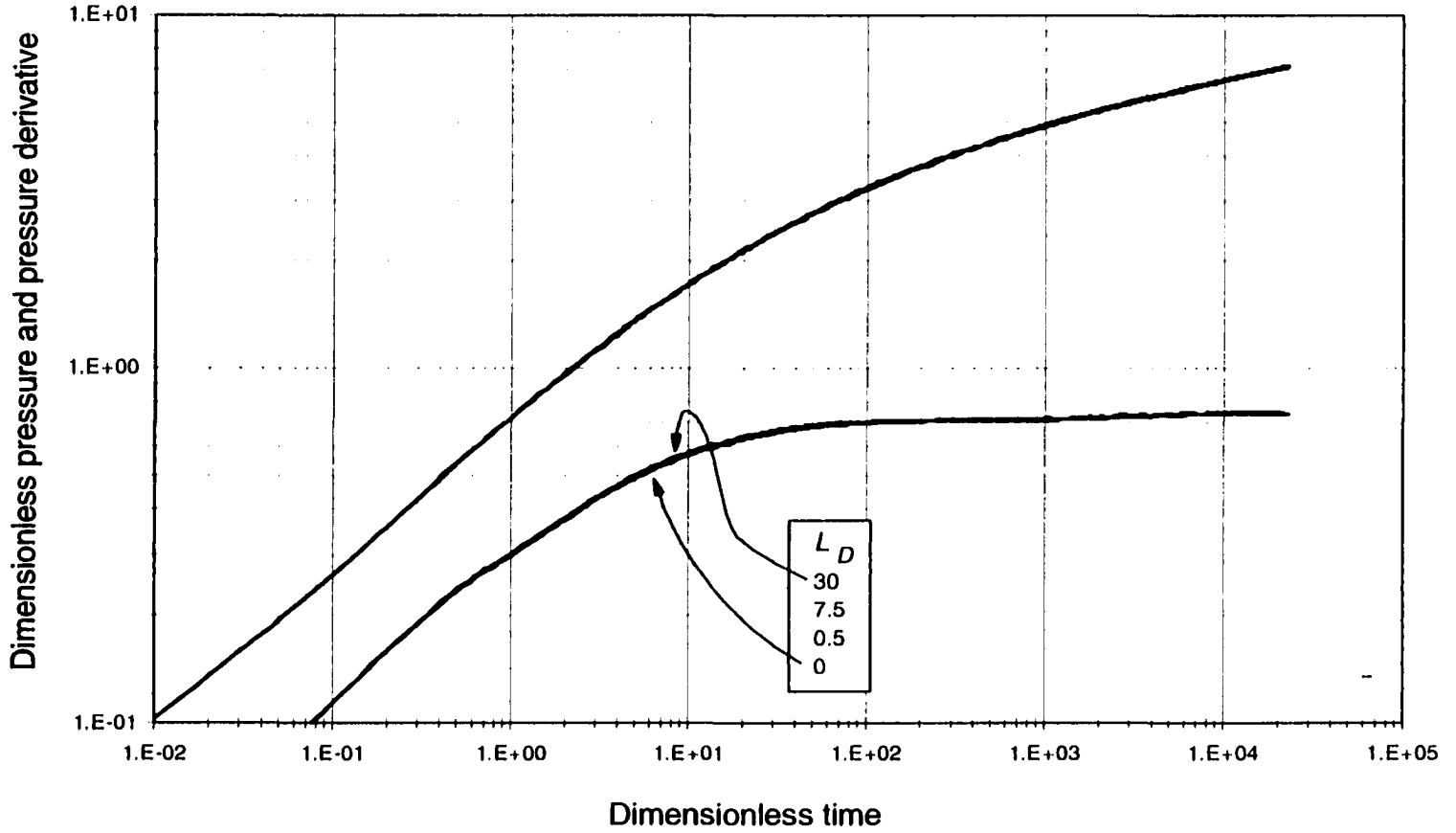

Fig. B.9.b. Dimensionless pressure and pressure derivative curve for a hydraulic fracture intersecting a fault at its tip forming an angle of 75°. C_{fD}=50

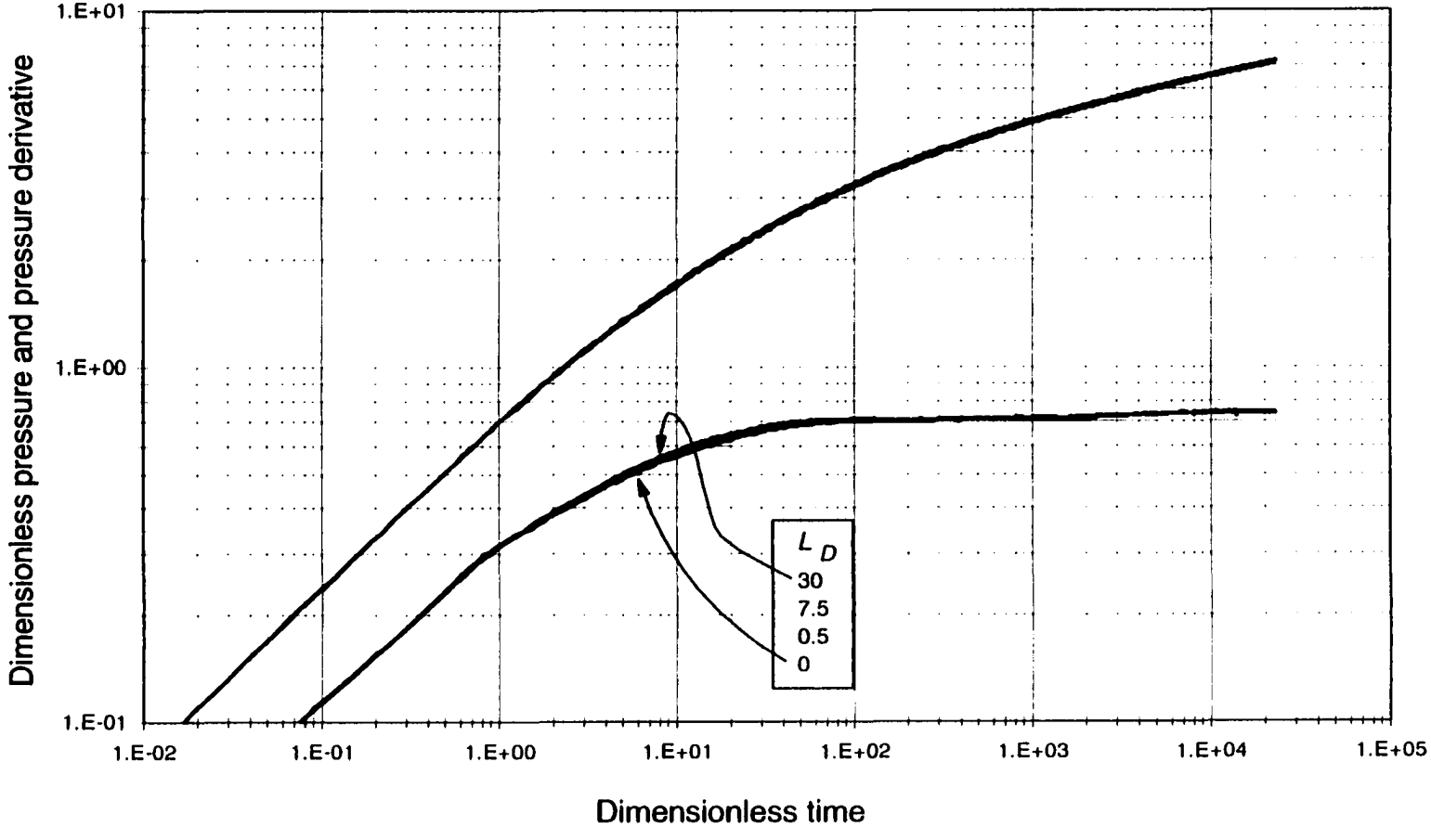

Fig. B.9.c. Dimensionless pressure and pressure derivative curve for a hydraulic fracture intersecting a fault at its tip forming an angle of 75°. C_D=300

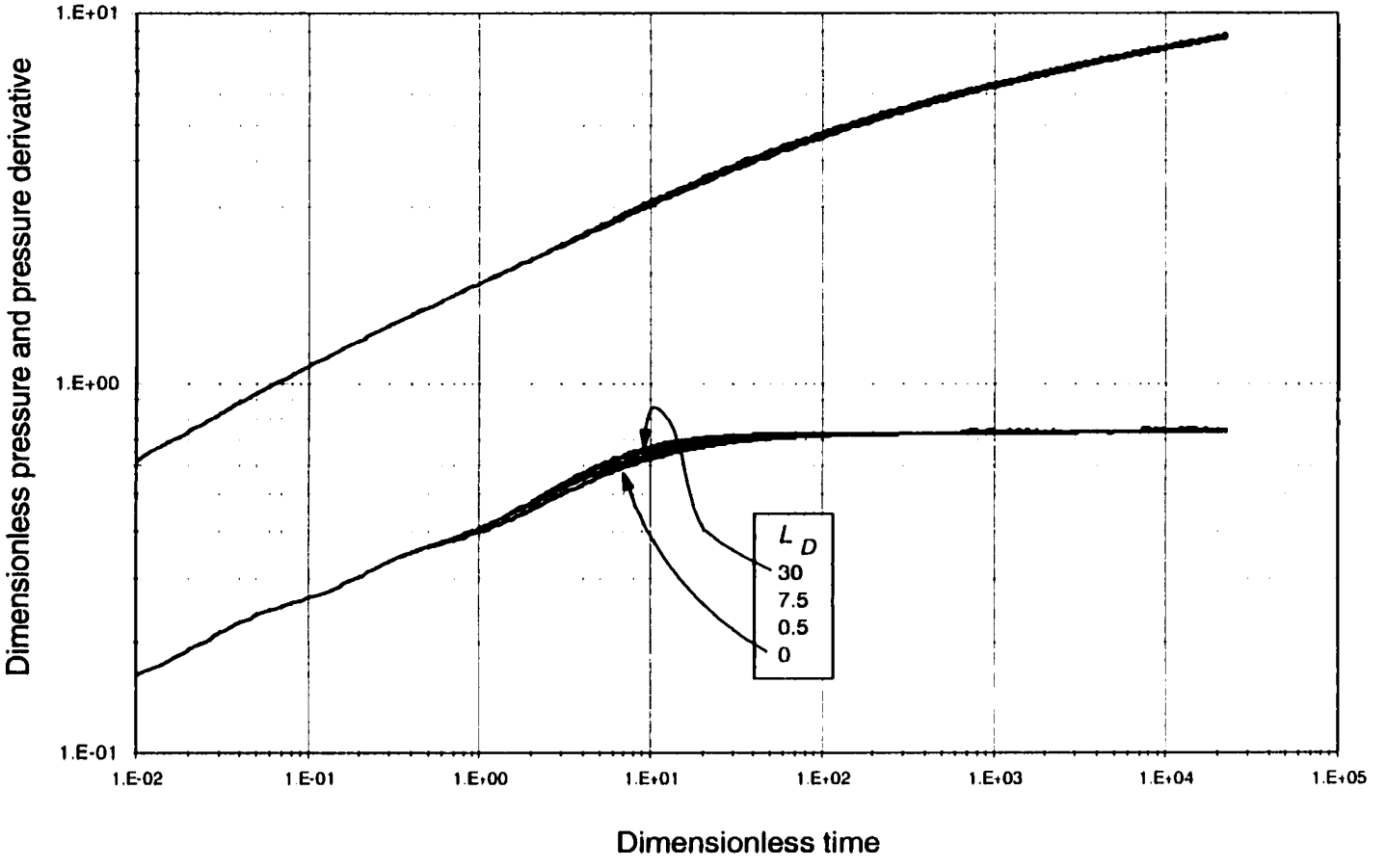

Fig. B.10.a. Dimensionless pressure and pressure derivative curve for a hydraulic fracture intersecting a fault at its middle part forming an angle of 60°. C_{fD}=1

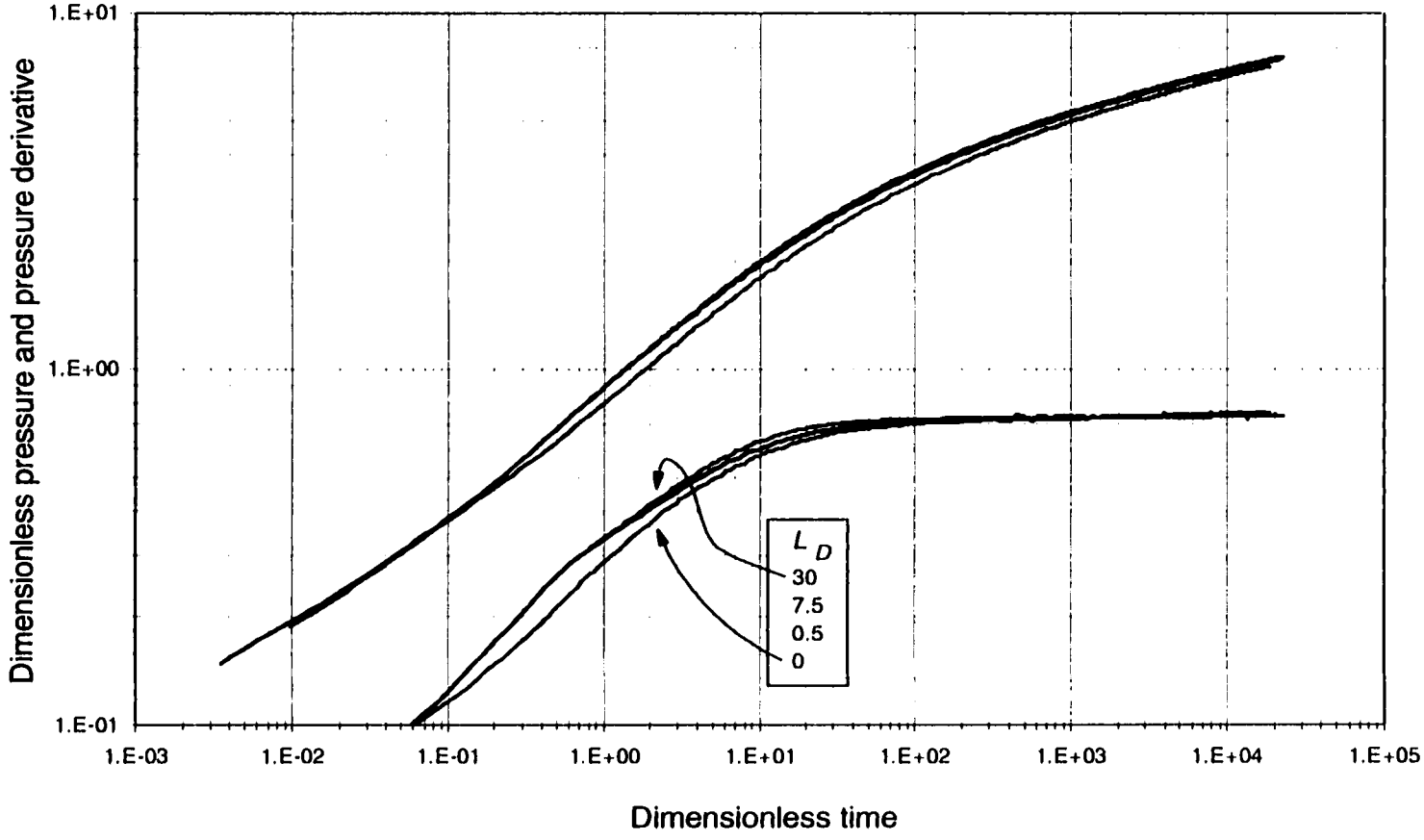

Fig. B.10.b. Dimensionless pressure and pressure derivative curve for a hydraulic fracture intersecting a fault at its middle part forming an angle of 60°. C_{fD}=10

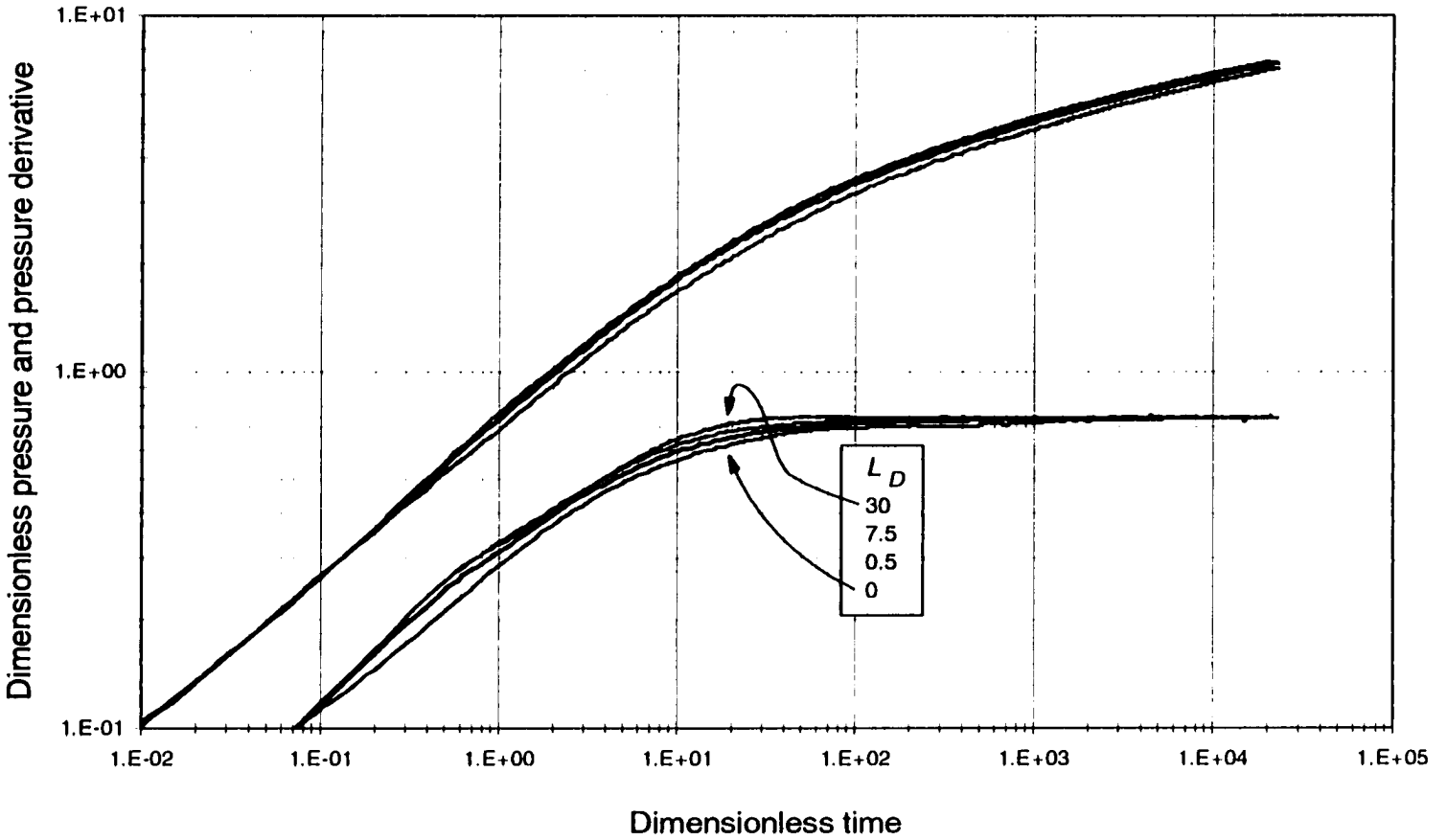

Fig. B.10.c. Dimensionless pressure and pressure derivative curve for a hydraulic fracture intersecting a fault at its middle part forming an angle of 60°. C_{fD}=50

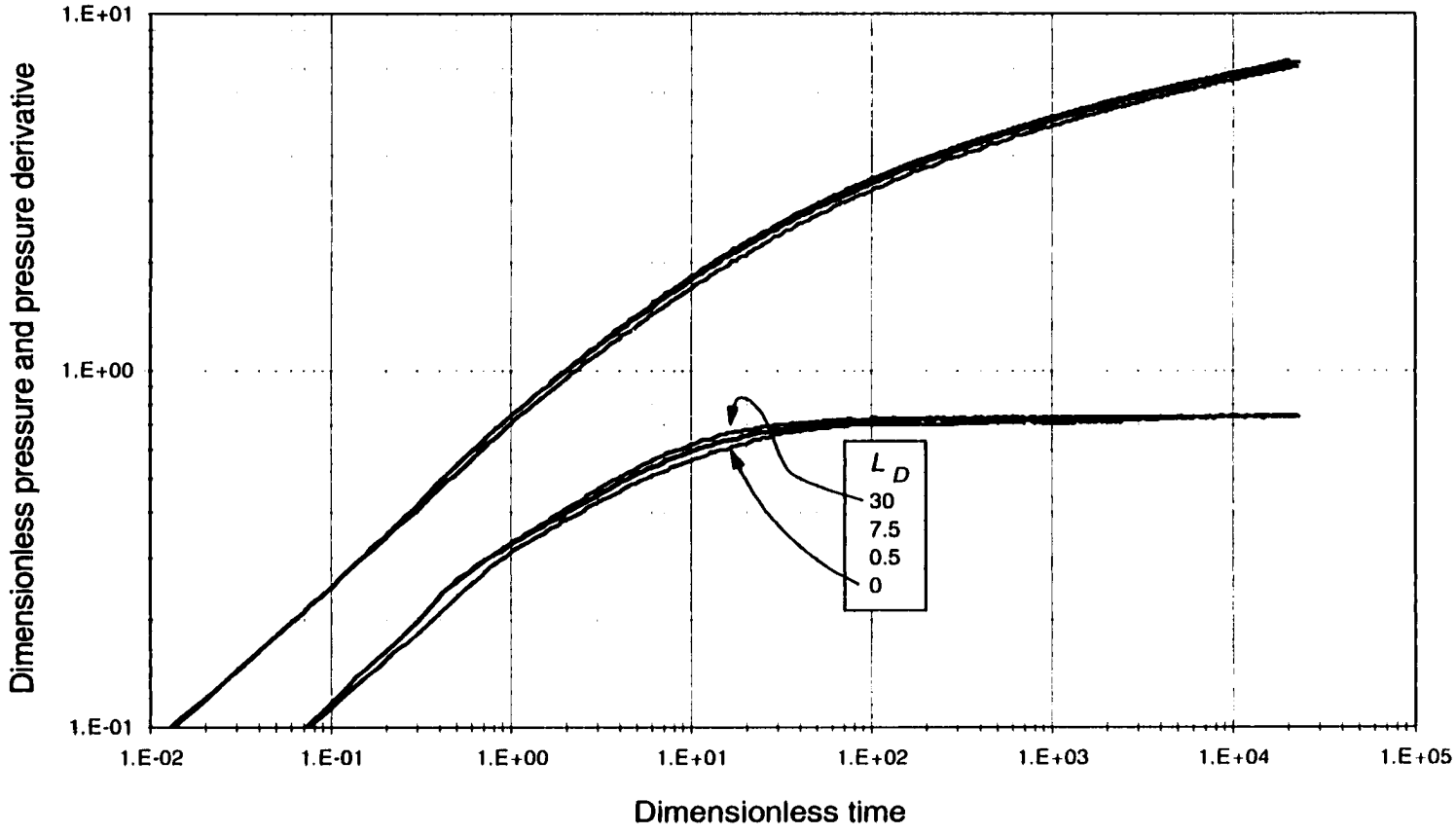

Fig. B.10.d. Dimensionless pressure and pressure derivative curve for a hydraulic fracture intersecting a fault at its middle part forming an angle of 60°. C_{fD}=100

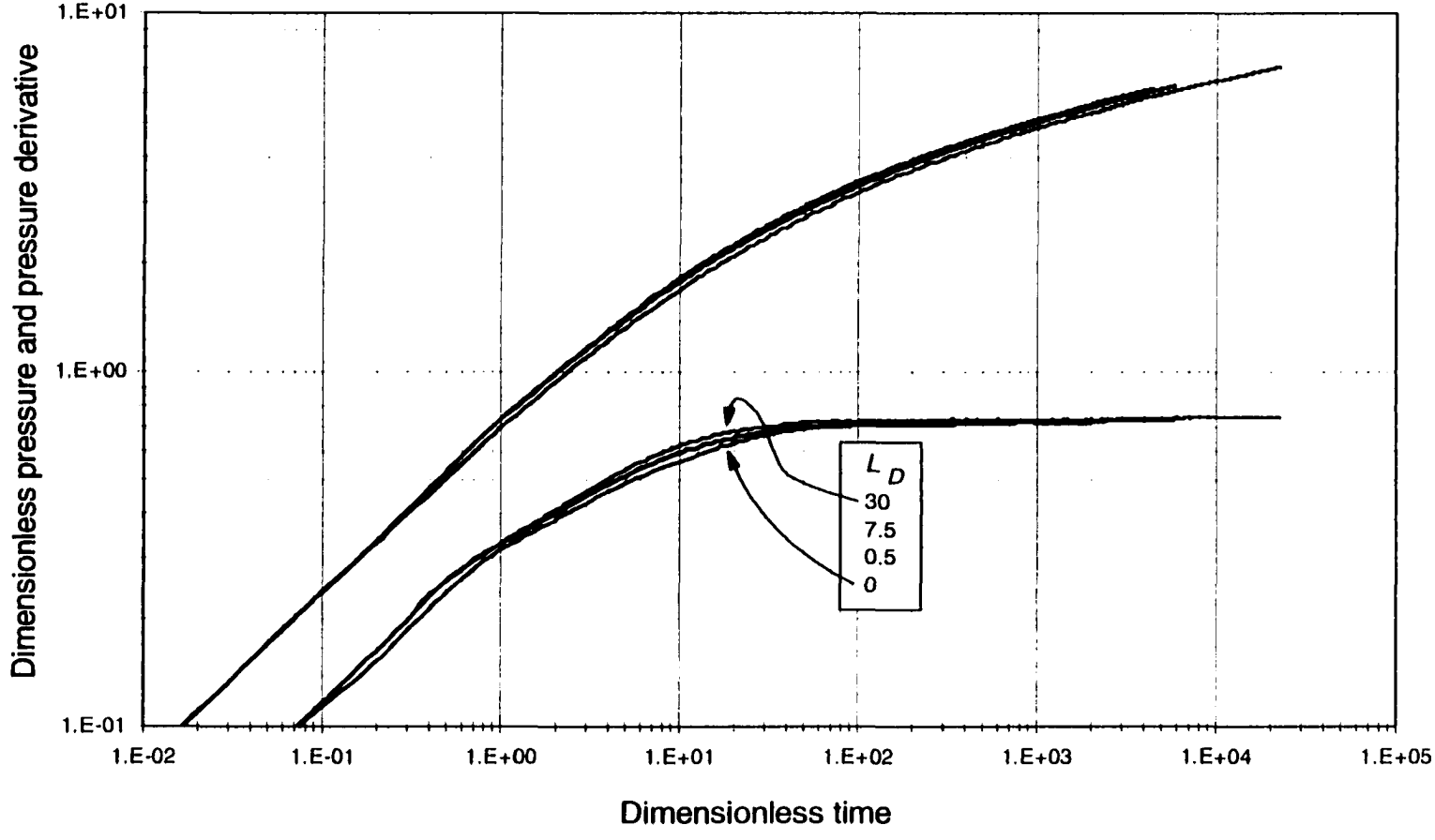

Fig. B.10.e. Dimensionless pressure and pressure derivative curve for a hydraulic fracture intersecting a fault at its middle part forming an angle of 60°. C_{fD}=300

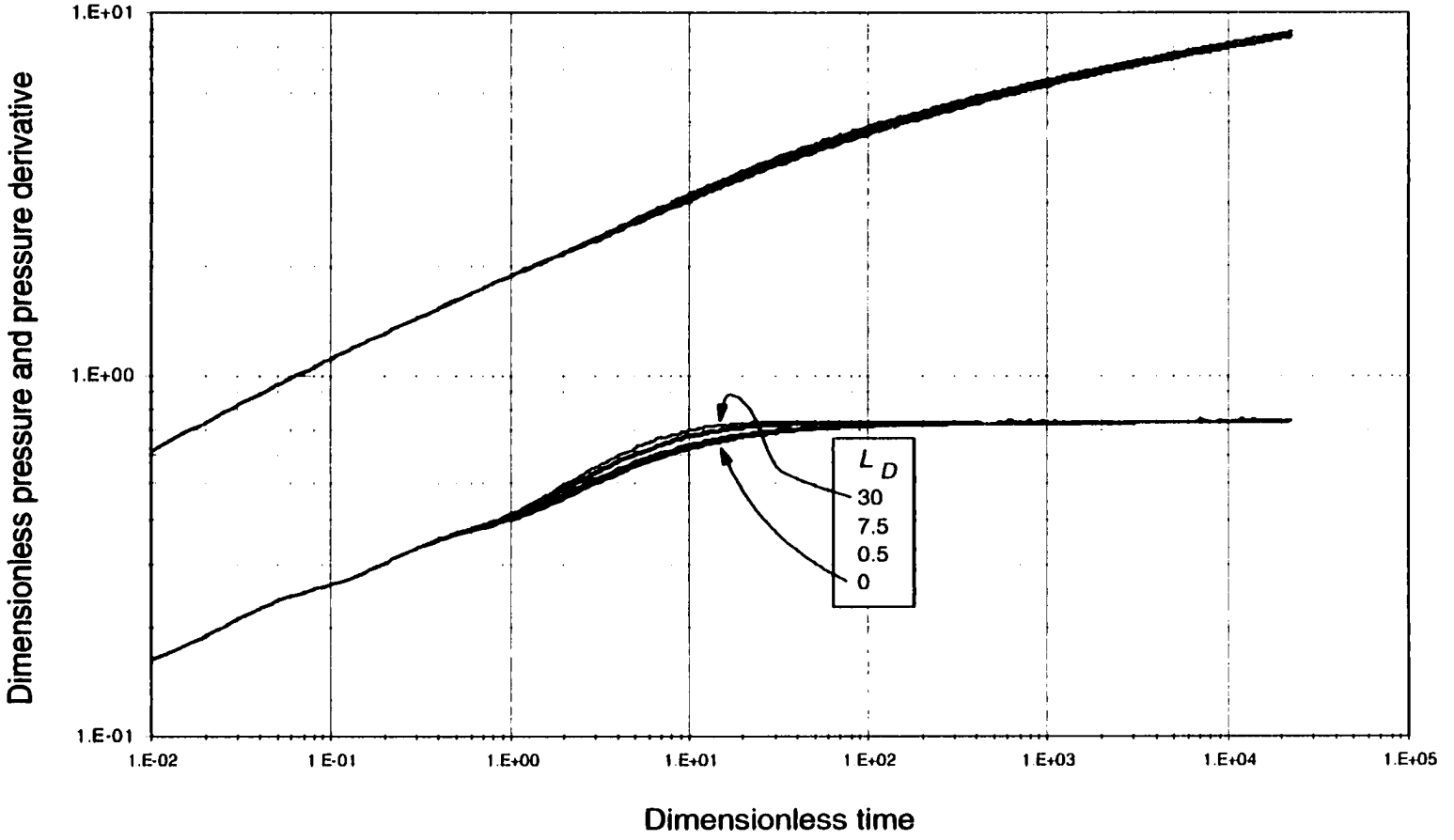

Fig. B.11.a. Dimensionless pressure and pressure derivative curve for a hydraulic fracture intersecting a fault at its fourth part forming an angle of 60°. C_D=1

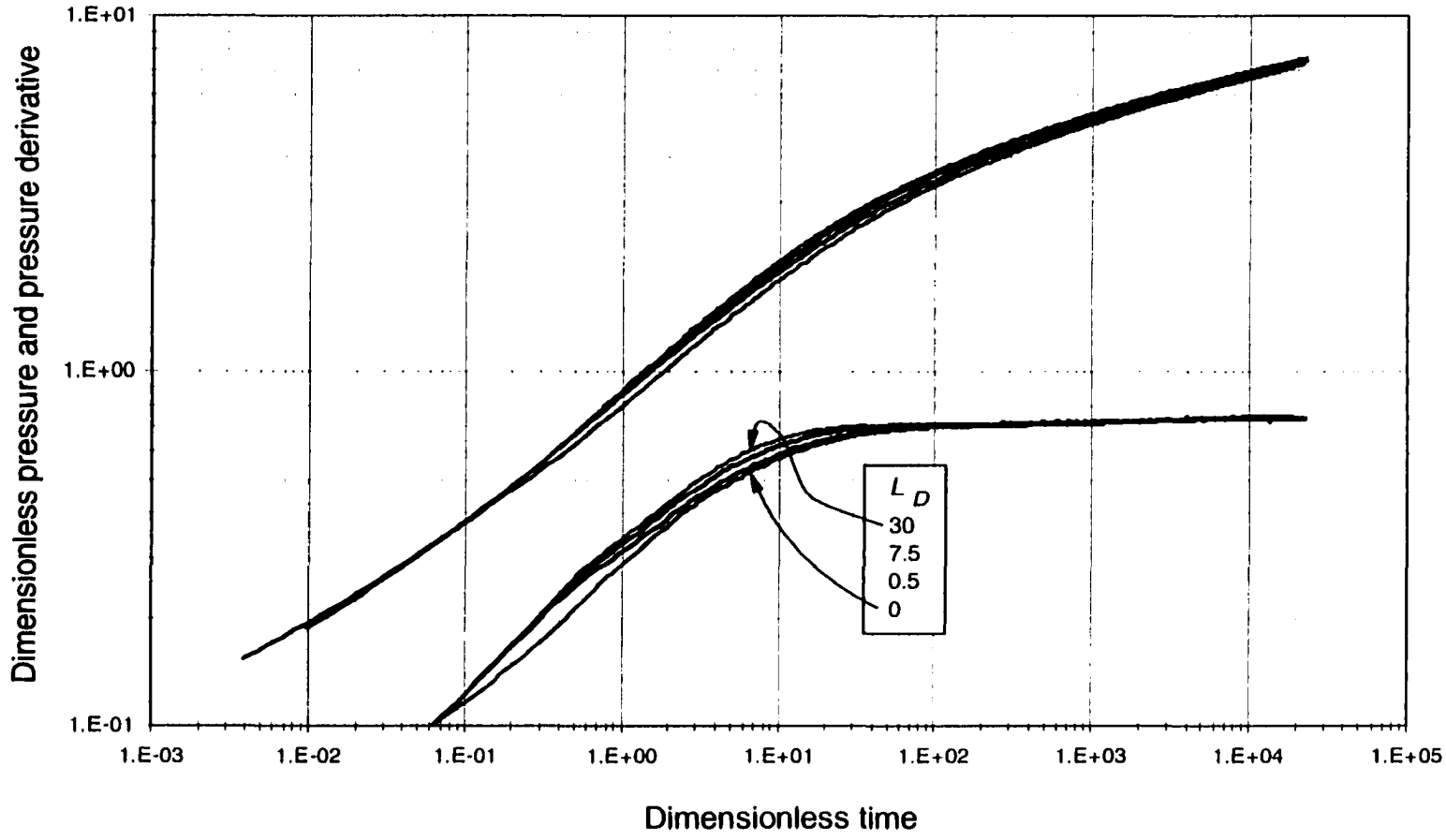

Fig. B.11.b. Dimensionless pressure and pressure derivative curve for a hydraulic fracture intersecting a fault at its fourth part forming an angle of 60°. C_{fD}=10

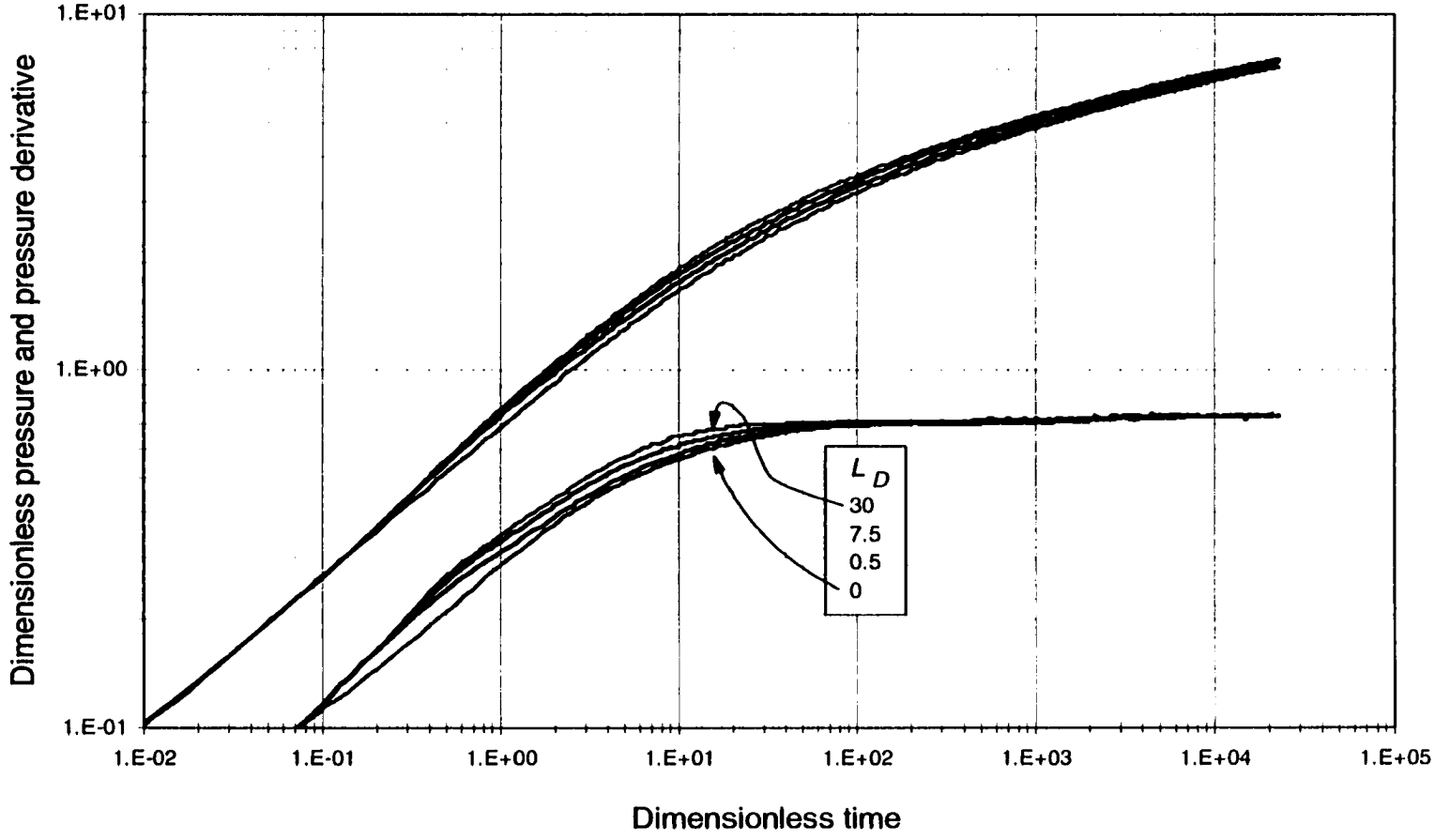

Fig. B.11.c. Dimensionless pressure and pressure derivative curve for a hydraulic fracture intersecting a fault at its fourth part forming an angle of 60°. C_D=50

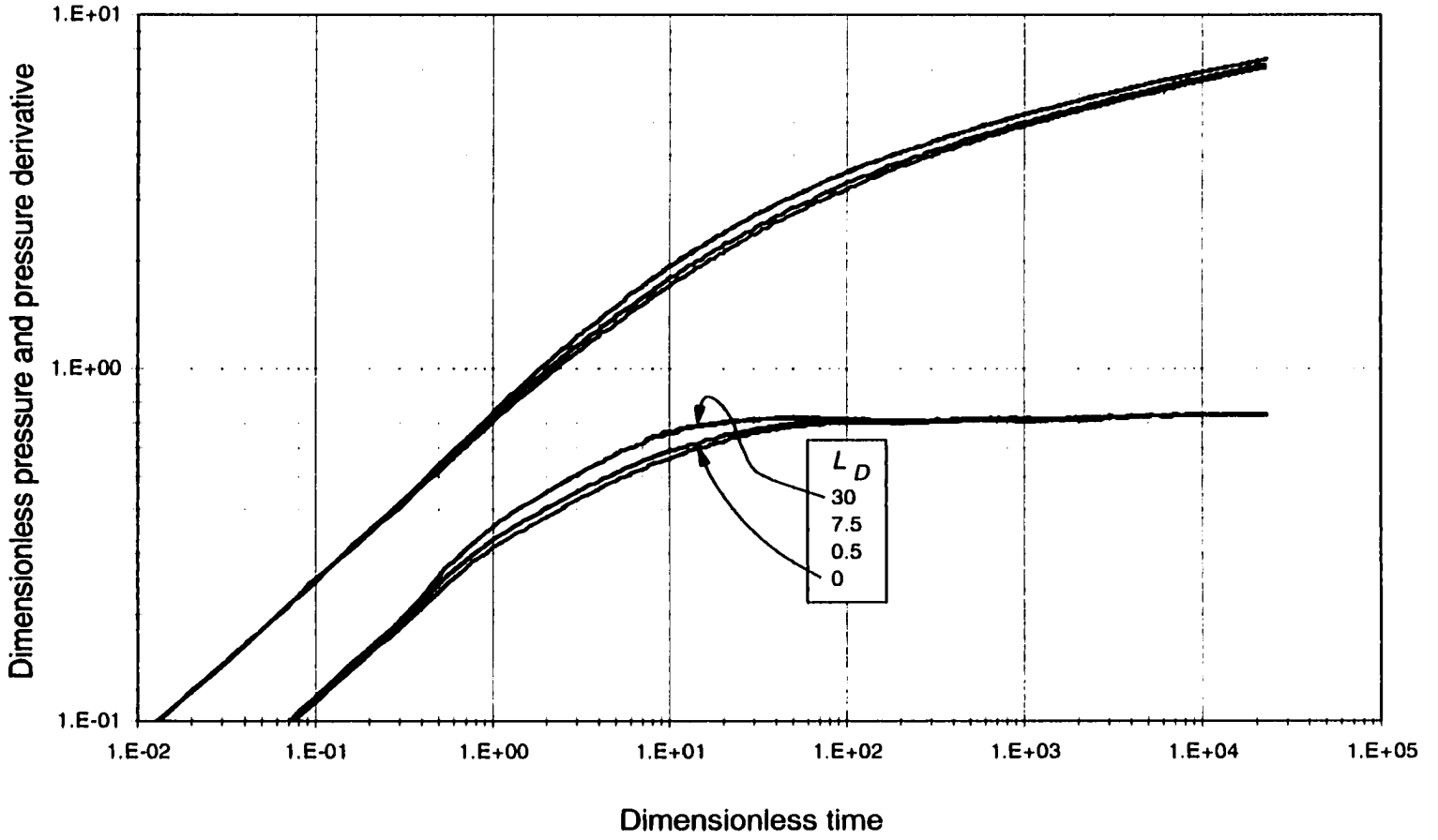

Fig. B.11.d. Dimensionless pressure and pressure derivative curve for a hydraulic fracture intersecting a fault at its fourth part forming an angle of 60°. C_{fD}=100

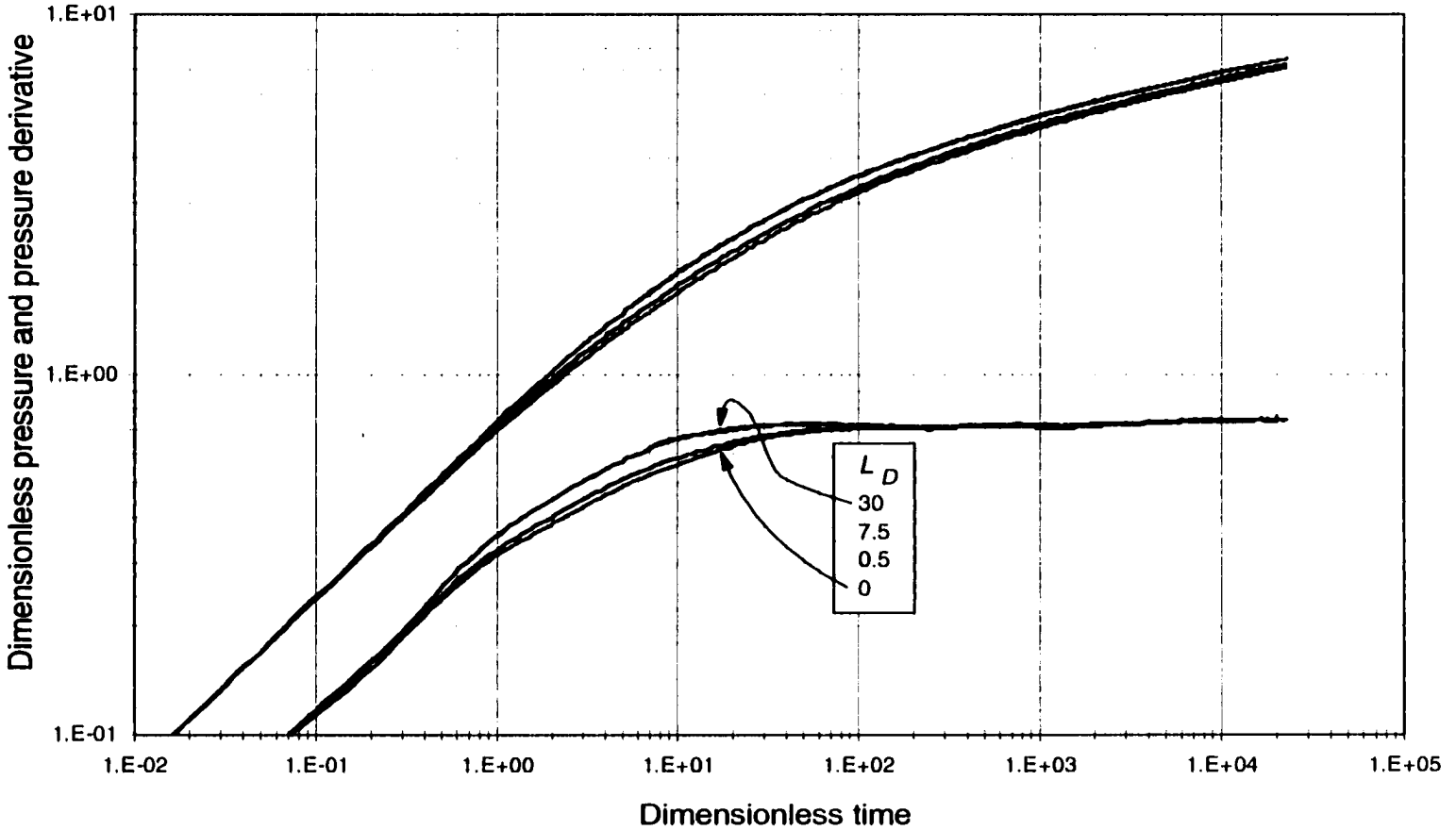

Fig. B.11.e. Dimensionless pressure and pressure derivative curve for a hydraulic fracture intersecting a fault at its fourth part forming an angle of 60°. C_{fD}=300

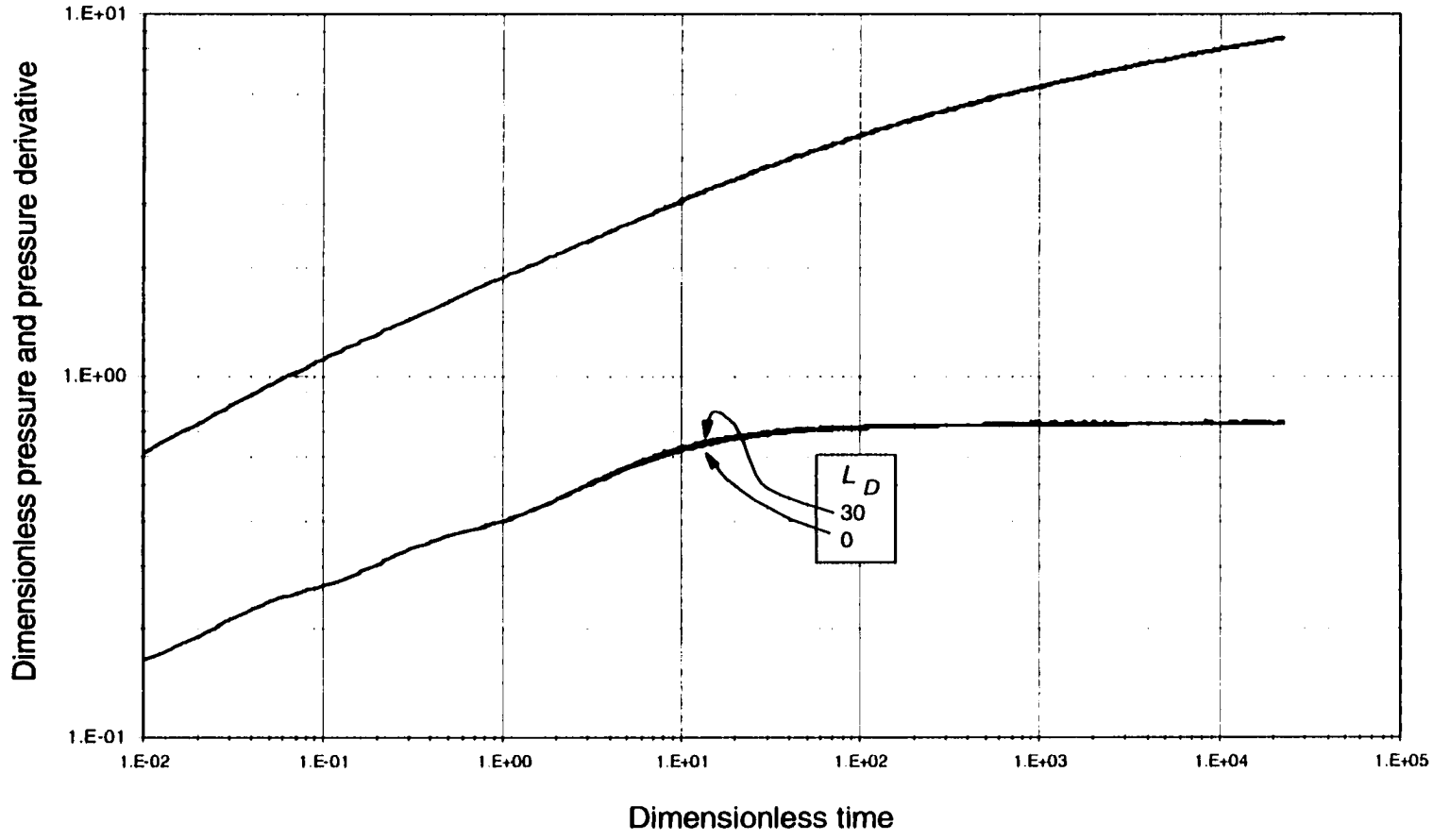

Fig. B.12.a. Dimensionless pressure and pressure derivative curve for a hydraulic fracture intersecting a fault at its tip forming an angle of 60°. $C_{fD}=1$

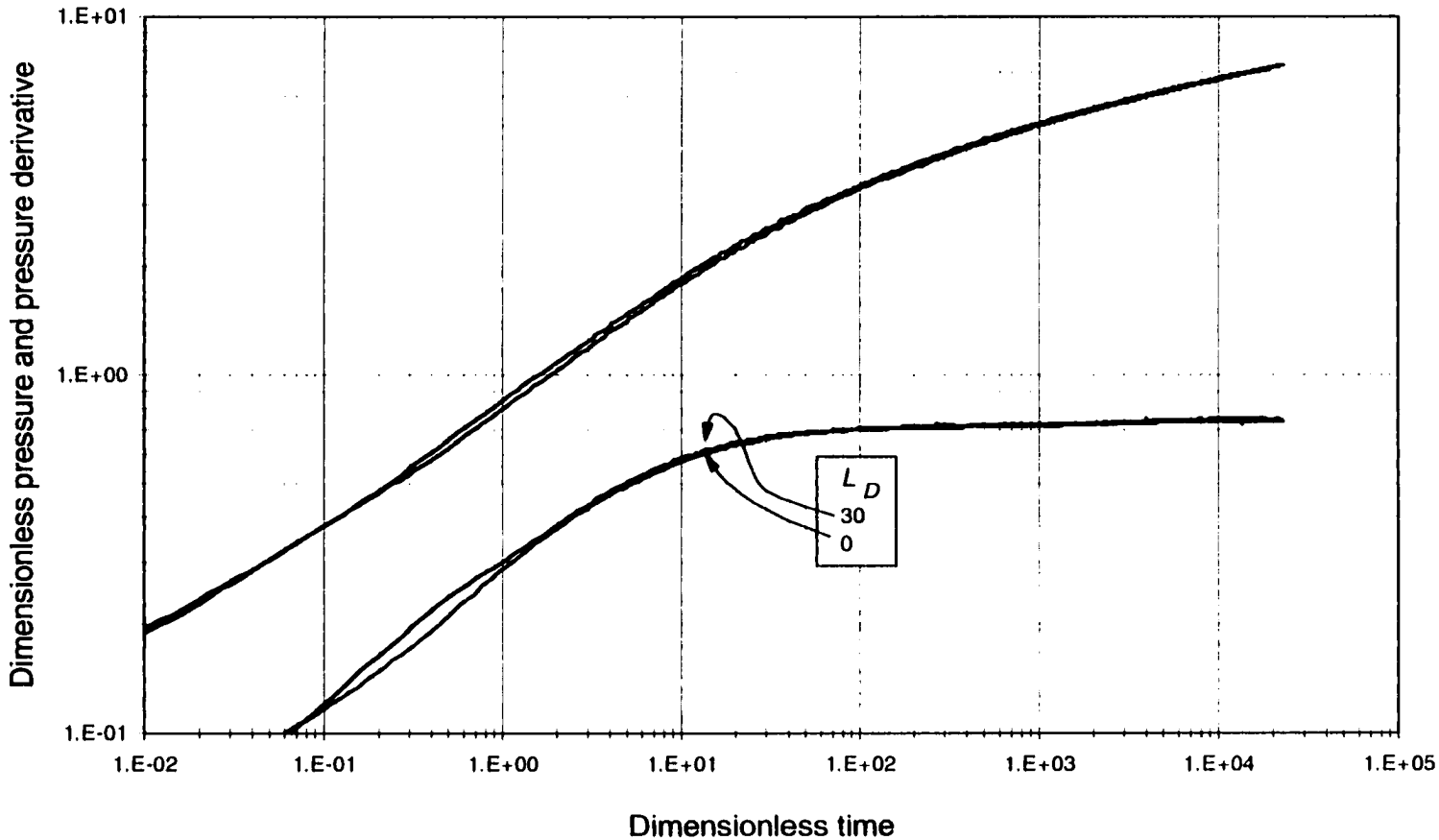

Fig. B.12.b. Dimensionless pressure and pressure derivative curve for a hydraulic fracture intersecting a fault at its tip forming an angle of 60°. C_D=10

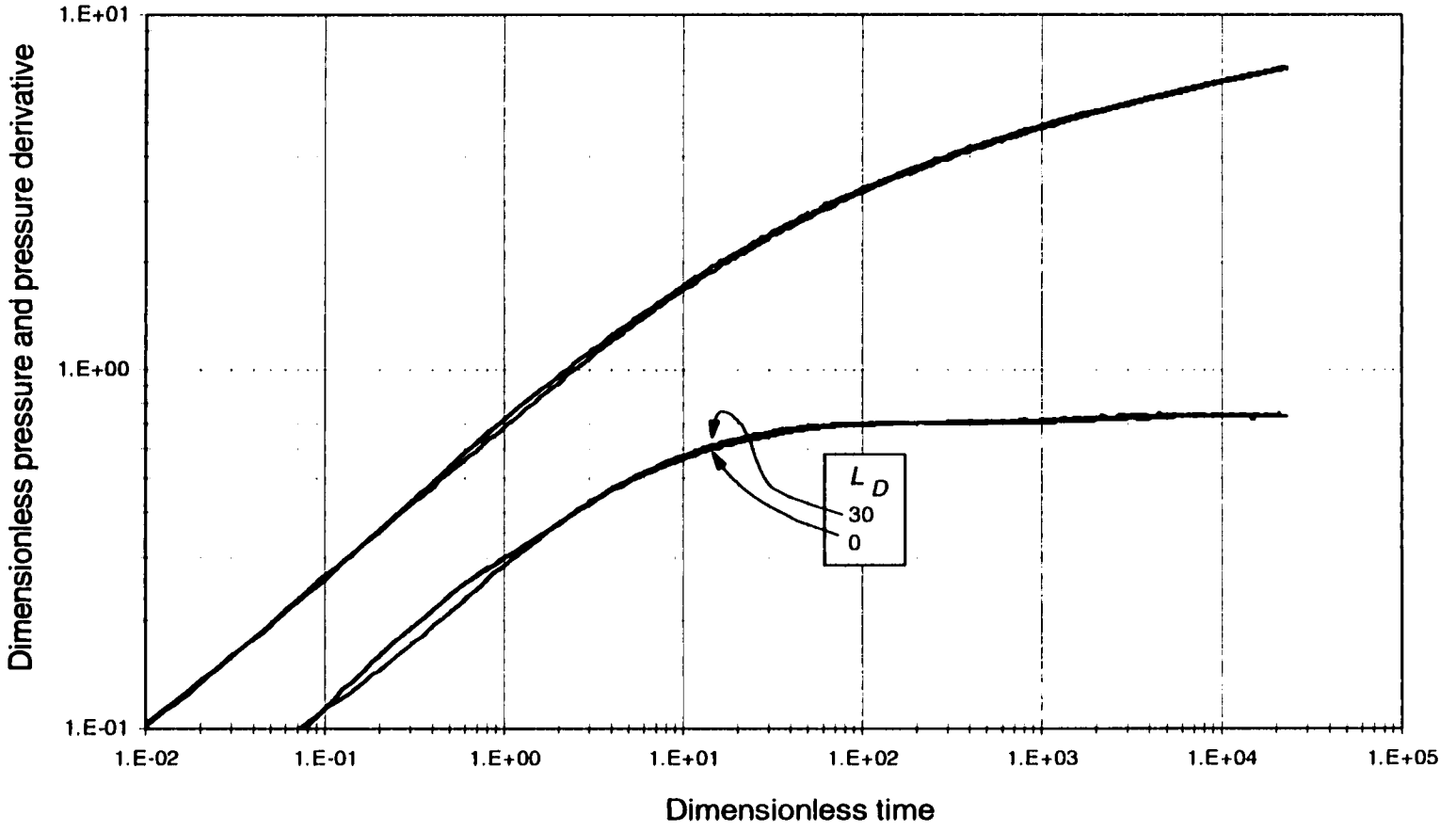

Fig. B.12.c. Dimensionless pressure and pressure derivative curve for a hydraulic fracture intersecting a fault at its tip forming an angle of 60°. C_{fD}=50

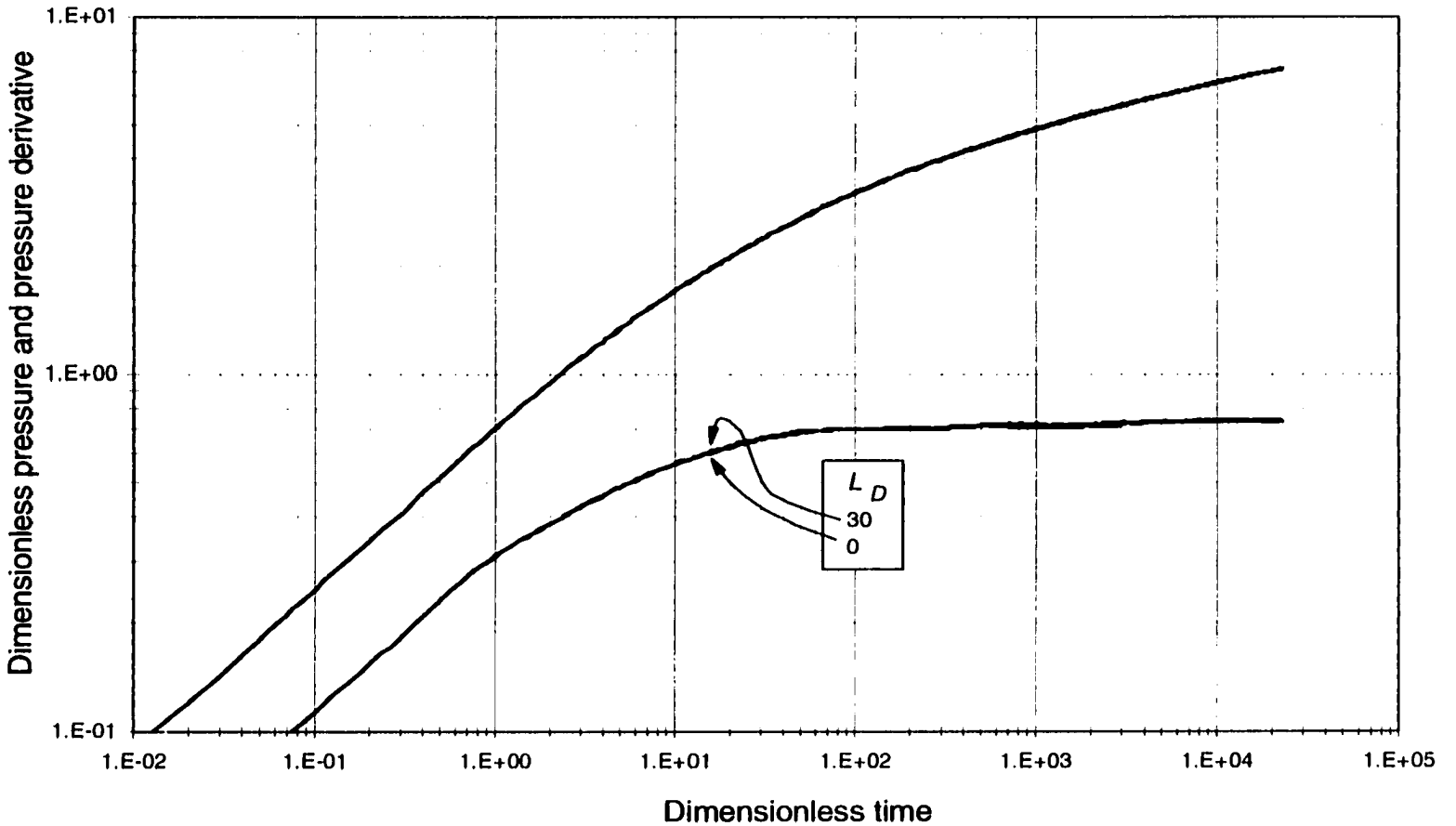

Fig. B.12.d. Dimensionless pressure and pressure derivative curve for a hydraulic fracture intersecting a fault at its tip forming an angle of 60°. C_D=100

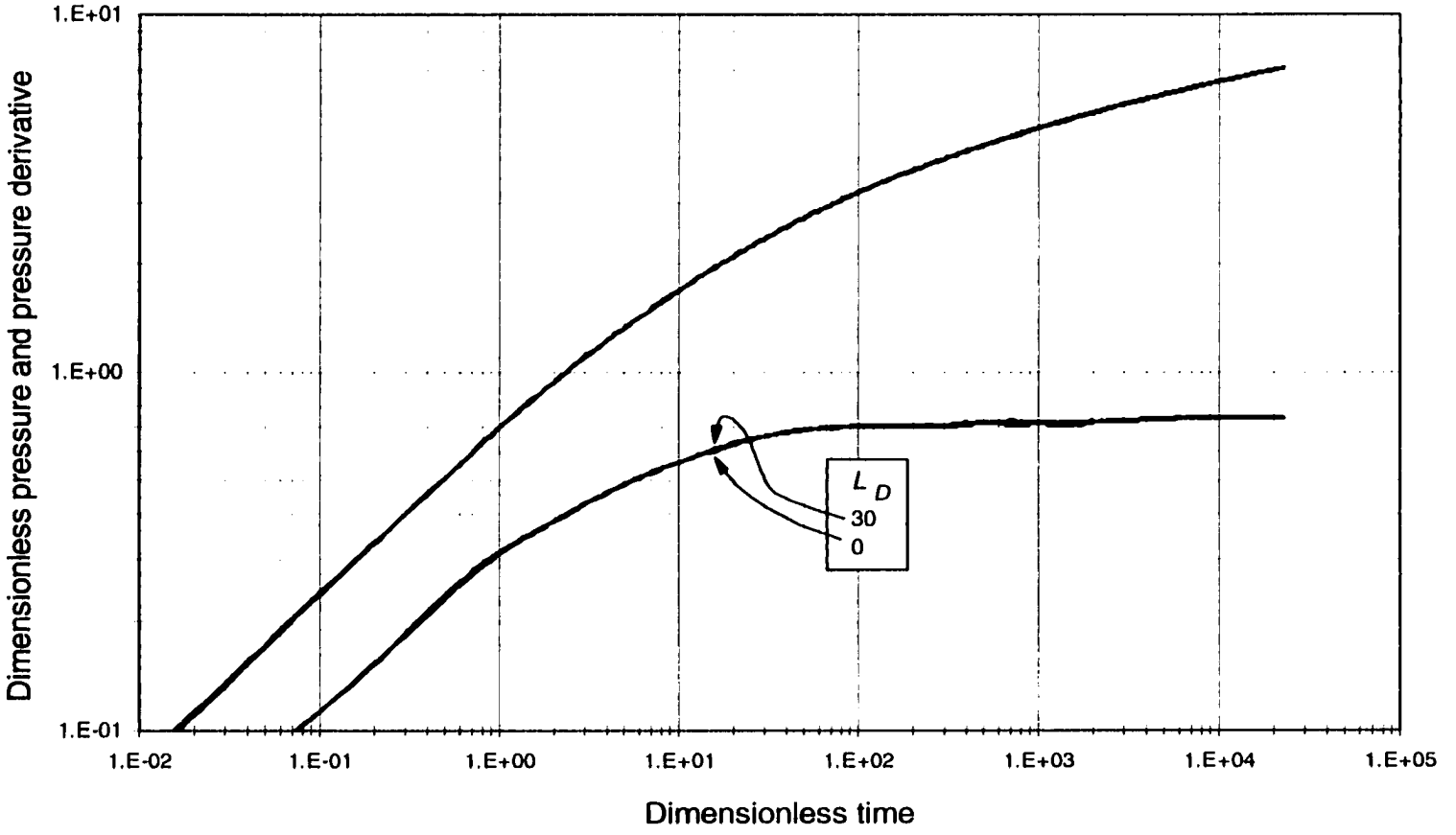

Fig. B.12.e. Dimensionless pressure and pressure derivative curve for a hydraulic fracture intersecting a fault at its tip forming an angle of 60°. C_D=300

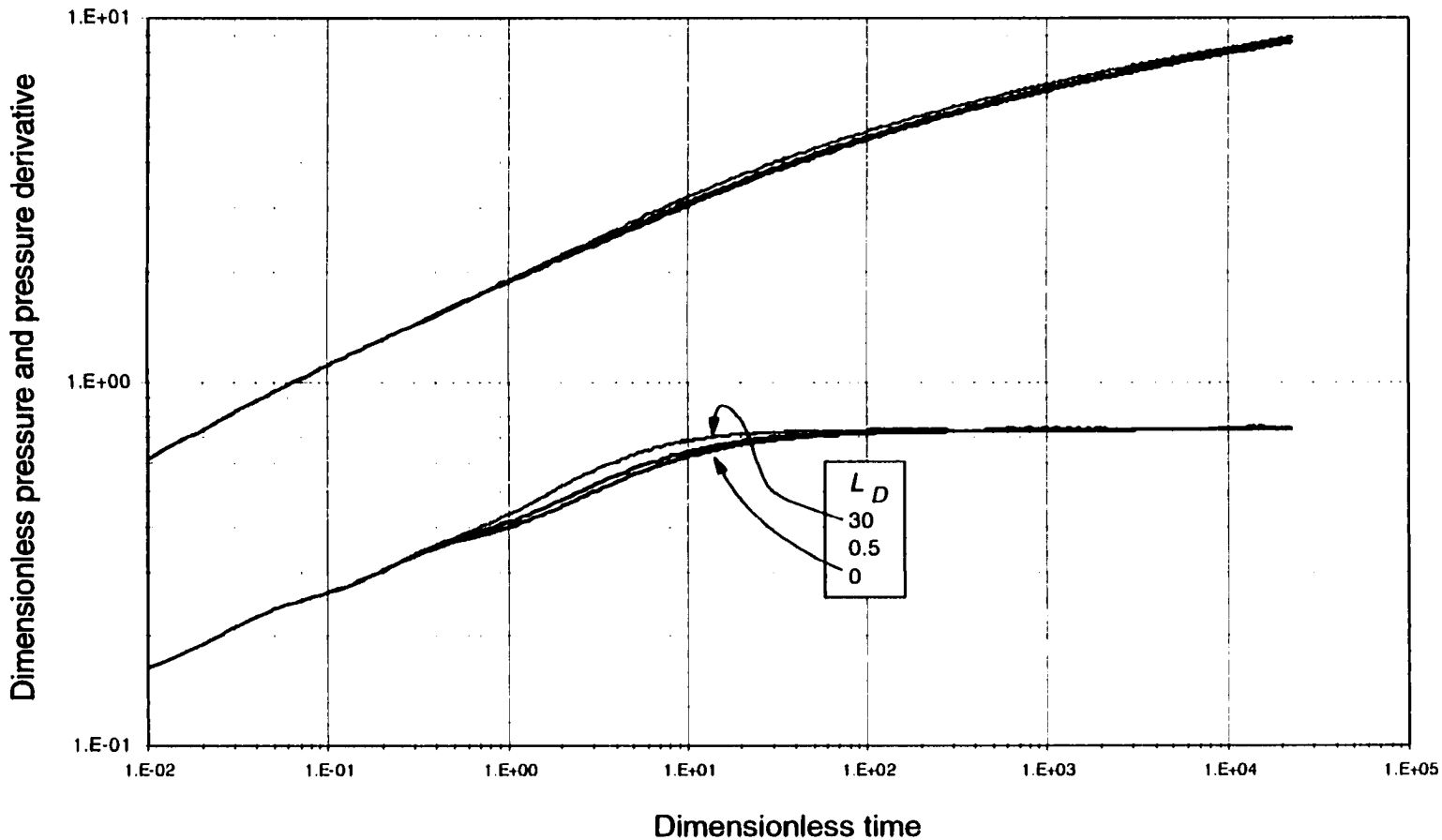

Fig. B.13.a. Dimensionless pressure and pressure derivative curve for a hydraulic fracture intersecting a fault at its middle part forming an angle of 30°. C_D=1

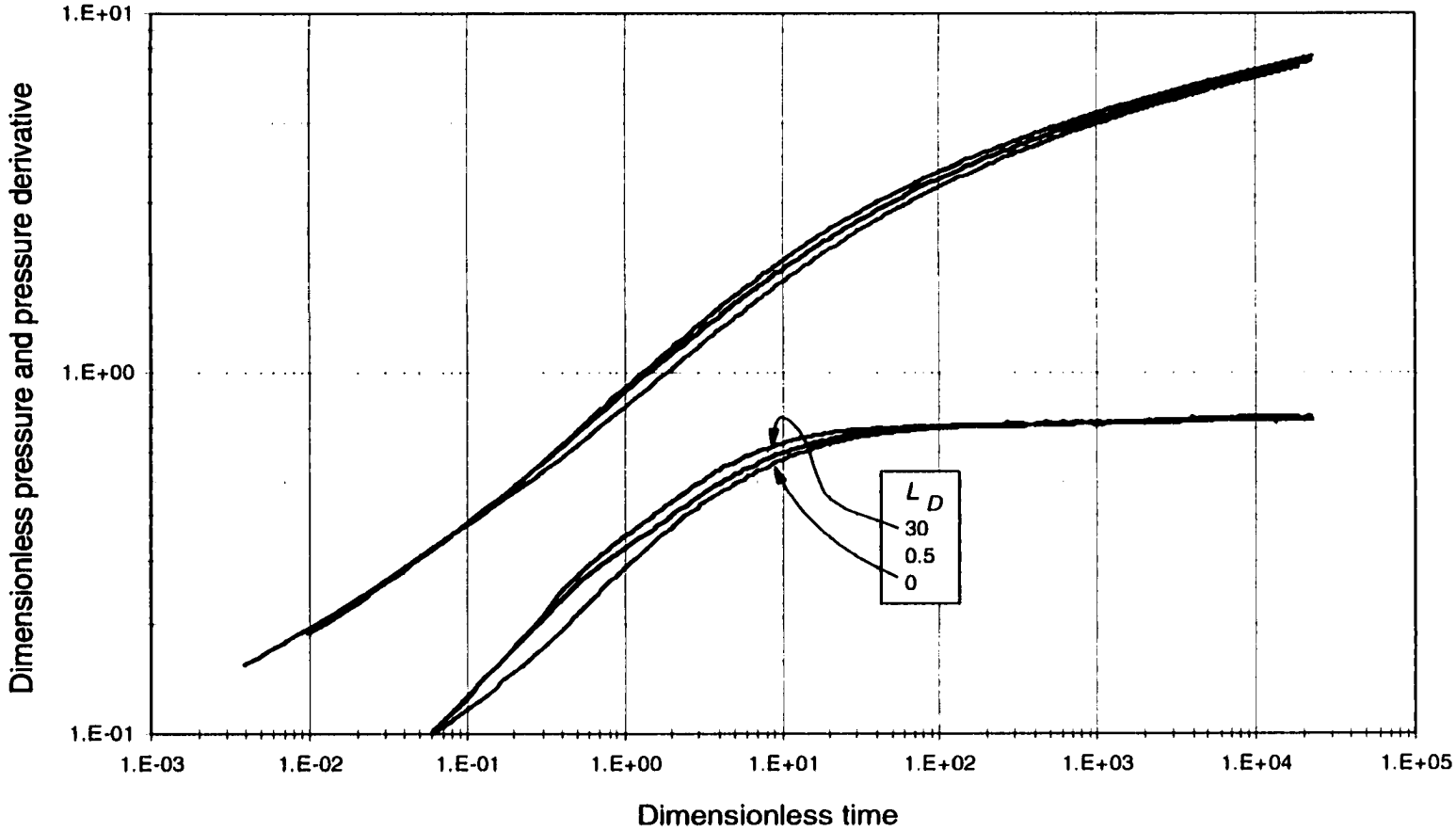

Fig. B.13.b. Dimensionless pressure and pressure derivative curve for a hydraulic fracture intersecting a fault at its middle part forming an angle of 30°. C_D=10

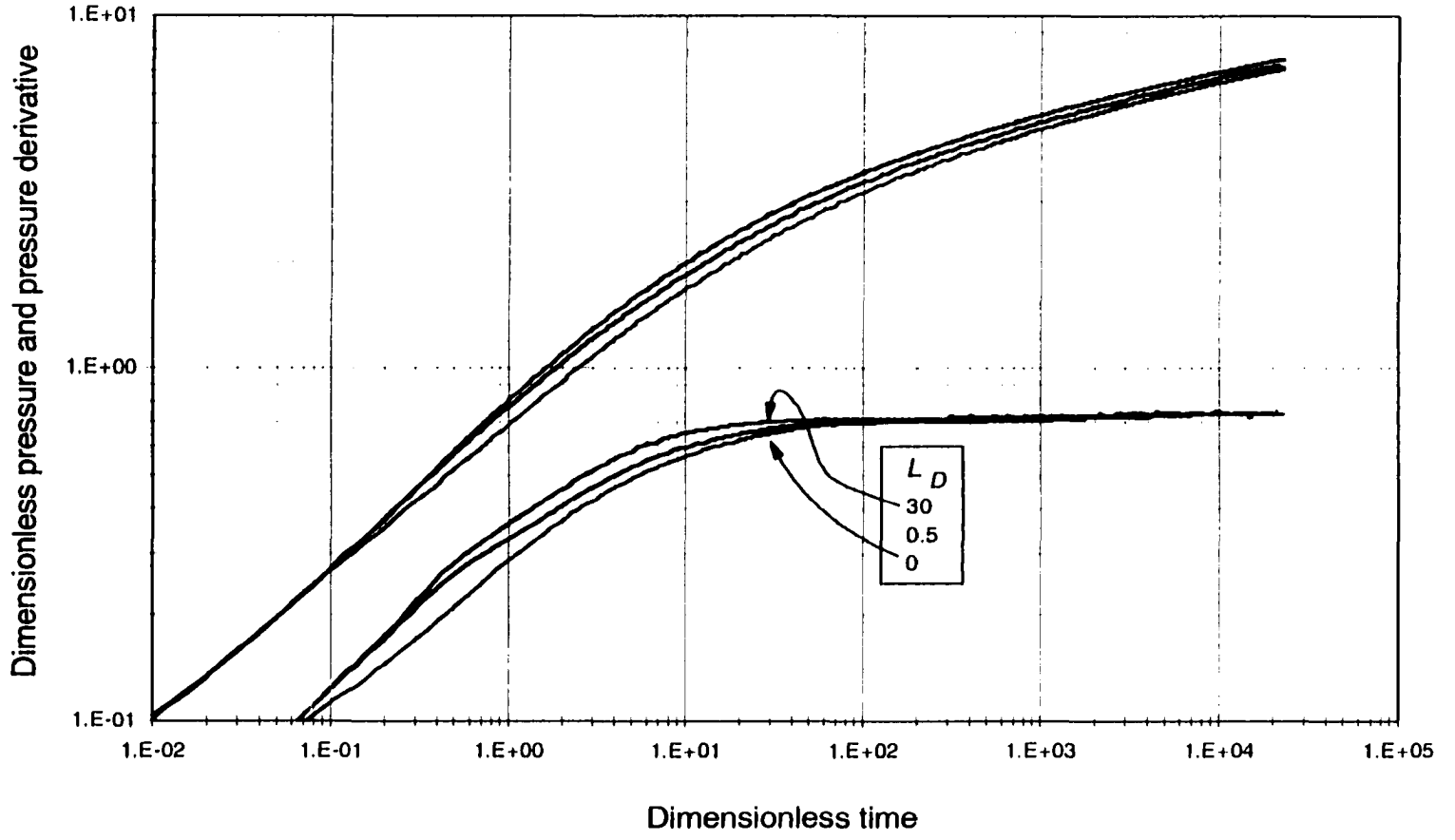

Fig. B.13.c. Dimensionless pressure and pressure derivative curve for a hydraulic fracture intersecting a fault at its middle part forming an angle of 30°. C_{fD}=50

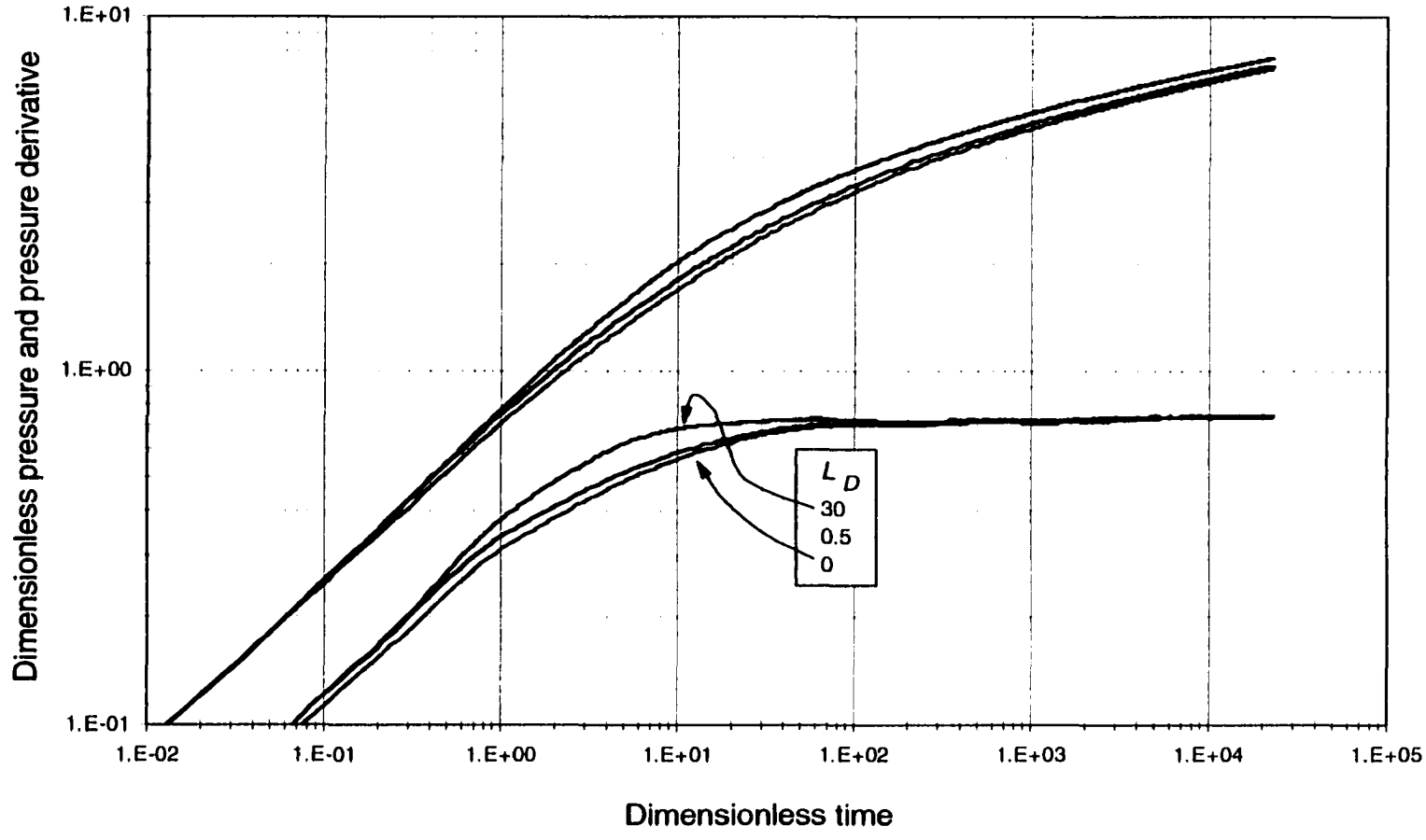

Fig. B.13.d. Dimensionless pressure and pressure derivative curve for a hydraulic fracture intersecting a fault at its middle part forming an angle of 30°. C_D=100

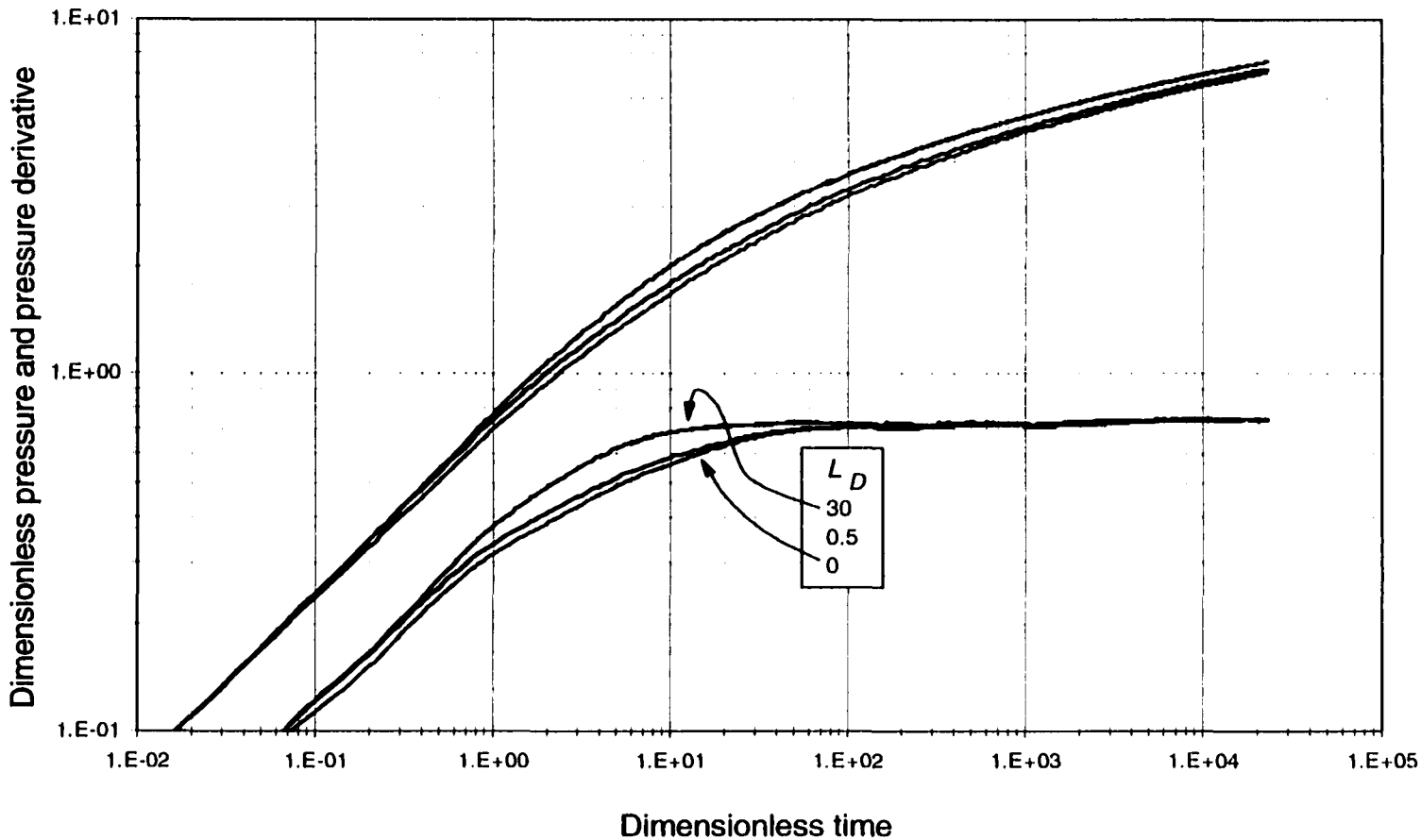

Fig. B.13.e. Dimensionless pressure and pressure derivative curve for a hydraulic fracture intersecting a fault at its middle part forming an angle of 30°. C_{fD}=300

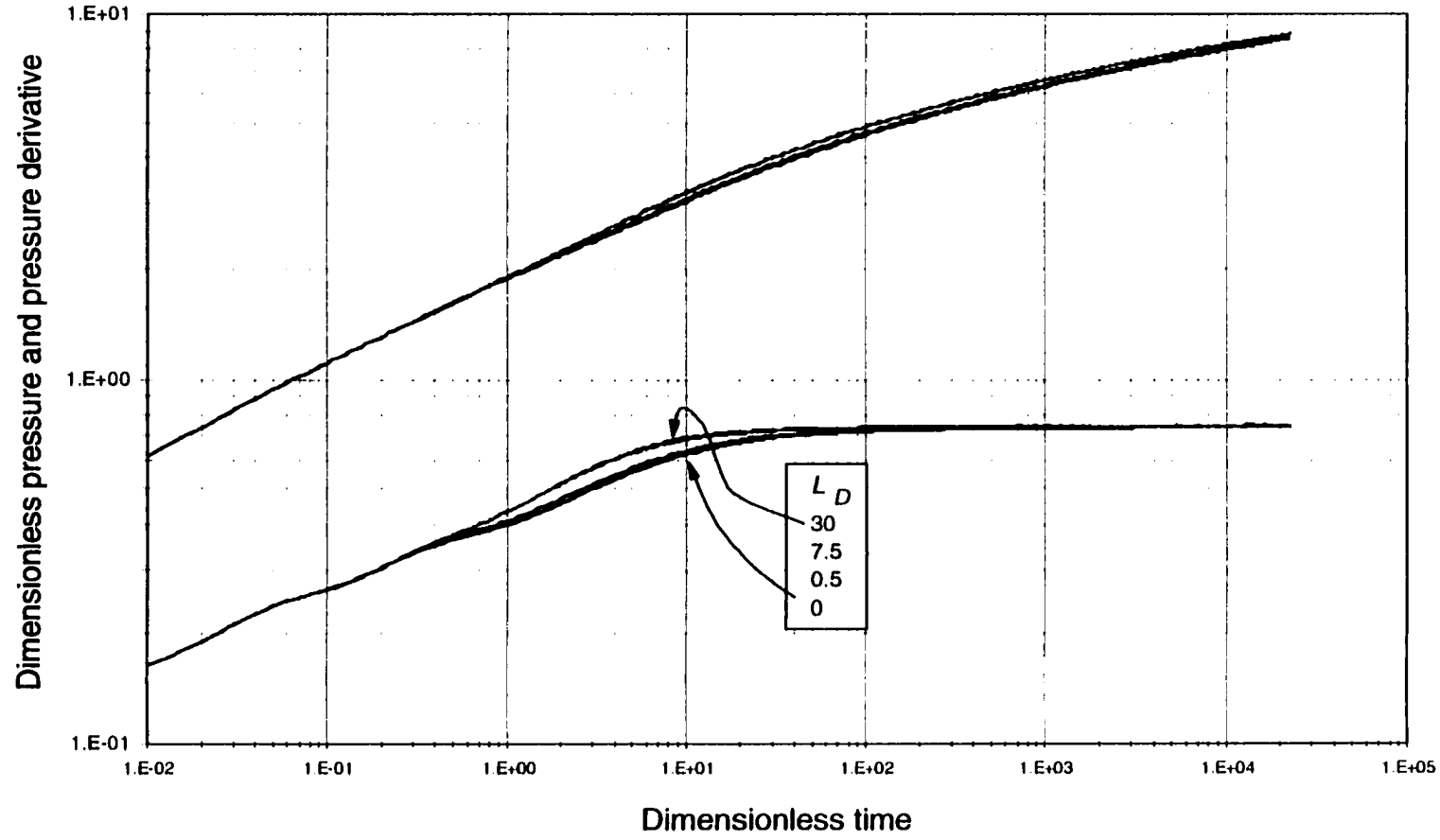

Fig. B.14.a. Dimensionless pressure and pressure derivative curve for a hydraulic fracture intersecting a fault at its fourth part forming an angle of 30°. C_D=1

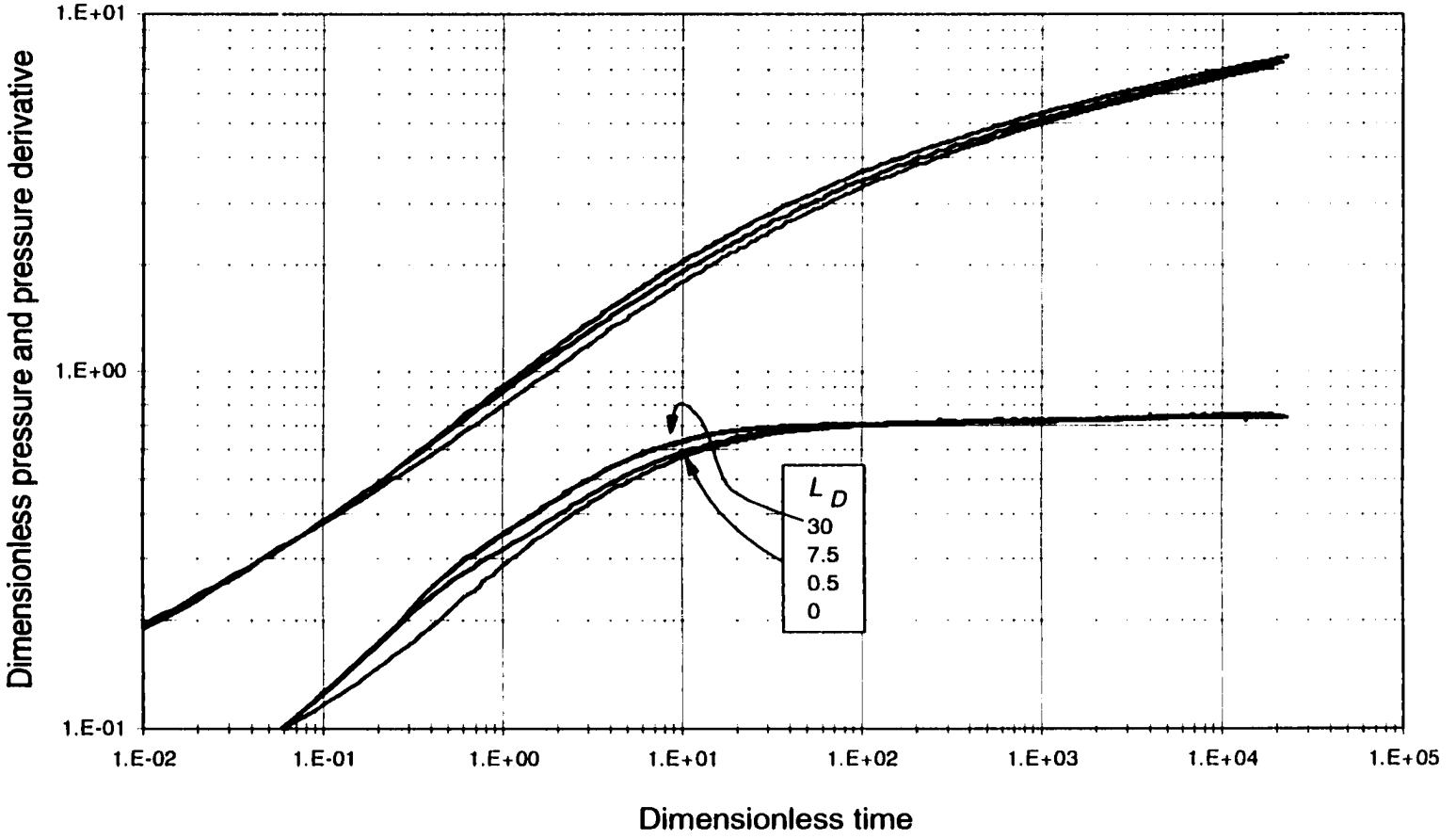

Fig. B.14.b. Dimensionless pressure and pressure derivative curve for a hydraulic fracture intersecting a fault at its fourth part forming an angle of 30°. C_D=10

Fig. B.14.c: Dimensionless pressure and pressure derivative curve for a hydraulic fracture intersecting a fault at its fourth part forming an angle of 30°. C_D=50

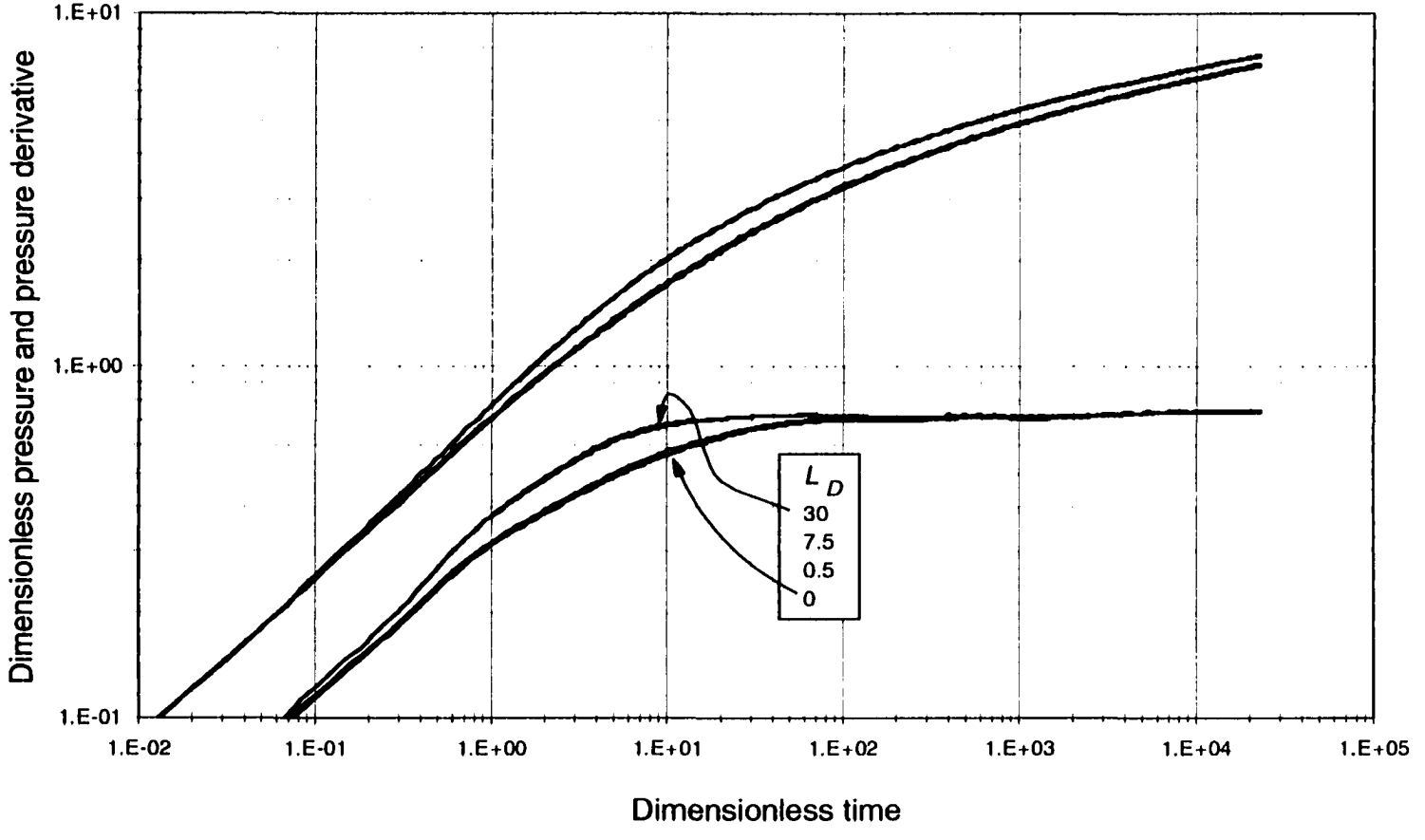

Fig. B.14.d. Dimensionless pressure and pressure derivative curve for a hydraulic fracture intersecting a fault at its fourth part forming an angle of 30°. C_D=100

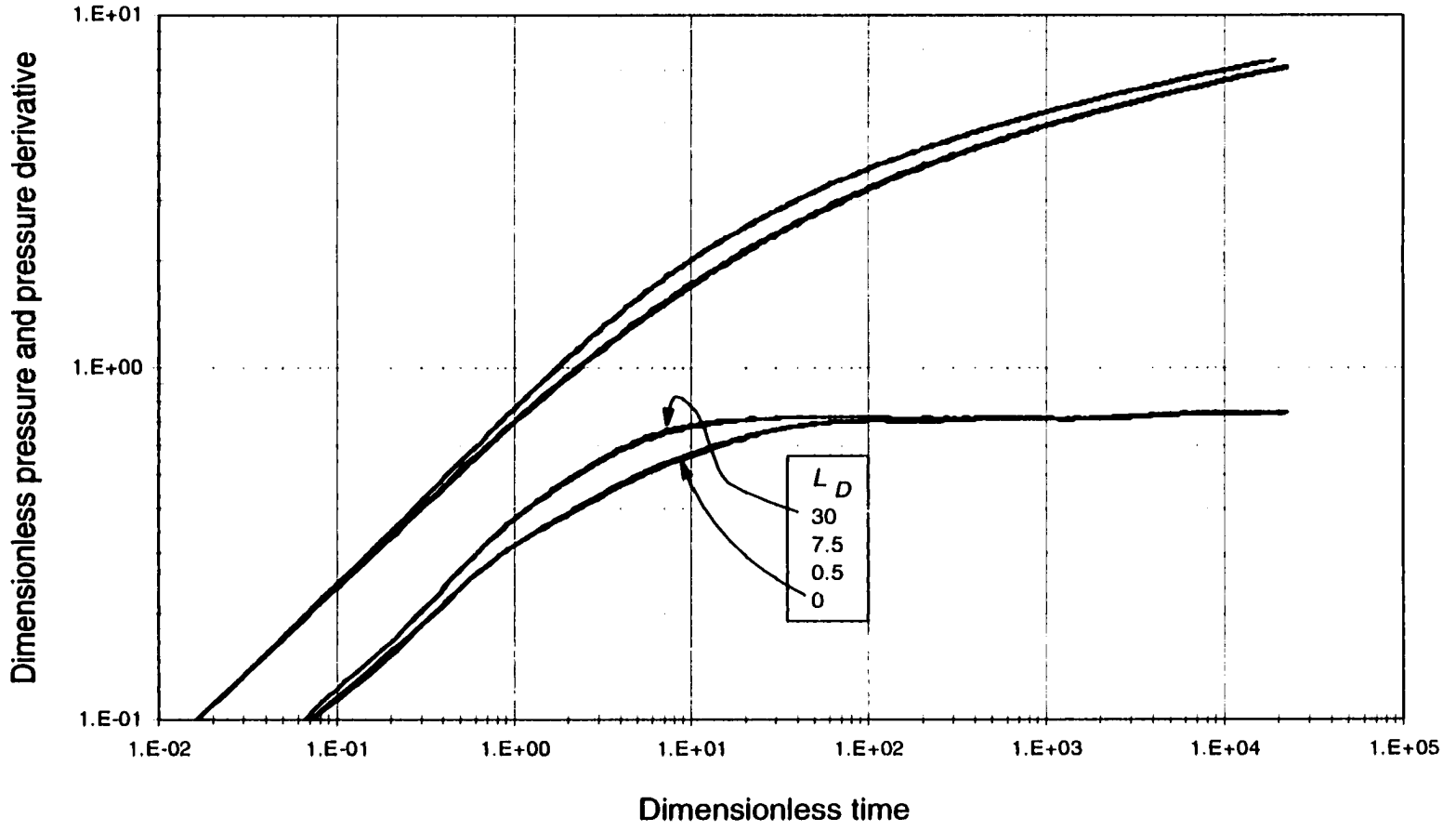

Fig. B.14.e. Dimensionless pressure and pressure derivative curve for a hydraulic fracture intersecting a fault at its fourth part forming an angle of 30°. C_{fD}=300

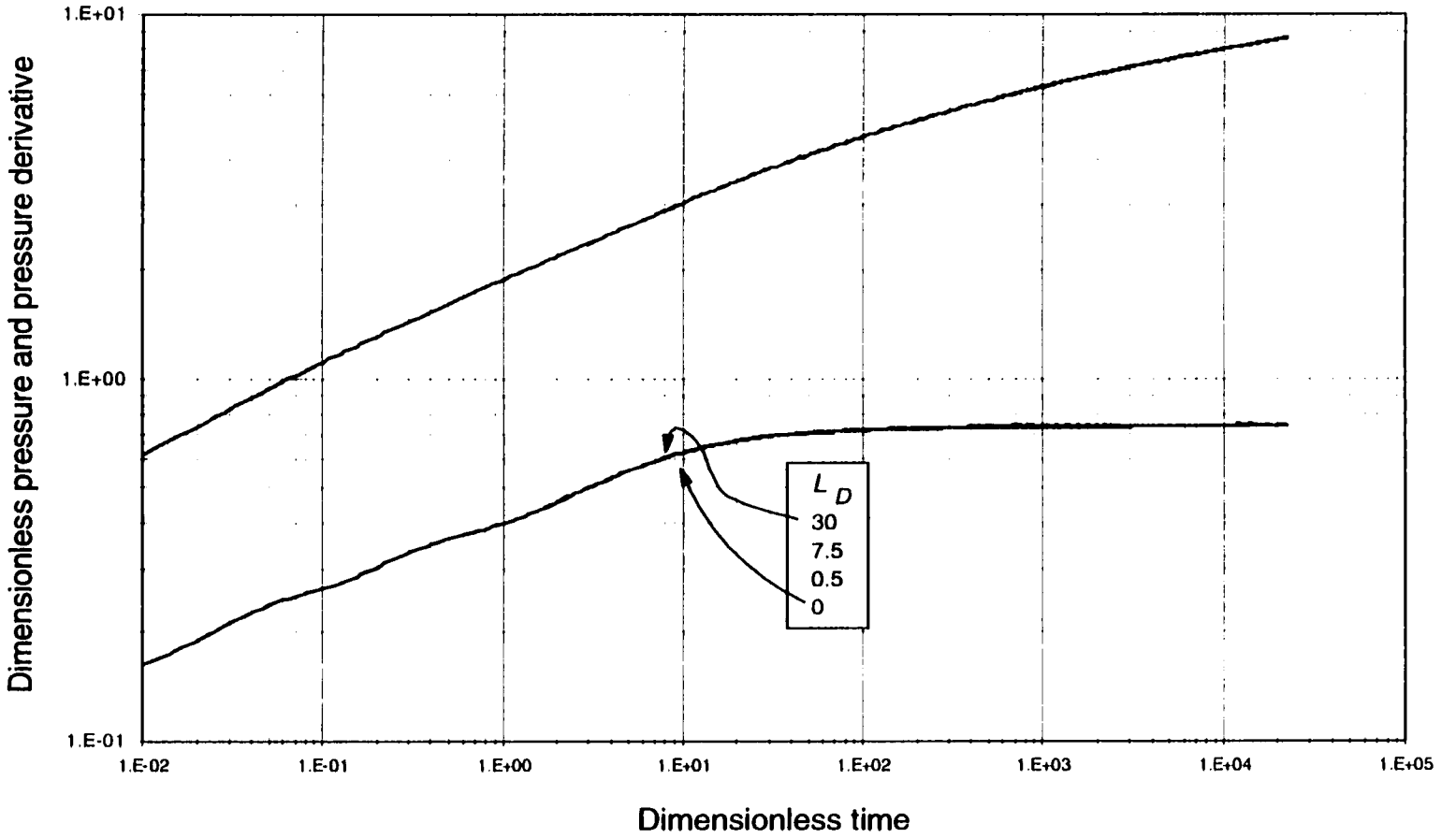

Fig. B.15.a. Dimensionless pressure and pressure derivative curve for a hydraulic fracture intersecting a fault at its tip forming an angle of 30°. $C_{fD}=1$

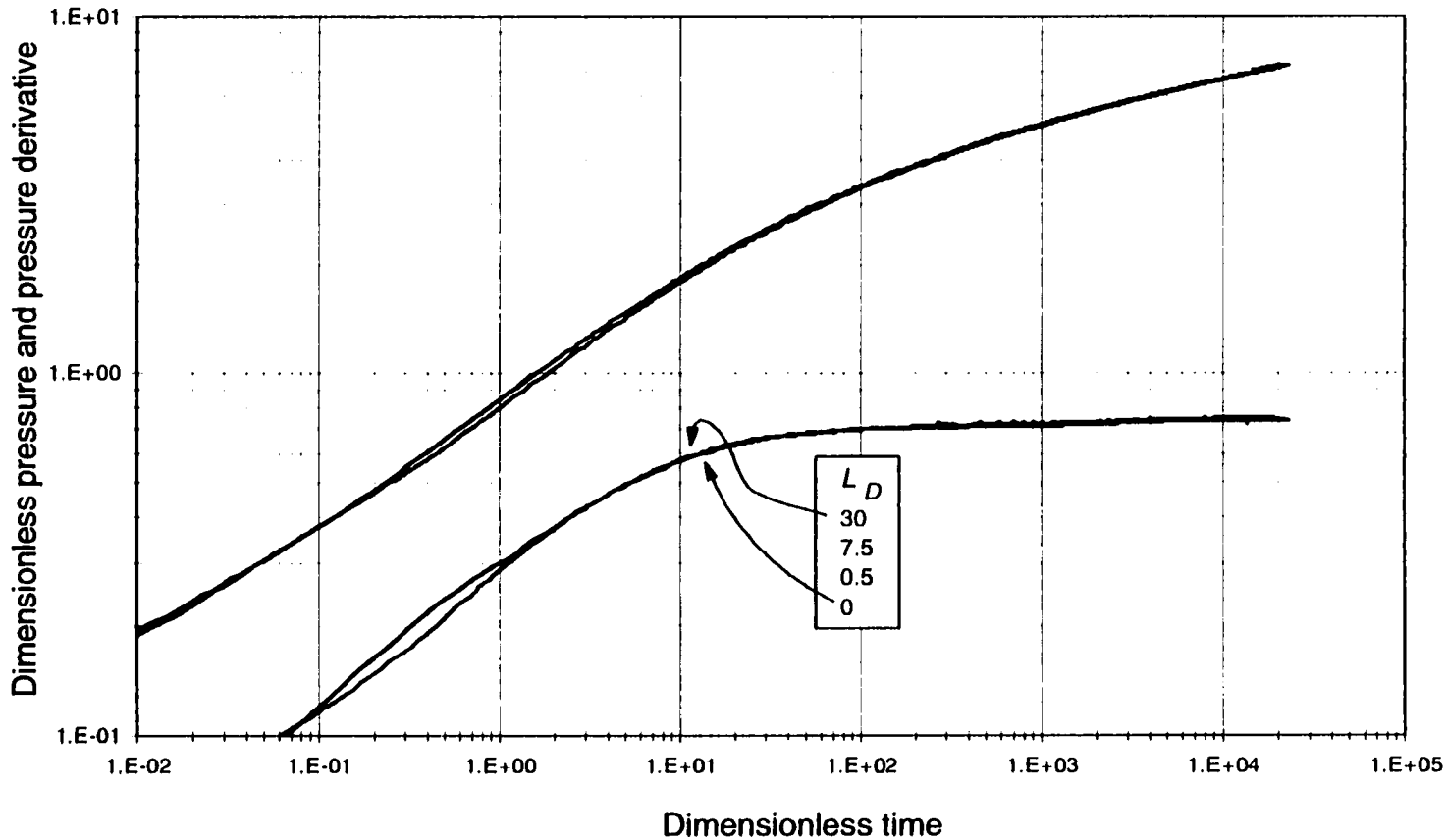

Fig. B.15.b. Dimensionless pressure and pressure derivative curve for a hydraulic fracture intersecting a fault at its tip forming an angle of 30°. C_{fD}=10

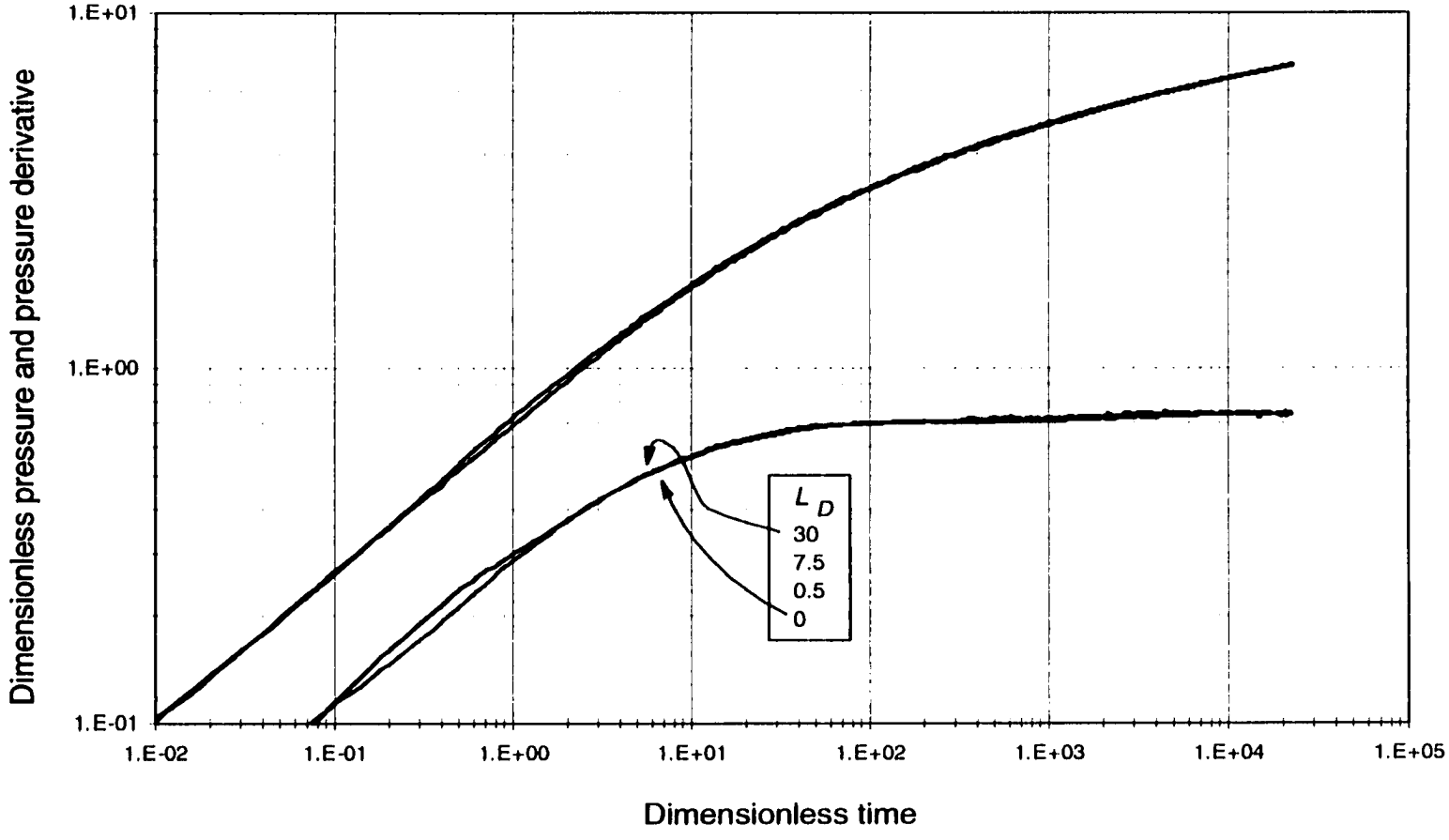

Fig. B.15.c. Dimensionless pressure and pressure derivative curve for a hydraulic fracture intersecting a fault at its tip forming an angle of 30°. C_D=50

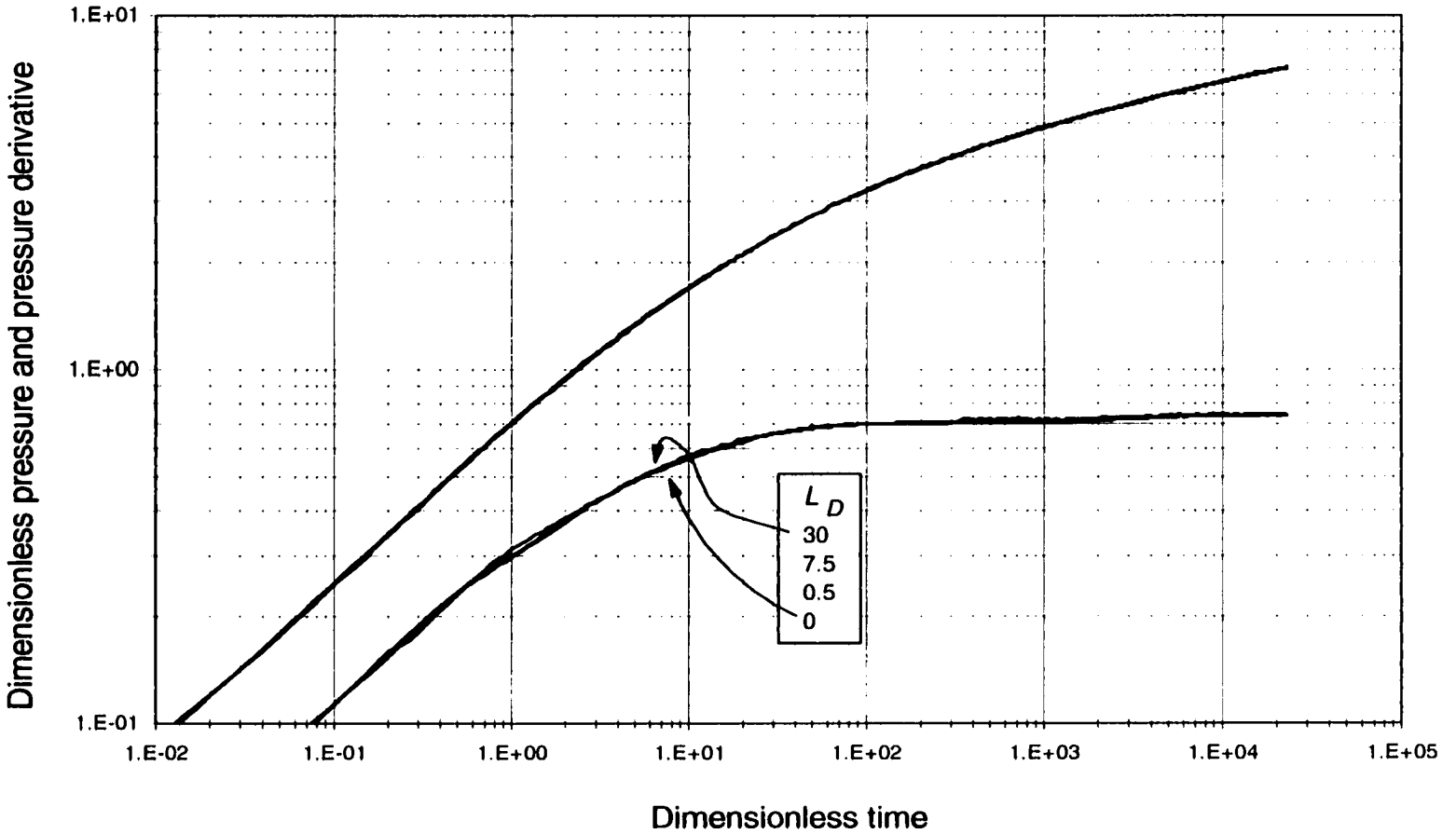

Fig. B.15.d. Dimensionless pressure and pressure derivative curve for a hydraulic fracture intersecting a fault at its tip forming an angle of 30°. C_D=100

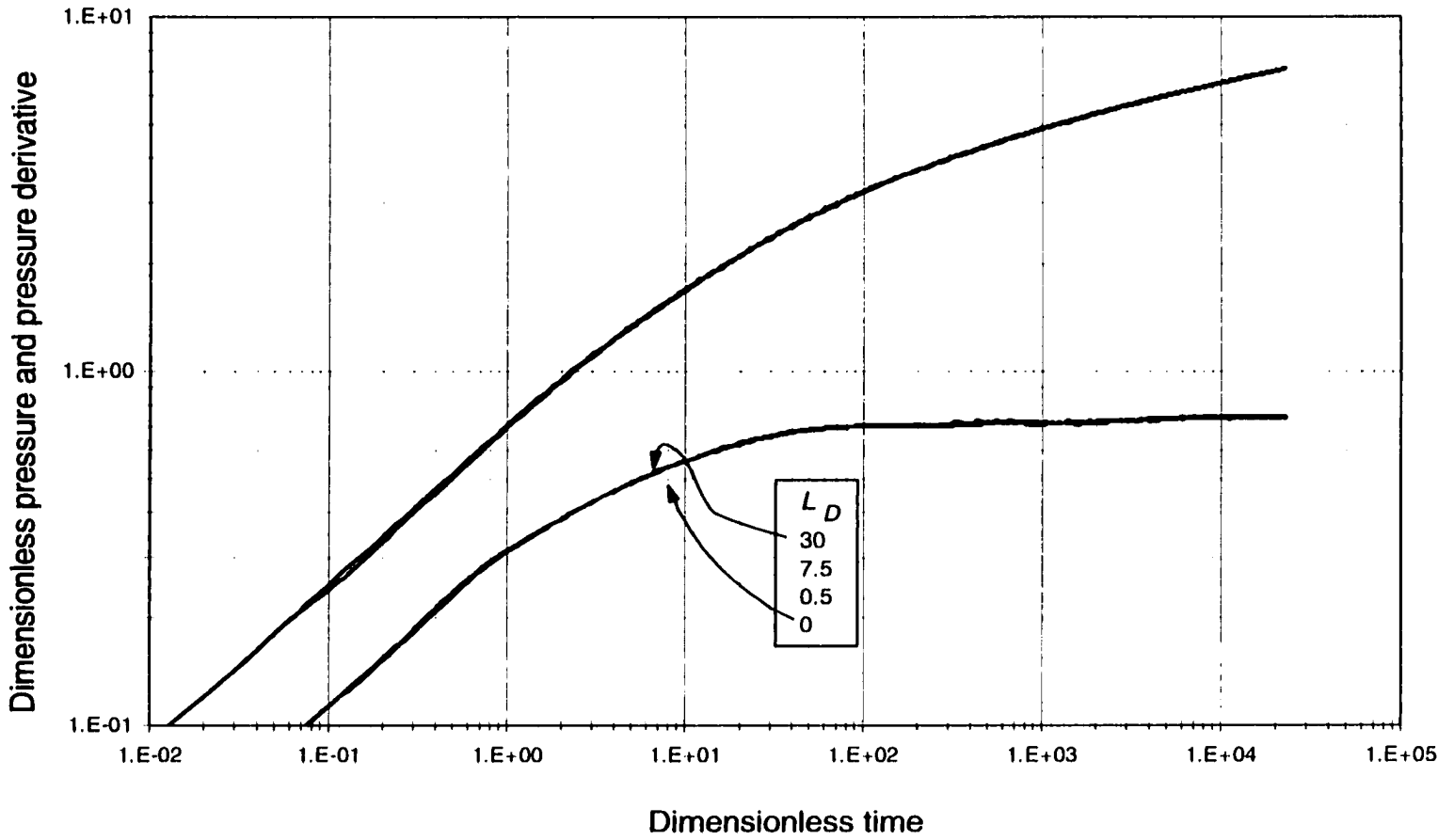

Fig. B.15.e. Dimensionless pressure and pressure derivative curve for a hydraulic fracture intersecting a fault at its tip forming an angle of 30°. C_{fD}=300

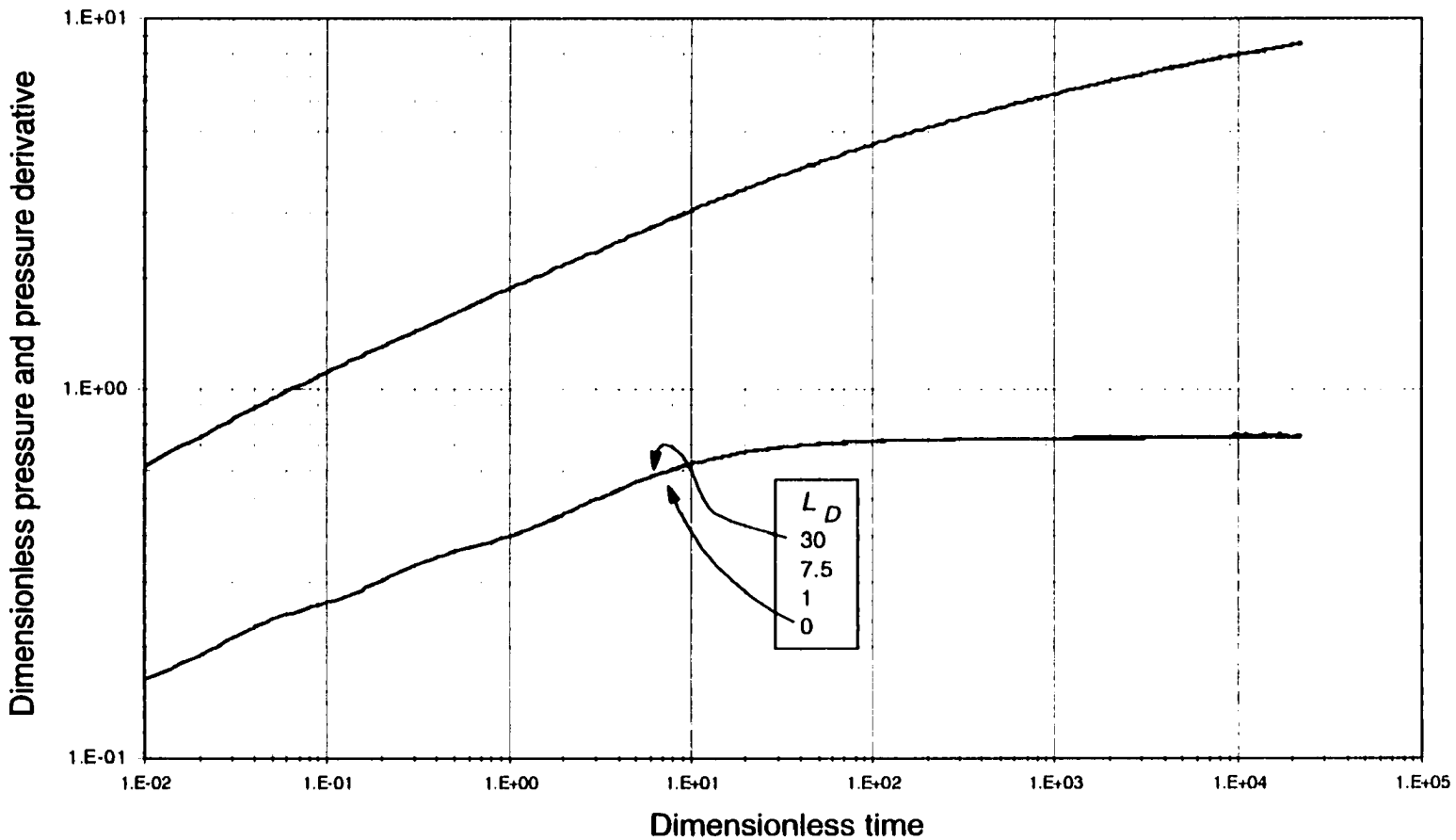

Fig. B.16.a. Dimensionless pressure and pressure derivative curve for a hydraulic fracture intersecting a fault at its tip forming an angle of 0°. $C_{fD}=1$

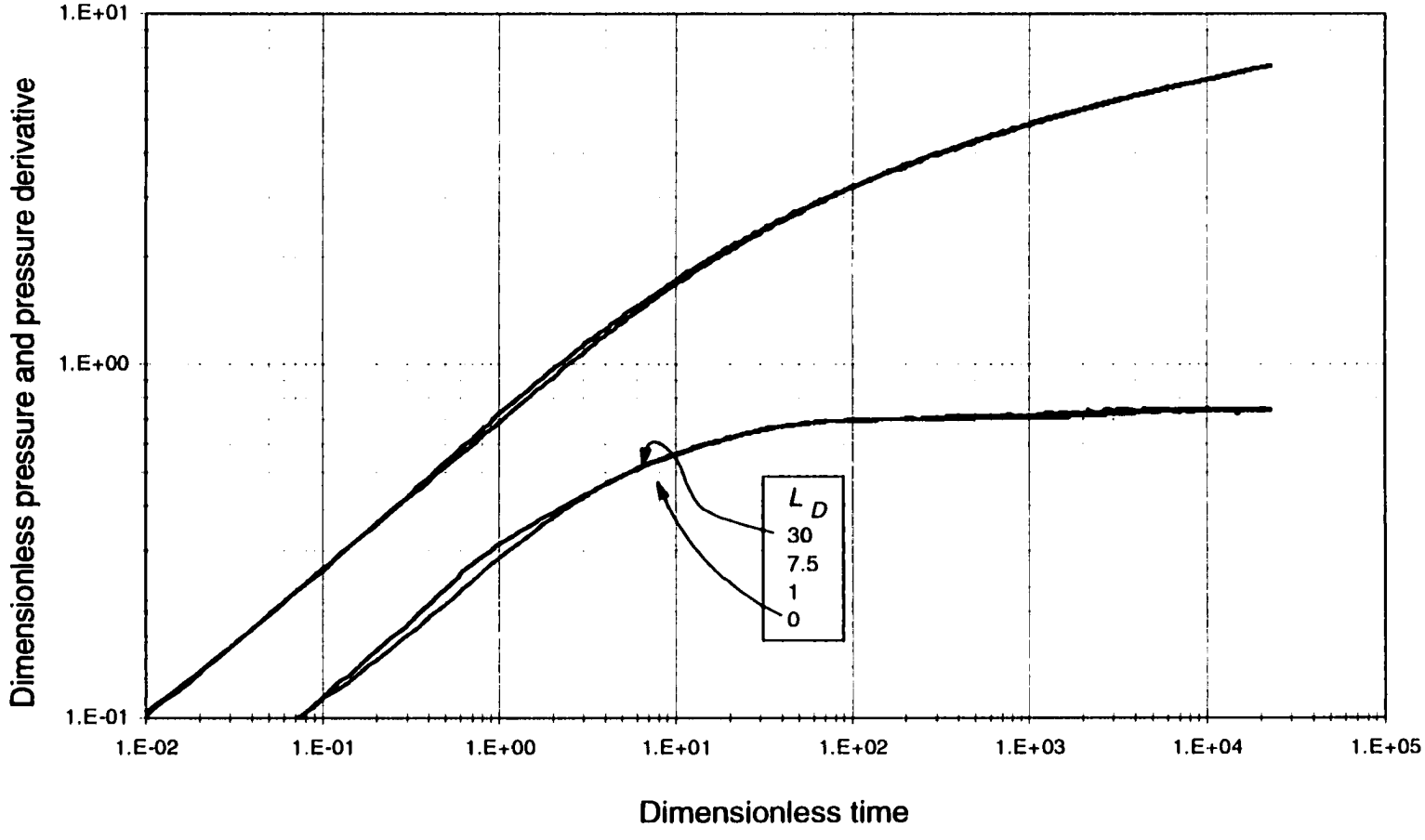

Fig. B.17.b. Dimensionless pressure and pressure derivative curve for a hydraulic fracture intersecting a fault at its tip forming an angle of 0°. C_{fD}=50

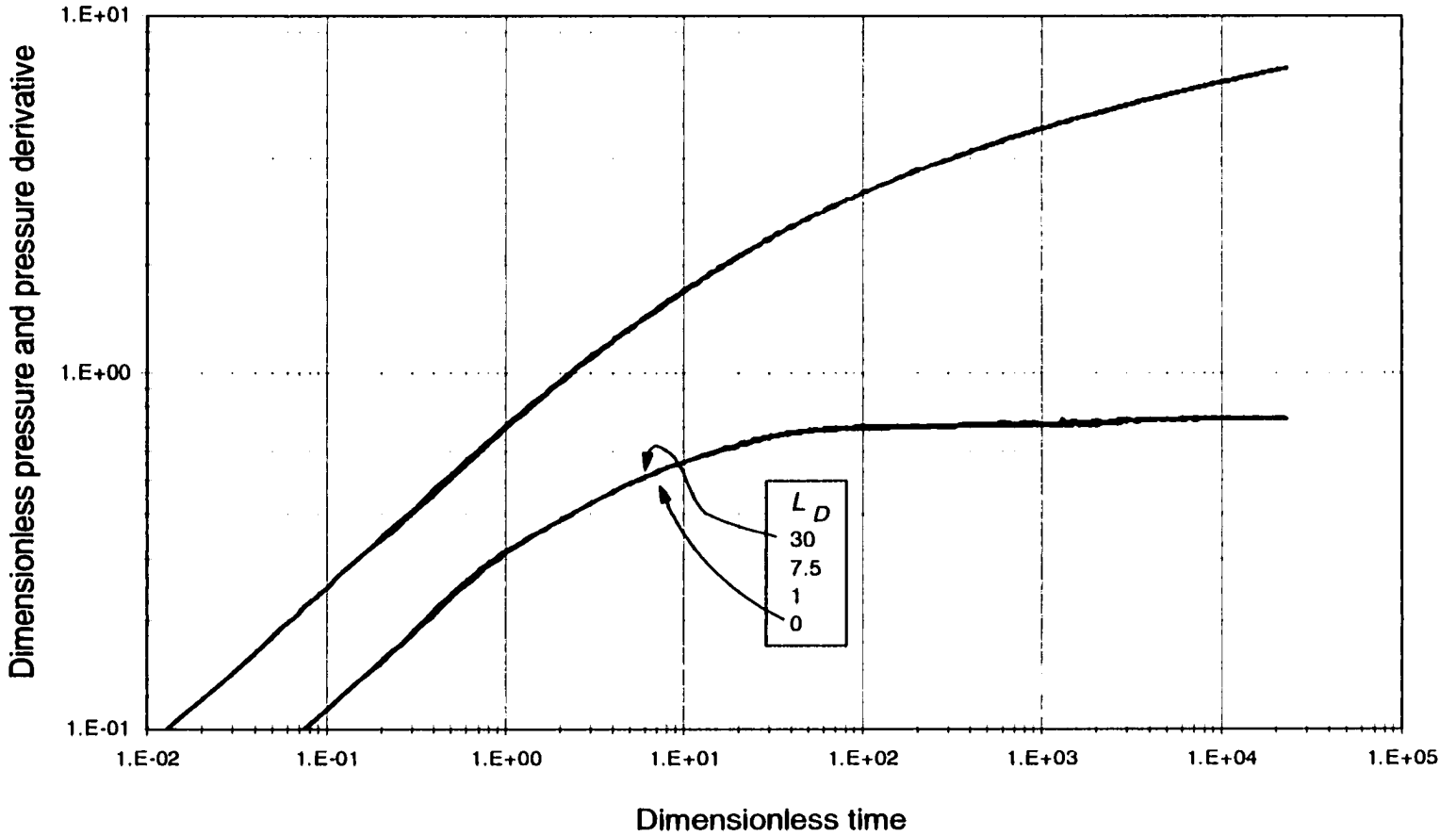

Fig. B.17.c. Dimensionless pressure and pressure derivative curve for a hydraulic fracture intersecting a fault at its tip forming an angle of 0°. C_D=300

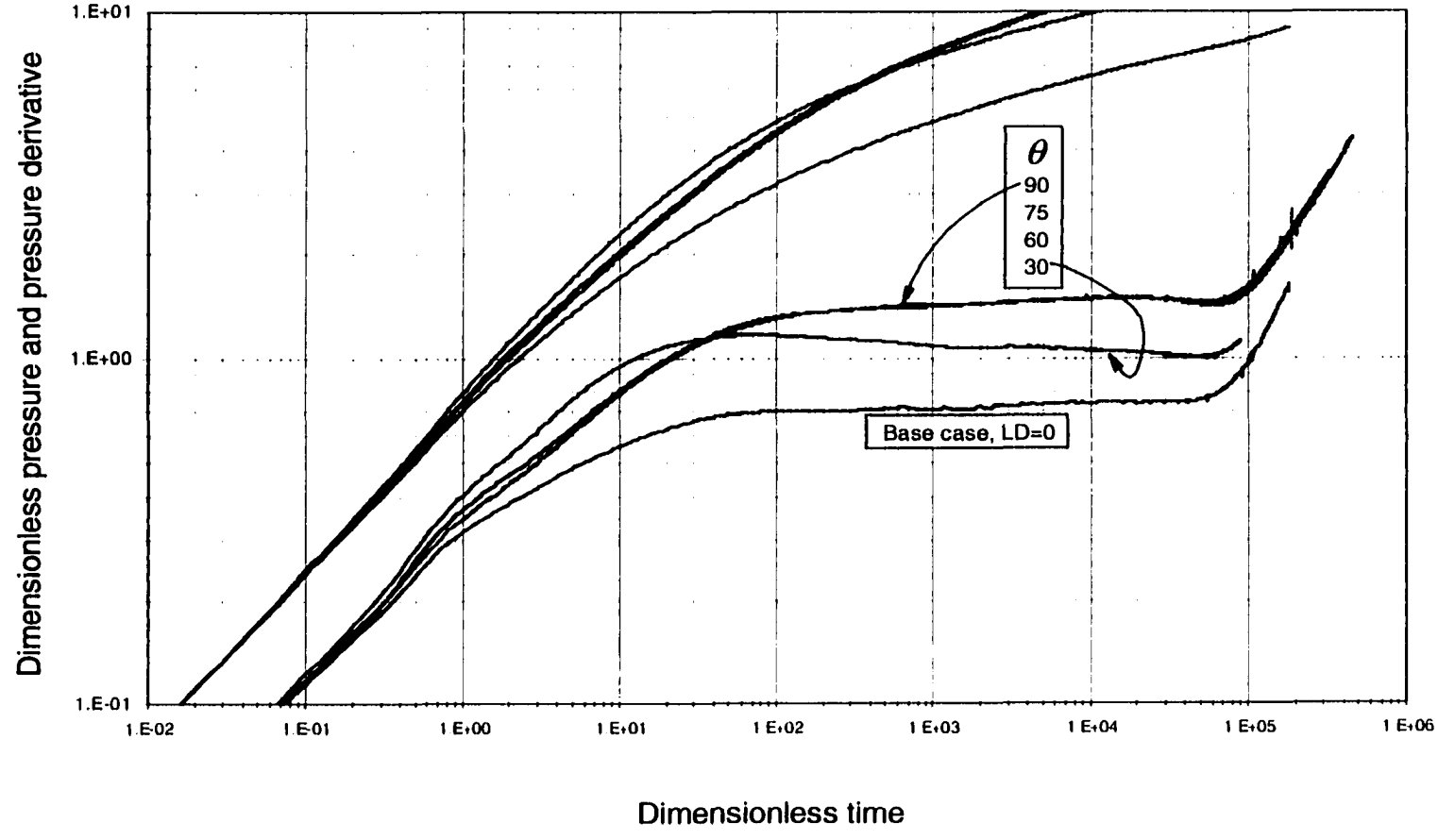

Fig. B.18.a. Dimensionless pressure and pressure derivative curve for a hydraulic fracture intersecting a fault at its middle part. C_D=300 and L_D=80

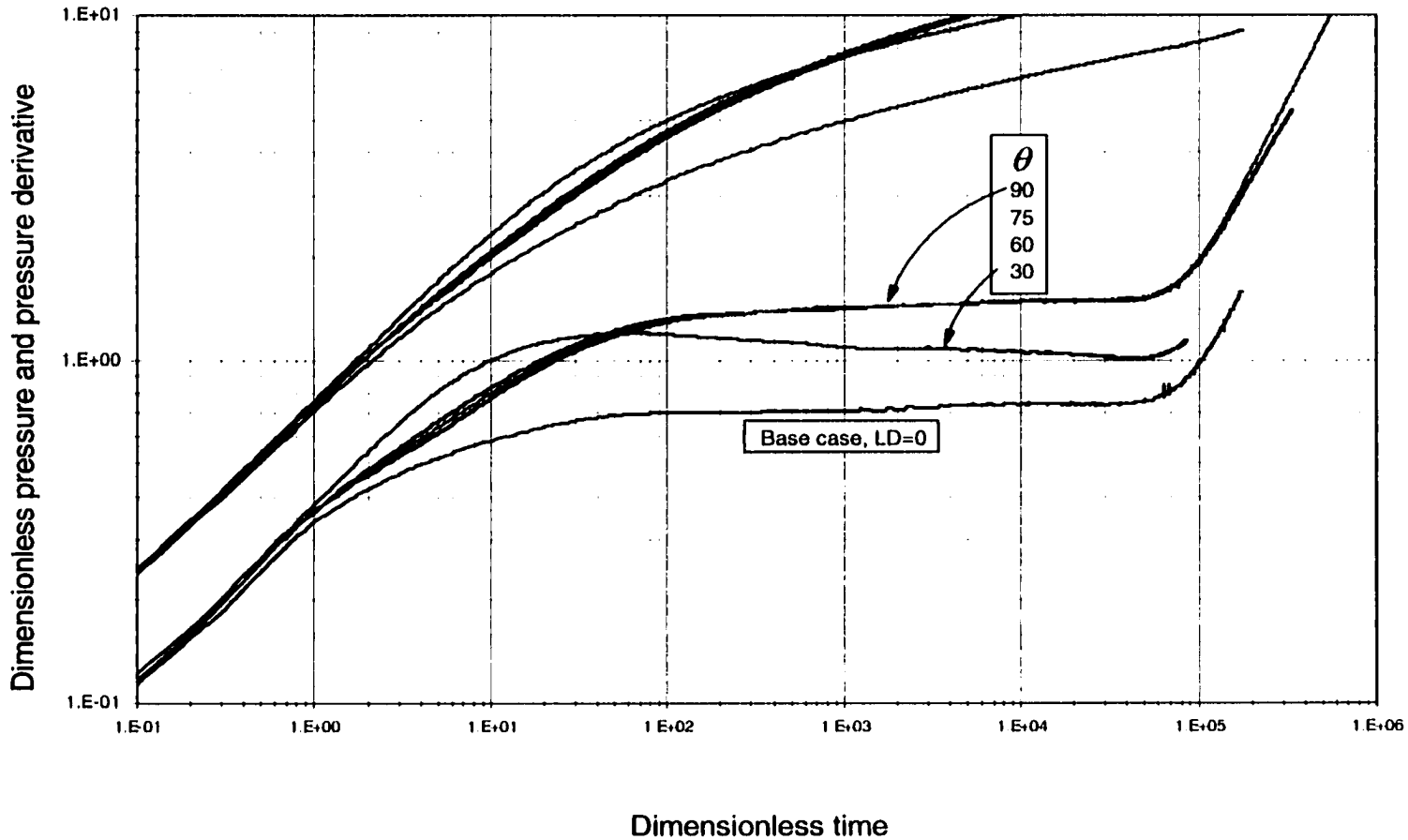

Fig. B.18.b. Dimensionless pressure and pressure derivative curve for a hydraulic fracture intersecting a fault at its middle part. C_{fD}=300 and L_D=162

APPENDIX C

GRIDS

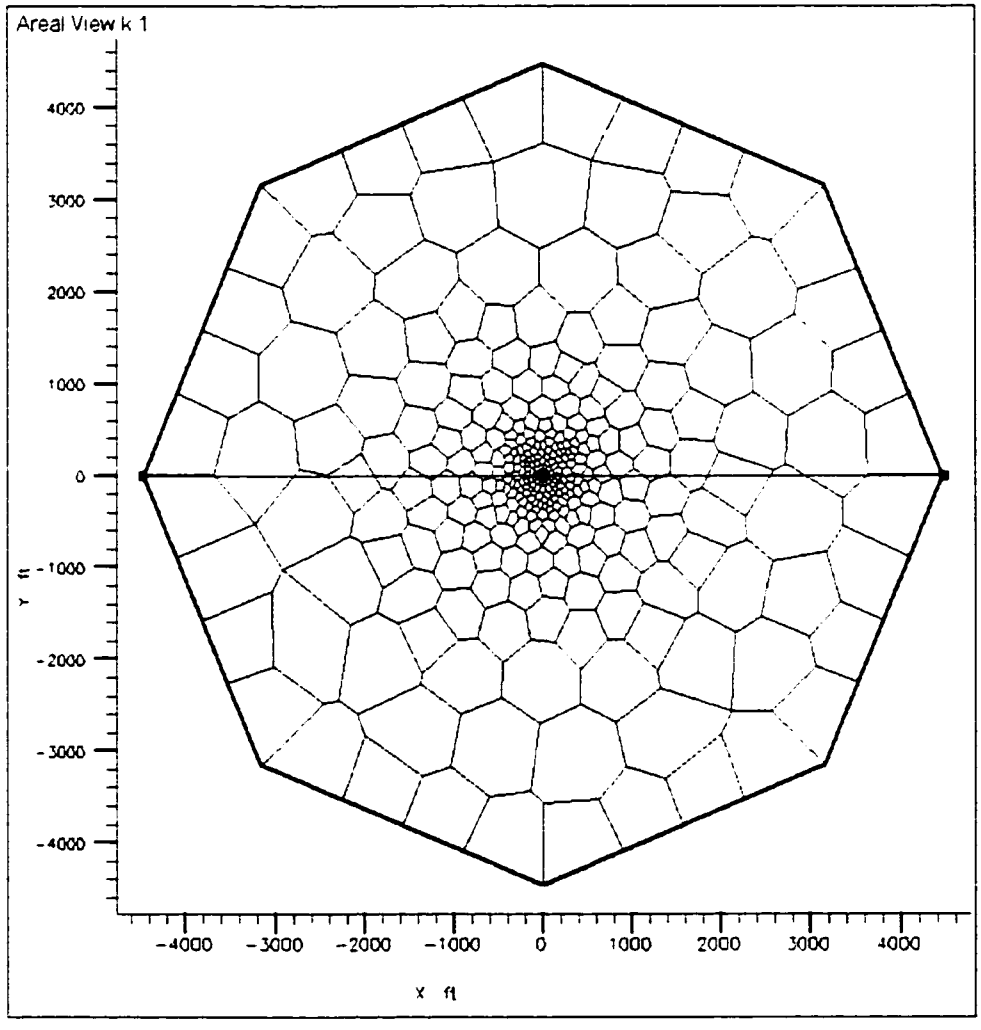

Fig. C.1.a. Variable PEBI grid for a vertical well without wellbore storage

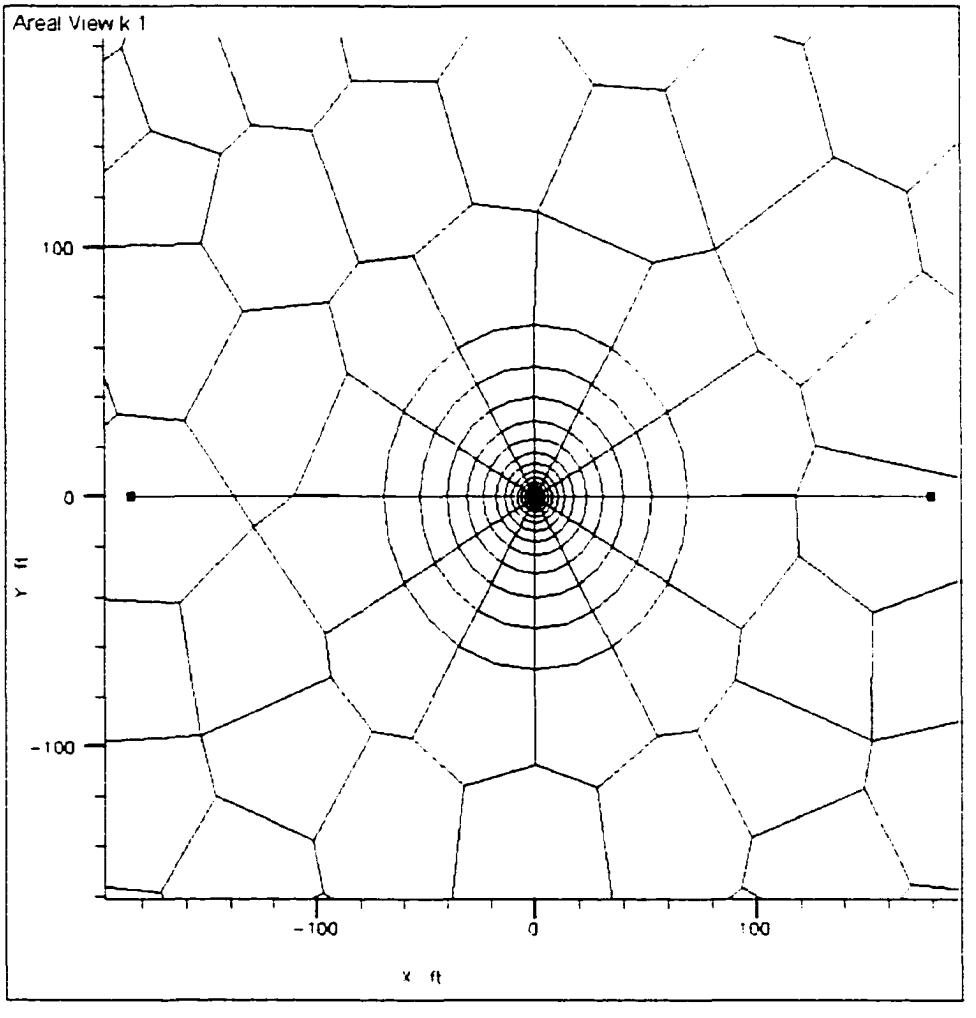

Fig. C.1.b. Variable PEBI grid for a vertical well without wellbore storage (closer view)

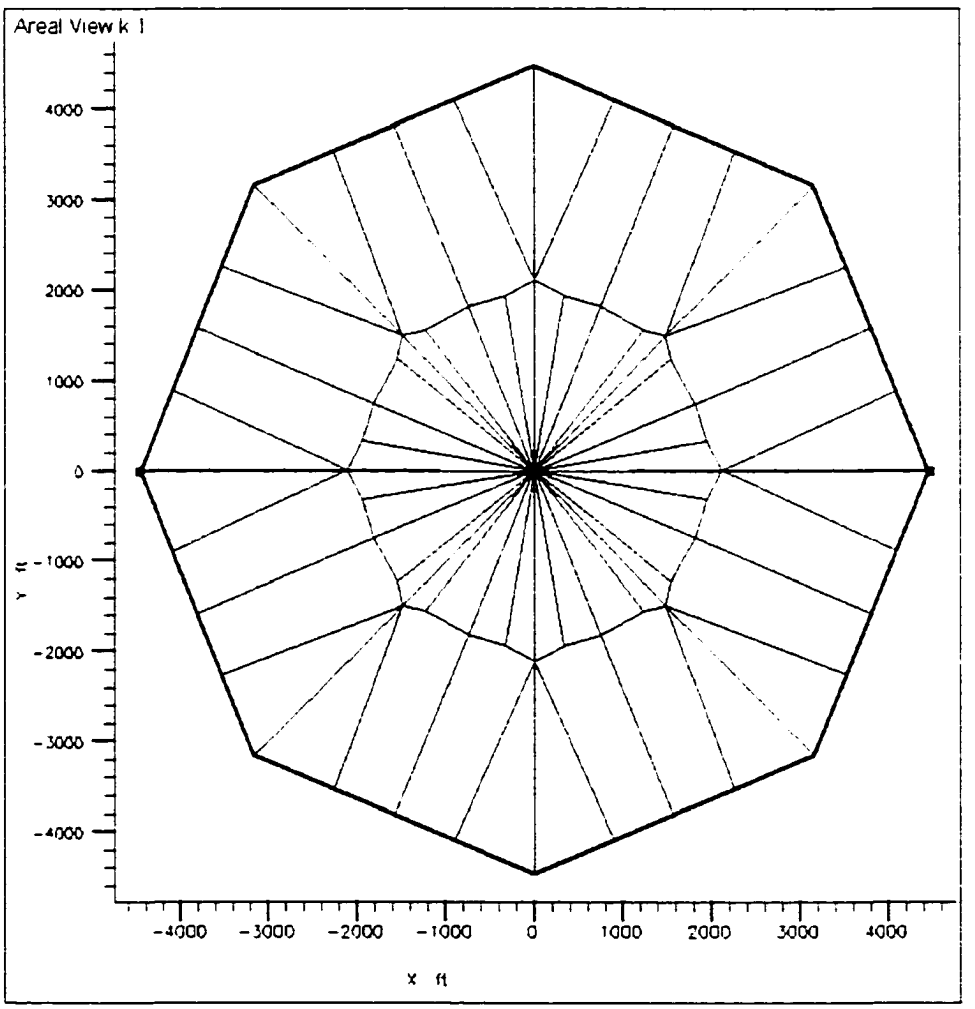

Fig. C.2.a. Elliptical PEBI grid for a vertical well without wellbore storage

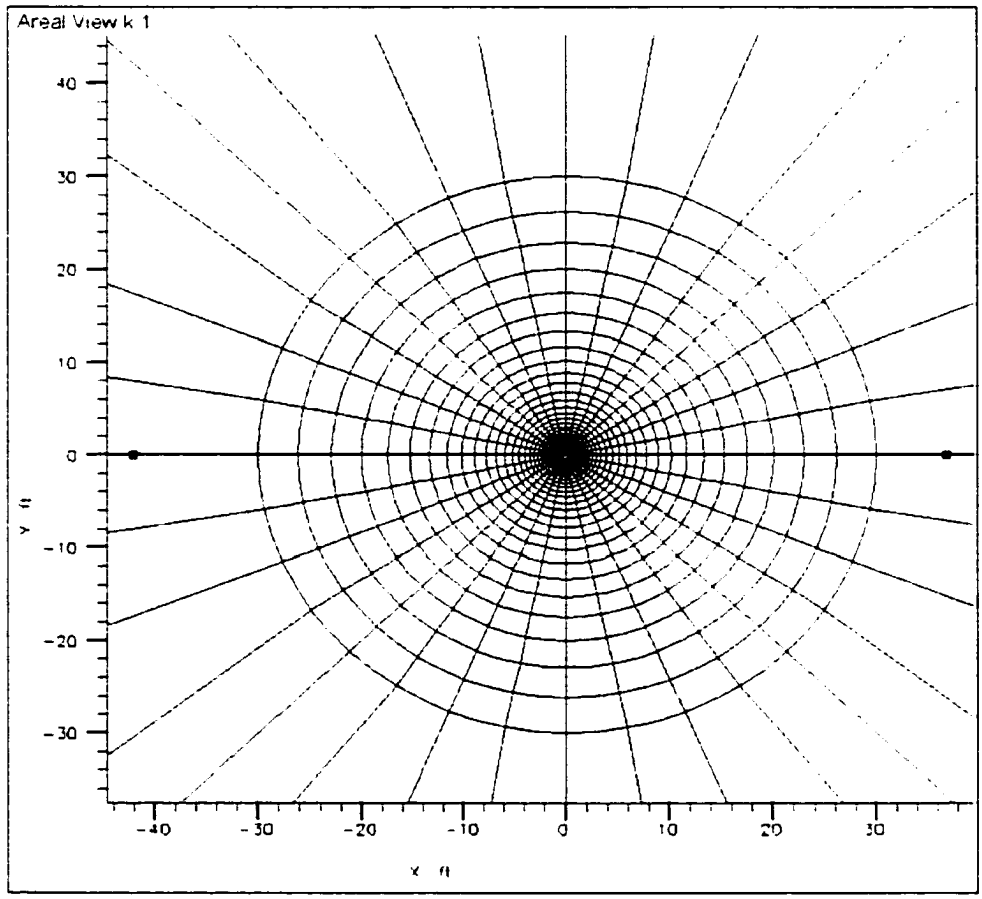

Fig. C.2.b. Elliptical PEBI grid for a vertical well without wellbore storage (closer view)

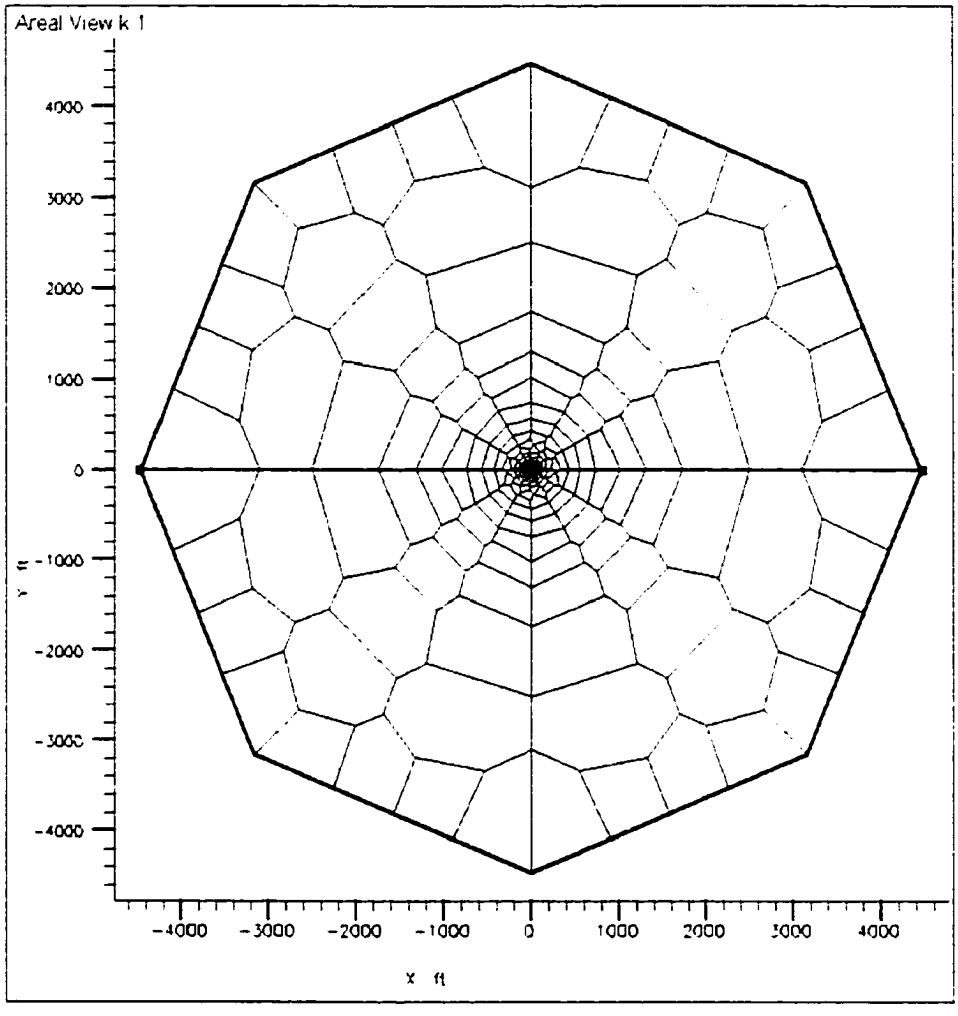

Fig. C.3.a. Circular PEBI grid for a vertical well without wellbore storage

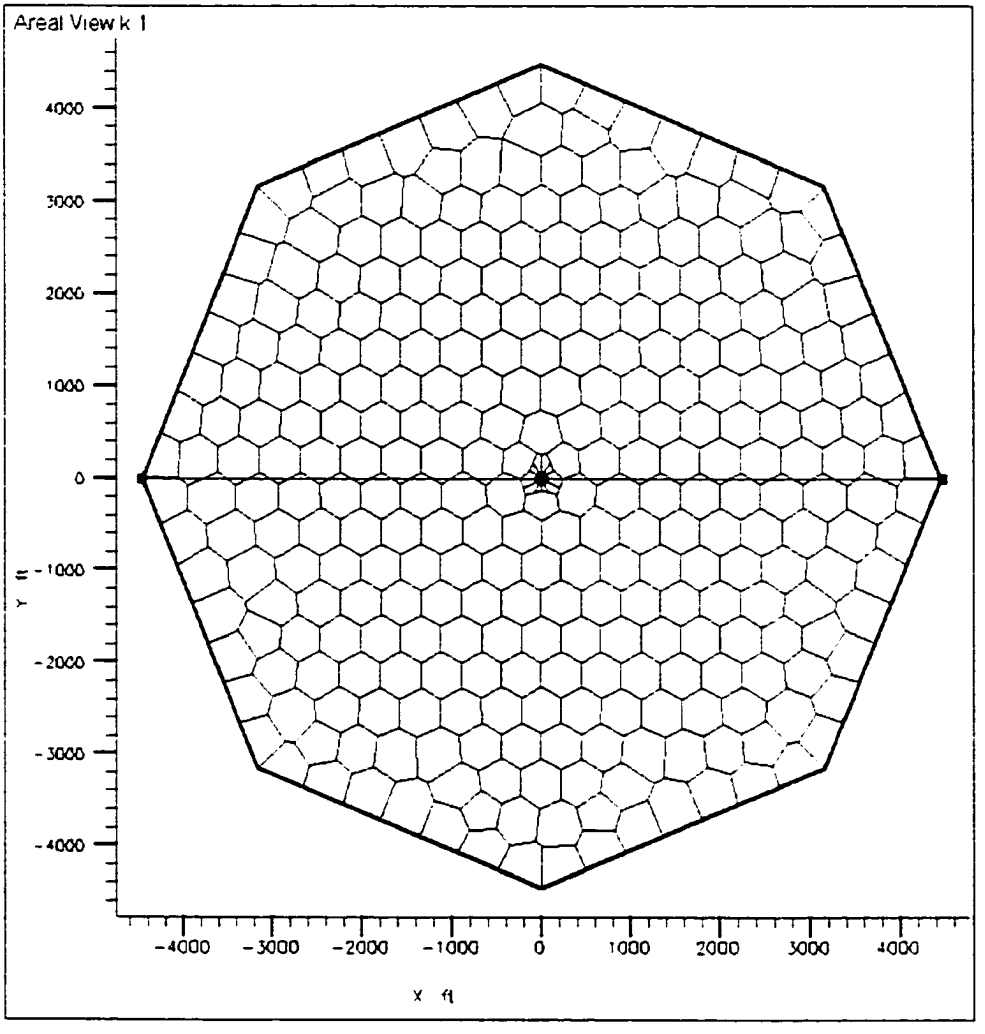

Fig. C.4.a. Hecagonal PEBI grid for a vertical well without wellbore storage

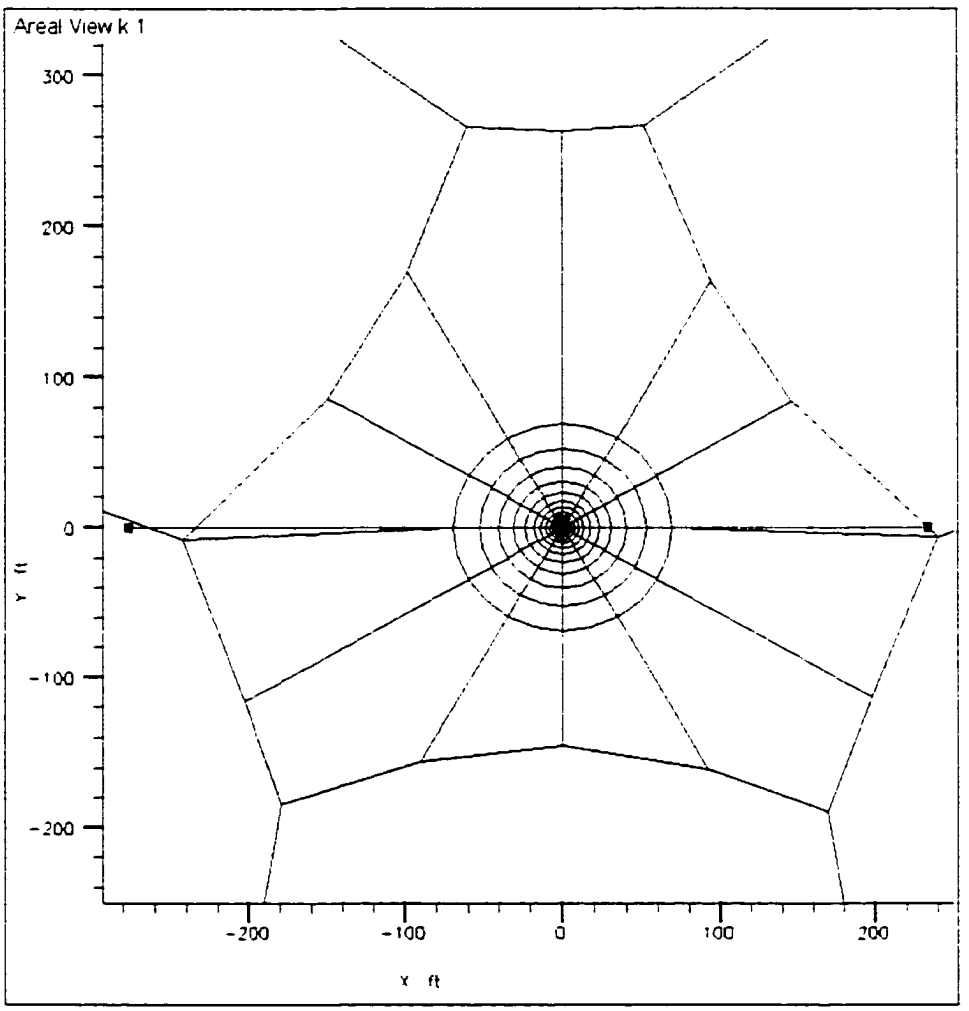

Fig. C.4.b. Hexagonal PEBI grid for a vertical well without wellbore storage (closer view)

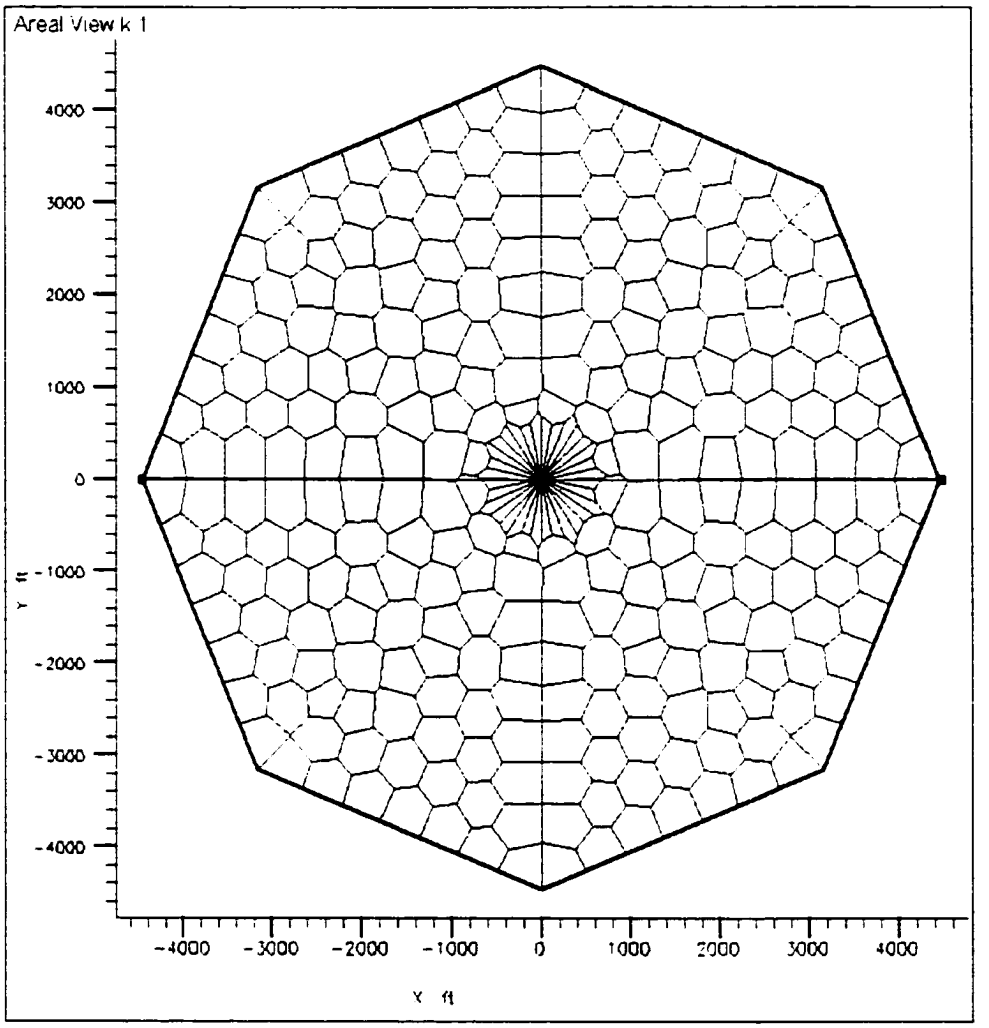

Fig. C.5.a. Rectangular PEBI grid for a vertical well without wellbore storage

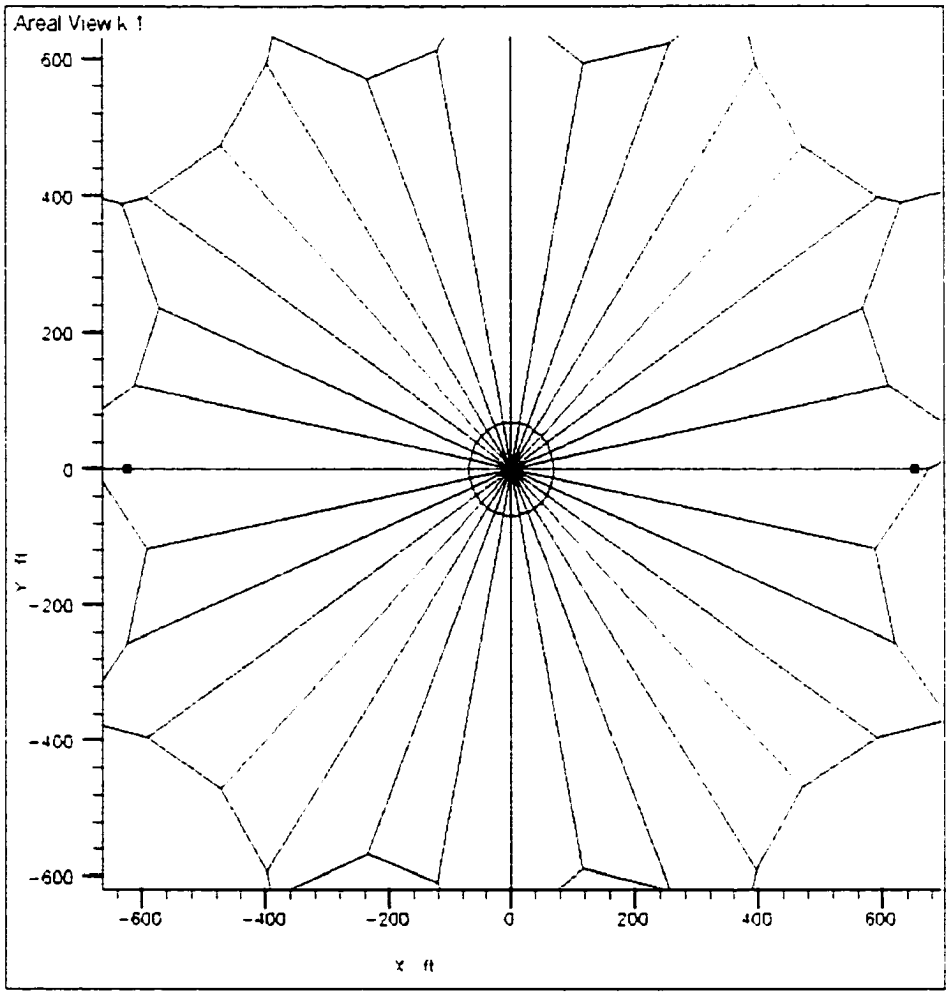

Fig. C.5.b. Rectangular PEBI grid for a vertical well without wellbore storage (closer view)

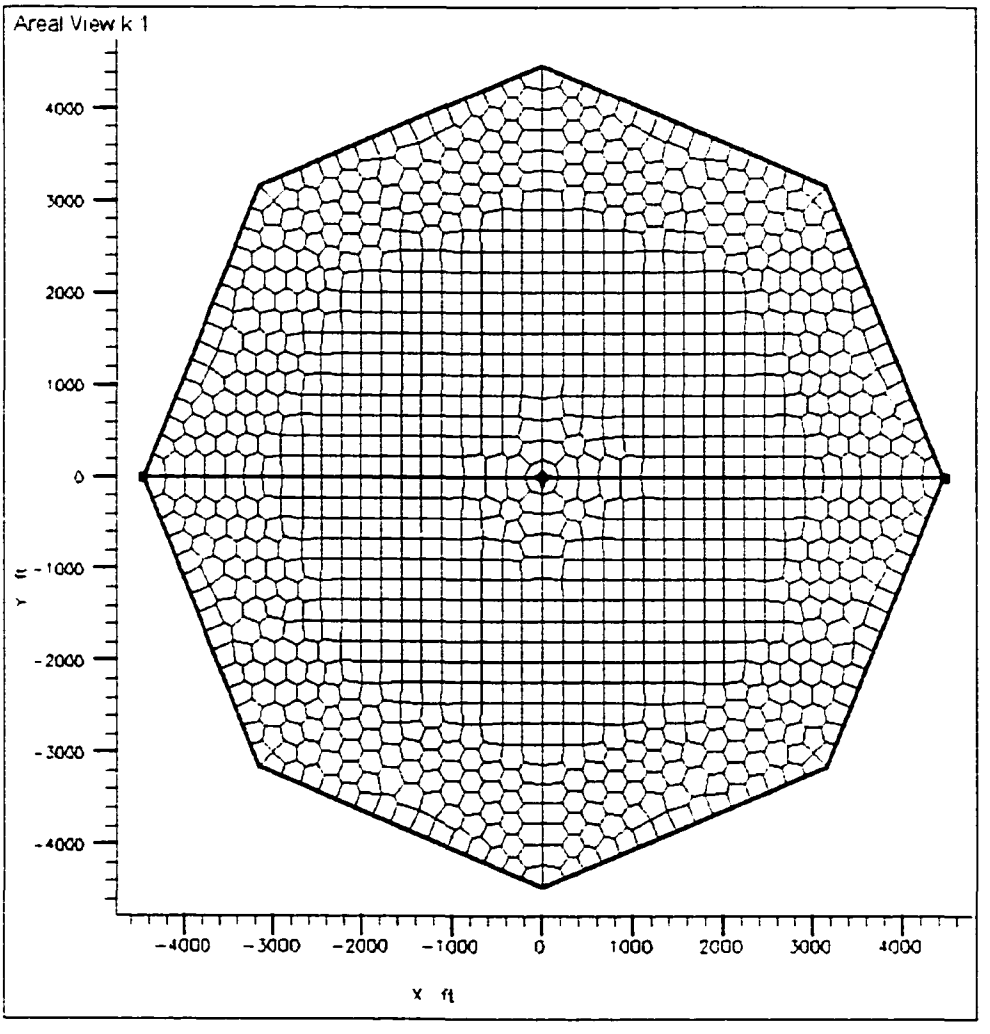

Fig. C.6. Rectangular PEBI grid for a vertical well without wellbore storage. 3708 gridpoints

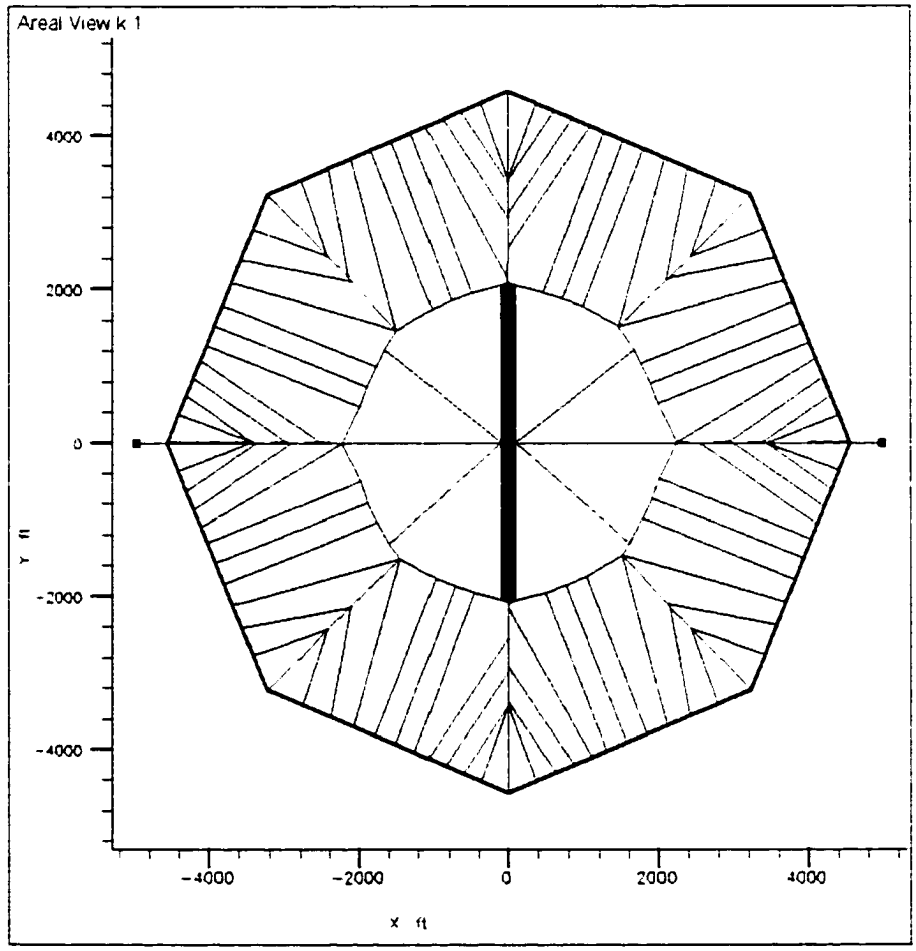

Fig. C.7.a. Circular PEBI grid used to simulate fractured well pressure behavior. $C_{fD}=1$

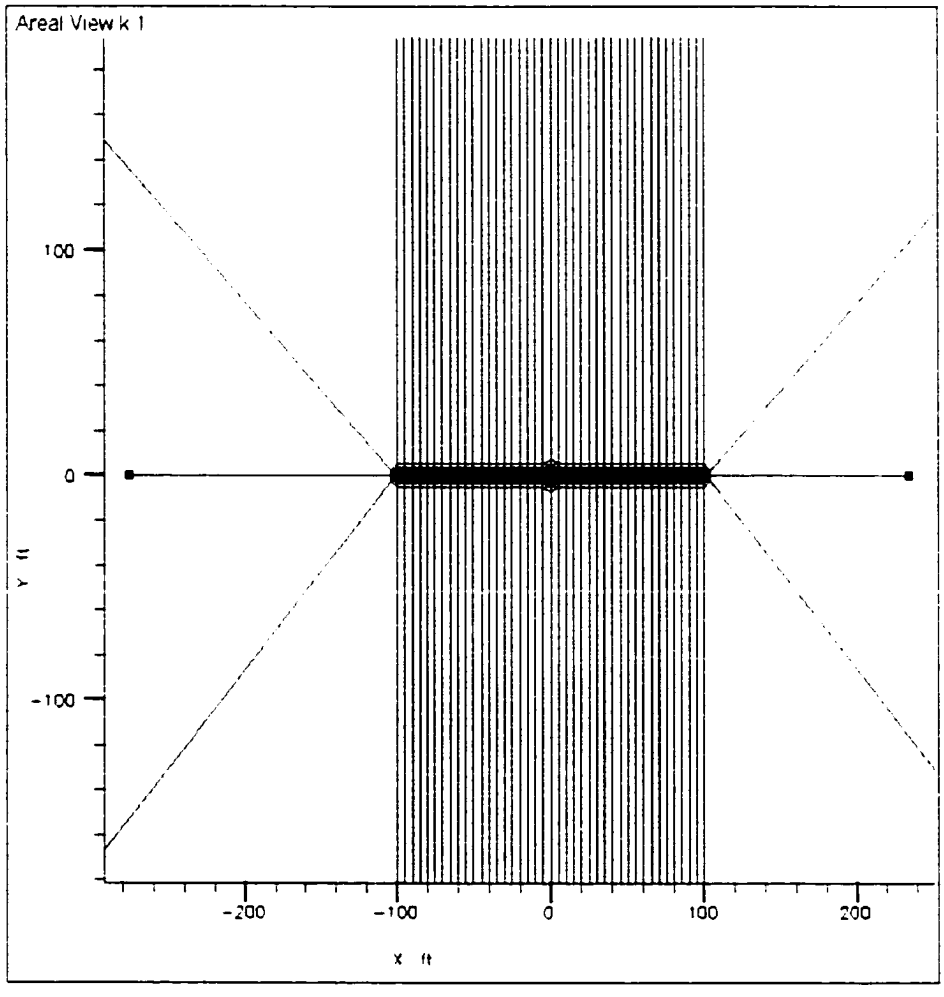

Fig. C.7.b. Circular PEBI grid used to simulate fractured well pressure behavior. $C_{fD}=1$ (closer view)

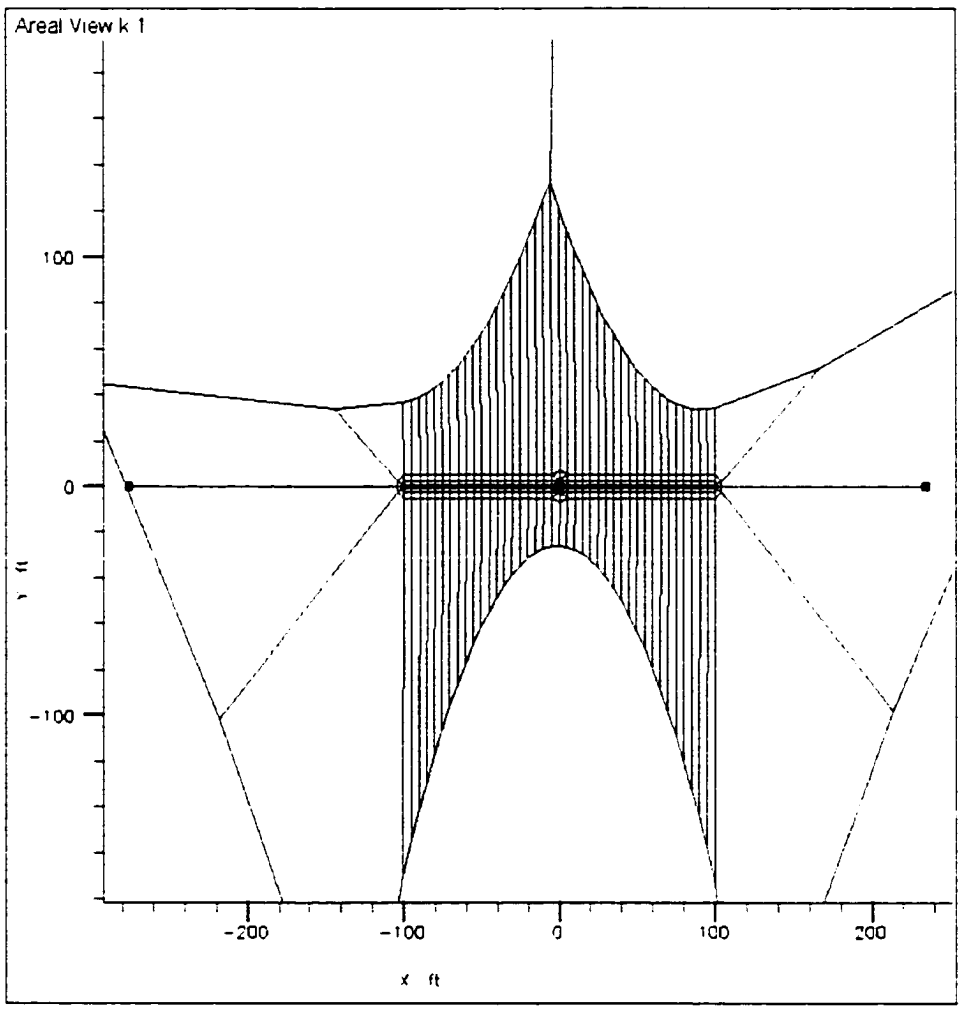

Fig. C.8. Hexagonal PEBI grid used to simulate fractured well pressure behavior. $C_{fD}=1$ (closer view)

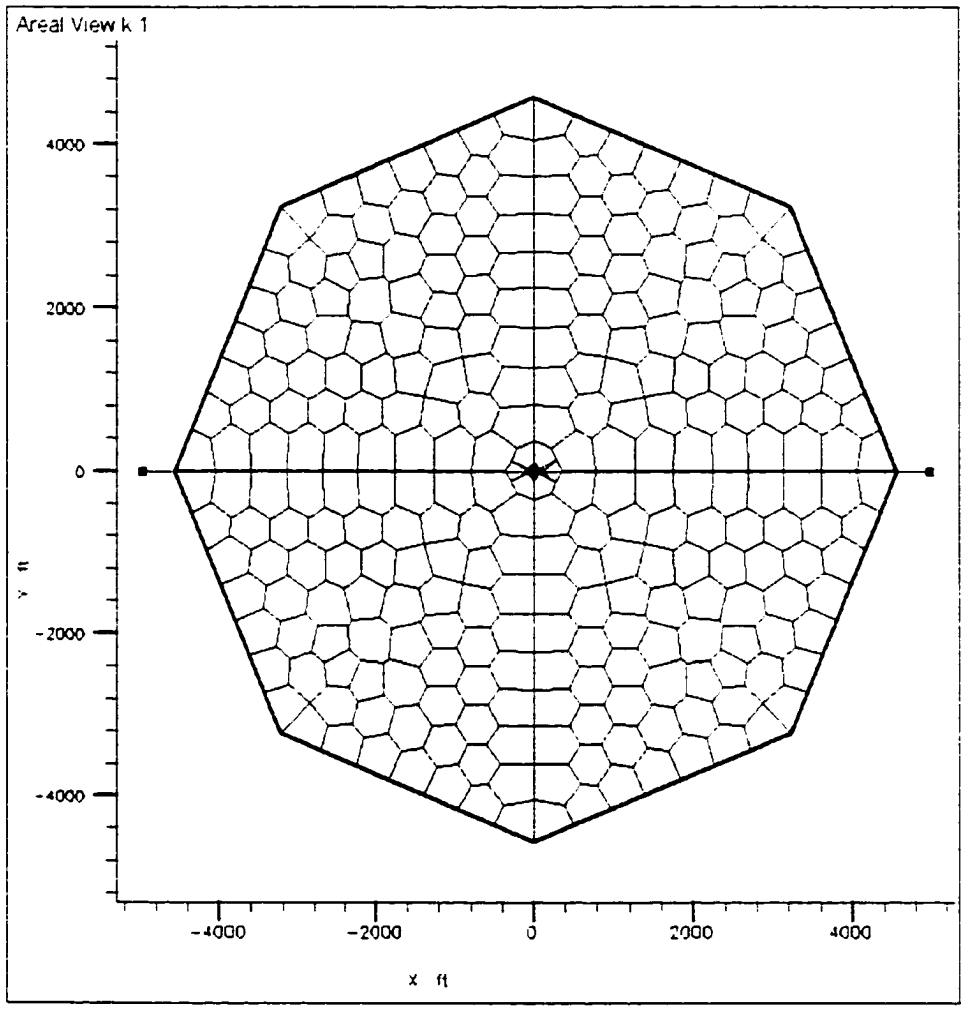

$C_{fD}=1$, *rectangular grid*

Fig. C.9.a. Rectangular PEBI grid used to simulate fractured well pressure behavior. $C_{fD}=1$

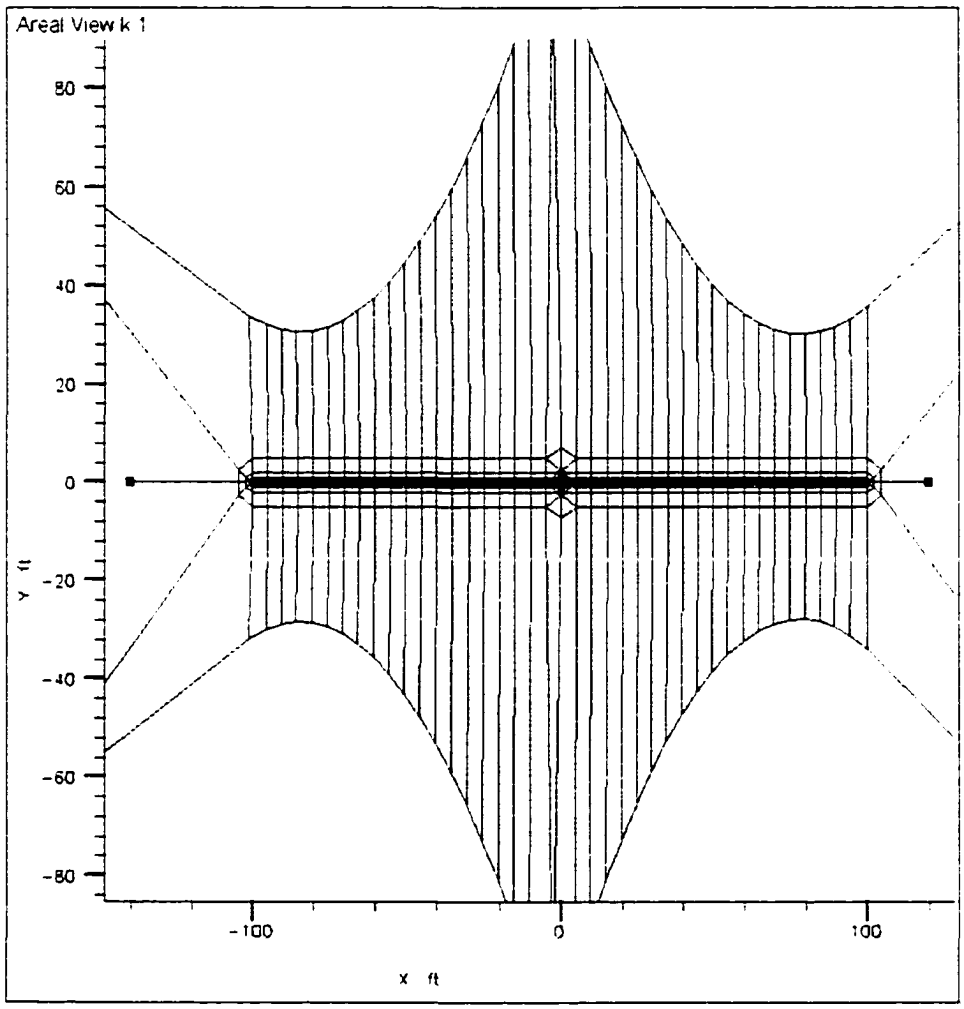

Fig. C.9.b. Rectangular PEBI grid used to simulate fractured well pressure behavior. $C_{fD}=1$ (closer view)

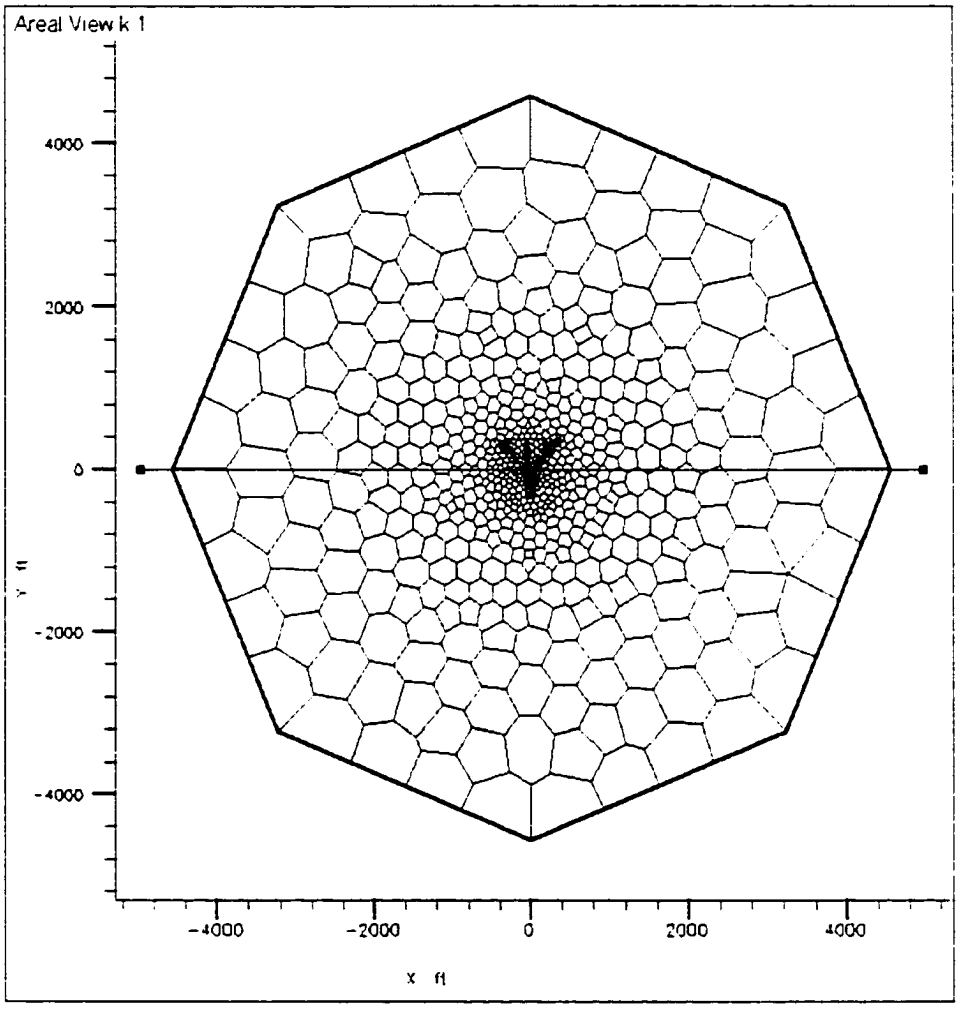

Fig. C.10.a. Variable PEBI grid used to simulate fractured well pressure behavior. $C_{fD}=1$

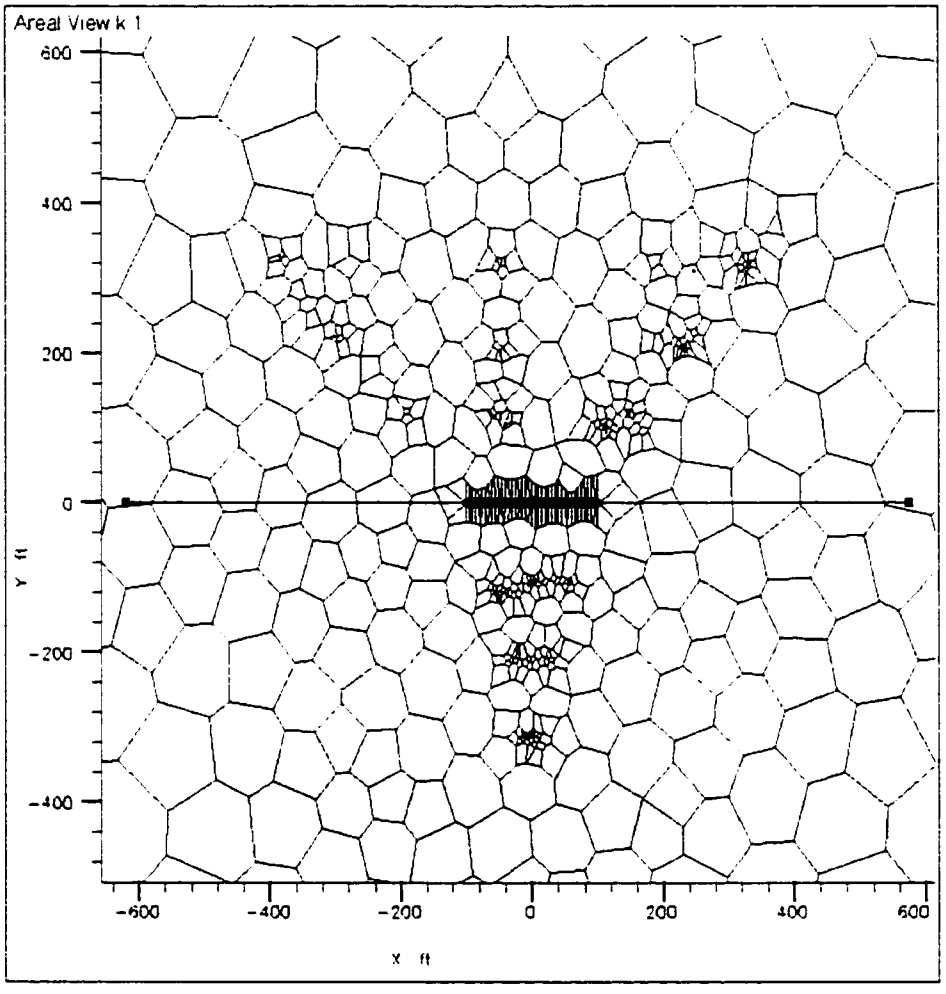

Fig. C.10.b. Variable PEBI grid used to simulate fractured well pressure behavior. C_{fD}=1 (closer view)

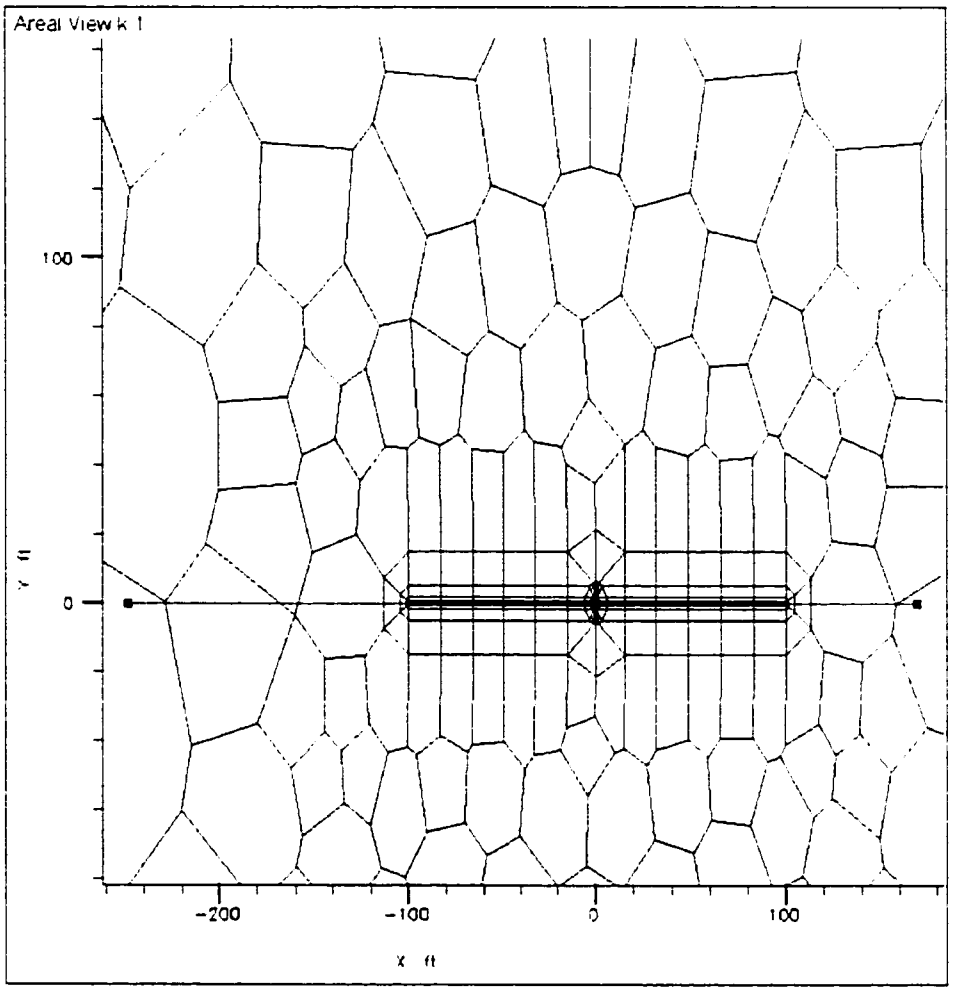

Fig. C.11. Elliptical PEBI grid used to simulate fractured well pressure behavior. $C_{fD}=1$ (closer view)

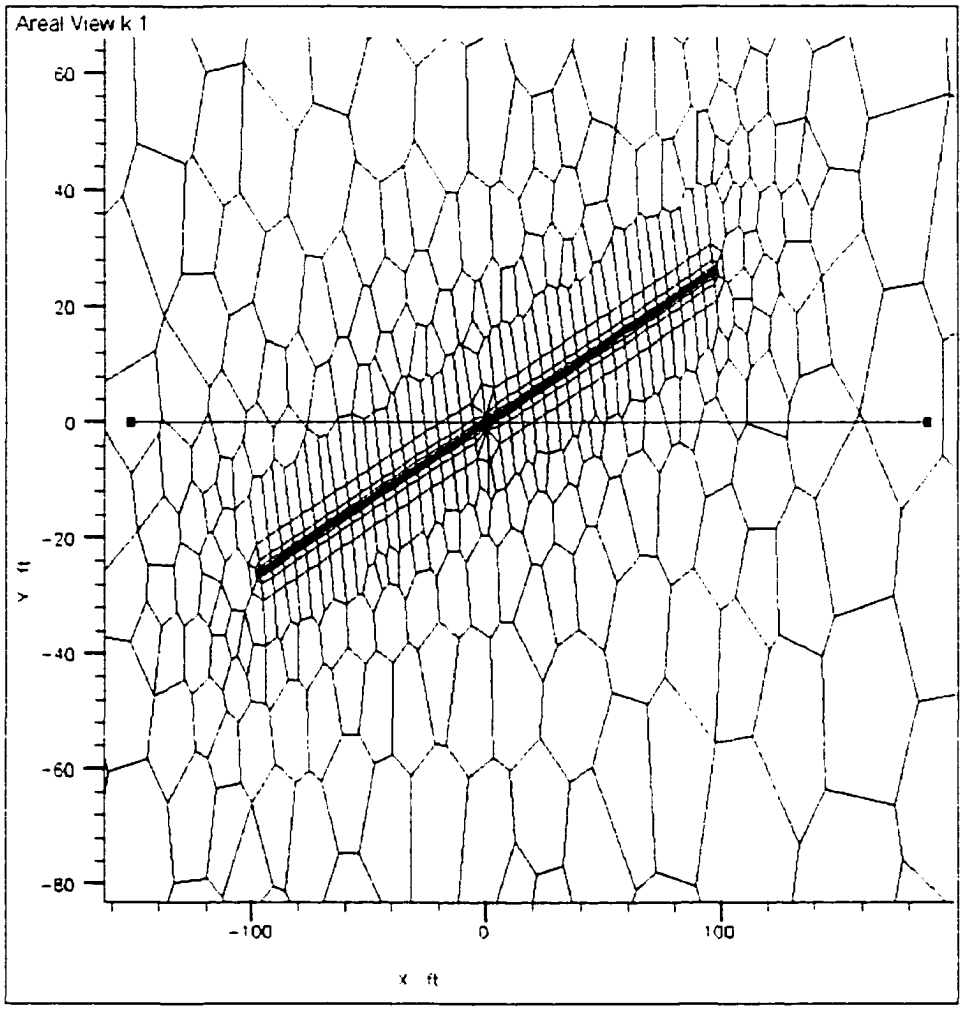

Fig. C.12. Elliptical PEBI grid used to simulate fractured well pressure behavior. C_{fD}=300 and θ=15° (closer view)

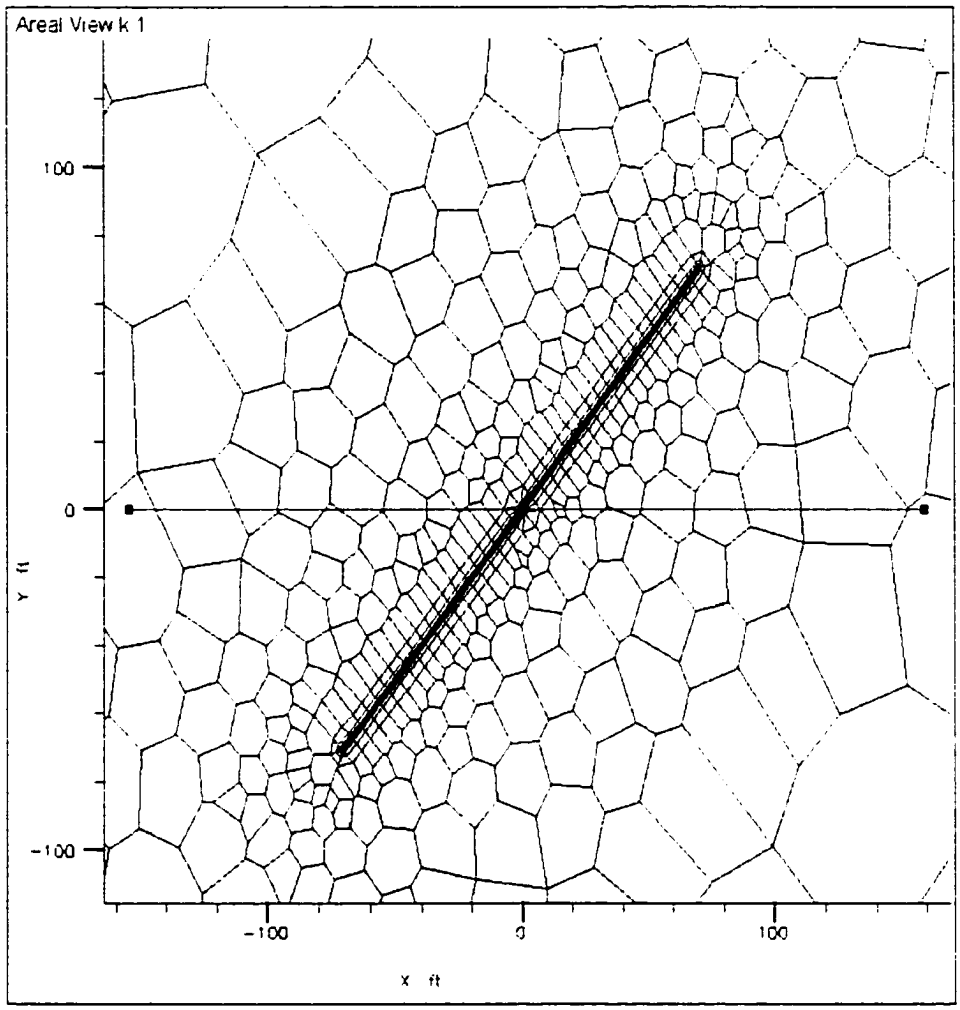

Fig. C.13. Elliptical PEBI grid used to simulate fractured well pressure behavior. C_{fD}=50 and θ=45° (closer view)

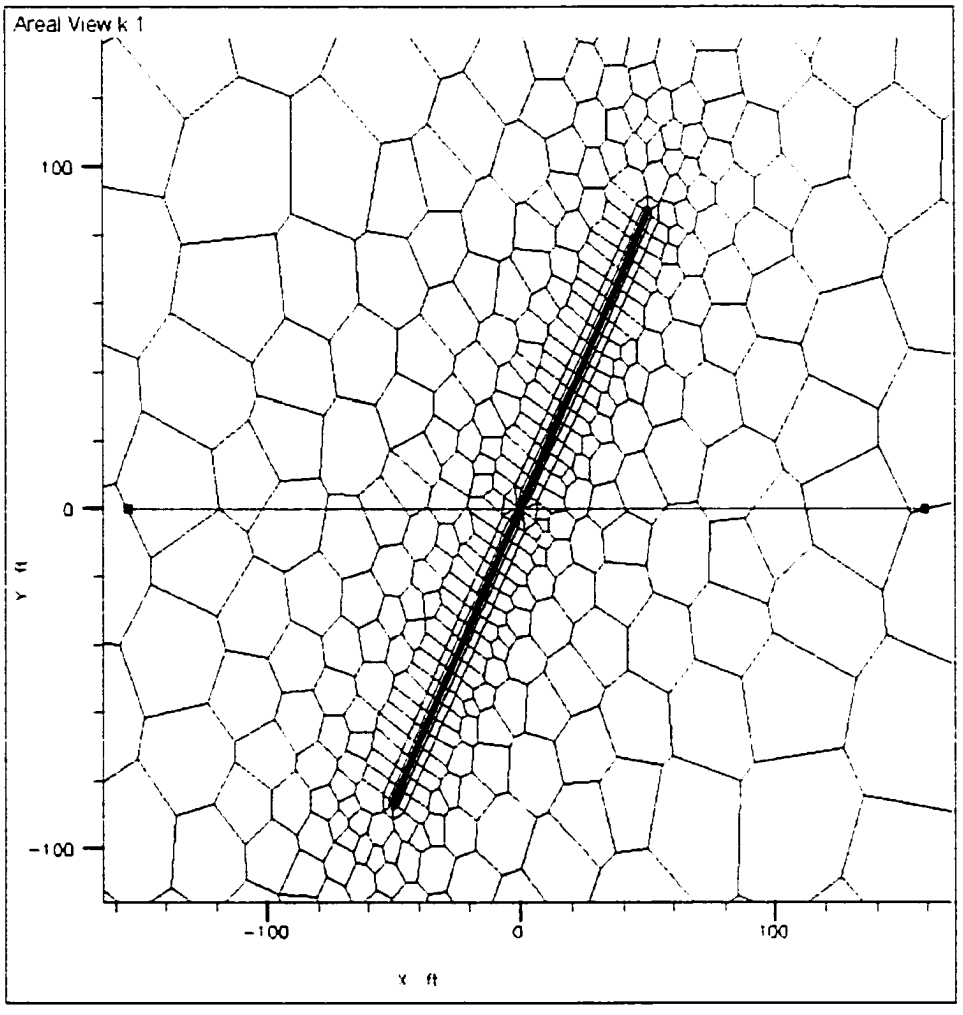

Fig. C.14. Elliptical PEBI grid used to simulate fractured well pressure behavior. C_{fD}=50 and θ=60° (closer view)

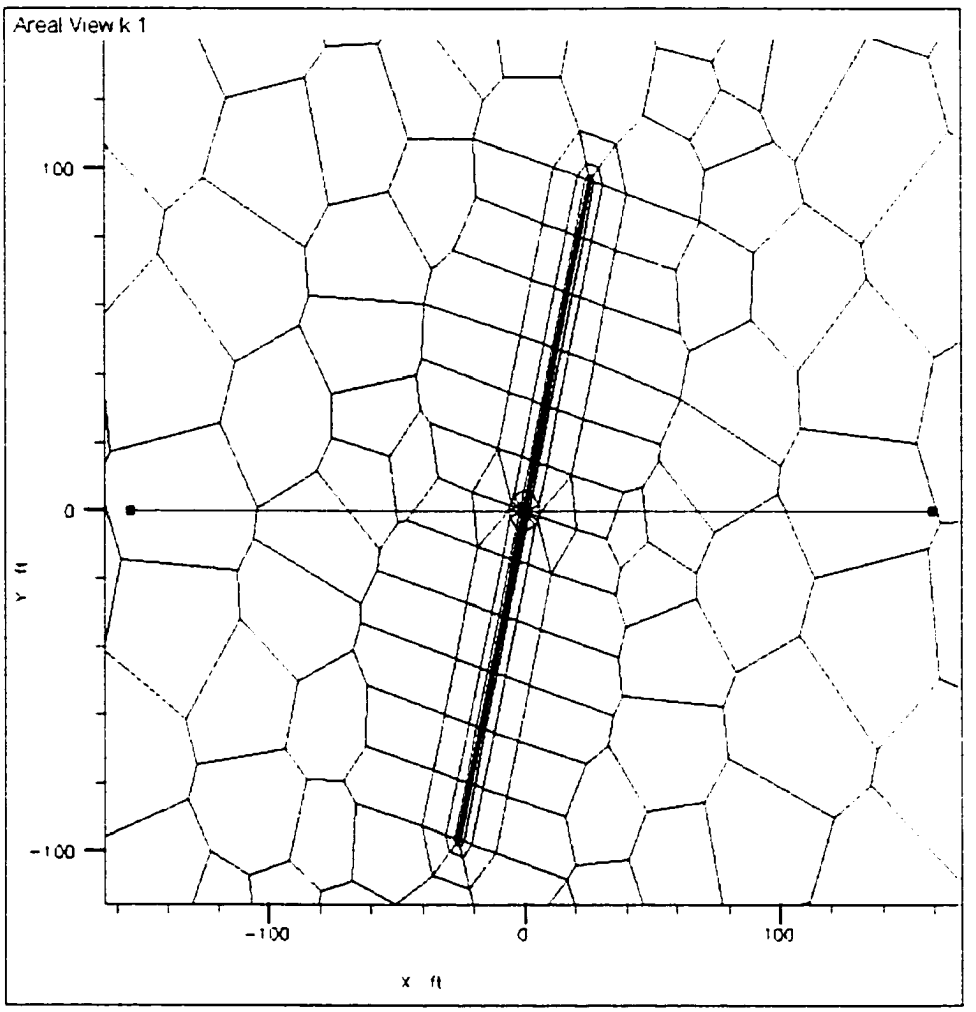

Fig. C.15. Elliptical PEBI grid used to simulate fractured well pressure behavior. C_{fD}=1 and θ=75° (closer view)

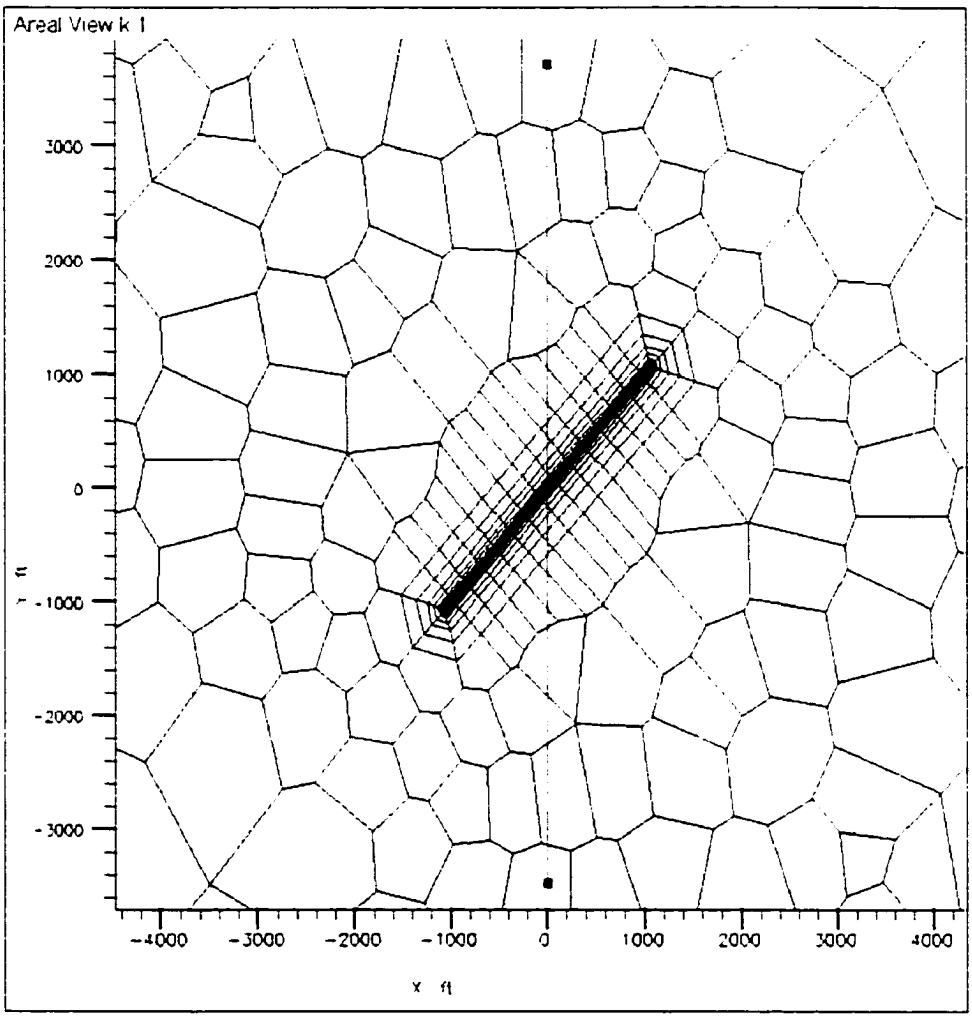

Fig. C.16. Elliptical PEBI grid used to simulate horizontal well pressure behavior. θ=45° (closer view)

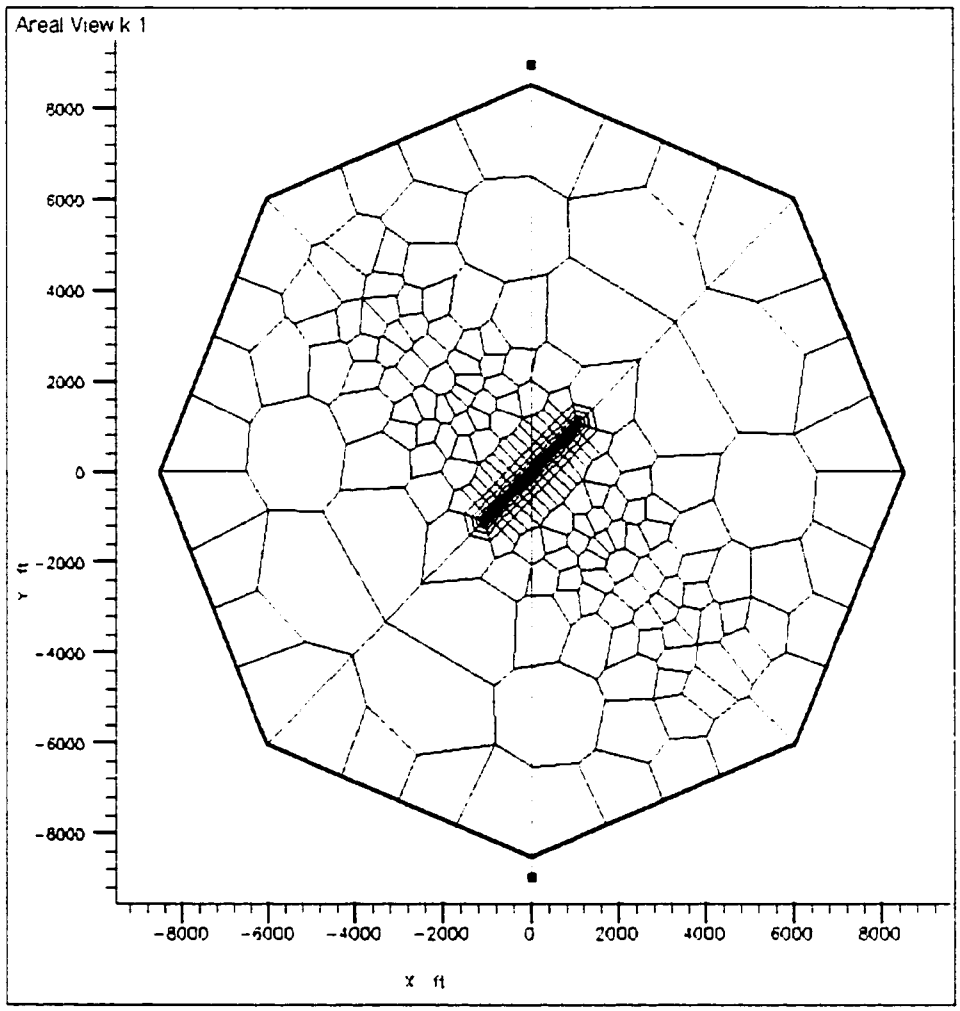

Fig. C.17. Circular PEBI grid used to simulate horizontal well pressure behavior. θ=45°

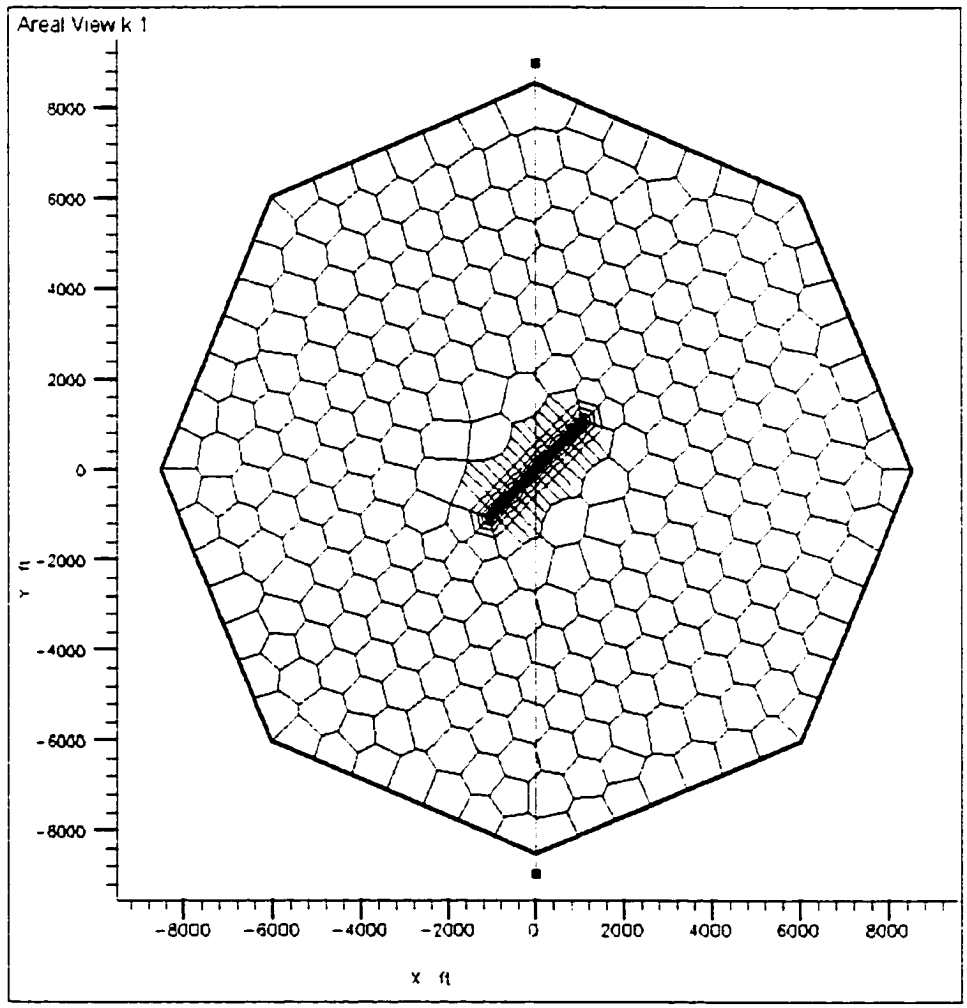

Fig. C.18. Hexagonal PEBI grid used to simulate horizontal well pressure behavior. θ=45°

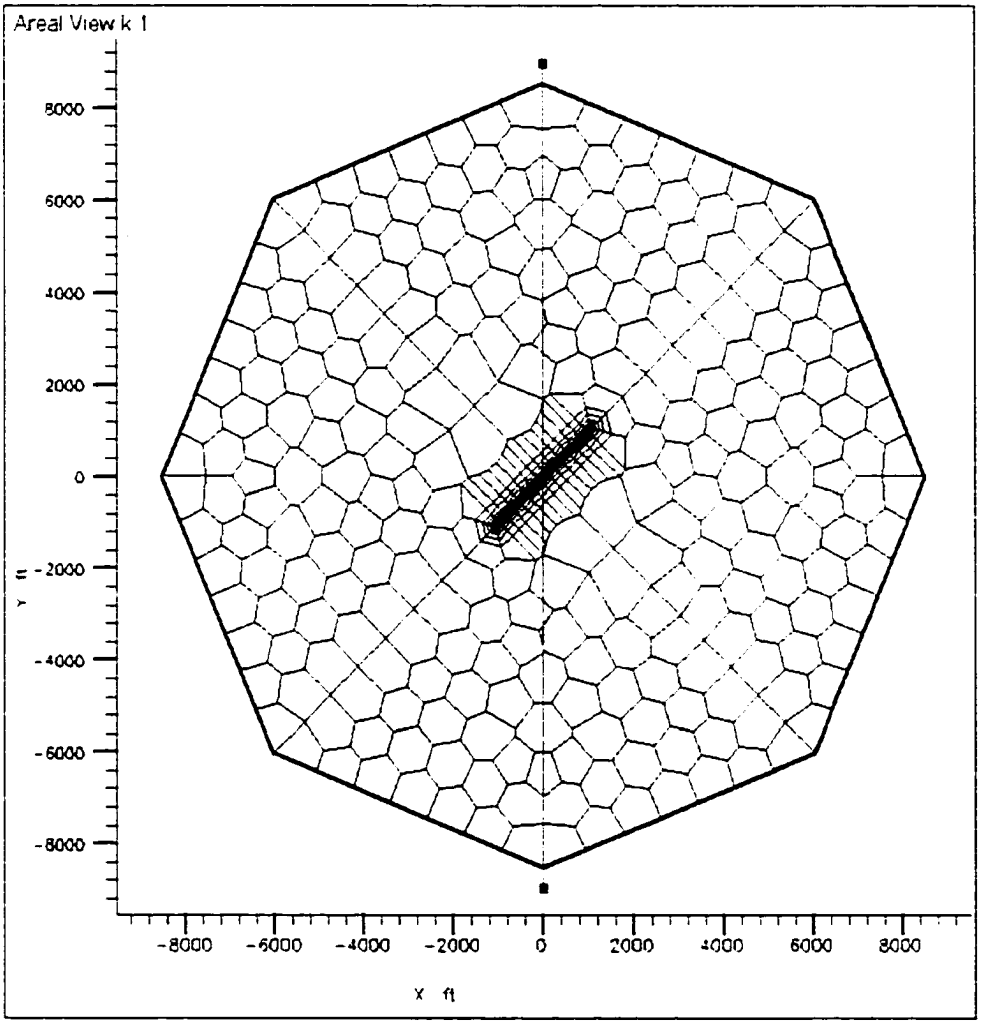

Fig. C.19. Rectangular PEBI grid used to simulate horizontal well pressure behavior. θ=45°

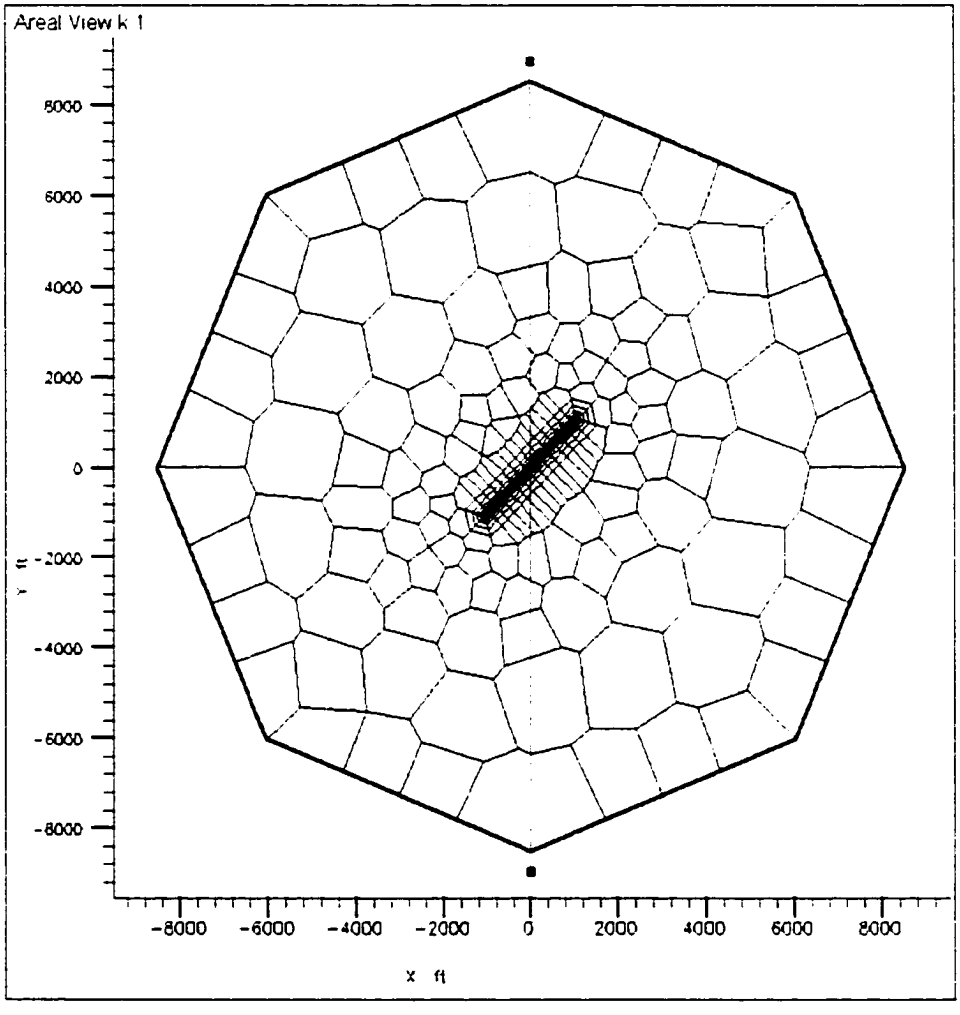

Fig. C.20. Variable PEBI grid used to simulate horizontal well pressure behavior. θ=45°

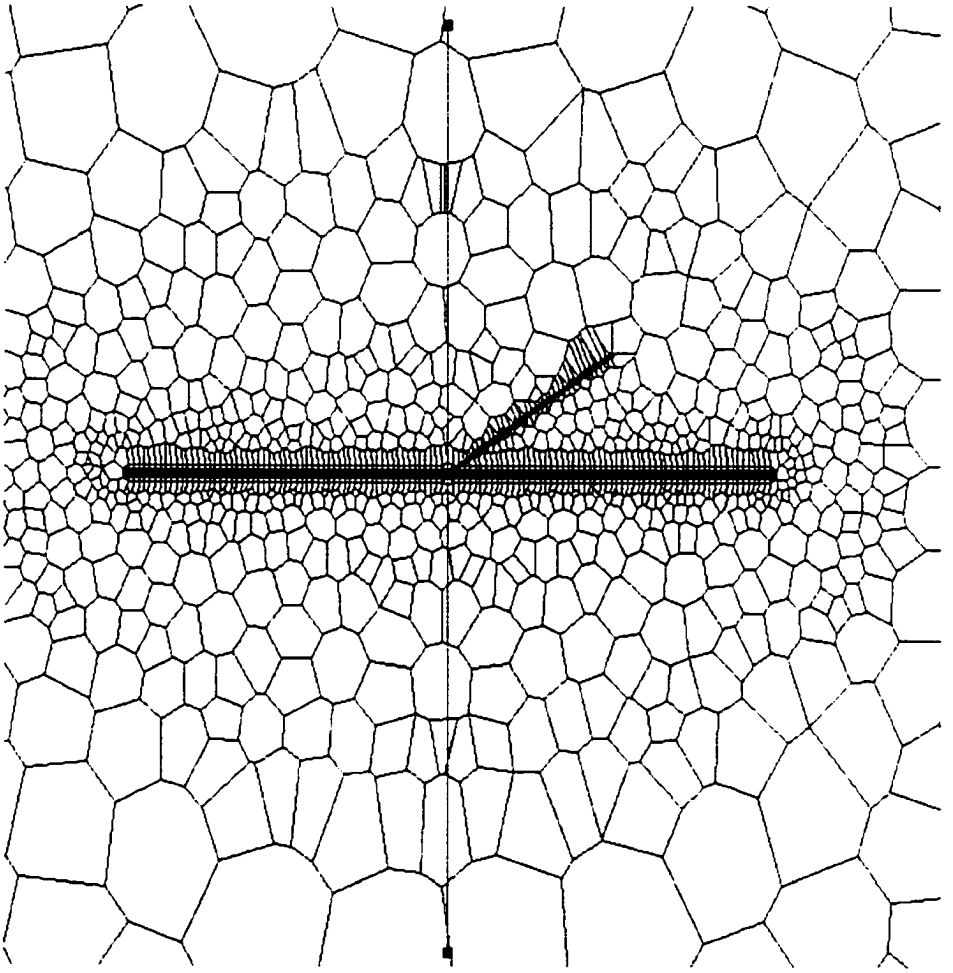

Fig. C.21.a. Close view of an elliptical PEBI grid for a hydraulically fractured well with a Branch fracture starting from the wellbore (Horizontal well) for $\theta=30°$ and $X_{fbD}=0.6$

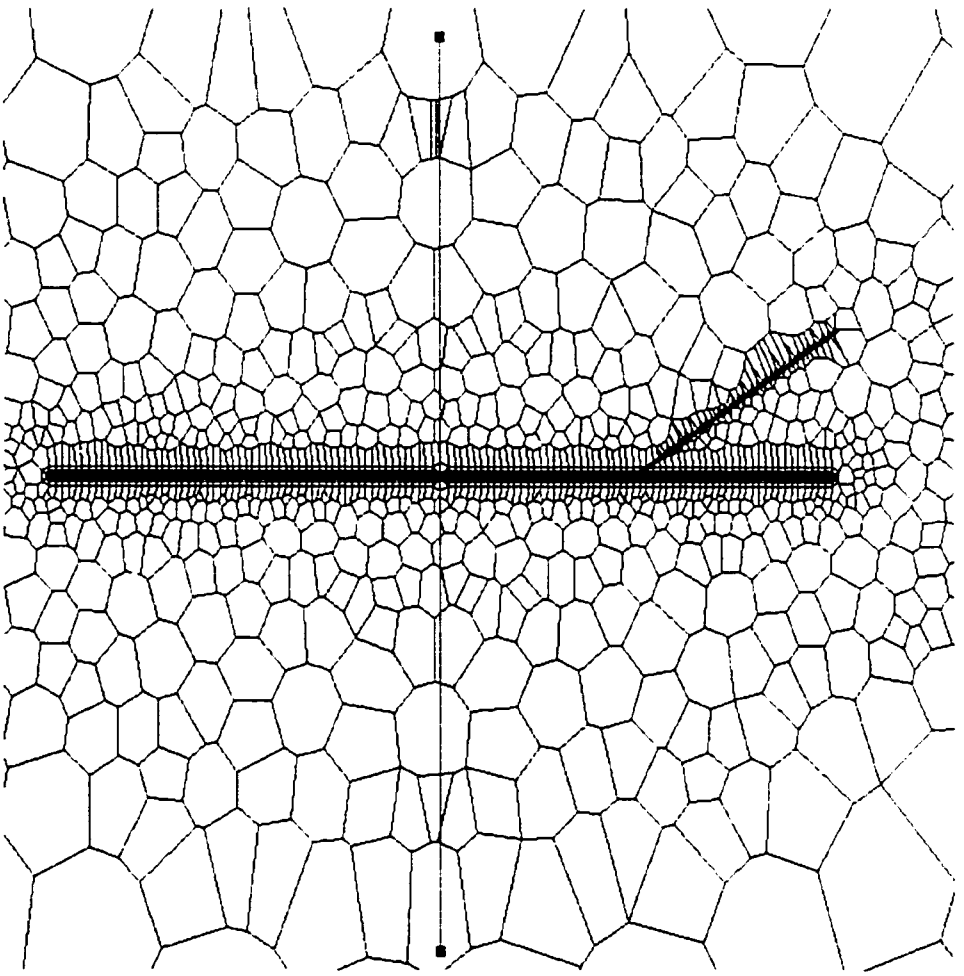

Fig. C.21.b. Close view of an elliptical PEBI grid for a hydraulically fractured well with a Branch fracture starting at the middle distance between wellbore and main fracture tip (Horizontal well) for θ=30° and X_{fbD}=0.6

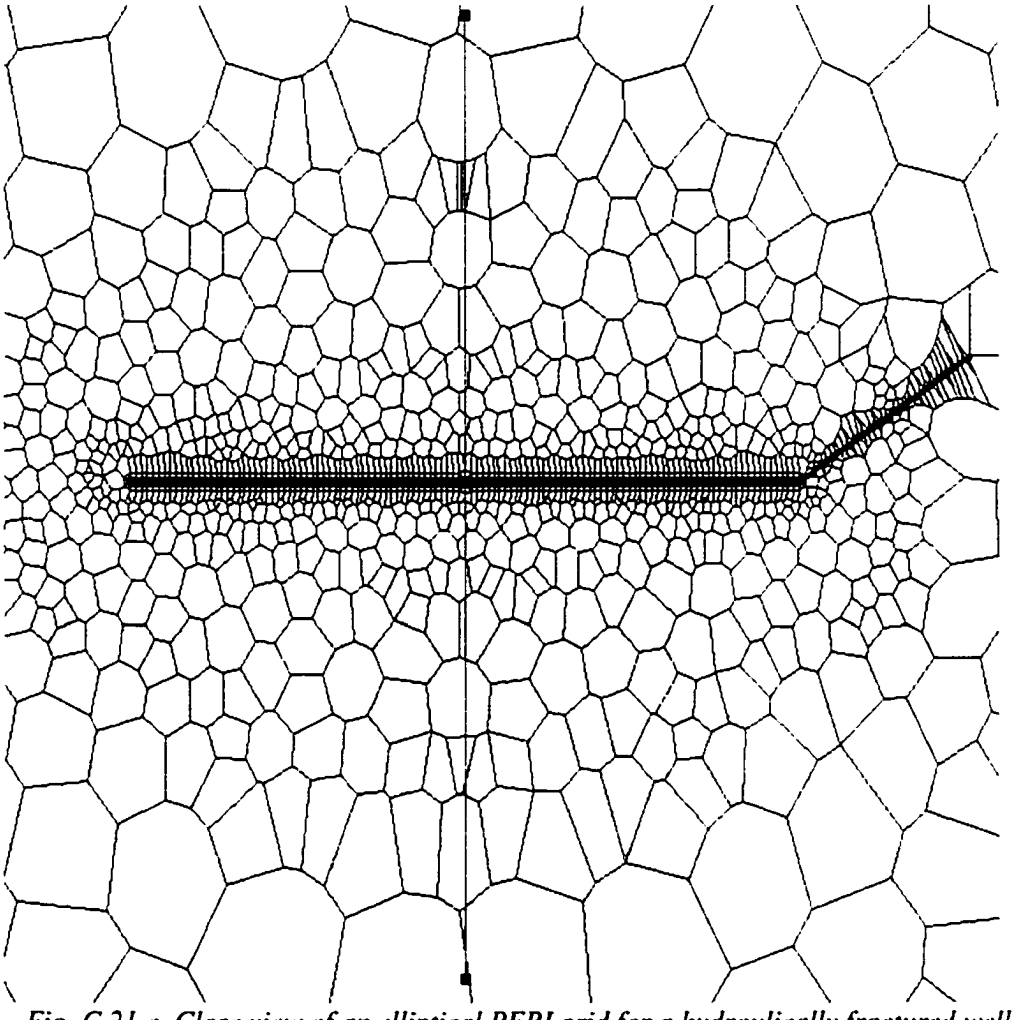

Fig. C.21.c. Close view of an elliptical PEBI grid for a hydraulically fractured well with a Branch fracture starting at the main fracture tip (Horizontal well) for θ=30° and X_{fbD}=0.6

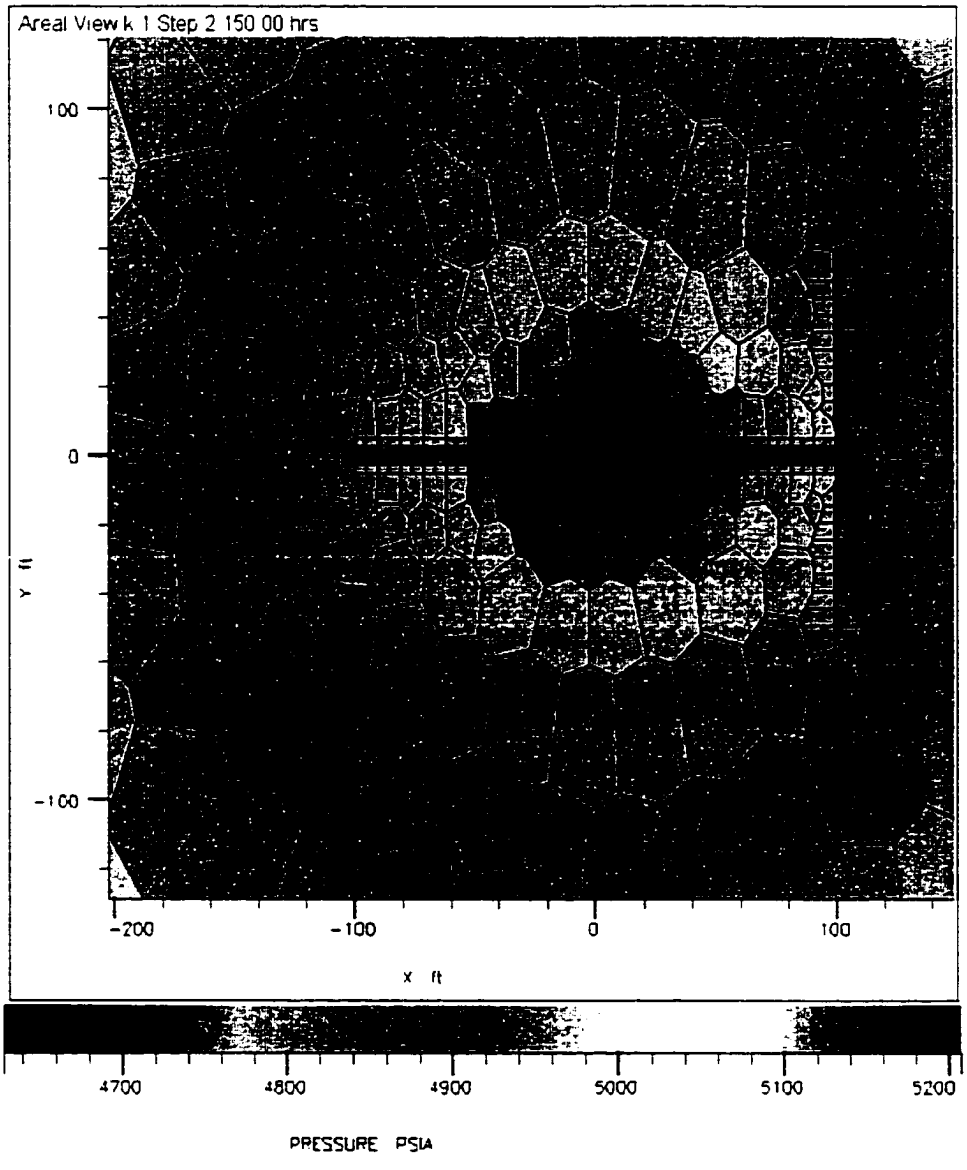

Fig. C.22.a. Close view of an elliptical PEBI grid (showing centers and pressure profile) for a hydraulically fractured well with $C_{fD}=1$ intersecting a fault with L_D of 1 and an angle of 90°

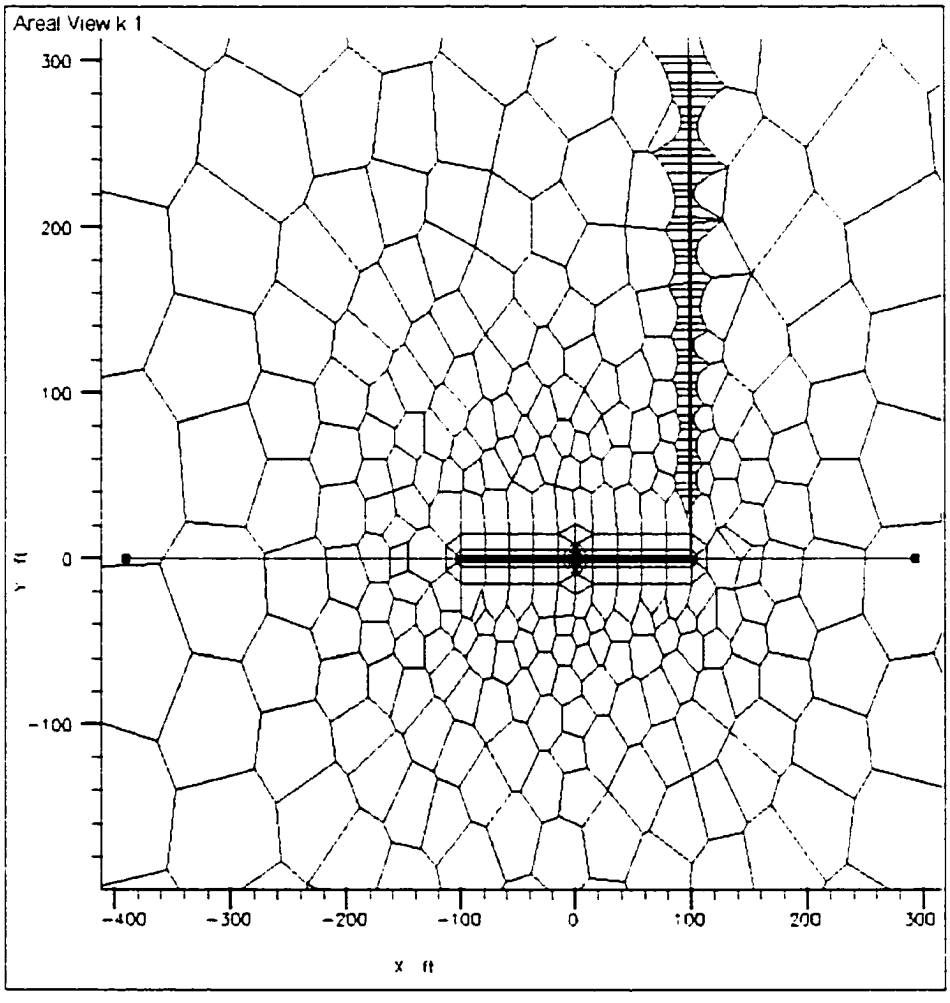

Fig. C.22.b. Close view of an elliptical PEBI grid for a hydraulically fractured well with $C_{fD}=1$ intersecting a fault at its tip. L_D of 3 and an angle of 90°

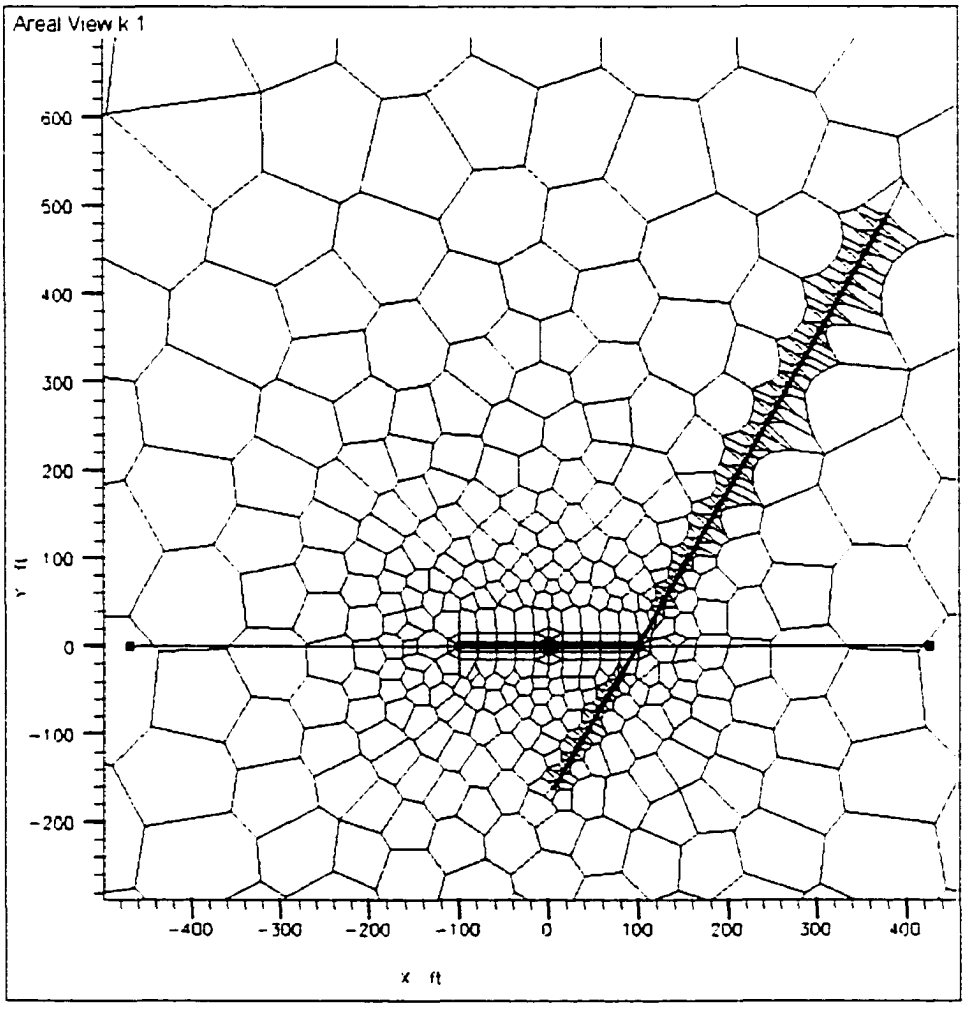

Fig. C.2.c. Close view of an elliptical PEBI grid for a hydraulically fractured well with $C_{fD}=1$ intersecting a fault at its fourth part. L_D of 7.5 and an angle of 60°

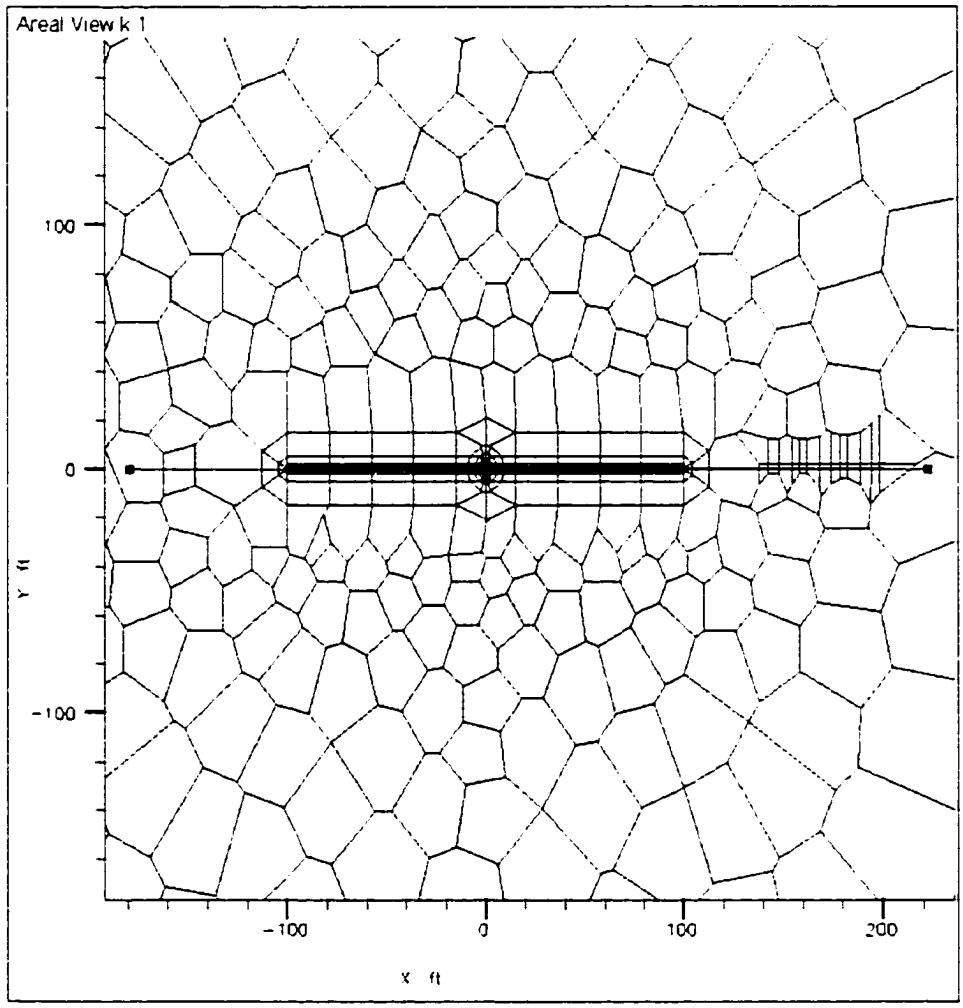

Fig. C.22.d. Close view of an elliptical PEBI grid for a hydraulically fractured well with $C_{fD}=1$ intersecting a fault at its tip. L_D of 1 and an angle of 0°

APPENDIX D

TABLES

Table D.1.a. Dimensionless pressure for a vertical well. Numerical solutions were obtained using Hexagonal, Circular and rectangular PEBI grids

	Analytic	Hexagonal		Circular		Rectangular	
t_D	P_D	P_D	Error, %	P_D	Error, %	P_D	Error, %
1028.29	3.79286	3.82867	0.944	3.83023	0.985	3.83104	1.007
1160.14	3.88169	3.91667	0.901	3.91672	0.902	3.91679	0.904
1308.47	3.97086	4.00436	0.844	4.00343	0.820	4.00274	0.803
1475.43	4.05961	4.09183	0.794	4.09034	0.757	4.08911	0.727
1664.61	4.14836	4.17967	0.755	4.17792	0.713	4.17651	0.679
1877.43	4.23744	4.26725	0.703	4.26549	0.662	4.26427	0.633
2117.48	4.32664	4.35484	0.652	4.35326	0.615	4.35251	0.598
2388.35	4.41531	4.44249	0.616	4.44123	0.587	4.44112	0.585
2693.61	4.50430	4.53012	0.573	4.52927	0.555	4.52988	0.568
3038.28	4.59350	4.61790	0.531	4.61753	0.523	4.61880	0.551
3427.38	4.68189	4.70583	0.511	4.70597	0.514	4.70777	0.553
3865.93	4.77069	4.79378	0.484	4.79444	0.498	4.79655	0.542
4360.37	4.85993	4.88181	0.450	4.88297	0.474	4.88514	0.519
4917.86	4.94927	4.96994	0.418	4.97155	0.450	4.97353	0.490
5547.02	5.03810	5.05827	0.400	5.06026	0.440	5.06179	0.470
6257.14	5.12721	5.14681	0.382	5.14911	0.427	5.14998	0.444
7057.56	5.21654	5.23547	0.363	5.23797	0.411	5.23803	0.412
7960.44	5.30557	5.32431	0.353	5.32690	0.402	5.32608	0.387
8978.70	5.39455	5.41334	0.348	5.41589	0.396	5.41418	0.364
10127.37	5.48376	5.50258	0.343	5.50496	0.387	5.50245	0.341
11422.94	5.57308	5.59203	0.340	5.59409	0.377	5.59093	0.320
12884.75	5.66195	5.68171	0.349	5.68332	0.377	5.67973	0.314
14532.88	5.75104	5.77156	0.357	5.77256	0.374	5.76884	0.310
16392.39	5.84034	5.86163	0.364	5.86189	0.369	5.85835	0.308
18489.81	5.92939	5.95188	0.379	5.95128	0.369	5.94826	0.318
20855.23	6.01838	6.04227	0.397	6.04071	0.371	6.03853	0.335
23523.04	6.10758	6.13278	0.413	6.13018	0.370	6.12914	0.353
26531.95	6.19688	6.22337	0.427	6.21970	0.368	6.22003	0.373
29926.37	6.28578	6.31401	0.449	6.30927	0.374	6.31113	0.403
33755.04	6.37487	6.40460	0.466	6.39888	0.377	6.40230	0.430
38073.84	6.46415	6.49507	0.478	6.48853	0.377	6.49342	0.453
42944.41	6.55321	6.58528	0.489	6.57819	0.381	6.58430	0.474
48439.11	6.64221	6.67515	0.496	6.66787	0.386	6.67480	0.491
54636.06	6.73139	6.76449	0.492	6.75754	0.389	6.76469	0.495
61625.55	6.82070	6.85312	0.475	6.84720	0.388	6.85378	0.485
69509.31	6.90960	6.94083	0.452	6.93682	0.394	6.94186	0.467
78402.02	6.99869	7.02740	0.410	7.02639	0.396	7.02872	0.429
88432.66	7.08795	7.11254	0.347	7.11589	0.394	7.11415	0.370
99745.96	7.17703	7.19596	0.264	7.20528	0.394	7.19794	0.291
112506.74	7.26603	7.27735	0.156	7.29454	0.392	7.27990	0.191
126900.61	7.35521	7.35639	0.016	7.38365	0.387	7.35988	0.064
143135.36	7.44451	7.43277	0.158	7.47257	0.377	7.43771	0.091

Table D.1.a. Continued

Grid	Analytic	Hexagonal		Circular		Rectangular	
t_D	P_D	P_D	Error, %	P_D	Error, %	P_D	Error, %
161447.45	7.53342	7.50619	0.361	7.56126	0.370	7.51328	0.267
182102.05	7.62251	7.57643	0.604	7.64971	0.357	7.58649	0.473
205399.36	7.71176	7.64332	0.887	7.73788	0.339	7.65728	0.706
231676.94	7.80085	7.70681	1.206	7.82576	0.319	7.72562	0.964
261315.94	7.88985	7.76696	1.558	7.91331	0.297	7.79154	1.246
294747.09	7.97901	7.82397	1.943	8.00055	0.270	7.85508	1.553
332455.47	8.06831	7.87822	2.356	8.08746	0.237	7.91632	1.884
374987.84	8.15724	7.93020	2.783	8.17407	0.206	7.97542	2.229
422961.91	8.24632	7.98052	3.223	8.26039	0.171	8.03252	2.593
477072.72	8.33555	8.02989	3.667	8.34646	0.131	8.08784	2.972
538107.06	8.42466	8.07904	4.102	8.43231	0.091	8.14161	3.360
606949.25	8.51367	8.12871	4.522	8.51798	0.051	8.19412	3.753
684598.88	8.60282	8.17958	4.920	8.60353	0.008	8.24565	4.152
772182.38	8.69212	8.23223	5.291	8.68900	0.036	8.29654	4.551
870969.50	8.78106	8.28714	5.625	8.77445	0.075	8.34711	4.942
982397.13	8.87014	8.34469	5.924	8.85990	0.115	8.39774	5.326
1108077.38	8.95936	8.40508	6.187	8.94541	0.156	8.44879	5.699
1249837.63	9.04847	8.46846	6.410	9.03100	0.193	8.50061	6.055
1409741.63	9.13749	8.53484	6.595	9.11670	0.228	8.55358	6.390
1590089.63	9.22663	8.60416	6.746	9.20252	0.261	8.60804	6.704
1793518.25	9.31592	8.67631	6.866	9.28848	0.295	8.66434	6.994
2022973.25	9.40486	8.75113	6.951	9.37459	0.322	8.72277	7.253
2281778.75	9.49395	8.82843	7.010	9.46084	0.349	8.78363	7.482
2573697.75	9.58316	8.90801	7.045	9.54724	0.375	8.84716	7.680
2902957.00	9.67228	8.98967	7.057	9.63379	0.398	8.91357	7.844
3274351.25	9.76130	9.07322	7.049	9.72046	0.418	8.98303	7.973
3693247.25	9.85044	9.15845	7.025	9.80726	0.438	9.05565	8.069
4165743.25	9.93971	9.24519	6.987	9.89418	0.458	9.13150	8.131
4698682.50	10.02867	9.33328	6.934	9.98119	0.473	9.21060	8.157
5299804.00	10.11775	9.42255	6.871	10.06830	0.489	9.29290	8.153
5977828.00	10.20696	9.51286	6.800	10.15549	0.504	9.37831	8.119
6742601.00	10.29609	9.60410	6.721	10.24274	0.518	9.46668	8.056
7605237.00	10.38510	9.69615	6.634	10.33005	0.530	9.55782	7.966
8578204.00	10.47425	9.78890	6.543	10.41740	0.543	9.65148	7.855
9675640.00	10.56350	9.88226	6.449	10.50477	0.556	9.74738	7.726
10913453.00	10.65249	9.97614	6.349	10.59216	0.566	9.84519	7.578
12309631.00	10.74156	10.07047	6.248	10.67956	0.577	9.94458	7.420
13884521.00	10.83076	10.16518	6.145	10.76695	0.589	10.04519	7.253
15660770.00	10.91989	10.26019	6.041	10.85431	0.601	10.14662	7.081
17664316.00	11.00891	10.35545	5.936	10.94164	0.611	10.24851	6.907
19924184.00	11.09805	10.45090	5.831	11.02892	0.623	10.35050	6.736
22473188.00	11.18730	10.54650	5.728	11.11613	0.636	10.45225	6.570
25348306.00	11.27630	10.64217	5.624	11.20327	0.648	10.55346	6.410

Table D.1.a. Continued

Grid	Analytic	Hexagonal		Circular		Rectangular	
t_D	P_D	P_D	Error, %	P_D	Error, %	P_D	Error, %
28591172.00	11.36537	10.73787	5.521	11.29030	0.660	10.65388	6.260
32249004.00	11.45457	10.83355	5.422	11.37723	0.675	10.75330	6.122
36374764.00	11.54370	10.92916	5.324	11.46401	0.690	10.85161	5.995
41028280.00	11.63272	11.02465	5.227	11.55063	0.706	10.94876	5.880
46277200.00	11.72186	11.11997	5.135	11.63707	0.723	11.04477	5.776
52197696.00	11.81114	11.21507	5.047	11.72329	0.744	11.13978	5.684
58875540.00	11.90014	11.30988	4.960	11.80926	0.764	11.23398	5.598
66407684.00	11.98914	11.40436	4.878	11.89494	0.786	11.32767	5.517
74903696.00	12.07838	11.49846	4.801	11.98028	0.812	11.42122	5.441
84486472.00	12.16749	11.59210	4.729	12.06522	0.841	11.51505	5.362
Average error			**3.153**		**0.455**		**3.364**

Table D.1.b. Dimensionless pressure for a vertical well generated by analytical solution and Variable and Elliptical PEBI grids

Grid	Analytic	Variable		Elliptical	
t_D	P_D	P_D	Error, %	P_D	Error, %
1028.29	3.79286	3.82994	0.978	3.82275	0.788
1160.14	3.88169	3.91693	0.908	3.90979	0.724
1308.47	3.97086	4.00388	0.832	3.99679	0.653
1475.43	4.05961	4.09083	0.769	4.08381	0.596
1664.61	4.14836	4.17835	0.723	4.17138	0.555
1877.43	4.23744	4.26580	0.669	4.25885	0.505
2117.48	4.32664	4.35342	0.619	4.34645	0.458
2388.35	4.41531	4.44123	0.587	4.43421	0.428
2693.61	4.50430	4.52912	0.551	4.52203	0.394
3038.28	4.59350	4.61725	0.517	4.61006	0.361
3427.38	4.68189	4.70558	0.506	4.69830	0.350
3865.93	4.77069	4.79398	0.488	4.78662	0.334
4360.37	4.85993	4.88247	0.464	4.87507	0.312
4917.86	4.94927	4.97105	0.440	4.96369	0.291
5547.02	5.03810	5.05980	0.431	5.05255	0.287
6257.14	5.12721	5.14871	0.419	5.14168	0.282
7057.56	5.21654	5.23766	0.405	5.23094	0.276
7960.44	5.30557	5.32672	0.399	5.32035	0.279
8978.70	5.39455	5.41585	0.395	5.40984	0.283
10127.37	5.48376	5.50508	0.389	5.49927	0.283
11422.94	5.57308	5.59438	0.382	5.58844	0.276
12884.75	5.66195	5.68378	0.386	5.67708	0.267
14532.88	5.75104	5.77319	0.385	5.76471	0.238
16392.39	5.84034	5.86268	0.382	5.85084	0.180
18489.81	5.92939	5.95220	0.385	5.93478	0.091
20855.23	6.01838	6.04174	0.388	6.01570	0.045
23523.04	6.10758	6.13129	0.388	6.09270	0.244
26531.95	6.19688	6.22083	0.386	6.16481	0.518
29926.37	6.28578	6.31037	0.391	6.23109	0.870
33755.04	6.37487	6.39987	0.392	6.29067	1.321
38073.84	6.46415	6.48932	0.389	6.34292	1.875
42944.41	6.55321	6.57868	0.389	6.38746	2.529
48439.11	6.64221	6.66793	0.387	6.42427	3.281
54636.06	6.73139	6.75703	0.381	6.45366	4.126
61625.55	6.82070	6.84593	0.370	6.47623	5.050
69509.31	6.90960	6.93459	0.362	6.49281	6.032
78402.02	6.99869	7.02296	0.347	6.50438	7.063
88432.66	7.08795	7.11095	0.325	6.51193	8.127
99745.96	7.17703	7.19850	0.299	6.51642	9.205
112506.74	7.26603	7.28551	0.268	6.51869	10.285
126900.61	7.35521	7.37190	0.227	6.51946	11.363
143135.36	7.44451	7.45757	0.175	6.51932	12.428

Table D.1.b. Continued

Grid	Analytic	Variable		Elliptical	
t_D	P_D	P_D	Error, %	P_D	Error, %
161447.45	7.53342	7.54244	0.120	6.51870	13.470
182102.05	7.62251	7.62648	0.052	6.51790	14.491
205399.36	7.71176	7.70969	0.027	6.51715	15.491
231676.94	7.80085	7.79217	0.111	6.51657	16.463
261315.94	7.88985	7.87412	0.199	6.51624	17.410
294747.09	7.97901	7.95585	0.290	6.51618	18.333
332455.47	8.06831	8.03779	0.378	6.51640	19.235
374987.84	8.15724	8.12037	0.452	6.51686	20.109
422961.91	8.24632	8.20400	0.513	6.51754	20.964
477072.72	8.33555	8.28898	0.559	6.51840	21.800
538107.06	8.42466	8.37541	0.585	6.51941	22.615
606949.25	8.51367	8.46327	0.592	6.52053	23.411
684598.88	8.60282	8.55237	0.586	6.52174	24.191
772182.38	8.69212	8.64248	0.571	6.52301	24.955
870969.50	8.78106	8.73332	0.544	6.52434	25.700
982397.13	8.87014	8.82464	0.513	6.52570	26.431
1108077.38	8.95936	8.91624	0.481	6.52712	27.148
1249837.63	9.04847	9.00796	0.448	6.52858	27.849
1409741.63	9.13749	9.09966	0.414	6.53011	28.535
1590089.63	9.22663	9.19125	0.383	6.53173	29.208
1793518.25	9.31592	9.28268	0.357	6.53346	29.868
2022973.25	9.40486	9.37393	0.329	6.53534	30.511
2281778.75	9.49395	9.46495	0.305	6.53741	31.141
2573697.75	9.58316	9.55575	0.286	6.53971	31.758
2902957.00	9.67228	9.64632	0.268	6.54230	32.360
3274351.25	9.76130	9.73667	0.252	6.54522	32.947
3693247.25	9.85044	9.82681	0.240	6.54855	33.520
4165743.25	9.93971	9.91674	0.231	6.55234	34.079
4698682.50	10.02867	10.00647	0.221	6.55667	34.621
5299804.00	10.11775	10.09602	0.215	6.56162	35.147
5977828.00	10.20696	10.18540	0.211	6.56727	35.659
6742601.00	10.29609	10.27462	0.209	6.57372	36.153
7605237.00	10.38510	10.36370	0.206	6.58105	36.630
8578204.00	10.47425	10.45263	0.206	6.58938	37.090
9675640.00	10.56350	10.54144	0.209	6.59881	37.532
10913453.00	10.65249	10.63013	0.210	6.60948	37.954
12309631.00	10.74156	10.71873	0.213	6.62150	38.356
13884521.00	10.83076	10.80724	0.217	6.63502	38.739
15660770.00	10.91989	10.89567	0.222	6.65020	39.100
17664316.00	11.00891	10.98405	0.226	6.66720	39.438
19924184.00	11.09805	11.07237	0.231	6.68620	39.753
22473188.00	11.18730	11.16066	0.238	6.70741	40.044
25348306.00	11.27630	11.24894	0.243	6.73104	40.308

Table D.1.b. Continued

Grid	Analytic	Variable		Elliptical	
t_D	P_D	P_D	Error, %	P_D	Error, %
28591172.00	11.36537	11.33720	0.248	6.75735	40.544
32249004.00	11.45457	11.42549	0.254	6.78659	40.752
36374764.00	11.54370	11.51380	0.259	6.81907	40.928
41028280.00	11.63272	11.60215	0.263	6.85511	41.070
46277200.00	11.72186	11.69058	0.267	6.89510	41.177
52197696.00	11.81114	11.77910	0.271	6.93947	41.246
58875540.00	11.90014	11.86772	0.272	6.98867	41.272
66407684.00	11.98914	11.95648	0.272	7.04326	41.253
74903696.00	12.07838	12.04540	0.273	7.10387	41.185
84486472.00	12.16749	12.13451	0.271	7.17120	41.063
Average error			**0.375**		**18.775**

Table D.2.a. Dimensionless pressure for a vertical well. Numerical solution generated using Circular PEBI grids (S=0)

	C_D=0, S=0			C_D=100, S=0		
	Analytical	Numerical		Analytical	Numerical	
t_D	P_D	P_D	Error, %	P_D	P_D	Error, %
3224.38	0.46369	0.46627	0.552	0.23806	0.23146	2.851
4299.38	0.48496	0.48739	0.498	0.28658	0.27871	2.824
5374.38	0.50146	0.50382	0.468	0.32558	0.31830	2.288
6449.38	0.51496	0.51727	0.446	0.35810	0.35172	1.815
7523.75	0.52637	0.52865	0.431	0.38546	0.38014	1.400
8598.75	0.53626	0.53853	0.421	0.40898	0.40456	1.094
9673.75	0.54500	0.54725	0.410	0.42970	0.42572	0.937
10854.38	0.55350	0.55578	0.411	0.44841	0.44591	0.560
12178.75	0.56202	0.56432	0.408	0.46717	0.46551	0.357
13664.38	0.57057	0.57287	0.400	0.48588	0.48441	0.302
15331.88	0.57907	0.58142	0.404	0.50284	0.50259	0.049
17202.50	0.58759	0.58997	0.405	0.51958	0.52000	0.081
19301.88	0.59613	0.59854	0.402	0.53617	0.53663	0.087
21656.88	0.60464	0.60710	0.406	0.55132	0.55250	0.213
24299.38	0.61315	0.61567	0.409	0.56597	0.56762	0.290
27264.38	0.62169	0.62424	0.408	0.58047	0.58203	0.268
30591.25	0.63021	0.63281	0.410	0.59394	0.59578	0.309
34323.75	0.63872	0.64138	0.414	0.60678	0.60892	0.351
38511.88	0.64726	0.64994	0.413	0.61952	0.62148	0.315
43211.25	0.65578	0.65850	0.413	0.63163	0.63353	0.300
48483.75	0.66429	0.66705	0.414	0.64304	0.64511	0.321
54399.38	0.67282	0.67559	0.411	0.65445	0.65627	0.277
61037.50	0.68135	0.68412	0.404	0.66556	0.66706	0.224
68485.00	0.68986	0.69263	0.400	0.67595	0.67750	0.229
76841.25	0.69838	0.70111	0.389	0.68641	0.68764	0.179
86217.51	0.70693	0.70956	0.371	0.69683	0.69752	0.099
96737.50	0.71543	0.71797	0.355	0.70651	0.70716	0.091
108541.25	0.72395	0.72634	0.329	0.71632	0.71659	0.037
121785.63	0.73249	0.73464	0.292	0.72623	0.72583	0.056
136646.25	0.74100	0.74288	0.253	0.73550	0.73490	0.081
153319.38	0.74951	0.75103	0.202	0.74487	0.74383	0.139
172026.89	0.75805	0.75910	0.138	0.75437	0.75263	0.232
193016.89	0.76657	0.76707	0.066	0.76344	0.76130	0.280
216568.75	0.77508	0.77496	0.016	0.77250	0.76987	0.341
242994.38	0.78362	0.78276	0.109	0.78173	0.77835	0.434
272644.38	0.79214	0.79051	0.205	0.79067	0.78674	0.500
305911.25	0.80065	0.79825	0.301	0.79952	0.79506	0.561
343238.75	0.80918	0.80601	0.393	0.80855	0.80331	0.651
385120.00	0.81771	0.81386	0.473	0.81744	0.81152	0.729
432111.88	0.82622	0.82182	0.535	0.82612	0.81971	0.782
484837.53	0.83474	0.82993	0.580	0.83500	0.82790	0.858

Table D.2.a. Continued

C_D=0, S=0				C_D=100, S=0		
analytical		Numerical		Analytical	Numerical	
t_D	P_D	P_D	Error, %	P_D	P_D	Error, %
543996.88	0.84328	0.83819	0.607	0.84388	0.83611	0.928
610373.75	0.85178	0.84660	0.613	0.85244	0.84440	0.952
684851.25	0.86031	0.85513	0.606	0.86121	0.85280	0.986
768413.13	0.86885	0.86375	0.590	0.87009	0.86135	1.015
862176.88	0.87735	0.87245	0.562	0.87856	0.87005	0.977
967377.50	0.88588	0.88120	0.531	0.88723	0.87892	0.945
1085412	0.89441	0.88997	0.499	0.89610	0.88792	0.921
1217857	0.90292	0.89876	0.463	0.90453	0.89701	0.838
1366461	0.91144	0.90755	0.429	0.91313	0.90612	0.773
1533194	0.91998	0.91633	0.398	0.92193	0.91523	0.732
1720270	0.92849	0.92509	0.367	0.93040	0.92428	0.663
1930169	0.93701	0.93384	0.339	0.93894	0.93326	0.608
2165686	0.94554	0.94257	0.315	0.94768	0.94217	0.585
2429946	0.95406	0.95128	0.292	0.95620	0.95100	0.547
2726443	0.96257	0.95997	0.271	0.96469	0.95977	0.512
3059114	0.97110	0.96864	0.255	0.97337	0.96848	0.505
3851203	0.98814	0.98592	0.226	0.99039	0.98575	0.470
4321119	0.99667	0.99452	0.216	0.99902	0.99434	0.471
4848376	1.00520	1.00312	0.208	1.00767	1.00290	0.476
5439967	1.01371	1.01169	0.200	1.01606	1.01143	0.457
6103738	1.02223	1.02024	0.195	1.02465	1.01995	0.461
6848513	1.03077	1.02879	0.193	1.03337	1.02846	0.477
7684132	1.03928	1.03731	0.190	1.04171	1.03696	0.458
8621775	1.04780	1.04582	0.189	1.05026	1.04544	0.461
9673775	1.05634	1.05432	0.191	1.05901	1.05393	0.483
10748644	1.06412	1.06208	0.192	1.06660	1.06169	0.463
11823506	1.07118	1.06910	0.195	1.07374	1.06870	0.471
12898369	1.07762	1.07550	0.197	1.08015	1.07511	0.469
13973231	1.08355	1.08138	0.201	1.08613	1.08100	0.474
15048100	1.08903	1.08682	0.203	1.09154	1.08645	0.468
16122962	1.09415	1.09188	0.208	1.09685	1.09153	0.487
17197824	1.09891	1.09661	0.210	1.10142	1.09628	0.469
18272694	1.10340	1.10105	0.213	1.10600	1.10074	0.478
19347556	1.10764	1.10524	0.217	1.11029	1.10495	0.484
20422418	1.11163	1.10920	0.219	1.11416	1.10892	0.472
21497280	1.11543	1.11295	0.223	1.11802	1.11270	0.478
22572150	1.11905	1.11652	0.227	1.12178	1.11629	0.492
23647012	1.12248	1.11993	0.228	1.12505	1.11971	0.477
24721876	1.12577	1.12318	0.231	1.12831	1.12298	0.475
25796738	1.12893	1.12629	0.234	1.13158	1.12611	0.485
26871600	1.13196	1.12928	0.237	1.13467	1.12912	0.492
27946470	1.13485	1.13215	0.239	1.13743	1.13200	0.479

Table D.2.a. Continued

	C_D=0, S=0			C_D=100, S=0		
	Analytical	Numerical		Analytical	Numerical	
t_D	P_D	P_D	Error, %	P_D	P_D	Error, %
29021332	1.13764	1.13491	0.241	1.14019	1.13478	0.476
30096194	1.14034	1.13757	0.243	1.14295	1.13746	0.483
31171062	1.14295	1.14014	0.246	1.14571	1.14004	0.497
32245924	1.14545	1.14262	0.248	1.14811	1.14253	0.488
33320786	1.14787	1.14502	0.249	1.15044	1.14495	0.480
34395648	1.15022	1.14734	0.251	1.15277	1.14728	0.478
35470520	1.15250	1.14959	0.253	1.15510	1.14955	0.483
36545380	1.15472	1.15178	0.255	1.15743	1.15175	0.494
37620244	1.15686	1.15390	0.257	1.15959	1.15388	0.495
38695108	1.15894	1.15596	0.258	1.16156	1.15595	0.485
39769976	1.16097	1.15797	0.259	1.16353	1.15797	0.480
40844836	1.16294	1.15992	0.260	1.16550	1.15993	0.480
41919700	1.16487	1.16183	0.262	1.16747	1.16184	0.484
42994572	1.16675	1.16368	0.263	1.16944	1.16371	0.493
44069432	1.16858	1.16549	0.265	1.17136	1.16553	0.501
45144296	1.17036	1.16726	0.265	1.17303	1.16730	0.491
46219160	1.17209	1.16899	0.266	1.17469	1.16903	0.484
47294020	1.17379	1.17067	0.266	1.17636	1.17072	0.481
48368888	1.17546	1.17232	0.267	1.17802	1.17238	0.482
49443752	1.17709	1.17394	0.268	1.17969	1.17400	0.485
50518612	1.17868	1.17552	0.269	1.18135	1.17558	0.491
51593480	1.18025	1.17707	0.270	1.18301	1.17713	0.500
52668344	1.18178	1.17858	0.271	1.18451	1.17865	0.498
53743204	1.18326	1.18007	0.271	1.18592	1.18013	0.490
54818076	1.18473	1.18153	0.271	1.18732	1.18159	0.485
55892940	1.18615	1.18296	0.270	1.18873	1.18302	0.482
56967804	1.18757	1.18436	0.271	1.19013	1.18442	0.482
58042664	1.18895	1.18574	0.271	1.19155	1.18580	0.485
59117528	1.19031	1.18709	0.271	1.19295	1.18715	0.489
60192388	1.19165	1.18842	0.272	1.19436	1.18848	0.495
61267256	1.19297	1.18973	0.272	1.19576	1.18978	0.503
62342120	1.19425	1.19101	0.272	1.19699	1.19106	0.498
63417000	1.19551	1.19227	0.272	1.19818	1.19232	0.492
64491872	1.19675	1.19351	0.271	1.19937	1.19356	0.487
65566688	1.19797	1.19474	0.271	1.20057	1.19477	0.485
66641564	1.19917	1.19594	0.270	1.20175	1.19597	0.483
67716440	1.20037	1.19713	0.271	1.20294	1.19715	0.484
68791312	1.20153	1.19829	0.271	1.20413	1.19831	0.486
69866184	1.20268	1.19944	0.270	1.20531	1.19945	0.489
70941064	1.20381	1.20057	0.270	1.20650	1.20057	0.494
72015880	1.20493	1.20169	0.270	1.20770	1.20168	0.501
73090752	1.20603	1.20279	0.270	1.20882	1.20277	0.503

Table D.2.a. Continued

	C_D=0, S=0			C_D=100, S=0		
	Analytical	Numerical		Analytical	Numerical	
t_D	P_D	P_D	Error, %	P_D	P_D	Error, %
74165624	1.20711	1.20387	0.268	1.20983	1.20385	0.497
75240504	1.20817	1.20494	0.268	1.21084	1.20491	0.492
76315376	1.20922	1.20600	0.267	1.21184	1.20595	0.488
77390192	1.21025	1.20704	0.265	1.21284	1.20698	0.486
78465064	1.21127	1.20807	0.265	1.21385	1.20799	0.484
79539936	1.21228	1.20908	0.264	1.21485	1.20900	0.484
80614816	1.21327	1.21008	0.263	1.21585	1.20998	0.485
81689688	1.21425	1.21107	0.262	1.21686	1.21096	0.487
82764560	1.21523	1.21205	0.262	1.21787	1.21192	0.491
83839376	1.21618	1.21301	0.261	1.21887	1.21287	0.495
84914248	1.21713	1.21397	0.260	1.21988	1.21381	0.500
85989120	1.21806	1.21491	0.259	1.22088	1.21474	0.506
87064000	1.21898	1.21584	0.258	1.22174	1.21565	0.501
88138872	1.21988	1.21676	0.256	1.22259	1.21655	0.496
89213752	1.22077	1.21767	0.255	1.22344	1.21745	0.492
90288560	1.22166	1.21857	0.254	1.22429	1.21833	0.489
91363440	1.22253	1.21946	0.252	1.22513	1.21920	0.486
92438320	1.22339	1.22033	0.251	1.22598	1.22006	0.485
93513184	1.22426	1.22120	0.250	1.22683	1.22091	0.485
94588064	1.22511	1.22206	0.249	1.22768	1.22175	0.485
95662936	1.22594	1.22292	0.248	1.22853	1.22259	0.486
96737744	1.22677	1.22376	0.246	1.22938	1.22341	0.488
97812624	1.22758	1.22459	0.244	1.23023	1.22422	0.491
98887504	1.22840	1.22542	0.243	1.23108	1.22503	0.494
99962376	1.22920	1.22624	0.242	1.23193	1.22582	0.498
101037256	1.22999	1.22705	0.240	1.23278	1.22661	0.503
102112064	1.23078	1.22785	0.239	1.23359	1.22739	0.506
103186944	1.23155	1.22864	0.237	1.23431	1.22816	0.501
104261808	1.23232	1.22943	0.235	1.23503	1.22892	0.497
105336688	1.23307	1.23021	0.233	1.23574	1.22968	0.493
Average error			**0.301**			**0.545**

Table D.2.b. Dimensionless pressure for a vertical well. Numerical solutions generated using Circular PEBI grids (C_D=10000, S=0 and S=5)

	C_D=10000, S=0			C_D=10000, S=5		
	Analytical	**Numerical**		**Analytical**	**Numerical**	
t_D	P_D	P_D	**Error, %**	P_D	P_D	**Error, %**
3224.38	0.00333	0.00335	0.635	0.00346	0.00349	0.801
4299.38	0.00444	0.00443	0.271	0.00461	0.00461	0.072
5374.38	0.00555	0.00556	0.081	0.00576	0.00574	0.363
6449.38	0.00667	0.00664	0.438	0.00691	0.00686	0.608
7523.75	0.00778	0.00781	0.485	0.00805	0.00799	0.731
8598.75	0.00889	0.00889	0.051	0.00920	0.00913	0.779
9673.75	0.01000	0.01002	0.207	0.01034	0.01026	0.784
10854.38	0.01122	0.01121	0.116	0.01160	0.01151	0.755
12178.75	0.01259	0.01259	0.028	0.01301	0.01292	0.711
13664.38	0.01413	0.01410	0.226	0.01459	0.01449	0.658
15331.88	0.01585	0.01589	0.203	0.01636	0.01626	0.584
17202.50	0.01779	0.01778	0.045	0.01834	0.01824	0.504
19301.88	0.01996	0.01996	0.017	0.02056	0.02047	0.424
21656.88	0.02239	0.02239	0.031	0.02304	0.02296	0.344
24299.38	0.02512	0.02510	0.086	0.02583	0.02576	0.267
27264.38	0.02818	0.02818	0.006	0.02894	0.02889	0.198
30591.25	0.03161	0.03161	0.002	0.03243	0.03239	0.135
34323.75	0.03546	0.03558	0.353	0.03633	0.03630	0.081
38511.88	0.03976	0.03978	0.051	0.04070	0.04068	0.040
43211.25	0.04458	0.04446	0.279	0.04558	0.04558	0.007
48483.75	0.04998	0.04966	0.628	0.05104	0.05105	0.018
54399.38	0.05601	0.05595	0.103	0.05713	0.05715	0.029
61037.50	0.06275	0.06288	0.206	0.06394	0.06396	0.031
68485.00	0.07026	0.07026	0.006	0.07154	0.07156	0.031
76841.25	0.07864	0.07866	0.025	0.08001	0.08003	0.020
86217.51	0.08798	0.08806	0.092	0.08947	0.08947	0.003
96737.50	0.09834	0.09834	0.004	0.09998	0.09997	0.014
108541.25	0.10984	0.10983	0.008	0.11169	0.11165	0.034
121785.63	0.12260	0.12261	0.013	0.12473	0.12464	0.068
136646.25	0.13663	0.13658	0.035	0.13917	0.13907	0.077
153319.38	0.15210	0.15207	0.014	0.15521	0.15507	0.093
172026.89	0.16913	0.16913	0.001	0.17301	0.17280	0.120
193016.89	0.18767	0.18773	0.035	0.19265	0.19242	0.121
216568.75	0.20786	0.20787	0.005	0.21436	0.21411	0.117
242994.38	0.22986	0.22982	0.018	0.23833	0.23803	0.127
272644.38	0.25350	0.25358	0.030	0.26467	0.26438	0.113
305911.25	0.27881	0.27870	0.040	0.29356	0.29332	0.081
343238.75	0.30598	0.30606	0.025	0.32528	0.32505	0.070
385120.00	0.33473	0.33479	0.018	0.35990	0.35974	0.046
432111.88	0.36479	0.36487	0.021	0.39748	0.39753	0.013
484837.53	0.39648	0.39652	0.011	0.43840	0.43857	0.040

Table D.2.b. Continued

	C_D=10000, S=0			C_D=10000, S=5		
	Analytical	Numerical		Analytical	Numerical	
t_D	P_D	P_D	Error, %	P_D	P_D	Error, %
543996.88	0.42944	0.42948	0.011	0.48268	0.48296	0.058
610373.75	0.46287	0.46290	0.005	0.53004	0.53076	0.135
684851.25	0.49737	0.49747	0.020	0.58101	0.58198	0.166
768413.13	0.53262	0.53271	0.016	0.63560	0.63657	0.151
862176.88	0.56712	0.56732	0.035	0.69276	0.69439	0.236
967377.50	0.60191	0.60190	0.002	0.75329	0.75524	0.259
1085412	0.63677	0.63686	0.014	0.81718	0.81881	0.199
1217857	0.66977	0.67040	0.094	0.88227	0.88469	0.274
1366461	0.70220	0.70270	0.071	0.94965	0.95239	0.288
1533194	0.73396	0.73435	0.052	1.01916	1.02131	0.211
1720270	0.76345	0.76376	0.040	1.08798	1.09076	0.255
1930169	0.79160	0.78507	0.831	1.15673	1.16001	0.283
2165686	0.81865	0.81426	0.539	1.22558	1.22827	0.219
2429946	0.84350	0.84145	0.244	1.29141	1.29470	0.255
2726443	0.86663	0.86655	0.010	1.35408	1.35852	0.326
3059114	0.88862	0.88955	0.105	1.41455	1.41894	0.309
3432385	0.90882	0.91049	0.183	1.47018	1.47528	0.346
3851203	0.92734	0.92950	0.232	1.52000	1.52696	0.456
4321119	0.94491	0.94673	0.192	1.56617	1.57351	0.467
5439967	0.97617	0.97667	0.050	1.64151	1.65045	0.542
6103738	0.99043	0.98984	0.060	1.67240	1.68098	0.510
6848513	1.00394	1.00211	0.182	1.69936	1.70669	0.430
7684132	1.01641	1.01371	0.266	1.72111	1.72826	0.414
8621775	1.02845	1.02481	0.355	1.74064	1.74648	0.334
9673775	1.04007	1.03556	0.436	1.75804	1.76222	0.237
10748644	1.05007	1.04518	0.468	1.77135	1.77515	0.214
11823506	1.05900	1.05376	0.497	1.78287	1.78608	0.180
12898369	1.06689	1.06151	0.507	1.79249	1.79567	0.177
13973231	1.07405	1.06858	0.512	1.80102	1.80429	0.181
15048100	1.08051	1.07507	0.506	1.80846	1.81215	0.203
16122962	1.08653	1.08106	0.506	1.81536	1.81938	0.221
17197824	1.09198	1.08662	0.493	1.82144	1.82606	0.253
18272694	1.09712	1.09181	0.486	1.82715	1.83226	0.279
19347556	1.10192	1.09666	0.480	1.83245	1.83803	0.304
20422418	1.10637	1.10121	0.469	1.83731	1.84341	0.331
21497280	1.11062	1.10549	0.464	1.84194	1.84843	0.351
22572150	1.11465	1.10953	0.462	1.84632	1.85313	0.367
23647012	1.11840	1.11335	0.454	1.85035	1.85753	0.386
24721876	1.12200	1.11697	0.451	1.85423	1.86167	0.400
25796738	1.12546	1.12041	0.450	1.85794	1.86556	0.408
26871600	1.12875	1.12369	0.451	1.86146	1.86923	0.416
27946470	1.13187	1.12682	0.448	1.86478	1.87270	0.423

Table D.2.b. Continued

	C_D=10000, S=0			C_D=10000, S=5		
	Analytical	Numerical		Analytical	Numerical	
t_D	P_D	P_D	Error, %	P_D	P_D	Error, %
50518612	1.17829	1.17207	0.531	1.91340	1.91977	0.332
51593480	1.17993	1.17364	0.536	1.91508	1.92134	0.325
52668344	1.18152	1.17518	0.539	1.91671	1.92288	0.320
53743204	1.18306	1.17669	0.541	1.91831	1.92438	0.316
54818076	1.18457	1.17817	0.543	1.91987	1.92586	0.311
55892940	1.18606	1.17963	0.545	1.92140	1.92731	0.307
56967804	1.18752	1.18105	0.548	1.92291	1.92874	0.302
58042664	1.18896	1.18245	0.551	1.92439	1.93014	0.298
59117528	1.19038	1.18383	0.553	1.92584	1.93152	0.294
60192388	1.19177	1.18518	0.556	1.92727	1.93288	0.290
61267256	1.19313	1.18651	0.558	1.92867	1.93421	0.287
62342120	1.19446	1.18783	0.559	1.93003	1.93553	0.284
63417000	1.19576	1.18912	0.559	1.93136	1.93683	0.282
64491872	1.19704	1.19039	0.559	1.93267	1.93811	0.281
65566688	1.19830	1.19164	0.559	1.93396	1.93937	0.279
66641564	1.19954	1.19287	0.559	1.93523	1.94062	0.278
67716440	1.20077	1.19409	0.559	1.93648	1.94185	0.276
68791312	1.20197	1.19529	0.559	1.93771	1.94307	0.276
69866184	1.20315	1.19647	0.558	1.93893	1.94428	0.275
70941064	1.20432	1.19764	0.558	1.94012	1.94547	0.275
73090752	1.20661	1.19993	0.557	1.94246	1.94781	0.275
74165624	1.20772	1.20105	0.555	1.94359	1.94897	0.276
75240504	1.20881	1.20217	0.552	1.94470	1.95011	0.277
76315376	1.20988	1.20326	0.550	1.94580	1.95124	0.279
77390192	1.21094	1.20435	0.547	1.94688	1.95236	0.281
78465064	1.21199	1.20542	0.545	1.94795	1.95348	0.283
79539936	1.21302	1.20648	0.542	1.94901	1.95458	0.285
80614816	1.21405	1.20753	0.539	1.95005	1.95567	0.288
81689688	1.21505	1.20857	0.536	1.95107	1.95676	0.290
82764560	1.21605	1.20960	0.533	1.95209	1.95783	0.293
83839376	1.21703	1.21062	0.530	1.95309	1.95890	0.296
84914248	1.21800	1.21163	0.526	1.95408	1.95996	0.300
85989120	1.21897	1.21263	0.523	1.95505	1.96101	0.304
87064000	1.21990	1.21361	0.518	1.95601	1.96205	0.308
88138872	1.22082	1.21459	0.513	1.95695	1.96309	0.313
89213752	1.22174	1.21556	0.508	1.95788	1.96412	0.317
90288560	1.22265	1.21652	0.504	1.95881	1.96514	0.322
91363440	1.22354	1.21748	0.498	1.95971	1.96616	0.328
92438320	1.22442	1.21842	0.493	1.96061	1.96717	0.333
93513184	1.22529	1.21936	0.487	1.96150	1.96817	0.339
94588064	1.22617	1.22028	0.482	1.96238	1.96917	0.345
95662936	1.22702	1.22120	0.476	1.96326	1.97016	0.351

Table D.2.b. Continued

C_D=10000, S=0				C_D=10000, S=5		
Analytical		Numerical		Analytical	Numerical	
t_D	P_D	P_D	Error, %	P_D	P_D	Error, %
96737744	1.22787	1.22212	0.471	1.96412	1.97115	0.357
97812624	1.22871	1.22302	0.465	1.96497	1.97213	0.363
98887504	1.22953	1.22392	0.459	1.96581	1.97310	0.370
99962376	1.23036	1.22481	0.453	1.96664	1.97407	0.376
101037256	1.23117	1.22570	0.447	1.96747	1.97503	0.383
102112064	1.23198	1.22657	0.440	1.96828	1.97599	0.390
103186944	1.23277	1.22744	0.434	1.96907	1.97695	0.398
104261808	1.23355	1.22831	0.426	1.96987	1.97790	0.406
105336688	1.23431	1.22917	0.419	1.97066	1.97884	0.414
Average Error			0.837			1.369

Table D.3.a. Dimensionless pressure for a vertical well intersected by a hydraulic fracture. Numerical solutions generated using Hexagonal, Circular, and Rectangular PEBI grids. C_{fD}=1

ANALYTICAL		HEXAGONAL		CIRCULAR		RECTANGULAR	
t_D	P_D	P_D	Error, %	P_D	Error, %	P_D	Error, %
0.0172	0.71347	0.95558	33.93	0.69196	3.02	0.95791	34.26
0.0860	1.04335	1.35038	29.43	0.98699	5.40	1.32946	27.42
0.1204	1.12969	1.41737	25.47	1.01892	9.80	1.38368	22.48
0.1548	1.19693	1.46253	22.19	1.03390	13.62	1.41796	18.47
0.1949	1.26045	1.50186	19.15	1.04247	17.29	1.44579	14.70
0.2453	1.32734	1.54110	16.10	1.04755	21.08	1.47207	10.90
0.3088	1.39878	1.58216	13.11	1.05038	24.91	1.49948	7.20
0.3888	1.47518	1.62674	10.27	1.05201	28.69	1.53116	3.79
0.4895	1.55560	1.67614	7.75	1.05318	32.30	1.57022	0.94
0.6162	1.64002	1.73109	5.55	1.05443	35.71	1.61901	1.28
0.7757	1.72872	1.79172	3.64	1.05609	38.91	1.67864	2.90
0.9766	1.82173	1.85756	1.97	1.05835	41.90	1.74872	4.01
1.2295	1.91924	1.92763	0.44	1.06129	44.70	1.82773	4.77
1.5478	2.02036	2.00064	0.98	1.06490	47.29	1.91340	5.29
1.9486	2.12549	2.07510	2.37	1.06915	49.70	2.00322	5.75
2.4531	2.23625	2.14956	3.88	1.07394	51.98	2.09485	6.32
3.0883	2.35320	2.22281	5.54	1.07917	54.14	2.18623	7.10
3.8879	2.47664	2.29404	7.37	1.08474	56.20	2.27576	8.11
4.8946	2.60555	2.36296	9.31	1.09051	58.15	2.36219	9.34
6.1619	2.73918	2.42990	11.29	1.09637	59.97	2.44470	10.75
7.7574	2.87809	2.49584	13.28	1.10221	61.70	2.52292	12.34
9.7660	3.02171	2.56237	15.20	1.10795	63.33	2.59700	14.06
12.2946	3.16932	2.63160	16.97	1.11352	64.87	2.66785	15.82
15.4780	3.31820	2.70601	18.45	1.11889	66.28	2.73738	17.50
19.4857	3.46996	2.78823	19.65	1.12406	67.61	2.80873	19.06
24.5311	3.62869	2.88087	20.61	1.12910	68.88	2.88638	20.46
30.8827	3.78973	2.98623	21.20	1.13412	70.07	2.97586	21.48
38.8791	3.95213	3.10612	21.41	1.13931	71.17	3.08290	21.99
48.9458	4.11553	3.24162	21.23	1.14496	72.18	3.21195	21.96
61.6192	4.27984	3.39295	20.72	1.15143	73.10	3.36478	21.38
77.5740	4.44628	3.55939	19.95	1.15916	73.93	3.53972	20.39
97.6598	4.61324	3.73927	18.94	1.16873	74.67	3.73213	19.10
154.7804	4.94671	4.12872	16.54	1.19612	75.82	4.14485	16.21
189.1761	5.09099	4.30546	15.43	1.21282	76.18	4.32746	15.00
257.9674	5.32218	4.57978	13.95	1.24640	76.58	4.60549	13.47
292.3631	5.41474	4.68943	13.40	1.26315	76.67	4.71543	12.92
326.7587	5.49647	4.78588	12.93	1.27982	76.72	4.81187	12.46
361.1544	5.57026	4.87172	12.54	1.29639	76.73	4.89765	12.08
395.5500	5.63779	4.94888	12.22	1.31286	76.71	4.97479	11.76
429.9456	5.70004	5.01884	11.95	1.32920	76.68	5.04483	11.49

Table D.3.a. Continued

ANALYTICAL		HEXAGONAL		CIRCULAR		RECTANGULAR	
t_D	P_D	P_D	Error, %	P_D	Error, %	P_D	Error, %
739.5065	6.09912	5.45795	10.51	1.47067	75.89	5.48695	10.04
773.9022	6.13312	5.49384	10.42	1.48581	75.77	5.52315	9.95
808.2978	6.16581	5.52809	10.34	1.50085	75.66	5.55766	9.86
842.6935	6.19688	5.56086	10.26	1.51579	75.54	5.59066	9.78
877.0893	6.22608	5.59228	10.18	1.53063	75.42	5.62226	9.70
911.4848	6.25426	5.62245	10.10	1.54539	75.29	5.65257	9.62
945.8804	6.28154	5.65147	10.03	1.56005	75.16	5.68171	9.55
980.2761	6.30795	5.67944	9.96	1.57463	75.04	5.70976	9.48
1014.6720	6.33334	5.70641	9.90	1.58913	74.91	5.73680	9.42
1049.0670	6.35796	5.73247	9.84	1.60355	74.78	5.76289	9.36
1083.4629	6.38188	5.75767	9.78	1.61790	74.65	5.78811	9.30
1117.8591	6.40514	5.78205	9.73	1.63217	74.52	5.81252	9.25
1152.2540	6.42778	5.80567	9.68	1.64637	74.39	5.83615	9.20
1186.6500	6.44952	5.82857	9.63	1.66051	74.25	5.85907	9.16
1221.046	6.47059	5.85077	9.58	1.67458	74.12	5.88131	9.11
1255.441	6.49115	5.87232	9.53	1.68859	73.99	5.90292	9.06
1289.837	6.51120	5.89324	9.49	1.70254	73.85	5.92392	9.02
1324.233	6.53080	5.91355	9.45	1.71643	73.72	5.94436	8.98
1358.628	6.54994	5.93329	9.41	1.73027	73.58	5.96427	8.94
1393.024	6.56824	5.95247	9.37	1.74406	73.45	5.98366	8.90
1427.420	6.58565	5.97111	9.33	1.75779	73.31	6.00257	8.85
1461.815	6.60269	5.98922	9.29	1.77148	73.17	6.02102	8.81
1496.211	6.61937	6.00683	9.25	1.78512	73.03	6.03904	8.77
1530.607	6.63572	6.02395	9.22	1.79871	72.89	6.05664	8.73
1565.002	6.65175	6.04058	9.19	1.81226	72.76	6.07384	8.69
1599.398	6.66746	6.05675	9.16	1.82577	72.62	6.09067	8.65
1633.793	6.68287	6.07246	9.13	1.83924	72.48	6.10713	8.62
1668.189	6.69801	6.08772	9.11	1.85267	72.34	6.12324	8.58
Average Error			**12.35**		**64.29**		**11.72**

Table D.3.b. Dimensionless pressure for a vertical well intersected by a hydraulic fracture. Numerical solutions generated using Variable and Elliptical PEBI grids. C_{fD}=1

ANALYTICAL		VARIABLE		ELLIPTICAL	
t_D	P_D	P_D	Error, %	P_D	Error, %
0.0172	0.71347	0.97051	36.03	0.71987	0.90
0.0860	1.04335	1.36026	30.37	1.06577	2.15
0.1204	1.12969	1.43795	27.29	1.15029	1.82
0.1548	1.19693	1.49931	25.26	1.21763	1.73
0.1949	1.26045	1.55976	23.75	1.28255	1.75
0.2453	1.32734	1.62530	22.45	1.35053	1.75
0.3088	1.39878	1.69663	21.29	1.42156	1.63
0.3888	1.47518	1.77414	20.27	1.49562	1.39
0.4895	1.55560	1.85800	19.44	1.57278	1.10
0.6162	1.64002	1.94820	18.79	1.65318	0.80
0.7757	1.72872	2.04464	18.27	1.73706	0.48
0.9766	1.82173	2.14715	17.86	1.82474	0.17
1.2295	1.91924	2.25555	17.52	1.91659	0.14
1.5478	2.02036	2.36968	17.29	2.01300	0.36
1.9486	2.12549	2.48936	17.12	2.11436	0.52
2.4531	2.23625	2.61445	16.91	2.22104	0.68
3.0883	2.35320	2.74479	16.64	2.33329	0.85
3.8879	2.47664	2.88022	16.30	2.45129	1.02
4.8946	2.60555	3.02054	15.93	2.57506	1.17
6.1619	2.73918	3.16552	15.56	2.70450	1.27
7.7574	2.87809	3.31486	15.18	2.83937	1.35
9.7660	3.02171	3.46819	14.78	2.97929	1.40
12.2946	3.16932	3.62510	14.38	3.12376	1.44
15.4780	3.31820	3.78512	14.07	3.27223	1.39
19.4857	3.46996	3.94776	13.77	3.42408	1.32
24.5311	3.62869	4.11250	13.33	3.57869	1.38
30.8827	3.78973	4.27885	12.91	3.73547	1.43
38.8791	3.95213	4.44638	12.51	3.89392	1.47
48.9458	4.11553	4.61469	12.13	4.05363	1.50
61.6192	4.27984	4.78349	11.77	4.21432	1.53
77.5740	4.44628	4.95258	11.39	4.37583	1.58
97.6598	4.61324	5.12185	11.02	4.53812	1.63
154.7804	4.94671	5.46083	10.39	4.86533	1.65
189.1761	5.09099	5.60877	10.17	5.00918	1.61
257.9674	5.32218	5.83775	9.69	5.23317	1.67
292.3631	5.41474	5.93025	9.52	5.32411	1.67
326.7587	5.49647	6.01247	9.39	5.40516	1.66
361.1544	5.57026	6.08647	9.27	5.47824	1.65
395.5500	5.63779	6.15372	9.15	5.54478	1.65
429.9456	5.70004	6.21536	9.04	5.60584	1.65

Table D.3.b. Continued

ANALYTICAL		VARIABLE		ELLIPTICAL	
t_D	P_D	P_D	Error, %	P_D	Error, %
464.3413	5.75630	6.27223	8.96	5.66224	1.63
498.7370	5.80906	6.32502	8.88	5.71464	1.63
533.1326	5.85790	6.37427	8.81	5.76355	1.61
567.5283	5.90398	6.42042	8.75	5.80940	1.60
601.9239	5.94744	6.46385	8.68	5.85254	1.60
636.3196	5.98802	6.50485	8.63	5.89328	1.58
670.7152	6.02672	6.54369	8.58	5.93186	1.57
705.1109	6.06371	6.58059	8.52	5.96851	1.57
739.5065	6.09912	6.61574	8.47	6.00340	1.57
773.9022	6.13312	6.64930	8.42	6.03669	1.57
808.2978	6.16581	6.68142	8.36	6.06854	1.58
842.6935	6.19688	6.71222	8.32	6.09905	1.58
877.0893	6.22608	6.74181	8.28	6.12835	1.57
911.4848	6.25426	6.77030	8.25	6.15653	1.56
945.8804	6.28154	6.79777	8.22	6.18367	1.56
980.2761	6.30795	6.82430	8.19	6.20986	1.55
1014.6720	6.33334	6.84996	8.16	6.23516	1.55
1049.0670	6.35796	6.87482	8.13	6.25965	1.55
1083.4629	6.38188	6.89893	8.10	6.28337	1.54
1117.8591	6.40514	6.92235	8.08	6.30638	1.54
1152.2540	6.42778	6.94513	8.05	6.32873	1.54
1186.6500	6.44952	6.96730	8.03	6.35046	1.54
1221.046	6.47059	6.98891	8.01	6.37161	1.53
1255.441	6.49115	7.00999	7.99	6.39222	1.52
1289.837	6.51120	7.03058	7.98	6.41233	1.52
1324.233	6.53080	7.05072	7.96	6.43196	1.51
1358.628	6.54994	7.07042	7.95	6.45114	1.51
1393.024	6.56824	7.08972	7.94	6.46990	1.50
1427.420	6.58565	7.10864	7.94	6.48827	1.48
1461.815	6.60269	7.12720	7.94	6.50627	1.46
1496.211	6.61937	7.14543	7.95	6.52392	1.44
1530.607	6.63572	7.16334	7.95	6.54123	1.42
1565.002	6.65175	7.18095	7.96	6.55824	1.41
1599.398	6.66746	7.19829	7.96	6.57496	1.39
1633.793	6.68287	7.21536	7.97	6.59140	1.37
1668.189	6.69801	7.23219	7.98	6.60758	1.35
Average Error			**12.59**		**1.43**

Table D.4. Dimensionless pressure for a vertical well intersected by a hydraulic fracture (C_{fD}=0.1). Numerical solutions generated using an Elliptical PEBI grid

Analytical		CASE 1 899 gridpoints		CASE 2 3462 gridpoints	
t_D	P_D	P_D	Error, %	P_D	Error, %
0.01297	1.2970	1.8169	40.08	1.8704	44.20
0.01467	1.3334	1.8720	40.39	1.9251	44.37
0.01877	1.4092	1.9910	41.28	2.0430	44.97
0.02124	1.4488	2.0546	41.82	2.1052	45.31
0.02718	1.5313	2.1896	42.99	2.2339	45.89
0.03074	1.5755	2.2608	43.49	2.2998	45.97
0.03934	1.6686	2.4099	44.43	2.4335	45.85
0.04450	1.7170	2.4876	44.88	2.5011	45.67
0.05034	1.7668	2.5674	45.32	2.5689	45.40
0.06442	1.8699	2.7325	46.13	2.7053	44.68
0.07287	1.9234	2.8177	46.50	2.7737	44.21
0.09325	2.0341	2.9928	47.13	2.9111	43.11
0.10549	2.0913	3.0825	47.39	2.9801	42.50
0.13499	2.2081	3.2655	47.88	3.1188	41.24
0.15270	2.2667	3.3586	48.17	3.1886	40.67
0.17274	2.3252	3.4525	48.48	3.2588	40.15
0.19541	2.3851	3.5471	48.72	3.3293	39.59
0.22105	2.4465	3.6423	48.88	3.4003	38.99
0.28286	2.5740	3.8334	48.93	3.5438	37.67
0.31998	2.6401	3.9290	48.82	3.6163	36.98
0.36196	2.7077	4.0244	48.63	3.6894	36.26
0.40946	2.7767	4.1194	48.36	3.7631	35.52
0.46319	2.8464	4.2138	48.04	3.8374	34.81
0.52396	2.9170	4.3075	47.67	3.9123	34.12
0.59272	2.9885	4.4004	47.24	3.9879	33.44
0.67049	3.0604	4.4923	46.79	4.0642	32.80
0.75847	3.1338	4.5832	46.25	4.1411	32.14
0.85799	3.2082	4.6732	45.66	4.2187	31.50
0.97058	3.2823	4.7621	45.09	4.2969	30.91
1.09793	3.3573	4.8502	44.47	4.3758	30.34
1.24200	3.4331	4.9375	43.82	4.4554	29.78
1.40497	3.5094	5.0241	43.16	4.5356	29.24
1.58932	3.5832	5.1100	42.61	4.6165	28.84
1.79787	3.6583	5.1956	42.02	4.6979	28.42
2.30065	3.8127	5.3660	40.74	4.8627	27.54
2.60252	3.8918	5.4510	40.06	4.9459	27.08
2.94403	3.9721	5.5360	39.37	5.0297	26.63
3.76732	4.1364	5.7065	37.96	5.1989	25.69
4.26166	4.2197	5.7921	37.26	5.2843	25.23
4.82086	4.3040	5.8780	36.57	5.3701	24.77
5.45343	4.3893	5.9642	35.88	5.4565	24.31

Table D.4. Continued

Analytical		CASE 1 899 gridpoints		CASE 2 3462 gridpoints	
t_D	P_D	P_D	Error, %	P_D	Error, %
6.16902	4.4741	6.0507	35.24	5.5432	23.90
7.89419	4.6472	6.2246	33.94	5.7181	23.04
8.93004	4.7346	6.3121	33.32	5.8061	22.63
10.1018	4.8225	6.3998	32.71	5.8945	22.23
11.4273	4.9108	6.4878	32.11	5.9833	21.84
12.9268	4.9993	6.5761	31.54	6.0724	21.46
14.6230	5.0870	6.6647	31.01	6.1618	21.13
16.5418	5.1748	6.7534	30.51	6.2515	20.81
18.7124	5.2634	6.8424	30.00	6.3414	20.48
21.1677	5.3532	6.9316	29.49	6.4317	20.15
23.9452	5.4439	7.0209	28.97	6.5221	19.81
27.0873	5.5348	7.1104	28.47	6.6127	19.47
30.6416	5.6257	7.2000	27.98	6.7035	19.16
34.6622	5.7161	7.2898	27.53	6.7945	18.87
39.2105	5.8072	7.3796	27.08	6.8856	18.57
44.3556	5.8984	7.4696	26.64	6.9768	18.28
50.1757	5.9891	7.5596	26.22	7.0681	18.02
56.7596	6.0797	7.6497	25.82	7.1595	17.76
64.2074	6.1703	7.7398	25.44	7.2509	17.51
72.6325	6.2613	7.8300	25.05	7.3423	17.26
82.1631	6.3534	7.9202	24.66	7.4338	17.01
92.9443	6.4440	8.0105	24.31	7.5253	16.78
105.1401	6.5351	8.1007	23.96	7.6168	16.55
118.9367	6.6267	8.1911	23.61	7.7084	16.32
134.5432	6.7179	8.2814	23.27	7.7999	16.11
152.1973	6.8075	8.3717	22.98	7.8914	15.92
172.1674	6.8971	8.4621	22.69	7.9830	15.74
194.7585	6.9878	8.5525	22.39	8.0745	15.55
220.3145	7.0794	8.6429	22.08	8.1662	15.35
281.9251	7.2648	8.8237	21.46	8.3495	14.93
318.9188	7.3553	8.9141	21.19	8.4413	14.77
408.1044	7.5381	9.0950	20.65	8.6250	14.42
461.6550	7.6296	9.1854	20.39	8.7169	14.25
522.2314	7.7210	9.2759	20.14	8.8087	14.09
668.2743	7.9027	9.4570	19.67	8.9921	13.78
755.9626	7.9944	9.5475	19.43	9.0833	13.62
855.1573	8.0857	9.6381	19.20	9.1739	13.46
967.3685	8.1771	9.7288	18.98	9.2638	13.29
1094.3030	8.2687	9.8195	18.76	9.3525	13.11
1237.9000	8.3600	9.9102	18.54	9.4397	12.92
1400.3270	8.4505	10.0010	18.35	9.5248	12.71
Average Error			**35.25**		**27.16**

Table D.5. Dimensionless pressure for a vertical well intersected by a hydraulic fracture (C_{fD}=0.5). Numerical solutions generated using an Elliptical PEBI grid

Analytical		CASE 1 899 gridpoints		CASE 2 3462 gridpoints	
t_D	P_D	P_D	Error, %	P_D	Error, %
0.01297	0.85792	0.93208	8.64	0.91098	6.18
0.01660	0.90730	0.98942	9.05	0.96261	6.10
0.02124	0.95953	1.05971	10.44	1.02432	6.75
0.02403	0.98676	1.09762	11.23	1.05746	7.16
0.03074	1.04462	1.17668	12.64	1.12646	7.84
0.03478	1.07550	1.21741	13.19	1.16192	8.04
0.04450	1.14002	1.30079	14.10	1.23415	8.26
0.05034	1.17371	1.34344	14.46	1.27084	8.28
0.06442	1.24370	1.43090	15.05	1.34538	8.18
0.08244	1.31749	1.52156	15.49	1.42170	7.91
0.09325	1.35576	1.56821	15.67	1.46065	7.74
0.10549	1.39498	1.61578	15.83	1.50018	7.54
0.13499	1.47563	1.71372	16.13	1.58121	7.15
0.15270	1.51643	1.76407	16.33	1.62280	7.01
0.17274	1.55745	1.81532	16.56	1.66517	6.92
0.19541	1.59955	1.86745	16.75	1.70837	6.80
0.22105	1.64280	1.92040	16.90	1.75242	6.67
0.25005	1.68720	1.97414	17.01	1.79737	6.53
0.28286	1.73312	2.02862	17.05	1.84324	6.35
0.31998	1.78049	2.08381	17.04	1.89007	6.15
0.36196	1.82932	2.13967	16.97	1.93789	5.94
0.40946	1.87938	2.19617	16.86	1.98673	5.71
0.46319	1.93044	2.25327	16.72	2.03662	5.50
0.52396	1.98259	2.31096	16.56	2.08758	5.30
0.59272	2.03583	2.36923	16.38	2.13965	5.10
0.67049	2.08998	2.42808	16.18	2.19285	4.92
0.75847	2.14547	2.48752	15.94	2.24720	4.74
0.85799	2.20222	2.54757	15.68	2.30274	4.56
0.97058	2.25962	2.60826	15.43	2.35949	4.42
1.09793	2.31823	2.66961	15.16	2.41747	4.28
1.24200	2.37801	2.73167	14.87	2.47672	4.15
1.40497	2.43881	2.79449	14.58	2.53725	4.04
1.58932	2.49908	2.85812	14.37	2.59909	4.00
1.79787	2.56081	2.92261	14.13	2.66224	3.96
2.03378	2.62406	2.98802	13.87	2.72673	3.91
2.30065	2.68882	3.05439	13.60	2.79256	3.86
2.60252	2.75517	3.12179	13.31	2.85975	3.80
2.94403	2.82317	3.19026	13.00	2.92828	3.72
3.33033	2.89286	3.25985	12.69	2.99816	3.64
3.76732	2.96425	3.33058	12.36	3.06938	3.55
4.26166	3.03681	3.40249	12.04	3.14193	3.46

Table D.5. Continued

Analytical		CASE 1 899 gridpoints		CASE 2 3462 gridpoints	
t_D	P_D	P_D	Error, %	P_D	Error, %
4.82086	3.11079	3.47559	11.73	3.21578	3.37
5.45343	3.18625	3.54990	11.41	3.29090	3.28
6.16902	3.26195	3.62542	11.14	3.36727	3.23
6.97849	3.33933	3.70213	10.86	3.44484	3.16
7.89419	3.41822	3.78001	10.58	3.52358	3.08
8.93004	3.49802	3.85904	10.32	3.60343	3.01
10.10181	3.57883	3.93917	10.07	3.68435	2.95
11.42732	3.66054	4.02035	9.83	3.76627	2.89
12.92680	3.74294	4.10253	9.61	3.84915	2.84
14.62297	3.82484	4.18562	9.43	3.93290	2.83
16.54179	3.90724	4.26958	9.27	4.01748	2.82
18.71238	3.99084	4.35432	9.11	4.10281	2.81
21.16766	4.07620	4.43975	8.92	4.18883	2.76
23.94522	4.16334	4.52581	8.71	4.27547	2.69
27.08727	4.25089	4.61241	8.50	4.36268	2.63
30.64160	4.33864	4.69948	8.32	4.45039	2.58
34.66222	4.42592	4.78693	8.16	4.53854	2.54
39.21047	4.51459	4.87471	7.98	4.62709	2.49
44.35560	4.60349	4.96274	7.80	4.71597	2.44
50.17569	4.69202	5.05098	7.65	4.80515	2.41
56.75959	4.78063	5.13938	7.50	4.89459	2.38
64.20740	4.86940	5.22789	7.36	4.98424	2.36
72.63250	4.95893	5.31650	7.21	5.07410	2.32
82.16307	5.04998	5.40518	7.03	5.16412	2.26
92.94428	5.13927	5.49392	6.90	5.25430	2.24
105.1401	5.22919	5.58273	6.76	5.34462	2.21
118.9367	5.31988	5.67161	6.61	5.43507	2.17
134.5432	5.41027	5.76057	6.47	5.52564	2.13
172.1674	5.58699	5.93881	6.30	5.70714	2.15
194.7585	5.67685	6.02814	6.19	5.79806	2.14
220.3145	5.76814	6.11762	6.06	5.88908	2.10
249.2229	5.86088	6.20728	5.91	5.98020	2.04
281.9251	5.95379	6.29713	5.77	6.07140	1.98
318.9188	6.04359	6.38715	5.68	6.16266	1.97
360.7668	6.13456	6.47735	5.59	6.25395	1.95
461.6550	6.31725	6.65815	5.40	6.43645	1.89
590.7568	6.49896	6.83921	5.24	6.61850	1.84
755.9626	6.68117	7.02010	5.07	6.79954	1.77
855.1573	6.77238	7.11033	4.99	6.88949	1.73
967.3685	6.86377	7.20039	4.90	6.97894	1.68
1094.3030	6.95528	7.29028	4.82	7.06783	1.62
Average Error			**11.33**		**4.15**

Table D.6.a. Dimensionless pressure for a vertical well intersected by a hydraulic fracture (C_{fD}=1 and C_{fD}=50). Numerical solutions generated using an Elliptical PEBI grid

	C_{fD}=1			C_{fD}=50		
	Analytical	Numerical Elliptical		Analytical	Numerical Elliptical	
t_D	P_D	P_D	Error, %	P_D	P_D	Error, %
0.10319	1.08938	1.11080	1.96634	0.25343	0.25874	2.09844
0.13758	1.16529	1.18561	1.74428	0.28637	0.29079	1.54397
0.15478	1.19693	1.21763	1.72947	0.30116	0.30509	1.30473
0.17367	1.22828	1.24971	1.74442	0.31640	0.31980	1.07429
0.19486	1.26045	1.28255	1.75358	0.33240	0.33525	0.85649
0.24531	1.32734	1.35053	1.74734	0.36689	0.36859	0.46495
0.27524	1.36244	1.38566	1.70464	0.38550	0.38657	0.27908
0.30883	1.39878	1.42156	1.62829	0.40510	0.40549	0.09610
0.38879	1.47518	1.49562	1.38546	0.44749	0.44633	0.25823
0.43623	1.51489	1.53380	1.24811	0.47029	0.46836	0.41184
0.48946	1.55560	1.57278	1.10447	0.49423	0.49152	0.54922
0.77574	1.72872	1.73706	0.48278	0.60232	0.59660	0.95095
0.97660	1.82173	1.82474	0.16544	0.66441	0.65730	1.06989
1.09576	1.86991	1.87012	0.01106	0.69761	0.68987	1.10934
1.37948	1.96975	1.96420	0.28184	0.76864	0.75966	1.16847
1.54780	2.02036	2.01300	0.36459	0.80559	0.79695	1.07250
1.73666	2.07225	2.06304	0.44461	0.84428	0.83590	0.99226
2.18634	2.18015	2.16702	0.60212	0.92731	0.91886	0.91138
2.45311	2.23625	2.22104	0.68011	0.97184	0.96292	0.91840
2.75243	2.29384	2.27646	0.75781	1.01835	1.00871	0.94641
3.08827	2.35320	2.33329	0.84588	1.06564	1.05625	0.88151
3.46510	2.41415	2.39157	0.93553	1.11504	1.10554	0.85180
3.88791	2.47664	2.45129	1.02363	1.16650	1.15657	0.85104
4.36231	2.54042	2.51245	1.10071	1.21958	1.20934	0.84035
4.89458	2.60555	2.57506	1.17026	1.27440	1.26382	0.83021
5.49182	2.67194	2.63908	1.22985	1.33092	1.31999	0.82157
6.91379	2.80792	2.77128	1.30499	1.44816	1.43728	0.75089
7.75740	2.87809	2.83937	1.34539	1.50988	1.49833	0.76497
8.70395	2.94954	2.90873	1.38359	1.57343	1.56091	0.79542
9.76598	3.02171	2.97929	1.40380	1.63795	1.62498	0.79175
10.95762	3.09498	3.05099	1.42140	1.70411	1.69048	0.79961
12.29461	3.16932	3.12376	1.43745	1.77183	1.75735	0.81734
13.79483	3.24358	3.19754	1.41936	1.83957	1.82554	0.76260
15.47804	3.31820	3.27223	1.38535	1.90795	1.89497	0.68015
17.36659	3.39320	3.34777	1.33889	1.97695	1.96558	0.57500
19.48571	3.46996	3.42408	1.32222	2.04845	2.03731	0.54410
21.86337	3.54848	3.50108	1.33575	2.12253	2.11009	0.58636
24.53110	3.62869	3.57869	1.37805	2.19912	2.18385	0.69441
27.52432	3.70965	3.65684	1.42347	2.27684	2.25852	0.80455
30.88271	3.78973	3.73547	1.43179	2.35341	2.33406	0.82233

Table D.6.a. Continued

	C_{fD}=1			C_{fD}=50		
	Analytical	Numerical Elliptical		Analytical	Numerical Elliptical	
t_D	P_D	P_D	Error, %	P_D	P_D	Error, %
34.65098	3.87006	3.81451	1.43517	2.43032	2.41039	0.82031
38.87913	3.95213	3.89392	1.47277	2.50974	2.48745	0.88788
43.62309	4.03359	3.97364	1.48637	2.58850	2.56520	0.90015
48.94582	4.11553	4.05363	1.50410	2.66800	2.64358	0.91557
54.91816	4.19828	4.13387	1.53424	2.74871	2.72253	0.95260
61.61924	4.27984	4.21432	1.53082	2.82796	2.80202	0.91743
69.13790	4.36225	4.29498	1.54215	2.90845	2.88199	0.90958
77.57401	4.44628	4.37583	1.58449	2.99123	2.96242	0.96305
87.03946	4.52941	4.45688	1.60146	3.07286	3.04327	0.96317
97.65980	4.61324	4.53812	1.62838	3.15549	3.12449	0.98227
109.5762	4.69790	4.61958	1.66713	3.23930	3.20608	1.02555
122.9461	4.78121	4.70125	1.67231	3.32139	3.28798	1.00584
137.9484	4.86416	4.78317	1.66513	3.40309	3.37020	0.96658
154.7804	4.94671	4.86533	1.64504	3.48430	3.45270	0.90705
171.9783	5.02194	4.94076	1.61665	3.55822	3.52843	0.83720
189.1761	5.09099	5.00918	1.60697	3.62643	3.59712	0.80829
206.3739	5.15486	5.07182	1.61100	3.68985	3.65997	0.80989
223.5717	5.21435	5.12958	1.62570	3.74917	3.71790	0.83421
240.7696	5.27004	5.18318	1.64833	3.80493	3.77163	0.87534
257.9674	5.32218	5.23317	1.67230	3.85727	3.82173	0.92146
275.1652	5.36971	5.28003	1.67016	3.90460	3.86866	0.92044
292.3631	5.41474	5.32411	1.67377	3.94959	3.91281	0.93120
309.5609	5.45700	5.36573	1.67244	3.99174	3.95448	0.93351
326.7587	5.49647	5.40516	1.66138	4.03093	3.99394	0.91764
343.9565	5.53418	5.44259	1.65492	4.06846	4.03141	0.91078
361.1544	5.57026	5.47824	1.65195	4.10444	4.06709	0.91004
378.3522	5.60469	5.51226	1.64915	4.13880	4.10113	0.91008
395.5500	5.63779	5.54478	1.64981	4.17191	4.13369	0.91592
412.7478	5.66967	5.57594	1.65324	4.20385	4.16489	0.92664
429.9456	5.70004	5.60584	1.65258	4.23419	4.19484	0.92929
447.1435	5.72865	5.63458	1.64205	4.26258	4.22363	0.91384
464.3413	5.75630	5.66224	1.63396	4.29010	4.25135	0.90314
481.5391	5.78309	5.68891	1.62866	4.31677	4.27808	0.89625
498.7370	5.80906	5.71464	1.62534	4.34268	4.30389	0.89334
515.9348	5.83388	5.73950	1.61777	4.36735	4.32883	0.88192
533.1326	5.85790	5.76355	1.61068	4.39126	4.35297	0.87194
550.3304	5.88125	5.78683	1.60547	4.41454	4.37636	0.86494
567.5283	5.90398	5.80940	1.60199	4.43722	4.39904	0.86045
584.7261	5.92612	5.83129	1.60028	4.45932	4.42104	0.85842
601.9239	5.94744	5.85254	1.59559	4.48057	4.44242	0.85131
619.1217	5.96798	5.87320	1.58818	4.50099	4.46321	0.83943
636.3196	5.98802	5.89328	1.58215	4.52094	4.48344	0.82960
653.5174	6.00759	5.91283	1.57732	4.54044	4.50313	0.82173

Table D.6.a. Continued

C_{fD}=1				C_{fD}=50		
Analytical		Numerical Elliptical		Analytical	Numerical Elliptical	
T_D	P_D	P_D	Error, %	P_D	P_D	Error, %
670.7152	6.02672	5.93186	1.57395	4.55952	4.52232	0.81586
687.9131	6.04542	5.95042	1.57150	4.57819	4.54103	0.81176
705.1110	6.06371	5.96851	1.57008	4.59646	4.55928	0.80890
722.3087	6.08160	5.98616	1.56929	4.61434	4.57710	0.80705
739.5065	6.09912	6.00340	1.56952	4.63188	4.59450	0.80700
756.7043	6.11629	6.02023	1.57044	4.64907	4.61151	0.80782
773.9022	6.13312	6.03669	1.57233	4.66593	4.62815	0.80986
791.1000	6.14962	6.05279	1.57464	4.68250	4.64442	0.81326
808.2978	6.16581	6.06854	1.57760	4.69875	4.66034	0.81742
825.4957	6.18169	6.08395	1.58112	4.71472	4.67594	0.82263
842.6935	6.19688	6.09905	1.57874	4.72987	4.69121	0.81737
859.8913	6.21162	6.11385	1.57398	4.74451	4.70618	0.80785
894.2870	6.24028	6.14257	1.56585	4.77305	4.73526	0.79184
911.4849	6.25426	6.15653	1.56266	4.78698	4.74938	0.78547
928.6826	6.26801	6.17022	1.56014	4.80068	4.76325	0.77981
945.8804	6.28154	6.18367	1.55805	4.81418	4.77686	0.77514
963.0782	6.29484	6.19688	1.55622	4.82747	4.79023	0.77137
980.2761	6.30795	6.20986	1.55498	4.84054	4.80336	0.76809
997.4739	6.32075	6.22262	1.55256	4.85331	4.81627	0.76324
1014.6720	6.33334	6.23516	1.55008	4.86587	4.82896	0.75856
1031.8700	6.34574	6.24751	1.54804	4.87826	4.84144	0.75470
1049.0670	6.35796	6.25965	1.54625	4.89046	4.85372	0.75132
1066.2650	6.37001	6.27160	1.54482	4.90249	4.86579	0.74847
1083.4630	6.38188	6.28337	1.54356	4.91437	4.87768	0.74652
1100.6610	6.39359	6.29496	1.54261	4.92607	4.88938	0.74484
1117.8590	6.40514	6.30638	1.54180	4.93764	4.90090	0.74404
1135.0570	6.41653	6.31764	1.54118	4.94905	4.91225	0.74353
1152.2540	6.42778	6.32873	1.54091	4.96030	4.92343	0.74344
1169.4520	6.43880	6.33967	1.53959	4.97134	4.93444	0.74227
1186.6500	6.44952	6.35046	1.53598	4.98205	4.94529	0.73776
1203.8480	6.46014	6.36111	1.53295	4.99262	4.95599	0.73374
1221.0460	6.47059	6.37161	1.52972	5.00307	4.96654	0.73012
1238.2430	6.48094	6.38198	1.52684	5.01340	4.97694	0.72714
1272.6390	6.50124	6.40234	1.52129	5.03368	4.99732	0.72221
1289.8370	6.51120	6.41233	1.51852	5.04365	5.00731	0.72050
1307.0350	6.52106	6.42220	1.51597	5.05349	5.01716	0.71891
1341.4301	6.54041	6.44160	1.51078	5.07289	5.03649	0.71748
1358.6279	6.54994	6.45114	1.50847	5.08241	5.04597	0.71701
1496.2109	6.61937	6.52392	1.44205	5.15130	5.11779	0.65055
Average Error			**1.45963**			**0.84133**

Table D.6.b. Dimensionless pressure for a vertical well intersected by a hydraulic fracture (C_{fD}=100 and C_{fD}=300). Numerical solutions generated using an Elliptical PEBI grid

	C_{fD}=100			C_{fD}=300		
	Analytical	Numerical Elliptical		Analytical	Numerical Elliptical	
t_D	P_D	P_D	Error, %	P_D	P_D	Error, %
0.10319	0.23950	0.24814	3.60898	0.22556	0.23256	3.10223
0.13758	0.27230	0.28183	3.50130	0.25821	0.26366	2.11275
0.15478	0.28699	0.29724	3.57097	0.27281	0.27769	1.78783
0.17367	0.30212	0.31328	3.69546	0.28784	0.29220	1.51564
0.19486	0.31804	0.33031	3.85805	0.30369	0.30754	1.26864
0.24531	0.35245	0.36744	4.25207	0.33806	0.34087	0.82966
0.27524	0.37103	0.38757	4.45854	0.35662	0.35892	0.64491
0.30883	0.39059	0.40877	4.65359	0.37614	0.37795	0.48053
0.38879	0.43284	0.45436	4.97198	0.41827	0.41904	0.18351
0.43623	0.45560	0.47878	5.08754	0.44099	0.44118	0.04162
0.48946	0.47943	0.50429	5.18522	0.46474	0.46442	0.06832
0.77574	0.58714	0.61760	5.18707	0.57218	0.56933	0.49835
0.97660	0.64906	0.68134	4.97279	0.63391	0.62961	0.67801
1.09576	0.68215	0.71508	4.82788	0.66687	0.66188	0.74749
1.37948	0.75293	0.78651	4.46080	0.73736	0.73096	0.86754
1.54780	0.78973	0.82428	4.37546	0.77401	0.76787	0.79351
1.73666	0.82827	0.86347	4.25035	0.81243	0.80641	0.74057
2.18634	0.91110	0.94628	3.86184	0.89508	0.88858	0.72573
2.45311	0.95556	0.98997	3.60096	0.93950	0.93227	0.76984
2.75243	1.00202	1.03523	3.31417	0.98593	0.97773	0.83215
3.08827	1.04918	1.08208	3.13595	1.03297	1.02498	0.77393
3.88791	1.14981	1.18067	2.68411	1.13338	1.12485	0.75177
4.36231	1.20278	1.23243	2.46517	1.18624	1.17748	0.73838
4.89458	1.25750	1.28584	2.25415	1.24083	1.23187	0.72205
5.49182	1.31390	1.34090	2.05438	1.29713	1.28801	0.70351
6.16192	1.37137	1.39758	1.91163	1.35447	1.34585	0.63650
6.91379	1.43091	1.45588	1.74454	1.41393	1.40537	0.60568
7.75740	1.49254	1.51575	1.55518	1.47547	1.46650	0.60826
8.70395	1.55601	1.57718	1.36043	1.53886	1.52919	0.62811
9.76598	1.62042	1.64010	1.21454	1.60315	1.59339	0.60885
10.95762	1.68650	1.70448	1.06647	1.66914	1.65902	0.60581
12.29461	1.75415	1.77025	0.91776	1.73672	1.72602	0.61583
13.79483	1.82180	1.83736	0.85414	1.80428	1.79432	0.55204
15.47804	1.89010	1.90573	0.82723	1.87250	1.86384	0.46231
17.36659	1.95900	1.97530	0.83178	1.94131	1.93451	0.35025
19.48571	2.03042	2.04599	0.76712	2.01266	2.00626	0.31783
21.86337	2.10444	2.11774	0.63205	2.08661	2.07901	0.36421
24.53110	2.18098	2.19046	0.43455	2.16311	2.15270	0.48116
27.52432	2.25866	2.26409	0.24001	2.24076	2.22727	0.60210
30.88271	2.33520	2.33854	0.14319	2.31723	2.30264	0.62978

Table D.6.b. Continued

	C_{fD}=100			C_{fD}=300		
	Analytical	Numerical Elliptical		Analytical	Numerical Elliptical	
t_D	P_D	P_D	Error, %	P_D	P_D	Error, %
34.65098	2.41204	2.41376	0.07132	2.39401	2.37877	0.63671
38.87913	2.49142	2.48968	0.06975	2.47335	2.45561	0.71729
43.62309	2.57015	2.56624	0.15199	2.55205	2.53310	0.74271
48.94582	2.64962	2.64339	0.23526	2.63151	2.61121	0.77177
54.91816	2.73032	2.72107	0.33876	2.71223	2.68989	0.82351
61.61924	2.80954	2.79925	0.36603	2.79140	2.76912	0.79836
69.13790	2.89000	2.87789	0.41897	2.87183	2.84886	0.80002
77.57401	2.97276	2.95696	0.53136	2.95457	2.92908	0.86264
87.03946	3.05437	3.03644	0.58700	3.03617	3.00976	0.86984
97.65980	3.13697	3.11631	0.65870	3.11877	3.09086	0.89485
109.5762	3.22078	3.19656	0.75207	3.20259	3.17236	0.94372
122.9461	3.30285	3.27717	0.77765	3.28467	3.25423	0.92649
137.9484	3.38455	3.35816	0.77991	3.36633	3.33645	0.88786
154.7804	3.46575	3.43950	0.75737	3.44751	3.41896	0.82829
171.9783	3.53964	3.51426	0.71699	3.52138	3.49471	0.75741
189.1761	3.60785	3.58214	0.71271	3.58956	3.56340	0.72887
206.3739	3.67126	3.64432	0.73373	3.65297	3.62624	0.73180
223.5717	3.73057	3.70169	0.77419	3.71227	3.68415	0.75772
240.7696	3.78635	3.75496	0.82920	3.76805	3.73783	0.80188
257.9674	3.83869	3.80466	0.88641	3.82040	3.78787	0.85131
275.1652	3.88601	3.85126	0.89423	3.86772	3.83474	0.85263
292.3631	3.93100	3.89513	0.91257	3.91269	3.87881	0.86589
309.5609	3.97315	3.93655	0.92109	3.95484	3.92040	0.87075
326.7587	4.01232	3.97580	0.91032	3.99403	3.95980	0.85703
343.9565	4.04986	4.01308	0.90814	4.03155	3.99722	0.85171
361.1544	4.08583	4.04859	0.91155	4.06753	4.03286	0.85237
378.3522	4.12018	4.08248	0.91504	4.10189	4.06689	0.85317
395.5500	4.15328	4.11490	0.92416	4.13498	4.09947	0.85881
412.7478	4.18522	4.14597	0.93791	4.16693	4.13072	0.86878
429.9456	4.21557	4.17578	0.94377	4.19727	4.16076	0.86976
447.1435	4.24397	4.20445	0.93108	4.22567	4.18969	0.85147
464.3413	4.27147	4.23205	0.92281	4.25318	4.21760	0.83642
481.5391	4.29816	4.25866	0.91896	4.27986	4.24457	0.82452
498.7370	4.32406	4.28435	0.91830	4.30576	4.27068	0.81482
515.9348	4.34873	4.30917	0.90978	4.33043	4.29598	0.79547
533.1326	4.37264	4.33319	0.90230	4.35433	4.32055	0.77589
550.3304	4.39590	4.35645	0.89756	4.37760	4.34442	0.75783
567.5283	4.41858	4.37899	0.89581	4.40027	4.36766	0.74105
584.7261	4.44068	4.40087	0.89654	4.42238	4.39031	0.72519
601.9239	4.46195	4.42212	0.89260	4.44362	4.41240	0.70259
619.1217	4.48235	4.44277	0.88316	4.46403	4.43398	0.67314
636.3196	4.50230	4.46285	0.87619	4.48397	4.45508	0.64418
653.5174	4.52180	4.48240	0.87125	4.50346	4.47574	0.61565

Table D.6.b. Continued

C_{fD}=100				C_{fD}=300		
Analytical		Numerical Elliptical		Analytical	Numerical Elliptical	
t_D	P_D	P_D	Error, %	P_D	P_D	Error, %
670.7152	4.54087	4.50145	0.86808	4.52252	4.49597	0.58712
687.9131	4.55954	4.52001	0.86699	4.54118	4.51581	0.55876
705.1110	4.57781	4.53811	0.86716	4.55945	4.53528	0.53011
722.3087	4.59569	4.55578	0.86850	4.57733	4.55441	0.50055
739.5065	4.61322	4.57303	0.87115	4.59485	4.57322	0.47072
756.7043	4.63041	4.58989	0.87507	4.61204	4.59173	0.44031
773.9022	4.64727	4.60637	0.88021	4.62890	4.60996	0.40915
791.1000	4.66384	4.62248	0.88670	4.64544	4.62792	0.37726
808.2978	4.68009	4.63825	0.89395	4.66170	4.64563	0.34462
825.4957	4.69606	4.65369	0.90224	4.67767	4.66311	0.31116
842.6935	4.71121	4.66881	0.89999	4.69281	4.68037	0.26510
859.8913	4.72585	4.68363	0.89345	4.70745	4.69743	0.21281
894.2870	4.75439	4.71240	0.88324	4.73599	4.73098	0.10578
911.4849	4.76832	4.72637	0.87970	4.74992	4.74749	0.05106
928.6826	4.78202	4.74009	0.87682	4.76362	4.76385	0.00475
945.8804	4.79551	4.75356	0.87484	4.77711	4.78006	0.06171
963.0782	4.80879	4.76679	0.87347	4.79040	4.79613	0.11955
980.2761	4.82188	4.77979	0.87299	4.80348	4.81207	0.17868
997.4739	4.83465	4.79256	0.87060	4.81626	4.82789	0.24146
1014.6720	4.84722	4.80512	0.86838	4.82881	4.84359	0.30599
1031.8700	4.85959	4.81748	0.86644	4.84119	4.85919	0.37169
1049.0670	4.87179	4.82964	0.86521	4.85340	4.87469	0.43858
1066.2650	4.88383	4.84160	0.86465	4.86543	4.89010	0.50695
1083.4630	4.89571	4.85338	0.86460	4.87730	4.90542	0.57644
1100.6610	4.90741	4.86497	0.86474	4.88903	4.92066	0.64706
1117.8590	4.91897	4.87640	0.86537	4.90058	4.93583	0.71937
1135.0570	4.93038	4.88766	0.86662	4.91198	4.95093	0.79292
1152.2540	4.94165	4.89875	0.86803	4.92325	4.96597	0.86755
1169.4520	4.95268	4.90969	0.86800	4.93428	4.98095	0.94576
1186.6500	4.96339	4.92047	0.86456	4.94498	4.99587	1.02912
1203.8480	4.97396	4.93111	0.86147	4.95556	5.01075	1.11373
1221.0460	4.98441	4.94161	0.85861	4.96601	5.02558	1.19968
1238.2430	4.99472	4.95197	0.85600	4.97634	5.04038	1.28690
1272.6390	5.01502	4.97229	0.85204	4.99662	5.06986	1.46569
1289.8370	5.02497	4.98225	0.85013	5.00659	5.08455	1.55725
1307.0350	5.03483	4.99210	0.84865	5.01645	5.09922	1.65012
1341.4301	5.05422	5.01144	0.84645	5.03582	5.12850	1.84034
1358.6279	5.06375	5.02095	0.84531	5.04536	5.14311	1.93739
1496.2109	5.13262	5.09332	0.76582	5.11423	5.25973	2.84504
Average Error			**1.48830**			**0.76686**

Table D.7.a. Dimensionless pressure for a vertical well intersected by a rotated hydraulic fracture. Numerical solutions generated using an Elliptical PEBI grid

	C_{fD}=300, θ = 15°			C_{fD} =100, θ = 30°			C_{fD} =50, θ = 45°		
	Analyt.	Num.	Error	Analyt.	Num.	Error	Analyt.	Num.	Error
t_D	P_D	P_D	%	P_D	P_D	%	P_D	P_D	%
0.01720	0.0974	0.1065	9.35	0.1105	0.1076	2.65	0.1234	0.1297	5.08
0.05159	0.1627	0.1721	5.81	0.1763	0.1830	3.76	0.1898	0.1981	4.34
0.08599	0.2070	0.2180	5.33	0.2209	0.2284	3.41	0.2347	0.2440	3.96
0.12038	0.2425	0.2528	4.23	0.2565	0.2659	3.67	0.2705	0.2786	3.00
0.15478	0.2728	0.2820	3.36	0.2870	0.2984	3.99	0.3012	0.3078	2.21
0.19486	0.3037	0.3117	2.64	0.3180	0.3319	4.35	0.3324	0.3376	1.58
0.24531	0.3381	0.3447	1.96	0.3525	0.3690	4.69	0.3669	0.3708	1.07
0.30883	0.3761	0.3813	1.36	0.3906	0.4100	4.98	0.4051	0.4077	0.64
0.38879	0.4183	0.4218	0.84	0.4328	0.4553	5.18	0.4475	0.4487	0.26
0.48946	0.4647	0.4666	0.41	0.4794	0.5050	5.33	0.4942	0.4940	0.04
0.61619	0.5158	0.5162	0.06	0.5307	0.5595	5.42	0.5457	0.5441	0.29
0.77574	0.5722	0.5707	0.25	0.5871	0.6190	5.42	0.6023	0.5993	0.50
0.97660	0.6339	0.6307	0.51	0.6491	0.6838	5.35	0.6644	0.6598	0.69
1.54780	0.7740	0.7684	0.72	0.7897	0.8302	5.13	0.8056	0.7986	0.87
1.94857	0.8528	0.8469	0.69	0.8687	0.9122	5.00	0.8848	0.8774	0.84
2.45311	0.9395	0.9321	0.79	0.9556	1.0001	4.66	0.9718	0.9629	0.92
3.88791	1.1334	1.1237	0.85	1.1498	1.1940	3.84	1.1665	1.1546	1.02
4.89458	1.2408	1.2302	0.86	1.2575	1.2998	3.36	1.2744	1.2610	1.05
6.16192	1.3545	1.3438	0.79	1.3714	1.4114	2.92	1.3885	1.3743	1.02
7.75740	1.4755	1.4642	0.77	1.4925	1.5285	2.41	1.5099	1.4945	1.02
9.76598	1.6031	1.5911	0.75	1.6204	1.6510	1.89	1.6379	1.6211	1.03
15.478	1.8725	1.8625	0.53	1.8901	1.9109	1.10	1.9079	1.8919	0.84
19.486	2.0127	2.0060	0.33	2.0304	2.0477	0.85	2.0485	2.0352	0.65
24.531	2.1631	2.1539	0.43	2.1810	2.1888	0.36	2.1991	2.1828	0.74
30.883	2.3172	2.3054	0.51	2.3352	2.3339	0.06	2.3534	2.3342	0.82
48.946	2.6315	2.6173	0.54	2.6496	2.6349	0.56	2.6680	2.6459	0.83
61.619	2.7914	2.7766	0.53	2.8095	2.7902	0.69	2.8280	2.8052	0.81
77.574	2.9546	2.9377	0.57	2.9728	2.9485	0.82	2.9912	2.9661	0.84
97.660	3.1188	3.1002	0.60	3.1370	3.1094	0.88	3.1555	3.1284	0.86
122.946	3.2847	3.2640	0.63	3.3029	3.2726	0.92	3.3214	3.2920	0.89
154.780	3.4475	3.4290	0.54	3.4657	3.4378	0.81	3.4843	3.4566	0.80
189.176	3.5896	3.5736	0.44	3.6079	3.5831	0.69	3.6264	3.6009	0.71
223.572	3.7123	3.6944	0.48	3.7306	3.7048	0.69	3.7492	3.7216	0.74
257.967	3.8204	3.7982	0.58	3.8387	3.8094	0.76	3.8573	3.8254	0.83
292.363	3.9127	3.8890	0.61	3.9310	3.9011	0.76	3.9496	3.9164	0.84
326.759	3.9940	3.9696	0.61	4.0123	3.9827	0.74	4.0309	3.9976	0.83
361.154	4.0675	4.0420	0.63	4.0858	4.0561	0.73	4.1044	4.0707	0.82
395.550	4.1350	4.1076	0.66	4.1533	4.1228	0.73	4.1719	4.1373	0.83
429.946	4.1973	4.1674	0.71	4.2156	4.1839	0.75	4.2342	4.1984	0.84
464.341	4.2532	4.2223	0.73	4.2715	4.2403	0.73	4.2901	4.2549	0.82
498.737	4.3058	4.2730	0.76	4.3241	4.2926	0.73	4.3427	4.3072	0.82

Table D.7.a. Continued

	C_{fD}=300, θ = 15°			C_{fD} =100, θ = 30°			C_{fD} =50, θ = 45°		
	Analyt.	Num.	Error	Analyt.	Num.	Error	Analyt.	Num.	Error
t_D	P_D	P_D	%	P_D	P_D	%	P_D	P_D	%
533.133	4.3543	4.3199	0.79	4.3726	4.3414	0.71	4.3913	4.3561	0.80
567.528	4.4003	4.3635	0.84	4.4186	4.3871	0.71	4.4372	4.4019	0.80
601.924	4.4436	4.4042	0.89	4.4619	4.4301	0.71	4.4806	4.4449	0.80
636.320	4.4840	4.4421	0.93	4.5023	4.4707	0.70	4.5209	4.4855	0.78
670.715	4.5225	4.4777	0.99	4.5409	4.5091	0.70	4.5595	4.5239	0.78
705.111	4.5595	4.5111	1.06	4.5778	4.5456	0.70	4.5965	4.5603	0.79
739.507	4.5949	4.5425	1.14	4.6132	4.5804	0.71	4.6319	4.5949	0.80
773.902	4.6289	4.5721	1.23	4.6473	4.6135	0.73	4.6659	4.6278	0.82
808.298	4.6617	4.6000	1.32	4.6801	4.6453	0.74	4.6988	4.6592	0.84
842.693	4.6928	4.6262	1.42	4.7112	4.6757	0.75	4.7299	4.6892	0.86
877.089	4.7218	4.6511	1.50	4.7402	4.7049	0.75	4.7589	4.7179	0.86
911.485	4.7499	4.6745	1.59	4.7683	4.7330	0.74	4.7870	4.7454	0.87
980.276	4.8035	4.7178	1.78	4.8219	4.7863	0.74	4.8405	4.7971	0.90
1014.67	4.8288	4.7376	1.89	4.8472	4.8116	0.74	4.8659	4.8215	0.91
1049.07	4.8534	4.7565	2.00	4.8718	4.8361	0.73	4.8905	4.8449	0.93
1083.46	4.8773	4.7743	2.11	4.8957	4.8598	0.73	4.9144	4.8675	0.95
1117.86	4.9006	4.7912	2.23	4.9190	4.8829	0.73	4.9376	4.8893	0.98
1152.25	4.9233	4.8073	2.36	4.9416	4.9053	0.74	4.9603	4.9104	1.01
1186.65	4.9450	4.8224	2.48	4.9634	4.9271	0.73	4.9820	4.9307	1.03
1221.05	4.9660	4.8368	2.60	4.9844	4.9483	0.72	5.0031	4.9503	1.05
1255.44	4.9865	4.8504	2.73	5.0049	4.9690	0.72	5.0236	4.9694	1.08
1289.84	5.0066	4.8633	2.86	5.0250	4.9892	0.71	5.0436	4.9878	1.11
1324.23	5.0262	4.8755	3.00	5.0446	5.0089	0.71	5.0632	5.0056	1.14
1358.63	5.0454	4.8870	3.14	5.0637	5.0282	0.70	5.0824	5.0228	1.17
1427.42	5.0808	4.9082	3.40	5.0992	5.0655	0.66	5.1179	5.0558	1.21
1461.82	5.0977	4.9180	3.53	5.1161	5.0836	0.63	5.1348	5.0716	1.23
Average Error			**1.57**			**1.82**			**1.09**

Table D.7.b. Dimensionless pressure for a vertical well intersected by a rotated hydraulic fracture. Numerical solutions generated using an Elliptical PEBI grid

	C_{fD}=50, θ = 60°			C_{fD}=1, θ = 75°			C_{fD}=1, θ = 90°		
	Analyt.	Num.	Error	Analyt.	Num.	Error	Analyt.	Num.	Error
t_D	P_D	P_D	%	P_D	P_D	%	P_D	P_D	%
0.01720	0.1234	0.1279	3.60	0.7135	0.7195	0.84	0.7135	0.7198	0.89
0.05159	0.1898	0.1980	4.28	0.9237	0.9479	2.62	0.9237	0.9481	2.64
0.08599	0.2347	0.2440	3.95	1.0433	1.0657	2.14	1.0433	1.0658	2.15
0.12038	0.2705	0.2791	3.16	1.1297	1.1505	1.84	1.1297	1.1503	1.83
0.15478	0.3012	0.3087	2.49	1.1969	1.2182	1.78	1.1969	1.2176	1.73
0.19486	0.3324	0.3387	1.90	1.2604	1.2835	1.83	1.2604	1.2825	1.75
0.24531	0.3669	0.3720	1.39	1.3273	1.3518	1.84	1.3273	1.3505	1.75
0.30883	0.4051	0.4088	0.92	1.3988	1.4231	1.74	1.3988	1.4216	1.63
0.38879	0.4475	0.4496	0.48	1.4752	1.4974	1.51	1.4752	1.4956	1.39
0.48946	0.4942	0.4947	0.09	1.5556	1.5747	1.23	1.5556	1.5728	1.10
0.61619	0.5457	0.5445	0.22	1.6400	1.6551	0.92	1.6400	1.6532	0.80
0.77574	0.6023	0.5994	0.49	1.7287	1.7389	0.59	1.7287	1.7371	0.48
0.97660	0.6644	0.6598	0.70	1.8217	1.8265	0.26	1.8217	1.8248	0.17
1.54780	0.8056	0.7987	0.86	2.0204	2.0144	0.29	2.0204	2.0130	0.36
1.94857	0.8848	0.8779	0.78	2.1255	2.1156	0.46	2.1255	2.1144	0.52
2.45311	0.9718	0.9640	0.81	2.2362	2.2222	0.63	2.2362	2.2210	0.68
3.88791	1.1665	1.1572	0.80	2.4766	2.4526	0.97	2.4766	2.4513	1.02
4.89458	1.2744	1.2644	0.79	2.6055	2.5766	1.11	2.6055	2.5751	1.17
6.16192	1.3885	1.3785	0.72	2.7392	2.7064	1.20	2.7392	2.7045	1.27
7.75740	1.5099	1.4992	0.71	2.8781	2.8417	1.26	2.8781	2.8394	1.35
9.76598	1.6379	1.6262	0.72	3.0217	2.9821	1.31	3.0217	2.9793	1.40
15.478	1.9079	1.8971	0.57	3.3182	3.2762	1.26	3.3182	3.2722	1.39
19.486	2.0485	2.0401	0.41	3.4700	3.4287	1.19	3.4700	3.4241	1.32
24.531	2.1991	2.1872	0.54	3.6287	3.5838	1.24	3.6287	3.5787	1.38
30.883	2.3534	2.3381	0.65	3.7897	3.7412	1.28	3.7897	3.7355	1.43
48.946	2.6680	2.6488	0.72	4.1155	4.0604	1.34	4.1155	4.0536	1.50
61.619	2.8280	2.8078	0.71	4.2798	4.2216	1.36	4.2798	4.2143	1.53
77.574	2.9912	2.9687	0.75	4.4463	4.3836	1.41	4.4463	4.3758	1.59
97.660	3.1555	3.1313	0.77	4.6132	4.5465	1.45	4.6132	4.5381	1.63
122.946	3.3214	3.2952	0.79	4.7812	4.7103	1.48	4.7812	4.7012	1.67
154.780	3.4843	3.4603	0.69	4.9467	4.8751	1.45	4.9467	4.8653	1.65
189.176	3.6264	3.6049	0.59	5.0910	5.0196	1.40	5.0910	5.0092	1.61
223.572	3.7492	3.7259	0.62	5.2144	5.1406	1.41	5.2144	5.1296	1.63
257.967	3.8573	3.8298	0.71	5.3222	5.2448	1.45	5.3222	5.2332	1.67
292.363	3.9496	3.9209	0.73	5.4147	5.3361	1.45	5.4147	5.3241	1.67
326.759	4.0309	4.0021	0.72	5.4965	5.4175	1.44	5.4965	5.4052	1.66
361.154	4.1044	4.0752	0.71	5.5703	5.4909	1.42	5.5703	5.4782	1.65
395.550	4.1719	4.1419	0.72	5.6378	5.5577	1.42	5.6378	5.5448	1.65
429.946	4.2342	4.2031	0.74	5.7000	5.6189	1.42	5.7000	5.6059	1.65
464.341	4.2901	4.2597	0.71	5.7563	5.6755	1.40	5.7563	5.6623	1.63
498.737	4.3427	4.3124	0.70	5.8091	5.7280	1.40	5.8091	5.7147	1.62

Table D.7.b. Continued

	C_{fD}=50, θ = 60°			C_{fD}=1, θ = 75°			C_{fD}=1, θ = 90°		
	Analyt.	Num.	Error	Analyt.	Num.	Error	Analyt.	Num.	Error
t_D	P_D	P_D	%	P_D	P_D	%	P_D	P_D	%
533.133	4.3913	4.3617	0.67	5.8579	5.7770	1.38	5.8579	5.7636	1.61
567.528	4.4372	4.4081	0.66	5.9040	5.8229	1.37	5.9040	5.8094	1.60
601.924	4.4806	4.4518	0.64	5.9474	5.8660	1.37	5.9474	5.8526	1.60
636.320	4.5209	4.4933	0.61	5.9880	5.9068	1.36	5.9880	5.8933	1.58
670.715	4.5595	4.5328	0.59	6.0267	5.9453	1.35	6.0267	5.9319	1.57
705.111	4.5965	4.5705	0.57	6.0637	5.9820	1.35	6.0637	5.9685	1.57
739.507	4.6319	4.6065	0.55	6.0991	6.0168	1.35	6.0991	6.0034	1.57
773.902	4.6659	4.6410	0.53	6.1331	6.0501	1.35	6.1331	6.0367	1.57
808.298	4.6988	4.6743	0.52	6.1658	6.0819	1.36	6.1658	6.0686	1.58
842.693	4.7299	4.7063	0.50	6.1969	6.1124	1.36	6.1969	6.0991	1.58
877.089	4.7589	4.7372	0.46	6.2261	6.1416	1.36	6.2261	6.1284	1.57
911.485	4.7870	4.7672	0.41	6.2543	6.1697	1.35	6.2543	6.1565	1.56
980.276	4.8405	4.8244	0.33	6.3079	6.2230	1.35	6.3079	6.2099	1.55
1014.67	4.8659	4.8518	0.29	6.3333	6.2483	1.34	6.3333	6.2352	1.55
1049.07	4.8905	4.8785	0.25	6.3580	6.2727	1.34	6.3580	6.2596	1.55
1083.46	4.9144	4.9045	0.20	6.3819	6.2965	1.34	6.3819	6.2834	1.54
1117.86	4.9376	4.9299	0.16	6.4051	6.3195	1.34	6.4051	6.3064	1.54
1152.25	4.9603	4.9548	0.11	6.4278	6.3418	1.34	6.4278	6.3287	1.54
1186.65	4.9820	4.9791	0.06	6.4495	6.3636	1.33	6.4495	6.3505	1.54
1221.05	5.0031	5.0030	0.00	6.4706	6.3847	1.33	6.4706	6.3716	1.53
1255.44	5.0236	5.0264	0.06	6.4911	6.4054	1.32	6.4911	6.3922	1.52
1289.84	5.0436	5.0494	0.11	6.5112	6.4256	1.32	6.5112	6.4123	1.52
1324.23	5.0632	5.0720	0.17	6.5308	6.4453	1.31	6.5308	6.4319	1.51
1358.63	5.0824	5.0943	0.23	6.5499	6.4645	1.30	6.5499	6.4511	1.51
1427.42	5.1179	5.1378	0.39	6.5856	6.5019	1.27	6.5856	6.4883	1.48
1461.82	5.1348	5.1591	0.47	6.6027	6.5200	1.25	6.6027	6.5062	1.46
Average Error			**0.80**			**1.35**			**1.48**

Table D.8. Dimensionless pressure for a horizontal well (θ=0, 45 and 90°). Numerical solutions generated using all available PEBI grids

	Analyt.	Numerical Circular		Numerical Elliptical		Numerical Hexagonal		Numerical Rectangular		Numerical Variable	
t_D	P_D	P_D	Er. %	P_D	Er. %	P_D	Er. %	P_D	Er. %	P_D	Er. %
1.414	7.45E-06	7.41E-06	0.54	7.40E-06	0.58	7.41E-06	0.48	7.41E-06	0.54	7.41E-06	0.49
1.595	7.62E-06	7.65E-06	0.38	7.65E-06	0.35	7.65E-06	0.40	7.65E-06	0.36	7.65E-06	0.38
1.801	7.78E-06	7.88E-06	1.17	7.87E-06	1.16	7.87E-06	1.15	7.87E-06	1.14	7.87E-06	1.14
2.032	7.93E-06	8.08E-06	1.87	8.08E-06	1.87	8.08E-06	1.82	8.08E-06	1.84	8.08E-06	1.82
2.294	8.06E-06	8.26E-06	2.47	8.27E-06	2.49	8.26E-06	2.41	8.26E-06	2.45	8.26E-06	2.42
2.589	8.19E-06	8.43E-06	2.95	8.43E-06	2.98	8.42E-06	2.89	8.43E-06	2.93	8.43E-06	2.89
2.922	8.30E-06	8.58E-06	3.36	8.58E-06	3.40	8.57E-06	3.31	8.58E-06	3.35	8.57E-06	3.32
3.298	8.40E-06	8.71E-06	3.68	8.71E-06	3.72	8.71E-06	3.63	8.71E-06	3.68	8.71E-06	3.64
3.723	8.50E-06	8.83E-06	3.91	8.83E-06	3.95	8.83E-06	3.89	8.83E-06	3.93	8.83E-06	3.90
4.202	8.59E-06	8.94E-06	4.10	8.94E-06	4.13	8.94E-06	4.09	8.94E-06	4.12	8.94E-06	4.10
6.041	8.83E-06	9.22E-06	4.40	9.22E-06	4.40	9.22E-06	4.43	9.22E-06	4.43	9.22E-06	4.44
9.803	9.12E-06	9.54E-06	4.55	9.53E-06	4.51	9.54E-06	4.59	9.54E-06	4.55	9.54E-06	4.58
11.065	9.20E-06	9.62E-06	4.58	9.61E-06	4.54	9.62E-06	4.62	9.62E-06	4.57	9.62E-06	4.60
12.488	9.27E-06	9.70E-06	4.61	9.70E-06	4.57	9.70E-06	4.63	9.70E-06	4.59	9.70E-06	4.62
17.956	9.52E-06	9.96E-06	4.70	9.96E-06	4.68	9.96E-06	4.69	9.96E-06	4.67	9.96E-06	4.68
20.266	9.60E-06	1.01E-05	4.73	1.01E-05	4.71	1.01E-05	4.71	1.01E-05	4.69	1.01E-05	4.70
47.287	1.04E-05	1.09E-05	4.65	1.09E-05	4.70	1.09E-05	4.62	1.09E-05	4.67	1.09E-05	4.64
53.372	1.05E-05	1.10E-05	4.59	1.10E-05	4.64	1.10E-05	4.57	1.10E-05	4.62	1.10E-05	4.59
60.239	1.07E-05	1.11E-05	4.52	1.12E-05	4.57	1.11E-05	4.50	1.12E-05	4.55	1.11E-05	4.52
67.990	1.08E-05	1.13E-05	4.44	1.13E-05	4.48	1.13E-05	4.43	1.13E-05	4.48	1.13E-05	4.45
76.738	1.10E-05	1.15E-05	4.34	1.15E-05	4.38	1.15E-05	4.34	1.15E-05	4.38	1.15E-05	4.36
86.612	1.12E-05	1.16E-05	4.24	1.16E-05	4.28	1.16E-05	4.26	1.16E-05	4.29	1.16E-05	4.27
97.756	1.14E-05	1.18E-05	4.13	1.18E-05	4.16	1.18E-05	4.15	1.18E-05	4.17	1.18E-05	4.17
110.33	1.16E-05	1.20E-05	4.02	1.20E-05	4.03	1.20E-05	4.04	1.20E-05	4.05	1.20E-05	4.06
124.53	1.18E-05	1.22E-05	3.90	1.22E-05	3.90	1.22E-05	3.94	1.22E-05	3.93	1.22E-05	3.94
140.56	1.20E-05	1.24E-05	3.78	1.24E-05	3.76	1.24E-05	3.81	1.24E-05	3.80	1.24E-05	3.82
158.64	1.22E-05	1.27E-05	3.66	1.27E-05	3.64	1.27E-05	3.70	1.27E-05	3.67	1.27E-05	3.69
179.05	1.25E-05	1.29E-05	3.54	1.29E-05	3.50	1.29E-05	3.57	1.29E-05	3.53	1.29E-05	3.57
202.09	1.27E-05	1.32E-05	3.41	1.32E-05	3.37	1.32E-05	3.44	1.32E-05	3.40	1.32E-05	3.43
228.09	1.30E-05	1.35E-05	3.29	1.35E-05	3.25	1.35E-05	3.32	1.35E-05	3.27	1.35E-05	3.31
257.44	1.33E-05	1.38E-05	3.17	1.38E-05	3.11	1.38E-05	3.19	1.38E-05	3.13	1.38E-05	3.17
290.57	1.37E-05	1.41E-05	3.05	1.41E-05	3.00	1.41E-05	3.06	1.41E-05	3.01	1.41E-05	3.04
327.95	1.40E-05	1.44E-05	2.93	1.44E-05	2.88	1.44E-05	2.94	1.44E-05	2.88	1.44E-05	2.91
370.15	1.44E-05	1.48E-05	2.80	1.48E-05	2.75	1.48E-05	2.80	1.48E-05	2.75	1.48E-05	2.78
417.78	1.48E-05	1.52E-05	2.69	1.52E-05	2.65	1.52E-05	2.68	1.52E-05	2.64	1.52E-05	2.66
471.54	1.52E-05	1.56E-05	2.56	1.56E-05	2.53	1.56E-05	2.54	1.56E-05	2.51	1.56E-05	2.52
532.21	1.56E-05	1.60E-05	2.44	1.60E-05	2.42	1.60E-05	2.42	1.60E-05	2.40	1.60E-05	2.40
600.69	1.61E-05	1.64E-05	2.32	1.64E-05	2.31	1.64E-05	2.29	1.64E-05	2.28	1.64E-05	2.28
677.98	1.66E-05	1.69E-05	2.18	1.69E-05	2.18	1.69E-05	2.15	1.69E-05	2.16	1.69E-05	2.14
765.21	1.71E-05	1.74E-05	2.06	1.74E-05	2.08	1.74E-05	2.03	1.74E-05	2.05	1.74E-05	2.03
863.67	1.76E-05	1.80E-05	1.92	1.80E-05	1.96	1.80E-05	1.89	1.80E-05	1.93	1.80E-05	1.90

Table D.8. Continued

	Analyt.	Numerical Circular		Numerical Elliptical		Numerical Hexagonal		Numerical Rectangular		Numerical Variable	
t_D	P_D	P_D	Er. %	P_D	Er. %	P_D	Er. %	P_D	Er. %	P_D	Er. %
974.80	1.82E-05	1.85E-05	1.79	1.85E-05	1.84	1.85E-05	1.77	1.85E-05	1.81	1.85E-05	1.78
1100.22	1.88E-05	1.91E-05	1.67	1.91E-05	1.72	1.91E-05	1.64	1.91E-05	1.70	1.91E-05	1.66
1241.80	1.94E-05	1.97E-05	1.52	1.98E-05	1.58	1.97E-05	1.50	1.97E-05	1.57	1.97E-05	1.52
1401.58	2.01E-05	2.04E-05	1.40	2.04E-05	1.46	2.04E-05	1.39	2.04E-05	1.45	2.04E-05	1.42
1581.91	2.08E-05	2.11E-05	1.27	2.11E-05	1.33	2.11E-05	1.27	2.11E-05	1.32	2.11E-05	1.29
1785.46	2.15E-05	2.18E-05	1.14	2.18E-05	1.19	2.18E-05	1.14	2.18E-05	1.18	2.18E-05	1.17
2015.20	2.23E-05	2.25E-05	1.02	2.26E-05	1.06	2.25E-05	1.03	2.26E-05	1.05	2.26E-05	1.05
2274.49	2.31E-05	2.33E-05	0.89	2.33E-05	0.90	2.33E-05	0.90	2.33E-05	0.89	2.33E-05	0.91
2567.15	2.40E-05	2.42E-05	0.78	2.41E-05	0.77	2.42E-05	0.79	2.41E-05	0.76	2.42E-05	0.80
2897.46	2.48E-05	2.50E-05	0.67	2.50E-05	0.63	2.50E-05	0.67	2.50E-05	0.59	2.50E-05	0.67
3270.27	2.58E-05	2.59E-05	0.55	2.59E-05	0.47	2.59E-05	0.55	2.59E-05	0.42	2.59E-05	0.53
3691.06	2.67E-05	2.68E-05	0.45	2.68E-05	0.34	2.68E-05	0.44	2.68E-05	0.25	2.68E-05	0.40
4165.99	2.77E-05	2.78E-05	0.33	2.78E-05	0.17	2.78E-05	0.30	2.78E-05	0.06	2.78E-05	0.25
4702.03	2.88E-05	2.88E-05	0.23	2.88E-05	0.03	2.88E-05	0.19	2.87E-05	0.13	2.88E-05	0.11
5307.04	2.99E-05	2.99E-05	0.12	2.98E-05	0.12	2.99E-05	0.06	2.98E-05	0.33	2.99E-05	0.05
5989.89	3.10E-05	3.10E-05	0.01	3.09E-05	0.28	3.10E-05	0.09	3.09E-05	0.56	3.10E-05	0.22
6760.61	3.22E-05	3.22E-05	0.11	3.21E-05	0.41	3.22E-05	0.21	3.20E-05	0.77	3.21E-05	0.37
7630.49	3.35E-05	3.34E-05	0.24	3.33E-05	0.57	3.34E-05	0.37	3.31E-05	1.01	3.33E-05	0.56
8612.30	3.48E-05	3.47E-05	0.36	3.46E-05	0.70	3.46E-05	0.52	3.44E-05	1.24	3.45E-05	0.73
9720.47	3.62E-05	3.60E-05	0.49	3.59E-05	0.84	3.59E-05	0.67	3.56E-05	1.47	3.58E-05	0.91
10971.2	3.76E-05	3.74E-05	0.64	3.72E-05	0.98	3.73E-05	0.84	3.70E-05	1.72	3.72E-05	1.11
12382.8	3.91E-05	3.88E-05	0.77	3.87E-05	1.08	3.87E-05	0.99	3.83E-05	1.94	3.86E-05	1.28
13976.1	4.07E-05	4.03E-05	0.93	4.02E-05	1.20	4.02E-05	1.15	3.98E-05	2.17	4.01E-05	1.46
15774.4	4.23E-05	4.19E-05	1.08	4.18E-05	1.29	4.18E-05	1.30	4.13E-05	2.38	4.16E-05	1.63
17804.2	4.40E-05	4.35E-05	1.23	4.34E-05	1.35	4.34E-05	1.44	4.29E-05	2.57	4.32E-05	1.78
20095.0	4.58E-05	4.52E-05	1.40	4.51E-05	1.42	4.51E-05	1.59	4.45E-05	2.75	4.49E-05	1.94
22680.6	4.76E-05	4.69E-05	1.54	4.70E-05	1.42	4.68E-05	1.68	4.63E-05	2.88	4.67E-05	2.04
25598.9	4.96E-05	4.87E-05	1.70	4.89E-05	1.43	4.87E-05	1.78	4.81E-05	2.99	4.85E-05	2.15
28892.7	5.16E-05	5.06E-05	1.85	5.08E-05	1.40	5.06E-05	1.85	5.00E-05	3.06	5.04E-05	2.22
			2.36		**2.38**		**2.38**		**2.57**		**2.44**

Table D.9. Number of gridblocks used for simulating hydraulic fracture well with a branch fracture (horizontal well)

Branch Fracture starting at the main fracture tip			
Angle,	**Number of grid blocks**		
Degrees	X_{fbD}=0.2	X_{fbD}=0.4	X_{fbD} =0.6
0	1454	1476	1498
10	1457	1479	1501
20	1458	1480	1502
30	1458	1481	1502
Branch fracture starting at middle distance between wellbore and main fracture tip			
Angle,	**Number of grid blocks**		
Degrees	X_{fbD}=0.2	X_{fbD}=0.4	X_{fbD} =0.6
10	1461	1483	1505
20	1463	1485	1507
30	1463	1485	1509
Branch fracture starting at the wellbore			
Angle,	**Number of grid blocks**		
Degrees	X_{fbD}=0.2	X_{fbD}=0.4	X_{fbD} =0.6
10	1461	1483	1505
20	1462	1485	1507
30	1463	1485	1509

Table D.10. Dimensionless pressure for a hydraulic fractured well with a branch fracture starting from the wellbore, $\theta = 30°$ and X_{fbD}=0.6

	C_{fD}=1		C_{fD} =10		C_{fD} =50	
t_D			P_D			
	X_{fbD}=0	X_{fbD} =0.6	X_{fbD} =0	X_{fbD} =0.6	X_{fbD} =0	X_{fbD} =0.6
1.E-07	0.041813	0.041866	0.013144	0.013163	0.005866	0.005872
5.E-07	0.066557	0.066651	0.020953	0.020976	0.009350	0.009366
1.E-06	0.078204	0.078288	0.024756	0.024793	0.011112	0.011126
5.E-06	0.117017	0.117208	0.037069	0.037130	0.016577	0.016606
1.E-05	0.139551	0.139745	0.044057	0.044091	0.019630	0.019645
5.E-05	0.207125	0.207479	0.066012	0.066083	0.029822	0.029847
1.E-04	0.246848	0.247217	0.078229	0.078343	0.036058	0.036114
5.E-04	0.369484	0.369870	0.118022	0.118175	0.060052	0.060100
1.E-03	0.436329	0.436724	0.140851	0.140992	0.076591	0.076678
5.E-03	0.641164	0.642110	0.220633	0.220931	0.145449	0.145696
1.E-02	0.757672	0.758714	0.272681	0.272948	0.194811	0.195035
5.E-02	1.090808	1.091793	0.474104	0.474827	0.387225	0.387577
1.E-01	1.281124	1.282513	0.609776	0.610804	0.517449	0.518171
5.E-01	1.830350	1.832356	1.079367	1.080367	0.979284	0.980423
1.E+00	2.120543	2.122878	1.346578	1.348840	1.238784	1.240117
5.E+00	2.871910	2.877022	2.070215	2.072769	1.969664	1.971550
1.E+01	3.216446	3.219915	2.406539	2.410629	2.312414	2.315497
5.E+01	4.018462	4.022331	3.224253	3.226560	3.104332	3.108082
1.E+02	4.377249	4.382546	3.560712	3.563561	3.459812	3.463311
5.E+02	5.186461	5.194307	4.372194	4.378748	4.254039	4.258842
1.E+03	5.537279	5.545215	4.717460	4.720977	4.608720	4.616414

Table D.10. Continued

	C_{fD} =100		C_{fD} =300	
t_D	P_D			
	X_{fbD}=0	X_{fbD} =0.6	X_{fbD} =0	X_{fbD} =0.6
1.E-07	0.004144	0.004148	0.001944	0.001946
5.E-07	0.006597	0.006604	0.003119	0.003124
1.E-06	0.007898	0.007906	0.003793	0.003797
5.E-06	0.011732	0.011745	0.006228	0.006238
1.E-05	0.014045	0.014070	0.008018	0.008029
5.E-05	0.022123	0.022147	0.015471	0.015497
1.E-04	0.027628	0.027654	0.020889	0.020920
5.E-04	0.050173	0.050233	0.044215	0.044260
1.E-03	0.066779	0.066878	0.061173	0.061227
5.E-03	0.134125	0.134313	0.132027	0.132219
1.E-02	0.183111	0.183286	0.183238	0.183487
5.E-02	0.375113	0.375432	0.384127	0.384466
1.E-01	0.506465	0.507314	0.522699	0.523255
5.E-01	0.959700	0.961192	0.997102	0.998175
1.E+00	1.231894	1.233199	1.274817	1.276195
5.E+00	1.945557	1.948284	2.032734	2.036311
1.E+01	2.291382	2.294128	2.393823	2.396356
5.E+01	3.093217	3.097334	3.222690	3.225729
1.E+02	3.442905	3.448702	3.593569	3.597845
5.E+02	4.255263	4.258636	4.437931	4.444555
1.E+03	4.605587	4.613353	4.810211	4.817008

Table D.11. Dimensionless pressure for a hydraulic fractured well with a branch fracture starting from the middle distance from the wellbore and the main fracture tip, θ = 30° and X_{fbD}=0.6

	C_{fD}=1		C_{fD} =10		C_{fD} =50	
t_D	P_D					
	X_{fbD}=0	X_{fbD} =0.6	X_{fbD} =0	X_{fbD} =0.6	X_{fbD} =0	X_{fbD} =0.6
1.E-07	0.041813	0.041845	0.013144	0.013154	0.005866	0.005876
5.E-07	0.066557	0.066607	0.020953	0.020969	0.009350	0.009363
1.E-06	0.078204	0.078260	0.024756	0.024774	0.011112	0.011132
5.E-06	0.117017	0.117066	0.037069	0.037084	0.016577	0.016609
1.E-05	0.139551	0.139662	0.044057	0.044093	0.019630	0.019651
5.E-05	0.207125	0.207324	0.066012	0.066076	0.029822	0.029863
1.E-04	0.246848	0.246862	0.078229	0.078234	0.036058	0.036122
5.E-04	0.369484	0.369619	0.118022	0.118066	0.060052	0.060147
1.E-03	0.436329	0.436663	0.140851	0.140961	0.076591	0.076691
5.E-03	0.641164	0.641544	0.220633	0.220766	0.145449	0.145689
1.E-02	0.757672	0.757898	0.272681	0.272765	0.194811	0.195060
5.E-02	1.090808	1.091514	0.474104	0.474416	0.387225	0.387931
1.E-01	1.281124	1.281481	0.609776	0.609953	0.517449	0.518476
5.E-01	1.830350	1.831859	1.079367	1.080268	0.979284	0.980485
1.E+00	2.120543	2.122634	1.346578	1.347919	1.238784	1.241236
5.E+00	2.871910	2.872562	2.070215	2.070705	1.969664	1.972685
1.E+01	3.216446	3.219599	2.406539	2.408922	2.312414	2.317037
5.E+01	4.018462	4.020607	3.224253	3.226006	3.104332	3.107486
1.E+02	4.377249	4.381624	3.560712	3.564306	3.459812	3.463618
5.E+02	5.186461	5.186543	4.372194	4.372307	4.254039	4.261692
1.E+03	5.537279	5.537833	4.717460	4.717979	4.608720	4.613539

Table D.11. Continued

	C_{fD} =100		C_{fD} =300	
t_D	P_D			
	X_{fbD}=0	X_{fbD} =0.6	X_{fbD} =0	X_{fbD} =0.6
1.E-07	0.004144	0.004150	0.001944	0.001945
5.E-07	0.006597	0.006608	0.003119	0.003120
1.E-06	0.007898	0.007913	0.003793	0.003796
5.E-06	0.011732	0.011744	0.006228	0.006233
1.E-05	0.014045	0.014072	0.008018	0.008023
5.E-05	0.022123	0.022161	0.015471	0.015477
1.E-04	0.027628	0.027670	0.020889	0.020906
5.E-04	0.050173	0.050241	0.044215	0.044257
1.E-03	0.066779	0.066863	0.061173	0.061176
5.E-03	0.134125	0.134292	0.132027	0.132075
1.E-02	0.183111	0.183305	0.183238	0.183379
5.E-02	0.375113	0.375625	0.384127	0.384354
1.E-01	0.506465	0.507051	0.522699	0.522855
5.E-01	0.959700	0.960906	0.997102	0.997748
1.E+00	1.231894	1.233793	1.274817	1.275173
5.E+00	1.945557	1.949328	2.032734	2.034410
1.E+01	2.291382	2.294833	2.393823	2.396183
5.E+01	3.093217	3.096642	3.222690	3.223422
1.E+02	3.442905	3.447931	3.593569	3.597090
5.E+02	4.255263	4.262055	4.437931	4.440300
1.E+03	4.605587	4.610279	4.810211	4.815018

Table D.12.a. Absolute errors obtained between the pressure solutions for a branch fracture starting from the wellbore and a fractured well with X_{fbD}=0 (no branch) and X_{fbD} =0.6 and angle of 30°

	C_{fD} =1	C_{fD} =10	C_{fD} =50	C_{fD} =100	C_{fD} =300
t_D	ABSOLUTE ERROR, %				
1.E-07	0.1269	0.1409	0.0977	0.0873	0.1249
5.E-07	0.1423	0.1114	0.1730	0.1054	0.1403
1.E-06	0.1064	0.1490	0.1284	0.1066	0.1044
5.E-06	0.1630	0.1662	0.1749	0.1071	0.1610
1.E-05	0.1389	0.0756	0.0766	0.1750	0.1369
5.E-05	0.1711	0.1064	0.0850	0.1048	0.1691
1.E-04	0.1495	0.1467	0.1549	0.0933	0.1475
5.E-04	0.1044	0.1292	0.0796	0.1180	0.1024
1.E-03	0.0906	0.0998	0.1132	0.1483	0.0886
5.E-03	0.1476	0.1348	0.1699	0.1403	0.1456
1.E-02	0.1375	0.0979	0.1151	0.0956	0.1355
5.E-02	0.0903	0.1525	0.0910	0.0851	0.0883
1.E-01	0.1085	0.1686	0.1397	0.1676	0.1064
5.E-01	0.1096	0.0927	0.1163	0.1555	0.1076
1.E+00	0.1101	0.1680	0.1076	0.1060	0.1081
5.E+00	0.1780	0.1234	0.0958	0.1402	0.1760
1.E+01	0.1078	0.1699	0.1333	0.1198	0.1058
5.E+01	0.0963	0.0716	0.1208	0.1331	0.0943
1.E+02	0.1210	0.0800	0.1011	0.1684	0.1190
5.E+02	0.1513	0.1499	0.1129	0.0793	0.1493
1.E+03	0.1433	0.0746	0.1669	0.1686	0.1413
Average	0.1283	0.1242	0.1216	0.1241	0.1263

Table D.12.b. Absolute errors obtained between the pressure solutions for a branch fracture starting from the middle distance between wellbore and main fracture tip and a fractured well with X_{fbD}=0 (no branch) and X_{fbD} =0.6 and angle of 30°

	C_{fD} =1	C_{fD} =10	C_{fD} =50	C_{fD} =100	C_{fD} =300
t_D	ABSOLUTE ERROR, %				
1.E-07	0.0775	0.0785	0.1709	0.1429	0.0533
5.E-07	0.0761	0.0771	0.1414	0.1561	0.0290
1.E-06	0.0709	0.0719	0.1790	0.1914	0.0775
5.E-06	0.0414	0.0424	0.1962	0.1023	0.0761
1.E-05	0.0790	0.0800	0.1056	0.1916	0.0709
5.E-05	0.0962	0.0972	0.1364	0.1678	0.0414
1.E-04	0.0056	0.0066	0.1767	0.1514	0.0790
5.E-04	0.0364	0.0374	0.1592	0.1353	0.0962
1.E-03	0.0767	0.0777	0.1298	0.1270	0.0056
5.E-03	0.0592	0.0602	0.1648	0.1244	0.0364
1.E-02	0.0298	0.0308	0.1279	0.1061	0.0767
5.E-02	0.0648	0.0658	0.1825	0.1365	0.0592
1.E-01	0.0279	0.0289	0.1986	0.1156	0.0298
5.E-01	0.0825	0.0835	0.1227	0.1257	0.0648
1.E+00	0.0986	0.0996	0.1980	0.1542	0.0279
5.E+00	0.0227	0.0237	0.1534	0.1939	0.0825
1.E+01	0.0980	0.0990	0.1999	0.1506	0.0986
5.E+01	0.0534	0.0544	0.1016	0.1107	0.0227
1.E+02	0.0999	0.1009	0.1100	0.1460	0.0980
5.E+02	0.0016	0.0026	0.1799	0.1596	0.0534
1.E+03	0.0100	0.0110	0.1046	0.1019	0.0999
Average	0.0575	0.0585	0.1542	0.1424	0.0609

Table D.13.a. Pressure solution obtained in this study for a hydraulically fractured well with no branch

	C_{fD} =1	C_{fD} =10	C_{fD} =50	C_{fD} =100	C_{fD} =300
t_D	P_D				
1.00E-07	0.041813	0.013144	0.005866	0.004144	0.001944
5.00E-07	0.066557	0.020953	0.009350	0.006597	0.003119
1.00E-06	0.078204	0.024756	0.011112	0.007898	0.003793
5.00E-06	0.117017	0.037069	0.016577	0.011732	0.006228
1.00E-05	0.139551	0.044057	0.019630	0.014045	0.008018
5.00E-05	0.207125	0.066012	0.029822	0.022123	0.015471
1.00E-04	0.246848	0.078229	0.036058	0.027628	0.020889
5.00E-04	0.369484	0.118022	0.060052	0.050173	0.044215
1.00E-03	0.436329	0.140851	0.076591	0.066779	0.061173
5.00E-03	0.641164	0.220633	0.145449	0.134125	0.132027
1.00E-02	0.757672	0.272681	0.194811	0.183111	0.183238
5.00E-02	1.090808	0.474104	0.387225	0.375113	0.384127
1.00E-01	1.281124	0.609776	0.517449	0.506465	0.522699
5.00E-01	1.830350	1.079367	0.979284	0.959700	0.997102
1.00E+00	2.120543	1.346578	1.238784	1.231894	1.274817
5.00E+00	2.871910	2.070215	1.969664	1.945557	2.032734
1.00E+01	3.216446	2.406539	2.312414	2.291382	2.393823
5.00E+01	4.018462	3.224253	3.104332	3.093217	3.222690
1.00E+02	4.377249	3.560712	3.459812	3.442905	3.593569
5.00E+02	5.186461	4.372194	4.254039	4.255263	4.437931
1.00E+03	5.537279	4.717460	4.608720	4.605587	4.810211

Table D.13.b. Pressure solution obtained in Ref. 36 for a symmetric hydraulic fractured well

	C_{fD} =1	C_{fD} =10	C_{fD} =50	C_{fD} =100	C_{fD} =500
t_D	P_D				
1.00E-07	0.041770	0.013130	0.005860	0.004140	0.001850
5.00E-07	0.066490	0.020930	0.009340	0.006590	0.002970
1.00E-06	0.078120	0.024730	0.011100	0.007890	0.003610
5.00E-06	0.116900	0.037030	0.016560	0.011720	0.005930
1.00E-05	0.139400	0.044010	0.019610	0.014030	0.007630
5.00E-05	0.206910	0.065940	0.029790	0.022100	0.014720
1.00E-04	0.246580	0.078150	0.036020	0.027600	0.019890
5.00E-04	0.369080	0.117900	0.059990	0.050120	0.042070
1.00E-03	0.435870	0.140700	0.076510	0.066710	0.058230
5.00E-03	0.640520	0.220400	0.145300	0.133980	0.125620
1.00E-02	0.756880	0.272400	0.194600	0.182910	0.174510
5.00E-02	1.089650	0.473600	0.386800	0.374730	0.365800
1.00E-01	1.279810	0.609150	0.516920	0.505910	0.497430
5.00E-01	1.828370	1.078200	0.978210	0.958690	0.949580
1.00E+00	2.118300	1.345100	1.237480	1.230540	1.213670
5.00E+00	2.868780	2.068100	1.967500	1.943610	1.934190
1.00E+01	3.213010	2.403900	2.310100	2.289070	2.278960
5.00E+01	4.014350	3.220860	3.101200	3.089880	3.068760
1.00E+02	4.372830	3.556800	3.456080	3.439450	3.420340
5.00E+02	5.180930	4.367820	4.249770	4.250850	4.224940
1.00E+03	5.531430	4.712700	4.603940	4.600550	4.579730

Table D.13.c. Absolute error between the pressure solution of this study and the one from Ref. 36 (tables D.13.a and D.13.b)

t_D	C_{fD} =1	C_{fD} =10	C_{fD} =50	C_{fD} =100	C_{fD} =300
	ABSOLUTE ERROR, %				
1.00E-07	0.10291	0.10763	0.10403	0.10778	--
5.00E-07	0.10005	0.10749	0.10780	0.10950	--
1.00E-06	0.10803	0.10698	0.10950	0.10046	--
5.00E-06	0.10035	0.10404	0.10046	0.10353	--
1.00E-05	0.10851	0.10779	0.10353	0.10756	--
5.00E-05	0.10363	0.10950	0.10755	0.10581	--
1.00E-04	0.10860	0.10046	0.10581	0.10287	--
5.00E-04	0.10938	0.10353	0.10288	0.10637	--
1.00E-03	0.10514	0.10756	0.10636	0.10269	--
5.00E-03	0.10043	0.10581	0.10269	0.10814	--
1.00E-02	0.10458	0.10288	0.10813	0.10974	--
5.00E-02	0.10612	0.10637	0.10974	0.10216	--
1.00E-01	0.10253	0.10268	0.10216	0.10968	--
5.00E-01	0.10818	0.10812	0.10968	0.10523	--
1.00E+00	0.10577	0.10974	0.10523	0.10987	--
5.00E+00	0.10899	0.10216	0.10987	0.10006	--
1.00E+01	0.10684	0.10968	0.10006	0.10089	--
5.00E+01	0.10233	0.10522	0.10091	0.10787	--
1.00E+02	0.10096	0.10987	0.10787	0.10036	--
5.00E+02	0.10665	0.10005	0.10036	0.10371	--
1.00E+03	0.10563	0.10089	0.10371	0.10937	--
Average	0.10503	0.10564	0.10516	0.10541	--

Table D.14.a. Pressure solution obtained in this study for a hydraulically fractured well with dimensionless branch fracture length, X_{fbD}, of 0.2 (angle = 0°)

	C_{fD} =1	C_{fD} =10	C_{fD} =50	C_{fD} =100	C_{fD} =300
t_D			P_D		
1.E-07	0.04218	0.01330	0.00594	0.00420	0.00187
5.E-07	0.06726	0.02120	0.00946	0.00668	0.00304
1.E-06	0.08006	0.02527	0.01127	0.00796	0.00370
5.E-06	0.11943	0.03768	0.01681	0.01192	0.00617
1.E-05	0.14182	0.04479	0.01999	0.01432	0.00792
5.E-05	0.21175	0.06690	0.03042	0.02279	0.01509
1.E-04	0.25193	0.07963	0.03705	0.02861	0.02047
5.E-04	0.37546	0.11978	0.06191	0.05189	0.04301
1.E-03	0.44429	0.14363	0.07926	0.06876	0.05961
5.E-03	0.65340	0.22661	0.14895	0.13742	0.12784
1.E-02	0.76927	0.28192	0.19906	0.18735	0.17755
5.E-02	1.11288	0.48859	0.39550	0.38293	0.37252
1.E-01	1.30448	0.62662	0.52982	0.51637	0.50579
5.E-01	1.87202	1.10246	0.99526	0.98186	0.97026
1.E+00	2.17097	1.37506	1.26619	1.25112	1.23943
5.E+00	2.93786	2.11491	2.00077	1.98670	1.97438
1.E+01	3.28376	2.45560	2.34415	2.32682	2.31617
5.E+01	4.09757	3.26644	3.15195	3.13707	3.12527
1.E+02	4.45388	3.62228	3.50549	3.49275	3.47811
5.E+02	5.27372	4.43907	4.32794	4.30959	4.29999
1.E+03	5.62644	4.79578	4.67983	4.66624	4.65485

Table D.14.b. Pressure solution obtained in Ref. 36 for a hydraulically fractured well with fracture asymmetric factor of 0.2

	C_{fD} =1	C_{fD} =10	C_{fD} =50	C_{fD} =100	C_{fD} =500
t_D			P_D		
1.E-07	0.04164	0.01312	0.00586	0.00414	0.00185
5.E-07	0.06634	0.02091	0.00933	0.00659	0.00300
1.E-06	0.07903	0.02492	0.01112	0.00785	0.00365
5.E-06	0.11780	0.03719	0.01658	0.01177	0.00609
1.E-05	0.13995	0.04420	0.01973	0.01413	0.00781
5.E-05	0.20885	0.06599	0.03002	0.02248	0.01489
1.E-04	0.24846	0.07856	0.03655	0.02823	0.02019
5.E-04	0.37045	0.11821	0.06108	0.05121	0.04242
1.E-03	0.43857	0.14170	0.07822	0.06783	0.05881
5.E-03	0.64472	0.22364	0.14694	0.13562	0.12619
1.E-02	0.75893	0.27808	0.19645	0.18480	0.17519
5.E-02	1.09831	0.48185	0.39011	0.37765	0.36751
1.E-01	1.28669	0.61844	0.52251	0.50963	0.49917
5.E-01	1.84692	1.08726	0.98227	0.96832	0.95702
1.E+00	2.14118	1.35670	1.24873	1.23441	1.22281
5.E+00	2.89817	2.08571	1.97405	1.95927	1.94729
1.E+01	3.24084	2.42405	2.31179	2.29692	2.28488
5.E+01	4.04456	3.22420	3.11145	3.09651	3.08442
1.E+02	4.39379	3.57298	3.46016	3.44521	3.43311
5.E+02	5.20309	4.38191	4.26903	4.25409	4.24198
1.E+03	5.55367	4.73245	4.61957	4.60462	4.59251

Table D.14.c. Absolute error between the pressure solution of this study (X_{fbD}=0.2) and the one from Ref. 36 for fracture asymmetric factor of 0.2 (tables D.14.a and D.14.b)

	C_{fD} =1	C_{fD} =10	C_{fD} =50	C_{fD} =100	C_{fD} =300
t_D			ABSOLUTE ERROR, %		
1.E-07	1.28468	1.32365	1.35236	1.32365	--
5.E-07	1.36262	1.36030	1.32365	1.36029	--
1.E-06	1.28774	1.37697	1.36028	1.37697	--
5.E-06	1.36731	1.28880	1.37698	1.28880	--
1.E-05	1.31971	1.31878	1.28880	1.31878	--
5.E-05	1.36817	1.35802	1.31878	1.35801	--
1.E-04	1.37577	1.34102	1.35801	1.34102	--
5.E-04	1.33443	1.31237	1.34102	1.31236	--
1.E-03	1.28853	1.34641	1.31237	1.34641	--
5.E-03	1.32898	1.31053	1.34640	1.31053	--
1.E-02	1.34396	1.36361	1.31053	1.36361	--
5.E-02	1.30901	1.37932	1.36361	1.37931	--
1.E-01	1.36411	1.30542	1.37932	1.30542	--
5.E-01	1.34070	1.37873	1.30542	1.37873	--
1.E+00	1.37201	1.33531	1.37872	1.33532	--
5.E+00	1.35101	1.38061	1.33531	1.38061	--
1.E+01	1.30708	1.28485	1.38061	1.28485	--
5.E+01	1.29368	1.29307	1.28485	1.29307	--
1.E+02	1.34916	1.36110	1.29307	1.36110	--
5.E+02	1.33934	1.28776	1.36111	1.28776	--
1.E+03	1.29335	1.32053	1.28776	1.32053	--
Average	1.33244	1.33463	1.33614	1.33463	

Table D.15.a. Pressure solution obtained in this study for a hydraulically fractured well with dimensionless branch fracture length, X_{fbD}, of 0.4 (angle = 0°)

	C_{fD} =1	C_{fD} =10	C_{fD} =50	C_{fD} =100	C_{fD} =300
t_D			P_D		
1.E-07	0.04221	0.01331	0.00595	0.00420	0.00190
5.E-07	0.06725	0.02121	0.00946	0.00668	0.00315
1.E-06	0.08019	0.02526	0.01128	0.00799	0.00388
5.E-06	0.11947	0.03773	0.01688	0.01217	0.00656
1.E-05	0.14205	0.04482	0.02021	0.01477	0.00840
5.E-05	0.21181	0.06699	0.03152	0.02414	0.01574
1.E-04	0.25206	0.07992	0.03886	0.03042	0.02114
5.E-04	0.37579	0.12206	0.06577	0.05466	0.04375
1.E-03	0.44472	0.14791	0.08400	0.07182	0.06037
5.E-03	0.65400	0.23896	0.15500	0.14084	0.12878
1.E-02	0.77148	0.29800	0.20542	0.19091	0.17853
5.E-02	1.12886	0.51054	0.40212	0.38645	0.37341
1.E-01	1.32928	0.65020	0.53616	0.52015	0.50729
5.E-01	1.91295	1.12443	1.00225	0.98497	0.97149
1.E+00	2.21197	1.39742	1.27218	1.25465	1.24169
5.E+00	2.98028	2.13578	2.00702	1.98968	1.97512
1.E+01	3.32716	2.47783	2.34921	2.33171	2.31765
5.E+01	4.14072	3.28880	3.16188	3.14348	3.13062
1.E+02	4.49431	3.64452	3.51536	3.49646	3.48190
5.E+02	5.31799	4.46486	4.33401	4.31723	4.30356
1.E+03	5.67315	4.81827	4.69033	4.67407	4.66173

Table D.15.b. Pressure solution obtained in Ref. 36 for a hydraulically fractured well with fracture asymmetric factor of 0.4

	C_{fD} =1	C_{fD} =10	C_{fD} =50	C_{fD} =100	C_{fD} =500
t_D			P_D		
1.E-07	0.04161	0.01313	0.00586	0.00414	0.00187
5.E-07	0.06632	0.02090	0.00933	0.00659	0.00310
1.E-06	0.07902	0.02491	0.01111	0.00787	0.00383
5.E-06	0.11782	0.03718	0.01664	0.01199	0.00647
1.E-05	0.13997	0.04418	0.01991	0.01456	0.00828
5.E-05	0.20881	0.06601	0.03106	0.02379	0.01551
1.E-04	0.24837	0.07874	0.03830	0.02999	0.02084
5.E-04	0.37025	0.12031	0.06486	0.05388	0.04312
1.E-03	0.43835	0.14586	0.08280	0.07076	0.05952
5.E-03	0.64494	0.23555	0.15277	0.13889	0.12690
1.E-02	0.76048	0.29371	0.20253	0.18810	0.17589
5.E-02	1.11259	0.50336	0.39624	0.38086	0.36817
1.E-01	1.31059	0.64070	0.52845	0.51271	0.49980
5.E-01	1.88500	1.10826	0.98753	0.97103	0.95757
1.E+00	2.18016	1.37689	1.25376	1.23700	1.22334
5.E+00	2.93649	2.10485	1.97883	1.96174	1.94782
1.E+01	3.27898	2.44303	2.31653	2.29938	2.28543
5.E+01	4.08257	3.24305	3.11615	3.09896	3.08497
1.E+02	4.43179	3.59181	3.46486	3.44766	3.43367
5.E+02	5.24107	4.40072	4.27374	4.25654	4.24254
1.E+03	5.59165	4.75126	4.62427	4.60707	4.59307

Table D.15.c. Absolute error between the pressure solution of this study (X_{fbD}=0.4) and the one from Ref. 36 for fracture asymmetric factor of 0.4 (Tables D.15.a and D.15.b)

	C_{fD} =1	C_{fD} =10	C_{fD} =50	C_{fD} =100	C_{fD} =300
t_D			ABSOLUTE ERROR, %		
1.E-07	1.41003	1.38203	1.45982	1.39876	--
5.E-07	1.38203	1.45982	1.38507	1.38852	--
1.E-06	1.45983	1.38508	1.46450	1.46868	--
5.E-06	1.38509	1.46449	1.41698	1.45697	--
1.E-05	1.46450	1.41699	1.46535	1.40883	--
5.E-05	1.41698	1.46535	1.47294	1.44207	--
1.E-04	1.46536	1.47293	1.43169	1.42233	--
5.E-04	1.47293	1.43169	1.38588	1.43521	--
1.E-03	1.43169	1.38588	1.42624	1.46945	--
5.E-03	1.38588	1.42624	1.44119	1.38287	--
1.E-02	1.42623	1.44120	1.40632	1.46969	--
5.E-02	1.44119	1.40631	1.46131	1.44656	--
1.E-01	1.40633	1.46131	1.43794	1.43061	--
5.E-01	1.46131	1.43794	1.46918	1.41504	--
1.E+00	1.43794	1.46918	1.44823	1.40690	--
5.E+00	1.46919	1.44823	1.40438	1.40438	--
1.E+01	1.44823	1.40440	1.39102	1.38660	--
5.E+01	1.40439	1.39102	1.44639	1.41615	--
1.E+02	1.39102	1.44639	1.43658	1.39580	--
5.E+02	1.44639	1.43658	1.39069	1.40568	--
1.E+03	1.43658	1.39068	1.40833	1.43336	--
Average	1.43062	1.42970	1.43095	1.42307	

Table D.16.a. Pressure solution obtained in this study for a hydraulically fractured well with dimensionless branch fracture length, X_{fbD}, of 0.6 (angle = 0°)

	C_{fD} =1	C_{fD} =10	C_{fD} =50	C_{fD} =100	C_{fD} =300
t_D			P_D		
1.E-07	0.04222	0.01333	0.00594	0.00421	0.00199
5.E-07	0.06729	0.02122	0.00948	0.00676	0.00345
1.E-06	0.08026	0.02528	0.01132	0.00817	0.00431
5.E-06	0.11960	0.03772	0.01735	0.01299	0.00732
1.E-05	0.14218	0.04487	0.02112	0.01608	0.00928
5.E-05	0.21189	0.06771	0.03450	0.02697	0.01683
1.E-04	0.25211	0.08160	0.04312	0.03398	0.02229
5.E-04	0.37586	0.12997	0.07323	0.05953	0.04498
1.E-03	0.44509	0.16051	0.09255	0.07702	0.06163
5.E-03	0.66014	0.26476	0.16537	0.14668	0.13012
1.E-02	0.78551	0.32922	0.21628	0.19665	0.17991
5.E-02	1.17683	0.55004	0.41285	0.39239	0.37495
1.E-01	1.39303	0.69002	0.54709	0.52625	0.50895
5.E-01	1.99614	1.16320	1.01225	0.99069	0.97358
1.E+00	2.29650	1.43510	1.28273	1.26152	1.24409
5.E+00	3.06439	2.17150	2.01855	1.99682	1.97830
1.E+01	3.41131	2.51643	2.36044	2.34077	2.32118
5.E+01	4.22540	3.32757	3.17179	3.15008	3.13497
1.E+02	4.57930	3.68341	3.52774	3.50431	3.48659
5.E+02	5.40382	4.50089	4.34887	4.32838	4.30906
1.E+03	5.75933	4.85709	4.70267	4.68097	4.66758

Table D.16.b. Pressure solution obtained in Ref. 36 for a hydraulically fractured well with fracture asymmetric factor of 0.6

	C_{fD} =1	C_{fD} =10	C_{fD} =50	C_{fD} =100	C_{fD} =500
t_D			P_D		
1.E-07	0.04158	0.01312	0.00585	0.00414	0.00196
5.E-07	0.06629	0.02089	0.00933	0.00666	0.00340
1.E-06	0.07901	0.02489	0.01115	0.00804	0.00425
5.E-06	0.11783	0.03715	0.01708	0.01279	0.00721
1.E-05	0.13996	0.04417	0.02080	0.01584	0.00914
5.E-05	0.20868	0.06665	0.03396	0.02656	0.01657
1.E-04	0.24817	0.08039	0.04244	0.03345	0.02195
5.E-04	0.36996	0.12800	0.07211	0.05862	0.04429
1.E-03	0.43829	0.15802	0.09118	0.07586	0.06070
5.E-03	0.65035	0.26070	0.16285	0.14442	0.12809
1.E-02	0.77354	0.32426	0.21295	0.19369	0.17708
5.E-02	1.15873	0.54157	0.40664	0.38628	0.36933
1.E-01	1.37209	0.67964	0.53856	0.51797	0.50094
5.E-01	1.96503	1.14508	0.99671	0.97583	0.95869
1.E+00	2.26125	1.41252	1.26264	1.24168	1.22450
5.E+00	3.01640	2.13893	1.98736	1.96628	1.94903
1.E+01	3.35860	2.47685	2.32500	2.30391	2.28665
5.E+01	4.16196	3.27667	3.12459	3.10348	3.08621
1.E+02	4.51115	3.62541	3.47329	3.45218	3.43491
5.E+02	5.32042	4.43431	4.28217	4.26106	4.24378
1.E+03	5.67100	4.78484	4.63270	4.61159	4.59431

Table D.16.c. Absolute error between the pressure solution of this study (X_{fbD}=0.6) and the one from Ref. 36 for fracture asymmetric factor of 0.4 (tables D.16.a and D.16.b)

	C_{fD} =1	C_{fD} =10	C_{fD} =50	C_{fD} =100	C_{fD} =300
t_D			ABSOLUTE ERROR, %		
1.E-07	1.50713	1.55298	1.47919	1.54660	--
5.E-07	1.47919	1.55161	1.55683	1.51800	--
1.E-06	1.55683	1.54660	1.48223	1.55449	--
5.E-06	1.48223	1.51801	1.56149	1.57112	--
1.E-05	1.56150	1.55450	1.51408	1.48329	--
5.E-05	1.51408	1.57112	1.56235	1.51315	--
1.E-04	1.56235	1.48329	1.56992	1.55224	--
5.E-04	1.56992	1.51316	1.52875	1.53530	--
1.E-03	1.52876	1.55224	1.48302	1.50677	--
5.E-03	1.48302	1.53530	1.52331	1.54068	--
1.E-02	1.52331	1.50677	1.53824	1.50494	--
5.E-02	1.53824	1.54068	1.50343	1.55781	--
1.E-01	1.50343	1.50494	1.55831	1.57346	--
5.E-01	1.55831	1.55780	1.53499	1.49985	--
1.E+00	1.53498	1.57346	1.56618	1.57287	--
5.E+00	1.56618	1.49985	1.54526	1.52962	--
1.E+01	1.54526	1.57287	1.50151	1.57475	--
5.E+01	1.50151	1.52962	1.48815	1.47936	--
1.E+02	1.48816	1.57475	1.54342	1.48754	--
5.E+02	1.54342	1.47935	1.53363	1.55532	--
1.E+03	1.53363	1.48755	1.48783	1.48227	--
Average	1.52769	1.53364	1.52677	1.53045	

Table D.17.a. Pressure solution for a branch fracture inclined 10° with respect to the main fracture and its deviation with respect to the pressure solution obtained for the angle of 0°. C_{fD}=1

	X_{fbD} =0.2		X_{fbD} =0.4		X_{fbD} =0.6	
t_D	P_D	Deviation, %	P_D	Deviation, %	P_D	Deviation, %
1.E-07	0.045162	6.599	0.045179	6.583	0.045201	7.071
5.E-07	0.071983	6.566	0.071999	6.596	0.072024	7.043
1.E-06	0.085731	6.614	0.085825	6.565	0.085900	7.028
5.E-06	0.127911	6.628	0.127937	6.614	0.128071	7.080
1.E-05	0.151781	6.562	0.152078	6.593	0.152192	7.042
5.E-05	0.226777	6.628	0.226831	6.622	0.226779	7.028
1.E-04	0.269695	6.589	0.269883	6.603	0.269866	7.043
5.E-04	0.402118	6.629	0.402182	6.563	0.402217	7.012
1.E-03	0.475402	6.543	0.475894	6.551	0.476406	7.035
5.E-03	0.699207	6.551	0.700226	6.601	0.706472	7.019
1.E-02	0.823732	6.612	0.825931	6.592	0.840831	7.043
5.E-02	1.190830	6.546	1.207995	6.551	1.259849	7.054
1.E-01	1.396297	6.575	1.422712	6.567	1.491901	7.097
5.E-01	2.004835	6.625	2.047427	6.568	2.136622	7.038
1.E+00	2.323805	6.577	2.367470	6.568	2.457902	7.028
5.E+00	3.143982	6.556	3.191815	6.628	3.279327	7.014
1.E+01	3.515748	6.598	3.560992	6.566	3.653399	7.097
5.E+01	4.386091	6.578	4.431247	6.556	4.525025	7.091
1.E+02	4.767104	6.571	4.810751	6.578	4.901868	7.044
5.E+02	5.643979	6.560	5.694038	6.604	5.782440	7.006
1.E+03	6.023572	6.593	6.073862	6.597	6.166514	7.070
Average deviation		**6.586**		**6.584**		**7.047**

Table D.17.b. Pressure solution for a branch fracture inclined 10° with respect to the main fracture and its deviation with respect to the pressure solution obtained for the angle of 0°. C_{fD}=10

	X_{fbD} =0.2		X_{fbD} =0.4		X_{fbD} =0.6	
t_D	P_D	Deviation, %	P_D	Deviation, %	P_D	Deviation, %
1.E-07	0.014210	6.435	0.014222	6.387	0.014241	6.859
5.E-07	0.022656	6.434	0.022673	6.453	0.022668	6.830
1.E-06	0.027004	6.429	0.026991	6.414	0.027016	6.865
5.E-06	0.040253	6.403	0.040336	6.455	0.040298	6.828
1.E-05	0.047872	6.436	0.047863	6.368	0.047955	6.882
5.E-05	0.071512	6.451	0.071554	6.376	0.072385	6.899
1.E-04	0.085047	6.372	0.085415	6.437	0.087168	6.823
5.E-04	0.127971	6.399	0.130363	6.371	0.138932	6.898
1.E-03	0.153511	6.434	0.158024	6.401	0.171512	6.853
5.E-03	0.242154	6.419	0.255434	6.450	0.283034	6.900
1.E-02	0.301179	6.393	0.318389	6.402	0.351613	6.802
5.E-02	0.522130	6.424	0.545338	6.381	0.587502	6.810
1.E-01	0.669405	6.392	0.694836	6.424	0.737497	6.880
5.E-01	1.178336	6.439	1.201354	6.403	1.242351	6.805
1.E+00	1.469921	6.453	1.492901	6.396	1.533236	6.838
5.E+00	2.259202	6.387	2.281457	6.385	2.321221	6.895
1.E+01	2.624988	6.453	2.647766	6.418	2.688557	6.840
5.E+01	3.490299	6.414	3.513942	6.407	3.554378	6.816
1.E+02	3.872218	6.455	3.893304	6.390	3.936268	6.865
5.E+02	4.741001	6.368	4.770164	6.400	4.808813	6.841
1.E+03	5.122373	6.376	5.150339	6.448	5.188958	6.833
Average deviation		**6.417**		**6.408**		**6.851**

Table D.17.c. Pressure solution for a branch fracture inclined 10° with respect to the main fracture and its deviation with respect to the pressure solution obtained for the angle of 0°. C_{fD}=50

	X_{fbD} =0.2		X_{fbD} =0.4		X_{fbD} =0.6	
t_D	P_D	Deviation, %	P_D	Deviation, %	P_D	Deviation, %
1.E-07	0.006343	6.347	0.006350	6.346	0.006340	6.779
5.E-07	0.010096	6.346	0.010102	6.342	0.010122	6.796
1.E-06	0.012037	6.342	0.012035	6.316	0.012077	6.706
5.E-06	0.017945	6.316	0.018023	6.349	0.018520	6.736
1.E-05	0.021343	6.349	0.021579	6.364	0.022551	6.777
5.E-05	0.032489	6.364	0.033638	6.284	0.036831	6.759
1.E-04	0.039538	6.284	0.041474	6.311	0.046019	6.730
5.E-04	0.066081	6.311	0.070229	6.347	0.078183	6.765
1.E-03	0.084631	6.347	0.089676	6.331	0.098779	6.728
5.E-03	0.159013	6.331	0.165435	6.305	0.176585	6.782
1.E-02	0.212455	6.305	0.219315	6.336	0.230981	6.799
5.E-02	0.422258	6.336	0.429170	6.304	0.440601	6.723
1.E-01	0.565464	6.304	0.572524	6.352	0.584276	6.798
5.E-01	1.062766	6.352	1.070394	6.366	1.080609	6.753
1.E+00	1.352270	6.366	1.357709	6.299	1.369955	6.800
5.E+00	2.135272	6.299	2.143453	6.365	2.153826	6.702
1.E+01	2.503509	6.365	2.507859	6.326	2.518828	6.710
5.E+01	3.364811	6.326	3.376889	6.367	3.386835	6.780
1.E+02	3.743860	6.367	3.750945	6.281	3.764257	6.705
5.E+02	4.617978	6.281	4.624825	6.288	4.641901	6.738
1.E+03	4.993852	6.288	5.008324	6.349	5.022207	6.795
Average deviation		**6.330**		**6.330**		**6.755**

Table D.17.d. Pressure solution for a branch fracture inclined 10° with respect to the main fracture and its deviation with respect to the pressure solution obtained for the angle of 0°. C_{fD}=100

	X_{fbD} =0.2		X_{fbD} =0.4		X_{fbD} =0.6	
t_D	P_D	Deviation, %	P_D	Deviation, %	P_D	Deviation, %
1.E-07	0.004472	6.175	0.004475	6.166	0.004479	6.506
5.E-07	0.007115	6.107	0.007120	6.140	0.007205	6.536
1.E-06	0.008484	6.179	0.008513	6.173	0.008704	6.577
5.E-06	0.012703	6.136	0.012970	6.188	0.013846	6.559
1.E-05	0.015262	6.180	0.015729	6.108	0.017128	6.530
5.E-05	0.024292	6.187	0.025716	6.135	0.028738	6.565
1.E-04	0.030489	6.150	0.032424	6.171	0.036195	6.528
5.E-04	0.055267	6.108	0.058250	6.155	0.063453	6.582
1.E-03	0.073257	6.145	0.076505	6.130	0.082103	6.599
5.E-03	0.146439	6.158	0.150083	6.160	0.156247	6.523
1.E-02	0.199582	6.127	0.203368	6.128	0.209624	6.598
5.E-02	0.408140	6.176	0.411888	6.176	0.418108	6.553
1.E-01	0.550239	6.155	0.554474	6.190	0.560983	6.600
5.E-01	1.046572	6.184	1.049214	6.123	1.055099	6.502
1.E+00	1.333309	6.165	1.337434	6.190	1.343647	6.510
5.E+00	2.116319	6.125	2.120075	6.150	2.128213	6.580
1.E+01	2.478307	6.113	2.485603	6.191	2.493028	6.505
5.E+01	3.343106	6.163	3.347852	6.105	3.356040	6.538
1.E+02	3.721788	6.154	3.724084	6.112	3.735412	6.595
5.E+02	4.590154	6.112	4.601295	6.174	4.611462	6.540
1.E+03	4.970872	6.128	4.978094	6.107	4.985989	6.516
Average deviation		**6.149**		**6.151**		**6.550**

Table D.17.e. Pressure solution for a branch fracture inclined 10° with respect to the main fracture and its deviation with respect to the pressure solution obtained for the angle of 0°. C_{fD}=300

	X_{fbD} =0.2		X_{fbD} =0.4		X_{fbD} =0.6	
t_D	P_D	Deviation, %	P_D	Deviation, %	P_D	Deviation, %
1.E-07	0.002007	6.608	0.002031	6.546	0.002132	7.079
5.E-07	0.003254	6.604	0.003369	6.617	0.003699	7.096
1.E-06	0.003961	6.578	0.004157	6.575	0.004616	7.006
5.E-06	0.006606	6.611	0.007028	6.618	0.007836	7.036
1.E-05	0.008480	6.626	0.008998	6.625	0.009941	7.077
5.E-05	0.016146	6.547	0.016846	6.588	0.018016	7.059
1.E-04	0.021910	6.574	0.022619	6.547	0.023852	7.030
5.E-04	0.046056	6.609	0.046835	6.583	0.048161	7.065
1.E-03	0.063813	6.594	0.064633	6.596	0.065959	7.028
5.E-03	0.136824	6.568	0.137830	6.565	0.139332	7.082
1.E-02	0.190093	6.599	0.191171	6.614	0.192682	7.099
5.E-02	0.398697	6.566	0.399766	6.593	0.401286	7.023
1.E-01	0.541613	6.614	0.543259	6.622	0.545070	7.098
5.E-01	1.039130	6.628	1.040167	6.603	1.042253	7.053
1.E+00	1.326468	6.562	1.328911	6.563	1.332421	7.100
5.E+00	2.114520	6.628	2.113589	6.551	2.116808	7.002
1.E+01	2.479540	6.589	2.481457	6.601	2.483893	7.010
5.E+01	3.347162	6.629	3.351568	6.592	3.356921	7.080
1.E+02	3.721627	6.543	3.725990	6.551	3.730811	7.005
5.E+02	4.601424	6.551	4.606029	6.567	4.612339	7.038
1.E+03	4.984413	6.612	4.989430	6.568	4.998741	7.095
Average deviation		**6.592**		**6.585**		**7.055**

Table D.18.a. Pressure solution for a branch fracture inclined 20° with respect to the main fracture and its deviation with respect to the pressure solution obtained for the angle of 0°. C_{fD}=1

	X_{fbD} =0.2		X_{fbD} =0.4		X_{fbD} =0.6	
t_D	P_D	Deviation. %	P_D	Deviation. %	P_D	Deviation. %
1.E-07	0.045242	6.764	0.045250	6.730	0.045268	7.229
5.E-07	0.072110	6.731	0.072078	6.699	0.072141	7.217
1.E-06	0.085878	6.773	0.085935	6.685	0.086008	7.163
5.E-06	0.128092	6.760	0.128103	6.735	0.128305	7.276
1.E-05	0.152053	6.729	0.152275	6.715	0.152434	7.212
5.E-05	0.227222	6.810	0.227280	6.806	0.227212	7.232
1.E-04	0.269980	6.687	0.270228	6.722	0.270323	7.225
5.E-04	0.402666	6.756	0.402649	6.672	0.402717	7.145
1.E-03	0.476243	6.708	0.476566	6.683	0.476933	7.153
5.E-03	0.700321	6.699	0.701425	6.761	0.707656	7.198
1.E-02	0.824801	6.733	0.827280	6.745	0.842155	7.212
5.E-02	1.192792	6.700	1.209428	6.662	1.261238	7.172
1.E-01	1.398083	6.695	1.424250	6.668	1.493817	7.235
5.E-01	2.008493	6.795	2.051329	6.746	2.139390	7.177
1.E+00	2.328420	6.762	2.371697	6.735	2.461100	7.167
5.E+00	3.147840	6.671	3.195932	6.748	3.285819	7.226
1.E+01	3.522709	6.783	3.566803	6.719	3.658069	7.233
5.E+01	4.392818	6.721	4.437577	6.690	4.530287	7.215
1.E+02	4.776636	6.757	4.818261	6.723	4.908780	7.195
5.E+02	5.649711	6.655	5.704935	6.783	5.792344	7.190
1.E+03	6.030199	6.696	6.080073	6.693	6.176585	7.245
Average deviation		**6.733**		**6.720**		**7.206**

Table D.18.b. Pressure solution for a branch fracture inclined 20° with respect to the main fracture and its deviation with respect to the pressure solution obtained for the angle of 0°. C_{fD}=10

	X_{fbD} =0.2		X_{fbD} =0.4		X_{fbD} =0.6	
t_D	P_D	Deviation, %	P_D	Deviation, %	P_D	Deviation, %
1.E-07	0.014234	6.587	0.014238	6.490	0.014264	7.028
5.E-07	0.022681	6.536	0.022711	6.611	0.022693	6.948
1.E-06	0.027050	6.587	0.027041	6.585	0.027051	7.002
5.E-06	0.040327	6.575	0.040398	6.599	0.040351	6.966
1.E-05	0.047946	6.580	0.047932	6.502	0.048018	7.022
5.E-05	0.071614	6.585	0.071661	6.516	0.072528	7.110
1.E-04	0.085175	6.512	0.085540	6.574	0.087279	6.959
5.E-04	0.128158	6.536	0.130546	6.502	0.139093	7.022
1.E-03	0.153727	6.566	0.158191	6.499	0.171754	7.004
5.E-03	0.242409	6.518	0.255939	6.635	0.283518	7.083
1.E-02	0.301775	6.578	0.318831	6.532	0.352187	6.976
5.E-02	0.522856	6.554	0.546151	6.520	0.588199	6.937
1.E-01	0.670403	6.531	0.695860	6.561	0.738294	6.995
5.E-01	1.180074	6.577	1.203311	6.555	1.244719	7.008
1.E+00	1.472316	6.606	1.494627	6.504	1.535973	7.029
5.E+00	2.261815	6.495	2.285232	6.540	2.324215	7.033
1.E+01	2.629331	6.607	2.651448	6.548	2.692945	7.014
5.E+01	3.495152	6.544	3.520211	6.574	3.559455	6.969
1.E+02	3.879126	6.621	3.900132	6.554	3.942413	7.031
5.E+02	4.749315	6.532	4.778906	6.571	4.818015	7.046
1.E+03	5.131761	6.547	5.156572	6.561	5.194264	6.942
Average deviation		**6.561**		**6.549**		**7.006**

Table D.18.c. Pressure solution for a branch fracture inclined 20° with respect to the main fracture and its deviation with respect to the pressure solution obtained for the angle of 0°. C_{fD}=50

	X_{fbD} =0.2		X_{fbD} =0.4		X_{fbD} =0.6	
t_D	P_D	Deviation, %	P_D	Deviation, %	P_D	Deviation, %
1.E-07	0.006351	6.469	0.006358	6.467	0.006347	6.892
5.E-07	0.010112	6.500	0.010118	6.496	0.010137	6.953
1.E-06	0.012052	6.461	0.012051	6.435	0.012096	6.879
5.E-06	0.017978	6.486	0.018056	6.519	0.018543	6.871
1.E-05	0.021385	6.534	0.021622	6.549	0.022592	6.972
5.E-05	0.032529	6.478	0.033680	6.399	0.036889	6.929
1.E-04	0.039616	6.469	0.041556	6.496	0.046107	6.934
5.E-04	0.066182	6.455	0.070336	6.490	0.078316	6.946
1.E-03	0.084801	6.533	0.089855	6.518	0.098902	6.861
5.E-03	0.159175	6.426	0.165603	6.401	0.176781	6.901
1.E-02	0.212689	6.408	0.219556	6.439	0.231368	6.978
5.E-02	0.423018	6.504	0.429942	6.472	0.441295	6.891
1.E-01	0.566055	6.402	0.573123	6.449	0.584921	6.916
5.E-01	1.064234	6.481	1.071874	6.495	1.081997	6.891
1.E+00	1.354905	6.548	1.360355	6.481	1.371730	6.938
5.E+00	2.138264	6.430	2.146457	6.496	2.156629	6.840
1.E+01	2.506414	6.474	2.510769	6.435	2.523815	6.921
5.E+01	3.370351	6.480	3.382450	6.521	3.391164	6.916
1.E+02	3.749149	6.499	3.756244	6.413	3.768635	6.829
5.E+02	4.624103	6.405	4.630959	6.412	4.648447	6.889
1.E+03	4.999883	6.401	5.014372	6.462	5.030809	6.978
Average deviation		**6.469**		**6.469**		**6.911**

Table D.18.d. Pressure solution for a branch fracture inclined 20° with respect to the main fracture and its deviation with respect to the pressure solution obtained for the angle of 0°. C_{fD}=100

	X_{fbD} =0.2		X_{fbD} =0.4		X_{fbD} =0.6	
t_D	P_D	Deviation, %	P_D	Deviation, %	P_D	Deviation, %
1.E-07	0.004480	6.345	0.004481	6.294	0.004483	6.618
5.E-07	0.007123	6.205	0.007133	6.315	0.007215	6.693
1.E-06	0.008500	6.354	0.008529	6.355	0.008718	6.750
5.E-06	0.012721	6.265	0.012990	6.331	0.013864	6.694
1.E-05	0.015291	6.355	0.015745	6.207	0.017160	6.725
5.E-05	0.024340	6.369	0.025754	6.273	0.028784	6.734
1.E-04	0.030535	6.292	0.032476	6.323	0.036265	6.732
5.E-04	0.055325	6.207	0.058324	6.274	0.063560	6.763
1.E-03	0.073365	6.282	0.076645	6.301	0.082205	6.731
5.E-03	0.146676	6.310	0.150322	6.309	0.156420	6.641
1.E-02	0.199835	6.245	0.203757	6.307	0.209976	6.777
5.E-02	0.408887	6.348	0.412586	6.335	0.418766	6.721
1.E-01	0.551114	6.304	0.555164	6.307	0.561601	6.718
5.E-01	1.048572	6.362	1.050375	6.227	1.056455	6.638
1.E+00	1.335569	6.323	1.339675	6.347	1.345388	6.648
5.E+00	2.118951	6.241	2.123414	6.298	2.130981	6.719
1.E+01	2.481048	6.216	2.488345	6.295	2.497964	6.715
5.E+01	3.348709	6.320	3.352152	6.225	3.360330	6.674
1.E+02	3.727650	6.302	3.728909	6.234	3.739756	6.719
5.E+02	4.595217	6.216	4.607281	6.296	4.617965	6.690
1.E+03	4.977257	6.249	4.987949	6.293	4.994528	6.698
Average deviation		**6.291**		**6.293**		**6.705**

Table D.18.e. Pressure solution for a branch fracture inclined 20° with respect to the main fracture and its deviation with respect to the pressure solution obtained for the angle of 0°. C_{fD}=300

	X_{fbD} =0.2		X_{fbD} =0.4		X_{fbD} =0.6	
t_D	P_D	Deviation, %	P_D	Deviation, %	P_D	Deviation, %
1.E-07	0.002017	6.974	0.002041	6.931	0.002142	7.494
5.E-07	0.003270	6.994	0.003385	6.978	0.003716	7.495
1.E-06	0.003978	6.943	0.004178	7.004	0.004639	7.497
5.E-06	0.006634	6.935	0.007060	6.965	0.007876	7.494
1.E-05	0.008518	6.954	0.009036	6.923	0.009989	7.493
5.E-05	0.016230	7.023	0.016929	7.040	0.018091	7.500
1.E-04	0.022011	6.969	0.022744	7.026	0.023965	7.497
5.E-04	0.046265	6.961	0.047035	6.910	0.048391	7.494
1.E-03	0.064092	6.946	0.064920	6.953	0.066286	7.496
5.E-03	0.137530	7.020	0.138539	7.015	0.139915	7.498
1.E-02	0.191041	7.002	0.192021	6.968	0.193521	7.495
5.E-02	0.400540	6.970	0.401525	6.977	0.403180	7.498
1.E-01	0.544221	6.985	0.545662	6.956	0.547536	7.494
5.E-01	1.043543	6.931	1.044620	6.909	1.047561	7.493
1.E+00	1.333623	7.042	1.335840	7.027	1.337680	7.498
5.E+00	2.122488	6.887	2.125202	6.971	2.128607	7.493
1.E+01	2.490116	6.936	2.492004	6.947	2.496506	7.496
5.E+01	3.362162	6.953	3.368489	6.969	3.373224	7.493
1.E+02	3.739122	6.979	3.744899	7.021	3.748140	7.500
5.E+02	4.624136	7.000	4.630624	7.054	4.632668	7.499
1.E+03	5.008384	6.985	5.011433	6.904	5.021380	7.494
Average deviation		**6.971**		**6.974**		**7.496**

Table D.19.a. Pressure solution for a branch fracture inclined 30° with respect to the main fracture and its deviation with respect to the pressure solution obtained for the angle of 0°. C_{fD}=1

	X_{fbD} =0.2		X_{fbD} =0.4		X_{fbD} =0.6	
t_D	P_D	Deviation, %	P_D	Deviation, %	P_D	Deviation, %
1.E-07	0.045286	6.854	0.045286	6.804	0.045304	7.314
5.E-07	0.072114	6.736	0.072147	6.789	0.072144	7.222
1.E-06	0.085909	6.807	0.085940	6.690	0.086041	7.204
5.E-06	0.128190	6.831	0.128150	6.769	0.128427	7.378
1.E-05	0.152143	6.784	0.152392	6.786	0.152495	7.255
5.E-05	0.227290	6.838	0.227415	6.861	0.227249	7.249
1.E-04	0.270155	6.748	0.270309	6.750	0.270498	7.294
5.E-04	0.402779	6.782	0.402910	6.732	0.402883	7.189
1.E-03	0.476635	6.785	0.476699	6.709	0.477088	7.188
5.E-03	0.701011	6.791	0.702004	6.838	0.707803	7.220
1.E-02	0.824989	6.754	0.828095	6.836	0.842647	7.274
5.E-02	1.193961	6.791	1.209702	6.683	1.261816	7.221
1.E-01	1.398830	6.745	1.425645	6.759	1.494208	7.263
5.E-01	2.010500	6.888	2.052424	6.795	2.140201	7.217
1.E+00	2.328457	6.764	2.374067	6.828	2.463363	7.266
5.E+00	3.148154	6.680	3.195982	6.749	3.287882	7.293
1.E+01	3.525523	6.857	3.567160	6.728	3.658427	7.244
5.E+01	4.393019	6.725	4.441122	6.764	4.533433	7.290
1.E+02	4.778461	6.793	4.818480	6.728	4.912878	7.285
5.E+02	5.655070	6.743	5.707114	6.818	5.795491	7.248
1.E+03	6.032619	6.733	6.085840	6.781	6.179243	7.291
Average deviation		**6.782**		**6.771**		**7.257**

Table D.19.b. Pressure solution for a branch fracture inclined 30° with respect to the main fracture and its deviation with respect to the pressure solution obtained for the angle of 0°. C_{fD}=10

	X_{fbD} =0.2		X_{fbD} =0.4		X_{fbD} =0.6	
t_D	P_D	Deviation, %	P_D	Deviation, %	P_D	Deviation, %
1.E-07	0.014244	6.653	0.014245	6.539	0.014267	7.056
5.E-07	0.022690	6.575	0.022712	6.616	0.022712	7.036
1.E-06	0.027071	6.661	0.027053	6.629	0.027067	7.065
5.E-06	0.040366	6.665	0.040424	6.657	0.040387	7.064
1.E-05	0.047948	6.586	0.047944	6.527	0.048051	7.096
5.E-05	0.071640	6.619	0.071721	6.594	0.072546	7.136
1.E-04	0.085240	6.584	0.085591	6.629	0.087288	6.971
5.E-04	0.128234	6.591	0.130665	6.587	0.139187	7.095
1.E-03	0.153773	6.593	0.158301	6.564	0.171853	7.066
5.E-03	0.242566	6.578	0.256002	6.658	0.283548	7.094
1.E-02	0.301860	6.604	0.318865	6.542	0.352287	7.006
5.E-02	0.523287	6.631	0.546520	6.584	0.588373	6.968
1.E-01	0.671064	6.623	0.696260	6.615	0.738517	7.028
5.E-01	1.180341	6.598	1.203435	6.565	1.245938	7.113
1.E+00	1.473758	6.697	1.495053	6.530	1.536400	7.059
5.E+00	2.263022	6.545	2.285908	6.567	2.324593	7.050
1.E+01	2.631959	6.701	2.652246	6.576	2.694049	7.058
5.E+01	3.495207	6.545	3.523660	6.665	3.561992	7.045
1.E+02	3.879514	6.631	3.901217	6.580	3.944909	7.099
5.E+02	4.753109	6.607	4.779684	6.587	4.818912	7.066
1.E+03	5.131995	6.551	5.158687	6.599	5.194684	6.950
Average deviation		**6.611**		**6.591**		**7.053**

Table D.19.c. Pressure solution for a branch fracture inclined 30° with respect to the main fracture and its deviation with respect to the pressure solution obtained for the angle of 0°. C_{fD}=50

	X_{fbD} =0.2		X_{fbD} =0.4		X_{fbD} =0.6	
t_D	P_D	Deviation, %	P_D	Deviation, %	P_D	Deviation, %
1.E-07	0.006352	6.474	0.006360	6.502	0.006351	6.959
5.E-07	0.010116	6.534	0.010126	6.567	0.010138	6.964
1.E-06	0.012061	6.533	0.012058	6.491	0.012105	6.953
5.E-06	0.017988	6.542	0.018062	6.547	0.018559	6.961
1.E-05	0.021391	6.562	0.021636	6.610	0.022605	7.030
5.E-05	0.032550	6.539	0.033689	6.425	0.036905	6.975
1.E-04	0.039627	6.496	0.041590	6.573	0.046130	6.988
5.E-04	0.066237	6.532	0.070406	6.582	0.078352	6.995
1.E-03	0.084884	6.626	0.089875	6.539	0.098942	6.904
5.E-03	0.159211	6.448	0.165766	6.492	0.176790	6.907
1.E-02	0.212897	6.500	0.219673	6.489	0.231594	7.082
5.E-02	0.423243	6.554	0.430372	6.565	0.441468	6.933
1.E-01	0.566621	6.495	0.573132	6.451	0.585207	6.968
5.E-01	1.064251	6.482	1.071981	6.504	1.082510	6.941
1.E+00	1.355041	6.557	1.361441	6.556	1.372592	7.006
5.E+00	2.139972	6.505	2.146555	6.501	2.156966	6.857
1.E+01	2.506529	6.478	2.511728	6.470	2.525466	6.991
5.E+01	3.371639	6.516	3.385658	6.609	3.392488	6.958
1.E+02	3.752705	6.588	3.757752	6.450	3.771589	6.912
5.E+02	4.625958	6.442	4.631701	6.427	4.651950	6.969
1.E+03	5.000685	6.416	5.017614	6.523	5.034998	7.067
Average deviation		**6.515**		**6.518**		**6.968**

Table D.19.d. Pressure solution for a branch fracture inclined 30° with respect to the main fracture and its deviation with respect to the pressure solution obtained for the angle of 0°. C_{fD}=100

	X_{fbD} =0.2		X_{fbD} =0.4		X_{fbD} =0.6	
t_D	P_D	Deviation, %	P_D	Deviation, %	P_D	Deviation, %
1.E-07	0.004480	6.353	0.004482	6.316	0.004487	6.700
5.E-07	0.007129	6.290	0.007140	6.407	0.007220	6.756
1.E-06	0.008506	6.427	0.008534	6.405	0.008721	6.781
5.E-06	0.012724	6.292	0.013003	6.424	0.013873	6.763
1.E-05	0.015300	6.414	0.015746	6.209	0.017165	6.755
5.E-05	0.024350	6.410	0.025756	6.282	0.028808	6.822
1.E-04	0.030552	6.345	0.032502	6.398	0.036300	6.837
5.E-04	0.055375	6.292	0.058326	6.278	0.063575	6.787
1.E-03	0.073366	6.284	0.076674	6.337	0.082285	6.836
5.E-03	0.146811	6.396	0.150464	6.398	0.156504	6.697
1.E-02	0.199970	6.309	0.203838	6.345	0.210186	6.883
5.E-02	0.409097	6.396	0.412653	6.350	0.418773	6.723
1.E-01	0.551308	6.337	0.555523	6.367	0.561658	6.728
5.E-01	1.048855	6.388	1.050808	6.266	1.057299	6.724
1.E+00	1.335894	6.346	1.340112	6.377	1.345450	6.653
5.E+00	2.119080	6.247	2.123855	6.317	2.131795	6.759
1.E+01	2.481954	6.251	2.489796	6.349	2.500333	6.817
5.E+01	3.349230	6.334	3.353687	6.268	3.361678	6.717
1.E+02	3.728609	6.326	3.729884	6.258	3.740356	6.736
5.E+02	4.597708	6.267	4.609027	6.331	4.620951	6.759
1.E+03	4.981929	6.337	4.992535	6.379	4.996590	6.743
		6.335		6.336		6.761

Table D.19.e. Pressure solution for a branch fracture inclined 30° with respect to the main fracture and its deviation with respect to the pressure solution obtained for the angle of 0°. C_{fD}=300

	X_{fbD} =0.2		X_{fbD} =0.4		X_{fbD} =0.6	
t_D	P_D	Deviation, %	P_D	Deviation, %	P_D	Deviation, %
1.E-07	0.002016	6.932	0.002040	6.907	0.002140	7.423
5.E-07	0.003267	6.912	0.003385	6.981	0.003716	7.510
1.E-06	0.003981	7.009	0.004175	6.942	0.004639	7.493
5.E-06	0.006632	6.907	0.007061	6.978	0.007876	7.502
1.E-05	0.008519	6.962	0.009036	6.920	0.009989	7.492
5.E-05	0.016226	7.004	0.016930	7.047	0.018099	7.546
1.E-04	0.022023	7.018	0.022743	7.025	0.023958	7.466
5.E-04	0.046278	6.988	0.047056	6.951	0.048378	7.464
1.E-03	0.064107	6.967	0.064901	6.926	0.066288	7.499
5.E-03	0.137432	6.954	0.138500	6.990	0.139910	7.494
1.E-02	0.190949	6.957	0.192027	6.970	0.193553	7.513
5.E-02	0.400687	7.005	0.401512	6.974	0.403296	7.529
1.E-01	0.543859	6.923	0.545754	6.972	0.547580	7.502
5.E-01	1.043830	6.957	1.044921	6.936	1.047278	7.464
1.E+00	1.333114	7.007	1.335947	7.034	1.337702	7.500
5.E+00	2.124256	6.964	2.124627	6.946	2.126879	7.405
1.E+01	2.491494	6.987	2.492044	6.948	2.496836	7.510
5.E+01	3.360427	6.905	3.365754	6.893	3.371895	7.450
1.E+02	3.739333	6.984	3.745395	7.034	3.748444	7.509
5.E+02	4.625401	7.026	4.628798	7.017	4.633463	7.518
1.E+03	5.006646	6.952	5.011840	6.911	5.019032	7.444
Average deviation		**6.968**		**6.967**		**7.487**

Table D.20.a. Pressure solution for a branch fracture (C_{fbD}=0.75) inclined 30° with respect to the main fracture (C_{fD}=1) and its deviation with respect to the pressure solution obtained for the angle of 30° with constant dimensionless fracture conductivity (C_{fbD}=1 and C_{fD}=1)

	X_{fbD} =0.2		X_{fbD} =0.4		X_{fbD} =0.6	
t_D	P_D	Deviation, %	P_D	Deviation, %	P_D	Deviation, %
1.E-07	0.045345	0.130	0.045364	0.171	0.045373	0.152
5.E-07	0.072187	0.101	0.072250	0.141	0.072220	0.105
1.E-06	0.086065	0.181	0.086094	0.179	0.086168	0.147
5.E-06	0.128324	0.104	0.128401	0.196	0.128635	0.162
1.E-05	0.152427	0.186	0.152553	0.106	0.152688	0.126
5.E-05	0.227602	0.137	0.227725	0.136	0.227665	0.183
1.E-04	0.270661	0.187	0.270787	0.176	0.270928	0.159
5.E-04	0.403564	0.195	0.403552	0.159	0.403653	0.191
1.E-03	0.477362	0.152	0.477317	0.130	0.477897	0.170
5.E-03	0.701750	0.105	0.703161	0.165	0.708684	0.124
1.E-02	0.826200	0.147	0.829155	0.128	0.843579	0.111
5.E-02	1.195899	0.162	1.211910	0.182	1.263931	0.168
1.E-01	1.400597	0.126	1.428477	0.198	1.496561	0.158
5.E-01	2.014179	0.183	2.054942	0.123	2.142562	0.110
1.E+00	2.332157	0.159	2.378768	0.198	2.466527	0.128
5.E+00	3.154171	0.191	3.200884	0.153	3.292142	0.130
1.E+01	3.531500	0.169	3.574292	0.200	3.663187	0.130
5.E+01	4.398484	0.124	4.445633	0.101	4.542408	0.198
1.E+02	4.783747	0.111	4.823781	0.110	4.919158	0.128
5.E+02	5.664549	0.167	5.717381	0.180	5.802230	0.116
1.E+03	6.042121	0.157	6.092204	0.104	6.187956	0.141
Average deviation		**0.151**		**0.154**		**0.145**

Table D.20.b. Pressure solution for a branch fracture (C_{fbD}=7.5) inclined 30° with respect the main fracture (C_{fD}=10) and its deviation with respect to the pressure solution obtained for the angle of 30° with constant dimensionless fracture conductivity (C_{fbD}=10 and C_{fD}=10)

	X_{fbD} =0.2		X_{fbD} =0.4		X_{fbD} =0.6	
t_D	P_D	Deviation, %	P_D	Deviation, %	P_D	Deviation, %
1.E-07	0.014269	0.179	0.014272	0.186	0.014294	0.187
5.E-07	0.022735	0.196	0.022743	0.137	0.022757	0.195
1.E-06	0.027100	0.106	0.027104	0.187	0.027108	0.152
5.E-06	0.040421	0.136	0.040502	0.195	0.040430	0.105
1.E-05	0.048033	0.176	0.048017	0.152	0.048122	0.147
5.E-05	0.071754	0.159	0.071796	0.105	0.072664	0.162
1.E-04	0.085351	0.130	0.085716	0.147	0.087399	0.126
5.E-04	0.128445	0.165	0.130877	0.162	0.139442	0.183
1.E-03	0.153969	0.128	0.158501	0.126	0.172126	0.159
5.E-03	0.243009	0.182	0.256470	0.183	0.284089	0.191
1.E-02	0.302459	0.198	0.319372	0.159	0.352884	0.170
5.E-02	0.523929	0.123	0.547565	0.191	0.589105	0.124
1.E-01	0.672392	0.198	0.697441	0.169	0.739334	0.111
5.E-01	1.182152	0.153	1.204932	0.124	1.248027	0.168
1.E+00	1.476705	0.200	1.496707	0.111	1.538821	0.158
5.E+00	2.265321	0.101	2.289740	0.167	2.327157	0.110
1.E+01	2.634854	0.110	2.656424	0.157	2.697509	0.128
5.E+01	3.501495	0.180	3.527547	0.110	3.566608	0.130
1.E+02	3.883571	0.104	3.906228	0.128	3.950042	0.130
5.E+02	4.759678	0.138	4.785877	0.129	4.828452	0.198
1.E+03	5.141995	0.194	5.165399	0.130	5.201324	0.128
Average deviation		**0.155**		**0.150**		**0.151**

Table D.20.c. Pressure solution for a branch fracture (C_{fbD}=37.5) inclined 30° with respect to the main fracture (C_{fD}=50) and its deviation with respect to the pressure solution obtained for the angle of 30° with constant dimensionless fracture conductivity (C_{fbD}=50 and C_{fD}=50)

	X_{fbD} =0.2		X_{fbD} =0.4		X_{fbD} =0.6	
t_D	P_D	Deviation, %	P_D	Deviation, %	P_D	Deviation, %
1.E-07	0.006359	0.123	0.006372	0.179	0.006363	0.186
5.E-07	0.010136	0.198	0.010146	0.196	0.010151	0.137
1.E-06	0.012080	0.153	0.012070	0.106	0.012127	0.187
5.E-06	0.018024	0.200	0.018086	0.136	0.018595	0.195
1.E-05	0.021413	0.101	0.021674	0.176	0.022639	0.152
5.E-05	0.032585	0.110	0.033743	0.159	0.036944	0.105
1.E-04	0.039698	0.180	0.041644	0.130	0.046197	0.147
5.E-04	0.066306	0.104	0.070522	0.165	0.078479	0.162
1.E-03	0.085002	0.138	0.089990	0.128	0.099067	0.126
5.E-03	0.159521	0.194	0.166068	0.182	0.177114	0.183
1.E-02	0.213196	0.140	0.220110	0.198	0.231962	0.159
5.E-02	0.423735	0.116	0.430900	0.123	0.442311	0.191
1.E-01	0.567554	0.164	0.574267	0.198	0.586199	0.170
5.E-01	1.065755	0.141	1.073625	0.153	1.083857	0.124
1.E+00	1.356838	0.132	1.364164	0.200	1.374111	0.111
5.E+00	2.142557	0.121	2.148735	0.101	2.160581	0.168
1.E+01	2.510498	0.158	2.514491	0.110	2.529444	0.158
5.E+01	3.376554	0.146	3.391748	0.180	3.396230	0.110
1.E+02	3.757439	0.126	3.761682	0.104	3.776433	0.128
5.E+02	4.632337	0.138	4.638103	0.138	4.657978	0.130
1.E+03	5.010283	0.192	5.027391	0.194	5.041549	0.130
Average deviation		**0.146**		**0.155**		**0.150**

Table D.20.d. Pressure solution for a branch fracture (C_{fbD}=75) inclined 30° with respect to the main fracture (C_{fD}=100) and its deviation with respect to the pressure solution obtained for the angle of 30° with constant dimensionless fracture conductivity (C_{fbD}=100 and C_{fD}=100)

	X_{fbD} =0.2		X_{fbD} =0.4		X_{fbD} =0.6	
t_D	P_D	Deviation, %	P_D	Deviation, %	P_D	Deviation, %
1.E-07	0.004485	0.104	0.004490	0.186	0.004495	0.177
5.E-07	0.007143	0.186	0.007150	0.137	0.007232	0.176
1.E-06	0.008518	0.137	0.008550	0.187	0.008736	0.171
5.E-06	0.012748	0.187	0.013028	0.195	0.013893	0.141
1.E-05	0.015330	0.195	0.015770	0.152	0.017195	0.179
5.E-05	0.024387	0.152	0.025783	0.105	0.028864	0.196
1.E-04	0.030584	0.105	0.032550	0.147	0.036339	0.106
5.E-04	0.055457	0.147	0.058421	0.162	0.063662	0.136
1.E-03	0.073485	0.162	0.076771	0.126	0.082431	0.177
5.E-03	0.146996	0.126	0.150740	0.183	0.156753	0.159
1.E-02	0.200336	0.183	0.204162	0.159	0.210458	0.130
5.E-02	0.409747	0.159	0.413441	0.191	0.419463	0.165
1.E-01	0.552362	0.191	0.556464	0.169	0.562376	0.128
5.E-01	1.050633	0.169	1.052116	0.124	1.059228	0.182
1.E+00	1.337556	0.124	1.341595	0.111	1.348122	0.199
5.E+00	2.121425	0.111	2.127415	0.167	2.134411	0.123
1.E+01	2.486114	0.167	2.493718	0.157	2.505284	0.198
5.E+01	3.354506	0.157	3.357387	0.110	3.366835	0.153
1.E+02	3.732722	0.110	3.734675	0.128	3.747834	0.200
5.E+02	4.603614	0.128	4.614999	0.129	4.625644	0.102
1.E+03	4.988384	0.129	4.999030	0.130	5.002086	0.110
Average deviation		**0.149**		**0.150**		**0.158**

Table D.20.e. Pressure solution for a branch fracture (C_{fbD}=225) inclined 30° with respect to the main fracture (C_{fD}=300) and its deviation with respect to the pressure solution obtained for the angle of 30° with constant dimensionless fracture conductivity (C_{fbD}=300 and C_{fD}=300)

	X_{fbD} =0.2		X_{fbD} =0.4		X_{fbD} =0.6	
t_D	P_D	Deviation, %	P_D	Deviation, %	P_D	Deviation, %
1.E-07	0.002019	0.179	0.002043	0.152	0.002143	0.137
5.E-07	0.003273	0.196	0.003388	0.105	0.003723	0.187
1.E-06	0.003985	0.106	0.004181	0.147	0.004648	0.195
5.E-06	0.006641	0.136	0.007072	0.162	0.007888	0.152
1.E-05	0.008534	0.176	0.009047	0.126	0.010000	0.105
5.E-05	0.016252	0.159	0.016961	0.183	0.018126	0.147
1.E-04	0.022052	0.130	0.022780	0.159	0.023997	0.162
5.E-04	0.046355	0.165	0.047146	0.191	0.048439	0.126
1.E-03	0.064189	0.128	0.065011	0.169	0.066409	0.183
5.E-03	0.137683	0.182	0.138672	0.124	0.140132	0.159
1.E-02	0.191328	0.198	0.192239	0.111	0.193923	0.191
5.E-02	0.401179	0.123	0.402185	0.167	0.403980	0.170
1.E-01	0.544935	0.198	0.546614	0.157	0.548261	0.124
5.E-01	1.045431	0.153	1.046074	0.110	1.048436	0.111
1.E+00	1.335780	0.200	1.337663	0.128	1.339944	0.168
5.E+00	2.126413	0.101	2.127380	0.129	2.130229	0.158
1.E+01	2.494235	0.110	2.495286	0.130	2.499590	0.110
5.E+01	3.366472	0.180	3.372417	0.198	3.376226	0.128
1.E+02	3.743243	0.104	3.750182	0.128	3.753301	0.130
5.E+02	4.631793	0.138	4.634181	0.116	4.639492	0.130
1.E+03	5.016401	0.194	5.018907	0.141	5.028968	0.198
Average deviation		**0.155**		**0.144**		**0.151**

Table D.21.a. Pressure solution for a branch fracture (C_{fbD}=0.5) inclined 30° with respect to the main fracture (C_{fD}=1) and its deviation with respect to the pressure solution obtained for the angle of 30° with constant dimensionless fracture conductivity (C_{fbD}=1 and C_{fD}=1)

	X_{fbD} =0.2		X_{fbD} =0.4		X_{fbD} =0.6	
t_D	P_D	Deviation, %	P_D	Deviation, %	P_D	Deviation, %
1.E-07	0.045384	0.217	0.045394	0.238	0.045420	0.255
5.E-07	0.072251	0.190	0.072332	0.256	0.072298	0.212
1.E-06	0.086048	0.161	0.086083	0.165	0.086183	0.165
5.E-06	0.128500	0.241	0.128401	0.196	0.128693	0.207
1.E-05	0.152394	0.164	0.152753	0.236	0.152834	0.222
5.E-05	0.227849	0.246	0.227913	0.219	0.227672	0.186
1.E-04	0.270688	0.197	0.270822	0.189	0.271155	0.243
5.E-04	0.403774	0.247	0.403816	0.224	0.403765	0.219
1.E-03	0.477850	0.254	0.477595	0.188	0.478286	0.251
5.E-03	0.702501	0.212	0.703706	0.242	0.709428	0.230
1.E-02	0.826353	0.165	0.830237	0.258	0.844200	0.184
5.E-02	1.196431	0.206	1.211913	0.182	1.263969	0.171
1.E-01	1.401939	0.222	1.429324	0.257	1.497609	0.228
5.E-01	2.014248	0.186	2.056803	0.213	2.144856	0.218
1.E+00	2.334114	0.242	2.380238	0.259	2.467558	0.170
5.E+00	3.155046	0.218	3.201146	0.161	3.294078	0.188
1.E+01	3.534376	0.250	3.573224	0.170	3.665363	0.190
5.E+01	4.403102	0.229	4.451776	0.239	4.542051	0.190
1.E+02	4.787271	0.184	4.826410	0.164	4.925552	0.258
5.E+02	5.664720	0.170	5.718426	0.198	5.806377	0.188
1.E+03	6.046350	0.227	6.101350	0.254	6.190135	0.176
Average deviation		**0.211**		**0.215**		**0.207**

Table D.21.b. Pressure solution for a branch fracture (C_{fbD}=5) inclined 30° with respect to the main fracture (C_{fD}=10) and its deviation with respect to the pressure solution obtained for the angle of 30° with constant dimensionless fracture conductivity (C_{fbD}=10 and C_{fD}=10)

	X_{fbD} =0.2		X_{fbD} =0.4		X_{fbD} =0.6	
t_D	P_D	Deviation, %	P_D	Deviation, %	P_D	Deviation, %
1.E-07	0.014278	0.240	0.014279	0.233	0.014294	0.189
5.E-07	0.022744	0.239	0.022759	0.204	0.022768	0.246
1.E-06	0.027135	0.233	0.027119	0.241	0.027127	0.222
5.E-06	0.040448	0.204	0.040528	0.259	0.040490	0.254
1.E-05	0.048065	0.241	0.048025	0.168	0.048163	0.233
5.E-05	0.071826	0.259	0.071864	0.199	0.072682	0.187
1.E-04	0.085384	0.168	0.085796	0.239	0.087440	0.174
5.E-04	0.128490	0.199	0.130955	0.222	0.139508	0.231
1.E-03	0.154141	0.239	0.158606	0.192	0.172232	0.221
5.E-03	0.243105	0.222	0.256585	0.227	0.284039	0.173
1.E-02	0.302442	0.192	0.319474	0.191	0.352962	0.191
5.E-02	0.524479	0.227	0.547862	0.245	0.589506	0.193
1.E-01	0.672345	0.191	0.698082	0.261	0.739943	0.193
5.E-01	1.183239	0.245	1.205669	0.185	1.249190	0.261
1.E+00	1.477614	0.261	1.498955	0.260	1.539332	0.191
5.E+00	2.267224	0.185	2.290854	0.216	2.328761	0.179
1.E+01	2.638828	0.260	2.659220	0.262	2.699545	0.204
5.E+01	3.502770	0.216	3.529459	0.164	3.570337	0.234
1.E+02	3.889715	0.262	3.907967	0.173	3.953837	0.226
5.E+02	4.760931	0.164	4.791293	0.242	4.827663	0.182
1.E+03	5.140873	0.173	5.167331	0.167	5.203570	0.171
		0.220		0.217		0.207

Table D.21.c. Pressure solution for a branch fracture (C_{fbD}=25) inclined 30° with respect to the main fracture (C_{fD}=50) and its deviation with respect to the pressure solution obtained for the angle of 30° with constant dimensionless fracture conductivity (C_{fbD}=50 and C_{fD}=50)

	X_{fbD} =0.2		X_{fbD} =0.4		X_{fbD} =0.6	
t_D	P_D	Deviation, %	P_D	Deviation, %	P_D	Deviation, %
1.E-07	0.006366	0.219	0.006373	0.192	0.006365	0.220
5.E-07	0.010136	0.192	0.010143	0.163	0.010155	0.172
1.E-06	0.012081	0.163	0.012087	0.243	0.012128	0.190
5.E-06	0.018032	0.243	0.018092	0.166	0.018594	0.192
1.E-05	0.021427	0.166	0.021690	0.248	0.022648	0.192
5.E-05	0.032630	0.248	0.033756	0.199	0.037001	0.260
1.E-04	0.039706	0.199	0.041694	0.249	0.046217	0.190
5.E-04	0.066402	0.249	0.070587	0.256	0.078492	0.178
1.E-03	0.085102	0.256	0.090068	0.214	0.099143	0.203
5.E-03	0.159552	0.214	0.166043	0.167	0.177203	0.233
1.E-02	0.213253	0.167	0.220132	0.208	0.232116	0.225
5.E-02	0.424127	0.208	0.431337	0.224	0.442265	0.181
1.E-01	0.567891	0.224	0.574212	0.188	0.586202	0.170
5.E-01	1.066256	0.188	1.074607	0.244	1.085245	0.253
1.E+00	1.358361	0.244	1.364449	0.220	1.375894	0.241
5.E+00	2.144700	0.220	2.151988	0.252	2.161085	0.191
1.E+01	2.512873	0.252	2.517543	0.231	2.531153	0.225
5.E+01	3.379445	0.231	3.391969	0.186	3.399438	0.205
1.E+02	3.759700	0.186	3.764240	0.172	3.779815	0.218
5.E+02	4.633945	0.172	4.642337	0.229	4.663737	0.253
1.E+03	5.012167	0.229	5.028628	0.219	5.043269	0.164
Average Deviation		**0.213**		**0.213**		**0.207**

Table D.21.d. Pressure solution for a branch fracture (C_{fbD}=50) inclined 30° with respect to the main fracture (C_{fD}=100) and its deviation with respect to the pressure solution obtained for the angle of 30° with constant dimensionless fracture conductivity (C_{fbD}=100 and C_{fD}=100)

	X_{fbD} =0.2		X_{fbD} =0.4		X_{fbD} =0.6	
t_D	P_D	Deviation, %	P_D	Deviation, %	P_D	Deviation, %
1.E-07	0.004490	0.222	0.004490	0.190	0.004497	0.239
5.E-07	0.007141	0.170	0.007152	0.161	0.007238	0.256
1.E-06	0.008526	0.229	0.008555	0.241	0.008735	0.166
5.E-06	0.012755	0.243	0.013024	0.164	0.013900	0.196
1.E-05	0.015333	0.214	0.015784	0.246	0.017205	0.237
5.E-05	0.024400	0.203	0.025807	0.197	0.028871	0.219
1.E-04	0.030616	0.210	0.032582	0.247	0.036369	0.190
5.E-04	0.055490	0.206	0.058475	0.254	0.063718	0.225
1.E-03	0.073513	0.200	0.076837	0.212	0.082440	0.188
5.E-03	0.147054	0.165	0.150713	0.165	0.156883	0.242
1.E-02	0.200486	0.257	0.204260	0.206	0.210729	0.259
5.E-02	0.409911	0.199	0.413570	0.222	0.419538	0.183
1.E-01	0.552460	0.209	0.556558	0.186	0.563107	0.258
5.E-01	1.051031	0.207	1.053362	0.242	1.059555	0.213
1.E+00	1.338872	0.222	1.343046	0.218	1.348947	0.260
5.E+00	2.122802	0.175	2.129188	0.250	2.135240	0.162
1.E+01	2.487549	0.225	2.495511	0.229	2.504584	0.170
5.E+01	3.355897	0.199	3.359871	0.184	3.369743	0.240
1.E+02	3.737498	0.238	3.736248	0.170	3.746511	0.165
5.E+02	4.608530	0.235	4.619518	0.227	4.630109	0.198
1.E+03	4.994049	0.243	5.003395	0.217	5.009324	0.255
Average deviation		**0.213**		**0.211**		**0.215**

Table D.21.e. Pressure solution for a branch fracture (C_{fbD}=150) inclined 30° with respect to the main fracture (C_{fD}=300) and its deviation with respect to the pressure solution obtained for the angle of 30° with constant dimensionless fracture conductivity (C_{fbD}=300 and C_{fD}=300)

	X_{fbD} =0.2		X_{fbD} =0.4		X_{fbD} =0.6	
t_D	P_D	Deviation, %	P_D	Deviation, %	P_D	Deviation, %
1.E-07	0.002020	0.226	0.002044	0.203	0.002145	0.226
5.E-07	0.003273	0.196	0.003393	0.243	0.003724	0.197
1.E-06	0.003990	0.231	0.004185	0.226	0.004650	0.232
5.E-06	0.006645	0.195	0.007075	0.196	0.007892	0.195
1.E-05	0.008540	0.249	0.009057	0.231	0.010014	0.249
5.E-05	0.016270	0.265	0.016963	0.195	0.018147	0.266
1.E-04	0.022065	0.189	0.022800	0.249	0.024004	0.190
5.E-04	0.046401	0.264	0.047181	0.265	0.048506	0.265
1.E-03	0.064248	0.220	0.065024	0.189	0.066434	0.220
5.E-03	0.137799	0.266	0.138867	0.264	0.140284	0.267
1.E-02	0.191271	0.168	0.192450	0.220	0.193880	0.169
5.E-02	0.401396	0.177	0.402584	0.266	0.404010	0.177
1.E-01	0.545201	0.246	0.546674	0.168	0.548931	0.247
5.E-01	1.045621	0.171	1.046771	0.177	1.049074	0.172
1.E+00	1.335850	0.205	1.339246	0.246	1.340447	0.205
5.E+00	2.129818	0.261	2.128272	0.171	2.132448	0.262
1.E+01	2.496655	0.207	2.497158	0.205	2.502008	0.207
5.E+01	3.366578	0.183	3.374567	0.261	3.378067	0.183
1.E+02	3.747996	0.231	3.753153	0.207	3.757128	0.232
5.E+02	4.635035	0.208	4.637271	0.183	4.643114	0.208
1.E+03	5.016640	0.199	5.023450	0.231	5.029050	0.200
Average deviation		**0.217**		**0.219**		**0.218**

Table D.22. Number of PEBI cells used to simulate a branch fracture

	Number of cells for branch fracture at the main fracture at tip		
Angle, °	X_{fbD}=0.2	X_{fbD}=0.4	X_{fbD}=0.6
0	1454	1476	1498
10	1457	1479	1501
20	1458	1480	1502
30	1458	1481	1502
	Number of cells for branch fracture at the main fracture at middle		
Angle, °	X_{fbD}=0.2	X_{fbD} =0.4	X_{fbD} =0.6
10	1461	1483	1505
20	1463	1485	1507
30	1463	1485	1509
	Number of cells for branch fracture at the main fracture at wellbore		
Angle, °	X_{fbD} =0.2	X_{fbD} =0.4	X_{fbD} =0.6
10	1461	1483	1505
20	1462	1485	1507
30	1463	1485	1509

Table D.23.a. Number of PEBI cells used to simulate a fracture well intersecting a fault at its middle part and forming an angle of 90°

L_D	C_{fD} =1	C_{fD} =10	C_{fD} =50	C_{fD} =100	C_{fD} =300
	Number of cells				
0.5	997	1078	700	632	632
1	1015	1096	711	640	640
2	1053	1137	731	678	678
3	1093	1177	769	718	718
4	1128	1211	847	758	758
5	1170	1254	887	797	797
7.5	1354	1354	988	897	897
10	1454	1454	1088	997	997
30	2250	2250	1887	1796	1796

Table D.23.b. Number of PEBI cells used to simulate a fracture well intersecting a fault at its fourth part and forming an angle of 90°

L_D	C_{fD} =1	C_{fD} =10	C_{fD} =50	C_{fD} =100	C_{fD} =300
	Number of cells				
0.5	1123	718	650	632	632
1	1143	733	666	645	645
2	1182	771	704	679	679
3	1222	811	744	717	717
4	1261	850	783	757	757
5	1301	889	823	798	798
7.5	1401	985	920	899	899
10	1501	1088	1022	996	996
30	2299	1886	1820	1795	1795

Table D.23.c. Number of PEBI cells used to simulate a fracture well intersecting a fault at its tip and forming an angle of 90°

L_D	C_{fD} =1	C_{fD} =10	C_{fD} =50	C_{fD} =100	C_{fD} =300
	Number of cells				
0.5	1118	723	656	636	636
1	1133	743	676	655	655
2	1172	782	716	695	695
3	1211	821	755	734	734
4	1250	861	795	774	774
5	1290	901	835	815	815
7.5	1385	1000	934	914	914
10	1488	1100	1034	1015	1015
30	2288	1899	1833	1813	1813

Table D.23.d. Number of PEBI cells used to simulate a fracture well intersecting a fault at its middle part and forming an angle of 75°

L_D	C_{fD} =1	C_{fD} =10	C_{fD} =50	C_{fD} =100	C_{fD} =300
	Number of cells				
0.5	1114	714	648	632	632
7.5	1384	985	918	898	898
30	2278	1884	1817	1796	1796

Table D.23.e. Number of PEBI cells used to simulate a fracture well intersecting a fault at its fourth part and forming an angle of 75°

L_D	C_{fD} =1	C_{fD} =10	C_{fD} =50	C_{fD} =100	C_{fD} =300
	Number of cells				
0.5	1117	717	649	632	632
7.5	1386	986	920	898	898
30	2282	1885	1817	1796	1796

Table D.23.f. Number of PEBI cells used to simulate a fracture well intersecting a fault at its tip and forming an angle of 75°

L_D	C_{fD} =1	C_{fD} =10	C_{fD} =50	C_{fD} =100	C_{fD} =300
	Number of cells				
0.5	1121		654		636
7.5	1399		932		914
30	2298		1831		1813

Table D.23.g. Number of PEBI cells used to simulate a fracture well intersecting a fault at its middle part and forming an angle of 60°

L_D	C_{fD} =1	C_{fD} =10	C_{fD} =50	C_{fD} =100	C_{fD} =300
	Number of cells				
0.5	1114	1114	1114	1114	1114
1	1128				
2	1167				
3	1206				
4	1245				
5	1284				
7.5	1383	1383	1383	1383	1383
10	1482				
30	2282	2282	2282	2282	2282

Table D.23.h. Number of PEBI cells used to simulate a fracture well intersecting a fault at its fourth part and forming an angle of 60°

L_D	C_{fD} =1	C_{fD} =10	C_{fD} =50	C_{fD} =100	C_{fD} =300
	Number of cells				
0.5	1117	716	732	632	632
7.5	1384	986	917	896	896
30	2282	1886	1817	1794	1794

Table D.23.i. Number of PEBI cells used to simulate a fracture well intersecting a fault at its tip and forming an angle of 60°

L_D	C_{fD} =1	C_{fD} =10	C_{fD} =50	C_{fD} =100	C_{fD} =300
	Number of cells				
0.5	1122	722	655	634	634
7.5	1401	1000	933	913	913
30	2301	1901	1833	1813	1813

Table D.23.j. Number of PEBI cells used to simulate a fracture well intersecting a fault at its middle part and forming an angle of 30°

L_D	C_{fD} =1	C_{fD} =10	C_{fD} =50	C_{fD} =100	C_{fD} =300
	Number of cells				
0.5	1114	714	648	632	632
7.5	1371	974	903	881	881
30	2270	1873	1804	1780	1780

Table D.23.k. Number of PEBI cells used to simulate a fracture well intersecting a fault at its fourth part and forming an angle of 30°

L_D	C_{fD} =1	C_{fD} =10	C_{fD} =50	C_{fD} =100	C_{fD} =300
	Number of cells				
0.5	1116	715	715	632	632
7.5	1371	973	973	876	876
30	2270	1873	1873	1780	1780

Table D.23.l. Number of PEBI cells used to simulate a fracture well intersecting a fault at its tip and forming an angle of 30°

L_D	C_{fD} =1	C_{fD} =10	C_{fD} =50	C_{fD} =100	C_{fD} =300
	Number of cells				
0.5	1120	720	653	653	634
7.5	1400	999	932	932	914
30	2300	1899	1832	1832	1832

Table D.23.m. Number of PEBI cells used to simulate a fracture well intersecting a fault at its tip and forming an angle of 0°

L_D	C_{fD} =1	C_{fD} =10	C_{fD} =50	C_{fD} =100	C_{fD} =300
	Number of cells				
0.5	1114		654		654
7.5	1361		874		874
30	2261		1774		1774

Table D.23.n. Number of PEBI cells used to simulate a fracture well intersecting a fault at its middle distance and forming different angles. L_D=80 (almost half reservoir is crossed by the fault)

Angle, °	C_{fD}	*Number of Grids*
none	1	1114
none	300	632
90	1	1832
90	300	1395
75	1	1868
75	300	1428
60	1	1947
60	300	1496
30	1	1938
30	300	1486

Table D.23.o. Number of PEBI cells used to simulate a fracture well intersecting a fault at its middle distance and forming different angles. L_D=162 (The whole reservoir is crossed by the fault)

Angle,°	C_{fD}	Number of Grids
none	1	1113
none	300	632
90	1	2696
90	300	2248
75	1	2460
75	300	2014
60	1	2452
60	300	2008
30	1	2457
30	300	2010

Table D.24.a. Pressure solution for a hydraulic fracture intersecting the a fault in its middle part forming and angle of 90°, C_{fD}=1

L_D = 0.5		L_D =1		L_D =2		L_D =3		L_D =4	
t_D	P_D	t_D	P_D	t_D	P_D	t_D	P_D	t_D	P_D
0.014497	0.679	0.014497	0.679	0.014497	0.679	0.014497	0.679	0.014497	0.679
0.042805	0.899	0.042805	0.899	0.042805	0.899	0.042805	0.899	0.042805	0.899
0.105696	1.124	0.105696	1.124	0.105696	1.124	0.105696	1.124	0.105696	1.124
0.199169	1.302	0.199167	1.302	0.199167	1.302	0.199167	1.302	0.199167	1.302
0.220009	1.333	0.220006	1.333	0.220006	1.333	0.220006	1.333	0.220006	1.333
0.321529	1.456	0.321508	1.456	0.32151	1.456	0.321512	1.455	0.321511	1.455
0.459777	1.580	0.459669	1.580	0.459685	1.580	0.459704	1.580	0.459691	1.580
0.501654	1.612	0.501512	1.612	0.50154	1.612	0.501544	1.612	0.50154	1.612
0.768022	1.772	0.767557	1.772	0.767553	1.772	0.767568	1.772	0.76755	1.772
0.834505	1.804	0.833907	1.805	0.833904	1.805	0.833919	1.805	0.833892	1.805
1.568063	2.067	1.562457	2.068	1.561952	2.068	1.561964	2.068	1.561838	2.068
1.688632	2.100	1.68126	2.101	1.680503	2.101	1.680537	2.101	1.680354	2.101
1.816457	2.133	1.806815	2.134	1.805726	2.135	1.80576	2.135	1.805496	2.135
1.951839	2.167	1.93933	2.168	1.937736	2.168	1.937794	2.168	1.937473	2.168
3.13576	2.402	3.076565	2.404	3.060434	2.405	3.060514	2.405	3.059012	2.405
4.826788	2.639	4.632395	2.642	4.531088	2.639	4.523005	2.639	4.5196	2.638
9.449414	3.048	8.647021	3.051	7.958786	3.033	7.84222	3.028	7.829264	3.028
19.46782	3.528	16.91131	3.532	14.15186	3.497	13.43379	3.481	13.34162	3.480
28.96538	3.804	24.56297	3.808	19.39364	3.767	17.80755	3.744	17.55795	3.741
36.99895	3.976	30.99839	3.981	23.607	3.938	21.13349	3.910	20.69999	3.906
54.56744	4.252	44.96005	4.258	32.45046	4.213	27.70134	4.179	26.7409	4.172
97.19283	4.667	78.80582	4.673	53.071	4.628	41.68225	4.586	38.95755	4.577
149.4101	4.979	120.2415	4.984	77.89961	4.939	57.22738	4.896	51.7541	4.884
513.5993	5.879	409.3323	5.884	250.4542	5.839	157.4392	5.795	125.1795	5.780
1043.603	6.398	830.2881	6.403	502.1868	6.359	301.4641	6.314	224.0269	6.299
2015.941	6.881	1604.958	6.887	966.3069	6.843	567.7197	6.798	404.9343	6.784
3064.664	7.189	2451.023	7.199	1472.856	7.154	859.1404	7.110	603.1771	7.095
4054.709	7.394	3244.094	7.405	1950.451	7.361	1134.699	7.318	790.8295	7.303
5083.001	7.561	4085.55	7.574	2465.744	7.534	1431.845	7.491	993.3063	7.476
10074.05	8.065	8135.546	8.082	4721.388	8.013	2880.682	8.009	1984.572	7.995
15423.47	8.381	14006.71	8.484	6367.69	8.235	5373.679	8.470	4540.662	8.610
17917.38	8.493	18124.79	8.676	8080.204	8.413	7593.448	8.727	6733.121	8.904
18057.37	8.499	18592.69	8.695	8209.83	8.424	7696.853	8.737	6761.073	8.907
18225.34	8.505	19154.02	8.717	8365.366	8.438	7820.929	8.749	6794.621	8.911
18426.9	8.514	19827.72	8.742	8552.02	8.455	7969.828	8.763	6834.886	8.915
18668.81	8.523	19908.55	8.745	8776.005	8.474	8148.502	8.780	6883.189	8.920
20223.38	8.583	21926.2	8.817	10215.55	8.586	9991.524	8.931	8088.883	9.041

Table D.24.a. Continued

L_D =5		L_D =7.5		L_D =10		L_D =30	
t_D	P_D	t_D	P_D	t_D	P_D	t_D	P_D
0.014497	0.679	0.014497	0.679	0.014497	0.679	0.014497	0.679
0.042805	0.899	0.042805	0.899	0.042805	0.899	0.042805	0.899
0.105696	1.124	0.105696	1.124	0.105696	1.124	0.105696	1.124
0.199167	1.302	0.199167	1.302	0.199167	1.302	0.199167	1.302
0.220006	1.333	0.220006	1.333	0.220006	1.333	0.220006	1.333
0.321511	1.455	0.321511	1.455	0.321509	1.456	0.321511	1.455
0.459699	1.580	0.459707	1.580	0.459691	1.580	0.459681	1.580
0.501523	1.612	0.501554	1.612	0.501546	1.612	0.501533	1.612
0.767533	1.772	0.767543	1.772	0.767545	1.772	0.767534	1.772
0.833879	1.805	0.83388	1.805	0.833873	1.805	0.833869	1.805
1.561459	2.068	1.561471	2.068	1.561459	2.068	1.561459	2.068
1.679884	2.101	1.679907	2.101	1.679884	2.101	1.679884	2.101
1.804958	2.135	1.804981	2.135	1.804969	2.135	1.804958	2.135
1.936808	2.168	1.936842	2.168	1.936831	2.168	1.936819	2.168
3.058118	2.405	3.058095	2.405	3.058095	2.405	3.058083	2.405
4.520402	2.639	4.520242	2.639	4.520254	2.639	4.520242	2.639
7.835467	3.028	7.834963	3.028	7.834963	3.028	7.834974	3.028
13.33989	3.480	13.33967	3.480	13.33978	3.480	13.33989	3.480
17.5153	3.741	17.51163	3.741	17.51174	3.741	17.51186	3.741
20.59589	3.906	20.5811	3.906	20.5819	3.906	20.5819	3.906
26.43352	4.171	26.36541	4.171	26.36782	4.171	26.36771	4.171
37.87454	4.574	37.51098	4.573	37.50972	4.573	37.50835	4.573
49.34962	4.880	48.34894	4.878	48.31293	4.878	48.3111	4.878
108.3223	5.773	98.37031	5.770	96.98003	5.770	96.78076	5.771
179.0855	6.293	149.1808	6.291	143.5709	6.291	142.2134	6.292
302.0878	6.778	225.178	6.777	208.1671	6.779	202.3703	6.782
434.9422	7.090	299.2101	7.090	266.4528	7.094	253.2976	7.097
560.499	7.297	365.6923	7.299	315.8725	7.303	293.9579	7.308
696.0843	7.470	435.5969	7.472	365.5902	7.478	332.6484	7.484
1360.979	7.990	769.5878	7.992	585.1124	8.000	481.2124	8.013
3107.808	8.611	1644.892	8.615	1116.027	8.625	747.9965	8.649
5548.179	9.043	3504.653	9.198	2232.048	9.212	1137.022	9.249
5606.87	9.051	3668.411	9.233	2330.019	9.247	1165.646	9.285
5677.3	9.061	3840.057	9.268	2432.736	9.281	1195.043	9.320
5761.811	9.072	4019.384	9.302	2537.597	9.315	1225.23	9.355
5863.22	9.085	4207.941	9.337	2650.208	9.350	1256.244	9.390
8113.373	9.326	5419.872	9.528	3919.591	9.656	1577.064	9.708

Table D.24.b. Pressure solution for a hydraulic fracture intersecting the a fault in its middle part forming and angle of 90°, C_{fD}=10

L_D = 0.5		L_D =1		L_D =2		L_D =3		L_D =4	
t_D	P_D	t_D	P_D	t_D	P_D	t_D	P_D	t_D	P_D
0.003811	0.150	0.003811	0.150	0.003811	0.150	0.003811	0.150	0.003811	0.150
0.107187	0.385	0.107187	0.385	0.107187	0.385	0.107187	0.385	0.107187	0.385
1.052651	0.839	1.047133	0.840	1.047006	0.840	1.04932	0.841	1.049088	0.841
2.158029	1.105	2.120779	1.106	2.113659	1.107	2.119185	1.108	2.120091	1.108
4.089219	1.405	3.941902	1.408	3.87428	1.409	3.877686	1.409	3.878442	1.409
6.290506	1.639	5.955046	1.644	5.740256	1.644	5.709552	1.643	5.711238	1.644
10.41798	1.941	9.631368	1.948	8.965755	1.949	8.775764	1.946	8.773952	1.945
15.05337	2.177	13.6764	2.185	12.31307	2.187	11.82511	2.181	11.80012	2.180
15.84699	2.211	14.36339	2.219	12.86489	2.221	12.31582	2.215	12.28464	2.214
20.41783	2.380	18.29608	2.388	15.95419	2.392	15.00441	2.384	14.92565	2.382
30.28755	2.649	26.7714	2.660	22.30913	2.665	20.27509	2.656	20.0185	2.653
40.59776	2.853	35.36802	2.861	28.60079	2.871	25.21511	2.860	24.69459	2.856
50.50406	3.007	62.09401	3.268	47.09074	3.279	38.69098	3.270	37.04171	3.266
70.24796	3.240	79.94524	3.451	59.12773	3.463	51.55598	3.542	48.35983	3.540
100.5654	3.496	113.0202	3.703	84.36703	3.743	69.53963	3.820	83.48455	4.089
130.1291	3.680	157.2019	3.943	110.6161	3.953	83.51379	3.986	114.4262	4.389
161.0393	3.833	199.512	4.115	132.7729	4.093	108.2423	4.211	137.977	4.561
201.4737	3.995	232.377	4.227	151.9439	4.196	122.0472	4.314	174.1509	4.767
517.697	4.674	857.8276	5.173	541.2213	5.135	381.1738	5.217	658.984	5.831
704.0251	4.897	1255.762	5.451	916.111	5.520	527.0641	5.462	942.5796	6.102
802.0871	4.991	1321.091	5.488	950.2659	5.547	586.4298	5.542	983.4015	6.134
901.4458	5.076	1413.524	5.537	1025.967	5.604	613.2905	5.575	1041.147	6.177
1014.876	5.162	1546.727	5.603	1135.126	5.678	808.8333	5.779	1170.048	6.264
1108.593	5.226	1688.219	5.667	1283.256	5.768	928.9578	5.882	1258.457	6.318
1208.766	5.290	1863.465	5.740	1480.332	5.872	1124.357	6.024	1467.17	6.432
1504.924	5.449	2147.458	5.844	1734.928	5.989	1432.9	6.203	1636.086	6.514
1704.786	5.541	2310.895	5.898	1872.018	6.045	1640.604	6.303	1738.207	6.559
1801.942	5.581	2357.191	5.912	1933.334	6.069	1753.055	6.352	1891.428	6.622
2000.577	5.658	2637.86	5.995	2230.042	6.174	2146.174	6.502	2191.014	6.731
2500.644	5.822	3079.993	6.110	2483.894	6.254	2384.009	6.580	2669.527	6.878
3004.357	5.957	3510.352	6.206	2883.456	6.364	2867.027	6.717	3281.895	7.032
4019.671	6.172	4494.583	6.390	3750.559	6.559	3726.654	6.912	4045.181	7.188
5003.387	6.335	5128.357	6.488	4550.43	6.702	4062.746	6.976	5025.377	7.350
6055.102	6.478	6525.6	6.669	5606 285	6.858	5036.957	7.137	6043.145	7.489
10309.98	6.877	10337.25	7.014	10477.45	7.328	8790.589	7.555	9388.568	7.821
15043.4	7.162	14254.36	7.256	15426.22	7.619	13563.58	7.882	13298.62	8.083
18877.6	7.333	18395.6	7.448	19533.63	7.797	19337.92	8.150	20202.97	8.399
20150.69	7.382	19274.63	7.483	20212.26	7.823	20043.15	8.177	20911.18	8.425

Table D.24.b. Continued

L_D =5		L_D =7.5		L_D =10		L_D =30	
t_D	P_D	t_D	P_D	t_D	P_D	t_D	P_D
0.003811	0.150	0.003811	0.150	0.003811	0.150	0.003811	0.150
0.107187	0.385	0.107187	0.385	0.107187	0.385	0.107187	0.385
1.048635	0.841	1.048792	0.841	1.048837	0.840	1.048789	0.840
2.119758	1.108	2.117373	1.107	2.117396	1.107	2.117327	1.107
3.876837	1.410	3.873982	1.409	3.874085	1.409	3.873833	1.409
5.704955	1.644	5.707018	1.643	5.707294	1.643	5.707041	1.643
8.753017	1.946	8.765159	1.945	8.766856	1.945	8.764298	1.945
11.75942	2.181	11.77455	2.180	11.77753	2.180	11.77386	2.180
12.23992	2.215	12.25517	2.214	12.25873	2.214	12.2546	2.213
14.85674	2.383	14.86775	2.382	14.8736	2.382	14.86924	2.382
19.8753	2.653	19.86372	2.651	19.87415	2.651	19.87197	2.651
24.43582	2.856	24.37964	2.854	24.39752	2.854	24.39764	2.854
36.2028	3.264	35.84188	3.261	35.88602	3.261	35.89656	3.261
46.59258	3.536	45.69336	3.534	45.71102	3.533	45.71171	3.533
74.90284	4.054	72.56084	4.081	72.33578	4.082	72.18616	4.078
86.59197	4.211	104.8219	4.529	103.3382	4.529	102.9183	4.526
98.82307	4.352	117.7936	4.671	143.0366	4.944	113.9837	4.659
134.4297	4.667	148.0974	4.946	161.8419	5.102	136.3214	4.894
359.9069	5.567	347.8776	5.887	376.6118	6.125	370.4951	6.254
613.5577	5.997	577.7828	6.365	457.1595	6.339	504.8869	6.686
657.4213	6.051	627.1141	6.438	483.3472	6.399	535.5472	6.768
713.0035	6.114	649.4346	6.469	496.4474	6.427	558.7218	6.827
808.6429	6.212	724.6832	6.564	529.489	6.495	585.179	6.892
892.7426	6.289	822.7509	6.671	564.4292	6.561	613.2297	6.958
1002.379	6.377	941.0949	6.784	607.9065	6.637	686.1061	7.115
1270.438	6.557	1147.198	6.946	730.261	6.817	778.7393	7.291
1586.603	6.725	1299.536	7.046	862.7908	6.975	861.65	7.432
1740.282	6.794	1411.345	7.111	924.4519	7.039	900.2259	7.493
2126.075	6.944	1756.036	7.283	1116.638	7.208	962.8616	7.586
2603.969	7.096	2225.834	7.466	1480.435	7.451	1139.596	7.819
3055.664	7.216	2442.447	7.537	2075.067	7.730	1319.474	8.018
3827.479	7.385	2859.872	7.658	2904.816	7.998	1596.623	8.274
4276.985	7.469	3347.052	7.779	3405.961	8.123	1960.346	8.543
5182.29	7.613	4211.667	7.954	4550.969	8.349	2473.598	8.836
8082.015	7.949	5505.311	8.158	8372.624	8.819	5007.847	9.641
11929.33	8.243	7879.298	8.431	11526.9	9.063	8764.723	10.190
15826.82	8.457	12228.69	8.765	15915.79	9.309	13703.8	10.584
16111.04	8.470	12689.36	8.793	16252.17	9.325	14447.78	10.629

Table D.24.c. Pressure solution for a hydraulic fracture intersecting the a fault in its middle part forming and angle of 90°, C_{fD}=50

L_D = 0.5		L_D =1		L_D =2		L_D =3		L_D =4	
t_D	P_D	t_D	P_D	t_D	P_D	t_D	P_D	t_D	P_D
0.004358	0.075	0.004358	0.075	0.004358	0.075	0.004358	0.075	0.004358	0.075
0.11418	0.284	0.11418	0.284	0.11418	0.284	0.11418	0.284	0.11418	0.284
1.1059	0.745	1.101702	0.744	1.098439	0.742	1.102705	0.745	1.102391	0.745
2.090361	0.980	2.050646	0.978	2.028438	0.975	2.04661	0.980	2.049155	0.979
3.050631	1.148	2.965765	1.146	2.909058	1.143	2.938283	1.148	2.946206	1.148
10.20777	1.816	9.558679	1.819	8.840795	1.821	8.731234	1.822	8.739706	1.822
21.0005	2.285	19.17718	2.291	16.56357	2.298	15.70563	2.296	15.56633	2.296
50.1445	2.883	44.12848	2.882	35.15327	2.908	30.7676	2.909	29.72438	2.908
100.9352	3.378	88.43329	3.383	62.11121	3.365	52.6766	3.413	49.19461	3.415
202.3783	3.871	178.51	3.886	118.4678	3.863	91.34385	3.907	79.47906	3.893
500.6092	4.512	501.523	4.621	335.5571	4.629	434.08	5.135	248.4765	4.903
831.7992	4.873	760.3881	4.919	734.3517	5.190	1051.226	5.783	367.5794	5.212
1004.043	5.010	937.88	5.069	906.4481	5.344	1252.644	5.913	423.9035	5.322
1534.803	5.317	1988.722	5.614	1699.776	5.802	2312.787	6.366	1063.934	6.009
2043.136	5.526	2705.596	5.842	2564.666	6.104	3145.93	6.594	1289.115	6.152
4016.266	6.027	7095.101	6.559	5179.412	6.628	5358.934	6.993	2701.515	6.701
5058.66	6.198	7571.263	6.608	5992.043	6.736	6345.092	7.119	3020.179	6.784
5143.961	6.211	7594.881	6.610	6069.617	6.746	6413.986	7.127	3036.242	6.788
5154.2	6.212	7623.234	6.613	6162.704	6.757	6422.253	7.128	3055.515	6.793
5166.479	6.214	7657.251	6.616	6173.871	6.759	6432.17	7.129	3078.64	6.799
5181.223	6.216	7698.08	6.620	6187.273	6.760	6444.083	7.131	3106.397	6.805
5198.903	6.219	7747.071	6.625	6203.359	6.762	6458.369	7.132	3139.704	6.813
5220.136	6.222	7805.852	6.630	6222.667	6.765	6475.509	7.135	3179.672	6.823
5245.601	6.225	7876.398	6.637	6245.826	6.767	6496.089	7.137	3184.464	6.824
5276.167	6.230	7961.058	6.645	6273.618	6.771	6520.774	7.140	3190.22	6.825
5312.844	6.235	8062.639	6.655	6306.97	6.775	6550.4	7.143	3197.133	6.827
5356.859	6.241	8184.537	6.666	6346.995	6.779	6585.941	7.147	3205.423	6.829
5409.68	6.248	8199.166	6.667	6395.034	6.785	6628.604	7.152	3215.363	6.831
9009.311	6.628	13872.91	7.058	11714.36	7.236	9605.066	7.429	6241.045	7.328
10030.3	6.708	15032.96	7.118	12878.31	7.306	10981.35	7.528	7458.158	7.461
10505.02	6.742	16189.69	7.173	14629.39	7.401	11864.78	7.586	8596.884	7.567
10710.12	6.757	17353.07	7.225	15011.41	7.420	12286.47	7.612	8695.198	7.576
11063.33	6.781	17888.95	7.247	15332.55	7.436	12520.71	7.626	9142.169	7.613
11609.33	6.817	18273.95	7.263	15459.01	7.442	12632.95	7.633	9403.908	7.634
12019.67	6.843	20036.27	7.331	17011.52	7.513	13941.93	7.706	10596.37	7.723
12514.86	6.873	20627.76	7.353	17729.47	7.544	14062.32	7.712	10935.81	7.747
12768.81	6.887	22017.92	7.401	18535.01	7.577	14882.43	7.755	11127.02	7.759
12910.98	6.896	22754.79	7.426	18664.34	7.582	15242.66	7.772	11344.94	7.774
13192.8	6.912	22868.18	7.429	19078.58	7.598	15279.47	7.774	11430.72	7.780

Table D.24.c. Continued

L_D =5		L_D =7.5		L_D =10		L_D =30	
t_D	P_D	t_D	P_D	t_D	P_D	t_D	P_D
0.004358	0.075	0.004358	0.075	0.004358	0.075	0.004358	0.075
0.11418	0.284	0.11418	0.284	0.11418	0.284	0.11418	0.284
1.103434	0.746	1.10257	0.745	1.10257	0.745	1.10257	0.745
2.049339	0.981	2.046243	0.980	2.046243	0.980	2.046243	0.980
2.940197	1.149	2.937733	1.148	2.937733	1.148	2.937733	1.148
8.688457	1.823	8.703923	1.821	8.702742	1.821	8.703751	1.821
15.45007	2.297	15.49409	2.294	15.48825	2.294	15.49834	2.294
29.12142	2.908	29.04506	2.902	29.02053	2.903	29.13724	2.904
47.23853	3.421	46.39939	3.415	46.22936	3.414	46.33347	3.411
74.03309	3.908	71.35837	3.919	70.44299	3.914	71.0769	3.917
234.9189	5.045	200.6115	5.144	184.8594	5.120	182.5905	5.124
400.6967	5.494	369.9539	5.779	309.0002	5.733	298.646	5.780
667.4832	5.894	576.0045	6.185	440.6736	6.120	402.0393	6.181
1353.412	6.433	1349.456	6.891	959.0505	6.871	849.0968	7.210
2033.586	6.738	2003.306	7.199	1357.344	7.173	1118.094	7.589
4063.548	7.258	4315.829	7.787	3019.64	7.819	2570.766	8.674
4699.547	7.367	4820.012	7.871	3441.537	7.921	2741.494	8.752
4751.587	7.375	4827.418	7.872	3488.292	7.932	2746.298	8.754
4814.038	7.385	4836.315	7.873	3544.403	7.944	2752.053	8.757
4888.987	7.397	4846.99	7.875	3551.145	7.946	2758.967	8.760
4978.92	7.410	4859.796	7.877	3559.216	7.948	2767.256	8.763
5086.842	7.426	4875.171	7.879	3568.916	7.950	2777.208	8.768
5216.341	7.445	4893.619	7.882	3580.553	7.952	2789.144	8.773
5231.876	7.447	4915.746	7.885	3594.518	7.955	2803.475	8.779
5250.531	7.450	4942.312	7.890	3611.269	7.959	2820.673	8.786
5272.911	7.453	4974.185	7.894	3631.378	7.963	2841.31	8.795
5299.762	7.457	5012.433	7.900	3655.501	7.968	2866.064	8.806
5331.979	7.462	5058.328	7.907	3684.462	7.975	2895.781	8.818
9046.813	7.857	9023.194	8.343	8015.735	8.571	5269.093	9.484
10301.43	7.954	10862.77	8.483	9322.174	8.685	6664.02	9.717
11412.41	8.031	11775.7	8.543	10391.82	8.767	7711.62	9.855
11668.72	8.047	11953.87	8.554	10678.03	8.788	8005.347	9.890
11884.16	8.061	12260.79	8.573	11019.35	8.812	8355.633	9.929
12428.41	8.094	12526.55	8.589	11508.33	8.844	8751.274	9.971
13210.68	8.140	14071.72	8.676	12409.03	8.901	9825.347	10.075
13950.76	8.181	14757.68	8.712	12619.42	8.914	9989.024	10.089
14675.13	8.218	15253.9	8.737	13032.28	8.938	10412.71	10.126
14844.48	8.227	15572.06	8.752	13143.96	8.944	10939.75	10.169
15122.39	8.241	15967.95	8.771	13393.78	8.959	11196.05	10.189

Table D.24.d. Pressure solution for a hydraulic fracture intersecting the a fault in its middle part forming and angle of 90°, C_{fD}=100

L_D = 0.5		L_D =1		L_D =2		L_D =3		L_D =4	
t_D	P_D	t_D	P_D	t_D	P_D	t_D	P_D	t_D	P_D
0.006155	0.059	0.006155	0.059	0.006155	0.059	0.006155	0.059	0.006155	0.059
0.100254	0.233	0.100254	0.233	0.100254	0.233	0.100254	0.233	0.100254	0.233
1.050723	0.735	1.04728	0.736	1.047209	0.736	1.048054	0.736	1.047908	0.736
2.116915	1.002	2.091519	1.004	2.085443	1.005	2.087942	1.005	2.087495	1.005
3.545377	1.236	3.46151	1.240	3.419306	1.242	3.424294	1.243	3.422952	1.243
5.253581	1.436	5.065424	1.441	4.926168	1.446	4.927544	1.447	4.921754	1.447
10.05798	1.803	9.451971	1.811	8.792183	1.821	8.683767	1.821	8.643203	1.821
20.22568	2.241	18.5036	2.250	16.02941	2.265	15.29804	2.266	15.03228	2.262
21.29641	2.274	19.44868	2.284	16.75091	2.299	15.93104	2.300	15.63179	2.296
30.35967	2.512	27.41826	2.521	22.68164	2.538	20.99258	2.541	20.35477	2.534
52.12099	2.886	46.44754	2.896	36.2036	2.915	31.80142	2.919	30.04609	2.911
102.3437	3.363	89.6337	3.369	65.96616	3.394	53.61159	3.401	48.28679	3.393
200.5725	3.839	171.9267	3.834	122.6228	3.871	92.34499	3.882	77.86385	3.875
410.5775	4.346	347.0154	4.332	245.8315	4.384	172.2729	4.391	134.448	4.390
1045.517	5.016	892.879	5.010	630.3691	5.069	424.1591	5.075	302.3252	5.067
2036.085	5.493	1744.983	5.489	1224.543	5.548	812.2201	5.554	562.2359	5.546
3107.223	5.796	2678.47	5.797	1876.443	5.854	1239.344	5.860	847.6419	5.854
4105.568	5.999	3556.465	6.002	2490.669	6.058	1645.683	6.065	1119.888	6.060
6226.794	6.305	5417.235	6.310	3802.921	6.366	2519.401	6.373	1707.756	6.368
8214.633	6.509	7153.917	6.515	5033.54	6.571	3338.614	6.578	2265.263	6.573
8605.437	6.544	7491.304	6.550	5273.702	6.606	3498.359	6.612	2374.263	6.607
8999.336	6.577	7844.995	6.584	5525.077	6.640	3666.714	6.647	2488.525	6.642
9429.74	6.612	8213.051	6.618	5787.963	6.674	3841.375	6.681	2607.821	6.676
9868.949	6.646	8599.36	6.652	6063.507	6.709	4024.933	6.715	2733.193	6.710
10339.7	6.681	9006.868	6.686	6348.807	6.743	4218.26	6.749	2864.413	6.744
10823.5	6.714	9428.308	6.720	6650.205	6.777	4418.374	6.783	3001.743	6.779
11334.17	6.749	9872.698	6.754	6965.796	6.811	4628.52	6.818	3145.471	6.813
11861	6.782	10337.14	6.788	7296.063	6.846	4848.618	6.852	3296.502	6.847
12422.22	6.816	10823.99	6.823	7641.178	6.879	5078.828	6.886	3453.633	6.881
13014.4	6.851	11335.65	6.857	8001.838	6.914	5322.647	6.920	3618.996	6.916
13622.17	6.885	11869.02	6.891	8375.169	6.948	5574.24	6.955	3791.49	6.950
14272.13	6.920	12428.3	6.925	8761.972	6.981	5836.656	6.989	3971.907	6.984
14934.71	6.953	13014.17	6.960	9180.143	7.015	6109.138	7.022	4162.562	7.019
15647.84	6.988	13625.38	6.994	9610.993	7.049	6396.41	7.056	4359.947	7.053
16953.04	7.048	17959.46	7.199	12651.18	7.253	8437.438	7.261	5761.582	7.258
17995.35	7.093	21609.41	7.336	15222.71	7.391	10140.14	7.398	6932.707	7.396

Table D.24.d. Continued

L_D =5		L_D =7.5		L_D =10		L_D =30	
t_D	P_D	t_D	P_D	t_D	P_D	t_D	P_D
0.006155	0.059	0.006155	0.059	0.006155	0.059	0.006155	0.059
0.100254	0.233	0.100254	0.233	0.100254	0.233	0.100254	0.233
1.048206	0.736	1.046766	0.736	1.046766	0.736	1.046779	0.736
2.088401	1.005	2.083712	1.005	2.083712	1.005	2.084055	1.005
3.422482	1.243	3.417541	1.243	3.417587	1.243	3.418309	1.243
4.915678	1.447	4.913247	1.448	4.913556	1.448	4.913499	1.447
8.609324	1.822	8.607684	1.822	8.609805	1.822	8.607214	1.822
14.89687	2.263	14.8447	2.263	14.85445	2.263	14.85617	2.262
15.48194	2.297	15.42198	2.297	15.43276	2.297	15.43551	2.296
20.06161	2.534	19.92127	2.534	19.94054	2.534	19.95659	2.533
29.30257	2.909	28.86816	2.907	28.90622	2.907	28.97066	2.907
46.10772	3.389	44.5465	3.385	44.57975	3.385	44.7711	3.385
71.94218	3.872	66.99459	3.866	66.78214	3.865	67.15911	3.865
117.8407	4.388	101.6456	4.371	99.72481	4.366	100.9006	4.374
244.0933	5.069	178.823	5.038	165.6495	5.010	166.7845	5.030
433.5538	5.546	279.7054	5.520	243.1108	5.483	236.5767	5.496
641.1762	5.855	382.1689	5.830	316.7771	5.794	298.4098	5.809
838.4434	6.060	475.6896	6.035	380.777	6.001	347.9774	6.018
1265.565	6.368	673.4669	6.343	502.791	6.300	436.7296	6.331
1672.89	6.573	860.1584	6.548	611.8964	6.499	506.8887	6.537
1753.055	6.607	896.8483	6.583	633.6895	6.533	519.7699	6.572
1837.175	6.642	935.3428	6.617	654.9391	6.565	532.8723	6.606
1924.723	6.676	975.7679	6.651	678.3729	6.600	546.3222	6.641
2016.17	6.710	1018.154	6.685	701.207	6.631	560.1573	6.676
2112.57	6.744	1062.646	6.720	726.7022	6.666	574.3019	6.711
2213.521	6.778	1109.306	6.754	751.0944	6.697	588.7997	6.745
2321.603	6.813	1158.342	6.788	778.8403	6.731	603.1828	6.779
2432.22	6.847	1209.752	6.822	806.6916	6.763	618.2252	6.814
2548.42	6.881	1263.719	6.856	837.1937	6.798	633.858	6.848
2669.779	6.915	1320.254	6.891	867.4951	6.830	649.1205	6.882
2797.1	6.950	1379.541	6.925	900.907	6.864	665.3208	6.916
2930.475	6.984	1441.568	6.959	934.1836	6.897	681.9729	6.950
3069.583	7.018	1505.945	6.994	970.799	6.931	698.5355	6.984
3212.554	7.051	1572.982	7.026	1007.334	6.964	715.9536	7.018
4245.639	7.257	2061.71	7.232	1278.486	7.168	829.4867	7.223
5105.702	7.393	2470.502	7.368	1507.974	7.305	910.2683	7.352

Table D.24.e. Pressure solution for a hydraulic fracture intersecting the a fault in its middle part forming and angle of 90°, C_{fD}=300

L_D = 0.5		L_D =1		L_D =2		L_D =3		L_D =4	
t_D	P_D	t_D	P_D	t_D	P_D	t_D	P_D	t_D	P_D
0.006155	0.063	0.006155	0.063	0.006155	0.063	0.006155	0.063	0.006155	0.063
0.100254	0.241	0.100254	0.241	0.100254	0.241	0.100254	0.241	0.100254	0.241
1.058651	0.743	1.055182	0.744	1.05514	0.744	1.055911	0.744	1.055789	0.744
3.093213	1.177	3.031621	1.180	3.005423	1.183	3.009585	1.183	3.008611	1.183
5.261102	1.443	5.072235	1.449	4.932405	1.454	4.931958	1.455	4.925858	1.454
10.05207	1.811	9.445413	1.818	8.783159	1.828	8.671659	1.829	8.631383	1.828
20.18773	2.248	18.46462	2.258	15.98859	2.272	15.25344	2.273	14.99112	2.269
51.9802	2.893	46.30251	2.904	36.06097	2.923	31.66212	2.926	29.92422	2.918
102.0109	3.370	89.83938	3.381	65.63344	3.401	53.3105	3.408	48.05554	3.400
509.9935	4.513	491.1734	4.592	466.2835	4.860	305.5939	4.842	231.5653	4.866
1017.747	5.007	802.2476	4.944	973.9771	5.393	617.4788	5.364	459.0868	5.404
5198.398	6.184	2499.555	5.760	5805.287	6.688	3878.523	6.700	3878.374	6.978
6055.653	6.297	3011.271	5.895	6819.374	6.808	5105.049	6.903	5052.458	7.174
7105.568	6.416	3756.808	6.055	8338.286	6.958	6014.367	7.024	5912.177	7.292
8075.308	6.510	4181.64	6.134	9347.328	7.043	6893.485	7.126	6749.688	7.390
9028.55	6.593	4600.544	6.204	9854.103	7.082	7612.4	7.200	7336.845	7.452
10132.42	6.679	5705.597	6.362	11414.87	7.191	9171.898	7.338	8744.326	7.583
12029.76	6.807	7687.761	6.583	14514.85	7.371	11171.95	7.485	10971.1	7.753
13236.94	6.878	8799.577	6.682	15075.84	7.399	11775.58	7.524	11689.48	7.800
14000.52	6.920	9358.679	6.728	16104.39	7.448	12735.11	7.582	11925.32	7.815
15279.12	6.985	9503.37	6.740	16519.09	7.467	12983.44	7.597	12535.61	7.852
16017.37	7.020	11128.47	6.857	18840.45	7.565	15273.96	7.718	13926.46	7.931
17064.37	7.067	12006.26	6.914	20254.22	7.619	16120.33	7.759	15407.65	8.006
18165.84	7.114	12611.97	6.950	21269.93	7.655	16989.16	7.798	16659.54	8.065
20578.57	7.206	12884.96	6.966	21876.09	7.676	17457.74	7.818	17811.21	8.115
20651.15	7.209	12967.05	6.971	21899.6	7.677	17598.65	7.824	17845.84	8.116
20738.17	7.212	13065.65	6.977	21927.8	7.678	17767.76	7.831	17887.46	8.118
20842.62	7.216	13183.85	6.983	21961.74	7.679	17970.58	7.840	17937.33	8.120
20855.23	7.216	13325.68	6.991	22002.44	7.680	17995	7.841	17997.18	8.122
20909.92	7.218	13540.88	7.003	22020.21	7.681	18101.29	7.845	18258.59	8.133
20935.95	7.219	13570.35	7.005	22028.58	7.682	18151.85	7.847	18382.64	8.138
20967.13	7.220	13605.66	7.007	22038.79	7.682	18212.38	7.850	18531.57	8.144
21004.62	7.221	13647.97	7.009	22050.82	7.682	18285.07	7.853	18549.46	8.145
21049.45	7.223	13698.87	7.012	22065.5	7.683	18372.32	7.856	18570.9	8.146
21103.45	7.225	13759.87	7.015	22082.93	7.683	18477	7.860	18596.58	8.147
21168.12	7.227	13833.01	7.019	22103.91	7.684	18602.66	7.865	18627.54	8.148
21245.74	7.230	13920.84	7.024	22129.13	7.685	18753.43	7.872	18664.57	8.149
21338.83	7.233	14026.32	7.029	22159.28	7.686	18934.35	7.879	18709.06	8.151

Table D.24.e. Continued

L_D =5		L_D =7.5		L_D =10		L_D =30	
t_D	P_D	t_D	P_D	t_D	P_D	t_D	P_D
0.006155	0.063	0.006155	0.063	0.006155	0.063	0.006155	0.063
0.100254	0.241	0.100254	0.241	0.100254	0.241	0.100254	0.241
1.056093	0.744	1.054592	0.744	1.054592	0.744	1.054614	0.744
3.009161	1.183	3.003899	1.183	3.003933	1.183	3.004609	1.183
4.92016	1.455	4.91757	1.455	4.917868	1.455	4.91781	1.455
8.598328	1.829	8.596425	1.829	8.598649	1.829	8.596448	1.829
14.85777	2.270	14.80584	2.270	14.81558	2.270	14.81822	2.270
29.18964	2.917	28.75866	2.915	28.79616	2.914	28.86013	2.914
45.90042	3.397	44.35273	3.393	44.3861	3.392	44.57493	3.392
192.5182	4.872	151.8327	4.864	146.3546	4.867	146.3053	4.871
357.9143	5.404	245.9553	5.401	226.9368	5.414	221.0735	5.419
3060.227	7.029	2137.644	7.272	1956.058	7.528	1039.019	7.551
4663.821	7.339	3461.395	7.634	3204.471	7.916	1719.163	8.225
5473.954	7.459	5118.371	7.926	4244.424	8.133	2529.938	8.709
6224.249	7.555	5598.145	7.994	5058.614	8.267	3543.039	9.099
7117.171	7.655	6408.529	8.096	6020.053	8.399	3842.992	9.190
8027.75	7.744	7762.227	8.240	6984.129	8.513	4777.132	9.422
11924.29	8.039	10727.32	8.483	9884.634	8.776	7665.254	9.886
13153.01	8.113	11510.16	8.536	10552.59	8.825	8121.088	9.939
14344.82	8.177	12154.96	8.577	10888.49	8.849	9065.032	10.038
14932.76	8.207	12579.75	8.603	11148.74	8.867	9547.855	10.084
16054.86	8.262	15263.42	8.748	12877.85	8.976	11679.27	10.259
18169.73	8.354	17311.79	8.843	13589.61	9.017	12671.7	10.329
19715.13	8.415	17924.84	8.869	14844.25	9.083	14084.45	10.417
20297.1	8.437	18726.48	8.902	15156.9	9.099	14790.13	10.458
20472.18	8.443	18967.6	8.911	15206.2	9.101	14817.42	10.460
20682.22	8.451	19256.86	8.923	15265.36	9.104	14850.32	10.461
20934.23	8.460	19291.6	8.924	15336.45	9.108	14889.76	10.464
21236.56	8.471	19333.22	8.925	15421.63	9.112	14937.11	10.466
21368.64	8.475	19515.18	8.932	15458.9	9.114	15143.95	10.478
21431.36	8.477	19601.51	8.936	15476.55	9.114	15242.09	10.483
21506.68	8.480	19705.15	8.940	15497.76	9.115	15253.9	10.484
21596.91	8.483	19829.55	8.944	15523.22	9.117	15268	10.484
21705.26	8.487	19978.83	8.950	15553.83	9.118	15284.97	10.485
21835.39	8.491	20157.92	8.957	15590.4	9.120	15305.38	10.486
21991.43	8.497	20372.89	8.965	15634.43	9.122	15329.8	10.488
22178.66	8.503	20398.69	8.966	15687.17	9.125	15359.15	10.489
22403.38	8.511	20429.64	8.967	15750.57	9.128	15394.23	10.491

APPENDIX E

RESERVOIR MODEL

Consider the flow of oil through a porous material. The oil volumetric factor is assumed to be equal to the unity. The continuity equation describing the oil flow is given by[87]:

$$\nabla(\rho\vec{v}) \pm G = -\frac{\partial}{\partial t}(\phi\rho) \qquad \text{(E.1)}$$

where G represents the source/sink term confined at the fracture plane at any node i,j and time t.

$$G = \frac{\rho Q(x_i, y_i, t)}{h}$$

where Q expresses the mass flow rate per unit area of grid block:

$$Q = \frac{q}{\Delta x \Delta y x_f}$$

then, Eq. E. E.1 can be written as:

$$\nabla(\rho\vec{u}) \pm \frac{\rho Q(x_i, y_i, t)}{h} = -\frac{\partial}{\partial t}(\phi\rho) \qquad \text{(E.2)}$$

If the gravitational effects are neglected, Forchheimer equation[88-91], used to include the effects of rapid flow, is given by:

$$-\vec{\nabla}p = \mu\vec{k}^{-1}u + \rho|u|\vec{\beta}u \qquad \text{(E.3)}$$

Since the porous medium is assumed to be isotropic and homogeneous, then Eq. E.3 can be written as follows:

$$-\vec{\nabla}p = \frac{\mu}{k}u + \rho u^2\beta \qquad \text{(E.4)}$$

Many correlations are given in the literature to determine β. Among them, it can be cited the ones developed by Liu et al[92], Geertsma[93] and Firoozabadi and Katz[94], respectively:

$$\beta = \frac{8.91 x 10^{8} \tau}{\phi k}$$

$$\beta = \frac{4.8511 x 10^{4}}{\phi^{5.5} \sqrt{k}}$$

$$\beta = \frac{2.6 x 10^{10}}{k^{1.2}}$$

Eq. E.4 can be rewritten as:

$$-\frac{k}{\mu}\vec{\nabla}p = \left(1 + \frac{k\rho u\beta}{\mu}\right)u \qquad \text{(E.5)}$$

Define the Reynolds number for porous media and the rapid flow parameter as:

$$R_e = \frac{k\rho u\beta}{\mu} \qquad \text{(E.6)}$$

$$\delta = (1 + R_e)^{-1} \qquad \text{(E.7)}$$

Combination of Eqs. E.5 through E.7 gives.

$$-\frac{k}{\mu}\vec{\nabla}p = (1 + R_e)u = \frac{u}{\delta} \qquad \text{(E.8)}$$

solving for u.

$$u = -\frac{k}{\mu}\delta\vec{\nabla}p \qquad \text{(E.9)}$$

Replacement of Eq. E.9 into Eq. E.2 yields.

$$-\bar{\nabla}\left(\rho\delta\frac{k}{\mu}\bar{\nabla}p\right)\pm\frac{\rho Q(x_i,y_i,t)}{h}=-\frac{\partial}{\partial t}(\phi\rho) \tag{E.10}$$

Expansion of the right-hand side (RHS) of Eq. E.10 gives:

$$\frac{\partial}{\partial t}(\phi\rho)=\phi\frac{\partial\rho}{\partial t}+\rho\frac{\partial\phi}{\partial t}=\phi\frac{\partial\rho}{\partial p}\frac{\partial p}{\partial t}+\rho\frac{\partial\phi}{\partial p}\frac{\partial p}{\partial t} \tag{E.11}$$

From the definition of pore and fluid compressibilities, respectively,

$$c_p=\frac{1}{\phi}\frac{\partial\phi}{\partial p}$$

$$c_{fl}=\frac{1}{\rho}\frac{\partial\rho}{\partial p}$$

c_p reflects the volume of excess fluid that can be stored in the pores due to an increase in pore pressure[95]. From the above definitions, we have:

$$\frac{\partial\phi}{\partial p}=\phi c_p \tag{E.12}$$

$$\frac{\partial\rho}{\partial p}=\rho c_f \tag{E.13}$$

Eqs. E.2 and E.3 lead to exponential relationships between porosity and pressure and density and pressure, respectively. Replacing this equations into Eq. E.11 yields:

$$\frac{\partial}{\partial t}(\phi\rho)=\phi\rho c_f+\rho\phi c_p=\phi\rho\left(c_f+c_p\right) \tag{E.14}$$

Letting the total compressibility, $c_t=c_f+c_p$, in the above equation, Eq. E.10 becomes:

$$\bar{\nabla}\left(\rho\delta\frac{k}{\mu}\bar{\nabla}p\right)\pm\frac{\rho Q(x_i,y_i,t)}{h}=\phi\rho c_t\frac{\partial p}{\partial t} \tag{E.15}$$

The physical system has been assumed to be bidimensional. Then, if μ and k are considered to be constant, Eq. E.15 is rewritten as:

$$\frac{\partial}{\partial x}\left(\rho\delta_x\frac{\partial p}{\partial x}\right)+\frac{\partial}{\partial y}\left(\rho\delta_y\frac{\partial p}{\partial y}\right)\pm\frac{\rho Q(x_i,y_i,t)}{h}\frac{\mu}{k}=\frac{\phi\rho c_t\mu}{k}\frac{\partial p}{\partial t}$$

Expanding further;

$$\rho\delta_x\frac{\partial^2 p}{\partial x^2}+\frac{\partial p}{\partial x}\left[\frac{\partial}{\partial x}(\rho\delta_x)\right]+\rho\delta_y\frac{\partial^2 p}{\partial y^2}+\frac{\partial p}{\partial y}\left[\frac{\partial}{\partial y}(\rho\delta_y)\right]\pm\frac{\rho Q(x_i,y_i,t)}{h}\frac{\mu}{k}=$$
$$\frac{\phi\rho c_t\mu}{k}\frac{\partial p}{\partial t}$$

$$\rho\delta_x\frac{\partial^2 p}{\partial x^2}+\frac{\partial p}{\partial x}\left[\rho\frac{\partial\delta_x}{\partial x}+\delta_x\frac{\partial\rho}{\partial x}\right]+\rho\delta_y\frac{\partial^2 p}{\partial y^2}+\frac{\partial p}{\partial y}\left[\rho\frac{\partial\delta_y}{\partial y}+\delta_y\frac{\partial\rho}{\partial y}\right]\pm$$
$$\frac{\rho Q(x_i,y_i,t)}{h}\frac{\mu}{k}=\frac{\phi\rho c_t\mu}{k}\frac{\partial p}{\partial t}$$

$$\rho\delta_x\frac{\partial^2 p}{\partial x^2}+\frac{\partial p}{\partial x}\left[\rho\frac{\partial\delta_x}{\partial p}\frac{\partial p}{\partial x}+\delta_x\frac{\partial\rho}{\partial p}\frac{\partial p}{\partial x}\right]+\rho\delta_y\frac{\partial^2 p}{\partial y^2}+\frac{\partial p}{\partial y}\left[\rho\frac{\partial\delta_y}{\partial p}\frac{\partial p}{\partial y}+\delta_y\frac{\partial\rho}{\partial p}\frac{\partial p}{\partial y}\right]\pm$$
$$\frac{\rho Q(x_i,y_i,t)}{h}\frac{\mu}{k}=\frac{\phi\rho c_t\mu}{k}\frac{\partial p}{\partial t}$$

$$\rho\delta_x\frac{\partial^2 p}{\partial x^2}+\left(\frac{\partial p}{\partial x}\right)^2\left[\rho\frac{\partial\delta_x}{\partial p}+\delta_x\frac{\partial\rho}{\partial p}\right]+\rho\delta_y\frac{\partial^2 p}{\partial y^2}+\left(\frac{\partial p}{\partial y}\right)^2\left[\rho\frac{\partial\delta_y}{\partial p}+\delta_y\frac{\partial\rho}{\partial p}\right]\pm$$
$$\frac{\rho Q(x_i,y_i,t)}{h}\frac{\mu}{k}=\frac{\phi\rho c_t\mu}{k}\frac{\partial p}{\partial t}$$

(E.16)

Divide by $\rho\delta_x\delta_y$:

$$\frac{1}{\delta_x}\frac{\partial^2 p}{\partial x^2}+\left(\frac{\partial p}{\partial x}\right)^2\left[\frac{1}{\delta_x\delta_y}\frac{\partial \delta_x}{\partial p}+\frac{1}{\rho\delta_y}\frac{\partial \rho}{\partial p}\right]+\frac{1}{\delta_x}\frac{\partial^2 p}{\partial y^2}+$$
$$\left(\frac{\partial p}{\partial y}\right)^2\left[\frac{1}{\delta_x\delta_y}\frac{\partial \delta_y}{\partial p}+\frac{1}{\rho\delta_x}\frac{\partial \rho}{\partial p}\right]\pm\frac{Q(x_t,y_t,t)\mu}{hk\delta_x\delta_y}=\frac{\phi\, c_t\mu}{k\delta_x\delta_y}\frac{\partial p}{\partial t} \qquad \text{(E.17)}$$

Define the high velocity flow modulus in the formation as $\delta'=\frac{1}{\delta}\frac{\partial \delta}{\partial p}$ and using the fluid compressibility concept defined before:

$$\frac{1}{\delta_x}\frac{\partial^2 p}{\partial x^2}+\left(\frac{\partial p}{\partial x}\right)^2\left[\frac{\delta_x'}{\delta_x}+\frac{c_f}{\delta_x}\right]+\frac{1}{\delta_x}\frac{\partial^2 p}{\partial y^2}+\left(\frac{\partial p}{\partial y}\right)^2\left[\frac{\delta_y'}{\delta_x}+\frac{c_f}{\delta_x}\right]\pm\frac{Q(x_t,y_t,t)\mu}{hk\delta_x\delta_y}=\frac{\phi\, c_t\mu}{k\delta_x\delta_y}\frac{\partial p}{\partial t}$$

Multiply by $\delta_x\delta_y$:

$$\delta_x\frac{\partial^2 p}{\partial x^2}+\left(\frac{\partial p}{\partial x}\right)^2\left[\delta_x(\delta_x'+c_f)\right]+\delta_y\frac{\partial^2 p}{\partial y^2}+\left(\frac{\partial p}{\partial y}\right)^2\left[\delta_y(\delta_y'+c_f)\right]\pm$$
$$\frac{Q(x_t,y_t,t)\mu}{hk}=\frac{\phi\, c_t\mu}{k}\frac{\partial p}{\partial t} \qquad \text{(E.18)}$$

Recalling Eq. E.7:

$$\delta=\frac{1}{1+\frac{k\rho\beta u}{\mu}} \qquad \text{(E.7)}$$

Since k, β and μ are assumed to be pressure independent, then:

$$\frac{\partial \delta}{\partial p}=-\frac{\frac{\partial}{\partial p}\left(1+\frac{k\rho\beta u}{\mu}\right)}{\left(1+\frac{k\rho\beta u}{\mu}\right)^2}=-\frac{\frac{k\beta}{\mu}\left(\rho\frac{\partial u}{\partial p}+u\frac{\partial \rho}{\partial p}\right)}{\left(1+\frac{k\rho\beta u}{\mu}\right)^2}$$

divide by δ:

$$\frac{1}{\delta}\frac{\partial \delta}{\partial p} = -\frac{\frac{k\beta}{\mu}\left(\rho\frac{\partial u}{\partial p} + u\frac{\partial \rho}{\partial p}\right)}{1+\frac{k\rho\beta u}{\mu}}$$

dividing and multiplying by $(k\,u\,\rho)^{-1}$;

$$\frac{\delta'}{ku\rho} = -\frac{\frac{\beta}{\mu}\left(\frac{1}{u}\frac{\partial u}{\partial p} + \frac{1}{\rho}\frac{\partial \rho}{\partial p}\right)}{1+\frac{k\rho\beta u}{\mu}}$$

let:

$$u' = \frac{1}{u}\frac{\partial u}{\partial p}$$

$$\delta' = -\frac{\frac{\beta}{\mu}\left(u'+c_f\right)ku\rho}{1+\frac{k\rho\beta u}{\mu}} = \frac{\beta}{\mu}\left(u'+c_f\right)ku\rho\delta \qquad \text{(E.19)}$$

The above equation can also be expressed as:

$$\delta' = -(1-\delta)\left\{u'+c_f\right\} \qquad \text{(E.20)}$$

Recalling Forchheimer's Equation, Eq. E.9.

$$u_r = -\delta_r\frac{k}{\mu}\frac{\partial p}{\partial x} \qquad \text{(E.9)}$$

then, taking derivative with respect to p, we obtain:

$$\frac{\partial u_r}{\partial p} = -\frac{k}{\mu}\frac{\partial p}{\partial x}\frac{\partial \delta_r}{\partial p}$$

divide by u_r,

$$\frac{1}{u_x}\frac{\partial u_x}{\partial p}=\frac{1}{-\delta_x\dfrac{k}{\mu}\dfrac{\partial p}{\partial x}}\left(-\frac{k}{\mu}\right)\frac{\partial p}{\partial x}\frac{\partial \delta_x}{\partial p}=\frac{1}{\delta_x}\frac{\partial \delta_x}{\partial p}$$

or:

$$u_x'=\delta_x' \tag{E.21}$$

Substituting Eq. E.21 into E.20 –for the x-direction– yields:

$$\delta_x'=-(1-\delta_x)\{\delta_x'+c_f\}$$

After some manipulations, the above equation results for the x- and y-directions:

$$\delta_x'=\frac{\delta_x(c_f-1)}{2-\delta_x}=\frac{c_f}{\left(\dfrac{1}{\delta_x-1}\right)-1} \tag{E.22}$$

$$\delta_y'=\frac{\delta_y(c_f-1)}{2-\delta_y}=\frac{c_f}{\left(\dfrac{1}{\delta_y-1}\right)-1} \tag{E.23}$$

Plugging Eqs. E.22 and E.23 into Eq. E.18:

$$\delta_x\frac{\partial^2 p}{\partial x^2}+\left(\frac{\partial p}{\partial x}\right)^2\left[\frac{\delta_x c_f}{2-\delta_x}\right]+\delta_y\frac{\partial^2 p}{\partial y^2}+\left(\frac{\partial p}{\partial y}\right)^2\left[\frac{\delta_y c_f}{2-\delta_y}\right]\pm\frac{Q(x_i,y_i,t)\mu}{hk}=\frac{\phi\, c_t\mu}{k}\frac{\partial p}{\partial t}$$

let:

$$\zeta_x=\frac{\delta_x c_f}{2-\delta_x}$$

$$\zeta_y=\frac{\delta_y c_f}{2-\delta_y}$$

Then, the diffusivity equation becomes:

$$\delta_x \frac{\partial^2 p}{\partial x^2} + \zeta_x \left(\frac{\partial p}{\partial x}\right)^2 + \delta_y \frac{\partial^2 p}{\partial y^2} + \zeta_y \left(\frac{\partial p}{\partial y}\right)^2 \pm \frac{Q(x_i, y_i, t)\mu}{hk} = \frac{\phi c_t \mu}{k} \frac{\partial p}{\partial t} \qquad \text{(E.24)}$$

Define the following dimensionless variables:

$$p_D(X_D, Y_D, t_D) = \frac{2\pi kh}{q\mu}\left(p_i - p(x, y, t)\right)$$

The dimensionless pressure drop in the fracture is given by:

$$p_{Df}(X_D, Y_D, t_D) = \frac{2\pi kh}{q_w \mu}\left(p_i - p_f(x, y, t)\right)$$

The dimensionless flow rate at the wellbore is:

$$q_{wD} = 1 = \frac{q_w \mu}{2\pi kh\left(p_i - p_f(x, y, t)\right)}$$

The dimensionless flow rate at the fracture is:

$$q_{fD} = \frac{2q_f(x, y, t)\mu x_f}{2\pi kh\left(p_i - p_f(x, y, t)\right)}$$

$$q_{fD} = \frac{2q_f(x, y, t)\mu x_f}{q_w}$$

The dimensionless distances are defined by:

$$X_D = \frac{x}{x_f}$$

$$Y_D = \frac{y}{x_f}$$

The dimensionless time is defined as follows:

$$t_D = \frac{t}{t_a} \qquad \text{(E.25)}$$

Replacing the dimensionless quantities into Eq. 24;

$$\delta_x\left[-\frac{\mu q_w}{2\pi kh\,x_f^2}\right]\frac{\partial^2 p_D}{\partial X_D^2}+\zeta_x\left(-\frac{\mu q_w}{2\pi kh\,x_f}\right)^2\left(\frac{\partial p_D}{\partial X_D}\right)^2+\delta_y\left[-\frac{\mu q_w}{2\pi kh\,x_f^2}\right]\frac{\partial^2 p_D}{\partial Y_D^2}+$$

$$\zeta_y\left(-\frac{\mu q_w}{2\pi kh\,x_f}\right)^2\left(\frac{\partial p_D}{\partial Y_D}\right)^2\pm\frac{Q(x_i,y_i,t)\mu}{hk}=\frac{\phi\,c_t\mu}{k}\left[-\frac{\mu q_w}{2\pi kh}\right]\frac{\partial p_D}{t_{ii}\partial t_D}$$

Multiplying by x_f^2 and dividing by $\mu q_w/2\pi kh$

$$\delta_x\frac{\partial^2 p_D}{\partial X_D^2}+\xi_x\left(\frac{\mu q_w}{2\pi kh}\right)\left(\frac{\partial p_D}{\partial X_D}\right)^2+\delta_y\frac{\partial^2 p_D}{\partial Y_D^2}+\zeta_y\left(\frac{\mu q_w}{2\pi kh}\right)\left(\frac{\partial p_D}{\partial Y_D}\right)^2\pm$$

$$\frac{q(x_i,y_i,t)\mu}{\Delta x\Delta yhk}\frac{2\pi khx_f^2}{\mu q_w}=\frac{\phi\,c_t\mu\,x_f^2}{kt_{ii}}\frac{\partial p_D}{\partial t_D}\qquad\text{(E.26)}$$

let:

$$\frac{\mu q_w}{2\pi kh}=1$$

$\frac{\phi\,c_t\mu\,x_f^2}{kt_{ii}}=1$, then

$$t_{ii}=\frac{\phi\,c_t\mu\,x_f^2}{k}\qquad\text{(E.27.a)}$$

Then Eq. E.25 results in:

$$t_D=\frac{kt}{\phi\,\mu\,cx_f^2}\qquad\text{(E.27.b)}$$

Replacing Eq. E.26 into E.25 yields:

$$\delta_x\frac{\partial^2 p_D}{\partial X_D^2}+\zeta_x\left(\frac{\partial p_D}{\partial X_D}\right)^2+\delta_y\frac{\partial^2 p_D}{\partial Y_D^2}+\zeta_y\left(\frac{\partial p_D}{\partial Y_D}\right)^2\pm\frac{q(x_i,y_i,t)\mu}{\Delta x\Delta y\,x_f hk}\frac{2\pi khx_f^2}{\mu q_w}=\frac{\partial p_D}{\partial t_D}$$

$$\delta_x\frac{\partial^2 p_D}{\partial X_D^2}+\zeta_x\left(\frac{\partial p_D}{\partial X_D}\right)^2+\delta_y\frac{\partial^2 p_D}{\partial Y_D^2}+\zeta_y\left(\frac{\partial p_D}{\partial Y_D}\right)^2\pm\frac{q(x_i,y_i,t)}{\Delta x\Delta y}\frac{2\pi x_f}{q_w}=\frac{\partial p_D}{\partial t_D}$$

The final equation will be:

$$\delta_x \frac{\partial^2 p_D}{\partial X_D^2} + \xi_x \left(\frac{\partial p_D}{\partial X_D} \right)^2 + \delta_y \frac{\partial^2 p_D}{\partial Y_D^2} + \zeta_y \left(\frac{\partial p_D}{\partial Y_D} \right)^2 \pm \frac{\pi q_{fD}(x_{Di}, y_{Di}, t_D)}{\Delta x_D \Delta y_D} = \frac{\partial p_D}{\partial t_D} \quad \text{(E.28)}$$

APPENDIX F

FRACTURE MODEL

Consider the flow of oil through a porous fracture. The oil volumetric factor is assumed to be one. The continuity equation describing the oil flow is given by[87]:

$$\nabla(\rho \vec{v}) \pm G'' = -\frac{\partial}{\partial t}(\phi \rho) \tag{F.1}$$

where G'' represents the source/sink term confined at the fracture plane at any node i,j (along the fracture) and time t.

$$G'' = \frac{\rho Q_f''(x_i, y_i, t)}{h}$$

Q_f'' expresses the mass flow rate per unit area of grid block;

$$Q_f'' = \frac{q_f''}{\Delta x \Delta y x_f}$$

then, Eq. F.1 can be written as:

$$\nabla(\rho \vec{v}) \pm \frac{\rho Q_f''(x_i, y_i, t)}{h} = -\frac{\partial}{\partial t}(\phi \rho) \tag{F.2}$$

The fracture model also includes the rapid flow effects, contrary to the reservoir case in which permeability and porosity are assumed to be pressure independent, the fracture model considers variation in fracture conductivity due to changes in pressure. Then, optionally, fracture porosity and fracture permeability will be considered to depend on pressure. The Forchheimer equation[88-91] for the flow velocity in the fracture is given by:

$$-\frac{\partial p_f}{\partial x} = \frac{\mu}{k_f(p)} \vec{u}_\tau + \rho \beta_f \vec{u}_\tau^2 \tag{F.3}$$

$$-\frac{\partial p_f}{\partial y}=\frac{\mu}{k_f(p)}\vec{u}_y+\rho\beta_f\vec{u}_y^2 \qquad \text{(F.4)}$$

Traditionally, the fracture flow has been considered to go along the x-axis. Eq. F.4 is introduced to account for the flow in the y-direction which is brought to the system due to the presence of the branched fracture system.

Solving for velocities from Eqs. F.1 and F.2, we obtained:

$$\vec{u}_x=-(R_{ef_x}+1)^{-1}\frac{k_f}{\mu}\frac{\partial p_f}{\partial x} \qquad \text{(F.5)}$$

$$\vec{u}_y=-(R_{ef_y}+1)^{-1}\frac{k_f}{\mu}\frac{\partial p_f}{\partial y} \qquad \text{(F.6)}$$

Define the Reynolds number for porous fractures as:

$$R_{ef}=\frac{k_f\rho u\beta}{\mu}$$

As for the case of the reservoir model, define the rapid flow parameter in the fracture as:

$$\delta_f=(1+R_{ef})^{-1}$$

Then, Eqs. F.3 and F.4 become:

$$u_x=-\delta_{fx}\frac{k_f}{\mu}\frac{\partial p_f}{\partial x} \qquad \text{(F.7)}$$

$$u_y=-\delta_{fy}\frac{k_f}{\mu}\frac{\partial p_f}{\partial y} \qquad \text{(F.8)}$$

Substituting the Forchheimer equation into Eq. F.2, letting $c_{tf}=c_f+c_{pf}$ and after treating the right-hand side with a similar procedure as for the reservoir model case –Appendix E–, we obtained:

$$\frac{\partial}{\partial x}\left(\rho\delta_{fx}\frac{k_f}{\mu}\frac{\partial p_f}{\partial x}\right)+\frac{\partial}{\partial y}\left(\rho\delta_{fx}\frac{k_f}{\mu}\frac{\partial p_f}{\partial y}\right)-\frac{\rho Q_f''(x_i,y_i,t)}{wh}=\phi_f\,\rho c_{tf}\frac{\partial p_f}{\partial t} \quad \text{(F.9)}$$

The suffix f stands for fracture property. Q_f'' represents the fluid mass flow from the reservoir to the fracture per unit of fracture length.

The dimensionless pressure drop in the fracture is given by:

$$p_{Df}(X_D,t_D)=\frac{2\pi kh}{q_w\mu}\left(p_i-p_f(x,y,t)\right)$$

The dimensionless flow rate at the wellbore is:

$$q_{wD}=1=\frac{q_w\mu}{2\pi kh\left(p_i-p_f(x,y,t)\right)}$$

The dimensionless flow rate at the fracture is:

$$q_{fD}=\frac{2q_f(x,y,t)\mu x_f}{2\pi kh\left(p_i-p_f(x,y,t)\right)}$$

$$q_{fD}=\frac{2q_f(x,y,t)\mu x_f}{q_w}$$

The dimensionless distances are given by:

$$X_D=\frac{x}{x_f}$$

$$Y_D=\frac{y}{x_f}$$

The dimensionless time, as derived in Appendix A, is:

$$t_D=\frac{kt}{\phi\mu c x_f^2} \quad \text{(A.27.b)}$$

Then, the following substitution can be obtained by using the above dimensionless parameters:

$$\frac{\partial}{\partial x}\left(-\rho\delta_{fx}\frac{k_f}{\mu}\frac{\partial p_f}{\partial x}\right)=\frac{\partial}{\partial X_D}\left(-\rho\delta_{fx}\frac{k_f}{\mu}\frac{\partial p_{fD}}{\partial X_D}\left[-\frac{q\mu}{2\pi khx_f^2}\right]\right)$$

$$\frac{\partial}{\partial y}\left(-\rho\delta_{fy}\frac{k_f}{\mu}\frac{\partial p_f}{\partial y}\right)=\frac{\partial}{\partial Y_D}\left(-\rho\delta_{fy}\frac{k_f}{\mu}\frac{\partial p_{fD}}{\partial Y_D}\left[-\frac{q\mu}{2\pi khx_f^2}\right]\right)$$

$$\frac{\partial p_f}{\partial t}=\frac{\partial p_f}{\partial t_D}\left[-\frac{q\mu}{2\pi khx_f^2}\right]\left(\frac{k}{\phi\mu c_{tf}x_f^2}\right)$$

Replacing the dimensionless parameters in Eq. F.9, it yields:

$$\frac{\partial}{\partial X_D}\left(\rho\delta_{fx}\frac{k_f}{\mu}\frac{q\mu}{2\pi khx_f^2}\frac{\partial p_{fD}}{\partial X_D}\right)+\frac{\partial}{\partial Y_D}\left(\rho\delta_{xx}\frac{k_f}{\mu}\frac{q\mu}{2\pi khx_f^2}\frac{\partial p_{fD}}{\partial Y_D}\right)-\frac{\rho Q_f''(x_t,y_t,t)}{h}=\phi_f\rho c_{tf}\frac{q\mu}{2\pi kh}\frac{k}{\phi_f\mu c_t x_f^2}\frac{\partial p_D}{\partial t_D}$$

multiply by $2\pi hx_f/q\mu$

$$\frac{\partial}{\partial X_D}\left(\rho\delta_{fx}\frac{k_f}{k}\frac{w}{x_f}\frac{\partial p_{fD}}{\partial X_D}\right)+\frac{\partial}{\partial Y_D}\left(\rho\delta_{fy}\frac{k_f}{\mu}\frac{w}{x_f}\frac{\partial p_{fD}}{\partial Y_D}\right)-\frac{\rho Q_f''(x_t,y_t,t)}{h}\frac{2\pi hx_f}{q\mu}=\frac{\phi_f\rho c_{tf}w}{\phi c_t x_f}\frac{\partial p_D}{\partial t_D} \qquad \text{(F.10)}$$

Define the dimensionless fracture storage capacity, C_{fD}^{*}, the dimensionless fracture conductivity, C_{fD}, and the dimensionless variable fracture conductivity, C'_{fD}:

$$C_{fD}^{*}=\frac{w\phi_f c_{tf}}{\pi\phi c_t x_f} \qquad \text{(F.11)}$$

$$C_{fD}=\frac{k_f w}{kx_f} \qquad \text{(F.12)}$$

Parameters defined by Eqs. F.11 and F.12 are not pressure dependent. After replacing the above definitions into Eq. F.10, it becomes:

$$C_{fD}\frac{\partial}{\partial X_D}\left(\rho\delta_f\frac{\partial p_{fD}}{\partial X_D}\right)+C_{fD}\frac{\partial}{\partial Y_D}\left(\rho\delta_{fy}\frac{\partial p_{fD}}{\partial Y_D}\right)-\rho\pi q_{fD}(X_{Dt},Y_{Dt},t_D)=\rho\pi C_{fD}^{\cdot}\frac{\partial p_D}{\partial t_D} \tag{F.13}$$

$$\rho\delta_{fx}\frac{\partial^2 p_{fD}}{\partial X_D^2}+\left\{\rho\delta_{fx}+\left(\delta_{fx}\frac{\partial\rho}{\partial p_{fD}}+\rho\frac{\partial\delta_{fx}}{\partial p_{fD}}\right)\right\}\left(\frac{\partial p_{fD}}{\partial X_D}\right)^2$$

$$\rho\delta_{fy}\frac{\partial^2 p_{fD}}{\partial Y_D^2}+\left\{\rho\delta_{fy}+\left(\delta_{fy}\frac{\partial\rho}{\partial p_{fD}}+\rho\frac{\partial\delta_{fy}}{\partial p_{fD}}\right)\right\}\left(\frac{\partial p_{fD}}{\partial Y_D}\right)^2-$$

$$\rho\pi q_{fD}(X_{Dt},Y_{Dt},t_D)=\rho\pi\frac{C_{fD}^{\cdot}}{C_{fD}}\frac{\partial p_D}{\partial t_D}$$

Divide by $\rho\delta_{fx}\delta_{fy}$:

$$\frac{1}{\delta_{fy}}\frac{\partial^2 p_{fD}}{\partial X_D^2}+\left\{\frac{1}{\delta_{fy}}+\left(\frac{1}{\delta_{fy}\rho}\frac{\partial\rho}{\partial p_{fD}}+\frac{1}{\delta_{fy}\delta_{fx}}\frac{\partial\delta_{fx}}{\partial p_{fD}}\right)\right\}\left(\frac{\partial p_{fD}}{\partial X_D}\right)^2+\frac{1}{\delta_{fx}}\frac{\partial^2 p_{fD}}{\partial Y_D^2}+$$

$$\left\{\frac{1}{\delta_{fy}}+\left(\frac{1}{\delta_{fx}\rho}\frac{\partial\rho}{\partial p_{fD}}+\frac{1}{\delta_{fy}\delta_{fx}}\frac{\partial\delta_{fy}}{\partial p_{fD}}\right)\right\}\left(\frac{\partial p_{fD}}{\partial X_D}\right)^2-\frac{\pi q_{fD}(X_{Dt},Y_{Dt},t_D)}{\delta_{fx}\delta_{fy}C_{fD}}=\frac{\pi C_{fD}^{\cdot}}{\delta_{fx}\delta_{fy}C_{fD}}\frac{\partial p_D}{\partial t_D}$$

Define the high velocity flow modulus in the formation as $\delta'=\frac{1}{\delta}\frac{\partial\delta}{\partial p}$ and using the fluid compressibility, the above equation becomes:

$$\frac{1}{\delta_{fy}}\frac{\partial^2 p_{fD}}{\partial X_D^2}+\left\{\frac{1}{\delta_{fy}}+\left(\frac{c_f}{\delta_{fx}}+\frac{\delta'_{fx}}{\delta_{fy}}\right)\right\}\left(\frac{\partial p_{fD}}{\partial X_D}\right)^2+\frac{1}{\delta_{fx}}\frac{\partial^2 p_{fD}}{\partial Y_D^2}+$$

$$\left\{\frac{1}{\delta_{fx}}+\left(\frac{c_f}{\delta_{fx}}+\frac{\delta'_{fy}}{\delta_{fx}}\right)\right\}\left(\frac{\partial p_{fD}}{\partial Y_D}\right)^2\frac{\pi q_{fD}(X_{Dt},Y_{Dt},t_D)}{\delta_{fx}\delta_{fy}C_{fD}}=\frac{\pi C_{fD}^{\cdot}}{\delta_{fx}\delta_{fy}C_{fD}}\frac{\partial p_D}{\partial t_D}$$

Multiply by $\delta_{fx}\delta_{fy}$:

$$\delta_{fx}\frac{\partial^2 p_{fD}}{\partial X_D^2}+\left(\delta_{fx}+c_f\delta_{fx}+\delta_{fx}\delta'_{fx}\right)\left(\frac{\partial p_{fD}}{\partial X_D}\right)^2+\delta_{fx}\frac{\partial^2 p_{fD}}{\partial Y_D^2}+$$

$$\left(\delta_{fx}+c_f\delta_{fx}+\delta_{fx}\delta'_{fx}\right)\left(\frac{\partial p_{fD}}{\partial Y_D}\right)^2-\frac{\pi}{C_{fD}}q_{fD}(X_{Di},Y_{Di},t_D)=\left(\frac{\pi C^*_{fD}}{C_{fD}}\right)\frac{\partial p_D}{\partial t_D} \qquad \text{(F.18)}$$

Recalling that:

$$\delta_f=\frac{1}{1+\dfrac{k_f\rho\beta u}{\mu}}$$

Since β and μ are assumed to be pressure independent, then:

$$\frac{\partial\delta_f}{\partial p_f}=-\frac{\dfrac{\partial}{\partial p_f}\left(1+\dfrac{k_f\rho\beta u}{\mu}\right)}{\left(1+\dfrac{k_f\rho\beta u}{\mu}\right)^2}=-\frac{\dfrac{\beta}{\mu}\left(k_f\rho\dfrac{\partial u}{\partial p_f}+k_f u\dfrac{\partial\rho}{\partial p_f}\right)}{\left(1+\dfrac{k_f\rho\beta u}{\mu}\right)^2}$$

divide both sides of the above equation by δ_f:

$$\frac{1}{\delta_f}\frac{\partial\delta_f}{\partial p_f}=-\frac{\dfrac{\beta}{\mu}\left(k_f\rho\dfrac{\partial u}{\partial p_f}+k_f u\dfrac{\partial\rho}{\partial p_f}\right)}{\left(1+\dfrac{k_f\rho\beta u}{\mu}\right)}$$

dividing and multiplying by $(k_f u\rho)^{-1}$:

$$\frac{\delta'_f}{k_f u\rho}=-\frac{\dfrac{\beta}{\mu}\left(k_f\rho\dfrac{\partial u}{\partial p_f}+k_f u\dfrac{\partial\rho}{\partial p_f}\right)}{\left[\dfrac{1}{k_f u\rho}\right]\left(1+\dfrac{k_f\rho\beta u}{\mu}\right)}$$

$$\frac{\delta'_f}{k_f u\rho}=-\frac{\dfrac{\beta}{\mu}\left(\dfrac{1}{u}\dfrac{\partial u}{\partial p_f}+\dfrac{1}{\rho}\dfrac{\partial\rho}{\partial p_f}\right)}{\left(1+\dfrac{k_f\rho\beta u}{\mu}\right)}$$

let:

$$u' = \frac{1}{u}\frac{\partial u}{\partial p}$$

and applying the definition of fracture permeability modulus and fluid compressibility, the resulting equation is:

$$\delta'_f = -\frac{\beta}{\mu}(u'+c_f)\delta_f k_f u\rho = \frac{\beta}{\mu}(u'+c_f)k_f u\rho\delta_f$$

The above equation can also be expressed as:

$$\delta'_f = -(1-\delta_f)(u'+c_f) \qquad \text{(F.19)}$$

Recalling Forchheimer's Equation, Eq. F.7,

$$u_x = -\delta_{fx}\frac{k_f}{\mu}\frac{\partial p}{\partial x}$$

then, taking derivative with respect to p, we obtain:

$$\frac{\partial u_x}{\partial p} = -\frac{1}{\mu}\frac{\partial p}{\partial x}\left(k_f\frac{\partial \delta_{fx}}{\partial p}\right)$$

divide by u_x,

$$\frac{1}{u_x}\frac{\partial u_x}{\partial p} = \frac{1}{-\delta_{fx}\dfrac{k_f}{\mu}\dfrac{\partial p}{\partial x}}\left\{-\frac{1}{\mu}\frac{\partial p}{\partial x}\left(k_f\frac{\partial \delta_{fx}}{\partial p}\right)\right\} = \frac{1}{\delta_{fx}}\frac{\partial \delta_{fx}}{\partial p}$$

or;

$$u_x' = \delta_x' \qquad \text{(F.20)}$$

Substituting Eq. F.19 into F.18 –for the x-direction– yields:

$$\delta_{fx}' = -(1-\delta_x)\{\delta_{fx}'+c_f\}$$

After performing various manipulations, the above equation results for the x- and y-directions:

$$\delta_{fx}' = \frac{c_f}{2-\delta_{fx}} = \frac{c_f}{\left(\frac{1}{\delta_{fx}-1}\right)-1} \tag{F.21}$$

$$\delta_{fy}' = \frac{c_f}{2-\delta_{fy}} = \frac{c_f}{\left(\frac{1}{\delta_{fy}-1}\right)-1} \tag{F.22}$$

Plugging Eqs. F.21 and F.22 into Eq. F.18:

$$\delta_{fx}\frac{\partial^2 p_{fD}}{\partial X_D^2} + \frac{\delta_{fx}(c_f+\delta_{fx})}{2-\delta_{fx}}\left(\frac{\partial p_{fD}}{\partial X_D}\right)^2 + \delta_{fy}\frac{\partial^2 p_{fD}}{\partial Y_D^2} + \frac{\delta_{fy}(c_f+\delta_{fy})}{2-\delta_{fy}}\left(\frac{\partial p_{fD}}{\partial Y_D}\right)^2$$
$$-\frac{\pi}{C_{fD}} q_{fD}(X_{Di}, Y_{Di}, t_D) = \left(\frac{\pi C_{fD}^*}{C_{fD}}\right)\frac{\partial p_D}{\partial t_D}$$

Assume $\delta_{fx} >> c_f$, and $\delta_{fy} >> c_f$, then the above expression can be rewritten as:

$$\delta_{fx}\frac{\partial^2 p_{fD}}{\partial X_D^2} + \delta_{fx}\zeta_{fx}\left(\frac{\partial p_{fD}}{\partial X_D}\right)^2 + \delta_{fy}\frac{\partial^2 p_{fD}}{\partial Y_D^2} + \delta_{fy}\zeta_{fy}\left(\frac{\partial p_{fD}}{\partial Y_D}\right)^2$$
$$-\frac{\pi}{C_{fD}} q_{fD}(X_{Di}, Y_{Di}, t_D) = \left(\frac{\pi C_{fD}^*}{C_{fD}}\right)\frac{\partial p_D}{\partial t_D} \tag{F.23}$$

where:

$$\zeta_{fx} = \frac{\delta_{fx}}{2-\delta_{fx}}$$

$$\zeta_{fy} = \frac{\delta_{fy}}{2-\delta_{fy}}$$

Eq. F.23 represents the flow equation in the nodes lying along the fracture. It is necessary to include a sink term at the wellbore node where the total fluid coming from the reservoir to the fracture and from the fracture to the well leaves is produced from the system. For the system given, the solution domain is taken as the complete reservoir domain, then q_w flow rate is considered. Then, Eq. F.23 becomes:

$$\delta_{fx}\frac{\partial^2 p_{fD}}{\partial X_D^2}+\delta_{fx}\zeta_{fx}\left(\frac{\partial p_{fD}}{\partial X_D}\right)^2+\delta_{fy}\frac{\partial^2 p_{fD}}{\partial Y_D^2}+\delta_{fy}\zeta_{fy}\left(\frac{\partial p_{fD}}{\partial Y_D}\right)^2$$
$$-\frac{\pi}{C_{fD}}q_{fD}(X_{Di},Y_{Di},t_D)+\frac{4\pi}{C_{fD}}q_{wD}(t_D)=\left(\frac{\pi C_{fD}^{*}}{C_{fD}}\right)\frac{\partial p_D}{\partial t_D}$$

Expressing the flow rate going from the formation to the fracture at each node in absolute value, the above equation becomes:

$$\delta_{fx}\frac{\partial^2 p_{fD}}{\partial X_D^2}+\delta_{fx}\zeta_{fx}\left(\frac{\partial p_{fD}}{\partial X_D}\right)^2+\delta_{fy}\frac{\partial^2 p_{fD}}{\partial Y_D^2}+\delta_{fy}\zeta_{fy}\left(\frac{\partial p_{fD}}{\partial Y_D}\right)^2$$
$$-\frac{\pi w_D}{C_{fD}\Delta X_{Di}\Delta Y_{Di}}q_{fD}(X_{Di},Y_{Di},t_D)+\frac{4\pi w_D}{C_{fD}\Delta X_{Dw}\Delta Y_{Dw}}q_{wD}(t_D)=\left(\frac{\pi C_{fD}^{*}}{C_{fD}}\right)\frac{\partial p_{fD}}{\partial t_D}$$

(F.24)